PROCEEDINGS OF THE ARMY SYMPOSIUM ON SOLID MECHANICS, 1974, HELD AT BASS RIVER, MASSACHUSETTS ON 10-12 SEPTEMBER 1974

THE ROLE OF MECHANICS IN DESIGN-STRUCTURAL JOINTS

ARMY MATERIALS AND MECHANICS RESEARCH CENTER

SEPTEMBER 1974

DISCLAIMER NOTICE

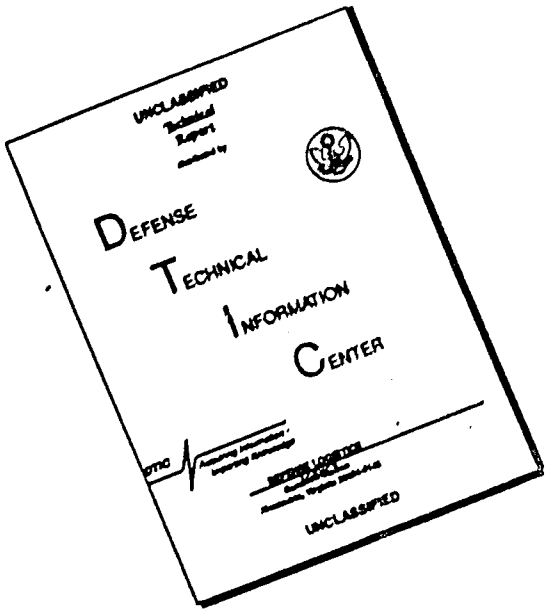

THIS DOCUMENT IS BEST QUALITY AVAILABLE. THE COPY FURNISHED TO DTIC CONTAINED A SIGNIFICANT NUMBER OF PAGES WHICH DO NOT REPRODUCE LEGIBLY.

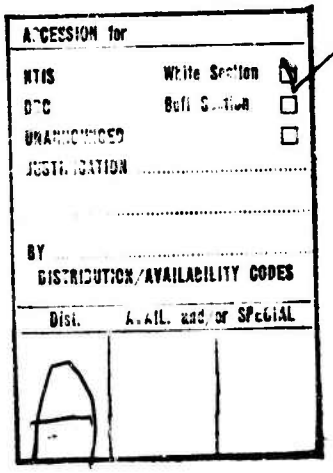

The findings in this report are not to be construed as an official Department of the Army position, unless so designated by other authorized documents.

Mention of any trade names or manufacturers in this report shall not be construed as advertising nor as an official indorsement or approval of such products or companies by the United States Government.

DISPOSITION INSTRUCTIONS

Destroy this report when it is no longer needed.
Do not return it to the originator.

REPORT DOCUMENTATION PAGE

READ INSTRUCTIONS BEFORE COMPLETING FORM

1. REPORT NUMBER: AMMRC MS 74-8	2. GOVT ACCESSION NO.
3. RECIPIENT'S CATALOG NUMBER: AD-786-543	
4. TITLE (and Subtitle): Proceedings of the Army Symposium on Solid Mechanics, 1974; The Role of Mechanics in Design - Structural Joints	5. TYPE OF REPORT & PERIOD COVERED: Final Report
6. PERFORMING ORG. REPORT NUMBER	
7. AUTHOR(s)	8. CONTRACT OR GRANT NUMBER(s)
9. PERFORMING ORGANIZATION NAME AND ADDRESS: Army Materials and Mechanics Research Center, Watertown, Massachusetts 02172, AMXMR-T	10. PROGRAM ELEMENT, PROJECT, TASK AREA & WORK UNIT NUMBERS
11. CONTROLLING OFFICE NAME AND ADDRESS: U. S. Army Materiel Command, Alexandria, Virginia 22304	12. REPORT DATE: September 1974
	13. NUMBER OF PAGES: 350
14. MONITORING AGENCY NAME & ADDRESS (if different from Controlling Office)	15. SECURITY CLASS. (of this report): Unclassified
	15a. DECLASSIFICATION/DOWNGRADING SCHEDULE

16. DISTRIBUTION STATEMENT (of this Report)

Approved for public release; distribution unlimited.

17. DISTRIBUTION STATEMENT (of the abstract entered in Block 20, if different from Report)

18. SUPPLEMENTARY NOTES

19. KEY WORDS (Continue on reverse side if necessary and identify by block number)

(See Reverse Side)

20. ABSTRACT (Continue on reverse side if necessary and identify by block number)

Proceedings of the Army Symposium on Solid Mechanics, 1974; The Role of Mechanics in Design - Structural Joints, held at Bass River (Cape Cod), Massachusetts, 10-12 September 1974.

Block No. 19

KEY WORDS

Adhesives	Fracture (mechanics)	Statistical analysis
Bonded joints	Joining	Stiffness
Composite Materials	Joints	Strain (mechanics)
Composite structures	Laminates	Stresses
Computerized simulation	Life (durability)	Stress concentrations
Cracking (fracturing)	Mathematical analysis	Structural mechanics
Deformation	Mathematical models	Structural properties
Elastic properties	Moire effects	Structural response
Failure	Optimization	Struts
Fastenings	Photoelasticity	Temperature
Fatigue (mechanics)	Plastic properties	Tolerances (mechanics)
Fibers	Predictions	Viscoelasticity
Filaments	Reliability	Vulnerability
Fittings	Shock (mechanics)	Welded joints

PREFACE

The Army Symposium on Solid Mechanics, 1974, was the fourth in a series of biennial meetings sponsored by the Technical Working Group (TWG) for Mechanics of Materials, one of nine TWG's of the U.S. Army Materiel Command Materials Advisory Group. The first such conference was held in 1968 at the Johns Hopkins University, Baltimore, Maryland, under the general theme of solid mechanics. The second meeting was held in 1970 at the U.S. Army Materials and Mechanics Research Center, Watertown, Massachusetts, under the theme "Lightweight Structures." The third symposium was held in 1972 at Ocean City, Maryland, on the theme "The Role of Mechanics in Design - Ballistic Problems." This 1974 symposium was held at Bass River (Cape Cod), Massachusetts, on the theme "The Role of Mechanics in Design - Structural Joints."

Participation in these symposia has been expanding with time. Starting with the 1972 meeting, papers have been solicited from in-house and contract researchers and designers for the Navy, Air Force and NASA, in addition to those for the Army. Beginning with this 1974 meeting, the Symposium Committee has been expanded and now includes representation from the Navy, Air Force, NASA and the U.S. Army Corps of Engineers. These expansions recognize that many mechanics research and/or design problems are not unique to a single service or government agency.

Essentially, these symposia are a vehicle for enhancing the responsiveness of the mechanics research efforts for the design of advanced military systems. They also facilitate communications and coordination between and among researchers and designers having common military theme interests whether they work for a government service or agency, industry, or at a university or research institute.

No endeavor of the magnitude of this 1974 symposium could have been successfully conducted without the enthusiastic cooperation and support of many individuals and groups. With fear of overlooking some whose contributions played a key role, it is nevertheless fitting to acknowledge:

Headquarters, U.S. Army Materiel Command and the Materials Advisory Group for their support and cooperation in this undertaking.

The many authors and participants and Session Chairmen who made this conference a success.

The reviewers from universities, industry and government organizations, for their diligence in carrying out a thankless task.

Dr. Alvin E. Gorum, Director of the U.S. Army Materials and Mechanics Research Center and Chairman of the U.S. Army Materiel Command Materials Advisory Group, who welcomed the participants at the meeting.

Professor Richard Hartenberg of Northwestern University who delivered the Keynote Address on "Jointing Through the Ages."

And finally the clerical staff of the Mechanics Research Laboratory and the Technical Reports Office of the Army Materials and Mechanics Research Center for their unflagging efforts in the preparation and printing of numerous symposium materials.

SYMPOSIUM COMMITTEE

R. SHEA, Chairman
E. M. LENOE, Vice Chairman
R. J. MORRISSEY, Executive Secretary
Army Materials and Mechanics Research Center

TECHNICAL PAPERS AND PROGRAM

E. M. LENOE, Chairman
Army Materials and Mechanics Research Center
W. H. BAER
Army Troop Service Command, Mobility Equipment R&D Center
J. I. BLUHM
Army Materials and Mechanics Research Center
E. N. CLARK
Army Armaments Command, Picatinny Arsenal
H. D. CURCHACK
Harry Diamond Laboratories
C. M. ELDRIDGE
Army Missile Command
J. FEROLI
Army Test & Evaluation Command, Aberdeen Proving Ground
G. L. FILBEY, JR.
Ballistic Research Laboratories, Aberdeen Proving Ground
R. FOYE [Representative of NASA]
Army Air Mobility Research and Development Laboratory, Langley Research Center
A. J. GUSTAFSON
Army Air Mobility Research and Development Laboratory, Eustis Directorate
D. J. HACKENBRACH
Army Tank-Automotive Command
G. W. FISCHER
Army Armaments Command, Rock Island Arsenal
J. J. HEALY [Representative of U.S. Army Corp. of Engineers]
Army Construction Engineering Research Laboratory
T. SIMKINS
Army Armaments Command, Watervliet Arsenal
G. E. MADDUX [Representative of U. S. Air Force]
Air Force Flight Dynamics Laboratory, Wright-Patterson Air Force Base
R. P. PAPIRNO
Army Materials and Mechanics Research Center
E. W. ROSS, JR.
Army Troop Support Command, Natick Laboratories
K. SACZALSKI [Representative of U. S. Navy]
Office of Naval Research
E. SAIBEL
Army Research Office
M. SCHWARTZ
Army Armaments Command, Frankford Arsenal

WORK IN PROGRESS SESSION

R. P. PAPIRNO, Chairman
Army Materials and Mechanics Research Center
G. E. MADDUX, Vice Chairman
Air Force Flight Dynamics Laboratory, Wright-Patterson Air Force Base

ARRANGEMENTS

S. VALENCIA, Chairman
Army Materials and Mechanics Research Center

CONTENTS

OPENING SESSION

SESSION I - BONDED JOINTS

SESSION II - WORK IN PROGRESS

This session was comprised of a series of brief presentations and discussions of current (but not necessarily complete) research relating to the theme of the symposium. Abstracts of these presentations were published under a separate cover from these proceedings.

SESSION III - FASTENERS-1

SESSION IV - FASTENERS-2

SESSION V - DESIGN APPLICATIONS

WELCOME

DR. ALVIN E. GORUM
Director, Army Materials and Mechanics Research Center
Chairman, Army Materiel Command Materials Advisory Group

It is a pleasure to welcome you all here today to open the Army Symposium on Solid Mechanics, 1974.

The Army Materials and Mechanics Research Center, under the Chairmanship of its Director, has the responsibility of operating the Materials Advisory Group (MAG) and its Technical Working Groups (TWG's).

The MAG functions directly under the Army Materiel Command (AMC) Deputy for Laboratories and concerns itself with matters of policy, management, and administration in connection with the Materials Research Program. It is composed of top echelon R&D representatives from each Subordinate Command and also of representatives from the Office of the Chief of Research and Development, the Office of the Surgeon General, and the Corps of Engineers.

Nominally functioning under the MAG are Technical Working Groups in Ceramics, Composites, Electronic Materials, Engineering Standardization, Mechanics of Materials, Metals, Organics, Materials Technology, and Test and Evaluation Methods. These groups are composed of technical people working at the bench and selected on the basis of their expertise in specific areas of the Materials and Mechanics Programs. One of the most important functions carried out by the TWG's is exchange of information.

The Mechanics of Materials Technical Working Group was created later than the others when it was noted that knowledge of the use of materials under complex loading, through fatigue, flow, wear and related phenomena were not adequately covered by the originally established TWG's. More recently, the area of effort assigned to this group was broadened to encompass not only Mechanics of Materials but also Structural Mechanics. It should be noted that although one of the last TWG's to be created, the Mechanics of Materials Technical Working Group has been the most active in relation to the "exchange of information" function of the Technical Working Groups.

This symposium is the fourth in a series of biennial meetings sponsored by the Mechanics of Materials Technical Working Group. The first such meeting was held in 1968 at The Johns Hopkins University, Baltimore, Maryland, under the general theme of solid mechanics. The second was held in 1970 at the Army Materials and Mechanics Research Center, Watertown, Massachusetts, under the theme "Lightweight Structures." The third was held in 1972 at Ocean City, Maryland under the theme "The Role of Mechanics in Design - Ballistic Problems." This meeting, of course, is being conducted under the theme "The Role of Mechanics in Design - Structural Joints."

Participation in these symposia has been expanding with time. Starting with the 1972 meeting, papers have been solicited from in-house and contract researchers and designers for the Navy, Air Force and NASA, in addition to those for the Army.

Beginning with this 1974 meeting, the Symposium Committee has been expanded and now includes representation from the Navy, Air Force, NASA and the U. S. Army Corps of Engineers. These expansions recognize that many mechanics research and/or design problems are not unique to a single service or government agency.

The object of these symposia is to improve the effectiveness of mechanics research for the design of advanced military systems. These meetings also facilitate communications and coordination between and among Army, Navy and Air Force researchers and designers having common military theme interests. The vis a vis exposure of the critical needs of designers with the capabilities of researchers provides for an earlier recogniation of potential technical barriers and motivates a sense of commonality of purpose -- vital for effective research and development.

KEYNOTE ADDRESS: JOINTING THROUGH THE AGES

RICHARD S. HARTENBERG
Professor of Mechanical Engineering
The Technological Institute
Northwestern University
Evanston, Illinois

ABSTRACT

Somewhere in the Old Stone Age the ancestral structural joint was devised by lashing a stone to a stick: two parts were united to form a single entity that may have been a hammer, an ax or an adz. The joint characteristic of force transmission across the interface between two parts had been materialized with the introduction of a third element, the fastener, in this case the lashing. With time, a great variety of fasteners would be contrived.

The advent of metal tools allowed elaborate joints in furniture, chariot wheels, and boats in even the timber-poor lands of antiquity, skills that would be greatly extended by later craftsmen in the forested areas across the Mediterranean Sea. The ancient practice of building hulls of boats and ships as shells from planks joined by sewing, dovetails, tenons or clinch nails, with internal structural reinforcing added later, would continue into Viking time. Man of the New Stone Age used the timber from his agricultural land-clearance projects for large structural frameworks of community housing. Massive roof-framing topping masonry walls came with Greek and Roman times, where heavy presses for oil and grape were also introduced. Machinery posing often unique structural problems accompanied the substantial powers derived from water wheels and windmills, themselves sometimes an impressive of collection of joints. With further industrialization, vats formed from riveted plates became boilers in the eighteenth century, and steam-driven mills would begin to supply iron plates and structural shapes for rivet-connected bridges and ships. The heavy bridge-loadings due to railway trains led, after 1840, to extensive tests on the strength of riveted joints, prompted the first experiments on fatigue of metals, stimulated analysis giving an understanding of horizontal shear in beams allowing rational spacing of rivets in built-up members, and created an awareness of web-crippling in thin-wall elements.

SESSION I - BONDED JOINTS

Chairman: R. Foye
Aerospace Technologist
Army Air Mobility Research Laboratory

"FATIGUE RESPONSE OF ANISOTROPIC ADHEREND BONDED JOINTS"

W. JAMES RENTON
Research Associate

J. R. VINSON
Professor and Chairman
Department of Mechanical and Aerospace Engineering
University of Delaware
Newark, Delaware

ABSTRACT

An extensive series of fatigue tests using a ductile adhesive, two different anisotropic adherend materials, subjected to constant amplitude and two-block, repeated spectrum loadings have been conducted. Results show the proportional limit stress of the adhesive to be an important fatigue parameter as is the ductility of the adhesive. A two parameter fatigue-life theory is advanced and an increase in life of a specimen is shown for certain two-block loading spectrums. The results are thought to be dependent on the increased fracture toughness of ductile adhesives.

INTRODUCTION

The application of advanced reinforced composite materials in aerospace structures during the remainder of this century is widely predicted. The joining of structural components by adhesive bonding is extremely desirable, because both bolting and riveting result in the cutting of fibers as well as the introduction of stress concentrations, of a more severe magnitude than for a bonded joint.

Because in aerospace structures dynamic loads are always present, it is absolutely essential that the fatigue behavior of bonded joints between composite material components be better understood, in order to have available design principles and rationale to take advantage of the desirable characteristics of composite materials.

To date the few isolated experimental studies of composite-composite or composite-metal adherend bonded joints have been conducted under static and/or constant amplitude cyclic loading, and no generally accepted cumulative damage theories have been evolved.

The present research is a systematic, analytical and experimental program of study concentrating on those parameters considered to be the most influential on the fatigue life of an adhesive bonded single lap joint. The objectives of the program are to better understand the reasons why certain parameters have such a large influence on the structural integrity of the joint. As a result it is hoped that considerable insight may be gained into improving the fatigue methodology of bonded joints. The experimental fatigue test portion of the program is reported on herein.

Fatigue failure involves the cumulative effect of small scale events taking place over numerous cycles of repeated loading. The fatigue damage process involves crack initiation, crack propagation to a critical crack size and finally, the unstable rupture due to peak loads exceeding the ultimate strength of the uncracked section.

Crack initiation in the joint of a real structure is begun by various types of flaws in the adhesive (i.e. bubbles, unbonded areas, foreign particles). Since prevention of such flaws is impossible, to maximize the fatigue life of a bonded joint, one looks for certain characteristics which minimize the crack growth rate. Ripling [1] states that this is best attained by an adhesive which possesses a high fracture toughness parameter. Landgraf [2] further states that such resistance is best attained by a material which has a high fracture strength coupled with a high fracture ductility.

Further complicating the study of fatigue in adhesive joints is the accurate determination of the stress concentration in tension and shear near to and at the ends of the overlap (Figure 1). These peak stresses are primarily a function of the elastic moduli of the adhesive and the adherends and the overlap length. Moreover, due to the complex stress field near the ends of the overlap, the resistance to crack growth in both tension and shear must be considered. Ripling [1] has shown for epoxies however, that the tensile fracture toughness is the critical crack growth resistance parameter.

The following parameters, deemed to be the most important, were selected for study: overlap length, adhesive thickness, orientation of the laminae of the laminated adherends (particularly the lamina immediately adjacent to the adhesive) and adherend material system. Additionally, the effect on the fatigue life of the mean value of the fatigue load causing maximum stresses above or below the shear proportional limit of the adhesive material, and the influence of a two-block repeated loading pattern on the fatigue life of the joint was studied. The determination of stresses in the test specimens is made by closed form analytical method [3] developed earlier in the program.

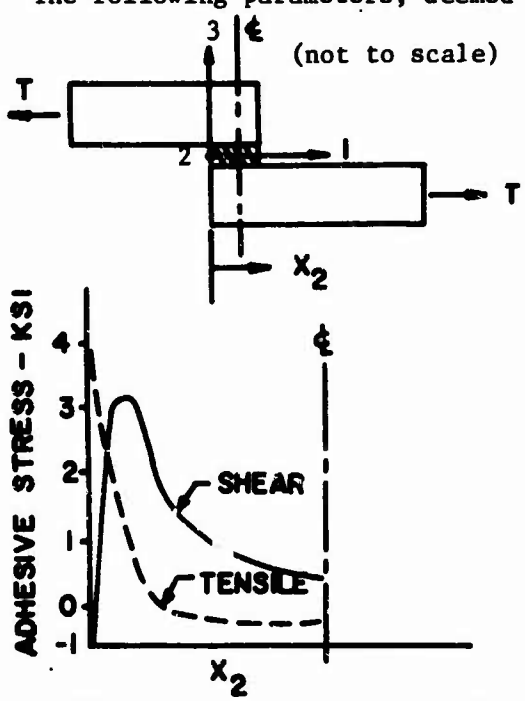

FIGURE (1) A Typical Stress Distribution In The Adhesive Of A Single-Lap Joint.

The initial phase of the test program involved specimens composed of 1002-S glass pre-preg tape adherends. A second series of screening tests using Kevlar-49 pre-preg material is also reported on herein. In both instances Hysol EA951 nylon-epoxy adhesive was

selected for its low moduli and high ductility coupled with it's high ultimate tensile and shear allowables. The specimens are nine inches in length and one inch wide. The adherends tested to date have been identical, each being 0.063 inches thick. The ultimate strength of the 1002-S glass in the filament direction was tested to be 230,000 psi, that of the Kevlar was 200,000 psi. Lap lengths are 0.30 and 0.60 inches, while adhesive thicknesses are 2.5 and 10 mils. Adherend ply orientations are all 0° and 45°/0°/-45°/0° repeated patterns. (Since there are seven plys in the adherend, it is symmetric with respect to the adherend midsurface). The ratio of lap length to adherend thickness varied from 4.3 to 8.7. The temperature for all tests was approximately 70°F and the relative humidity during testing varied from 8-55 percent. The fatigue stress ratio for all constant amplitude tests is +.10 (tension).

Static Test Results:

To discern the joint efficiency of the fatigue test items all specimens were tested to obtain their ultimate load capability. Table (1) summarizes the static ultimate strength test results. An adhesive failure was expected. The relatively low values attained by the Kevlar-49 specimens is attributed to the "fuzzy" nature of the failure surface. Initial evaluation of these surfaces with an electron-microscope shows that the fibers adjacent to the adhesive broke down. Possibly this was caused by a too lean fiber resin mixture, or could signal the need to study the adequacy of present day surface preparation techniques.

SPECIMEN	ULTIMATE SHEAR STRESS*	TYPE OF FAILURE
1002-S Glass		
.30 inch overlap (a)	5400.	adhesive
.60 inch overlap (a)	4800.	adhesive
.30 inch overlap (b)	3800.	adhesive
.60 inch overlap (b)	3500.	adhesive
Kevlar-49		
.30 inch overlap (a)	4200. (78% of glass specimens)	primarily in fibers adjacent to adhesive
.60 inch overlap (a)	3300. (69% of glass specimens)	primarily in fibers adjacent to adhesive
.60 inch overlap (b)	2100. (60% of glass specimens)	ply adjacent to adhesive

* Strain rate = .05 cm/min.
a All 0° plys
b 45°/0°/-45°/0° plys

TABLE I Summary of Single Lap Joint Ultimate Test Results

Fatigue Test Results:

Fatigue runout (i.e. the number of cycles at which the test is stopped) for the tests was defined to be 4.0×10^6 cycles. There have been a total of 124 lap joint fatigue tests to date. Fifty-two 0° and fifty-one $45^\circ/0^\circ/-45^\circ/0^\circ$ ply orientation specimens were run. Additionally, the results of nineteen lap joint fatigue tests using Kevlar-49 adherend material are included.

A. Constant Amplitude Test Results:

The objectives of the tests were three fold: (1) to study the influence of certain geometric variations of the lap joint configuration on the fatigue life of the joint; (2) to discern the relative importance of the shear proportional limit stress on the fatigue behavior of the single lap joint; (3) to introduce specific introductory comments on the type of adhesive failure surfaces observed.

The test results are summarized by the solid lines in Figures (6-10). The effect of lengthening the overlap length was to increase the joint load carrying capability for a fatigue life of 4×10^6 cycles. This was deemed logical as an increased overlap length reduces the stress concentrations in the adhesive for a given load. This was verified using the closed form Analysis [3] program. A maximum design load corresponding to 450 lbs. (20% of ultimate) was attained for a lap length of 0.30", and 600 lbs. (26%) for a lap length of 0.60", independent of the ply orientation. Moreover, while no distinct adhesive thickness effect was evident, a 20 to 40% penalty in load level associated with runout for the angle-ply construction was observed.

One of the primary objectives of the initial test program was to determine the influence of the shear proportional limit stress of the adhesive on the fatigue life of the joint.

Based on the criteria that fatigue runout was 4×10^6 cycles, runout was attained for the 1002-S glass and Kevlar-49 specimens as outlined in Table (2). The closed form analysis [3] which accounts for transverse shear, normal strain and anisotropic material properties was then used to determine the maximum shear stress in the joint corresponding to the mean load at runout. These peak stresses are compared with the shear proportional limit stresses of the adhesive from Reference 3. The results are summarized in Table 2 and given in detail in Reference 8. The correlation is considered to be good. In essence, it strongly indicates that if the peak shear stress in the adhesive at mean load remains below the shear proportional limit stress of the adhesive, a marked increase in fatigue life of the joint can be achieved, assuming an adhesive failure is the critical mode of failure in the construction. In this series of tests, in which 100 lb. load increments were used, an increase in life of the joint of 5 times or more was achieved. Moreover, for those specimens in which runout was attained, anywhere from 50 to 99 percent of the ultimate static strength of the joint remained, determined through statically testing these specimens to failure subsequent to the fatigue tests. This in turn indicates that a much longer life for those

parts which achieved runout could have been attained if the fatigue testing had continued past the 4×10^6 cycles.

TABLE II Comparison of Peak Shear Stress Values in the Adhesive

SPECIMEN	MEAN LOAD AT RUNOUT (LB)*	MAX. SHEAR PROPORT. LIMIT STRESS (PSI)**	MAX. SHEAR STRESS FOR MEAN LOAD AT RUNOUT (PSI)***
1002-S Glass			
.30 inch overlap (a)	247.	1015.	930.
.36 inch overlap (a)	275.	999.	1017.
.62 inch overlap (a)	330.	600.	731.
.30 inch overlap (b)	165.	925.	675.
.60 inch overlap (b)	275.	480.	428.
Kevlar-49			
.30 inch overlap (d)	275.	1100. (c)	972.
.60 inch overlap (d)	330.	600. (c)	610.
.60 inch overlap (b)	275.	550. (c)	524.

* Mean load varied in 100 lb. increments
** From shear test results, Reference [3]
*** From closed form Analysis, Reference [3]
a All 0° adherends-initial failure was in adhesive
b 45°/0°/-45°/0° adherends-initial failure in 45° ply adjacent to adhesive
c Estimated
d Initial failure was in fibers adjacent to adhesive

It is hypothesized that this significant increase in fatigue life associated with stressing only below the proportional limit stress of the adhesive at mean load is primarily due to the retention of a primarily elastic stress field in the crack region which experiences very little plastic flow. This in turn usually means a slower propagation of a crack, resulting in a longer life of the part.

The 1002-S glass, all 0° specimens which exhibited failure prior to four million cycles, exhibited an adhesive-cohesive failure as shown in Figure 2. Typically, the failed surfaces displayed distinct bands on their outer edges. It is assumed that the smooth nature of the outer bands was due to the minute motion of the adhesive after cracking was initiated. Further, it is believed the cracks initiated from the ends of the overlap, moving inward until the remaining net section of the adhesive, which was uncracked, could not withstand the magnitude of the maximum load from a static point of view. Such growth of the bands is believed realistic as the peak tensile stresses occur at the end of the overlap supplying a tension type capability for crack growth. This form of crack growth has been substantiated by Jemian [4-6].

The general appearance of the 45°/0°/-45°/0° fatigue failed surfaces differs from the all 0° specimens and its static test counterpart. Figure 3 displays the fatigue and static failure surfaces of a typical specimen. The static failure mode is seen to be in the adhesive. The fatigue failure mode is believed to be the result of resin degradation

in the 45 degree ply adjacent to the adhesive. Breaking of the fibers normal to their direction is evident. This is known to be the result of high inter-laminar shear and normal stresses in the resin. This has been documented in References (3,8) and summarized in Table (3) using the closed form analysis method developed earlier in this program. The all 0^{o} Kevlar specimens exhibited a generally "fuzzy" failure surface (Figure 4). This was thought to be the result of a premature failure due to a lean resin-fiber mixture. The $45^{o}/0^{o}/-45^{o}/0^{o}$ specimens failed in a manner analogous to that of Figure (3).

All 0^{o} 1002-S

Static Failure Surface | Adherends Fatigue Failure Surface

FIGURE (2)

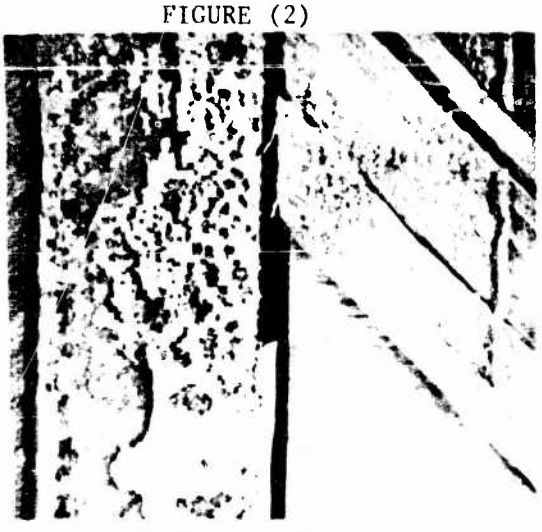

$45^{o}/0^{o}/-45^{o}/0^{o}$ Glass

Static Failure Surface | Adherends Fatigue Failure Surface

FIGURE (3)

Typical All 0^{o} Kevlar-49 Adherend Static and Fatigue Failure Surface

FIGURE (4)

Results of the constant amplitude fatigue tests using the Kevlar-49 specimens show in Figures 6, 8 and 10, that these specimens exhibited a superior ability to resist fatigue (symbol -●).

This is expected and due to the ability of a stiffer adherend material to reduce the peak shear and tensile stresses as shown in Figure (5). These results are from the closed form routine developed earlier in this program. Moreover, a reduction in peak tensile stresses results in a slowing down of the critical crack growth mode. This should lead to a longer life joint for a given loading. It does. This would suggest that use of Kevlar material in single lap bonded joints should result in a superior fatigue joint.

B. Two-Block Loading Fatigue Test Results:

Screening tests were run involving a two-block repeated spectrum

TABLE (3) Comparison of the stresses in a 0^o and 45^o Ply Adjacent to the Adhesive** (Load held constant).

SPECIMEN*	τ_{12} (PSI)	σ_2 (PSI)	σ_3 (PSI)	TYPE FAILURE
All 0^o Adherend	0.	3123.	500.	Adhesive
$45^o/0^o/-45^o/0^o$	3505.	9515.	654.	45^o ply adjacent to adhesive

* The specimens were identical except for the ply orientation - tensile allowable 1002-S Resin 6100 PSI.

** Stresses are at .005" from loaded edge of overlap. Stresses refer to axes defined in Figure (1).

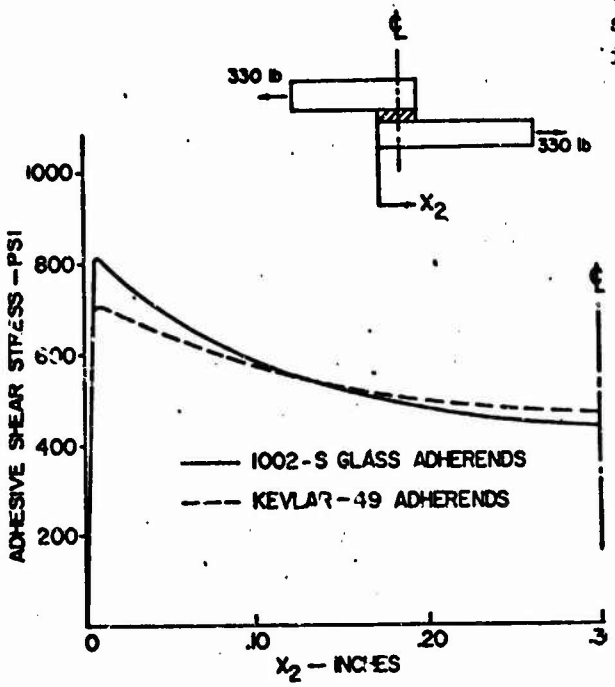

A Comparison of Adhesive Stresses with Fiberglass and Kevlar-49 Adherends. (Specimens are identical except for material properties)

FIGURE (5)

loading. The tests were run for the all 0^o and $45^o/0^o/-45^o/0^o$ adherends of 1002-S glass and Kevlar-49. The loading was changed every 50,000 cycles. Also, the loading sequence (i.e. low-high loading vs. high-low loading) was investigated. One series of tests used the fatigue runout load (mean + alternating load) used in the previous section as the low load block (S.R.= +.10) and varied only the mean load to obtain the high load block (stress ratio = +.38). Another series of tests varied only the alternating load. The stress ratio was again varied between +.38 to +.10 from the previous high mean load block. The load combinations are specified in Table (4).

One of the objectives of this section was to test the hypothesis that the fatigue life of an adhesive (resin) system under a two-block repeated loading spectrum can be described by a two parameter expression [7] composed of A) the number of cycles at the high stress level (α), B) a stress interaction factor (R^{α}). R is the ratio of fracture toughness at the lower load level vs. the higher load level and is function of (α). It is determined

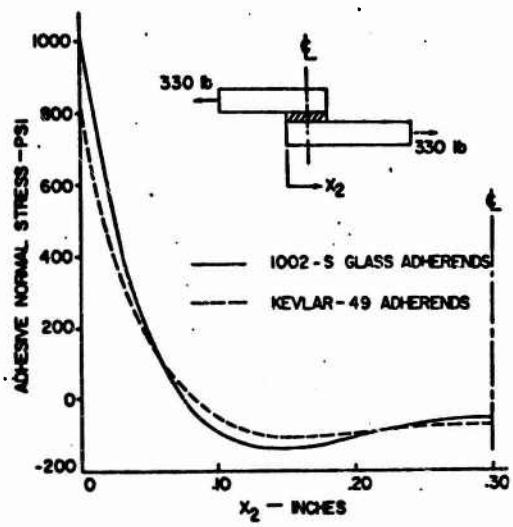

experimentally, (a) is a constant. The final expression for life is:

$$N_g = \frac{N_1}{\alpha + R^{\frac{1}{2}}(1-\alpha)} \qquad (1)$$

where:

N_g = the fatigue life of the test piece under the complex load history.

N_1 = fatigue life of the test piece at the maximum load level (mean + alternating) of the constant amplitude tests for S.R. = +.10-Fig.6-10.

The hypothesis assumes that damage is done at both load levels, but that more damage is done at the higher load level. Moreover, it is assumed that for the series of tests in which only mean load was varied the low load level, being approximately the proportional limit runout load, initiated no damage. Thus, only the high load level initiates the damage.

The 1002-S results to date are presented in Figures (6 to 10) and in Table (4). The data shows that whether the specimens failed in the adhesive or in the resin, that when looking at the mean load variation effect only, the all 0° and $45^\circ/0^\circ/-45^\circ/0^\circ$ adherend specimens showed an increase in life under the two block loading spectrum vs. the constant amplitude one. This increase in life is evident whether one looks at the total number of cycles to failure (symbols o, ▲) vs. the maximum load as a per cent of static load or considers only the number of cycles run at the high stress level (symbols ▫, ■) vs. the maximum load as a per cent of static load. Both are plotted on

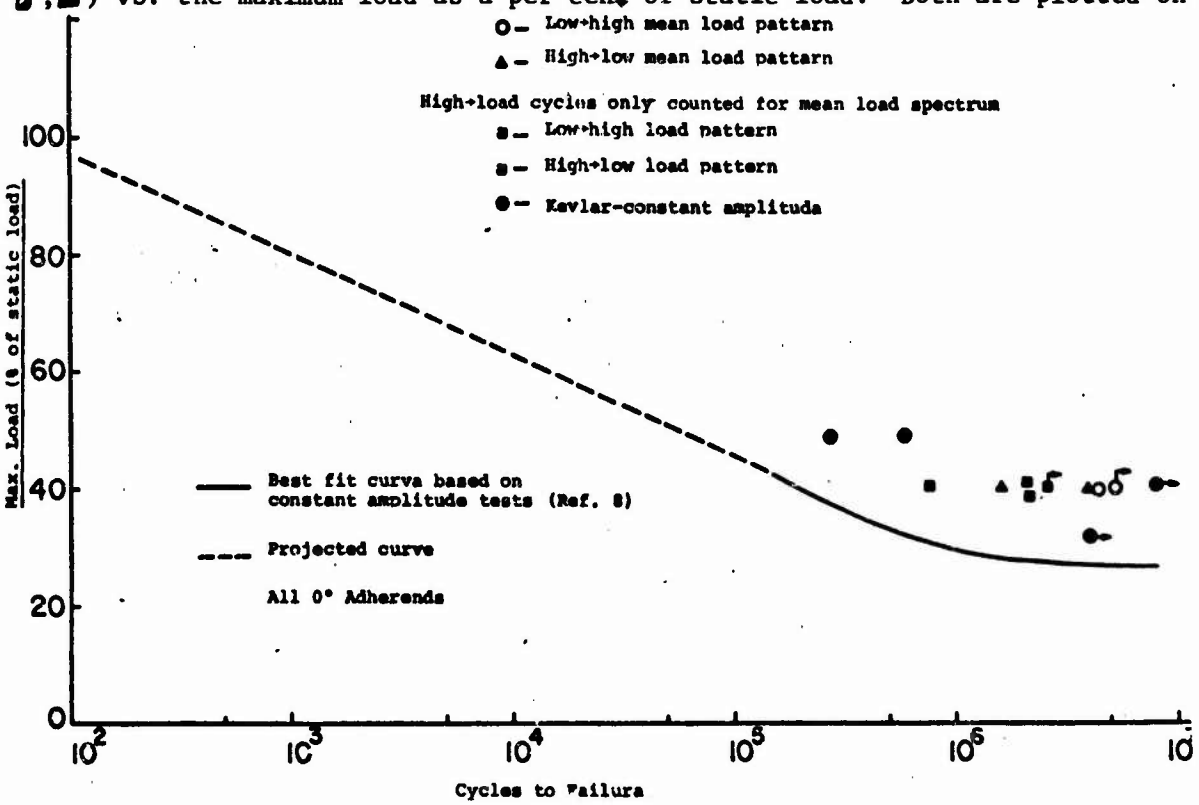

FIGURE (6) Fatigue Test Results of .30° Overlap Glass Specimens.

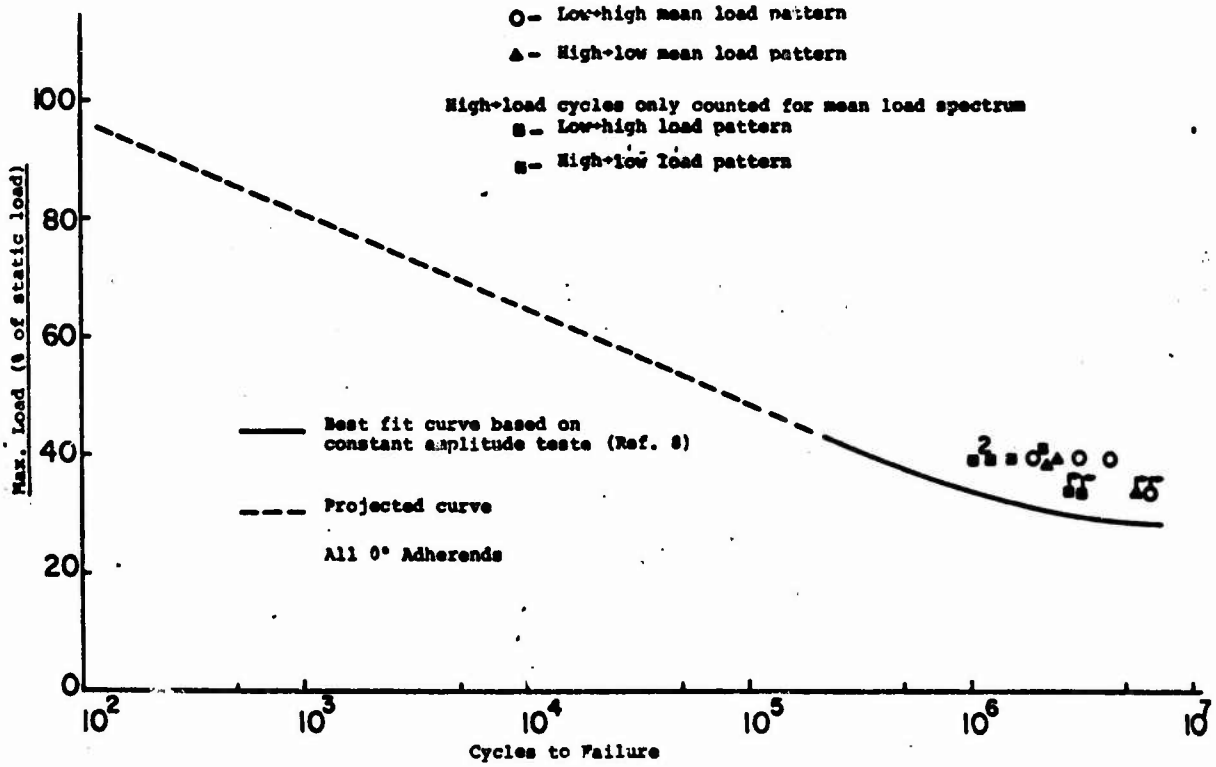

FIGURE (7) Fatigue Test Results of .36" Overlap Glass Specimens.

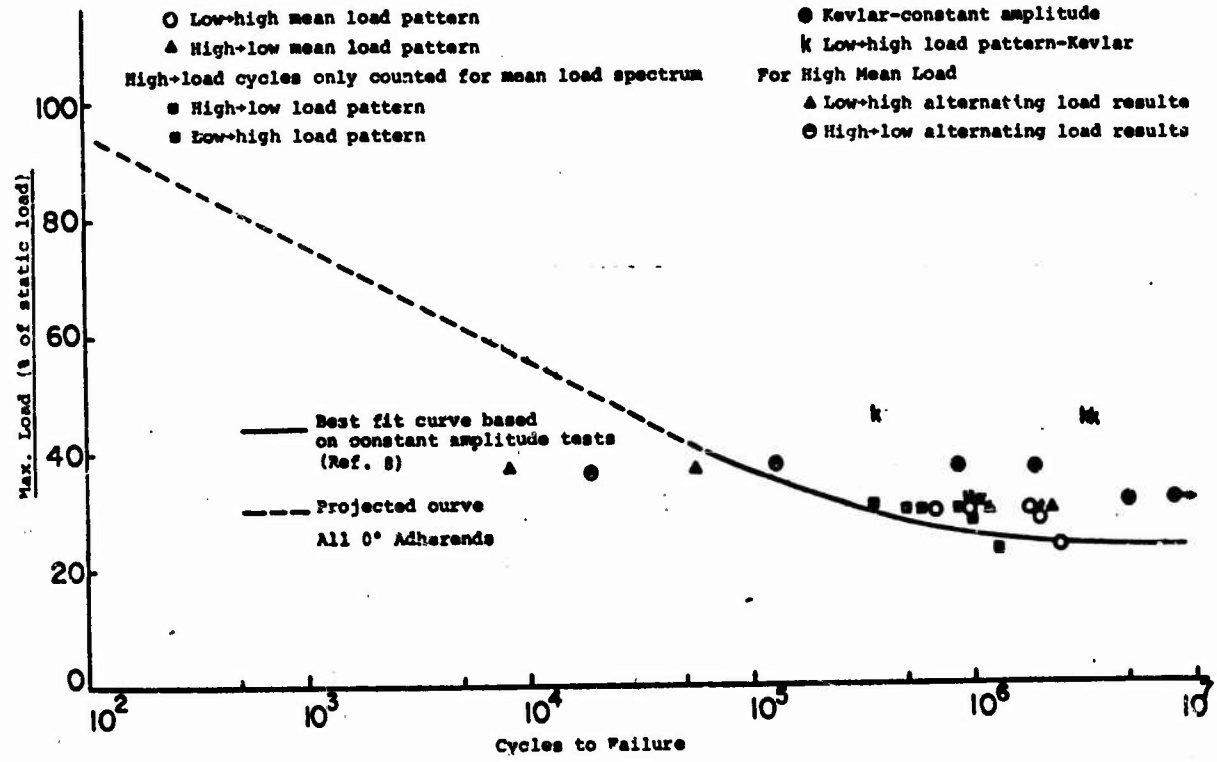

FIGURE (8) Fatigue Test Results of .60" Overlap Glass Specimens.

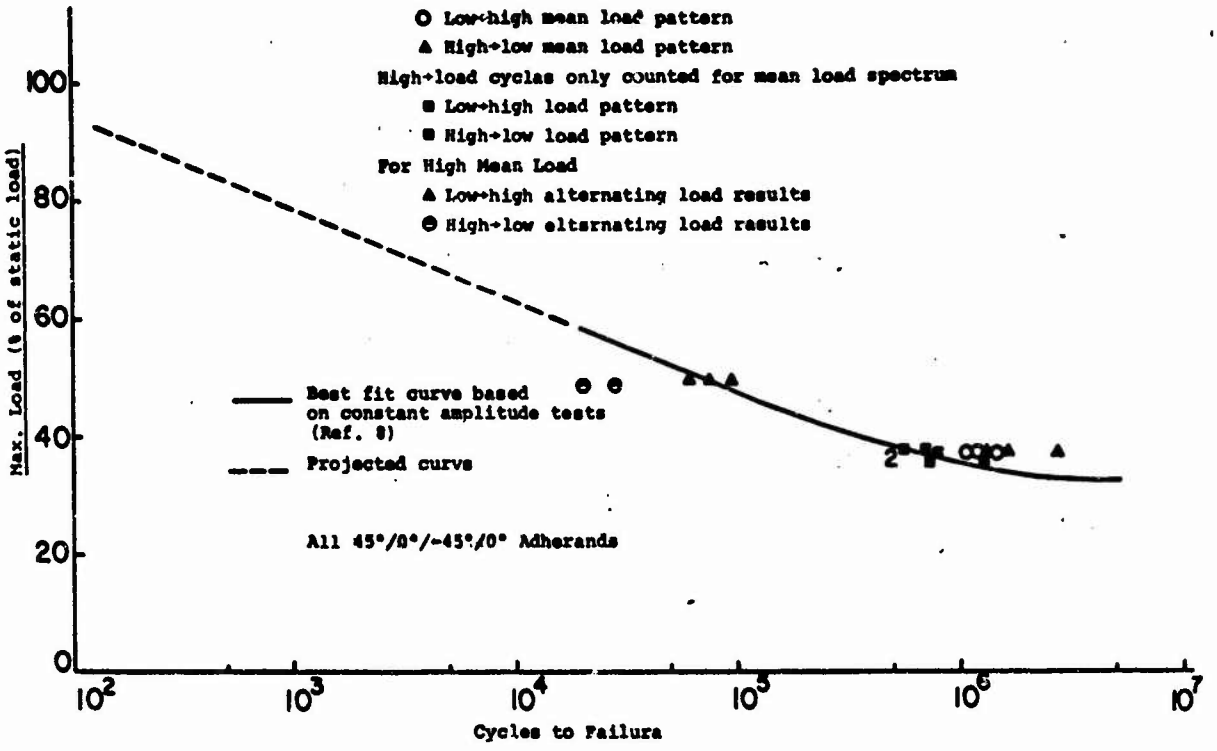

FIGURE (9) Fatigue Test Results of .30° Overlap Glass Specimens.

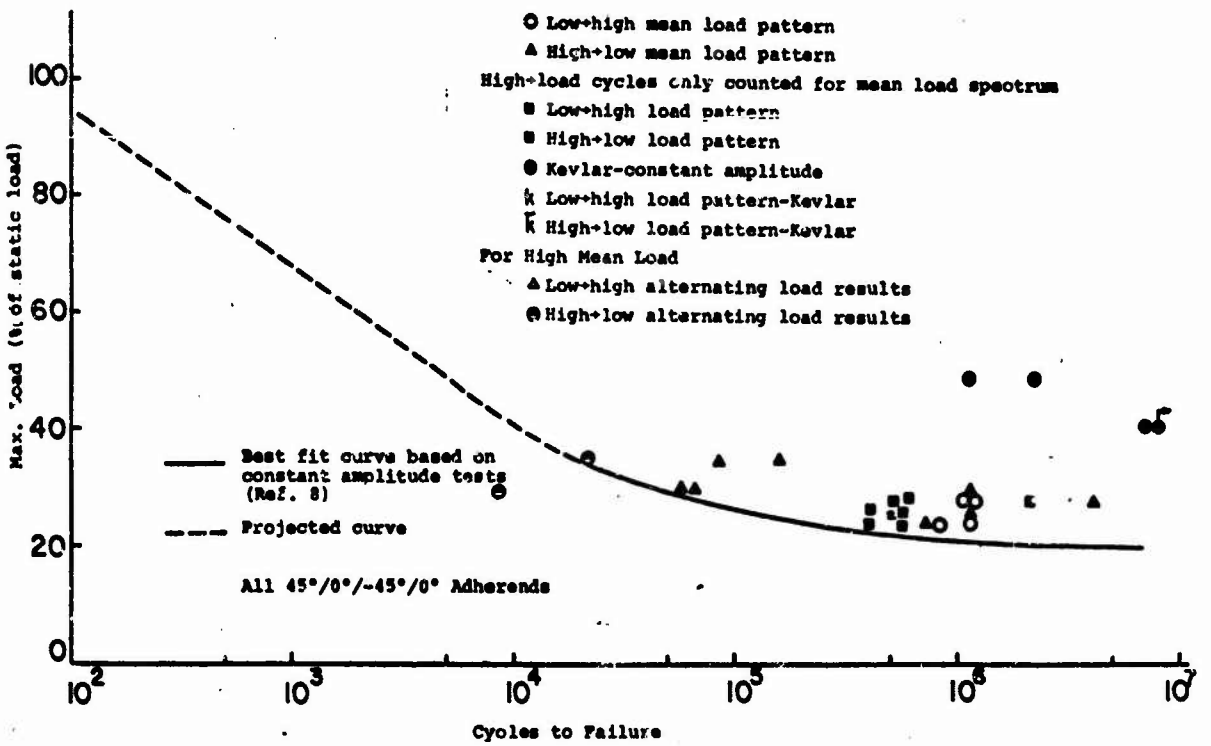

FIGURE (10) Fatigue Test Results of .60° Overlap Glass Specimens.

TABLE (4) - Summary of Two-block Loading Fatigue Tests

Specimen	Load and Sequence	Max. Load As % (ult.)	Stress Ratio	% Life @ High Stress = α	N_g,exp x 10^6	* N_1 = cycles to Failure @ High Stress x 10^6	R%	** N_g, theo. x 10^6	N_g,exp / N_g,theo	Type of Failure
.30 inch overlap(a) (Figure 6 Data)	247±202 500±202	40.	+.10→ +.425	.50	5.10	.190	-.925	2.71	1.88	Runout
" "	"	"	"	.497	4.23	"	-.845	2.26	1.87	Adhesive failure
" "	500±202 247±202	"	+.425 +.10	.50	4.11	"	-.907	2.71	1.51	" "
" "	"	"	"	.508	1.53	"	-.78	2.26	.67	" "
						Avg. =	-.86			
.36 inch overlap(a) (Figure 7 Data)	275±225 385±225	33.3	+.10→ +.26	.498	6.12	1.15	-.614	5.83	1.05	" "
" "	385±225 275±225	"	+.26→ +.10	.50	5.69	1.15	-.59	5.83	.975	" "
						Avg. =	-.60			
" "	275±225 500±225	39.5	+.10→ +.38	.503	1.91	.380	-.61	2.48	.77	Adhesive failure
" "	"	"	"	.497	3.01	"	-.737	2.69	1.11	" "
" "	"	"	"	.495	4.16	"	-.80	2.69	1.54	" "
" "	500±225 275±225	"	+.38→ +.10	.508	2.37	"	-.703	2.36	1.00	" "
" "	"	"	"	.502	2.29	"	-.67	2.48	.923	" "
						Avg. =	-.704			
.60 inch overlap(a) (Figure 8 Data)	330±270 600±270	29.5	+.10→ +.38	.499	2.49	.340	-.72	1.65	1.50	" "
" "	"	"	"	.490	1.84	.340	-.60	1.78	1.03	" "
" "	"	"	"	.500	.997	"	-.31	1.63	.61	" "
" "	"	"	"	.497	2.11	"	-.66	1.68	1.25	" "
" "	600±270 330±270	29.5	+.38→ +.10	.501	1.90	.340	-.645	1.63	1.16	" "
" "	"	"	"	.511	2.05	"	-.704	1.51	1.35	" "
" "	"	"	"	.52	1.15	"	-.46	1.42	.81	" "
						Avg. =	-.585			
" " a	600±270 600±490	37.	+.10→ +.38	.0196	.051	.080	1.58	.052	.99	Cohesive Failure
" " "	"	"	"	.074	.054	"	1.52	.053	1.01	" "
						Avg. =	1.55			
" " "	600±490 600±270	"	+.38→ +.10	1.00	.018	.080	-	-	-	Adhesive Failure
" " "	"	"	"	.585	.121	"	+.19	-	-	" "
.30 inch overlap(b) (Figure 9 Data)	165±135 300±135	36.6	+.10→ +.38	.494	1.12	.700	.27	1.45	.77	Ply adj. to adhesive
" "	"	"	"	.497	1.41	"	.002	1.44	.98	" "
" "	"	"	"	.499	1.19	"	.17	1.44	.83	" "
" "	300±135 165±135	"	+.38→ +.10	.502	1.41	.700	.009	1.43	.99	" "
" "	"	"	"	.510	1.53	"	-.10	1.40	1.09	" "
" "	"	"	"	.502	2.71	"	-.49	1.43	1.89	" "
						Avg. =	-.023			

TABLE (4) - Summary of Two-Block Loading Fatigue Tests

Specimen	Load and Sequence	Max. Load As % (ult.)	Stress	% Life @ High Stress = α	N_g,exp x 10^6	*N_1 = cycles to Failure @ High Stress x 10^6	R%	**N_g, theo. x 10^6	$\frac{N_g,exp}{N_g,theo}$	Type of Failure
.30 inch overlap(b) (Figure 9 Data) A	300+135 300±245	49.	+.38→ +.10	.315	.073	.075	1.06	.075	1.0	Ply adj. to adhesive
" " "	"	"	"	.18	.061	"	1.29	.075	.81	" "
" " "	"	"	"	.463	.093	"	.65	.075	1.24	" "
						Avg. =	1.00			
" " "	300±245 300±135	"	+.10→ +.38	1.0	.018	-	-	-	-	" "
" " "	"	"	"	1.0	.025	-	-	-	-	" "
.60 inch overlap(b) (Figure 10 Data)	275±225 500±225	23.7	+.10→ +.38	.486	.823	.200	-.472	1.04	.79	" "
" "	"	"	"	.499	1.10	"	-.636	.94	1.17	" "
" "	500±225 275±225	"	+.38→ +.10	.525	.756	"	-.547	.79	.96	" "
" "	"	"	"	.502	1.105	"	-.636	.921	1.19	" "
						Avg. =	-.572			
" " A	500±225 500±410	29.7	"	.152	.059	.045	.72	-	-	" "
" " "	"	"	"	.242	.066	"	.58	-	-	" "
" " "	500±410 500±225	"	+.10→ +.38	1.00	.009	.045	-	-	-	" "
" "	220±180 400±180	27.4	"	.497	1.11	.072	-.86	1.56	.71	" "
" "	"	"	"	.499	1.19	"	-.88	1.44	.83	" "
" "	400±180 220±180	-	+.38→ +.10	.519	1.16	"	-.95	1.16	.998	" "
						Avg. =	-.896			
" "	"	"	"	.507	4.13	.072	-	-	-	" "
" " A	400±180 400±325	34.2	+.38→ +.10	.384	.081	.020	-.225	-	-	" "
" " A	"	"	"	.370	.159	"	-.39	-	-	" "
" " A	400±325 400±180	"	+.10→ +.38	1.00	.021	"	-	-	-	" "

A - Varied Alternating Load Only

EA951 Nylon-Epoxy Adhesive

1002-S Material

** - Based on Average R for each group

a - All 0° Adherends

b - 45°/0°/-45°/0° Adherends

Figures (6 to 10). This improvement in life is further substantiated in Table (4) where the stress inter-action factor, if negative, implies an improvement in life.

The results of the second loading sequence, whereby only the alternating load was varied is also given in Figures (8 to 10) (symbols Δ, ⊖) and Table (4). They show a reduction in life especially for the high-low load pattern as one would expect as the mean stress is much above the proportional limit stress. Notice in this case that the stress interaction factor ($R^{\sim}$) is generally positive, indicating damage.

In all cases for all loading sequences, the specimens failed in a manner analogous to the constant amplitude results and no ordering effects as pertains to the loading sequence was visible. Moreover, the results of the two parameter life prediction process (Table 4) for the 1002-S glass data looks promising, yet much additional testing is needed to justify its use. Moreover, it could be extended possibly to a multiple amplitude loading spectrum by determining $R^{\sim}$ for various mean load levels and overlap lengths. In this instance the mean load effect was not accounted for.

The Kevlar-49 two-block loading screening tests (symbols K,$\bar{K}$) show results much improved vs. those for the 1002-S glass adherends in Figures (8 and 10). One would expect such an improvement in fatigue life vs. the glass adherend specimens for as was shown earlier (Figure 5) a more favorable (i.e. lower) peak stress condition exists in the stiffer Kevlar-49 joints. This in effect retards crack growth, improving the fatigue life of the joint for a specific load level. Insufficient data exists for the Kevlar specimens, in order to evaluate the two parameter damage theory.

DISCUSSION

It would now seem reasonable to attempt an explanation of how a crack propagates in a ductile adhesive system. Based on the closed form analysis of Reference [3], one can accurately determine the peak tensile and shear stresses for a given mean load. Knowing these, one knows when the proportional limit stress (determined in Reference [3]) of the adhesive is surpassed and damage has begun. For a ductile adhesive as EA951 is, one assumes it to ultimately propagate the crack when the material adjacent to the crack tip reaches its plastic strain limit. Moreover, Reference [1] states that the critical crack propagation mode of the adhesive is in tension (i.e. for epoxies) and that in general, a ductile adhesive has a higher fracture toughness than a brittle one. Therefore, it is hypothesised that the improvement in life noticed for the series of tests reported on herein,

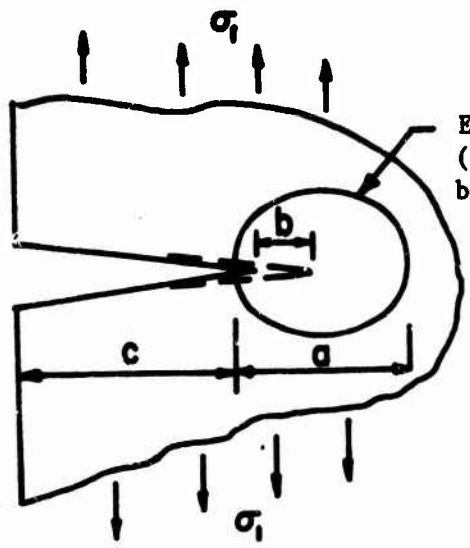

(A) Stress Region at Crack Tip Due To High Mean Stress (σ_1).

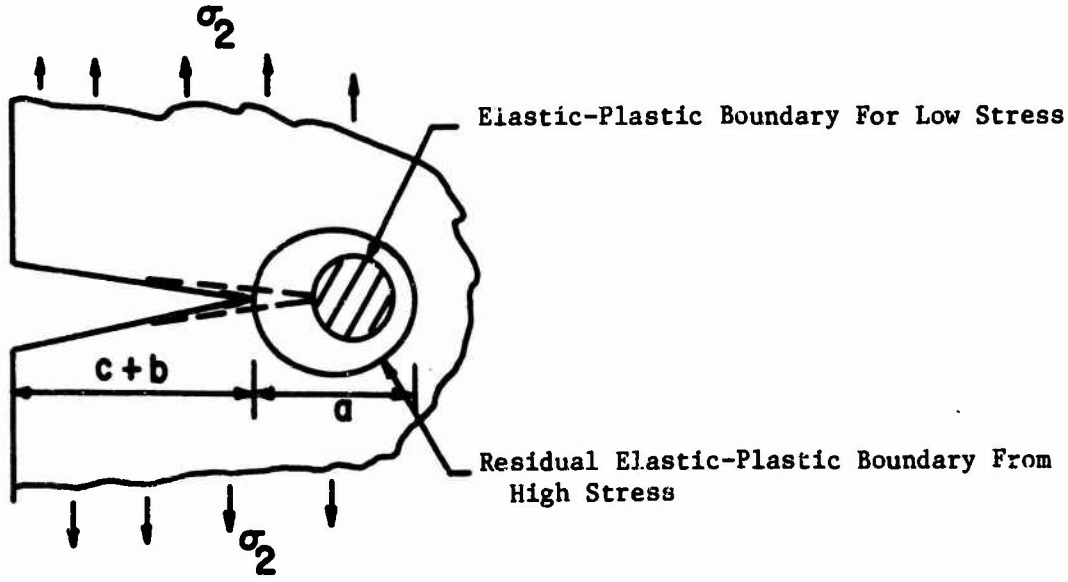

(B) Stress Region At Crack Tip Due to Low Mean Stress (σ_2).

FIGURE (11) Fatigue Crack Growth Process.

whereby only the mean load was varied is as follows. Referring to Figure (11a), a crack is formed at a flaw in the adhesive in the region of the high stress concentrations and at the high load level. This in turn forms a plastic zone ahead of the crack of length (a). The crack propagates a distance (b) under this load. Now the stress is reduced to the lower stress level, Figure (11b). The crack tip is now blunted due to the residual plastic deformation remaining in the region around the crack tip. This results in a toughening of that region which retards the crack growth rate for a given load level. This "toughening" effect is most probably due to the elastic region adjacent to the elastic-plastic boundary exerting clamping stresses on the plastically deformed region. These stresses effectively decrease the amount a crack opens for a given load level, leading to closure of the crack at significant tensile load levels (References 12 and 13). The net effect is to raise the load level required to fully open and propagate the crack. The crack must grow until the shaded region exceeds the residual elastic-plastic region before the toughening effect is dissipated. This may not occur in 50,000 cycles. When the stress level is again raised, the plastic zone extends, and the crack growth rate is more severe. The net effect is an increase in life of the joint vs. that seen for a constant amplitude stress only. This process continues until unstable crack growth occurs. Unknown at this time is the role the viscosity of the adhesive would play in this process.

SUMMARY

The major results are:

1. A 20 to 40% penalty in the load levels associated with runout in fatigue is experienced in the use of some angle ply construction compared to the uni-ply construction.

2. Failure in the 45° ply adjacent to the adhesive in the angle ply construction was due to excessive in-plane shear and normal stresses.

3. The proportional limit shear stress was seen to be an important damage parameter in the fatigue of adhesives.

4. An improvement in the fatigue life of a bonded joint was observed for a two-block loading when the mean load only was altered upward from a non-damaging level.

5. A two parameter fatigue theory was found to have promise in predicting the fatigue life for a two-block loading spectrum. No adhesive characteristics have been evaluated in this paper; these statements are quoted from References [1] and [2].

6. An "ideal" fatigue resistant adhesive for structural applications would be: (A) one of high fracture strength to resist applied loads. (B) have a high fracture ductility to accommodate large plastic strains at critical locations (i.e. cracks, discontinuities). (C) have a "soft" modulus to reduce the severity of stress concentrations.

7. The ideas presented here are based on screening tests. Therefore, much additional work is needed to justify them conclusively.

REFERENCES

1. E. J. Ripling, S. Mostovoy, and R. L. Patrick, "Application of Fracture Mechanics to Adhesive Joints", ASTM STP No. 360, 1963.

2. R. W. Landgraf, "The Resistance of Metals to Cyclic Deformation", ASTM STP No. 467, 1970.

3. W. J. Renton and J. R. Vinson, "The Analysis and Design of Composite Material Bonded Joints Under Static and Fatigue Loadings", AFOSR Report 73-1627, August, 1973.

4. Wilcox, Roy C. and Jemian, Wartan A., "Fracture Surface Features of Epoxy Bonded Joints", Department of Mechanical Engineering, Auburn University, Auburn, Alabama.

5. Jemian, Wartan A. and Ventrice, Marie B., "The Fracture Toughness of Adhesive-Bonded Joints", The Journal of Adhesion, Volume I, July 1969.

6. Wilcox, Roy C. and Jemian, Wartan A., "Scanning Electron Fractography of Lap-Shear Joints", Polymer Science and Engineering, Volume 13, No. 1, January 1973.

7. H. W. Liu and H. T. Corten, "Fatigue Damage During Complex Stress Histories", NASA Technical Note D-256, Nov. 1959.

8. W. J. Renton and J. R. Vinson, "On the Fatigue Behavior of Bonded Joints in Composite Material Structures", AIAA preprint No. 74-383, April 1974.

9. Douglas Y. Wang, "Influence of Stress Distribution on Fatigue Strength of Adhesive-bonded Joints", Journal of Experimental Mechanics, June 1964.

10. A. S. Tetelman and A. J. McEvily, Jr., "Fracture of Structural Materials", Wiley and Sons Inc., publishers.

11. R. Houwink and G. Salomon, "Adhesion and Adhesives", Volumes I and II, Second edition, 1965, Elsevier Publishing Co.

12. N. J. L. Adams, "Fatigue Crack Closure at Positive Stresses", Journal of Engineering Fracture Mechanics, Volume 4, 1972.

13. W. Elber, "The Significance of Fatigue Crack Closure", ASTM, STP 486, 1971.

14. R. M. Engle and J. L. Rudd, "Analysis of Crack Propagation Under Variable Amplitude Loading Using the Willenborg Retardation Model", AIAA paper No. 74-369, April, 1974.

COMPARISON OF THEORETICAL AND EXPERIMENTAL SHEAR STRESS IN THE ADHESIVE LAYER OF A LAP JOINT MODEL

WILLIAM N. SHARPE, JR.
National Research Council Associate
Air Force Materials Laboratory

THEODORE J. MUHA, JR.
Aerospace Engineer
Air Force Flight Dynamics Laboratory
Wright-Patterson Air Force Base
Dayton, Ohio 45433

ABSTRACT

The shear stress in the epoxy adhesive layer of a plexiglas single-lap joint model is measured by monitoring the fringe pattern generated by a laser incident on single wires imbedded on each side of the bond layer. The experimental stresses are compared with those predicted by analytical, numerical, and finite element solutions. Predictions of the Goland-Reissner theory and a BOND4 numerical solution agree well with the results.

INTRODUCTION

In recent years the adhesive bonded joint has received a great deal of attention in the aerospace industry. As weight and cost have become more critical, the bonded joint has been used more frequently to eliminate fastener weight and to reduce fabrication cost. Initial fears of putting fasteners through advanced composite materials in production aircraft led to the examination of bonded joints as an alternative.

An understanding of the mechanics of adhesive joints is necessary for full utilization of the weight- and cost-saving potential of advanced composites in aircraft structures. Many computer analyses have been developed based on either linear or nonlinear response of the materials; the Advanced Composites Branch of the Air Force Flight Dynamics Laboratory has collected twenty of these programs which are operational at Wright-Patterson AFB (see Table I). Gross properties such as maximum shear strength of the joint have been compared with experimental results to examine the validity of the analyses, but the difficulty of measuring strains in a thin adhesive layer sandwiched between two adherends has precluded detailed comparison of the theoretical prediction with experimental results. Thus, there has been no way to effectively compare and evaluate the various analysis methods.

This paper presents a new optical technique which is used to measure adhesive shear strain in a transparent elastic model and compares the results with stresses computed by a finite-element program (NASTRAN) and by the closed-form analysis programs, BONDJOI of Lockheed, JTSDL of Southwest Research Institute, and BOND4 of the University of Delaware. The single-lap joint is chosen because there are significant normal stresses present, and it

TABLE I

PROGRAM	JOINT TYPE				MATERIAL PROPERTIES					END CONDITION		DIMENSION		SOURCE
	S-L	D-L	ST.-L	SCARF	ISO	ORTHO	ANISO	LIN	NON-LIN	FIXED	PINNED	2D	3D	
BONJO	X	X			X	X			X	X		X		LOCKHEED
BONJOI	X	X			X	X		X		X		X		LOCKHEED
AC2O			X		X	X		X		X		X		COMPOSITES DESIGN GUIDE
JTSDL	X	X			X	X			X		X	X		SwRI
JTSTP			X		X	X			X		X	X		SwRI
BOND3	X		X		X	X		X			X	X		UNIVERSITY OF DELAWARE
BOND4	X				X	X		X			X	X		UNIVERSITY OF DELAWARE
STPS4			X		X	X		X		X		X		GRUMMAN
A4EA	X				X			X				X		DOUGLAS
A4EB		X			X				X			X		DOUGLAS
A4EC				X	X			X				X		DOUGLAS
A4ED				X	X				X			X		DOUGLAS
A4EE				X	X				X			X		DOUGLAS
A4EF			X		X			X				X		DOUGLAS
A4EG			X		X				X			X		DOUGLAS
PLSTR	X	X	X	X	X	X		X		X	X	X		OHIO STATE UNIVERSITY
MAGIC	X	X	X	X	X	X		X		X	X	X	X	AFFDL
NASTRAN 15.1	X	X	X	X	X	X	X	X	X	X	X	X	X	NASA
NAVY NASTRAN	X	X	X	X	X	X	X	X	X	X	X	X	X	NSRDC
NASTRAN 15.5	X	X	X	X	X	X	X	X	X	X	X	X	X	NASA

S-L = Single Lap
D-L = Double Lap
ST.-L = Step Lap

is presumed that the theory that can best predict the measurable shear stress under these complicated conditions will be the best theory.

REVIEW OF PREVIOUS WORK

Analytical Studies

Previous analytical studies of bonded joints have been reviewed and discussed by Pahoja [1] and Renton and Vinson [2] as introductions to their reports. The review here will be restricted to the particular isotropic single-lap joint under experimental consideration. The configuration of the joint and coordinate system are shown in Figure 1.

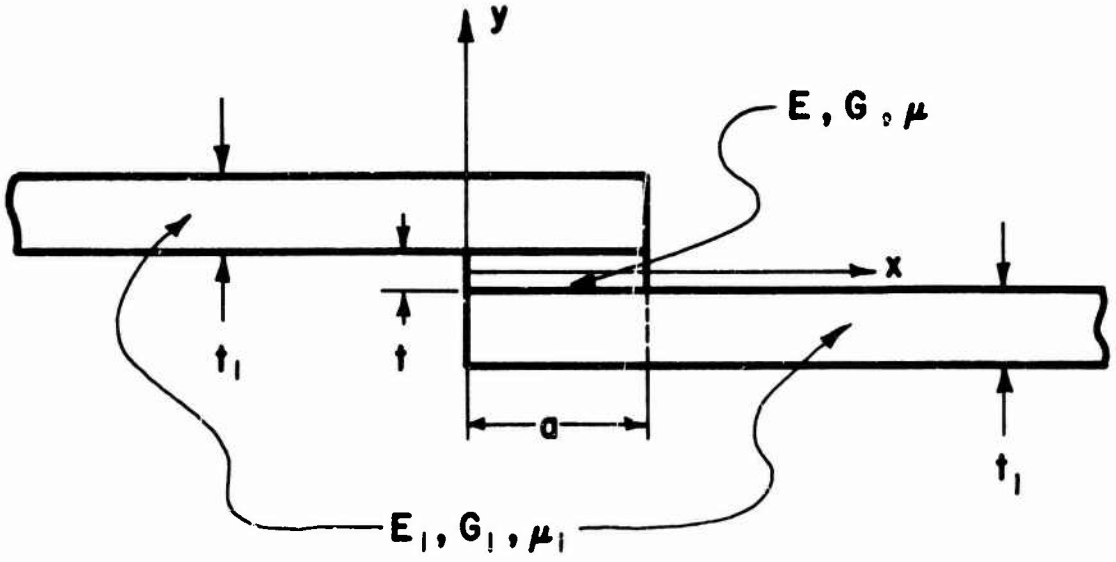

Figure 1. Schematic of a symmetric isotropic single-lap joint.

The analytical predictions will be compared (where possible) for a plexiglas joint having the following properties:

TABLE II

Adherend	Adhesive
E_1 = 510,000 psi	E = 5550 psi
μ_1 = 0.41	μ = 0.5
G_1 = 180,000 psi	G = 1850 psi
t_1 = 0.25 in.	t = 0.010 in.

overlap a = 1.0 in.

width = 1.0 in.

Many of the more recent studies are for anisotropic nonidentical adherends; however, they reduce to the isotropic identical adherend case in which the adherends and adhesive are assumed to be linearly elastic and isotropic. The adhesive is assumed to be in a state of plane strain or plane stress; the stress state is assumed not to vary across the width of the joint (z direction). The loading at the adherend ends is usually assumed to be a force in the x direction.

Volkersen [3] considered the adhesive stresses to arise only from differential straining of the adherends (no bending) in the region of the joint. His prediction of the local shear stress compared to the average shear stress is:

$$\frac{\tau}{\tau_{ave}} = \frac{(D/W)^{\frac{1}{2}}}{\sinh (DW)^{\frac{1}{2}}} \{(W-1) \cosh [(DW)^{\frac{1}{2}} x/a] + \cosh [(DW)^{\frac{1}{2}}(1- \frac{x}{a})]\} \qquad (1)$$

with $D = \frac{Ga^2}{E_1 t_1 t}$ and $W = 2$ for this case. This equation is plotted in Figure 2 for the plexiglas lap joint. It shows the shear stress variation that was accepted for some thirty years, i.e. the shear stress reaching a peak at the ends of the joint.

Goland and Reissner [4] recognized that bending of the adherends in the joint region would severely affect the stress state in the adhesive and developed a theory to account for this. They considered two cases, one in which the joint is flexible ($T_1/G_1 < 1/10\ t/G$) and the other in which it is inflexible ($t/G < 1/10\ t_1/G_1$). The experimental joint has $t_1/G_1 = 0.26\ t/G$ which does not quite satisfy their requirement for a flexible joint. The flexible case yields a closed-form solution (see Figure 2):

$$\frac{\tau}{\tau_{ave}} = \tfrac{1}{4} \{\frac{\beta a}{2\tau_1} (1+3k) \frac{\cosh \frac{\beta a}{2\tau_1} (\frac{x-a/2}{a/2})}{\sinh \frac{\beta a}{2\tau_1}} + 3(1-k)\}; \quad \beta^2 = \frac{8G}{E_1} \frac{\tau_1}{\tau} \qquad (2)$$

k is a factor related to the bending moment at the ends of the joint and is 0.85 for this case.

The inflexible case solution assumes the adhesive layer to be in a state of plane strain and produces a series expression for the stresses in the adhesive layer. The shear stress goes to zero at the ends of the joint and reaches a peak stress ratio of 2.8 at a distance of approximately 0.050 in. from the joint ends for this case.

Platema [5] (as described in Ref. [7]) combines the Volkersen and Goland-Reissner theory to compute the shear stress in the adhesive. The stress ratio is plotted in Figure 2; a result identical to the Goland-Reissner theory in this instance.

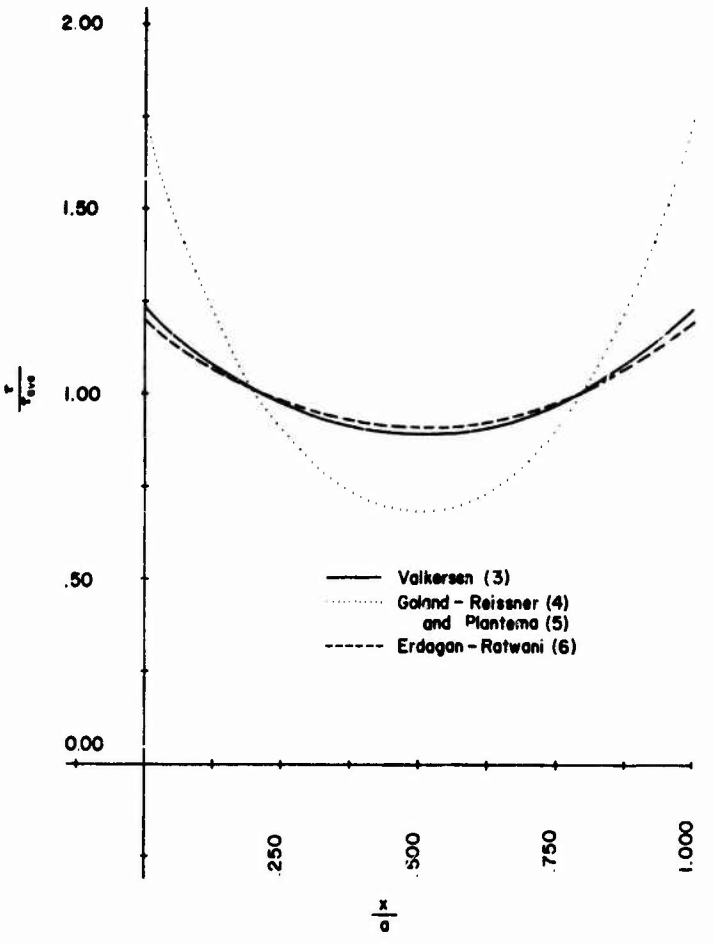

Figure 2. Closed form solutions for a joint with the properties in Table I.

Kelsey and Benson [6] (as described in Ref. [7]) employ the complimentary energy method to determine the shear and normal stresses in a single-lap joint. They apply the boundary condition that the shear stress at the ends of the joint vanish. The expression for shear stress ratio is:

$$\frac{\tau}{\tau_{ave}} = \frac{m_1 m_2 a^2}{4} \left\{ \frac{\cosh m_1(x-a/2)\ \cosh \frac{m_2 a}{2} - \cosh \frac{m_1 a}{2}\ \cosh m_2\ (x-a/2)}{m_1 \cosh \frac{m_1 a}{2} \sinh \frac{m_2 a}{2} - m_2 \sinh \frac{m_1 a}{2} \cosh \frac{m_2 a}{2}} \right\} \qquad (3)$$

with $m_1 = \frac{6E}{\tau^2 G}(1 + m_3)$

$$m_2 = \frac{6E}{\tau^2 G}(1 - m_3)$$

$$m_3 = (1 - \frac{2G^2\tau}{3EE_1\tau_1})^{\frac{1}{2}}$$

However, this equation is not dimensionally correct as m_1, m_2 have units of in.$^{-2}$ and cannot be used in the hyperbolic functions. Apparently there is a misprint in defining m_1 and m_2 in Ref. 7. For the case under consideration, $m_3 \simeq 1$, $m_1 = 3.6 \times 10^5$ in.$^{-2}$, and $m_2 = 2.9$ in.$^{-2}$. Even if one takes the square root of m_1, m_2 to correct the dimensions, the large value of m_1 makes computation difficult. If one divides Equation 3 by $m_1 \cosh m_1 a/2$ and approximates $\cosh m_1 a/2$ by $\frac{1}{2} \exp m_1 a/2$, the result is:

$$\frac{\tau}{\tau ave} = \frac{m_2}{2} \coth \frac{m_2 a}{2} \; e^{m_1(x-a)} - \frac{\cosh m_2(x-a/2)}{\sinh \frac{m_2 a}{2}} \qquad (4)$$

This equation does predict zero stresses at the end of the joint (x=a), but because of the large value of m the peak is located very close to the end. A plot in Ref. 7 for a typical case shows close agreement with Volkersen [3] except at the ends.

Erdogan and Ratwani [8], in a study of anisotropic step-lap joints, compute the shear stress in the adhesive for a single step-lap joint. This configuration has the thickness of each adherend equal to $2t_1$ with a step t_1 in thickness cut out of the joint end. The predicted shear stress distribution for the isotropic case is given in Figure 2 and shows less variation along the joint length than the others. This is because this configuration introduces less bending into the joint.

Numerical Studies

The following studies are analytical, but their solutions are not available in closed form. Any prediction requires numerical integration of the governing differential equations.

Pahoja [1] generated an elasticity solution and tested it experimentally. He was interested in variations of the stresses through the thickness (not width) of the adhesive layer and measured this by standard photoelastic techniques. His lap joint had the following characteristics: t=0.25 in., t_1=1.0 in., E=4.5 x 10^5 psi, and E_1=10 x 10^6 psi which is more nearly the flexible case of Goland-Reissner. His plot of the shear stress along the centerline of the adhesive layer is given in Figure 3.

Hadcock et al [9] developed a simplified analysis of anisotropic adherends for use in design. The shear stress ratio is plotted in Figure 3 for a 1 in. overlap of boron/epoxy bonded to titanium with a 0.008 in. thick layer of Metlbond 329 adhesive.

Wah [10] made a theoretical analysis of a single lap joint with anisotropic adherends. His numerical example for orthotropic adherends unequal in size and properties bonded with a 0.004 in. thick epoxy adhesive is plotted in Figure 3.

These numerical analyses are not for the experimental joint, thus comparison is difficult. They are included to show the general shape of the distribution; note in particular the very high shear stresses at the ends predicted by Hadcock et al and Wah.

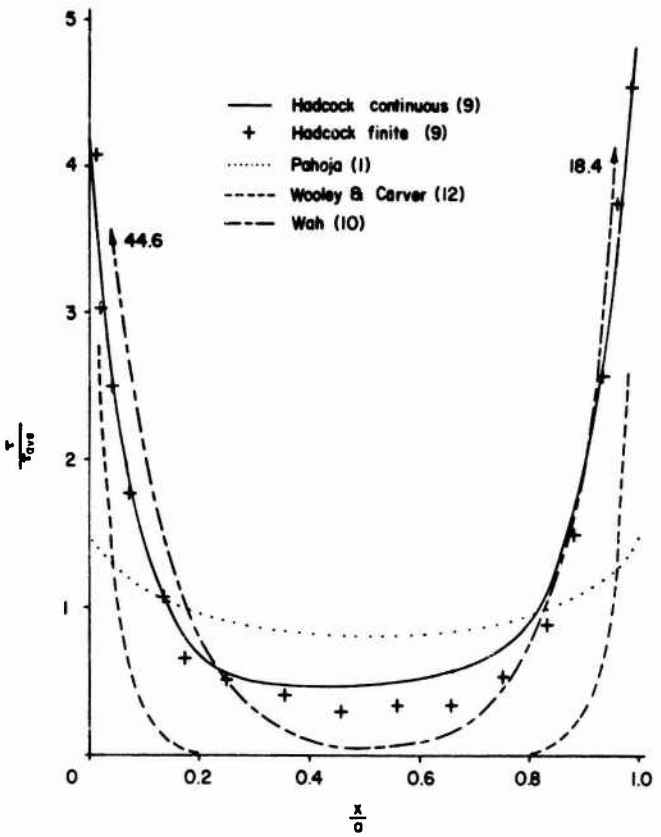

Figure 3. Numerical solutions for various joints.

Finite Element Studies

Finite element techniques are appropriate for theoretical examination of the stresses in the joint though they tend to be expensive because many elements are required to adequately model the thin adhesive layer. Hadcock

et al [9] performed finite element studies of representative joints which tended to support the predictions of their more workable analyses (see Figure 3).

Harrison and Harrison [11] use the finite element technique to calculate stresses in the elastic adhesive layer between perfectly rigid adherends. They compute stresses due to shrinkage, tensile loading, and shear loading, but these are not in a form suitable for experimental evaluation.

Wooley and Carver [12] conducted a finite element study of the single lap joint to evaluate stress concentration factors (τ_{max}/P and σ_{max}/P) for various properties and geometries. In general their factors agreed quite well with ones calculated by the Goland-Reissner theory. A typical stress distribution is plotted in Figure 3. Complete information was not given for this joint so the ordinate values are meaningless, but their analysis definitely shows zero shear stress over the middle six-tenths of the joint and very large stresses at the joint ends.

Experimental Studies

Many experimental investigations of the variations of geometry and properties of bonded joints have been made to develop design information. In some cases, strength tests have been used to evaluate a stress distribution and failure theory. A good example of this approach is a recent paper by DeVries et al [13] who used the Goland-Reissner stress distribution to develop a maximum stress criterion and an energy balance criterion. Their experiments tend to support the latter criterion. Only investigations which have attempted to measure the stresses in the adhesive layer are considered here.

Mylonas [14] performed the first photoelastic investigation of the stresses in the adhesive layer. The specimen is viewed from the side (perpendicular to the x-y plane of Figure 1), and the adhesive layer is photoelastic material. Of course the assumption of uniformity of stress in the z direction is implicit in this experimental approach. He tested a 0.5 in. thick, 2.8 in. long joint with 1 in. thick by ½ in. wide plastic adherends. The shear stress was found to be a maximum at the joint ends with a stress concentration τ_{max}/τ_{ave} of 1.83 at the edge and 1.70 at the center of the adhesive layer.

Cornell [15] used brittle-laquer techniques to measure the stresses in a fatigue specimen made of a tab brazed onto a cantilevered base bar. He also made measurements on a photoelastic model. These experimental results tended to confirm an analysis which treated the adherends as simple beams.

Mylonas [16] studied the stresses at the ends of the overlap as a function of shape at the end of the adhesive layer. His model has essentially rigid adherends and a step-lap configuration so that the shear stress was nearly uniform along its length. He found that the corner stresses were smallest when the concave end was semicircular and when the inclined ends were most nearly parallel to the interfaces.

McLaren and MacInnes [17] investigated a photoelastic lap joint model with zero thickness adhesive layer (i.e. the entire model was cast of the same material with t=0 in Figure 1). Their purpose was to examine the Goland-Reissner prediction that larger bending applied to the joint would generate more uniform stresses, and their results confirm this. They also studied the effects of inclined ends of the adhesive layer, getting results much like those of Mylonas [16].

Lundsford [18] in a report dealing with double-lap type joints develops simple theories and recommends their experimental verification. He suggests four ways of measuring strain in the adhesive layer. One of these involves placing small indentations on both sides of the layer along the edge of the joint and measuring their relative displacement with a microscope--a procedure somewhat similar to the one described in this paper.

Pahoja [1] performed a photoelastic investigation on a model with an adhesive layer 0.25 in. thick mounted between two 1 in. x 1 in. aluminum adherends. The model was subjected to shear as well as axial loading. His measured shear stresses generally agree with his theory except that they go to zero at the overlap ends in contrast to the theoretical prediction.

COMPUTER ANALYSIS

The intense interest in bonded joints has generated many computer analyses. Of the twenty programs which have been collected by the Advanced Composites Branch of the Air Force Flight Dynamics Laboratory, AFFDL/FBC, four were chosen for use in this study. These four programs are Lockheed Aircraft's BONJOI, Southwest Research Institute's JTSDL, the University of Delaware's BOND4, and NASA's general-purpose finite element program NASTRAN.

BONJOI was developed by the Lockheed-Georgia Company for AFFDL/FBC under contract F33615-70-C-1302. The program computes both the adhesive and adherend stresses for both single-lap and double-lap joints. The analysis covers both static and thermal load cases. The stresses are assumed to remain in the linear elastic range throughout the joint. The adhesive shear and normal stresses are calculated at twenty-seven bond-line locations which are fixed in the program and chosen to assure a good distribution of points in areas of high stress gradients. Adherend axial stresses are computed at the upper and lower surface of each layer and interlaminar shear and normal stresses are calculated at the interface of layers. All adherend stresses are calculated at eleven equidistant locations along the x-axis. Although the procedure was specifically designed for joints using advanced filamentary composites, it is equally applicable to joints using any other materials.

JTSDL was developed by Southwest Research Institute for AFFDL/FBC under contract F33615-69-C-1641. The program is a nonlinear analysis method applicable to single-lap and double-lap joints subjected to static loads at room temperature. The joint is assumed sufficiently wide to obtain a state of plane strain. The adherends may be either orthotropic or isotropic. The adhesive is assumed to be isotropic and of a constant thickness which is much smaller than either adherend thickness. The adherends are assumed to be flat

plates in bending and symmetrical about their middle surface. Interlaminar shear is neglected. All stresses are calculated at eleven equidistant points along the x-axis.

BOND4 was developed by Dr. W.J. Renton at the University of Delaware under AFOSR contract 1760-72. The program covers the linear analysis of single-lap joints. It determines the adhesive shear and normal stresses, incorporating the effects of transverse shear and normal strain. The stress distribution through the adherend thickness is calculated. This program, which is especially relevant for anisotropic adherends assumes that each adherend consists of an odd number of layers and is symmetrical about its midplane. The isotropic adhesive is used according to "effective" properties which are ascertained in tests described in AFOSR Report 1760-72.

NASTRAN is an extremely large, general-purpose, finite-element, structural analysis program which NASA has been developing over the past several years. AFFDL/FBC has three versions of NASTRAN operational. These versions are NASA Levels 15.1 and 15.5 and the Naval Ship Research and Development Center (NSRDC) Level 15.1. This study required only the linear elastic, static, two dimensional, isotropic, nonthermal aspects of the program. The elements used were the CQUAD2 and CTRIA2 elements; these quadrilateral and triangular elements have both plate and membrane properties and can accomodate isotropic or anisotropic materials whose properties may be temperature dependent. Level 15.5 was used throughout this study.

Analyses of a joint with a = 0.5 inch and t = 0.015 inch and the other dimensions and properties as in Table II are given in Figures 4 and 5. Note that only BONJOI and BOND4 satisfy the condition of zero shear stress at the joint edge.

When running the experiments, the end boundary conditions were one end fixed and one end pinned. These conditions could not be entirely duplicated in the computer analyses; both JTSDL and BOND4 assume both ends pinned, BONJOI assumes both ends fixed, and the fixed condition was input into NASTRAN.

EXPERIMENTAL INVESTIGATION

Theory of Measurement

Consider two wires imbedded in a plastic lap joint model, one wire on either side of the adhesive as shown in Figure 6. Let a laser beam be incident perpendicular to the model. It will be diffracted by each of the wires, and these diffracted patterns will overlap to generate interference fringes on a screen as shown. The position of these interference fringes, is related to the spacing between the wires. As the model is loaded, this spacing change changes, the fringes move, and this motion is related to the shear strain in the sample.

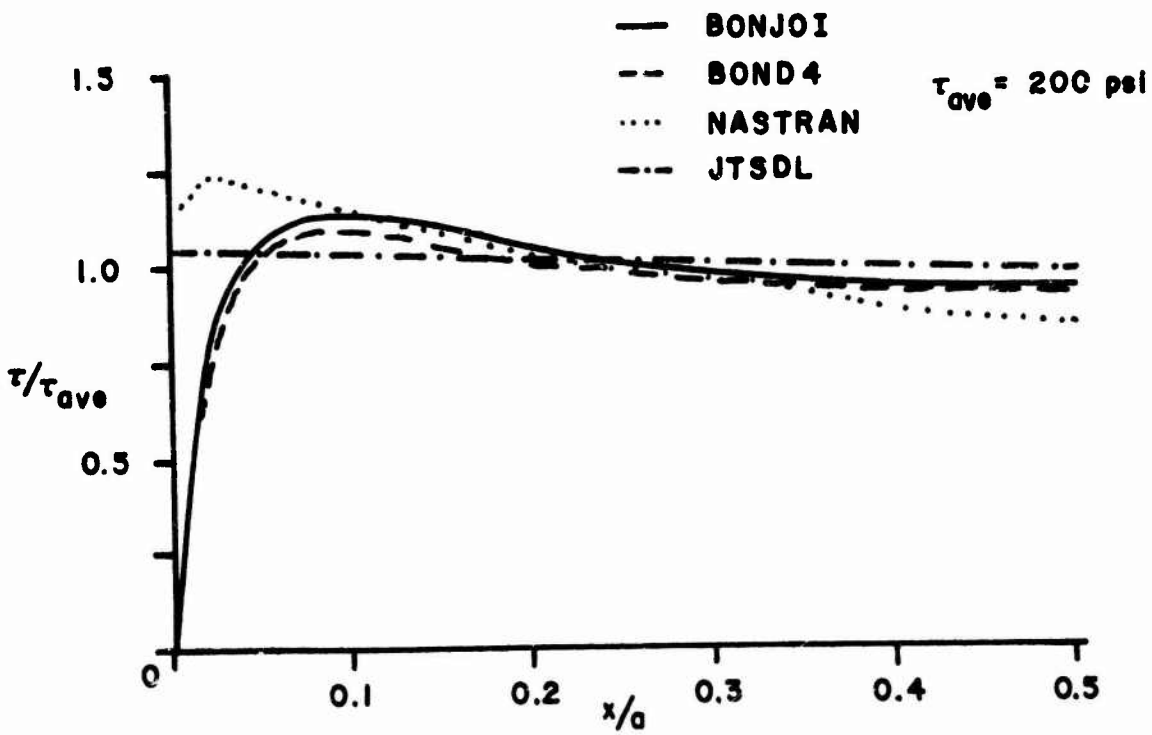

Figure 4. Shear stresses from computer analyses for a joint subjected to 100 lb end loads.

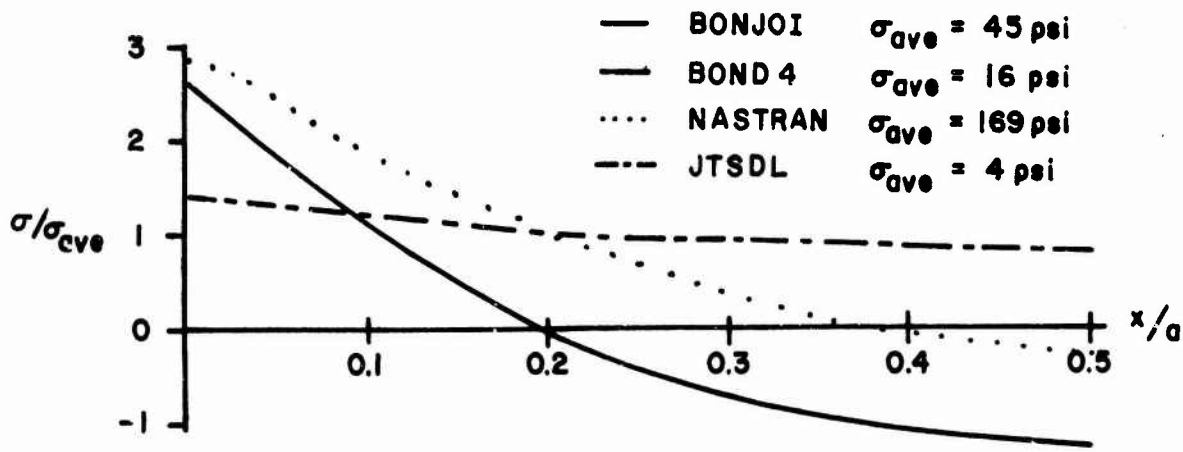

Figure 5. Normal stresses from computer analyses for a joint subjected to 100 lb end loads.

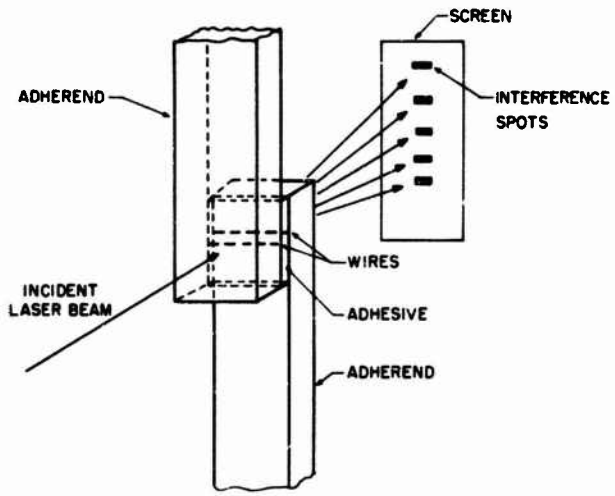

Figure 6. Schematic of technique for measuring shear strain.

The equation relating fringe motion to shear strain in the sample can be derived with the aid of Figure 7. A and B are the two imbedded wires.

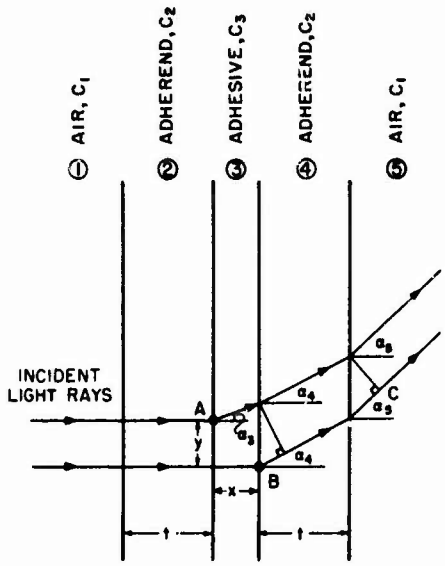

Figure 7. Optical paths for a single-lap joint model.

The media are numbered as shown with the adherends and adhesive having speeds of light propagation C_2 and C_3 respectively. The incident light rays are perpendicular to the model surface. Conditions for interference are derived by computing the path difference for a ray passing through A as compared to one through B. The ray passing through A takes a time

$$\frac{x}{C_3 \cos \alpha_2} + \frac{t}{C_2 \cos \alpha_4}$$

to pass from the 23 interface to the 45 interface. The ray passing through B takes a time

$$\frac{x}{C_3} + \frac{t}{C_2 \cos \alpha_4} + \frac{(y + x \tan \alpha_3)}{C_1} \sin \alpha_5$$

to pass from the 23 interface to C at which point it is parallel to and in the same medium as the ray through A. When the difference in time of propagation is equal to an integral number of periods, τ, of light amplitude vibration in the final medium the light rays interfere constructively. Thus the governing equation is:

$$\frac{(y + \tan \alpha_3)}{C_1} \sin \alpha_5 + \frac{x}{C_3} - \frac{x}{C_3 \cos \alpha_3} = m\tau = \frac{m\lambda}{C_1} \qquad (1)$$

$m = 0, \pm 1, \pm 2, \pm 3, \ldots$ $\quad \lambda$ = wavelength of light

After some simplification using the relations $n_1 C_1 = n_2 C_2$, etc. and $n_1 \sin \alpha_1 = n_2 \sin \alpha_2$ etc. where n is the index of refraction (n=1 for air), the equation becomes:

$$x\, n_3 (1 - \cos \alpha_3) + y \sin \alpha_5 = m\lambda \qquad (2)$$

If one considers the rays bending downward, the governing equation becomes:

$$x\, n_3 (\cos \alpha_3 - 1) + y \sin \alpha_5 = m\lambda \qquad (3)$$

The displacement in the x direction is related to normal strain, ε, and that in the y direction to shear strain, γ, in the adhesive layer. The gage length for the strain measurement is the original layer thickness, so the strains are

$$\varepsilon = \delta x / x \text{ and } \gamma = \delta y / x \qquad (4)$$

The displacements are related to the fringe shift, δm, observed at some position α_5 on the screen by:

$$\delta x\, N_3 (\pm 1 \mp \cos \alpha_3) + \delta y \sin \alpha_5 = \delta m \lambda) \qquad (5)$$

δm is measured by counting the number of fringes or fraction thereof that pass the observation position.

In practice an observation angle of 5° is typical, and the adhesive layer has an index of refraction of approximately 1.6. Equation 5 is then

$$\pm 0.0061\ \delta x + 0.087\ \delta y = \delta m\lambda \tag{6}$$

Most of the theories indicate that the maximum normal and shear strains observed are of the same order of magnitude, so that the error in assuming that the fringe motion is due soley to shear strain is 7 percent or less. If this is acceptable, one may use the simple equation:

$$\gamma = \frac{\delta m\lambda}{x \sin \alpha} \tag{7}$$

where α is the angle between the main beam and the observation position.

Figure 8 is a photograph of a fringe pattern produced by a laser beam passing over two wires with x = .010 in. and y = 0.015 in. Plotted alongside the photograph is Equation 2, assuming x = 0. The fringe pattern of Figure 8 is the same as would be produced by a Young's double-slit experiment with two slits separated by .015 in. The opaque wires are complementary to the slit by Babinet's principle [19].

Increasing the observation angle α means that more fringes pass the observation position and the displacement can be measured with greater sensitivity. However, a small angle is desirable because δm is then less sensitive to x displacement. It is easy to measure δm to one-fourth of a fringe shift, giving a minimum detectable shear strain of 0.007 when x = 0.010 in. and $\alpha = 5^{\circ}$. Fringe motions as small as 1/1000 can be measured using suitable techniques [20].

The surfaces in Figure 2 tilt approximately 1° maximum for these test conditions as the sample is loaded, and the fringes move accordingly. However, if one averages the fringe shift of the upper and lower pattern, this rotation is eliminated.

Techniques of Measurement

The lap-joint models were made of 0.25 in. plexiglas strips 1 in. wide. A measured value of E = 510,000 psi and a Poisson's ratio of 0.41 were used to compute an approximate shear modulus of G = 180,000 psi. The adhesive must be optically clear, linearly elastic, and have a shear modulus with a value relative to the adherend modulus typical of structural adhesives. A suitable adhesive is type PC-6C manufactured by Photolastic, Inc. which is used to bond photoelastic coatings to components. Its bulk tensile modulus is 30,000 psi, and assuming a Poisson's ratio of 0.5, it has an approximate shear modulus of 10,000 psi. The major consideration in producing the model is that it be linear; this linearity is demonstrated in Figure 9 which is a plot of load versus overall model elongation taken from the Instron recorder during a test. The shear stress in the adhesive is always 100 psi or less.

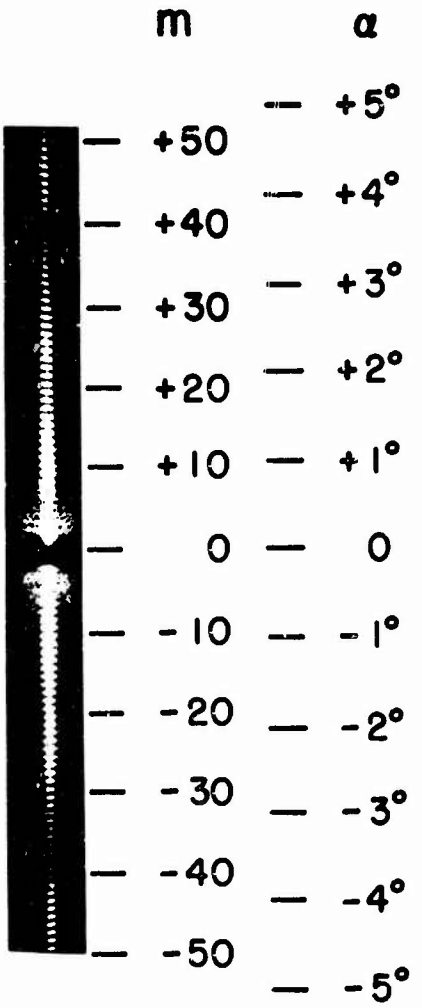

Figure 8. Photograph of fringe pattern.

The PC-6C adhesive is quite easy to use for its intended application; however, it contains small bubbles after it cures which don't hurt a photoelastic pattern, but destory the coherence of the transmitted laser beam. After considerable experimentation, a satisfactory procedure was developed. The epoxy adhesive is mixed at 150°F and spread on one half of the model. This half is then placed in a vacuum chamber at 100 microns and 150°F for 8 minutes (the timing is fairly critical). Upon removal, this half is clamped in a fixture and the other half clamped on top. The spacing of the adhesive layer is controlled by shims which are machined away after the model cures.

All of the theoretical discussion was based on wires as the diffracting agents. The original procedure was to rule shallow grooves on the adherends, lay 0.5 mil wire in them, and bond the ends with Eastman 910. The procedure required to free the adhesive of bubbles produces a rather viscous adhesive which distorts the wires as the adherends are clamped together. It turns out that the grooves do remain visible after the model is cured, and they produced very nice fringe patterns. In fact, the fringes in Figure 8 were produced by grooves in the plastic adherends. The decrease in intensity around $\pm 4^{\circ}$ is caused by diffraction of the light by the grooves. That is the first diffraction minimum and indicates that the opaque part of the grooves is approximately 9 microns wide.

The model was loaded in a table-model Instron testing machine equipped with load cycling controls. Before each test the load was cycled several times to reduce any viscoelastic behavior. A five milliwatt helium-neon laser was mounted on a separate optical bench so that the laser beam could be moved from point-to-point in the model. It would be possible to expand the laser beam so as to cover a whole set of lines and photograph fringe pattern change as the load is applied. For these tests, it was easier to just move the laser beam around in the model to measure strains at various points. δm was measured by selecting a particular observation position (at $\pm\alpha$) and counting the passing fringes. This counting can be done by eye, but

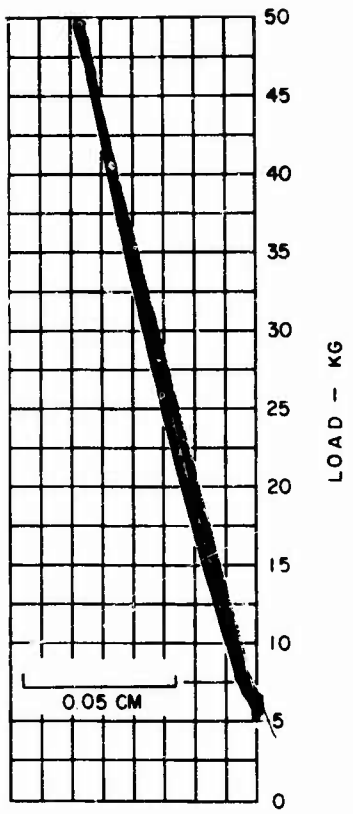

Figure 9. Load-elongation curve for typical model test.

when δm is small, say 2 or 3, this is not accurate enough. A photodetector with a 0.02 in. aperture was mounted at the observation position, and the intensity of the fringe pattern recorded as it moved. The fringe pattern intensity is described by a cosine-squared function modulated by the diffraction intensity variation; one can thus easily estimate δm to ¼ of a fringe shift. Note that the δm measurement can be made with much greater sensitivity [20]. A copy of a typical intensity plot is given in Figure 10. The variation in total intensity is caused by changes in the background intensity as the sample is loaded.

Results

The heat-vacuum procedure required to remove the air bubbles from the adhesive causes a reduction in elastic stiffness from the specified value of E = 10,000 psi. The shear modulus of the adhesive was determined by

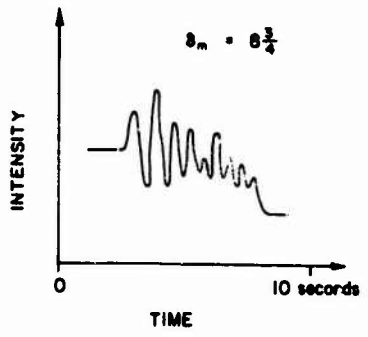

Figure 10. Typical intensity-time plot showing maxima and minima passing the photodetector.

equating the area under the shear strain versus x/L curve to γ_{ave} and dividing this into the applied shear stress (normally 100 psi). The adhesive shear modulus was about 1100 psi after one day's cure and stabilized at 5550 psi after two weeks.

The forces applied to the model do not exactly match the boundary conditions of the theories--most of which assume a single load applied to the adherend ends. The lower end of the model was clamped in a rigid holder attached to the moving crosshead, and the upper was clamped in a holder attached with a universal joint to the load cell. The lower adherend was shifted $2t_1$ from the axis of the testing machine so that the applied forces would be more parallel to the adherend. In reality, the lower end is a clamped connection and the upper end a pinned connection. However, the adherends are long (6.5 or 7.0 in.) which tends to mitigate these end effects on the joint behavior.

Figure 11 shows the variation in shear stress along the length of the joint with the properties in Table II as well as across the width. At each x/L position, readings were taken at the center, halfway over toward each edge, and within 0.050 in. of each edge. The typical uncertainty shown is of the fringe shift detection procedure. There is no detectable variation in shear stress across the model (within the sensitivity of the measurement and uniformity of the model).

The variation in shear stress along the centerline (z=0) of a model with the properties in Table II is examined more closely in the experiment reported in Figure 12. The end of the overlap was trimmed down to bring the grooves closer to the end, and corrections were applied in the computation of τ_{ave}. This figure shows the definite drop of the shear stress near (within 0.030 in.) the end of the overlap--a phenomenon first measured by Pahoja [1]--in larger models. The peak shear stress occurs at approximately x/L=0.05. Also plotted on Figure 12 are the predictions from Figures 2 and 4 of Goland-Reissner and the BOND4 program.

Figure 13a compiles experimental results showing that increasing the shear modulus makes the shear stress peak slightly higher. In Figure 13b, changing the adhesive thickness has little effect, while increasing the joint length steepens the shear stress gradient slightly. These results are in general agreement with theoretical predictions.

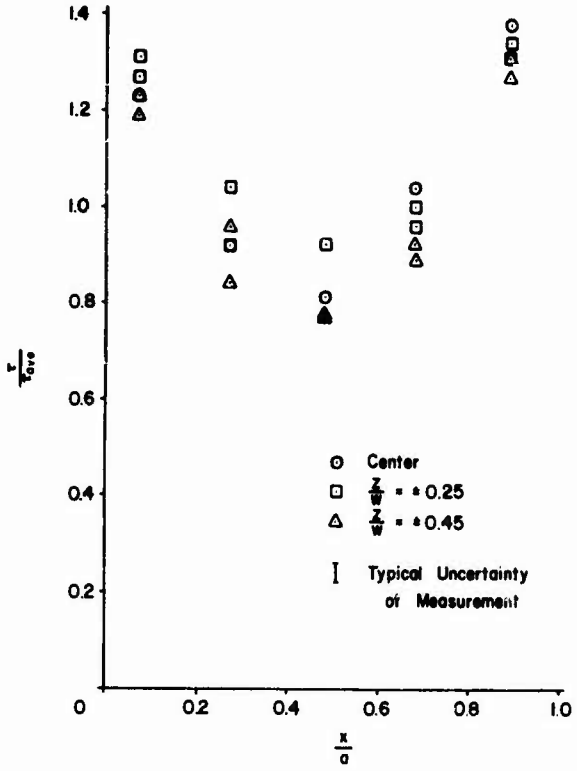

Figure 11. Shear stress variation across width and length of joint.

CONCLUSIONS

The closed form Goland-Reissner and Plantema solution and the numerical BOND4 program predict the shear stress distribution in the adhesive layer better than other theories in this particular case. The BONDJOI program also predicts the stresses fairly accurately; the difference between it and BOND4 may simply be the fact that the experimental boundary conditions are in reality closer to the pinned-end boundary conditions of BOND4 than the clamped ends of BONJOI. The numerical solutions satisfy the boundary conditions of zero shear stress at the end of the adhesive and thus give a better estimate of the maximum shear stress.

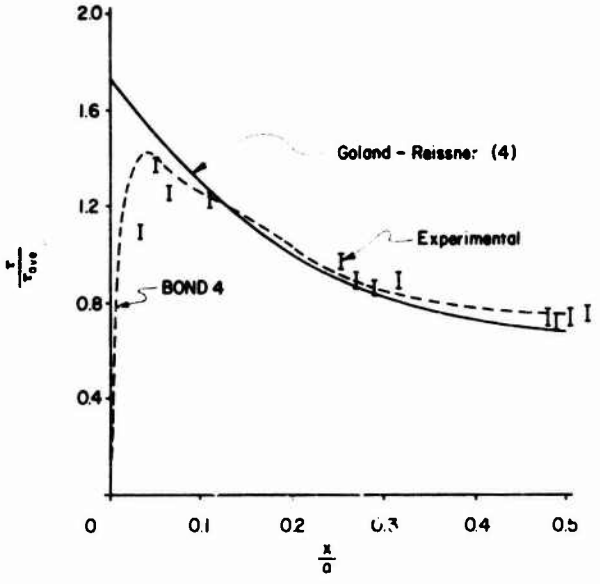

Figure 12. Variation of centerline shear stress with distance from joint end.

The ratio of adherend shear modulus to adhesive shear modulus is approximately 100 for the model of Figure 12. A decrease in this ratio by a factor of 9 has little effect on the general shape as shown in Figure 13a. Typical metal-epoxy lap joints have a shear modulus ratio on the order of 10; therefore, these comparisons are valid for practical joints. These results also tend to indicate that those theories that predict exceptionally large stresses at the joint ends and very small stresses in the center are incomplete or perhaps suffer from computational difficulties.

This new experimental technique has been shown to be workable. Considerable improvement could be made in the construction of models (e.g. develop adhesives with a wider range of shear modulus) and in the fringe measurement. However, the simple procedures used produced an uncertainty of measurement and uniformity of the model capable of evaluating the analytical solutions.

Theories have been evaluated experimentally for the first time by comparison of the shear stress in an adhesive layer of typical thickness. The single-lap joint studied is a simple case; this approach may have more value for complicated joints such as the stepped-lap joint where more simplifying assumptions must be made to generate a solution.

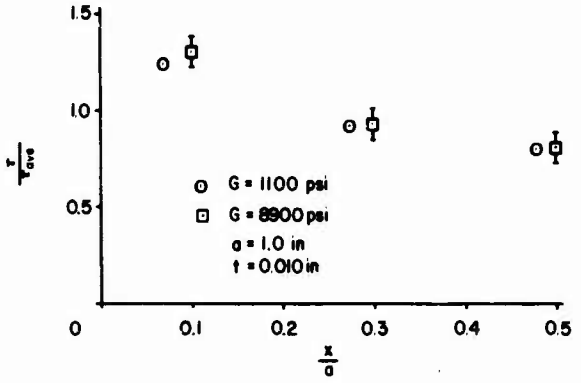

Fig. 13a

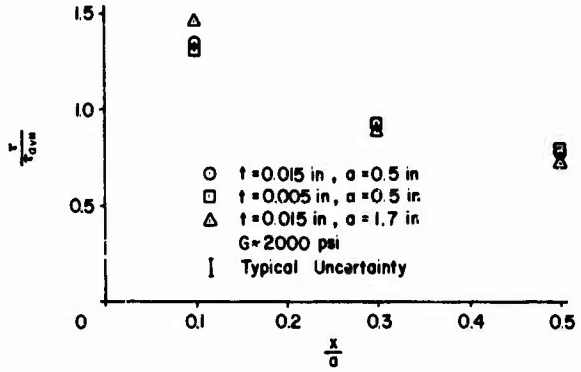

Fig. 13b

Figure 13. Effect of varying shear modulus, joint length and joint thickness.

ACKNOWLEDGEMENT

W.N. Sharpe, Jr. very gratefully acknowledges the support of the National Research Council and the Air Force Materials Laboratory while on sabbatical from Michigan State University.

REFERENCES

1. Pahoja, M.H., "Stress Analysis of an Adhesive Lap Joint Subjected to Tension, Shear Force and Bending Moments," Report No. 361, Dept. of Theoretical and Applied Mechanics, University of Illinois, 1972.

2. Renton, W.J., and Vinson, J.R., "The Analysis and Design of Composite Material Bonded Joints Under Static and Fatigue Loading," Report No. 169, Dept. of Mechanical and Aerospace Engineering, University of Delaware, 1973.

3. Volkersen, O., "Die Nietraftverteilung in zugbeanspruchten Nietverbindungen mit konstaten Laschenquerschnitten," Luftfahrtforschung, Vol. 15, 1938, pp. 41-47.

4. Goland, M., and Reissner, E., "The Stresses in Cemented Joints," Journal of Applied Mechanics, Vol. 11, No. 1, March 1944, pp. A-17-27.

5. Plantema, F.J., De Schuifspanning in eme lijmnaad, Report M1181, Nat Luchtvaartlaboratorium, Amsterdam, 1949.

6. Kelsey, S., and Benson, N.K., Institut fur Statik and Dynamik, Technische Hochschule, Stuttgart, ISD Report No. 10, 1966.

7. Benson, N.K., "Influence of Stress Distribution on the Strength of Bonded Joints," Adhesion-Fundamentals and Practice, Ministry of Technology, Maclaren, London, 1969, pp. 191-205.

8. Erdogan, F., and Ratwani, M., "Stress Distribution in Bonded Joints," Journal of Composite Materials, Vol. 5, July 1971, pp. 378-393.

9. Hadcock, R.N., Corvelli, N., and Torczyner, R.D., "Joints in Composite Structures," AFFDL-TR-72-130, Air Force Flight Dynamics Laboratory, Wright-Patterson Air Force Base, 1972.

10. Wah, T., "Stress Distribution in a Bonded Anisotropic Lap Joint," ASME paper No. 73-Mat-M, 1973.

11. Harrison, N.L. and Harrison, W.J., "The Stresses in an Adhesive Layer," J. Adhesion, Vol. 3, No. 3, Jan. 1972, pp. 195-212.

12. Wooley, G.R., and Carver, D.R., "Stress Concentration Factors for Bonded Lap Joints," J. Aircraft, Vol. 8, No. 10, Oct. 1971, pp. 817-820.

13. DeVries, K.L., Williams, M.L. and Chang, M.D., "Adhesive Fracture of a Lap Shear Joint," Experimental Mechanics, Vol. 14, No. 3, pp. 89-97, 1974.

14. Mylonas, C., "On the Stress Distribution in Glued Joints," Proc. 8th Intl. Cong. Appl. Mech., 4, pp. 137-145, 1948.

15. Cornell, R.W., "Determination of Stresses in Cemented Lap Joints," Journal of Applied Mechanics, Vol. 20, No. 1, March 1953, pp. 355-364.

16. Mylonas, C., "Experiments on Composite Models with Application to Cemented Joints," Proc. Soc. Exp. Stress Analysis, Vol. 12, No. 2, 1955, pp. 129-142.

17. McLaren, A.S., MacInnes, I., "The Influence on the Stress Distribution in an Adhesive Lap Joint of Bending of the Adherend Sheets," British Journal of Applied Mechanics, Vol. 9, Feb. 1958, pp. 72-77.

18. Lunsford, L.R., "Stress Distribution in Bonded Joints," Technical Report ERR-FW-130, General Dynamics--Fort Worth, 1961.

19. Jenkins, F.A., and White, H.E., Fundamentals of Optics, McGraw-Hill Book Co., New York, N.Y. 1957.

20. Sharpe, W.N., Jr., "A Short Gage-Length Optical Gage for Small Strain," to be published in Experimental Mechanics.

CRACK PROPAGATION BETWEEN DISSIMILAR MEDIA

D. R. MULVILLE (Code 8433)
Ocean Technology Division
Naval Research Laboratory
Washington, D. C. 20375

R. N. VAISHNAV
Department of Civil and Mechanical Engineering
The Catholic University of America
Washington, D. C. 20017

ABSTRACT

Interfacial crack propagation studies were conducted on specimens of epoxy bonded to aluminum. The effect of surface roughness of the aluminum on fracture toughness was measured for four different surface finishes. It was found that increased surface roughness resulted in greater fracture toughness if the surface was roughened, e.g., by sandblast or glass-peen finishes on the aluminum. This may be explained by the observation that the interfacial cracks replicated the surface features of the aluminum. Microscopic studies of the failure surfaces indicate that crack propagation occurs in the epoxy near the interface, and that a residue of epoxy remains bonded to the aluminum. The magnitude of the residual stresses due to casting and curing of the epoxy was determined by photoelastic techniques. Methods were developed for analyzing the birefrigent pattern in the epoxy to determine the magnitude of the elastic residual stress and the frozen stress. It was found that residual stresses can contribute 15 to 20 percent of the energy required for crack initiation at the interface.

INTRODUCTION

Due to their favorable strength and fabrication qualities, bonded materials and composites are finding increasing use in aircraft and other modern engineering structures. However, many problems are associated with the use of these materials, such as debonding and delamination, under service conditions. Although considerable theoretical developments have been reported in the analysis of interfacial problems, they have received limited experimental exploration.

The plane problem of a crack between dissimilar materials was initially considered by Williams [1]. Using an eigenfunction approach, he analyzed the character of the stresses near the crack tip between two dissimilar isotropic materials joined without residual stress. He found that the resulting stresses possess an oscillatory character of the form $r^{-\frac{1}{2}} \sin(\lambda \log r)$ and $r^{-\frac{1}{2}} \cos(\lambda \log r)$, where r is the radial distance from the crack tip and λ is a function of material properties. This is in contrast to the homogeneous problem, in which the form of the resulting stresses near the crack tip is a $r^{-\frac{1}{2}}$ type of singularity.

Erdogan [2] considered a similar problem and obtained expressions for the stress along the bond in terms of complex potential functions. His results verify the oscillatory behavior of the stresses previously described by Williams. In addition, he defined a pair of stress-intensity factors related to the Griffith-Irwin fracture theory. In the homogeneous problem, the stress-intensity factors, K_I and K_{II}, are associated with symmetric (normal) and skew-symmetric (shear) stress fields, respectively. However, for the non-homogeneous problem considered here, each of the stress-intensity factors is related to both symmetric and skew-symmetric stress fields. Later, Erdogan [3] analyzed the general plane problem of a series of through cracks along the interface subjected to known surface tractions and known dislocations in displacement along the bonded segments.

England [4] considered the plane problem of an internally pressurized crack between two dissimilar materials. He discussed the physical significance of the oscillatory behavior of the stresses and displacements near the crack tip. Mathematically, such oscillations implied that the upper and lower surfaces of the crack would have to wrinkle and overlap. England showed that these physically impossible interferences predicted by the analytic solution were confined to a very small region near the ends of the crack and he felt that on physical grounds the solution should provide a good approximation at points remote from this region. Rice and Sih [5], [6] analyzed the problem of bending of a bi-material plate with cracks along the bond, and later, considered the general plane problem for interfacial cracks between dissimilar materials. Using a combination of the eigenfunction approach and the complex variable method, they formulated a solution for the stress and displacement fields and defined the stress-intensity factors in terms of a complex potential function.

While all of the preceding studies have provided theoretical solutions to various types of interfacial problems for dissimilar materials, little experimental data was available to verify these results. Recently, Wu and Thomas [7] conducted an experimental study of crack propagation at the interface of a bi-material plate with loading normal to the bond. Using Rice and Sih's [6] analysis they determined the stress-intensity factors for interfacial failure. The failure mode observed in their studies was a small amount of slow crack growth along the interface, followed by rapid crack propagation away from the interface, leading to ultimate fracture. Wang [8] analyzed the plane problem of an interfacial crack between adhesively bonded dissimilar materials using numerical techniques. He also conducted an experimental compliance calibration to verify the results obtained in the numerical solutions. However, he did not include crack propagation studies in his investigation.

Williams [9,10,11] has conducted both analytic and experimental debonding studies using a pressurized blister test. This test was designed to treat the case of a soft elastomeric material cast, and cured on a relatively rigid substrate. A pressure inlet hole was drilled through the underside of the substrate, and pressure was applied which lifted the elastomeric layer off the surface of the substrate, forming a blister. This technique was

applied by Burton, et al, [12] to study debonding of solid propellant and compatible liner from the rocket motor case. It has also been applied to measure the adhesive quality of dental cements, paints, explosively welded metal parts and barnacle cement. These applications are presented briefly in a recent paper by Bennett, et al, [13] in which he discusses the advantages and limitations of this test method. Its advantages are 1) ease of sample preparation, 2) ease of testing with relatively inexpensive equipment and 3) determination of several data points from a single specimen. However, for some materials, with a higher adhesive strength than cohesive strength, failure often begins at the periphery of the blister and extends into the material rather than along the bond.

While this sampling of analytical effort indicates that there has been considerable theoretical work on interfacial stress analysis, little has been done experimentally. Prior to this investigation, experimental studies had not been conducted for combinations of residual stresses, uniform thermal loading, external forces applied parallel to the bond or external moments which cause interfacial failure, nor did a formulation exist for the strain energy release rate for interfacial failure under these combinations of loads. The objective of this study was to examine in detail the nature of the fracture process at the interface of two bonded dissimilar materials by studying experimentally crack propagation in bi-material specimen subjected to a variety of loading conditions. For ease in illustrating the phenomena, one of the materials in the example will be considered as a relatively rigid body, i.e., the Young's modulus of one material is much greater than the other material.

THEORETICAL ANALYSIS

Consider two elastic half-spaces S^L and S^R as shown in Figure 1 with a common boundary, A, along the entire X axis; the positive Y axis being directed normally to the X axis, and lying wholly in S^L. Let the internal segment A' of the X axis bounded by the end points $(-\ell,o)$ and (ℓ,o) correspond to an interfacial bond with the remaining segment A'' on either side of A' representing two cracks. The total boundary A separating S^L and S^R is the sum of A' and A''. Assume that each half-space is externally loaded by a system of self-equilibrating forces with A'' traction free. Under this loading there will be no resultant normal or shear forces transferred across A'. In addition, assume that the difference between the strains in S^L and S^R on A' is specified.

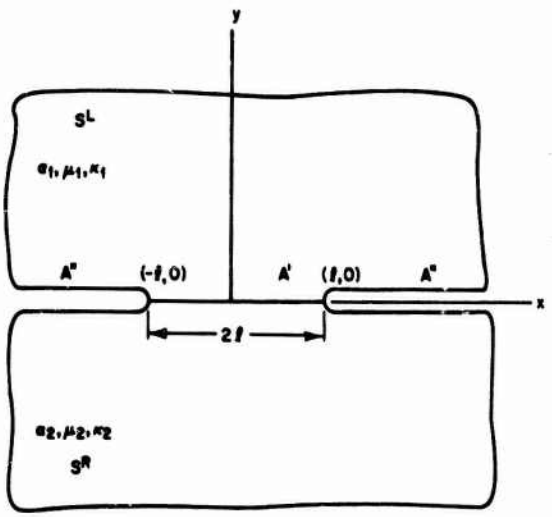

Figure 1 Two elastic half spaces bonded along A'

The boundary conditions can be

be expressed formally as follows: 1.) the surface tractions vanish along the unbonded section of the real axis, A''; 2.) the traction vector is continuous across A'; 3.) the strain difference is specified on A'; 4.) the components of the resultant force on A' are zero.

Using the complex potential function method as presented in [14], the stress field was analyzed for the plane problem of two bonded dissimilar materials with cracks along the intervace subjected to thermal loading or self-equilibrating tensile or bending loading applied to either half space, [15]. Each of the materials lying in S^L and S^R is assumed to be linearly elastic, homogeneous and isotropic. These results were used to formulate the strain energy release rate for crack propagation at the interface between the two materials. It should be noted that the resulting stresses obtained in this analysis possess an oscillatory character similar to that found by Williams.

The strain energy release rate, $\mathcal{G}$, defined as the decrease in stored elastic strain energy per unit of crack increase, was expressed as

$$\mathcal{G} = \frac{2\pi(1+4\lambda^2)}{a+b}\ \eta^2 \ell - \frac{2\eta\lambda\ell^2}{R} + \frac{\ell^3}{4R^2}(1+4\lambda^2) \qquad (1)$$

where $a = \frac{\kappa_1}{\mu_1} + \frac{1}{\mu_2}$, $b = \frac{1}{\mu_1} + \frac{\kappa_2}{\mu_2}$ $c = \frac{a}{b}$ is defined as the bi-elastic constant, $\lambda = (\log c)/2\pi$ and

$$\eta = (\eta_R^L - \eta_R^R) + (\eta_T^L - \eta_T^R) + (\eta_M^L - \eta_M^R) \qquad (2)$$

In equations (1) and (2), ηR is the strain due to residual stresses, ηT is the strain due to thermal loading, ηM is the strain due to mechanical loading, and R is the radius of curvature of A'. In the above μk is the shear modulus, $\kappa_\kappa = (3-4\nu)$ for plane strain and $\kappa_\kappa = (3-\nu_\kappa)/(1+\nu_\kappa)$ for generalized plane stress, where ν_κ is Poisson's ratio.

The expression for the strain energy release rate is based on the plane problem of two elastic half spaces bonded along A', and can be used to analyze the following loading conditions: residual stresses, uniform thermal loading, forces applied parallel to the bond to one or both half spaces, bending loads applied to one or both half space or any combinations of these loads. This analysis does not consider non-linear or time dependent effects, which may arise in bonding applications using polymeric adhesives. In addition, the strain function assumed along the bond in this analysis implies that one of the materials acts as a relatively rigid body, i.e., that the Young's modulus of one material is much greater than the other material. Otherwise, the resulting displacement on the interface must be considered an unknown function related to the material properties. This analysis also assumes that the crack growth will occur along the interface, i.e., along $y=0$.

EXPERIMENTAL INVESTIGATION

Experimental studies were undertaken to make quantitative measurements of the fracture parameter $\mathcal{J}$ for interfacial crack propagation. Using the analysis of the preceding section, a specimen design was chosen and loading conditions selected for which cracks would propagate at the interface between two dissimilar materials. Specimen design studies included photoelastic observations and strain gage instrumentation of various specimens to determine how closely the assumptions of the theoretical analysis were satisfied. Aluminum-epoxy specimens were fabricated to conduct a series of interfacial crack propagation studies for various surface finishes on the aluminum surface of the bond. Restrained shrinkage along the bond during solidification of the epoxy and differential thermal contraction during post-curing gave rise to a field of residual stresses, whose effect was included in the analysis.

The aluminum half of these specimens were 2 inch x 0.375 inch bar stock of 6061-T6 alloy 6 inches in length. The end faces were machined parallel and the plates were then cleaned and etched using methods similar to those currently used by the aircraft industry [16]. The aluminum plate was mounted in a mold with inserted teflon sides and end pieces, which were washed in detergent and air dried before casting of the epoxy. The epoxy consisted of 100 parts by weight of DER 332 epoxy resin and 12.5 parts by weight of tetraethylene pentamine hardener (TEPA). The mixture was heated to 110°F before casting to remove entrapped air bubbles and decrease viscosity. Solidification occurred in approximately one hour, and specimens were subsequently removed from the mold and post cured at 125°F for four hours. Dimensions of the epoxy plate were 2 inches in width x 4 inches in length x 0.375 inches in thickness. Values for the Young's modulus, E, and Poisson's ratio, ν, for the aluminum were $E = 10^7$ psi and $\nu = 0.33$, and for the epoxy $E = 5.7 \times 10^5$ psi and $\nu = 0.34$.

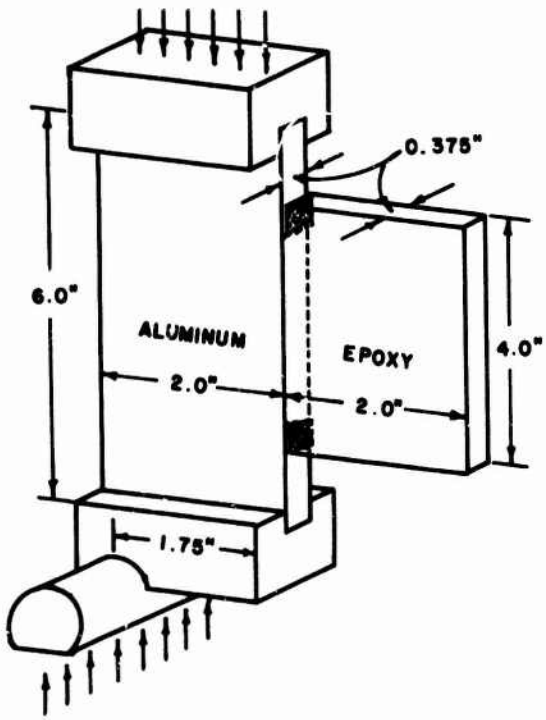

Figure 2 Specimen geometry and loading fixtures

After post-curing, a saw cut was made in each end of the epoxy along the interface with a .020" thick blade. A razor blade was then used as a wedge to initiate a crack from the sawed notch. Bending loads were then applied to the aluminum plates at a rate of 500 lb/min as shown in Figure 2, and the progress of interfacial failure was observed. Under this loading cracks did propagate along the interface, and for bond lengths

which were small with respect to other plate dimensions, the data could be analyzed using the techniques presented in the previous section.

For this specimen, strain along the interface was determined from

$$\eta = \eta_M^L - \eta_M^R = \frac{-y^L}{R^L} + \frac{y^R}{R^R} + \frac{XX_1}{E_1} - \frac{XX_2}{E_2} \qquad (3)$$

where, as shown in Figure 3, $y^L = y - h_e/2$ is the distance from the neutral axis of the epoxy plate of depth h_e, $y^R = y + h_a/2$ is the distance from the neutral axis of the aluminum plate of depth h_a, R^L and R^R are the radii of curvatures of the neutral axes, epoxy and aluminum respectively, due to flexure alone. This geometric description for bending analysis of two bonded plates follows closely the methods used by Boley, B.A. and Weiner, J.H. [17] for thermoelastic analysis of bending and buckling of bi-metallic beams. Evaluating this expression on A′ corresponds to setting y = 0 in the relations for y^L and y^R defined above. XX_1 and XX_2 are uniform stresses applied parallel to the bond in the epoxy and aluminum respectively and E_1 and E_2 are Young's moduli of the epoxy and aluminum respectively.

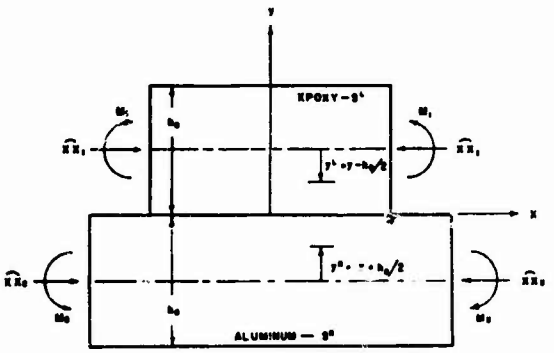

Figure 3 Plate specimen under self-equilibrating bending and compression loading

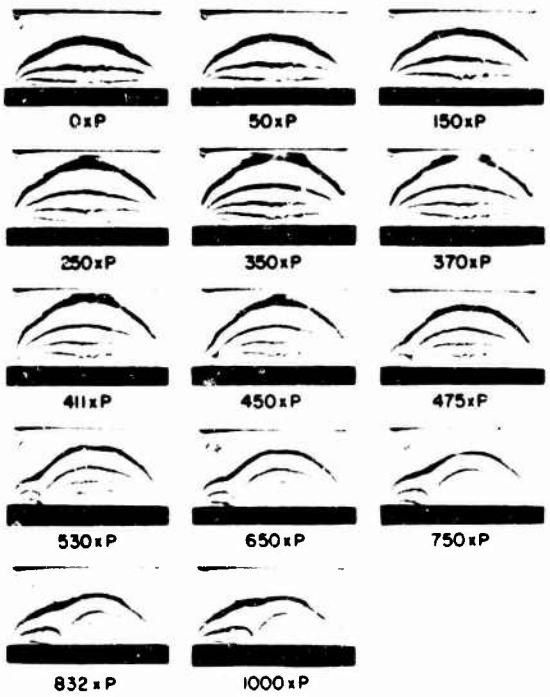

Figure 4 Isochromatic patterns for bonded plate under bending loads, P = 9.4 lbs

Light field isochromatic fringe patterns are shown in Figure 4 for a bending specimen under progressively increasing load (P = 9.4 lbs). As shown in this figure, an increase in the applied load parallel to the bond resulted in an increase in the fringe order along the bond. The fringe pattern showed a decrease in fringe order behind the crack tips. It was relatively easy to follow the progress of the crack since the fringes approach the interface near the crack tip. Non-symmetric crack growth was observed in a number of these specimens. However, analysis of interfacial failure involves only the total bonded length and is unaffected by non-symmetric crack growth.

A specimen of somewhat different design was used to determine the magnitude of the residual stress field induced due to casting and post-curing of the epoxy. This specimen was made by taking a 1" X 1" X 6" aluminum bar and casting a 2" X 4" X 3/8" epoxy with a 4" X 3/8" surface of the latter centrally located on a 1" X 6" aluminum surface. Compressive loads were then applied to the one inch square ends of the aluminum bar. Because of the difference in coefficient of thermal expansion of these materials and the elevated curing temperature, a tensile stress resulted in the epoxy when the specimen was returned to room temperature. Therefore, application of a compressive load to the aluminum parallel to the bond reduced the magnitude of the tensile residual stress. This was evidenced by a relaxation in the isochromatic pattern introduced during post-curing. Photographs of the light field isochromatic fringe patterns for the compression study are shown in Figure 5. Initial birefringence, as in the first frame of Figure 5, arose from two sources, elastic residual stresses and frozen stresses. The elastic stress field produced during the casting, post-curing and subsequent cooling process, stored elastic energy which was available for release to the fracture process. When the epoxy was debonded completely from the aluminum bar, birefringence due to the elastic stress field vanished, while birefringence due to the frozen stress field, which does not contribute to the fracture process, remained in the epoxy. To determine the magnitude of the elastic stress field, the position of the isochromatic fringes were measured along the center line perpendicular to the bond for various compressive loads applied to the aluminum bar. These results are shown in Figure 6. After crack propagation tests were completed on bending specimens, the epoxy was debonded and the position of the frozen isochromatic fringes were measured. The elastic strain required to produce an isochromatic pattern corresponding to the frozen isochromatic pattern was determined from Figure 6. Measurement of the position of the 1/2 order fringe taken from the frozen isochromatic patterns from eleven specimens ranged from 0.625" to 0.84". For these specimens the elastic strain due to residual stresses was 160 μ in./in. $\pm$ 20%. This value was used in calculations of the energy required for crack propagation along the bond. For the compression specimen, crack propagation did not occur at the interface. Rather, the cracks deviated from the

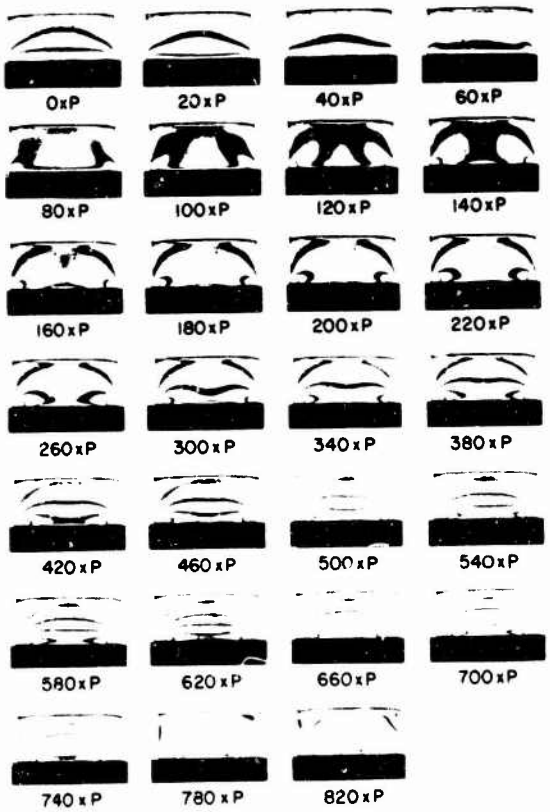

Figure 5 Isochromatic patterns for a bonded plate under compression loads, P = 47.1 lbs.

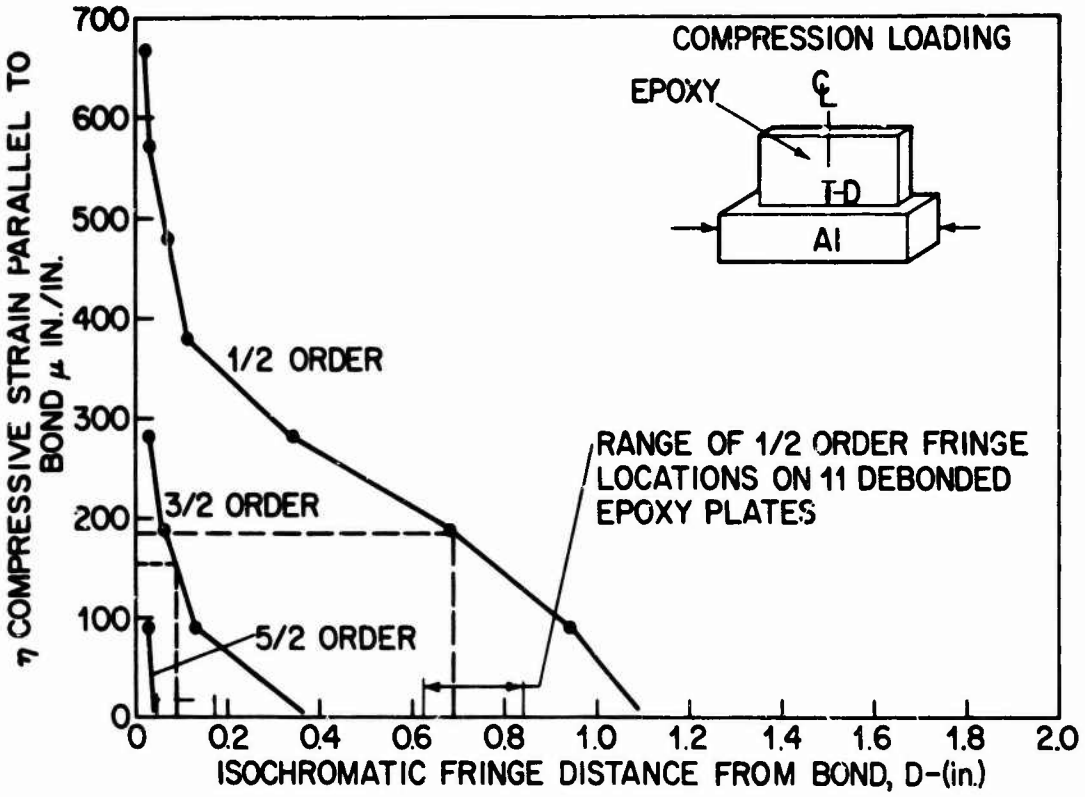

Figure 6 Strain vs isochromatic fringe distance from bond under compression loads

interface into the epoxy. This observation is in agreement with the theoretical analysis which predicts compressive normal stresses near the crack tip that may inhibit interfacial crack propagation.

RESULTS AND DISCUSSION

Using the formulation of the theoretical section, the strain energy release rate $\mathcal{J}$, was calculated at various crack lengths along the bond. This analysis is for two-dimensional bonded plates under either plane stress or plane strain conditions. In general, however, analysis of bonded plates is considered as a three-dimensional problem, since these plates experience a contraction in the thickness direction during curing or under mechanical loading. Durelli, et al [18] have shown that this pinching has little effect on the normal stress and strains along a bond for materials with similar Poisson's Ratio, and consequently, the two-dimensional analysis was considered adequate. Plane strain conditions were assumed in this analysis. From a physical point of view this is a reasonable assumption, since the aluminum constrains the epoxy at the interface. At regions remote from the interface, plane stress analysis may be more appropriate, since this constraint is no longer present.

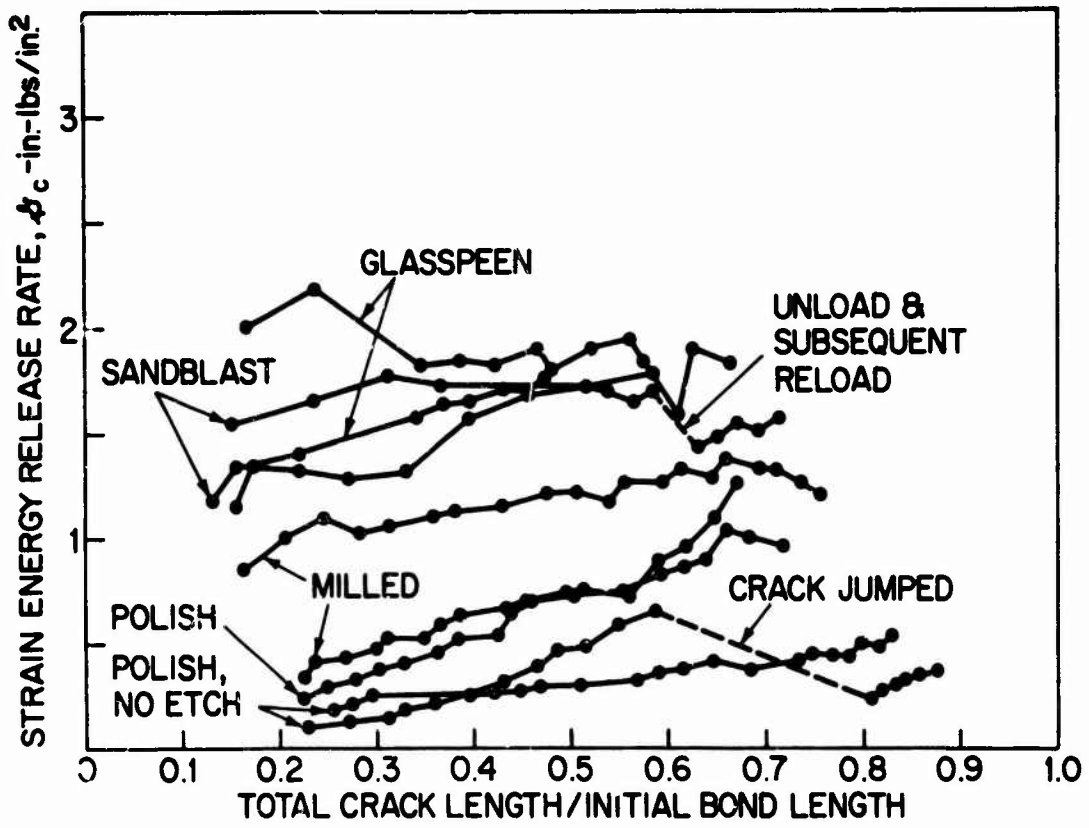

Figure 7 Strain energy release rate vs crack length/initial bond length for various finishes specimens under bending loads

Data shown in Figure 7 compares the results for bending tests on glass-peened, milled and sandblasted surfaces with polished aluminum surfaces. These values are generally greater than the value of $\mathcal{G} = 0.5$ in. lb/in.^{2} for the bulk epoxy system reported by Mostovoy and Ripling [19]. However, for the polished specimens, the value of $\mathcal{G}$ are approximately equal to the bulk values. A summary of the average strain energy release rates and crack velocities are presented in Table 1. It can be seen from Table 1 that the crack velocities measured, $\dot{m}$, were fairly uniform and indicate relatively slow crack growth. The $\mathcal{G}$ values quoted here can be taken as representative of these slow crack growth conditions. Polished, milled, glass-peened and sandblasted surfaces were etched prior to casting of the epoxy except as noted. Included also were measured values of the surface roughness for the various surface finishes. Surface roughness measurements were made with a profilometer which draws a tracer point across the surface and indicates the arithmetic average of the roughness. The tracer point used for these measurements was conical with a hemispherical tip having a 0.0005 radius. Figure 8 shows that for polished, glass-peened and sandblasted surfaces, which were etched prior to casting and were subjected to bending loading, there is a linear relation between surface roughness and strain energy release rate. This can be expressed as

$$\mathcal{G} = 0.014\ S + 0.9 \qquad (4)$$

	Spec	Polished (No etch)		Polished		Milled		Glass Peened		Sandblast	
		[1]$\bar{X}$	[2]S	$\bar{X}$	S	$\bar{X}$	S	$\bar{X}$	S	$\bar{X}$	S
Bending											
$\mathcal{G}$ in-lb/in^2	1	0.40	0.15	1.0	0.20	0.8	0.11	1.6	0.10	2.5	0.44
	2	0.42	0.07	—	—	1.3	0.06	1.9	0.13	1.8	—
$\dot{m} \times 10^{-3}$ in/sec	1	3.2	—	3.6	—	3.2	—	—	—	—	—
	2	3.3	—	—	—	—	—	—	—	—	—
Surface Roughness											
No Etch	[3]L	2.4	1.1	—	—	126	32.9	53	4.8	93	8.1
	[4]T	—	—	—	—	43	14.6	—	—	—	—
Etch	L	—	—	6.6	1.1	91	26.8	51	3.6	92	7.4
	T	—	—	—	—	56	11.4	—	—	—	—

[1]Average value
[2]Standard deviation
[3]L = Longitudinal or Lengthwise direction
[4]T = Transverse or thickness direction

Table 1 Average strain energy release rate, crack velocity and surface roughness for various surface finishes

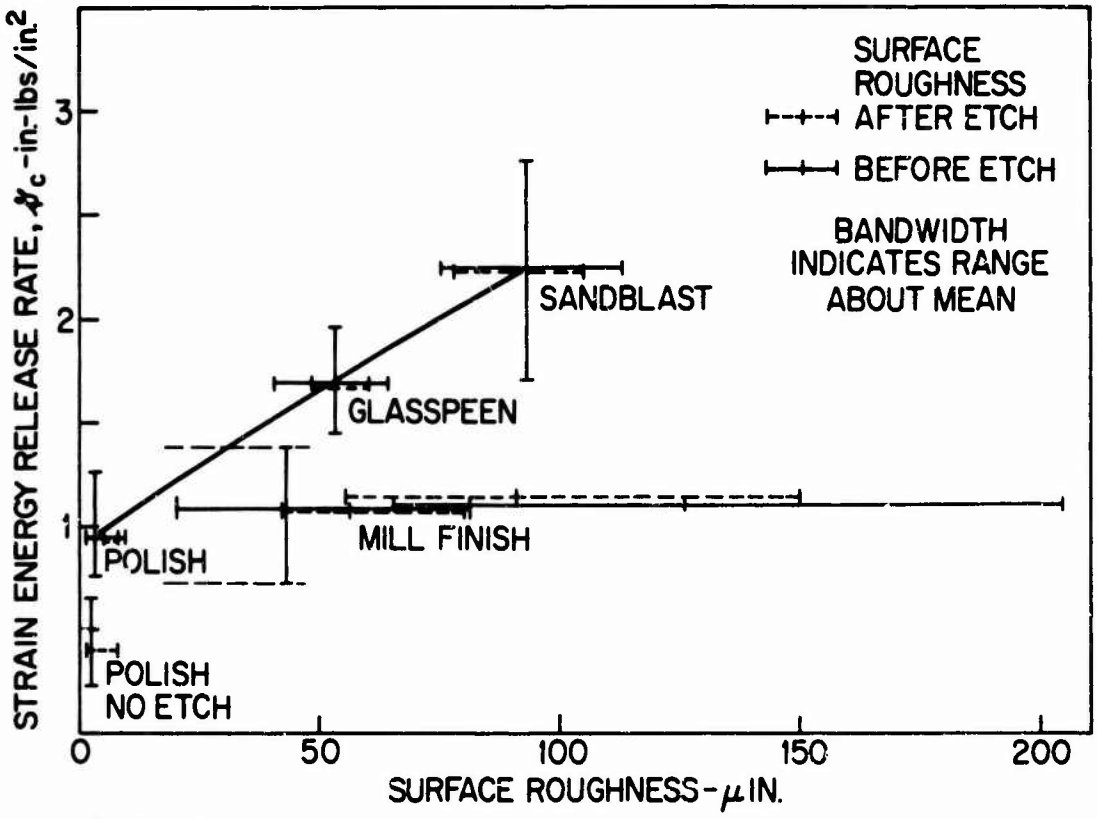

Figure 8 Strain energy release rate vs surface roughness for specimens under bending loads

where S is the surface roughness in microinches measured using the method described above. Data in Table 1 indicate that the milled surface roughness is non-uniform, i.e., the surface roughness along the length of the bond is greater than the roughness in the thickness direction. From fracture surface observations it is apparent that this variation is due to the milling operation, which produces high roughness values in the longitudinal or lengthwise direction but low values in the thickness direction. Roughness measurements in the thickness direction of the milled specimens fall within the range predicted from the relation between surface roughness and strain energy release rate for the other surface finishes studied. Therefore, the strain energy release rate may be determined from the minimum value of surface roughness over the range considered in this study. Indications from optical observations of the fracture surfaces show that the crack replicates the surface finish of the aluminum as it propagates along the bond. Based on the relation developed between initial surface roughness and $\mathcal{J}$, greater roughness of fracture surfaces in the epoxy indicate higher strain energy release rates were required for crack propagation. The effect of loading rate or crack velocity on this behavior was not considered here, although this is an important factor which may affect the failure mode. This result is useful in failure analysis of bonded structures. In many instances the circumstances which caused failure are unknown, and the origin, direction of crack propagation and energy required for crack growth must be determined from observations of the failure surface.

Higher magnification studies using the scanning electron microscope indicate that there is a residue of epoxy, which remains bonded to the aluminum surface. These studies also indicate that for stable crack propagation, crack growth occurs very near the interface. Studies conducted by Bascom [20] on scarf joints of aluminum bonded with epoxy also indicate that a residue of epoxy remains on the aluminum after interfacial failure. By radioisotope tagging with Carbon-14 he found that a 300 to 500 angstrom layer of resin is left on the aluminum. His fractured specimens also exhibit replication of the scratches and machining marks of the aluminum surface on the resin fracture surface.

CONCLUSIONS

The purpose of this investigation was to characterize crack propagation at the interface between two dissimilar materials using a formulation based on strain energy release rate and to determine the contribution of the residual stress field to the energy required for crack propagation at an epoxy-aluminum interface. To this end, a theoretical analysis was developed for the plane problem of two elastic half spaces in contact along an arc where one of the materials acts as a relatively rigid body. The stress analysis included the cases of residual stresses, thermal loading and self equilibrating tensile or bending loading applied to either half space. Using this analysis, the elastic strain energy release rate, $\mathcal{J}$, was formulated as a fracture criteria for interfacial failure.

Experimental studies were conducted on specimens of epoxy bonded to

aluminum. In the fabrication of these specimens, the epoxy was cast against the aluminum, and after initial curing, the specimens were post-cured at elevated temperature. This procedure resulted in residual stresses as evidenced by birefringent patterns in the epoxy. The magnitude of the residual stress due to this casting and curing process was determined by photoelastic techniques. Methods were developed for analyzing the birefringent pattern in the epoxy in order to separate the contribution of the elastic residual stress field from that of the frozen stress field. In analyzing interfacial failure of these specimens, knowledge of the magnitude of elastic residual stress field is required, since these stresses contribute to the energy necessary for interfacial crack propagation. As a result of these studies, it was found that elastic residual stresses in this particular geometry and material combination can contribute 15 to 20 percent of the energy required for initial crack initiation at the interface.

Following the casting and curing process, cracks were initiated in the epoxy at the interface, and then these specimens were subjected to mechanical loading. The process of interfacial crack propagation was observed, and the data was analyzed using the fracture mechanics fromulation derived from the theoretical stress analysis. Results of this analysis indicated that $\mathcal{G}$ can be used to characterize elastic debonding, since the strain energy release rate and crack velocity remained relatively constant as the crack propagated along the bond.

The effect of surface roughness of the aluminum on fracture toughness was measured for four different surface finishes. It was found that increased surface roughness resulted in greater fracture toughness, e.g., sandblast or glass-peen finishes on the aluminum resulted in higher toughness than machined or polished surfaces. This may be explained by the observation that the interfacial cracks replicated the surface fracture of the aluminum. Microscopic studies of the failure surfaces indicate that crack propagation occurs in the epoxy very near the interface, and that a residue of epoxy remains bonded to the aluminum. Therefore, greater surface roughness resulted in greater crack area and higher toughness. This implied that the $\mathcal{G}$ is dependent on the local character of the surface rather than on gross non-uniformity such as those present in the milled specimen. From this data a linear relation was suggested between strain energy release rate and surface roughness over the range of surfaces examined in this study.

The techniques presented in this paper provide a simple method for the study of interfacial failure in bonded materials, where one of the materials acts as a relatively rigid body. Results of this investigation have application in design of bonded structures, or in general problems of debonding and delamination between dissimilar bodies. The analysis can be applied to composite materials in analysis of glass-resin interfaces, in bonded joints or in welded structures where the crack propagates at the interface. This approach can be extended to consider the effects of crack velocity, fatigue loading, environment and various residual fields on the fracture toughness of bonded materials.

ACKNOWLEDGEMENTS

The authors acknowledge the support of the Office of Naval Research, The Naval Ships Systems Comman and The Catholic University of America for the work reported herein, conducted under Project Number RR-023-03-45-5451 and SF 51-544-102-12432.

REFERENCES

1. Williams, M. L., "The Stressed Around a Fault or Crack in Dissimilar Media," Bulletin of the Seismological Society of America, v. 49, no. 2, April 1959, 199-204.

2. Erdogan, F., "Stress Distribution in a Nonhomogeneous Elastic Plate with Cracks," J. of Applied Mechanics, Series E, v. 30, no. 2, June 1963, 232-236.

3. Erdogan, F., "Stress Distribution in Bonded Dissimilar Materials with Cracks," J. of Applied Mechanics, Series E, v. 32, no. 2, June 1965, 403-410.

4. England, A. H., "A Crack Between Dissimilar Media," J. of Applied Mechanics, Series E, v. 32, no. 2, June 1965, 400-402.

5. Sih, G. C. and Rice, J. R., "The Bending of Dissimilar Materials with Cracks," J. of Applied Mechanics, Series E, v. 31, no. 3, Sept. 1964, 477-482.

6. Rice, J. R. and Sih, G. C., "Plane Problems of Crack in Dissimilar Media," J. of Applied Mechanics, Series E, v. 32, no. 2, June 1965, 418-423.

7. Wu, E. and Thomas, R. L., "Interfacial Fracture Phenomena," Proceedings of the Fifth Int'l. Congress on Rheology, v. 1, 1969, 575-587, Univ. Park Press, Baltimore, Md.

8. Wang, C., "Fracture Mechanics for an Interfacial Crack Between Adhesively Bonded Dissimilar Materials," Dept. of Theoretical and Applied Mechanics, Report No. 353, Univ. of Illinois at Urbana-Champaign, March 1972.

9. Williams, M. L., "The Continuum Interpretation for Fracture and Adhesion," J. of Applied Polymer Science, v. 13, 1969, 29-40.

10. Williams, M. L., "The Fracture Threshold for an Adhesive Interlayer," J. of Applied Polymer Science, v. 14, 1970, 1121-1126.

11. Williams, M. L., "Cohesive-Adhesive Fracture in a Pressurized Double Blister," J. of Adhseion, v. 5, no. 1, Jan. 1973.

12. Burton, J. D., Jones, W. B. and Williams, M. L., "Theoretical and Experimental Treatment of Fracture in an Adhesive Interlayer," Trans. of the Society of Rheology, v. 15, no. 1, 1971, 39-50.

13. Bennett, S. J., DeVries, K. L. and Williams, M. L., "Adhesive Fracture Mechanics," International Journal of Fracture, v. 10, no. 1, March 1974.

14. Milne-Thomson, L. M., "Plane Elastic Systems," Springer-Verlag, Berlin, 1960.

15. Mulville, D. R., "Characteristics of Crack Propagation at the Interface of Two Dissimilar Media," Doctoral Dissertation, The Catholic University of America, 1974.

16. De Lollis, N. J., "Adhesive for Metals," Industrial Press, Inc., New York, N. Y., 1970.

17. Boley, B. A. and Weiner, J. H., "Theory of Thermal Stress," J. Wiley and Sons, New York, 1960, 429-432.

18. Durelli, A., Parks, V., Feng, H. and Chiang, R., "Strains and Stresses in Matrices with Inserts," Mechanics of Composite Systems, Proceedings of 5th Symposium on Naval Structural Mechanics, Edited by Wendt, J., Liebowitz, H. and Perrone, N., Peragammon Press, New York, 1970, 265-336.

19. Mostovoy, S. and Ripling, E., "Fracture Toughness of an Epoxy System," J. of Applied Polymer Science, v. 10, 1966, 1351-1371.

20. Bascom, W. D., "Surface Aspects of Bonding Metals with Polymer Adhesives," Polymer Conference Series on Adhesion, University of Utah, Salt Lake City, Utah, July 1973.

SESSION III - FASTENERS-1

Chairman: J.H. Crews
Aerospace Technologist
NASA - Langley Research Center

ELASTIC-PLASTIC ANALYSIS OF INTERFERENCE FIT FASTENERS

N. D. GHADIALI
Engineering Scientist

A. T. HOPPER
Associate Manager

S. G. SAMPATH
Researcher

F. A. SIMONEN
Engineering Scientist
Battelle's Columbus Laboratories
Columbus, Ohio 43201

ABSTRACT

The paper describes an elastic-plastic finite element capability suitable for interference fit fastener analyses. The effect of sequential application of cyclic loads may also be included. Numerical solutions for three problem cases are presented. A thick-walled Lamé cylinder under cyclic internal pressure has been analyzed to verify the computer program. A plugged, no-load-transfer specimen sequentially loaded by elastic fastener interference and axial tension has been analyzed, along with the case of a round fastener in an out-of-round hole.

INTRODUCTION

Interference fit fasteners are used to improve fatigue performance of structural joints. Stress analysis methods for such types of structures must take into account the effect of interference fit bolts on the elastic-plastic strain field of the structure as a function of load and geometric parameters and the effect of sequential and cyclic loads on the stress and strain distributions. This paper contains a description of an elastic-plastic finite element capability that has been developed for such types of analyses for axisymmetric and plane stress models. The effort is part of an overall Air Force-sponsored research program to develop methods of predicting fatigue performance of interference fit fastener under both constant amplitude and spectral loading via an integrated analytical and experimental approach.

A large quantity of experimental data on cyclic behavior of metals subjected to uniaxial loading is available. However, efforts at characterizing these results either through empirical relationships or rheological models as evinced by Martin, Topper, and Sinclair [1] have proved to be a formidable task. Biaxial or triaxial stress states around interference fit fasteners and stress and strain concentration effects make the problem additionally complex. A general discussion on the improvement in fatigue strength in joints resulting from interference fasteners and rivets has been given by Schjive [2]. A finite element analysis approach similar to the work presented

here has been used by Brombolich [3] to consider load sequence effects and the effect of friction and fretting on the stress distribution around the hole boundary. However, the sole emphasis by Brombolich is on the stress distribution around a fastener as the critical design factor to the exclusion of the plastic strain field. An important observation has been made by Brombolich that inclusion of frictional effects in the analysis leads to a small change in the maximum stress for values of friction coefficient less than 1.0. Some numerical methods of plastic analysis of structures subjected to cyclic loading are described by Armen, Isakson, and Pifko [4] but are not applied explicitly to the fastener problem. Experimental means for measurement of strain distributions around fasteners used by Carey [5] include photoelastic coatings, X-ray diffraction, and a replica strain technique. Each of these has limitations as techniques for measuring plastic strains or stresses. However, the technique of speckle photography appears to offer great promise.*

In this paper a brief description of a computer program used for fastener analysis is followed by three numerical solutions. These solutions include (1) a thick-walled Lamé cylinder under cyclic internal pressure which was analyzed to verify the finite element results with a known analytical solution, (2) a plugged no-load-transfer specimen sequentially loaded by fastener interference stresses and subsequent axial tension, and (3) the case of an oversized round fastener in an out-of-round hole in a square plate. All three solutions involve elastic-plastic analyses. Numerical solutions obtained for a coupon type of specimen is being reported by Adams and Griffith* in order to show the excellent correlation obtained with speckle photography experimental data.

DESCRIPTION OF COMPUTER PROGRAM

The elastic-plastic analysis is based on a constant strain finite element procedure for planar and axisymmetric configurations. In the plastic range the material response is governed by the von Mises yield criteria and the Prandtl-Reuss incremental flow rule. Kinematic strain hardening can be considered in relation to elastic unloading and yielding under stress reversal. In treating the transition of element response from elastic to plastic behavior, the "partial stiffness" approach of Marcal and King [6] is utilized.

Loadings may be applied in an arbitrary sequential fashion to represent loading cycles imposed on fasteners under service conditions. This general capability required modification of an existing elastic-plastic finite element program to permit specification of multiple load states as input data. For each load state, an incremental procedure is followed to follow the course of plastic deformation from one load state to the next. Special numerical procedures were developed for perform appropriate checks at the onset of each change in load state to determine which elements undergo elastic unloading

---

* Adams, F. D., and Griffith, W. I., "Interference-Fit-Fastener Displacement Measurement by Speckle Photography", to be presented at the Army Symposium on Solid Mechanics, 1974.

and which elements continue to yield. The procedure applies a small perturbation to the loading and an elastic analysis is performed to determine whether the von Mises effective stress increases or decreases as a result of the load change.

A second special feature of the computer program allows simulation of the contact conditions along surfaces such as a fastener-hole interface. The technique involves the use of a special type of element to represent the desired type of contact condition. In modeling the region of contact, pairs of nodal points are designated along the interface, with one node in each of the contacting materials. The coordinates of the paired nodal points are identical. These superimposed points, however, are in general allowed to displace independently, with the contact condition being imposed as a constraint through the stiffness characteristics of the special element. Thus, relative displacements normal to the contact surface can be maintained as zero, with the nodal point pairs being allowed to displace freely in the direction tangent to the contact surface. This procedure has been extended to also allow an initial clearance or interference between the contacting surfaces as well as frictional stresses along the surface.

The interfacial node and element configuration is shown in Figure 1 along with the interaction forces. If u_1 and u_2 are the displacement

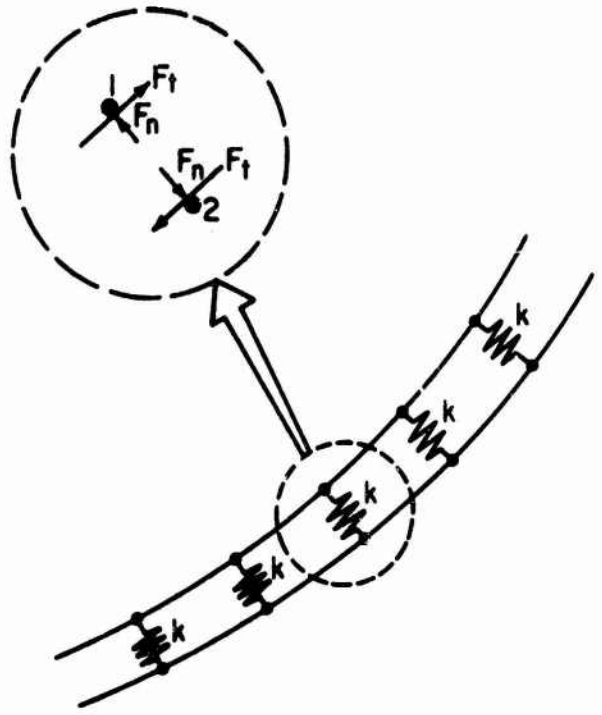

Figure 1 Linear Stiffness Elements and Frictional Forces Acting on Interface

components normal to the contact surface of adjacent nodes, the equal and opposite forces acting between these nodes is given by

$$F_n = k(u_2-u_1) - ku_0 \quad , \tag{1}$$

where u_0 is the initial clearance between the surfaces. The stiffness k is assigned by the computer program to be much larger than the nodal stiffness contributions of the adjacent elements.

The frictional forces F_t between adjacent nodes are treated as external loads and are determined by an iterative procedure. On the first iteration these forces are taken to be zero. On the second and successive iterations, these forces are taken as

$$F_t = \mu F_n \quad , \tag{2}$$

where F_n is the normal force from the previous iteration and μ is the coefficient of friction. This procedure was found to converge rapidly. It should be noted that the condition of Equation (2) could be imposed directly on the system of equations for the nodal point displacements and the iteration process could be avoided. However, this would introduce nonsymmetric terms into the system of equations and thereby prevent the use of the highly efficient solution methods which apply to symmetric systems of linear algebraic equations.

PROGRAM VERIFICATION

The cyclic load capability of the finite element code was demonstrated by analyzing the stresses in a thick-walled cylindrical tube under alternating internal pressure. These results were compared with results obtained from classical plasticity theory for an elastic ideally-plastic thick-walled cylinder for a load-unload internal pressure history as given by Davidson, et al. [7]

The analytical solution for the residual hoop stress (σ_t) upon release of an internal pressure is

$$\sigma_t = \frac{\sigma_y}{\sqrt{3}} \left(1+\frac{b^2}{r^2}\right) \left[\frac{R^2}{b^2} - \frac{a^2}{b^2-a^2}\left(\frac{b^2-R^2}{b^2} + 2 \log \frac{R}{a}\right)\right] , \quad r > R , \tag{3}$$

$$\sigma_t = \frac{\sigma_y}{\sqrt{3}}\left[\frac{b^2+R^2}{b^2} + 2\log\left(\frac{r}{R}\right) - \frac{a^2}{b^2-a^2}\left(\frac{b^2-R^2}{b^2} + 2\log\frac{R}{a}\right)\left(1+\frac{b^2}{r^2}\right)\right], \quad r < R, \quad (4)$$

$$P = \frac{2\sigma_y}{\sqrt{3}}\log\frac{R}{a} + \frac{2\sigma_y}{\sqrt{3}}\left(\frac{b^2-R^2}{2b^2}\right). \quad (5)$$

In the above equations, r is the radial coordinate, a and b are the inside and outside radii of the cylinder, σ_y is the yield strength, P is the pressure, and R is the overstrain radius which marks the interface between the elastic and plastic regions. The two sets of results have been plotted in Figure 2 and show good agreement.

SEQUENTIALLY LOADED FASTENER

The case of a 3/8-inch steel fastener installed in a plugged 7075-aluminum alloy tensile specimen which is subsequently subjected to axial tension has been studied. A plane stress condition was assumed. Due to symmetry only one quarter of the geometry needed to be modeled. The finite element model consisted of 287 nodes and 259 elements. Due to symmetry and the low value of axial load, a non-sliding condition was assumed at the interface of the fastener and the plate. An elastic interference (as opposed to a rigid interference) due to fastener insertion was modeled by artificially ascribing a thermal expansion to the fastener region. The first increment is the interference load which causes the specimen to reach yield. Analyses for several load increments into the plastic range were performed to reach the assumed fastener oversize of 0.005 inches. The stresses were found to be fairly constant around the periphery of the hole, but the plastic strains showed a greater variation. The width of the yield zone was found to be approximately 0.08 inches for the interference of 0.005 inches.

An axial tensile stress of 12,500 psi was then applied incrementally to the ends of the specimen model. The nominal stress at the minimum cross-section corresponding to this axial loading was 25,000 psi or 35% of the yield stress of the material. The von Mises effective stresses and the equivalent plastic strains are plotted in Figure 3 as a function of the radial distance from the hole edge.

Figure 4 shows the striking difference between the results of a sequential load type of analysis and one in which the loads are applied simultaneously. In Figure 4 the stresses and strains in the plate are shown around the fastener interface for the two types of analyses. It is evident that the latter type of solution can grossly underestimate the residual plastic strains.

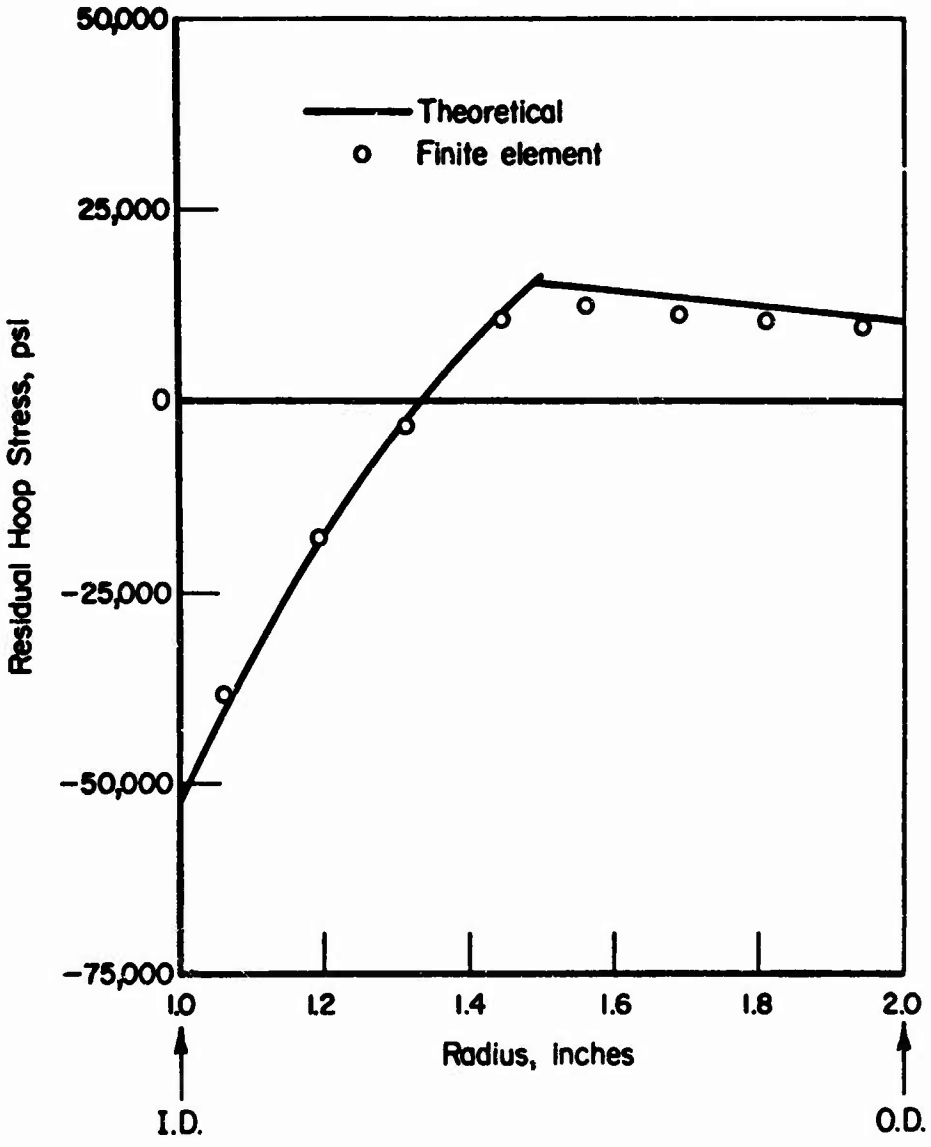

Figure 2 Residual Hoop Stress Distribution in a Thick-Walled Cylinder (Material Yield = 69,800 psi) Unloaded from an Internal Pressure of 50,000 psi

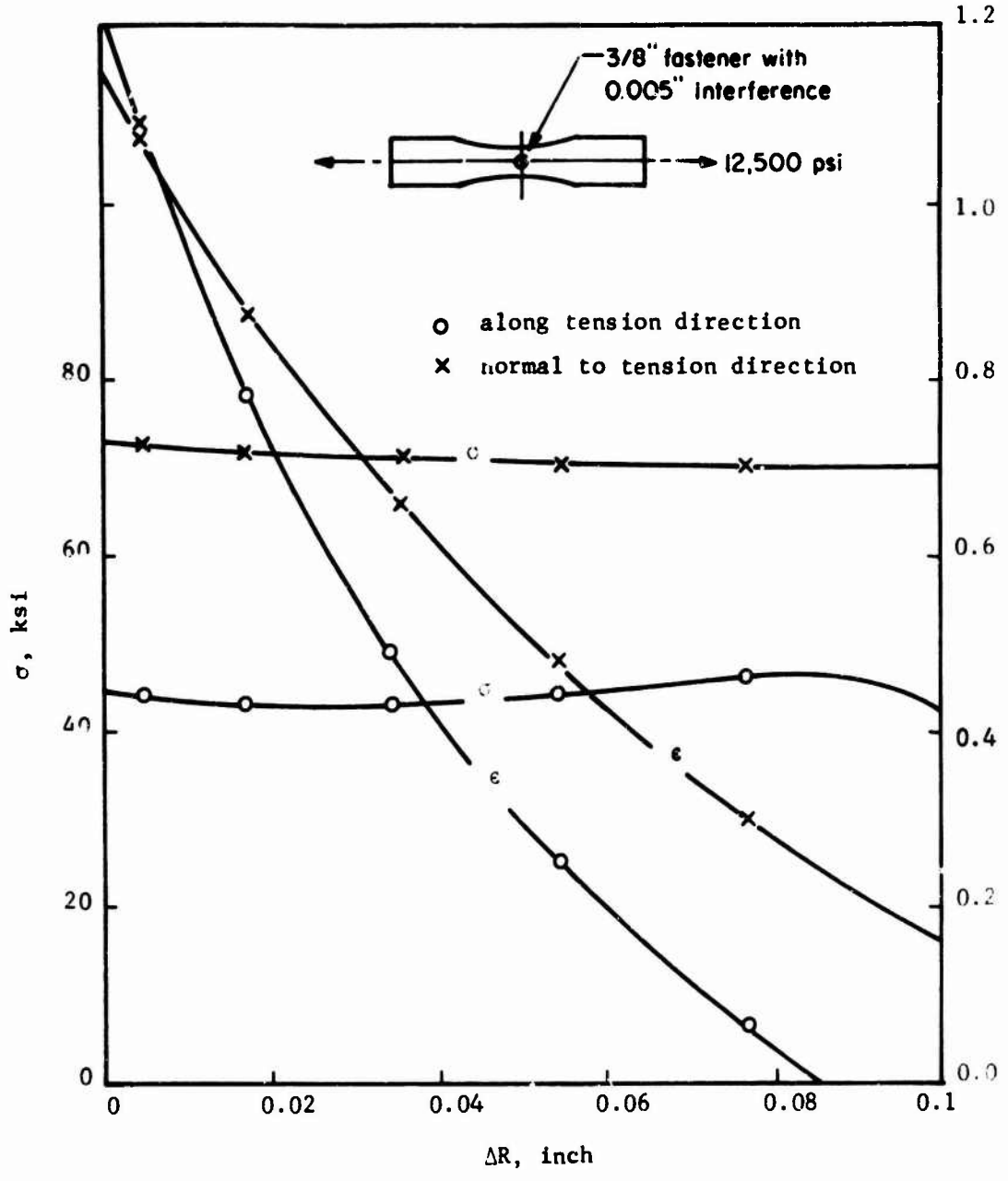

Figure 3 Von Mises Stress and Equivalent Plastic Strain at Various Distances from Hole Edge; σ_y = 69,800 psi

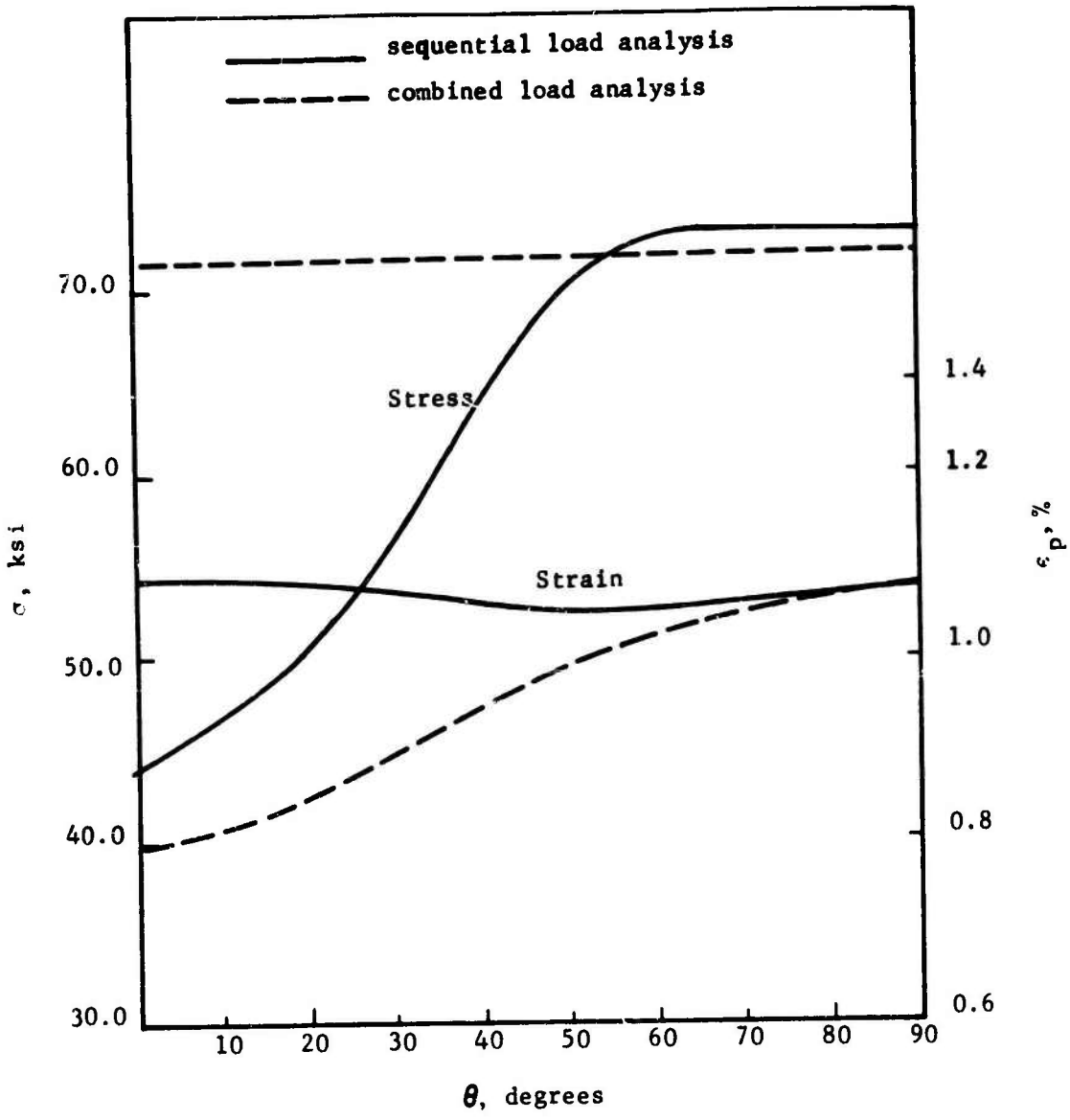

Figure 4 Von Mises Stress and Equivalent Plastic Strain Around the Hole Edge: Comparison Between Sequential and Combined Load Analysis

OUT-OF-ROUND HOLE

The case of an elliptical hole in a square aluminum plate specimen with a 3/8-inch round oversized fastener inserted in the hole has been investigated using the node coupling capability of the code. A plane stress condition was assumed. Again, due to symmetry, only one quarter of the fastener plate configuration was modeled. The finite element grid consisted of 163 nodes and 141 elements. Two sets of nodes on the interface were used in the model to represent the fastener and the plate and to allow the two surfaces to separate. The out-of-roundness of the hole was assumed to be four percent of the fastener diameter. Very small load increments were applied, and following each load increment coupling of the nodes in the radial direction was made in the area where newly-formed contact between the fastener and the hole was indicated. As before, the interference load was modeled by assuming thermal expansion of the fastener. The thermal load was incremented until a value corresponding to a diametral interference of 0.008 inch was reached. The growth of the contact area around one quadrant of the fastener-plate interface is shown in Figure 5. As the figure shows, contact is achieved over an angle of approximately 45° only in spite of the high value of interference imposed. Since fastener designs usually assume a contact area of around 90%, control of hole out-of-roundness in fabrication is seen to be a very sensitive factor in fastener performance. In Figure 6 the radial stress and the equivalent plastic strain around the edge of the hole in the plate have been plotted for the maximum interference value of 0.008 inch. Again, the high values of stress and strain in the contacting region stem from the low area of contact.

A second case of a round fastener in an out-of-round hole was analyzed to determine the stresses and the accompanying plastic strains when the fastener interference was greater than the out-of-roundness, resulting in a snug fit of the fastener in the hole. The geometrical data for this case was drawn from metrology performed on the hole in a certain coupon specimen. The slight experimentally observed asymmetry of the hole periphery was neglected in the analytical model, so that the hole in the finite element model had fourfold symmetry. The 6x6-inch coupon was assumed to be under a plane stress condition. The outer edges of the plate were assumed as clamped. The finite element model consisted of 208 nodes and 180 elements. Figures 7 and 8 depict the stresses around the edge of the hole for two levels of fastener interference. The out-of-roundness of the hole is also shown in the two figures by plotting the difference between the fastener size and the value of the hole radius. As before, high local stresses and plastic strains were indicated. It is interesting to note in Figure 7 that at the point with the least radial contact stress the von Mises stress is still high due to a large circumferential stress.

CONCLUSIONS

The computer program and the analysis procedure can be effectively utilized for stress analyses under cyclic conditions for plane stress or axisymmetric models of fastener insertions. The program has been applied to a number of fastener geometry and loading conditions. The importance of treating sequential loadings has been demonstrated. A number of areas for

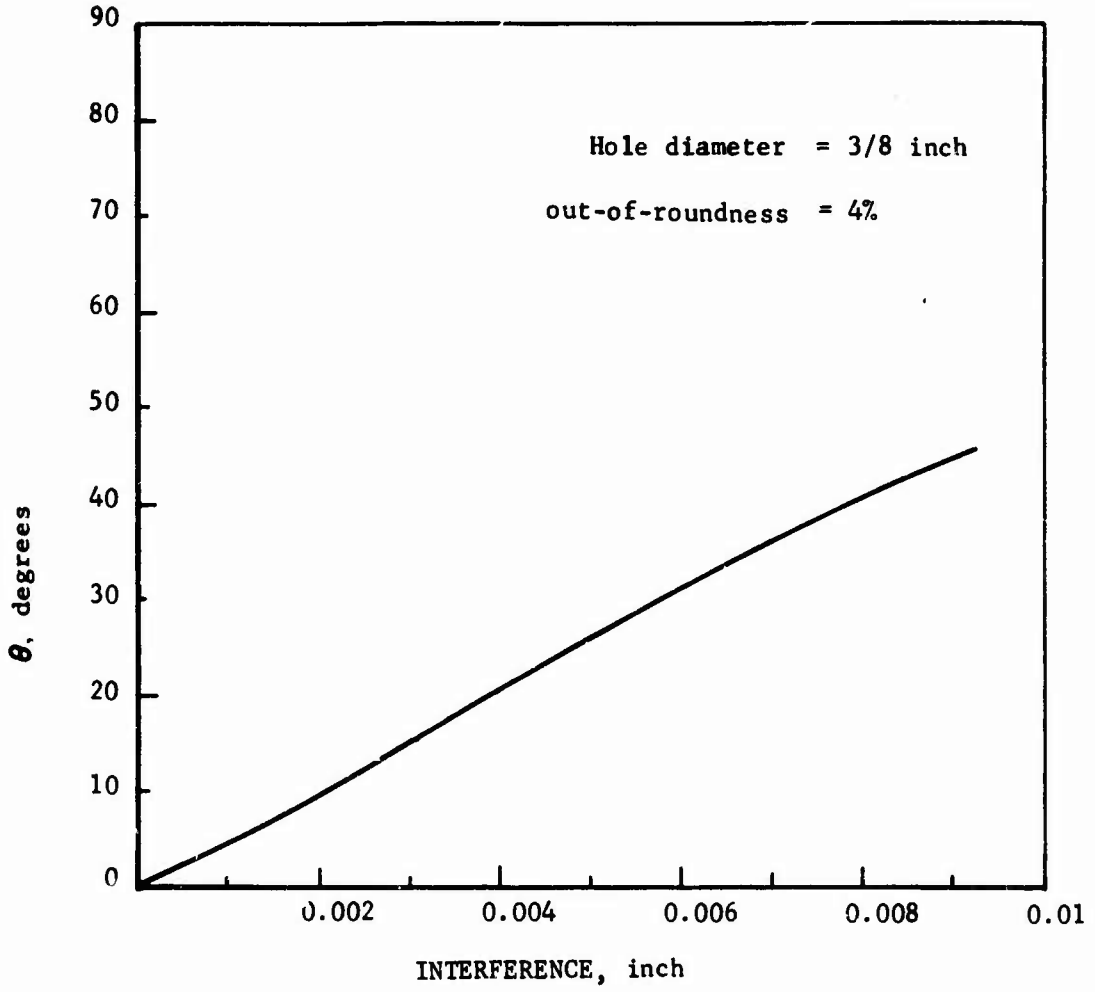

Figure 5 Contact Angle Achieved Between Fastener and Out-of-Round Hole Surfaces for Various Interferences

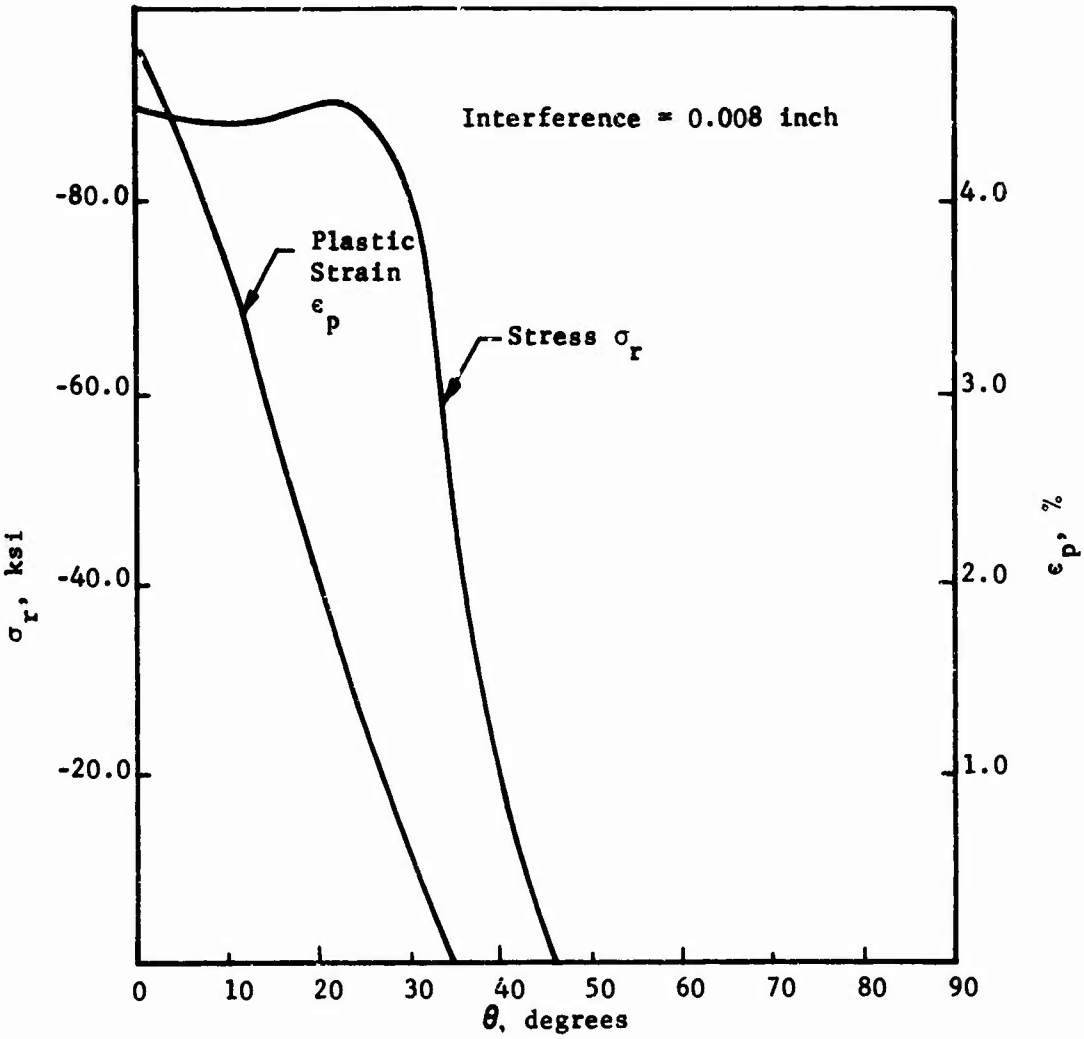

Figure 6 Radial Stress and Equivalent Plastic Strain Around Edge of Out-of-Round Hole

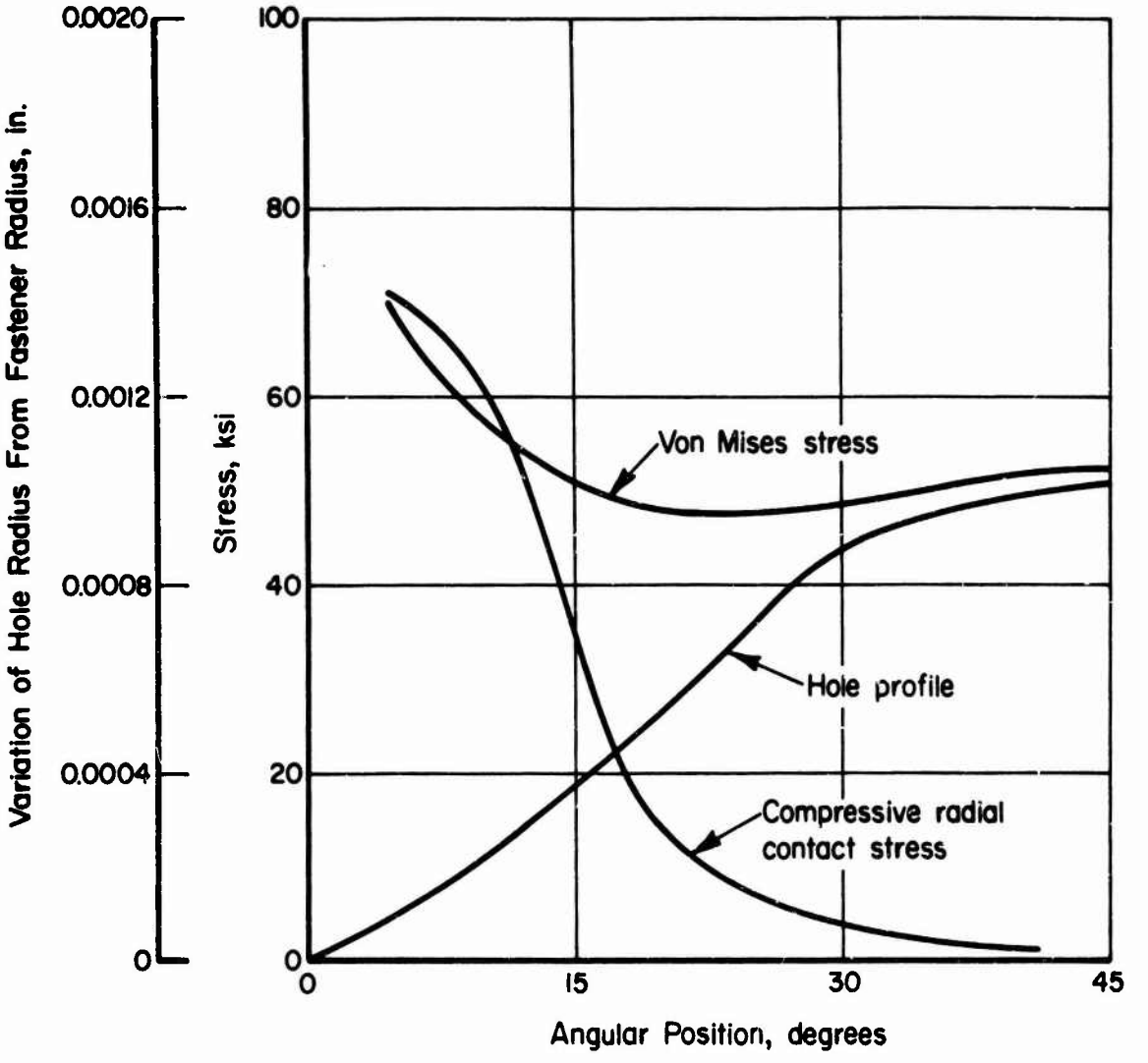

Figure 7 Geometry of Out-of-Roundness of Hole and Contact Stress Distribution Around the Edge for Interference Load Which Causes Initial Yield in Specimen; Diametrical Interference = 0.00271 inch

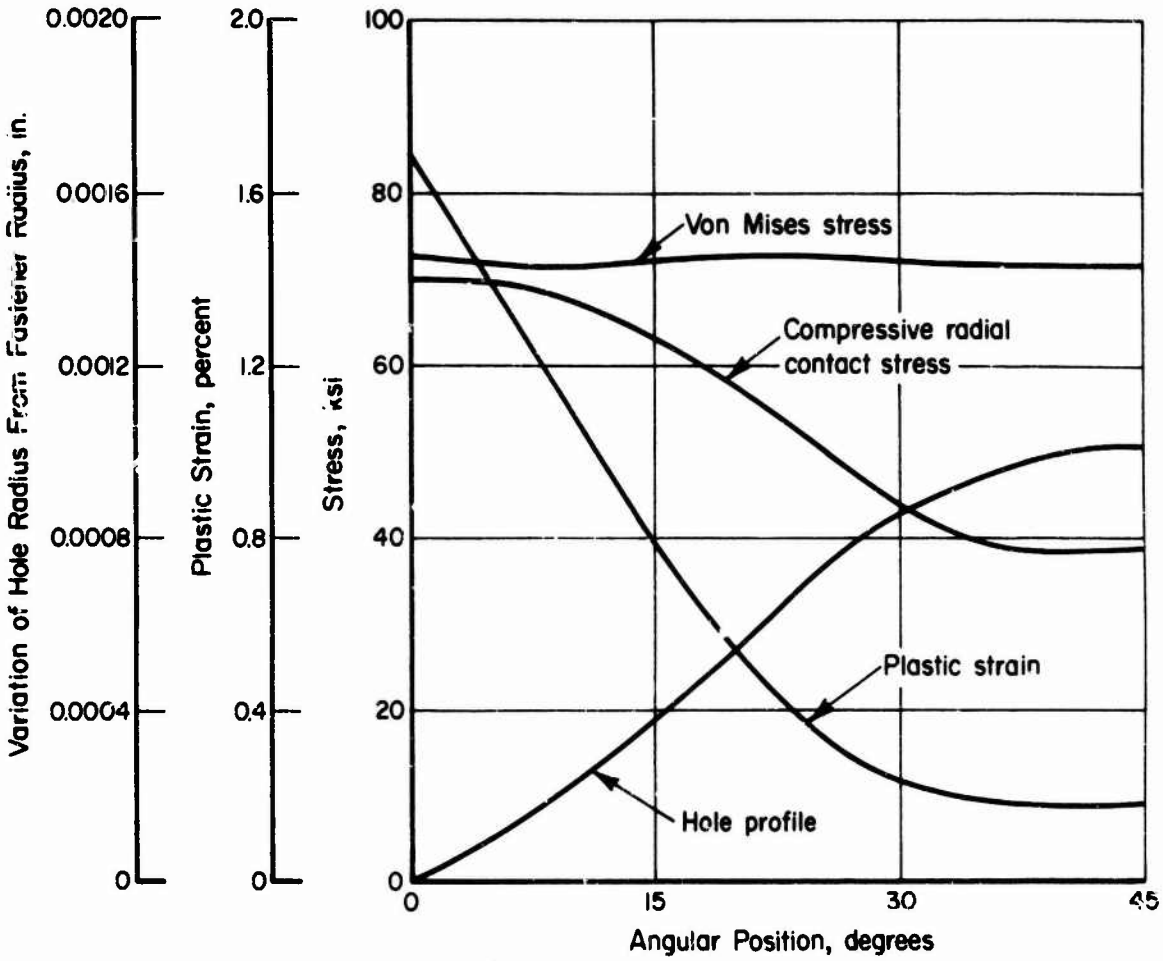

Figure 8 Stress and Plastic Strain Distribution Around the Edge of Out-of-Round Hole for Maximum Interference; Diametrical Interference = 0.005 inch

future study remain. The program can easily incorporate a Ramberg-Osgood type of stress-strain curve or yield stress changes due to cycling. Also, computer programs with three-dimensional solid elements can be similarly modified to treat more complicated geometries which are encountered in joints. Various factors like fastener size, sheet thickness, degree of roundness of fastener shank and hole, edge distance, angle and taper, hole perpendicularity, taper mismatch, types of bolt, nut and joint materials all influence the fatigue life of an interference fit fastened joint. Quantitative analyses to determine the degree of influence under cyclic load situations are goals of this research program.

ACKNOWLEDGEMENTS

The work reported herein was sponsored by the Air Force Flight Dynamics Laboratory, Wright-Patterson Air Force Base, Ohio, under Contract No. F33615-73-C-3121, with Dr. Frank Adams as the Program Monitor.

REFERENCES

1. Martin, J. F., Topper, T. H., and Sinclair, G. M., "Computer-Based Simulation of Cyclic Stress-Strain Behavior with Applications to Fatigue", Mat. Res. Stand. J., v. 11, February 1971, 23-28, 50-51.

2. Schjive, J., "Fatigue of Lugs", Contributions to the Theory of Aircraft Structures, Professor A. van der Neut, Anniversary Volume, NLR MP 72022 W, NIJGH-Wolters, Noordhoff University Press, 1972.

3. Brombolich, L. J., "Elastic-Plastic Analysis of Stresses Near Fastener Holes", presented at Eleventh Aerospace Sciences Meeting, AIAA, Washington, D.C., January 1973.

4. Armen, H., Isakson, G., and Pifko, A., "Discrete Element Methods for the Plastic Analysis of Structures Subject to Cyclic Loading", Int. J. Num. Meth. Engng., v. 2, 1970, 189-206.

5. Carey, R. P., "Experimental Determination of Strain Fields Resulting From Interference Fit Tapered Pins", Australian Defense Scientific Service Report, Aeronautical Research Laboratories, ARL/SL.377, June 1972.

6. Marcal, P. V., and King, I. P., "Elastic-Plastic Analysis of Two-Dimensional Stress Systems by the Finite Element Method", Int. J. Mech. Sci., v. 9, 1967, 143-155.

7. Davidson, T. E., Barton, E. E., Reiner, A. N., and Kendal, D. P., "The Autofrettage Principle as Applied to High-Strength Light-Weight Gun Tubes", Watervliet Arsenal Report, Watervliet, New York, October 1959.

INTERFERENCE-FIT FASTENER DISPLACEMENT MEASUREMENT BY SPECKLE PHOTOGRAPHY

FRANK D. ADAMS
Physicist
Air Force Flight Dynamics Laboratory
Wright-Patterson Air Force Base, Ohio

WILLIAM I. GRIFFITH
Researcher
Battelle's Columbus Laboratories
Columbus, Ohio 43201

ABSTRACT

A relatively new technique called laser-speckle photography has been used to measure displacements induced by the installation of an interference-fit fastener in a coupon specimen. The technique, itself, is described in detail. Experimental results are presented and compared to finite-element calculations. The correlation between theory and measurement is shown to be excellent.

I. INTRODUCTION

The objective of this paper is to report on a relatively new technique for experimental stress analysis being applied to an investigation of interference-fit fasteners. Before describing the technique, we shall include in the introduction a brief discussion of the fastener problem itself.

In any assembled structure, the jointing and fastening of two member elements has traditionally presented a problem to the designer. In recent years, the ever increasing requirement for high-performance aircraft has forced the use of high-strength metals. These materials are, in general, more susceptible to fatigue failure especially in the area of fasteners. In order to combat this difficulty, designers have turned to more fatigue-resistant fastening concepts such as the interference-fit fastener (IFF). If properly employed, an IFF will reduce stress amplitude excursions in the vicinity of the fastener and thus improve fatigue performance of the joint[1].

A common type of IFF is an oversize tapered bolt which is force fit into a tapered hole. These are being used by the millions in current military and civilian aircraft structures. In a majority of the locations where IFFs have been employed, satisfactory fatigue performance has been attained. However, a few failures have been noted and these have uncovered gaps in our understanding of the basic mechanism involved. In addition, it was learned that less than adequate analytical tools are available for design engineers to predict fatigue performance of joints fastened with IFFs.

The Air Force Flight Dynamics Laboratory is presently sponsoring a contract program with Battelle's Columbus Laboratories to develop methods of predicting the fatigue performance of tapered bolt IFFs.* This effort encompasses analytical and experimental work, as well as cyclic fatigue tests of joint specimens to validate methods which are developed. One part of this

* Air Force Contract F33615-73-C-3121.

program involves analytical computations of the stress/strain field in the vicinity of IFFs. Finite-element methods are being employed. In order to validate these analyses, experimental measurements are required, and a relatively new technique called speckle photography was chosen to provide part of these data.

It should be mentioned at the onset that speckle photography is not the only method being employed to verify our finite-element analyses. Conventional strain gages and a method called dislocation etching technique[2] are also being used. Other techniques such as photoelastic coatings and moire were considered but rejected because of low sensitivity. Holographic interferometry, which can detect very small displacements, was also discarded. This technique is relatively easy to apply when displacements are normal to the specimen surface but becomes overly complicated and difficult to use for measuring in-plane strain. Speckle photography has comparable sensitivity to holography and is ideally suited for in-plane measurements. This new technique and its application to the IFF problem is the subject of this report.

In Section II, speckle photography as a technique is explained and discussed. The specific apparatus required and procedures used to employ this method with IFFs are described in Section III. Results are presented and discussed in Section IV. The final section is devoted to a summary and a discussion of future plans.

The data reported in Section IV concern only coupon-type specimens in which tapered bolt IFFs are fitted into tapered holes. Speckle photography is used to obtain the displacement field within a few radii of the hole that is incurred as a result of force fitting the fastener. At this writing, similar data on joint specimens have not been obtained. These measurements will be made in the near future. In addition, we are planning to use speckle photography to obtain data on the displacement field near IFFs when joint specimens are uniaxially loaded.

II. SPECKLE PHOTOGRAPHY TECHNIQUE

When using coherent laser light for illumination, a uniform diffuse surface has a speckled or grainy appearance. This is due to random changes in phase when the light is scattered from a diffuse surface. The eye or a photographic system produces an image in superposition with random interference. The mean size of laser speckles is proportional to the wavelength of light and the numerical aperture of the imaging lens. With f/1 optics, speckles as small as 1 micron in diameter are possible. Figure 1 is a photograph illustrating laser speckle. An f/22 lens aperture was used to accent the speckle phenomena.

Several methods of exploiting the speckle phenomenon to measure small displacements or strains have been devised. Of particular interest to us is a technique called speckle photography[3,4,5]. A double exposure "specklegram" (photographic negative image) is made of the speckled surface. Exposures are made before and after a displacement has occurred. Thus, each bright speckle point is recorded on the specklegram as two dark points - one in the undisplaced position and the other in the displaced position. Conversely, each dark speckle is recorded as two clear transmission areas on the specklegram. Only knowledge of the photographic magnification factor is re-

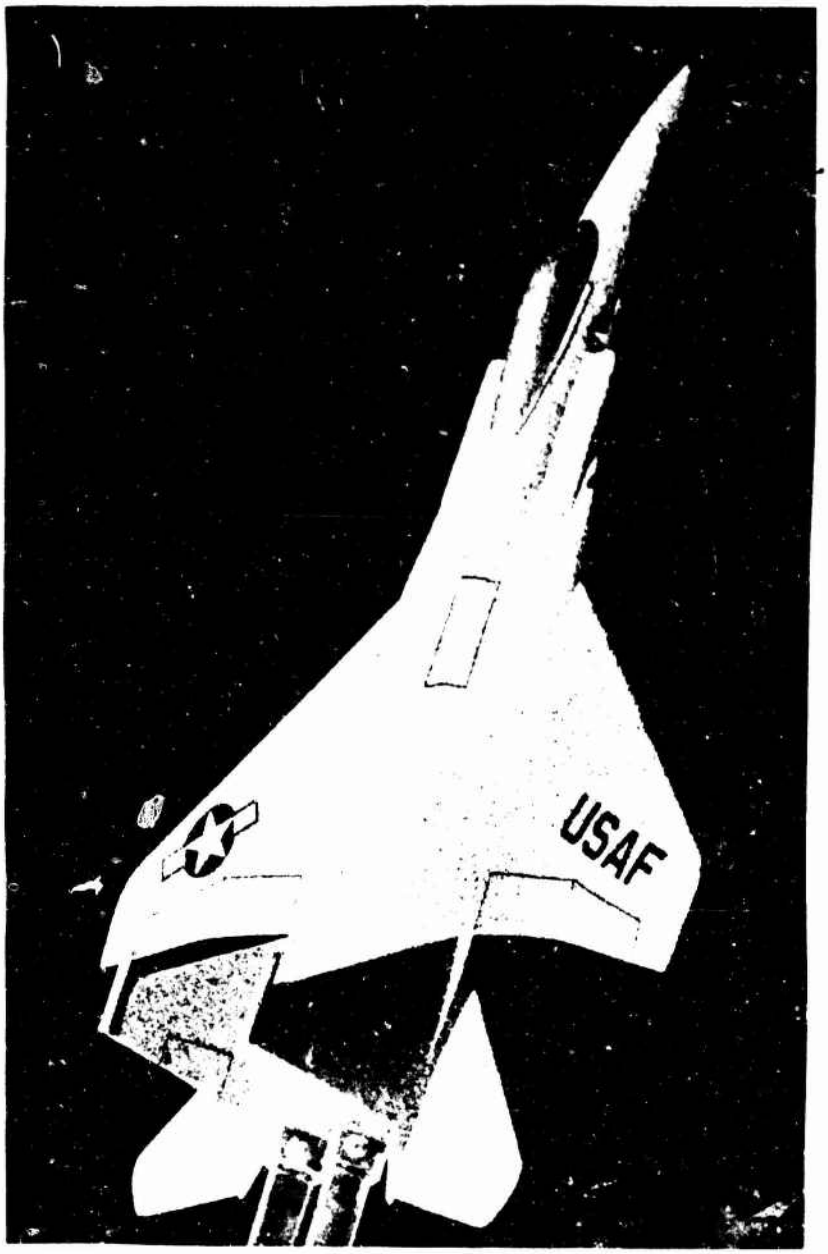

Figure 1 Photograph of Solid Aircraft Illuminated by Laser Light

quired to determine the local in-plane displacement vector once the length and direction of a line segment between the recorded speckle pairs are known.

A direct point-to-point measurement on a specklegram is virtually impossible or at best extremely tedious because of randomness in the speckle field. Fortunately, this is not necessary. If a narrow collimated laser beam (monochromatic and coherent) is directed through the specklegram, diffraction will modify the emerging light rays into a cone. This "diffraction halo" is the result of diffraction from the random distribution of small speckles. Since the speckles are recorded in pairs, however, a parallel fringe pattern (Young's fringes) also occurs in the emerging light cone. Figure 2 is a photograph of a typical speckle diffraction halo with a displacement induced fringe pattern.

For small diffraction angles, Young's fringes are perpendicular to the displacement vector and the spacing is inversely proportional to the displacement magnitude. This provides a measurement of local displacement since, in general, a narrow laser beam is used to interrogate only a small area of the image on a specklegram. The resolution depends on the laser beam diameter and magnification used in the photographic setup. The in-plane displacement distribution can be obtained by scanning the laser beam over the entire image area and taking measurements at selected points.

Other methods for extracting in-plane displacement data from a specklegram have been developed[3,4,5]. These provide a displacement contour fringe pattern superimposed on an optical image of the test specimen. Although such whole field methods are excellent for qualitative analyses and "quick look" at the displacement data, they do not provide the spatial resolution that can be attained using the point read-out technique. In addition, only one component of the displacement field can be contoured at one time. The point data acquisition method yields displacement magnitude and direction simultaneously.

Measurement accuracy is very dependent on signal-to-noise ratio in the diffraction halo. Signal amplitude is directly related to the fringe contrast. As can be seen in Figure 2, the primary source of noise is secondary speckle in the diffraction halo. These secondary speckles are not related to the speckles which are photographically recorded on the specklegram negative, but are generated by the coherent illumination of the acquisition laser beam. This type of noise effects accuracy if the fringe spacing approaches the speckle size. With larger fringe spacing, filtering or smoothing techniques will yield an acceptable signal-to-noise figure.

There are several items which can reduce fringe contrast (signal amplitude) and thus effect measurement accuracy. These are

(1) Insufficient isolation of the measuring apparatus and specimens from environmental vibration

(2) Steep gradients in the displacement field

(3) Out-of-plane displacements or rotations of the specimen about in-plane axes

(4) Changes in the surface characteristics of the specimen between photographic exposures.

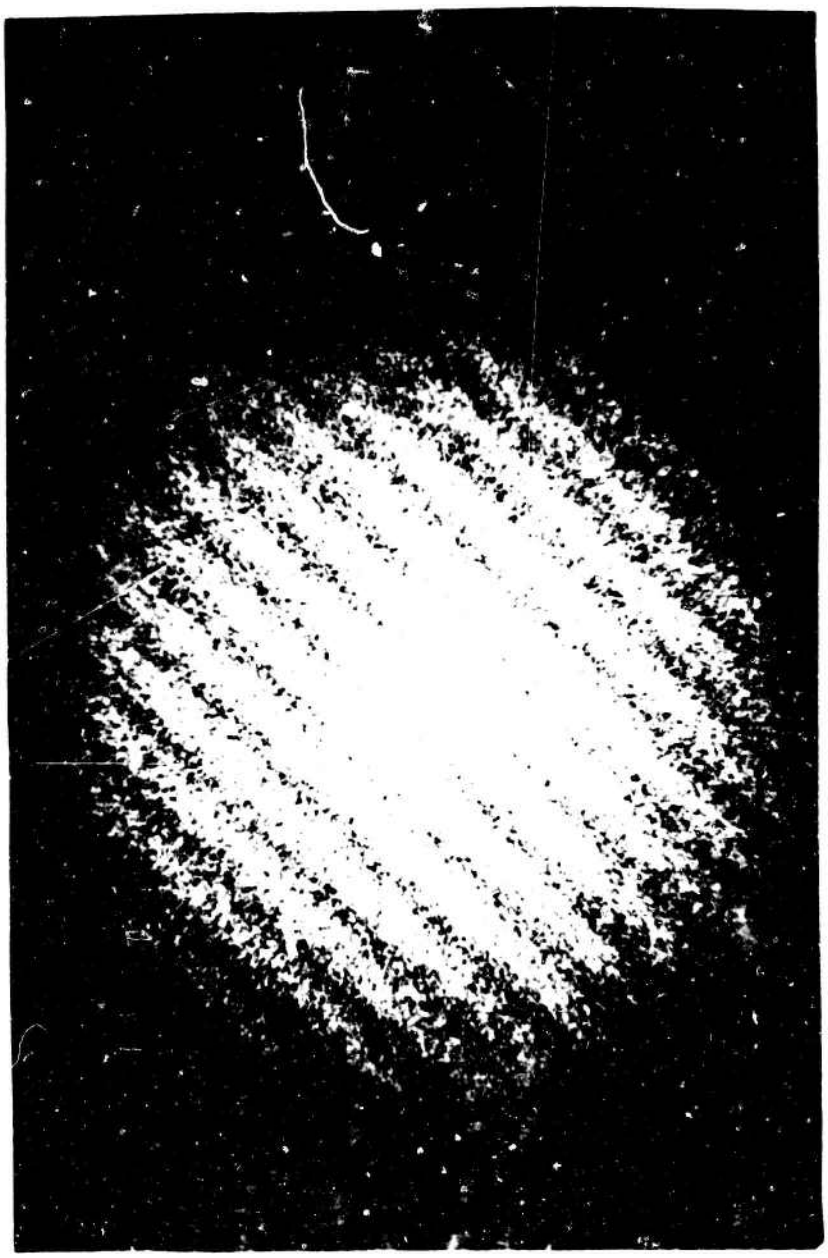

Each item will be discussed separately.

Relative motion between the test specimen and camera should be limited so as not to blur speckles in the film plane. When measuring very small displacements, tiny speckles are required and are generated by using a large aperture lens. Optical "stable tables" are employed for these measurements. Larger displacements allow for larger speckles which reduce the stability requirement proportionally. With lens opening of f/8 or smaller, the measurement can usually be made without a stable table.

Steep gradients in the displacement field can reduce contrast or wash out Young's fringes. This usually occurs when there is a significant change in displacement across the diameter of the readout laser beam. Since this diameter cannot be reduced to less than about 1 mm, it is necessary to use larger photographic magnification when this problem is encountered.*

Out-of-plane displacements and rotations of the specimen about in-plane axes which take place between double exposures will tend to wash out Young's fringes. This occurs because speckles are three-dimensional entities. Although a laser illuminated object "appears" to have a speckled surface, these speckles are, in reality, generated in the scattered light field. For most lens systems, the speckle is very much elongated in a direction parallel to the optical axis. This allows some out-of-plane displacement to occur with no effect on the Young's fringes. However, out-of-plane displacements which are many times larger than the in-plane displacements being measured will destroy speckle correlation between exposures. In such cases, speckle pairs are not recorded and Young's fringes cannot be produced.

Changes in surface characteristics which occur between exposures can also reduce or wash out fringe contrast. This is also a type of decorrelation in the speckle pattern which is independent of in-plane translation. The primary cause is usually local plastic yielding of the material which upsets the surface. Fortunately, this is not a "go or no go" situation. A small amount of plastic yielding will partially upset the surface and cause some reduction in fringe contrast. As loading and yielding are increased, the transition to complete fringe washout is not gradual, but neither is it sudden. As a result, it is possible to use speckle photography to study plastic yielding if measurements are obtained for small load increments. The resultant total displacement field is obtained by superposition of the incremental data.

For the investigation of IFFs reported herein, Item (1) above was not a problem since our specklegrams were recorded on an optical stable table. Item (2) was controlled by using magnification factors of unity or larger. Item (3) presented no problem because of the geometry and because test fixtures were constructed to minimize out-of-plane displacements. Incremental loading was used to control Item (4), since plastic yielding usually does occur when IFFs are installed in joints. Details are discussed in the next section.

III. APPARATUS AND PROCEDURE

The basic arrangement of apparatus required to record a specklegram is

---

* Secondary speckle size is inversely proportional to the diameter of the readout laser beam. Also, edge diffraction becomes a problem with very small diameter laser beams.

diagrammed in Figure 3. We are using a 50-milliwatt helium-neon laser to illuminate the test specimen. A microscope objective lens and a 25-micron pinhole are employed to expand and filter the laser beam.

A rather massive fixture was fabricated to hold the test specimen and camera. This was done to minimize whole body displacements of the specimen relative to the camera which might occur during torque up of a fastener. Figure 4 is a photograph of the test fixture with a 2" x 6" aluminum coupon test specimen bolted to the box frame. A single 3/8" tapered IFF is installed in the center of the coupon. The front surface of all test specimens was grit blasted to insure a diffuse scattering of the laser light.

The speckle camera was especially designed and fabricated for this program. A high quality half-silvered mirror was incorporated into it in order to permit two film plates to be exposed simultaneously. Figure 5 is a diagram of this camera. The horizontal film plate holder was equipped with a "dark slide". This enabled us to use the vertical image plane for making several specklegrams of small incremental displacements while recording the total displacement on the horizontal film plate. The small increment specklegrams provided good data in the plastic yield zone very near the fastener. Smaller displacements in the far field elastic zone are easier to obtain on the total increment specklegram.

In practice, the following procedure was used. Both film plates were exposed with an IFF placed in its hole but not torqued up. The dark slide was then used to shield the horizontal image plane. Twenty to thirty percent of the recommended interference was then achieved by torquing the IFF. In order to record this increment, a second exposure was made in the vertical film plane only. This film was then replaced with a fresh plate and a new exposure made. A second increment is recorded by further torquing of the fastener followed by exposing the vertical film plate. The process is repeated until the total interference recommended by the fastener manufacture is obtained. The final exposure is made with the dark slide removed to record the total displacement increment.

Once specklegrams have been obtained, the next step is to acquire and reduce data. As discussed in Section II, the point acquisition technique was found to be most acceptable for our purposes. This yields displacement magnitude and direction as a function of coordinate position. Figure 6 is a drawing of the basic configuration used for data acquisition.

Young's fringe formula states that the distance, D, between fringe minimum is approximately

$$D \approx L\lambda/d \ , \qquad (1)$$

where L is the distance from the specklegram to the viewing plane, λ is the wavelength of light, and d is the separation distance of speckle pairs. Young's fringes are, of course, perpendicular to the displacement direction.

The mechanics of measuring the fringe spacing is somewhat more difficult than it first appears. This is particularly true if high accuracy is required. Attempts to physically measure the fringe spacing with scales on a translucent view screen produced data scatter of 5 percent or more. We,

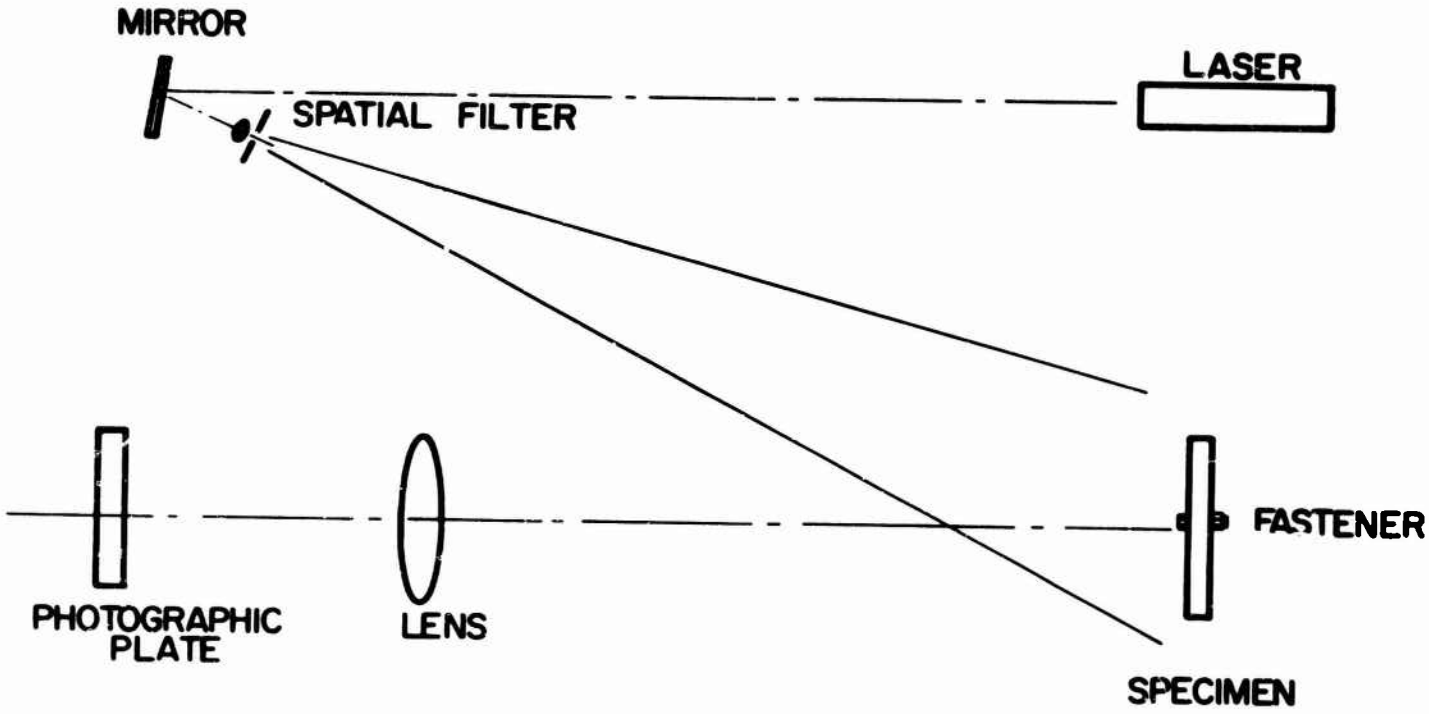

Figure 3 Specklegram Recording Procedure

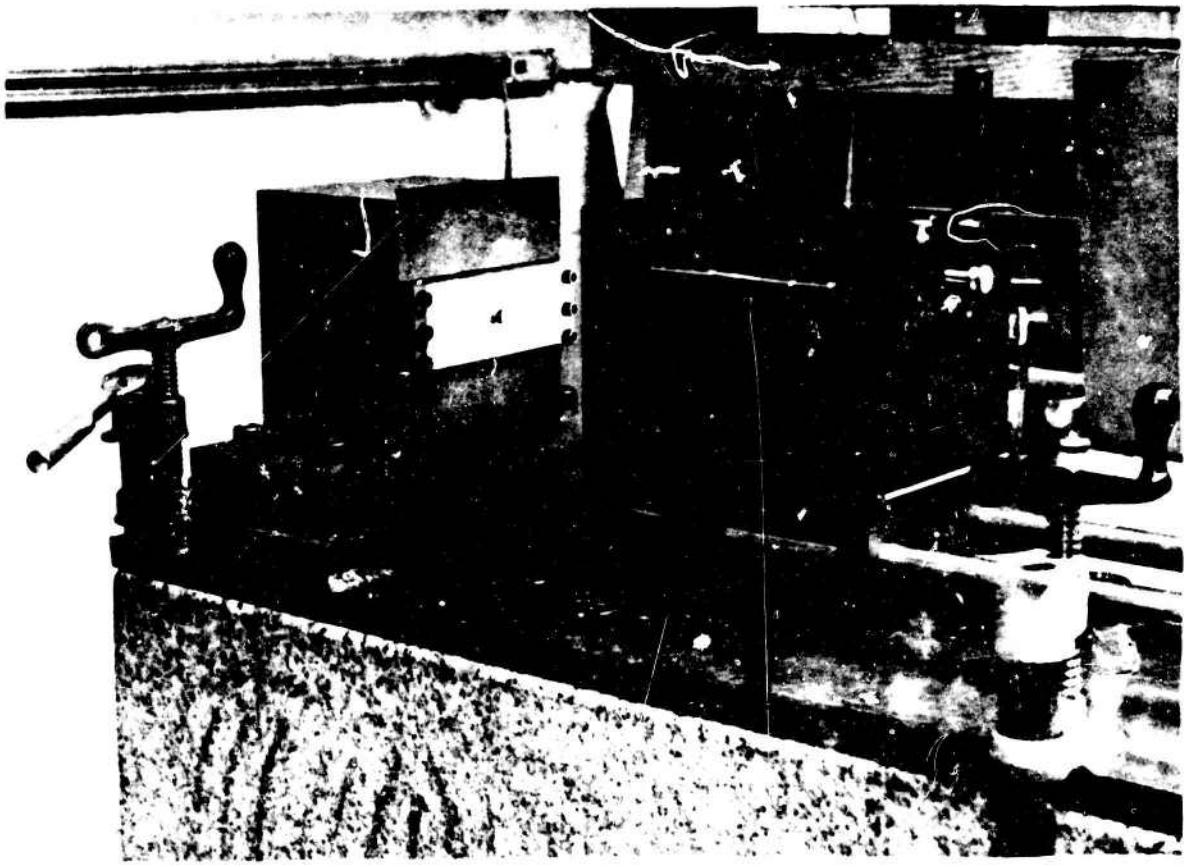

Figure 4. Photograph of the Loading Fixture and Crack

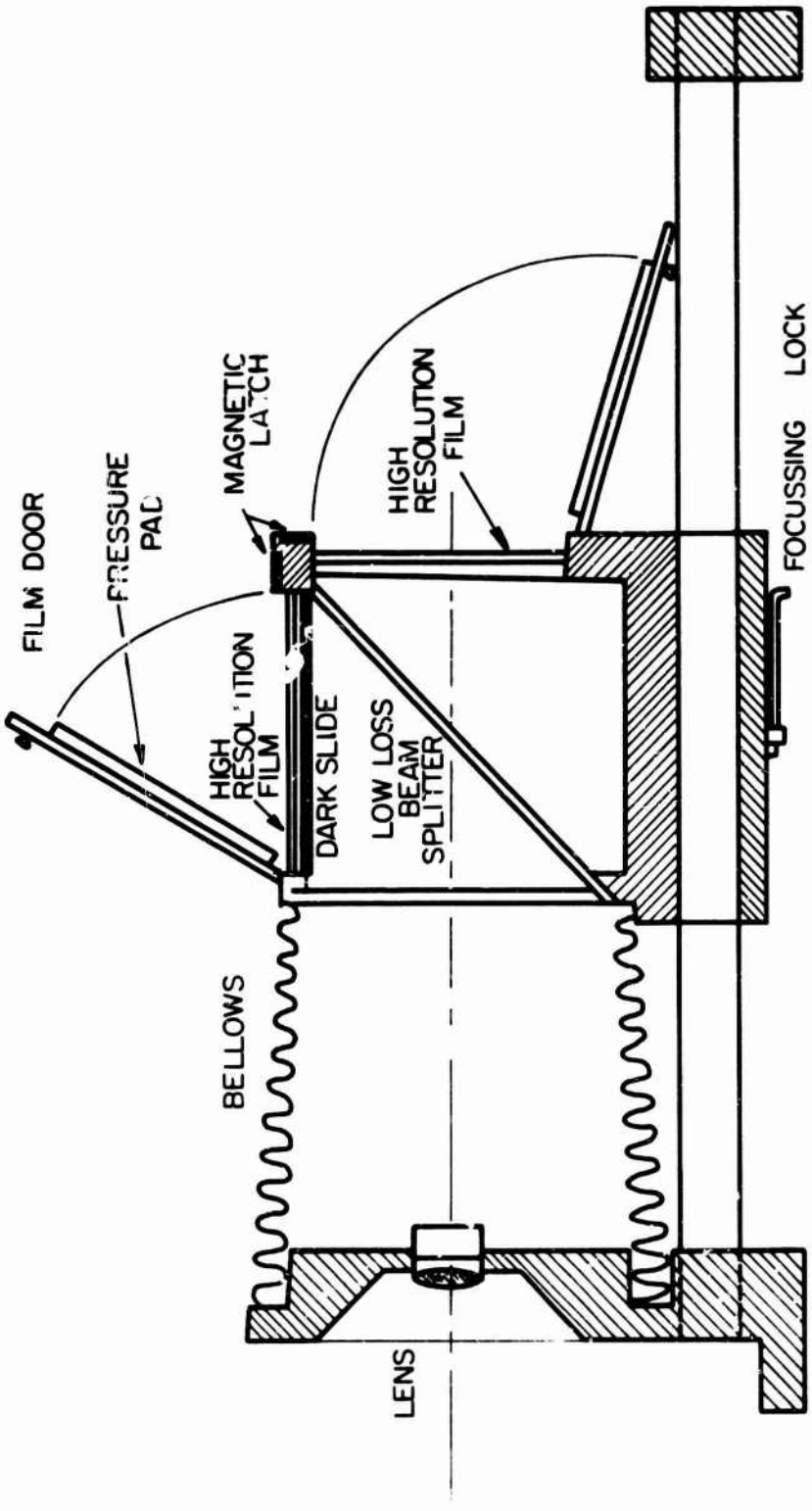

Figure 5 Cross Section of Camera

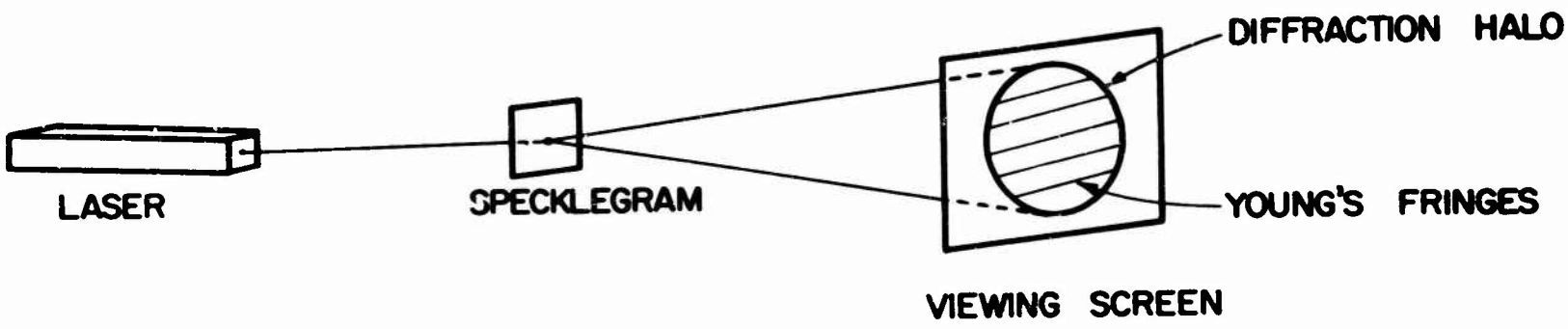

Figure 6 Data Acquisition Procedure

therefore, designed and fabricated a scanning device which employed a Bell and Howell Type 509 photodetector to plot light intensity in the diffraction halo.

Figure 7 is a photograph of the optical bench used for data acquisition readout. The major components are a 5-milliwatt laser, a X-Y positioner to locate the specklegram, a photodetector scanning device, and a translucent view screen. The scanner and view screen are attached in a rotatable mount. This allows the operator to position the scanner such that the fringes are traversed in a perpendicular direction. The angular orientation of the fringe pattern is measured in "degrees" from a scale attached to the view screen. The view screen is 18" in diameter. The scanning aperture is a 4" slit. This slit aperture is very effective in smoothing out speckle noise in the diffraction halo.

An X-Y recorder is used to plot light intensity versus scanner position. A typical plot is showing in Figure 8. Some further noise reduction can be accomplished by drawing a smooth curve over the recorded data. The distance between minimum light intensity locations is determined by direct measurement with scales.* The distance between speckle points is obtained by solving Young's fringe equation (Eq. 1) for d. Finally, the final displacement magnitude, δ, is calculated by dividing d by the camera magnification factor, M. Thus, we have

$$\delta = \frac{L\lambda}{DM} \quad . \tag{2}$$

In practice, the displacement magnitude δ, the displacement direction θ, and the X,Y coordinate at the point on the specklegram image which is interrogated are tabulated for each measurement.

IV. RESULTS AND DISCUSSION

Speckle photography measurements were made on a 6" x 6" x 0.5" 7075-T6 aluminum coupon specimen with a 3/8-inch steel Taper-Lok** fastener installed with a diametral interference of 0.00368 inch. This value of diametral interference was determined by measuring the fastener protrusion before and after installation. Since the shank taper is 1/4 inch per foot, diametral interference is the protrusion difference divided by 48. The results obtained from four different radial traverses out from the hole edge are shown in Figure 9. It can be seen from this figure that the radial displacement patterns from all four traverses have an 1/r type of distribution and are in good agreement with one another.

---

* The average intensity distribution in a diffraction halo is not uniform and falls off rapidly with distance from the center. This can cause a shift in the distance between maximum in a fringe pattern. For this reason, we always measure the distance between minima.

** Trade name for tapered bolt fastener manufactured by Omark Industries, El Segundo, California.

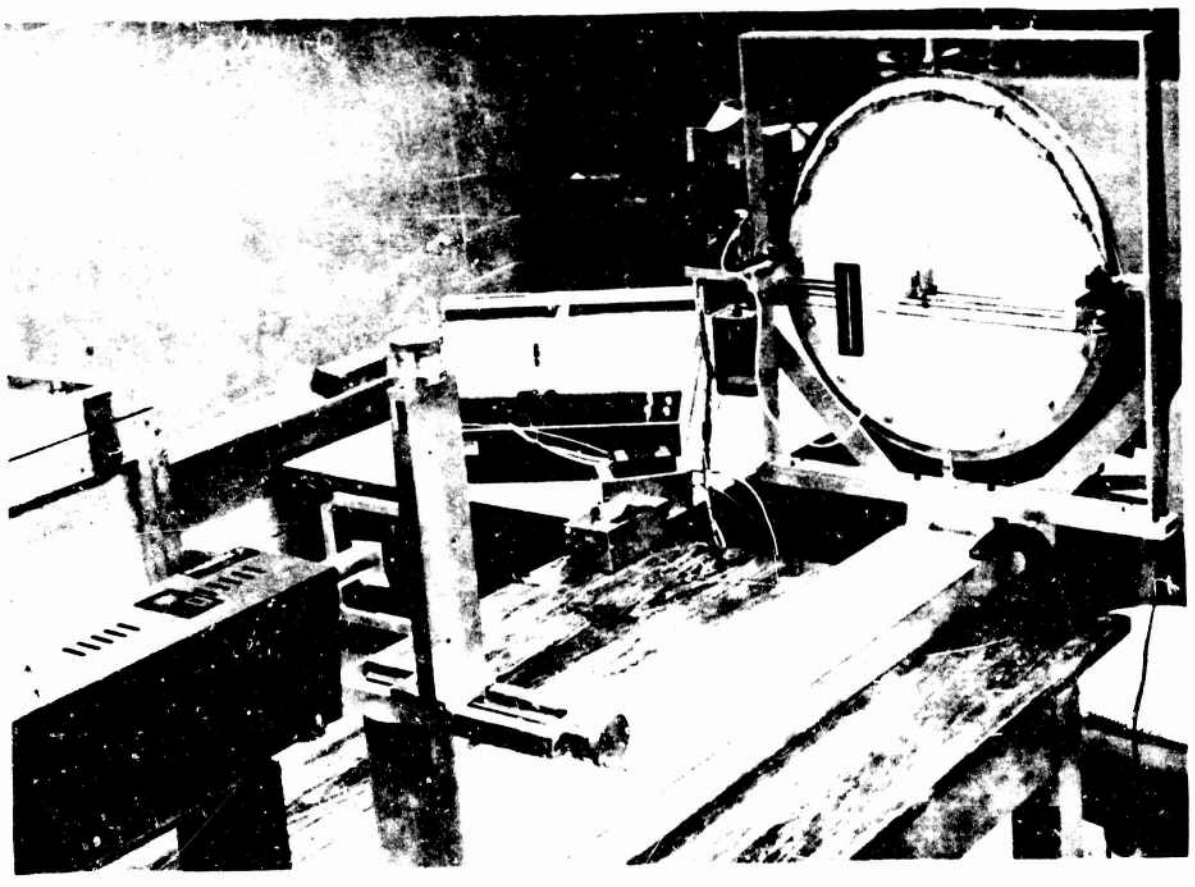

Figure 3. Front View of the DRI Azimuth Scanning Device

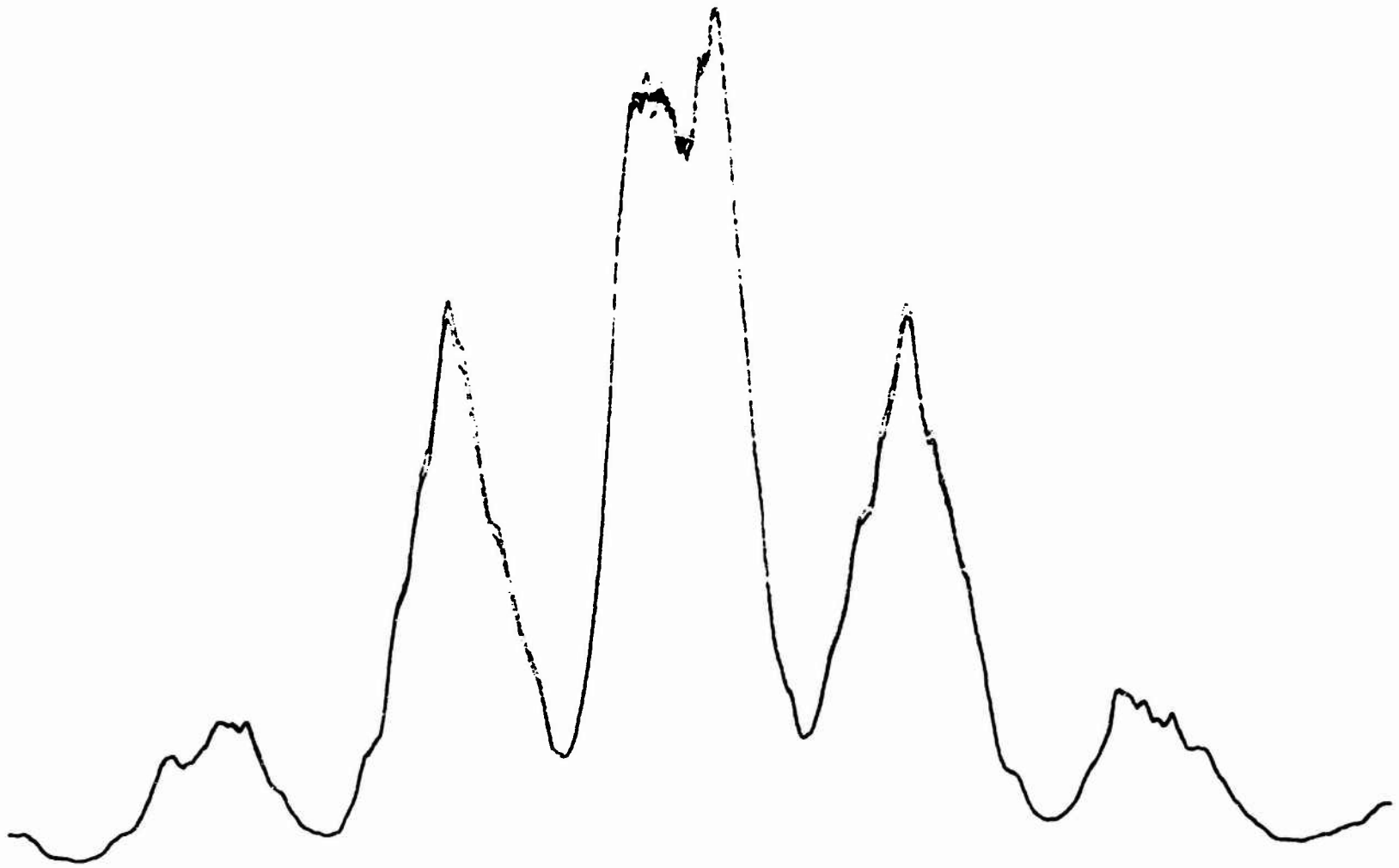

Figure 8 A Typical Plot of the Diffracted Halo with Young's Fringes

Radial displacements obtained from a finite-element analysis* are also plotted in Figure 9 and appear as a solid line. These results follow the shape of the experimental data points but are larger by approximately 30 percent. To explain this discrepancy, three incremental exposures were examined in detail. This examination revealed that the first load increment, which should have produced a radial edge displacement of about 0.0006 inch (diametral, interference of 0.0012 inch), caused an edge displacement of less than 0.0001 inch. The second and third increments produced the expected displacements. Thus, the effective interference is lower than that calculated by the protrusion method. If we assume that the second and third increments each force an edge displacement of 0.0006 inch, then a total displacement of 0.0013 inch at the edge of the hole would seem reasonable. Figure 10 is a comparison of the interference of 0.0026 inch.

To determine the cause of this "slack" interference, metrological measurements taken before the specimen was loaded were examined. A portion of these measurements are shown in Figure 11. The polar plot, Plot A, reveals that the hole was perpendicular and of uniform taper. Variations of up to 0.0007 inch, however, are discernible. Plot B is only a portion of the plot obtained from the hole surface in the logitudinal direction of the hole. Variations in this plot are again seen to be about 0.0007 inch. The above-mentioned irregularities required that local smoothing be accomplished during the first increment before complete interference could be obtained.

Speckle photography measurements were also made on a 2" x 2" x 0.5" silicon iron coupon specimen fitted with a 3/8-inch steel Taper-Lok fastener. This specimen was included in the test matrix so that eventually a comparison can be made between measurements obtained by speckle photography and the dislocation etching technique. Data from the dislocation etching technique were not available at the time this paper was submitted. However, a comparison between finite-element predictions and speckle photography measurements was accomplished.

Measured displacements are plotted in Figure 12. Also, presented are two theoretical curves obtained by finite-element analysis. The dashed curve shows the displacements resulting from a "protrusion determined" interference of 0.00243 inch. The solid line shows the predicted displacements for an interference level that best fits the experimental data, which is 0.00175 inch or 72 percent of the above value**.

Two equal incremental exposures were made for this specimen. These were again examined to see if the "slack" interference could be accounted for. Measured displacements in the first increment were only 1/2 of those found in the second. This would indicate that the total effective interference should be about 75 percent of the protrusion determined interference.

---

* All finite-element calculations were provided by S. G. Sampath via BCL internal communication.

** It should be noted in Figure 12 that the theoretical displacement at the edge of the fastener hole is not equal to 1/2 the diametral interference. This is due to compression of the fastener which is much greater with a steel specimen as compared to aluminum due to the difference in Young's modulus.

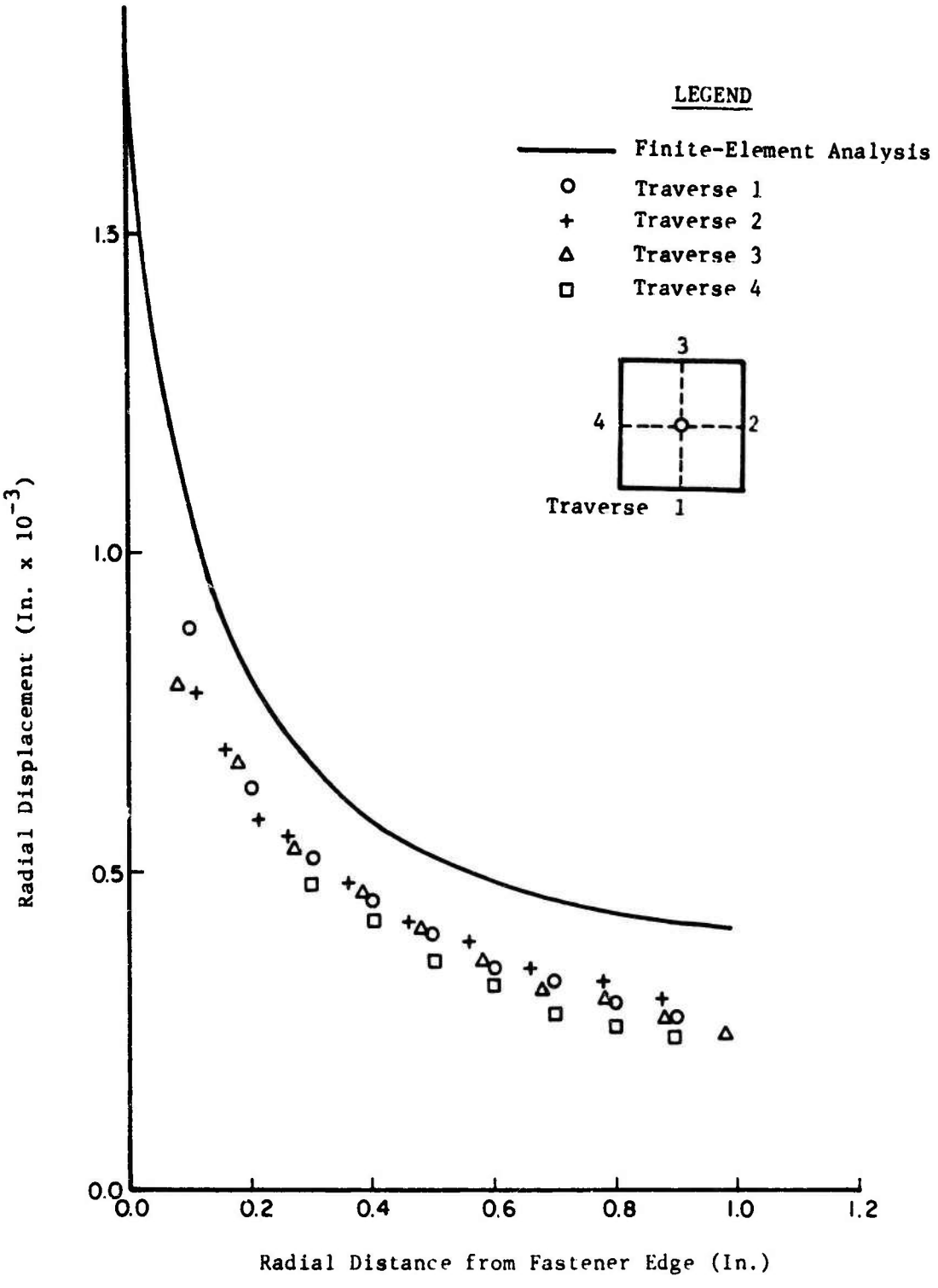

Figure 9 Radial Displacement Versus Radial Position for a 6" x 6" x 0.5" 7075-T6 Aluminum Specimen with 0.00378-Inch Interference

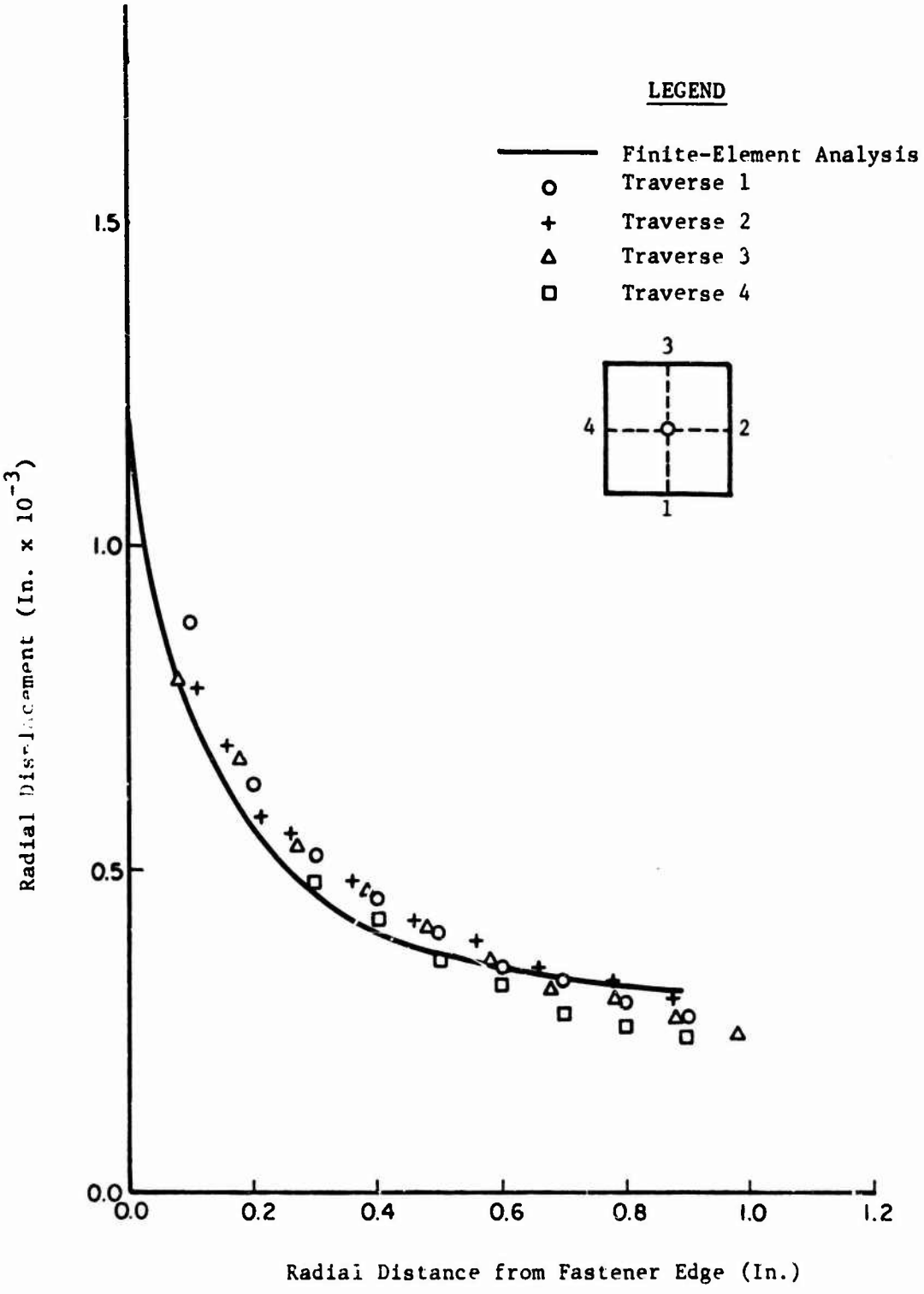

Figure 10 Radial Displacement Versus Radial Position for a 6" x 6" x 0.5" 7075-T6 Aluminum Specimen with 0.0026-Inch Interference

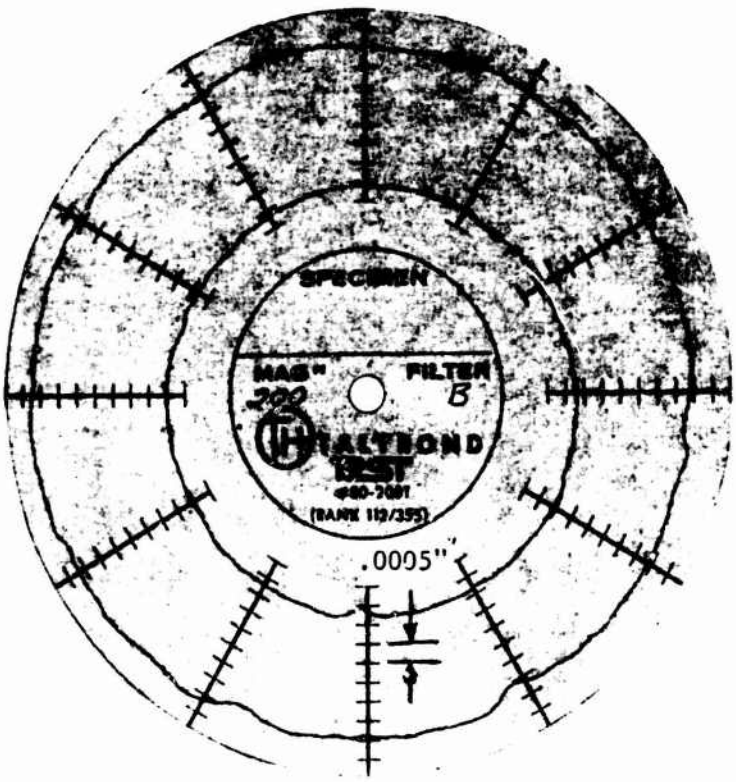

PLOT A

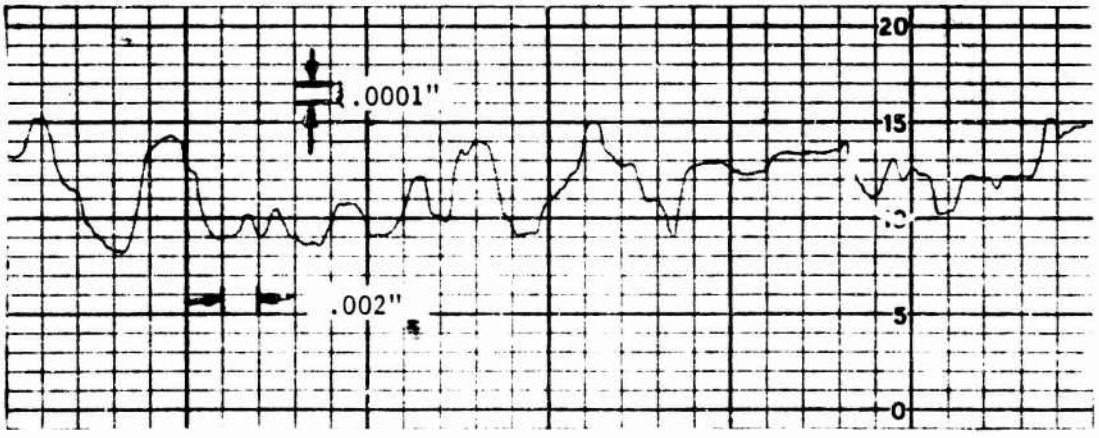

PLOT B

Figure 11 Metrological Data for a Aluminum Coupon Specimen

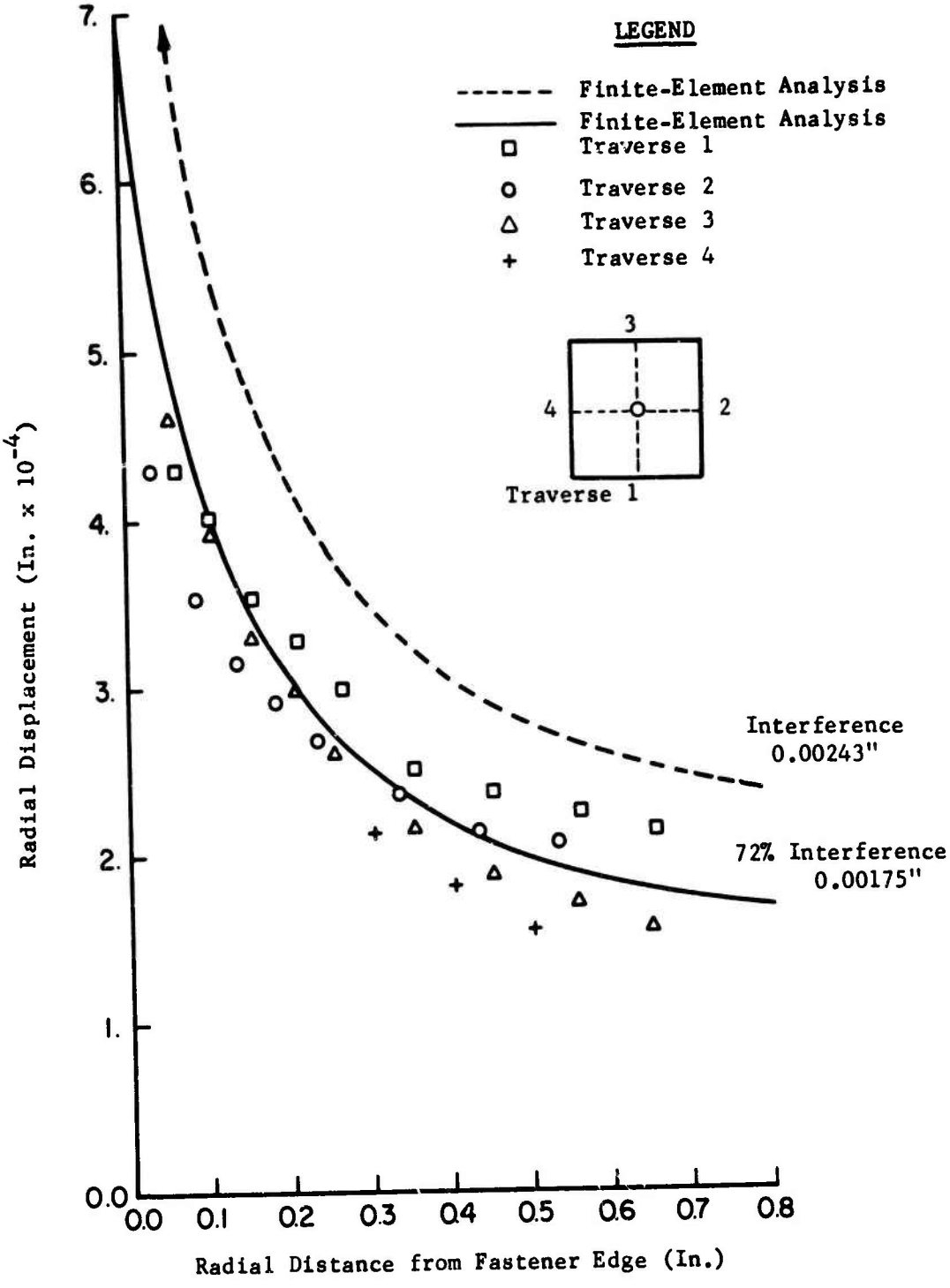

Figure 12 Radial Displacement Versus Radial Position for a 2" x 2" x 0.5" Silicon Iron Specimen with 0.00243-Inch Interference

This is quite close to the 72 percent value obtained by best fitting the data. Metrology of the steel hole is presented in Figure 13 and is consistent with these results.

The data presented in Figure 12 exhibit less symmetry in comparison to the measurements made on the aluminum specimen (Figure 10). Some of this is due to simple difference in the hole geometries. However, a steel-in-steel installation requires relatively high torque and some movement of the coupon could have occurred. The measured displacements would then have a component of rigid body translation or rotation superimposed on the interference-induced displacement.

Finally, measurements were obtained on a 6" x 6" x 0.5" aluminum coupon specimen which had a 3/8-inch tapered hole that was 0.5 percent out-of-round. Metrological data for this hole are presented in Figure 14. An interference of 0.00366 inch was applied to the specimen with a steel Taper-Lok fastener.

Out-of-round IFF holes are not an uncommon occurrence. They are often caused by high feed rates and/or dull reaming drills. When an out-of-round hole condition exists, the fastener shank is not initially in contact over its entire surface area. As the fastener is drawn into the hole, a greater portion of its shank contacts the specimen. For small amounts of out-of-roundness, the fastener will eventually make total contact. Additional interference will cause deformations similar to the "round hole" case, except that the strain field will lack symmetry.

Measured displacements are plotted in Figure 15. In addition, results obtained from a plane stress finite-element analysis are also plotted. The dashed line shows the displacements corresponding to the axis of maximum deformation (initial contact). The solid line represents the displacements along the axis of minimum deformation (largest gap). Data points from traverse 2 at the 45 degrees correspond to the dashed line. Data from traverses 1 and 3 relate to the solid line.

The experimental data are in good agreement with the finite-element analysis. However, there are several features worth examining in greater detail. In Figure 15, the measurements along traverse 2 fall below the theoretical curve. The hole metrology, as presented in Figure 14, helps explain this discrepancy. The orientation of out-of-roundness varies by about 30 degrees through the thickness of the specimen. This "spiraling" pattern effectively broadens the region of initial contact and has an attentuating influence on the displacement along traverse 2.

It is also interesting to note that this specimen appears to have an absence of slack interference. Incremental exposures also confirm this. The first increment showed relatively large displacements in the area of initial contact and little elsewhere. The first incremental exposure for the round hole specimens revealed generally small but symmetrical displacements. This difference probably results from the positive initial contact due to the out-of-roundness. The finite-element model for the out-of-round condition was constructed from the hole metrology. The spiraling effect, however, could not be included in the model since the analysis was performed under the assumption of plane stress.

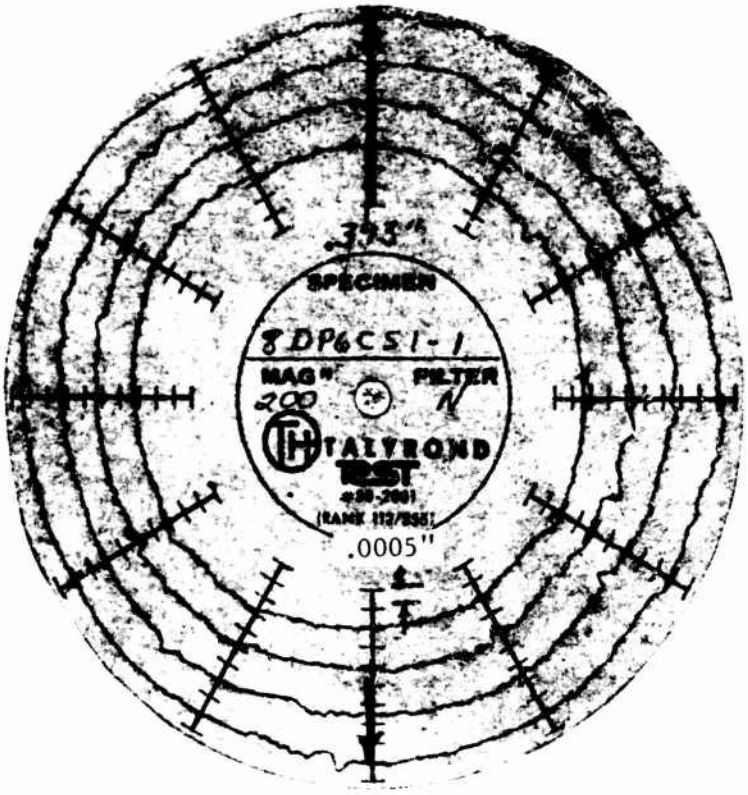

Polar Plot

Longitudinal Plot

Figure 13 Metrological Data for a Steel Coupon Specimen

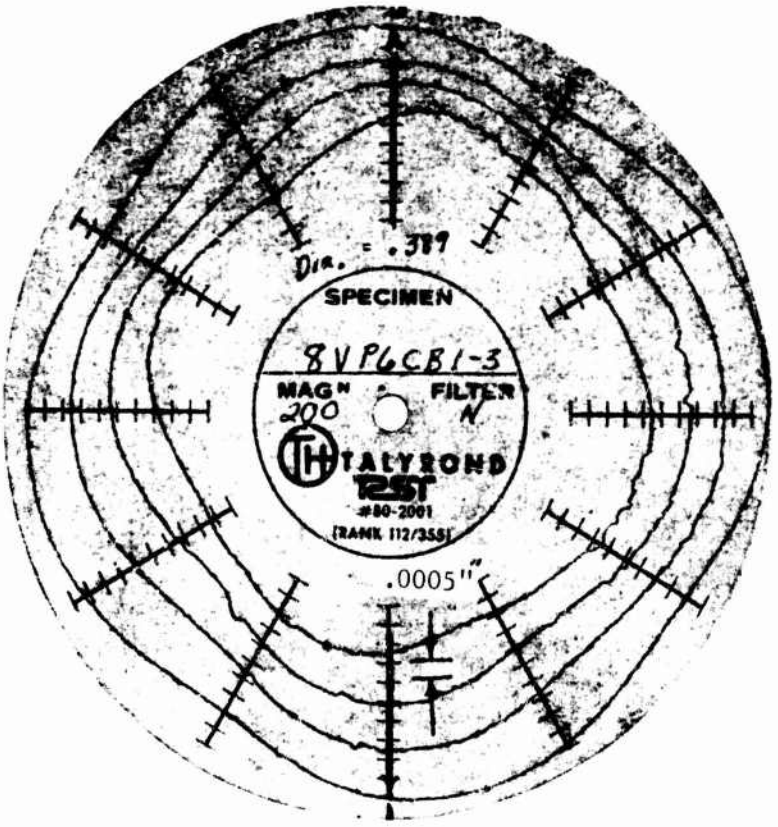

Polar Plot

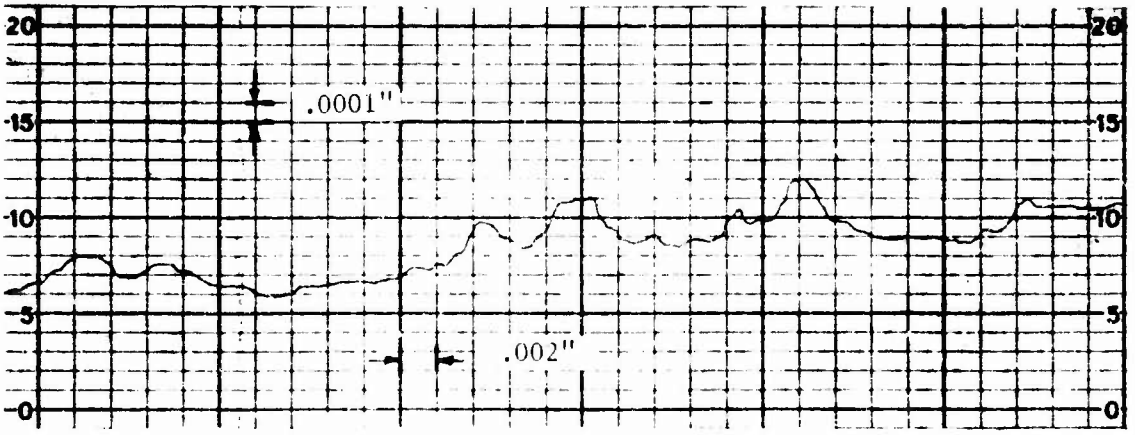

Longitudinal Plot

Figure 14 Metrological Data for a Out-of-Round Aluminum Coupon Specimen

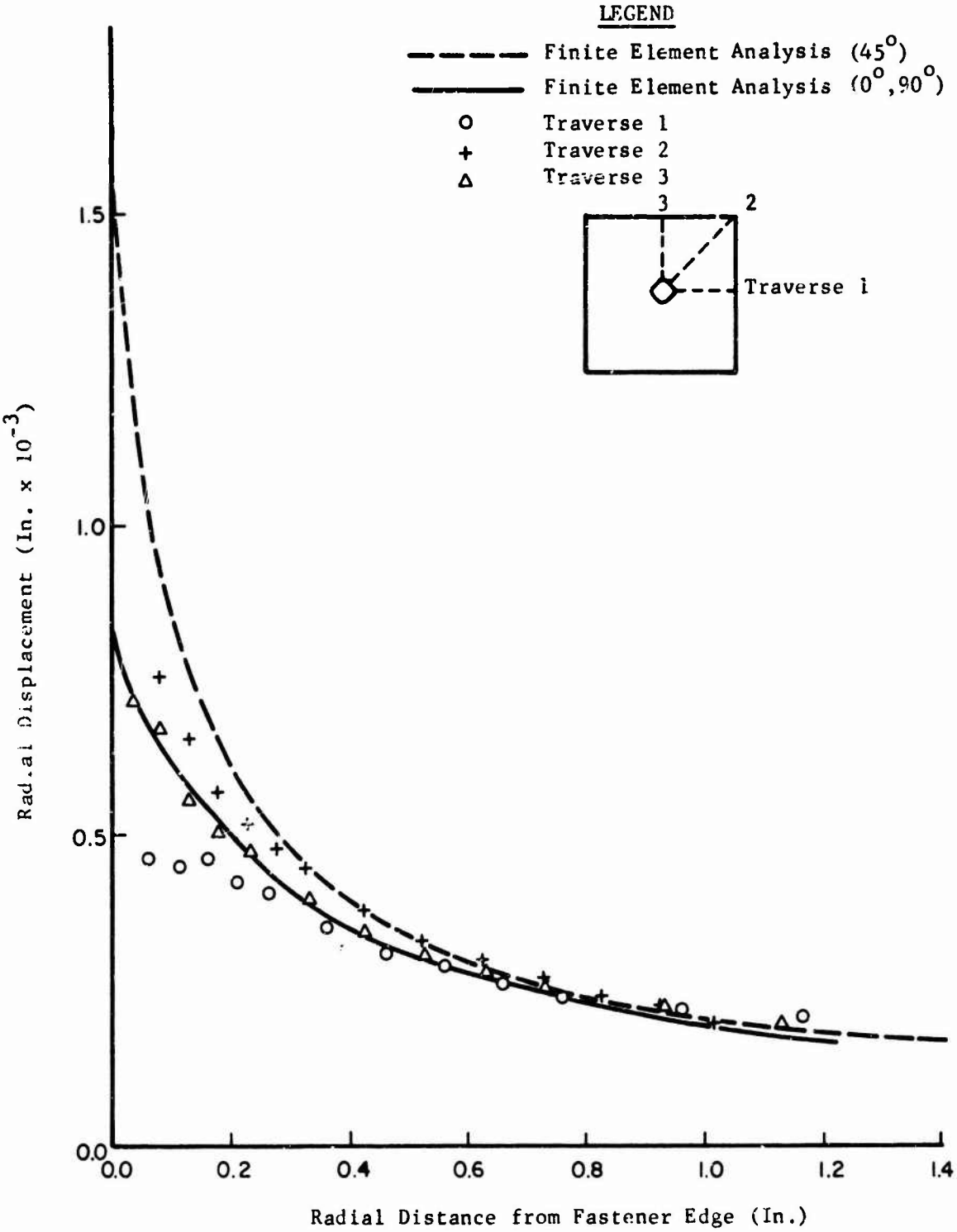

Figure 15 Radial Displacement Versus Radial Position for a 6" x 6" x 0.5" Aluminum Specimen With a 0.5% Out-of-Round Hole and 0.00366-Inch Interference

V. SUMMARY AND CONCLUSIONS

Speckle photography has been demonstrated as a useful technique for measuring in-plane displacements produced by the installation of an IFF in a coupon specimen. The measurements required a two-step process. First, a specklegram was made by obtaining a double-exposure photograph of the laser illuminated specimen before and after a displacement occurred. Displacement data were then acquired from Young's fringes which were produced when the specklegram was interrogated with a laser beam.

Measurements were made for 3/8-inch steel IFFs installed in 1/2-inch aluminum and steel plates. Both round and out-of-round fastener holes were examined. Experimental data were compared to finite-element model calculations. The results indicate that irregularities in otherwise round fastener holes cause the amount of interference to be less than that expected. Once this effect was taken into account, however, the agreement between theory and measurement was excellent.

Future work will include speckle photography measurements on structural joint specimens fastened with IFFs. Displacements caused by fastener installation as well as uniaxial loading will be determined. An attempt will be made to measure the change in strain distribution around an IFF when a joint undergoes cyclic loading. Such information should be extremely valuable in developing a method of predicting the fatigue life of joints fastened with IFFs.

VI. REFERENCES

(1) Smith, C.R., "Tapered Bolts - Their Influence on Fatigue of Airplane Structure", Convair Report No. ZR 659-053, May 1960.

(2) Hahn, G.T., Mincer, P.N., and Rosenfield, A.R., "The Fe-3Si Steel Etching Technique for Local Strain Measurement", Experimental Mechanics, June 1971.

(3) Archbold, E., Burch, J.M., and Ennos, A.E., Optics Acta, 17, no. 12, 883, (1970).

(4) Archbold, E. and Ennos, A.E., Optics Acta, 19, no. 4, 253, (1972).

(5) Adams, F.D. and Maddux, G.E., "On Speckle Diffraction Interferometry for Measuring Whole Field Displacements and Strains", AFFDL-TR-73-123, December 1973.

FINITE ELEMENT ANALYSIS OF THREADED CONNECTIONS

Peter O'Hara
Mechanical Engineer
Benet Weapons Laboratory
Watervliet Arsenal
Watervliet, New York 12189

ABSTRACT

In the analysis of threaded and thread like connections between two bodies two separate phases of the problem can be done using the finite element method. First the analysis of the shape of an individual thread is accomplished using 2-dimensional elements. This work is then correlated with the Heywood Equation. Second the analysis of the thread to thread load distribution is demonstrated using axi-symmetric elements and a computer program to generate the finite element data.

NOMENCLATURE

α	=	ALPHA = Angle of Loaded Face
β	=	BETA = Angle of the Back Face
R	=	Fillet Radius
$\overline{R}$	=	Nondimensional Fillet Radius
H	=	Total Height of the Projection
$\overline{H}$	=	Nondimensional Height
P1	=	Thread Space on the Datum Line
P	=	Pitch or Space on Datum Line
Z	=	Projected Bearing Height
S	=	Shear Length
W	=	Total Applied Load
WI	=	Load Supported
λ	=	GAMMA = Loading Angle Off Normal
T	=	Length of the Projection
σ_F	=	Maximum Fillet Stress
σ_b	=	Average Bearing Stress
τ_{avg}	=	Average Shear Stress
e,a,b	=	Heywood Geometry Factors

INTRODUCTION

The analysis of threaded connections and other joint problems involving the transfer of load by a series of interlocking projections has long been of interest to the design engineer.

This interest is related to the frequency of failures in this type of joint. Failure in threaded or thread-like connections can often be related to one of three failure modes. First, a failure of the bearing surface which usually takes the form of 'brunelling' or 'galling' and seldom causes gross structure failure. Second, shearing off of projections near the base of the projection usually related to some form of overload condition on the threads. Third, failure due to cracking of the fillet at the intersection of the bearing surface, the main body of component and the adjoining thread. This is the most difficult problem because of the complicated geometries and loading. These failures are also frequently fatigue failures in service.

The analysis of forces and stress on Thread-Like Projections will be the major concern of this paper. The study will be divided into two basic areas: 1) The study of individual thread shapes; 2) The study of the axisymmetric two-body problem approximating a threaded connection between two cylinders. The thread shape work is all 2-dimensional analysis and involves three different sources of data from both photoelastic and finite element methods of analysis. The two-body analysis is with the use of the NASTRAN (1-4)* axisymmetric ring elements.

This paper will use as a model of a threaded connection a thread like projection system used as a thrust carrying connection on a saboted subcaliber projectile. In this application the projectile has a smaller projection than the sabot because it is fabricated from a stronger material.

GEOMETRY OF A THREAD-LIKE PROJECTION

To define the shape and size of a thread-like projection, five parameters are required. These are shown in Figure 1. A projection has a loaded surface at some flank angle alpha (α) and an unloaded surface at some back angle beta (β). These are blended into the main body of the component using a fillet radius (R). The projection has a characteristic width (P) which is the length between the centers of the two fillets. This characteristic length becomes the pitch of most threads. These four numbers define a triangular pointed geometry, which must be truncated in real structures. In many projections it can be cut off at some height (H). (Figure 1a). In threads where clearance is required so that components fit together, the space is on the datum line (P1) (Figure 1b). In this case the datum line is half way between the top of the thread and the end of the flat bearing face. If length dimensions are nondimensionalized by the characteristic width, four parameters to define the shape of a projection remain.

*Numbers in parenthesis refer to items in the reference list.

FIG. 1

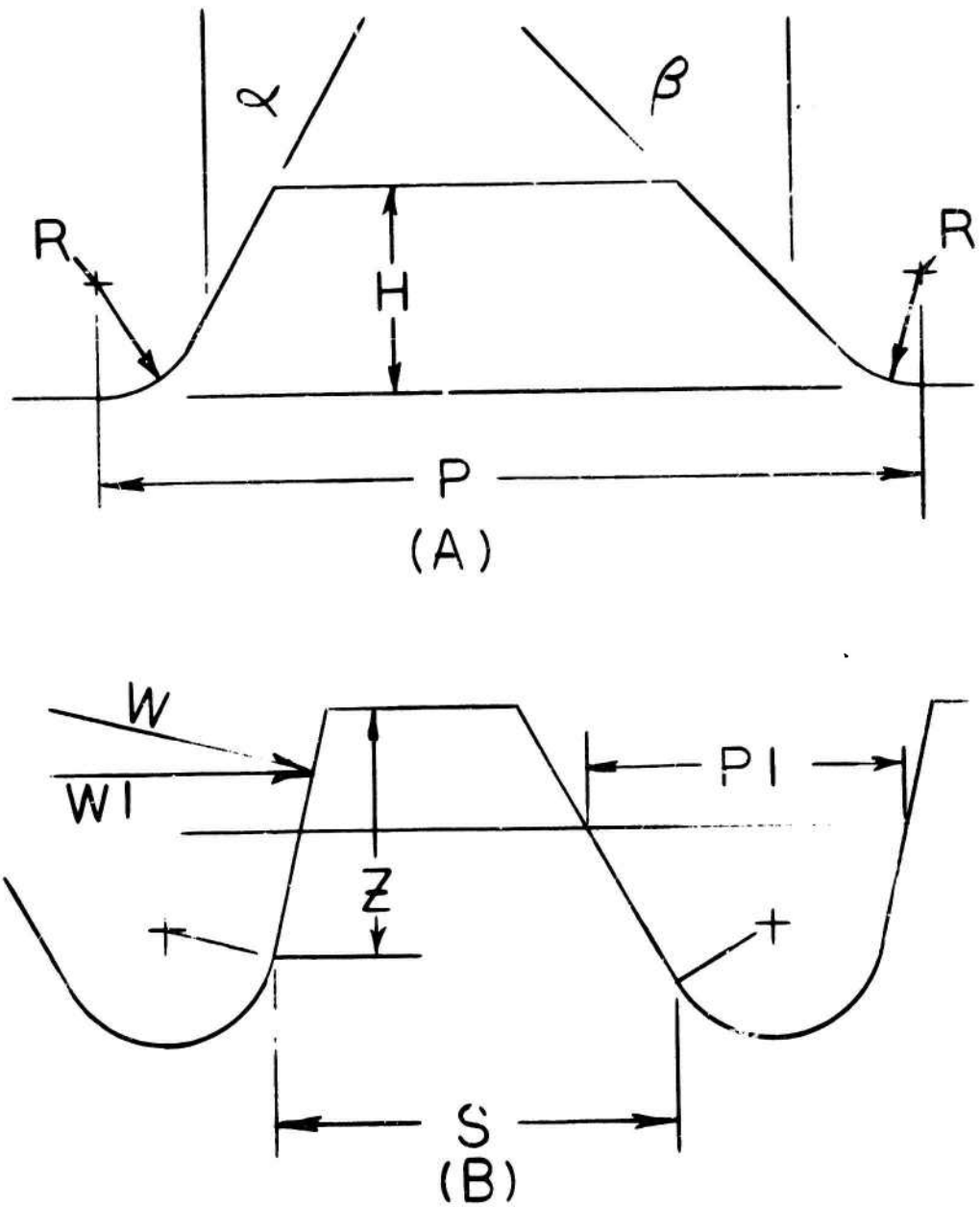

Figure 1. Geometry Factors for Loaded Projections

Projections are identified in this report by a notation, relating to geometry, which is a series of four numbers-alpha-beta-$\overline{R}$-$\overline{H}$ the flank angle, back angle, nondimensional root radius, and nondimensional height, respectively. Therefore, a projection designated 17-36-.1-.25 has a flank of 17 degrees, a back angle of 36 degrees, a root radius of 0.1 times the pitch and a height of .25 times the pitch. In the case of threads the height is dropped and only three numbers are used.

Two other dimensions of interest to the designs are the projected bearing height (Z) and the shear length (S) of a projection. These are shown in Figure 1(b).

When the bearing face of a projection is set at an angle to the direction of the applied load WI the resultant load W on the projection is larger than the applied load. If a zero friction bearing condition is assumed then the angle between the two loads is the flank angle α and the two loads can be related using the simple equation:

$$W = \frac{WI}{\cos\alpha} \tag{1}$$

This will be done for the 2-dimensional work and load will be the useful load supported by the projection.

TWO-DIMENSIONAL ANALYSIS

The first two stresses to be discussed are the average bearing stress (σ_b) and the average shear stress (τ_{avg}) which are simply calculated using the equations:

$$\tau_{avg} = \frac{WI}{ST} \qquad \sigma_b = \frac{WI}{ZT} \tag{2}$$

Where T is the thickness, Z and S are the appropriate dimensions and WI is the supported load. The calculation of the maximum fillet stress will be carried out using two different methods, the Heywood relation and NASTRAN finite element solution.

The Heywood relation (5) can be simply stated as:

$$\sigma_F = \left[1 + 0.26 \left(\frac{e}{R}\right)^{0.7}\right] \left[\frac{1.5a}{e^2} + \frac{0.36}{b\ e} \left(1 + \frac{1}{4} \sin\gamma\right)\right] \frac{W}{T} \quad (3)$$

Where W is the total applied load, T is thickness, R is root radius and b, e and a are geometry factors shown on Figure 2. The relation was developed on the basis of a large amount of 2-dimensional photoelastic data which varies in geometry from cantilever beams to threads. Heywoods idealized shape is a series of thread like projections the tops of which are rounded off at the same radius as the fillet. In evaluating this equation for this work the position of loading (b) varies only over a range equivalent to the flat bearing surface of the projection in question.

Two programs have been written which evaluate the Heywood equation for many combinations of values for the four basic geometric parameters - root radius (R), flank angle (α), back angle (β) and loading angle (γ). One program relates to a projection of fixed height, the other to a thread. The output is one page for each shape. This page contains the fillet stress data for each load angle (γ) at each of 7 positions spaced evenly along the flat bearing surface. Also on the page is a summary consisting of the average of fillet stresses on the page, the average bearing stress and the average shear stress.

This was done for each of the two shapes and for 17 variations having the same length, height and back angle. However, six different flank angles and three different fillet radii were used. The results of this study are given in Tables I-IV. Tables I and II give the summary data - average of the fillet stresses, average bearing stress and average shear stress for the original and each variation. Tables III and IV give fillet stresses for point loads at three positions on the bearing surface, center load at the center of the bearing surface, and tip load at the intersection of the bearing and the top surfaces.

FINITE ELEMENT ANALYSIS

The finite element data was obtained using the NASTRAN triangular and quadrilateral membrane elements (CTRMEM, CQDMEN). The grids used are shown in Figure 3 a, b, c. Figure 3a is the smaller projection, 3b is the larger projection and 3c is the 2000 series elements in the fillet region which was the same in both cases. The five elements which bound the fillet itself (2010, 2018, 2020, 2034, 2042) are indicated in Figure 3c for later reference. The position and direction of the force on

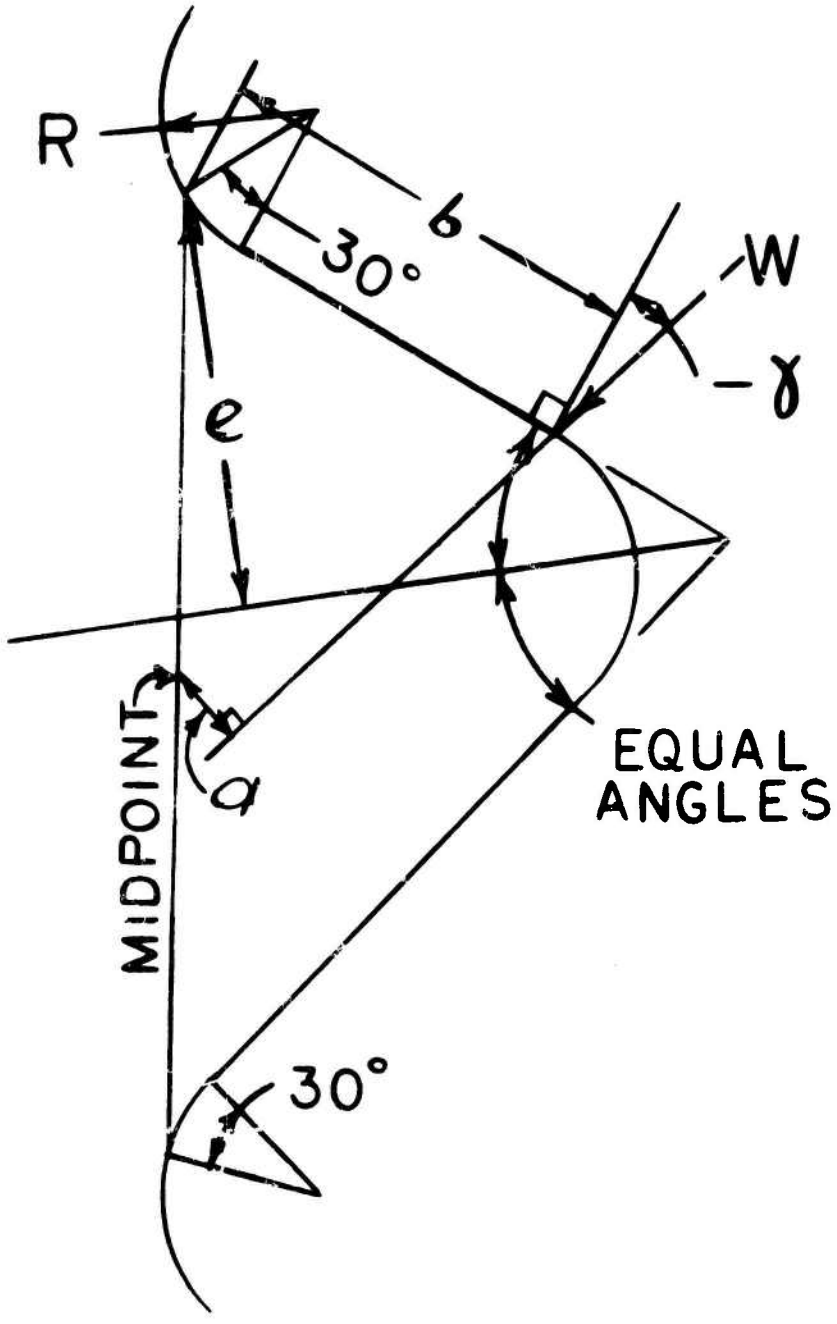

FIG. 2

Geometry Factors Used in the Heywood Equation

TABLE I

Stresses in 18 different small projections using;

WI = 1.0 BETA = 45.0 H = 3.75
T = 1.0 GAMMA = 0.0 P = 10.0
Stresses in psi

	$\sigma_{avg.\ of\ 7}$			$\sigma_{B\ avg.}$			$\tau_{avg.}$		
R→	0.26	0.52	1.04	0.26	0.52	1.04	0.26	0.52	1.04
ALPHA									
7	1.25	0.91	0.77	0.28	0.30	0.35	0.10	0.11	0.12
10	1.19	0.85	0.71	0.28	0.30	0.35	0.10	0.11	0.12
15	1.08	0.77	0.63	0.28	0.30	0.34	0.10	0.11	0.12
20	1.00	0.70	0.56	0.28	0.29	0.33	0.10	0.11	0.12
25	0.93	0.64	0.50	0.28	0.29	0.32	0.10	0.11	0.12
30	0.89	0.60	0.56	0.28	0.29	0.31	0.10	0.11	0.12

TABLE II

Stresses in 18 different large projections using;

WI = 1.0 BETA = 45.0 H = 3.77
T = 1.0 GAMMA = 0.0 P = 15.89
Stresses in psi

	$\sigma_{avg.\ of\ 7}$			$\sigma_{B\ avg.}$			$\tau_{avg.}$		
R→	0.26	0.52	1.04	0.26	0.52	1.04	0.26	0.52	1.04
ALPHA									
7	0.99	0.66	0.49	0.28	0.30	0.35	.065	.067	.071
10	0.94	0.62	0.46	0.28	0.30	0.34	.065	.067	.071
15	0.87	0.56	0.40	0.28	0.30	0.33	.065	.067	.070
20	0.81	0.51	0.36	0.28	0.29	0.32	.065	.067	.070
25	0.76	0.47	0.32	0.28	0.29	0.32	.065	.067	.070
30	0.72	0.44	0.30	0.27	0.28	0.31	.065	.066	.070

TABLE III

Fillet stresses in the small projection for three different point loads and 18 projection shapes using;

WI = 1.0 BETA = 45.0 H = 3.74
T = 1.0 GAMMA = 0.0 P = 10.0
Stresses in psi

	ROOT			CENTER			TIP		
R→	0.26	0.52	1.04	0.26	0.52	1.04	0.26	0.52	1.04
ALPHA									
7	2.20	1.20	0.76	0.99	0.79	0.72	1.32	1.05	0.93
10	2.15	1.15	0.71	0.92	0.73	0.66	1.25	0.99	0.87
15	2.08	1.08	0.64	0.81	0.64	0.57	1.14	0.90	0.70
20	2.04	1.03	0.57	0.72	0.57	0.50	1.06	0.83	0.79
25	2.02	0.99	0.53	0.64	0.50	0.44	0.99	0.77	0.66
30	2.04	0.97	0.49	0.58	0.45	0.39	0.95	0.73	0.63

TABLE IV

Fillet stresses in the large projection for three different point loads and 18 projection shapes using;

WI = 1.0 BETA =45.0 H = 3.77
T = 10. GAMMA = 0.0 P = 15.89
Stresses in psi

	ROOT			CENTER			TIP		
R→	0.26	0.52	1.04	0.26	0.52	1.04	0.26	0.52	1.04
ALPHA									
7	2.20	1.13	0.64	0.74	0.55	0.45	0.82	0.61	0.49
10	2.16	1.10	0.61	0.69	0.51	0.41	0.76	0.57	0.46
15	2.12	1.05	0.56	0.61	0.45	0.36	0.68	0.50	0.38
20	2.10	1.02	0.53	0.53	0.39	0.31	0.61	0.46	0.36
25	2.11	1.01	0.50	0.47	0.34	0.27	0.56	0.41	0.33
30	2.15	1.01	0.49	0.42	0.31	0.24	0.51	0.38	0.30

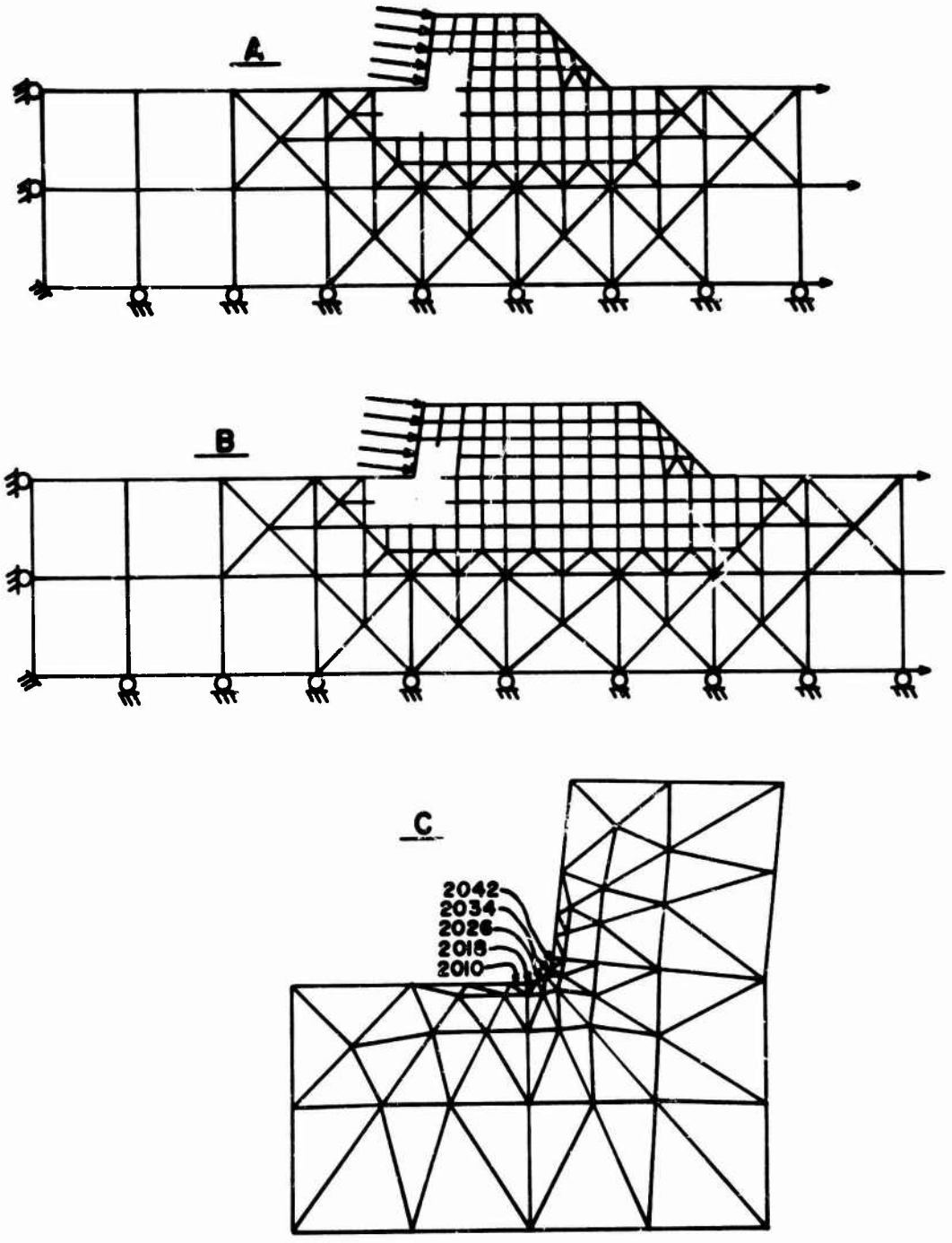

FIG. 3

NASTRAN Grids Used in 2-Dimensional Work

each possible loaded grid point is shown in Figure 3 along with an indication of the two surfaces with fixed constraints and the one fixed grid point used as boundary conditions.

Five loadings or subcase conditions will be reported on this section for each of the two projections. Four of these correspond to the data in the Heywood work. These are:

Subcase 1: Root Load
Subcase 2: Center Load
Subcase 3: Top Load
Subcase 4: Average of 5 Loads

The reader will note that in the finite element solution the flat bearing surface was divided into four equal parts instead of six as in the Heywood work. This gives the average of fillet stresses for only five loads. The fifth loading condition, subcase 5, is 1.0 psi tension in the body. Therefore, the resultant stresses can be considered as stress concentration factors for the projection on a body in tension.

The size of the finite element model is the same as the reported Heywood projections so that the data can be compared. However, in these solutions, stress will be given for the five elements which bound the fillet to give an idea of how stress varies in the fillet and to show that maximum stress is not always at the same position in the fillet. This data is in Table V.

TABLE V

First principal stress for 5 elements in each fillet of 2 different projections using;

WI = 1.0 (total) ALPHA = 7.0
T = 1.0 R = 0.26 BETA = 45.0
Stresses in psi

Elem. SUBC.	2010	2018	2026	2034	2042	2010	2018	2026	2034	2042
1	1.04	1.50	1.53	-1.67	-6.56	1.02	1.47	1.49	-1.68	-6.57
2	0.58	0.89	1.03	1.01	0.82	0.53	0.80	0.92	0.90	0.72
3	0.61	1.01	1.25	1.31	1.15	0.54	0.87	1.08	1.13	1.00
4	0.69	1.05	1.18	1.13	-1.26	0.64	1.00	1.08	1.02	-1.27
5	2.05	2.68	2.66	2.32	1.38	2.34	3.16	3.24	2.80	1.87

Subcase 1, Root load
Subcase 2, Center load
Subcase 3, Tip load
Subcase 4, Average of 5 loads
Subcase 5, 1.0 psi tension

DISCUSSION OF 2-DIMENSIONAL RESULTS

The reader will note the size of the projections analyzed. They are 1 inch thick and have characteristic lengths of 10.0 inches and 15.89 inches. Those are not the dimensions of the projections on the real component. This is because this work is intended as a relative comparison study. It would be very difficult at this point to use this type of data to calculate the stresses in an actual projection for the following reasons: On actual structures the projection would be 3-dimensional, not 2-dimensional. In an actual structure the distribution or magnitude of the contact stresses cannot be predetermined. Lastly, in a real structure the nature of the general stress field in the structure is not known. With these comments as a background the data can be shown to contain much information.

Tables I and II each give basic evaluation data for eighteen different projection shapes all having the same height. The two projections being studied are the two with an alpha of 7 degrees and a radius of 0.26. From the standpoint of fillet stress all of the eighteen shapes for each case are improvements. A substantial sensitivity to both flank angle and fillet radius is shown along with a difference in the two basic projections. The bearing stress data is essentially the same for both projections. This data shows only a small sensitivity to changes in flank angle and a larger sensitivity to changes in fillet radius. The average shear stress is relatively insensitive to either fillet radius or flank angle.

Tables III and IV show the sensitivity of maximum fillet stress to the position of the load on the bearing surface. When the load is very close to the fillet (root load), the "proximity effect" produces high stresses which as the load is moved out (center load), drop substantially. Then as the load moves to the top of the projection, it begins to act like a cantilever beam and stress begins to increase. This indicates an optimum position for the load to be applied if it were possible to select the point of application.

Table V gives some results of the finite element work. It can easily be seen that in 7 of 10 cases the maximum stress was recorded in the same element 2026 and that the only loading which shows any difference between the two projections is subcase 5.

These stresses can then be compared with the Heywood solution for the same loading and geometry. (7^{o} flank angle, .26 inch radius). In this comparison, the maximum error is for the root load. This large error is a result of the stress gradient in the elements because the load is being applied to a grid point

from element 2042. There is, of course, no Heywood information corresponding to subcase 5. Note, however, the higher stress value for the larger projection. Note also that the difference between two cases is often larger with the Heywood equation. This would indicate that the actual improvement may be somewhat less than that predicted by Heywood. This effect probably stems from the difference between the real geometry and that assumed by Heywood.

The increased stress in the tension case for the wider projection has been noted before by this author (6) in an investigation of square rifling projections. That report also showed that as a projection becomes wider relative to its height, the added material is not properly utilized to support loads and in the presence of tensile stress, can in fact, result in a higher stress. This poor utilization of the material on the back side of the projection is supported by the data reported here. For the two projections being analyzed, the average of fillet stresses is 10-17 times the shear stress. Under these conditions it would seem that the fillet would fail before the projection could shear off at the base.

THE TWO-BODY PROBLEM

The two-body problem is shown in schematic on Figure 4. The problem is of two cylinders (1 and 2) connected by two or more annular thread like projections. The six outer surfaces (sides 1 and 2, ends 1-4) may be loaded or constrained. R1 is the inner radius of the inner cylinder, R2 is the radius of the datum line of the projections and R3 is the outer radius of the outer cylinder. The length in the Z direction of either body is considered an integer product of the pitch of the thread. The NASTRAN finite element program was used to obtain a solution using axisymmetric ring elements CTRIARG and CTRAPRG. Because of the large number of possible problems in this class it has become apparent that an automated data generation program would be very useful. This program has been written in two steps (7) the most useful edition CONN5 was used in this study.

CONN5 is a FORTRAN IV program which can generate all but two cards of a NASTRAN bulk data deck. The user must input the Executive and Case Control decks as input to CONN5 and has the option of adding any other Bulk Data cards that may be required. The input data for CONN5 also contains a list of serial numbers, initial or default values, a master deck which defines the thread shape, and a card which gives specific geometry information. This seems like a great deal of data, however, once a master deck and serial number system are established, these need not be changed. Change in the Executive control deck is not common; which leaves changes in the case control deck, cards

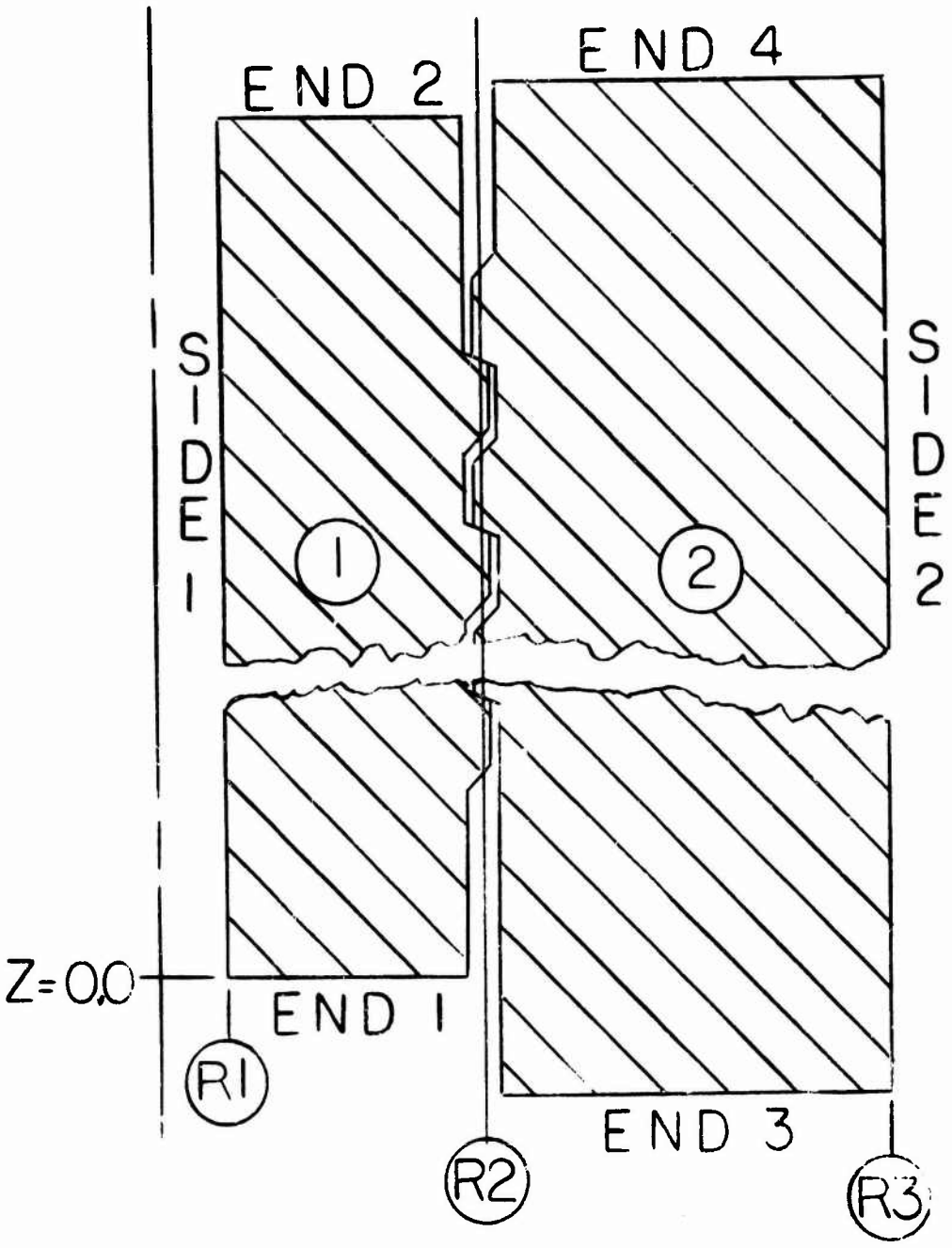

FIG. 4

Geometry of the Two-Body Problem

which control the specific geometry and loading and constraints which are the real problem. These cards are placed conveniently at the rear of the input deck to CONN5.

Referring again to figure 4 it is possible to place loads on five surfaces, side 1 and ends 1-4. Three surfaces can be constrained side 2 and ends 3-4 and in the case where R1 is equal to zero (0.0), side 1 is automatically constrained according to the special requirements of NASTRAN. The geometry information is the number of thread pairs (NUM), the pitch of the threads (P), the inner radius (R1), the datum radius (R2), and the outer radius (R3). The program will then look at the Master deck and place the threads on the datum radius using triangular ring element CTRIARG then fill in the remainder of the two bodies with trapizoidal ring element CTRAPRG. Multi-points constraint equations are written for the contact conditions, the requested fixed constraints are written, and all cards relating to the requested loads are generated. The entire data deck can be placed on tape or disk or punched and printed out on request.

The NASTRAN multi-point constraint equation is a linear first order equation which relates grid point displacements in the following way:

$$\sum_{1}^{n} a_n u_n = 0 \qquad (4)$$

where u_n is any of the displacements of grid point and a is a user selected coefficient. CONN5 writes equations which enforce two geometric conditions:

1) Bearing surfaces must remain parallel
2) Bearing surfaces must remain in contact.

Of these two, only the first may be written in an exact way, the equation for the second is an approximation. This in combination with the fact that in contact problems you do not know apriori what the deformed contact surface will be means that the multi-point constraint set generated by CONN5 is only a first approximation and may have to be changed to produce the correct solution.

Once the two-body problem has been solved, the displacement of grid points on the bearing surface can be used as input to a second run and the surface forces which are required to produce those displacements extracted. These forces are useful for such purposes as checking multi-point constraint equations and plotting the force transfer picture between the two bodies. (This process

could be simplified if the multi-point constraint forces could be directly extracted; which is mathematically possible but not supported in the NASTRAN code). If the problem is well defined and the structures well behaved bearing surface forces will have the proper sign and they will sum to the proper total input force.

The problem reported was done as an example and shows little relation to any real situation. The CONN5 generated grid is shown in Figure 5. In this problem both the projections from the 2-dimensional phase are used, however, the modelling is not detailed due to time and computer system size limitations. The inner body is a solid bar with seven of the smaller projection cut into its center surface. The outer body has seven of the larger projections on its inner surface. Three different loading subcases will be used:

1) A constant body force (gravity)

2) 1000 pounds pushing the inner body out of the outer (END 1)

3) 1000 pounds pulling the inner body out of the outer (END 2).

All loads are in the positive Z direction and the outer surface (SIDE 2) of the outer body is fixed in all degree of freedom. Both bodies have the same elastic constants; however, the density of the inner body is approximately ten times that of the outer.

RESULTS OF THE TWO-BODY WORK

The results of the sample two-body problem are shown in Tables VI and VII and in Figure 6. The tables give the axial component of bearing surface grid point forces, the total load for each thread tooth, the sum of the tooth loads, and the tooth load normalized to maximum tooth load. This information is presented for each subcase for the inner body in table VI and each subcase for the outer body in Table VII. The normalized loads are plotted against tooth number in Figure 6.

If Tables VI and VII are compared it can easily be seen that for subcases 1 and 2 the forces are equal and opposite in sign which would indicate that the multi-point constraints are working well for this simple case. In subcase 3 there is a problem: This was traced to an exponent error when the grid point displacements were input into the second run for the inner body. It is interesting to note that while the error was to thread number 4 the effect was propagated primarily to

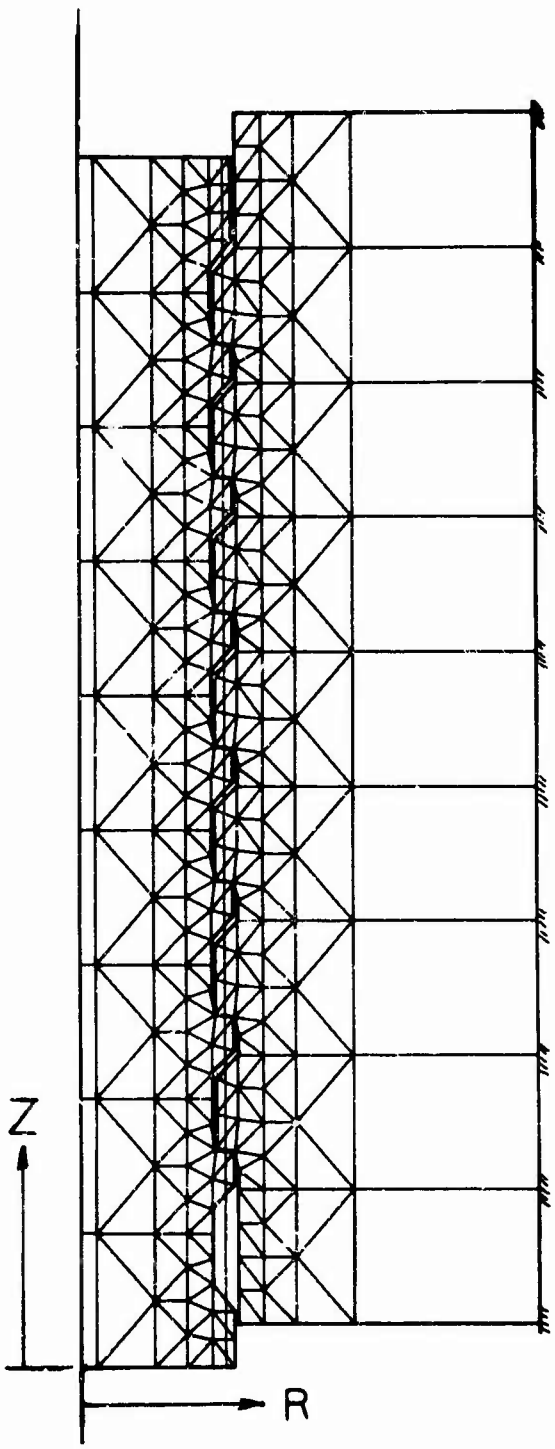

FIG. 5

NASTRAN Grid Used in Two-Body Problem

TABLE VI

Constraint forces on the inner body in the axial (z) direction.

Thread Number	Root Load	Tip Load	Total Load	Normalized Load
SUBCASE 1				
1	-0.863	-0.879	-1.742	0.985
2	-0.670	-0.692	-1.362	0.770
3	-0.615	-0.619	-1.234	0.697
4	-0.606	-0.597	-1.203	0.680
5	-0.630	-0.611	-1.241	0.701
6	-0.703	-0.676	-1.379	0.779
7	-0.917	-0.852	-1.769	1.000
			SUM=-9.930	
SUBCASE 2				
1	-268.4	-288.4	-556.8	1.000
2	-100.5	-125.4	-225.9	0.406
3	- 44.76	- 58.51	-103.3	0.186
4	- 22.10	- 29.56	- 51.6	0.093
5	- 12.22	- 16.45	- 28.6	0.051
6	- 8.07	- 10.42	- 18.4	0.033
7	- 7.05	- 8.10	- 15.4	0.027
			SUM=-1000.0	
SUBCASE 3				
1	- 5.90	- 7.11	- 13.0	0.023
2	- 3.38	- 8.01	- 11.4	0.021
3	9.62	- 11.10	- 1.6	0.003
4	- 31.56	- 16.26	- 47.9	0.086
5	- 22.6	- 32.89	-155.5	0.280
6	-117.1	- 98.04	-215.1	0.387
7	-307.7	-247.0	-554.7	1.000
			SUM=-999.2	

TABLE VII

Constraint forces on the outer body in the axial (z) direction.

Thread Number	Tip Load	Root Load	Total Load	Normalized Load
SUBCASE 1				
1	0.836	0.880	1.743	0.985
2	0.670	0.692	1.362	0.770
3	0.616	0.619	1.235	0.698
4	0.606	0.597	1.203	0.680
5	0.630	0.611	1.241	0.702
6	0.703	0.676	1.379	0.780
7	0.917	0.852	1.769	1.000
			SUM= 9.932	
SUBCASE 2				
1	268.4	288.4	556.8	1.000
2	100.5	125.4	225.9	0.406
3	44.76	58.51	103.3	0.185
4	22.10	29.56	51.7	0.093
5	12.18	16.45	28.6	0.051
6	8.07	10.42	18.5	0.033
7	7.05	8.10	15.1	0.027
			SUM= 999.9	
SUBCASE 3				
1	8.18	7.14	15.3	0.027
2	10.61	7.85	18.5	0.033
3	16.94	11.69	28.6	0.051
4	30.43	11.22	51.7	0.092
5	59.34	43.89	103.2	0.185
6	124.5	100.7	225.2	0.404
7	309.8	246.6	557.4	1.000
			SUM= 999.9	

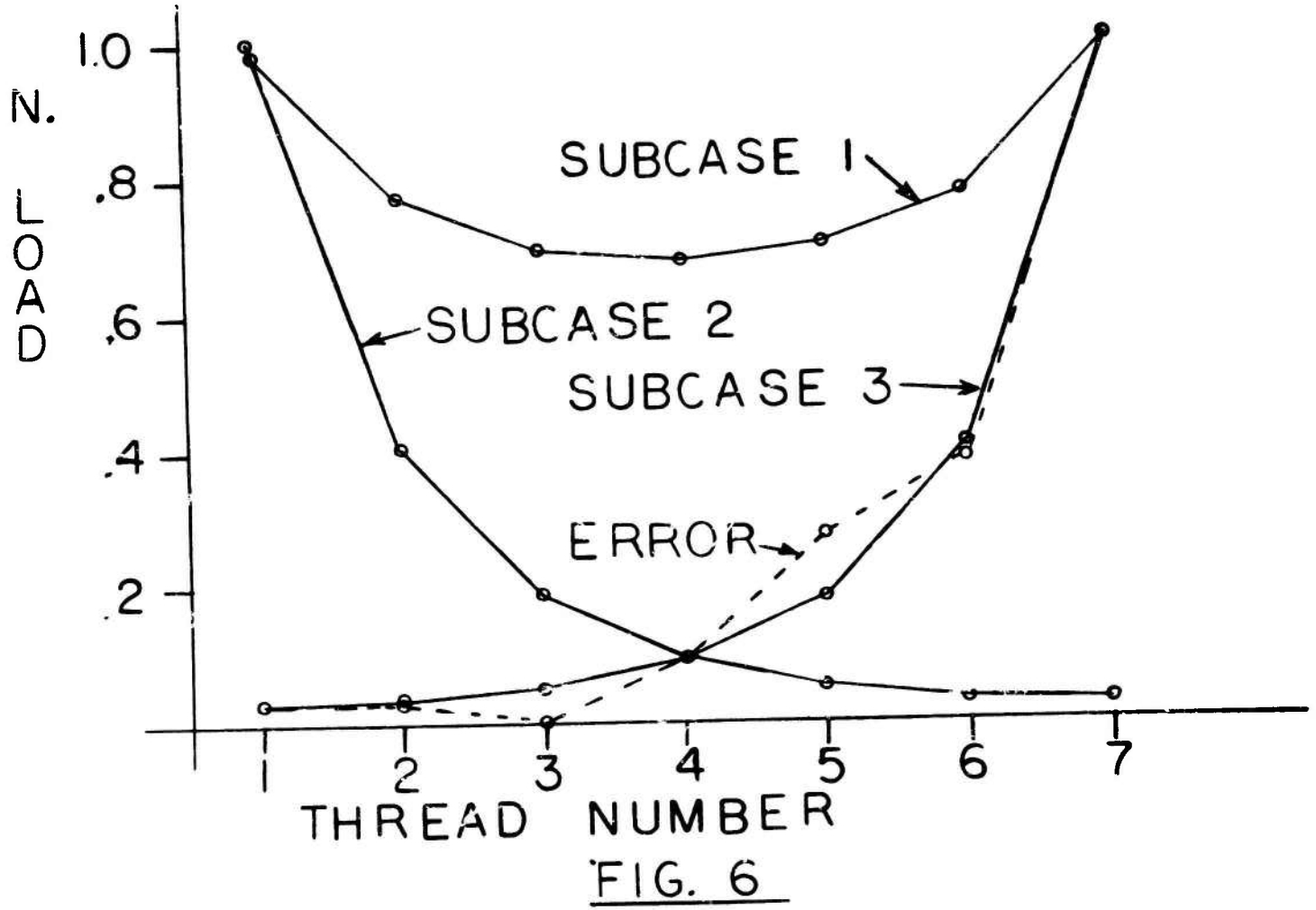

FIG. 6

Thread Load Distribution from Two-Body Problem

thread numbers 3 and 5. The distribution curve for this case is shown dashed in Figure 6.

Figure 6 clearly shows that the thread load distribution curve is a function of the loading. In subcase 1 where the load is distributed in the body all the individual thread loads are within a 32 percent spread. However, when the load is concentrated at one end of the inner body the load distribution peaks sharply on the thread nearest the load with that one carrying about 55 percent of the load.

It may seem that the bearing surface forces from this type of solution could be input into a 2-dimensional solution for a more detailed picture of an individual tooth. This is not possible because it would not account for the effect of the general stress field in the body on the tooth in question. The two-body solution would have to be run with a more detailed model of the thread tooth. Such a solution would require a very large computer system and be rather costly - however, it is possible.

CONCLUSION

It has only been possible to present a small fraction of the total data generated by the finite element solutions. The data which has been presented still demonstrate that useful information about the practical problem of thread design can be obtained using the NASTRAN finite element program. Two-dimensional finite element information has been correlated with the Heywood equation which is based on photoelastic data.

The two-body work has shown a method which can be used to calculate individual thread loads. By taking advantage of the finite element method to describe different geometries, it may be possible to control thread loads.

There are improvements which should be made in the NASTRAN program like the ability to extract multi-point constraint forces or a full contact capability.

REFERENCE LIST

1. "The NASTRAN User's Manual (level 15)" C. W. McCormick, Editor, NASA SP 222(01), June 1972.

2. "The NASTRAN Theoretical Manual," R. H. MacNeil, Editor, NASA SP 221, September 1970.

3. R. H. MacNeil and C. W. McCormick, "The NASTRAN Computer Program for Structural Analysis," Society of Automotive Engineers.

4. W. C. Hamann, "Finite Element Methods in Product Design," Mechanical Engineering, February 1974.

5. R. B. Heywood, "Tensile Fillet Stresses in Loaded Projections," Proceedings Institute of Mechanical Engineering, Vol. 160, 1949.

6. G. P. O'Hara, "Two-Dimensional Photoelastic Investigation of Stress in Rifling Projections," Watervliet Arsenal Report, WVT-6905, 1969.

7. G. P. O'Hara, "CONN4 a NASTRAN Threaded Connection Aid," Proceedings of the Fourth NAVY-NASTRAN Colloquium, Navy Ship Research and Development Center, March 1973.

EVALUATION OF BOLTED JOINTS IN GRAPHITE/EPOXY

Robert C. Van Siclen
Engineering Specialist
Northrop Corporation
Aircraft Division
Hawthorne, California

ABSTRACT

This paper discusses a program aimed at developing design procedures for bolted joints in graphite/epoxy laminates. The twofold objective of this program is the development of joint allowables for graphite/epoxy laminates and the evaluation of alternate reinforcing concepts for improving joint strength. The approach taken to establish design allowables was to obtain and evaluate actual joint test data for a particular graphite/epoxy system (Thornel 300/PR286) and from this data to establish semi-empirical procedures for predicting joint strength as a function of basic laminate properties and joint geometrical parameters. Those reinforcing concepts considered include: metallic interleaves, externally bonded on metallic doublers, laminate cross-ply buildups, and fiberglass "softening strips."

INTRODUCTION

The behavior of bolted joints in graphite/epoxy composites is a topic of primary importance, since it is one of the areas most critical to the design of graphite/epoxy structures. Although in most composite applications the use of bonded joints appears more weight efficient than bolted joints, in areas where the part is to be removed for inspection or maintenance, bolted joints are required. The main difficulty in designing mechanical joints in composite laminates is that the behavior of such joints in composites is not well understood. This is due, in part, to the general complexities associated with composite materials and partly to the lack of understanding of mechanical joints in general. Although this lack of understanding of mechanical joint behavior exists for conventional metals, it is minimized in these materials due to their ductility.

In the past, numerous studies have been conducted with the specific aim of solving the problems of mechanical joints in composite materials. Such investigations may be divided into three categories, the first concerned with predicting the elastic stress distribution around pinned joints (Refs. 1, 2), the second with semi-empirical approaches for predicting joint behavior (Refs. 3, 4, 5), and the third with optimizing the design of joints in composite laminates (Ref. 6). Whereas, the first type of study provides more insight into understanding the behavior of such joints, the second type may be more readily adapted to provide design data for such joints. The third type of investigation is forced to rely on only a very limited amount of substantiation but can provide guidelines to streamlining joint design. A rather complete survey of the work done in mechanically fastened joints in composites prior to 1968 is provided in Reference 7.

Finally, as a result of the knowledge gained from these investigations, other investigators have looked at ways for improving joint behavior by providing reinforcing around the fastener holes. The reinforcement studies conducted to date have included two primary approaches, one concerned with increased strength and/or stiffness at the joint by use of such reinforcements as metal (Refs. 8, 9), parent material build-up (Refs. 8, 10) and boron/polyimide film (Refs. 11, 12) and the other concerned with methods for reducing the stiffness of the material at the hole through use of "softening" materials (Refs. 10, 13).

An understanding of the various modes of failure which commonly occur in bolted joints in composites is fundamental in predicting the strength of such joints in composite laminates.

As pointed out in Reference 14, four basic failure modes are possible for mechanical joints in composite materials. These are (1) shearout (or cleavage) failure of the laminate, (2) tensile failure of the material, (3) bearing failure of the materials, and (4) various types of bolt or pin failures. Additionally, combinations of these failure modes are possible. The first three types of failures are shown in Figure 1.

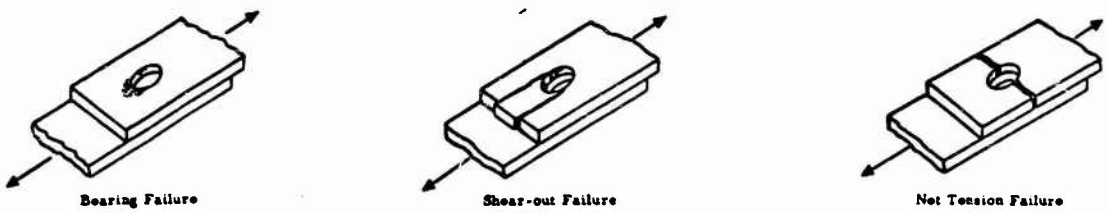

FIGURE 1. POTENTIAL MODES OF FAILURE IN GRAPHITE/EPOXY BOLTED JOINT SPECIMEN

The factors which influence the behavior of mechanical joints in composite materials also affect the behavior of such joints in conventional materials. However, some of these parameters have a more marked effect in composites than in conventional materials. Specific geometric properties which affect joint behavior are edge distance (e), side distance (s), hole diameter (D), and laminate thickness (t).

Because of the nature of composite materials, the material parameters which influence the behavior of mechanical joints in composite materials are more numerous than those for conventional materials. This is due primarily to the ability to tailor the strength and stiffness properties of the composite laminate by proper orientation of the individual lamina. Those material properties which affect laminate behavior are fiber orientation, stacking sequence, and type of material system.

The type of fastener used in the design can also greatly influence joint strength. When countersunk fasteners are used rather than protruding head fasteners, the bearing strength of the composite joint may be severely reduced due to the reduced bearing surface. In addition, other type fasteners, such as hi-loks, must be considered. Finally, the type of joint loading must be accounted for. Whether it is a double or single lap joint can greatly affect the joint strength.

APPROACH

The approach taken during this study was to combine experimental investigation and analytical assessment to arrive at procedures for predicting the mechanical joint strength of a particular graphite/epoxy composite system, Thornel 300/PR286. The study was limited to the family of 0°, ±45°, and 90° plies, since this family of laminates is the most commonly used.

Initially, an extensive review of all available data on mechanical joints in both composite and conventional materials was conducted. As previously mentioned, this review indicated that all previous studies fit into three primary categories, those concerned primarily with predicting the elastic stress distribution around pinned joints, those concerned principally with semi-empirical approaches for predicting joint behavior, and those concerned with joint optimization. As a result of this review, it was determined that the most realistic approach at this time for establishing design allowables would be to combine experimental investigation with an analytical assessment of the test results.

In order to provide the necessary data base for assessing the behavior of these joints for variations in significant parameters, an experimental study was planned and augmented. The test program was planned to provide the maximum amount of usable data for the minimum number of tests. To do this, the majority of data was gathered for an 8 ply $(0°, \pm 45°, 90°)_s$ laminate. In order to assess the effect of various reinforcing concepts on joint strength and behavior, both reinforced and unreinforced laminates were tested.

The final portion of this study consisted of an analytical assessment of the results of the experimental study. Alternate approaches currently used to predict joint behavior were evaluated, as well as new approaches for predicting joint behavior. A comparison of the results of the reinforcement study on the basis of weight, fabricability, and geometric considerations was made.

EXPERIMENTAL INVESTIGATION

The actual test program conducted during this study consisted of two phases, one to provide data to aid in developing joint allowables for graphite/epoxy laminates and the other to evaluate alternate reinforcing concepts for improving joint strength. The specific reinforcing concepts which were investigated during the Phase II tests included: metallic interleaves, externally bonded on metallic doublers, laminate cross-ply buildups, and both woven and unidirectional fiberglass.

The basic graphite/epoxy system tested during this investigation was Thornel 300/PR286. All data were gathered from single fastener straight-sided coupon specimens static tested at room temperature. The bolt diameter used for all specimens was 3/16-inch with each bolt torqued to a constant value of 25 in-lb. During Phase I, the maximum amount of data was gathered for the $(0°, \pm 45°, 90°)_s$ laminate since this laminate was felt to represent a fairly typical laminate for actual use with mechanical joints and had been selected as the basic laminate for the Phase II studies. A summary of all of the specimens tested during this study including detail of the layup and purpose of the test is provided in Table I.

All tests were conducted using a 20,000 lb. Instron test machine with the test setup as illustrated in Figure 2. Prior to test each specimen's overall alignment was checked to ensure that load eccentricities were kept to a minimum value. Machine loading rate was selected to ensure that specimen failure occurred in one to two minutes, thereby preventing impact loading of the specimen which could induce premature specimen failure. Specimen load was introduced into the double lap joint specimen through two 0.25-inch thick steel doubler plates. Load was introduced into the single shear protruding head fastener specimen through a steel plate designed to minimize any load eccentricities on the composite specimen. During each test a plot of load versus machine head travel was made, in order to record the load at which initial failure occurred. All specimens were tested until ultimate failure occurred.

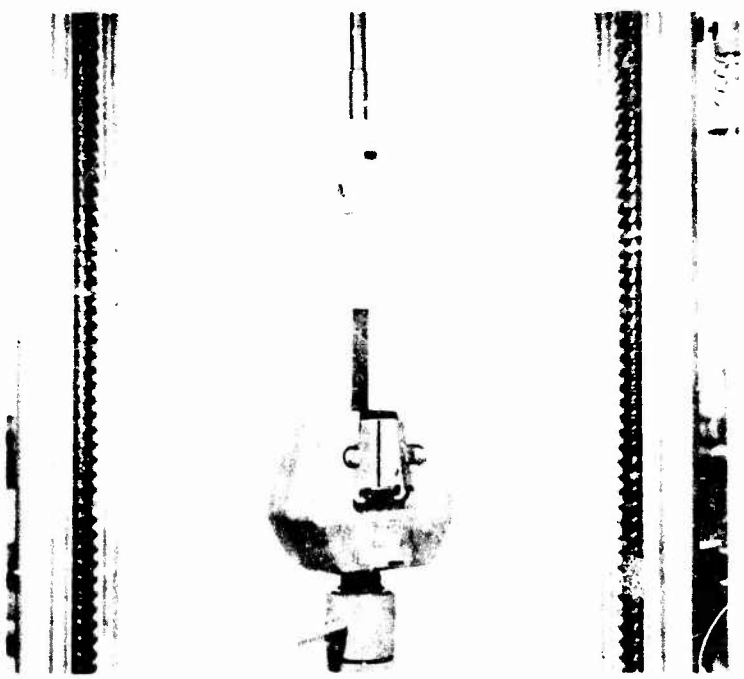

FIGURE 2. JOINT TEST SETUP

TABLE I. SUMMARY OF MECHANICAL JOINT EVALUATION TESTS

NOTE: All tests run at room temperature only (static tests only)

Hole Diameter, D = 3/16", e = Edge distance, a = Side distance

Specimen No.	No. of Specimens	e (in.)	s (in.)	Type of Test	Type of Laminate	Remarks
1	3	.75	.75	1	A	Select min. e/D and s/D values for max. P_{Fail} for double lap joint with protruding head fasteners
2	2	.56	.38	1	A	
3	3	.56	.50	1	A	
4	3	.56	.75	1	A	
5	3	.38	.50	1	A	
6	3	.38	.75	1	A	
7	2	.19	.50	1	A	
8	3	.75	.50	1	B	Evaluate affect of D/t variations
9	3	.56	.50	1	C	
10	3	.75	.75	2	B	Select min. e/D and s/D values for max. P_{Fail} for single lap joint with protruding head fasteners
11	3	.56	.50	2	B	
12	3	.56	.75	2	B	
13	3	.38	.50	2	B	
14	3	.38	.75	2	B	Evaluate effect of D/t variations
15	2	.75	.50	1	D	Evaluate externally bonded on doublers as a reinforcing technique
16	3	.56		1	D	
17	3	.38		1	D	
18	3	.75		1	E	Evaluate use of additional layers of graphite/epoxy as a reinforcing technique
19	3	.56		1	E	
20	3	.38		1	E	
21	3	.75		1	F	Evaluate the use of metallic interleaves as a reinforcing technique
22	3	.56		1	F	
23	3	.38		1	F	
24	3	.75		1	G	
25	3	.56		1	G	
26	3	.38		1	G	
27	3	.75		1	H	Evaluate the use of E-Glass/Epoxy as a reinforcing technique
28	3	.56		1	H (Woven Cloth)	
29	3	.38		1	H (Woven Cloth)	
30	3	.75		1	I	
31	3	.56		1	I (Unidirectional)	
32	3	.38	.50	1	I (Unidirectional)	
33	3	.56	.50	1	J	Evaluate the effect of laminate ply orientation on joint strength
34	3	.56	.50	1	K	
35	3	.56	.50	1	L	
36	3	.56	.50	1	M	
37	3	.56	.50	1	N	
38	5	.56	.50	1	A	Evaluate alternate hole fabrication technique
39	5	.56	.50	1	N	
40	1	.38	.50	1	B	Miscellaneous
41	2	.56	.25	1	B	

Total = 121 Specimens

Laminate Types (Preliminary) (For region of specimen with hole) - Unless otherwise noted all plies are Thornel 300/PR286 graphite/epoxy

A - $(0°/\pm45°/90°)_s$
B - $(0°/\pm45°/90°)_{2s}$
C - $(0°/\pm45°/90°)_{4s}$
D - $(M/0°/\pm45°/90°)_s$ - M = Outside bonded-on metal doubler (Titanium)
E - $(0°/\pm45°/90°/\pm45°/0°/\pm45°/90°)_s$
F - $(0°/ti/\pm45°/ti/90°)_s$ or $(0°/-45°/ti/+45°/ti/90°)_s$
G - $(0°/ti/+45°/ti/-45°/ti/90°)_s$
H - $(0°_{G2}/\pm45°/90°)_s$ G - Glass Layer
I - $(N/\pm45°/90°)_s$ N - Layer of woven E-glass fabric
J - $(0°/\pm45°/90°/\pm45°)_s$
K - $(0°_2/\pm45°/90)_s$
L - $(\pm45°)_{2s}$
M - $(0°/90°)_{2s}$
N - $(0°_2/\pm45°)_s$

PHASE I TESTS

Table II contains a summary of the test results obtained during Phase I. Tests run during this phase consisted of a detailed evaluation of the various parameters that potentially influence the behavior of mechanical joints in graphite/epoxy laminates. At this time both double and single lap protruding head fastener tests were run. In addition to varying the laminate layup, the geometric parameters, edge distance, side distance, and laminate thickness were also varied.

The specimen tested during this phase consisted of straight-sided single fastener coupon specimen with an overall length of 5.0 inches. Specimen width was twice the side distance, S. The fastener hole was located a distance e from the edge of the specimen. No tabs were required at the grip ends of the specimen since all specimens were designed to fail at loads considerably below the basic laminate tensile strength. Typical failed specimen from this phase of the test program is shown in Figure 3.

Specimen test results for this phase provided significant information on the behavior of graphite/epoxy bolted joints. From these tests, data was obtained on each of the three primary modes of failure: bearing, shearout, and net tension. As shown in Table II almost no delaminations occurred in the test specimen even after failure. In general, for those specimen in which initial failure was noticed, it occurred at stress levels no more than 20 percent below ultimate failure load.

PHASE II TESTS

In this phase of the test program a total of 54 double lap bolted joint specimens were fabricated and tested in order to evaluate alternate joint reinforcing techniques. The results of these tests are summarized in Table III. The specimens were fabricated in such a way that they included the transition from the baseline 8-ply laminate into the reinforced joint area. Specimens typical of each of the different reinforced joint concepts are shown in Figure 4. All specimens but the externally-bonded on titanium reinforced specimens were fabricated with the build-up being entirely on one side of the test specimen. This was done to minimize the difficulty of fabricating the specimen and was felt justified since this was probably more representative of a production situation. In the case of the externally bonded-on doublers, the same thickness doublers were bonded onto both sides of the specimen. With the exception of the fiberglass reinforced specimen, all specimen tested were tabbed to prevent premature failure of the specimen at the grips.

The materials selected as reinforcement for this study consisted of the following. For the metal reinforcement, 6Al-4V titanium was used both for the interleaves and the external doublers. The titanium interleaves were .006-inch/ply thick to be as compatible as possible with the .0055-inch/ply thickness of the graphite/epoxy. The bonded-on titanium doublers were made from .016 inch thick material. The fiberglass reinforcement used was unidirectional Scotchply 1009-26 and woven CORDOPREG E-203 (181 Weave). Both of these E-glass/epoxy systems were selected since they were compatible with the

TABLE II. RESULTS OF PHASE I TEST PROGRAM

TEST SPECIMEN NO.	THICKNESS t (IN.)	END DISTANCE e (IN.)	SIDE DISTANCE s (IN.)	INITIAL FAILING LOAD P_i (LBS.)	FAILING LOAD P_b (LBS.)	NET-SECTION STRESS F^{tu}_{nu} (KSI)	BEARING STRESS F_{br} (KSI)	NET TENSION STRESS F_{nt} (KSI)	MODE OF FAILURE
1A[1]	.040	.75	.75	395	514	9.8	87.4	9.8	B
1B[1]	.040	.75	.75	775	1020	19.5	116.0	19.5	B
1C	.035	.75	.75	1090	1240	35.9	138.0	25.9	B
2A	.041	.56	.38	908	914	56.2	120.0	50.8	NT
2B	.040	.56	.38	1038	1038	27.7	132.5	45.9	NT
2A	.042	.56	.38	1045	1090	37.9	137.0	35.0	NT
2B	.042	.56	.50	1136	1145	29.6	145.0	33.6	NT
2C	.042	.56	.50	1,[illegible]	1150	38.9	142.0	18.5	NT
4A	.043	.38	.75	1000	1002	25.1	123.0	17.0	SO/B
4B	.042	.56	.75	1040	1138	29.1	143.0	20.6	SO/B
4C	.043	.38	.75	1020	1095	27.6	136.0	19.5	SO/B
3B	--	.25	.50	--	--	--	--	--	--
3B	.042	.38	.50	930	820	57.5	112.0	26.4	COMB.
3C	.042	.38	.50	1038	1029	42.5	138.0	30.0	COMB.
6A	.042	.38	.75	930	930	38.2	112.0	18.7	SO
6B	.044	.38	.75	930	930	40.5	110.0	16.0	SO
6C	.043	.38	.75	1020	1020	41.8	125.0	18.1	SO
7A	.040	.18	.38	415	415	56.7	56.7	13.8	SO
7B	.041	.19	.38	474	874	60.8	60.9	14.2	SO
8A	.087	.75	.38	5075	5340	25.5	125.0	30.4	NT
8B	.088	.75	.38	2570	5378	25.1	156.0	30.1	NT
8C	.089	.75	.38	2620	2620	22.7	155.0	36.3	NT
9A	.172	.38	.38	4200	4350	27.5	132.0	21.5	NT
9B	.171	.38	.38	--	4320	27.0	125.0	51.1	NT
9C	.168	.38	.38	4590	4690	30.0	147.0	34.2	NT
10A	.082	.75	.72	1950	2135	19.8	138.0	18.8	B
10B	.088	.72	.75	1860	2210	19.5	132.0	19.2	B
10C	.083	.72	.75	2270	2350	21.2	147.0	31.8	B
11A	.090	.56	.38	1840	2310	36.2	129.0	30.3	B[3]
11B	.081	.56	.38	1961	2090	37.5	133.0	31.1	B
11C	.085	.56	.38	1730	3045	26.9	131.0	30.9	B[3]
12A	.084	.38	.75	1370	3055	22.9	127.0	18.4	B
12B	.090	.56	.75	2090	3230	38.7	180.2	18.8	B
12C	.082	.56	.75	1760	1920	24.9	151.8	17.7	B
13A	.087	.38	.38	1395	1730	34.8	105.0	24.2	BO
13B	.091	.38	.38	1980	3030	39.0	117.0	37.4	BT/SO
13C	.087	.38	.38	--	3030	50.8	125.0	28.7	COMB.
14A	.086	.38	.75	--	1745	33.9	107.0	12.5	COMB.[3]
14B	.085	.38	.75	1852	1960	50.4	121.5	17.8	COMB.[3]
14C	.085	.38	.75	--	1830	39.3	117.5	17.0	COMB.[3]
33A	.065	.56	.38	1895	17[illegible]	28.4	139.0	15.7	NT
33B	.041	|	|	1730	1730	28.6	139.0	32.7	NT
33C	.046	|	|	1830	1830	37.0	130.0	11.0	NT
34A	.054	|	|	1380	1340	27.5	134.0	51.8	SO
34B	.055	|	|	1425	1422	27.9	136.0	22.0	SO/CL
34C	.054	|	|	1380	1310	28.1	128.0	29.9	SO/NT
53A	.045	|	|	870	870	31.7	106.5	25.0	NT[4]
53B	.043	|	|	855	855	21.4	104.8	24.8	NT[4]
23C	.046	|	|	930	920	53.5	110.0	26.4	NT[4]
36A	.043	|	|	515	560	14.0	69.0	18.0	SO
36B	.044	|	|	690	738	18.5	91.0	31.3	SO
36C	.043	|	|	708	708	17.7	87.0	30.3	SO
37A	.044	|	|	--	--	--	--	--	--
37B	.042	|	|	956	983	31.5	123.0	28.8	B/CL
37C	.042	|	|	979	979	24.5	120.0	28.1	B/BO
38A	.047	.38	|	--	1030	24.0	118.0	37.6	NT
38B	.047	.27	|	--	1080	24.8	130.0	28.4	BT
38C	.048	.56	|	--	1080	25.1	134.0	29.0	NT
35B	.042	.37	|	--	1038	24.4	119.0	38.9	SO
35B	.030	.37	|	--	1060	32.8	112.0	26.2	NT
39A	.044	.56	|	--	970	31.3	104.0	34.4	SO
39B	.044	.55	|	--	730	18.3	89.5	21.0	SO
39C	.043	.54	|	--	890	22.2	109.0	33.8	SO
39B	.047	.22	|	--	905	20.7	101.0	33.8	SO
39E	.045	.56	|	--	930	33.0	107.3	35.2	20
40A	.040	.38	.38	1980	1980	38.8	116.0	37.2	NT/CL
41A	.040	.56	.25	1320	1230	14.8	71.4	41.7	NT
41E	.083	.56	.31	1270	1270	18.3	80.7	40.3	NT

1. Specimens not torqued prior to test
2. B - Bearing failure
   NT - Net tension failure
   SO - Shearout failure
   CL - Cleavage failure
   COMB - Combination of failures at hole
3. Delamination
4. Tearout at 45°

TABLE III. RESULTS OF PHASE II TEST PROGRAM

TEST SPECIMEN NO.	THICKNESS t (IN.)	EDGE DISTANCE e (IN.)	SIDE DISTANCE s (IN.)	INITIAL FAILURE LOAD P (LBS.)	FAILURE LOAD P_y (LBS.)	SHEAR-OUT STRESS F_{SO} (KSI)	BEARING STRESS F_{BR} (KSI)	NET TENSION STRESS F_{NT} (KSI)	MODE[1] OF FAILURE
15A	.045	.75	.50	2925	2825	28.0	193.0	45.3	PM
15B	.045	.75		3150	3150	31.2	215.0	51.5	PM
15C	.045	.75		--	--	--	--	--	--
16A	.045	.56		2830	2830	40.0	195.0	45.7	PM[2]
16B	.045	.56		2940	2940	41.0	201.0	47.2	PM[2]
16C	.045	.56		2925	2960	41.4	202.0	47.5	PM[2]
17A	.045	.38		2820	2820	64.2	193.0	45.2	COMB.
17B	.044	.38		2340	2340	54.0	162.0	38.0	PM
17C	.045	.38		2700	2700	81.5	135.0	45.3	COMB.
18A	.114	.75		3000	3000	20.1	139.0	32.7	PM
18B	.112	.75		3000	3000	20.3	141.0	33.0	PM
18C	.113	.75		3060	3060	20.7	143.0	33.5	PM
19A	.116	.56		3060	3060	29.8	145.0	34.9	PM[2]
19B	.111	.56		2850	2910	27.8	136.0	31.8	PM[2]
19C	.113	.56		2575	2950	28.6	140.0	32.8	PM[2]
20A	.112	.38		2350	2350	36.8	110.0	25.9	NT/CL
20B	.113	.38		2270	2270	35.3	106.0	24.9	NT
20C	.111	.38		2375	2375	37.6	113.0	26.4	NT/CL
21A	.072	.75		2310	2310	24.5	169.0	39.6	PM
21B	.073	.75		2260	2260	23.7	183.0	38.2	PM[2]
21C	.072	.75		2290	2290	24.3	167.5	39.2	PM[2]
22A	.070	.56		2175	2370	38.4	178.3	41.8	PM[2]
22B	.070	.56		2125	2310	38.6	188.5	44.2	PM[2]
22C	.070	.56		2125	2300	38.5	188.0	44.1	PM[2]
23A	.068	.38		2010	2010	51.8	135.5	43.4	B/SO[3]
23B	.073	.38		1825	1925	46.3	139.0	32.6	B/SO[3]
23C	.072	.38		1800	1975	48.2	144.0	33.8	B/SO[3]
24A	.081	.75		2240	2640	24.9	172.0	40.3	PM[2]
24B	.081	.75		2400	2590	24.4	168.0	39.5	PM[2,4]
24C	.081	.75		2330	2330	22.0	151.5	33.6	PM[2,3,4]
25A	.085	.56		2350	2580	23.2	156.0	37.5	PM[2,3,4]
25B	.085	.56		2325	2585	23.2	160.0	37.5	PM[2,3,4]
25C	.083	.56		2325	2325	22.7	156.0	36.8	PM[2,3,4]
26A	.08	.38		2290	2450	21.0	145.5	34.0	B/SO[3]
26B	.085	.38		2385	2385	21.4	149.0	23.0	PM[4]
26C	.089	.38		1975	2340	19.0	138.2	32.5	B/SO[3]
27A	.098	.75		1490	2290	17.9	123.0	28.9	NT
27B	.096	.75		1220	2270	18.1	126.0	29.2	NT
27C	.098	.75		1380	2260	17.8	121.5	28.5	NT
28A	.099	.56		1600	2010	21.8	107.0	25.0	NT/SO
28B	.098	.56		1490	2000	22.0	107.5	25.2	NT
28C	.099	.56		1540	1980	21.6	105.5	24.7	NT
29A	.101	.38		1480	1620	28.1	84.5	19.8	NT/SO
29B	.103	.38		1470	1620	27.6	83.0	19.4	NT/SO
29C	.101	.38		1360	1560	27.4	82.5	19.3	NT/SO
30A	.060	.75		1225	1515	19.3	133.0	31.2	COMB
30B	.060	.75		1440	1530	19.5	134.0	31.4	COMB
30C	.063	.75		1440	1500	18.2	125.0	29.4	COMB
31A	.061	.56		1175	1360	24.0	118.0	27.5	NT/SO
31B	.062	.56		1275	1275	22.2	108.0	25.4	NT/SO
31C	.062	.56		1350	1390	24.1	118.0	27.9	NT/SO
32A	.060	.38		1100	1100	32.2	96.5	22.6	NT/SO
32B	.060	.38		1090	1090	31.9	95.5	22.4	NT/SO
32C	.060	.38	.50	1090	1090	31.9	95.5	22.4	NT/SO

NOTES:

1. PM - Parent Material (away from hole)
   Comb - Combination failure at hole
   B - Bearing failure
   SO - Shearout failure
   NT - Net tension
   CL - Cleavage failure
2. Noticeable bearing at the hole
3. Specimen delamination
4. Parent material failure at start of buildup

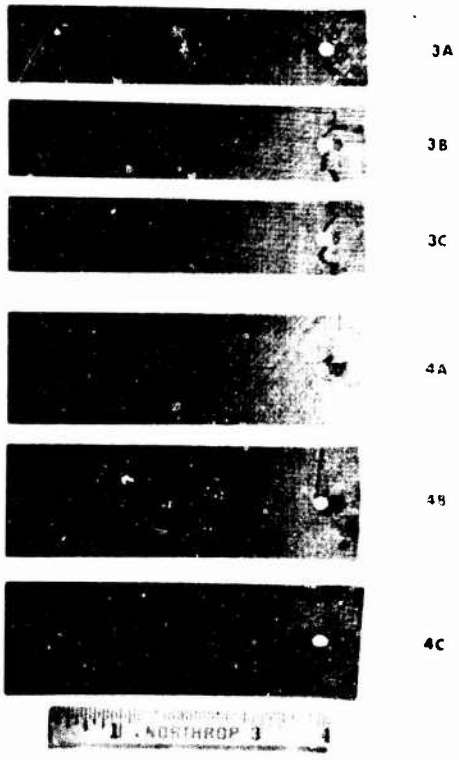

FIGURE 3. TYPICAL FAILED SPECIMEN FROM PHASE I TEST PROGRAM

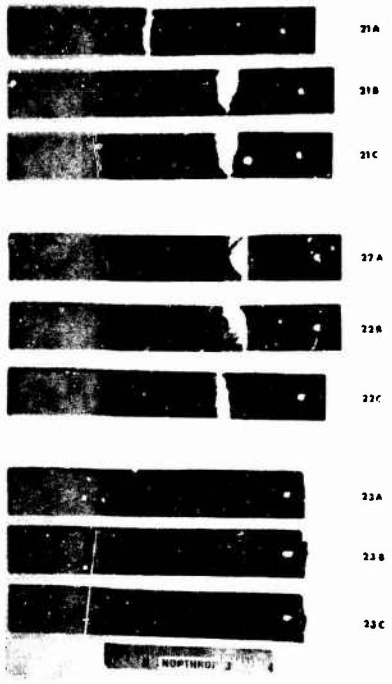

FIGURE 4. TYPICAL FAILED SPECIMEN FROM PHASE II TEST PROGRAM

Thornel 300/PR286 graphite/epoxy which cures at 350°F. Unidirectional and woven glass fabric were evaluated since each of these materials offer potential for use as "softening strip" materials for both loaded and unloaded holes.

The specimens were designed as nearly as possible to allow each joint to sustain a load of 3,000 lbs which was established from test as the tensile load capability for a one-inch wide strip of the basic laminate without a hole.

As shown in Table III a number of the reinforced specimens failed away from the loaded hole in the unreinforced laminate at loads close to 3,000 lbs. In the case of the titanium interleaf specimen, failure appeared to originate at the transition from the parent laminate to the area of the reinforced hole. For the metal interleaf, metal doubler, and parent material build-up specimen, at least one of the specimen configurations failed in the area of the joint at load levels close to the desired 3,000 lbs. However, for the glass reinforced specimens the failures occurred at load levels considerably below the 3,000 lbs.

ANALYTICAL ASSESSMENT

The data from the Phase I program was analyzed on the basis of considering each of the three potential joint failure modes which can occur in the composite laminate, i.e., bearing, shear-out, and net tension failure. This approach was followed since the results of the Phase I test program showed that specimen failure did indeed occur in one of these three distinct failure modes or by a combination of them. Therefore, by knowing the load level at which each of these modes of failure will occur, the load at which a particular joint will fail may be determined as the minimum of these three values.

NET TENSION FAILURE

As illustrated in Figure 5 for a $(0°, \pm45°, 90°)_s$ graphite/epoxy laminate the allowable net tensile stress for a laminate is significantly reduced as the ratio of side distance-to-diameter ratio (s/D), is increased. Thus, by increasing side distance so that the s/D value exceeds 3 or 4 will not significantly increase the net tensile load carried by the joint. This apparent reduction in strength is reasonable in light of the presence of high stress concentrations at the net section which become maximum at the edge of the fastener hole.

In Reference 8, Lehman presents an approach to predicting the elastic net tension stress concentration factor, SCF, for composite laminates. This work represents an extension to orthotropic laminates of the experimental work which had been done by Frocht and Hill (Reference 15) in determining elastic stress concentration factors for loaded holes in isotropic materials. This approach offers significant improvement over the more conventional approach used to predict the allowable net tensile load for a mechanical joint in a composite, which effectively treats the net tensile strength as being essentially independent of the geometric properties of the joint for a given range of s/D values. At best the conventional approach can be extremely conservative, while at worst it can lead to poorly designed understrength joints (e.g., extremely high s/D values). Further, to use such an approach with any degree of correctness, it is necessary to determine net tensile strength allowables for numerous values of s/D which implies a substantial amount of testing.

The approach presented by Lehman bears on being able to predict the maximum net tension stress concentration factor, SCF, at the edge of the hole, K_{tc}, from the following equation:

$$K_{tc} = 1 + A\left[\left(\frac{D}{2s}\right)^{-0.55} - 1\right]\left(\frac{e}{2s}\right)^{-.5} \qquad (1)$$

The value of A in equation (1) is taken as a constant for a particular laminate orientation and is determined from tests of the particular laminate orientation. A comparison of actual test results from $(0°, 90°, \pm45°)_s$ specimen of various e/D and s/D values with results obtained using equation (1) is provided in Figure 5. As can be seen from this figure, generally good agreement occurs between theory and test results.

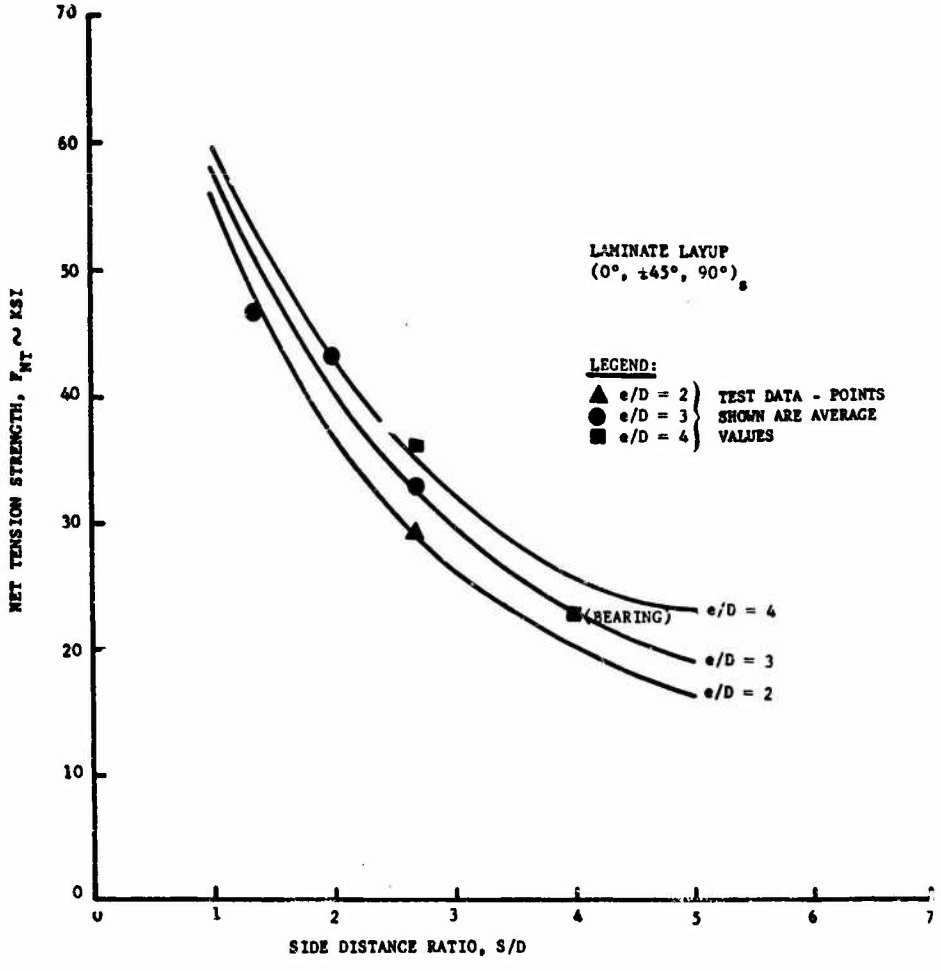

FIGURE 5. COMPARISON BETWEEN THEORETICAL NET TENSION STRENGTHS AND EXPERIMENTAL RESULTS SHOWS GOOD AGREEMENT

By knowing the value of K_{tc} and the parent ultimate tensile strength of the unflawed laminate, F_x^{tu}, the value of F_{NT} may be computed:

$$F_{NT} = \frac{F_x^{tu}}{K_{tc}} \tag{2}$$

Utilizing the value of F_{NT} determined from Equation (2), the net tensile strength of a given joint, P_{NT}, may be determined from the following equation:

$$P_{NT} = F_{NT}\,(2s - D)t \tag{3}$$

SHEAR-OUT FAILURE

As shown in Figure 6 from the data for a $(0°, \pm 45°, 90°)_s$ graphite/epoxy laminate, the allowable shearout strength for such a laminate is significantly reduced as the edge-distance-to-diameter ratio, e/D, is increased. Beyond a value of e/D equal 4.0 bearing at the hole becomes the mode of failure. Data of this type differs significantly with reported values such as those provided in the Air Force Design Guide (Reference 14) which imply that the shearout strength is a constant value for a particular laminate orientation. Further, the use of constant shearout equations can lead to excessively conservative designs, or worse, totally unconservative designs depending on the value of e/D for the specimen from which the shearout strength was determined.

For excessively large values of e/D, say e/D = 10, although the shearout strength continues to decrease, it will do so at a much slower rate than that shown in Figure 6 for low values of e/D. No consideration was given to the high e/D range in this investigation since in this range bearing failure precludes any shearout failure from occurring.

The phenomena of varying shearout strength as a function of e/D is similar to the apparent variation in shear strength of a bonded joint as the overlap length is increased. For a bonded joint, increasing the overlap length

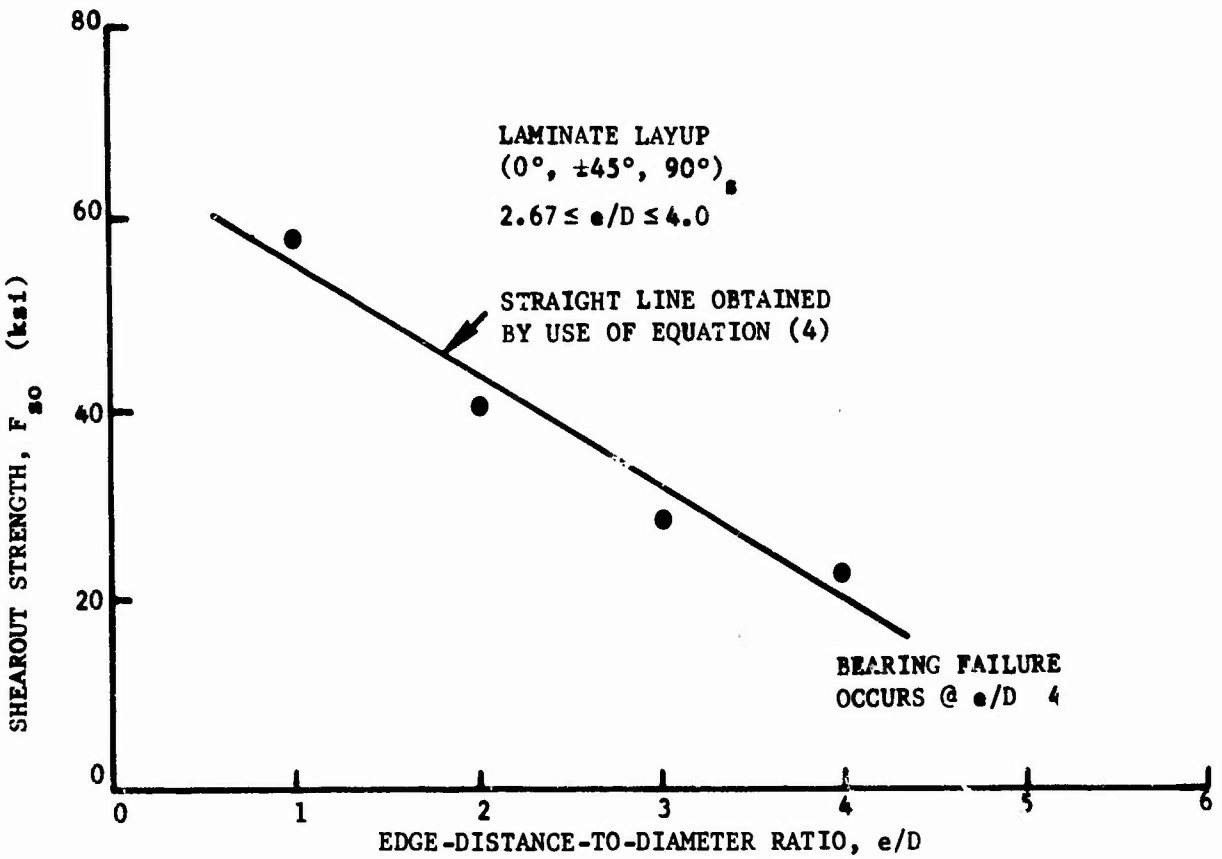

FIGURE 6. SHEAROUT STRENGTH IS NOT CONSTANT FOR A GIVEN LAMINATE

beyond a certain value does not appreciably increase the load that can be transferred across the bonded joint. As in the case of bonded joints, undoubtedly significantly high peak shear stresses are present at the portion of the laminate immediately adjacent to the mechanical fastener. However, as the length of the edge distance is increased, the magnitude of the peak stress is not significantly reduced.

The equation given below was found to approximate the results of the data shown in Figure 6 within normal data scatter. The equation for the shearout strength, F_{so}, is:

$$F_{so} = A_1 \left(\frac{e}{D}\right) + A_2 \qquad (4)$$

The values A_1 and A_2 are constants determined for a specific laminate orientation. The value of A_1 and A_2 found from the study were -11.7 ksi and 65.0 ksi, respectively, for a $(0°, \pm 45°, 90°)_s$ laminate. In order to determine the two constants required for this equation at least two specimens of different e/D values must be tested.

Knowing the shearout strength from equation (4), the value of the allowable load on the fastener at shearout failure P_{so}, is computed from the following equation:

$$P_{so} = F_{so} Dt \left(2\frac{s}{D} - 1\right) \qquad (5)$$

BEARING FAILURE

Based on the results of past investigations, the bearing strength of a given orientation laminate was assumed to be dependent only on the diamter-to-thickness ratio, D/t. Further, it was assumed that there is a theoretical maximum bearing strength for any given orientation, but that for high values of D/t this value is reduced due to local buckling at the hole. Since only limited tests could be run during this program, data was gathered for the eight ply specimen which corresponded to a D/t value of 4.4 (a reasonably high value of D/t). This was done to ensure that bearing allowables obtained from this program would not be overly optimistic for thin laminates.

It was found from the test program that true bearing failures could only be obtained by increasing the edge-distance-to-diameter ratio and the side-distance-to-diameter ratio to prevent shearout and net tension failures from occurring. Keeping this in mind, the equivalent bearing stress contour plot shown in Figure 7 was developed. Although the equivalent bearing values shown here were not obtained entirely from actual bearing failures, the plot represents at least minimum bearing allowables based on the maximum bearing stress at the time the joint in a particular laminate failed. Thus, although a laminate with 40% 0°, 40% ±45°, and 20% 90° plies failed in shearout, nevertheless this occurred at an equivalent bearing stress value of 133,000 psi. The use

of equivalent bearing allowables is conservative and can be improved by running additional tests to obtain actual bearing failures. It should be noted that the bearing values shown are fairly high, especially in light of the very low density of graphite/epoxy ($\rho = .055$ lb/in^3).

The allowable bearing load on the joint P_{BR} may be computed from the following equation:

$$P_{BR} = F_{BRu} Dt \tag{6}$$

Where F_{BRu} is the ultimate bearing strength of the laminate.

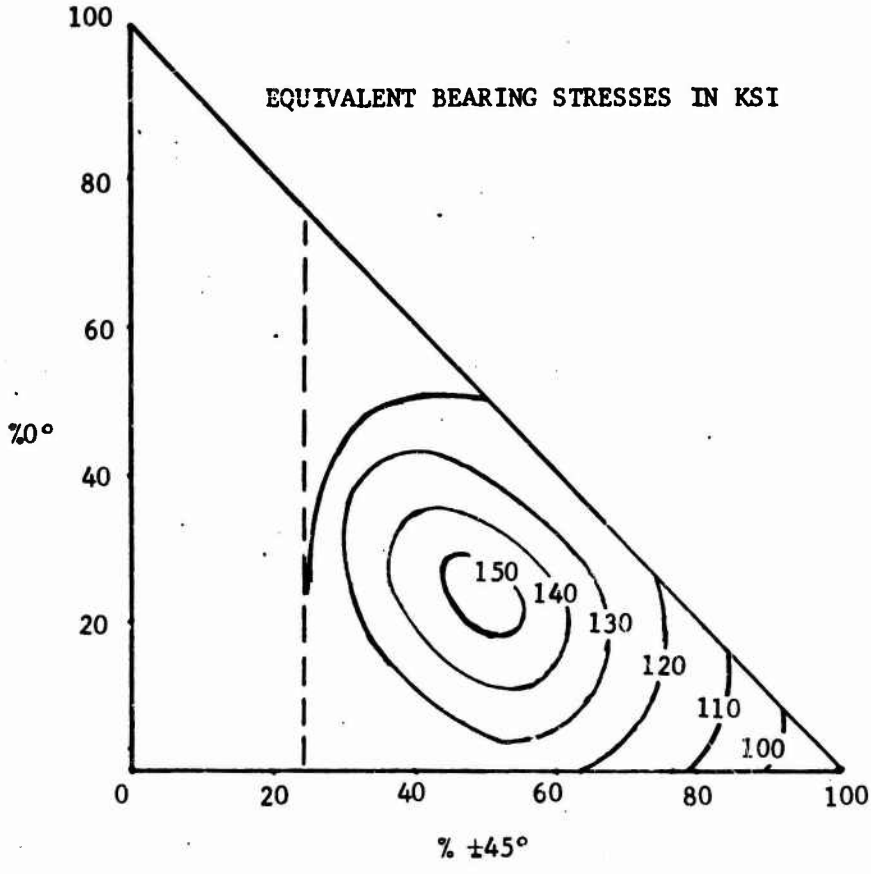

FIGURE 7. EQUIVALENT BEARING STRENGTH CONTOUR PLOT FOR (0°, ±45°, 90°) FAMILY OF LAMINATES

COMPARISON OF ALTERNATE REINFORCING CONCEPTS

Upon completion of the Phase II test program each of the alternate reinforcing concepts was compared on the basis of weight, fabrication, and geometric requirements (i.e., thickness, edge distance, etc.). Data for each of the different reinforcing approaches was compared by adjusting the joint thickness and weight by the ratio of actual specimen failure load to the desired 3,000 lb load. Figure 8 summarizes the results of this comparison made on the basis of weight and thickness. As can be seen from this figure the minimum weight reinforcing approach was to use ±45° graphite/epoxy plies to reinforce the laminate in the area of the joint. However, for the case of minimum thickness, the reinforcing concept utilizing internally bonded titanium interleaves was the smallest with a thickness of .087 in. required to carry the 3,000 lb. load.

The minimum weight edge distance required for those specimens reinforced with metal layers (bonded either internally or externally) was at an e/D of 2, while for the all graphite/epoxy or the hybrid composite (fiberglass and graphite) specimens, the optimum value of e/D was 3. Thus, for design of a mechanical joint in which the geometry of the joint must be kept to a minimum, the use of metallic reinforcement offers the most efficient approach.

From a fabrication standpoint the all graphite/epoxy laminate provided the most satisfactory approach due to ease of both fabrication and machining. The least desirable approach from a fabrication standpoint was the use of internally bonded titanium interleaves which were both difficult to fabricate (primarily due to the cleaning required) and difficult to machine (delaminations occurred at specimen edges and at the edge of the holes).

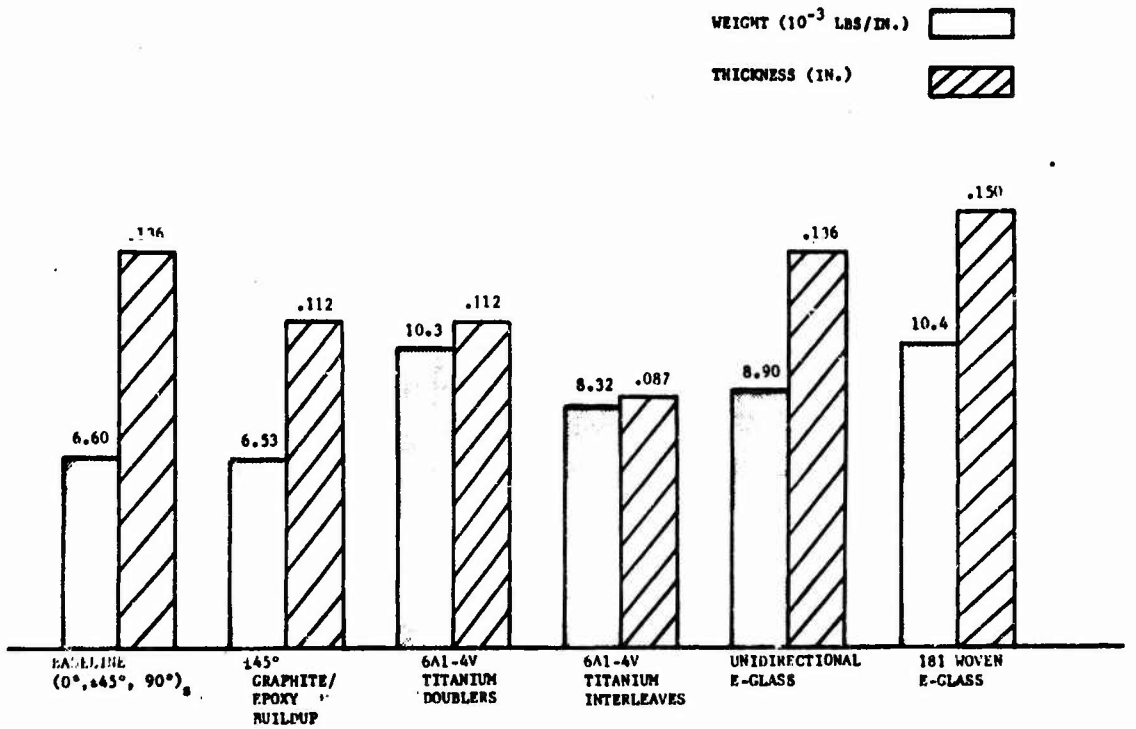

FIGURE 8. COMPARISON OF ALTERNATE REINFORCING CONCEPTS

One of the more unique characteristics which showed up from this study was the ratio of initial failure load to ultimate failure load. For all of the specimen but the woven fiberglass reinforced specimens this ratio is close to one, that is, initial and ultimate failures were close to one another. However, for the 181 fiberglass cloth reinforced specimen with high e/D (Specimen #22) as shown in Table III, initial failure occurred at approximately 60% of the ultimate failure load.

CONCLUSIONS

The following conclusions were drawn as a result of the Phase I study:

- It is possible to develop allowables for predicting joint failure by considering each of the three independent failure modes of bearing, shearout, and net tension.
- Net tension strength for a particular graphite/epoxy laminate is not a constant, but instead, varies with edge distance, side distance, and hole diameter.
- Shearout strength for a particular graphite/epoxy laminate is not constant but varies with edge-distance-to-diameter ratio.
- Bearing strength is a constant for a particular graphite/epoxy laminate and is the maximum load which can be transferred at the joint.
- Appreciably high bearing strengths may be obtained in graphite/epoxy laminates.
- Joints fabricated through the use of the congenital hole technique (i.e., holes layed up during laminate fabrication) appear to offer an alternative to machined holes although further fabrication and testing is needed.

From the Phase II studies, the following conclusions were drawn:

- Graphite/epoxy layers are the most weight efficient means for reinforcing a highly loaded hole in a graphite/epoxy laminate.
- Use of metals to reinforce joints in graphite/epoxy laminates is most efficient when edge distance and thickness requirements are to be minimized.
- For highly loaded graphite/epoxy joints, fiberglass reinforcement should be used only in those cases where the need for such material has been dictated by other requirements (e.g., softening strips or damage arrestment strips).

RECOMMENDATIONS

Work is now being conducted to further understand the phenomena involved in the shearout and net tensile behavior of graphite/epoxy joints through the use of finite element modelling techniques.

In the future, additional tests will be conducted to evaluate the behavior of graphite/epoxy bolted joints subjected to random fatigue loadings.

REFERENCES

1. Waszczak, J.P., and Cruse, T.A., "Failure Mode and Strength Predictions of Anisotropic Bolt Bearing Specimens," Journal of Composite Materials, Volume 5, July 1971, p. 421.

2. Dickson, J.N., Hsu, T.M., and McKinney, J.M., "Development of an Understanding of the Fatigue Phenomena of Bonded and Bolted Joints in Advanced Filamentary Composite Materials, Volume 1, Analysis Methods," AFFDL-TR-72-64, Volume 1, June 1972.

3. "Advanced Composite Wing Structures Boron Epoxy Design Data, Volume II - Analytical Data," Contract F33615-68-C-1301, Grumman Aerospace Corp., Nov. 1969.

4. "Structural Airframe Application of Advanced Composite Materials - Volume IV - Mechanical Properties - Static," AFML-TR-69-101, Volume IV, Contract AF33(615)-5257, General Dynamics/Fort Worth Division, October 1969.

5. "Advanced Composite Technology - Fuselage Program; Phase IV, Volume II," AFML-TR-70-41, Contract F33615-69-C-1494, General Dynamics/Convair Aerospace Division/Fort Worth, June 1971.

6. Waszczak, J.P., and Cruse, T.A., "A Synthesis Procedure for Mechanically Fastened Joints in Advanced Composite Materials," AFML-TR-73-145, Volume II, Contract F33615-72-C-1214, September, 1973.

7. "Feasibility of Joining Advanced Composite Flight Vehicle Structures," AFML-TR-68-391, Contract AF33(615)-3962, Mechanics of Materials Research Division/IIT Research Institute, January 1969.

8. Lehman, G.M., Hawley, A.V., et al, "Investigation of Joints in Advanced Fibrous Composites for Aircraft Structures, Joint and Attachment Investigation, Volume 1. Technical Discussion and Summary," AFFDL-TR-69-43, Vol. 1, June 1969.

9. "Exploratory Application of Filament-Wound Reinforced Plastics for Aircraft Landing Gear," Bendix Corporation, AFML-TR-66-309, December 1966.

10. Nelson, W.D., et al, "Composite Conceptual Wing Design," AFML-TR-73-57, Contract F33615-71-C-1340, McDonnell Douglas Corporation, Douglas Aircraft Company, March 1973.

11. Padawer, G.E., "The Strength of Bolted Connections in Graphite/Epoxy Composites Reinforced by Colaminated Boron Film," Composite Materials: Testing and Design, ASTM STP 497, American Society of Testing and Materials, Anaheim, Calif., 20-22 April 1971.

REFERENCES (Continued)

12. Padawer, G.E., "Film Reinforced Multifastened Mechanical Joints in Fibrous Composites," Journal of Aircraft, Volume 10, Number 9, September 1973.

13. Cherry, F.D., "The Elimination of Fastener Hole Stress Concentrations Through the Use of Softening Strips," Proceedings of the Conference on Fibrous Composites in Flight Vehicle Design, AFFDL-TR-72-130, Sept. 1972.

14. Advanced Composites Design Guide, Volume II, Analysis, Third Edition, Contract F33615-71-C-1362, North American Rockwell/Los Angeles Division, January 1973.

15. Frocht, M., and Hill, H., "Stress Concentration Factors Around a Central Circular Hole in a Plate Loaded Through a Pin in the Hole," ASME Vol. 62, 1940, pp. A-5.

DEVELOPMENT OF ELEMENTAL JOINT FATIGUE TEST STANDARDS FOR PERMANENT INSTALLED FASTENERS

ROBERT B. URZI
Senior Research Engineer
Lockheed-California Company
Burbank, California

ABSTRACT

A multiple task program was implemented to provide the data necessary to establish a Military Test Standard (part of MIL-STD-1312 "Fastener Test Methods") for use in evaluation of installed mechanical fasteners in fatigue. Upon completion of a survey of industry and government ad hoc standards, followed by the generation of substantiating data, two types of elemental joint configurations were found to be suitable for insertion into the standard. The first specimen was a simple lap joint/single shear high load transfer specimen. The second was a low load transfer specimen where two continuous dogbone shaped materials of different stiffness, due to geometric considerations, are fastened together. Metallic specimens were fabricated and constant amplitude fatigue tested to determine the sensitivity of the joints selected, in terms of cycles to failure, to variations in the fastener system. Experimental stress analysis techniques such as dimensional photoelastic models, photoelastic coatings, and strain gages were used to investigate high, medium, and low load transfer joints. Information gained from tests conducted on these models and instrumented specimens provided stress distribution and magnitudes associated with joint deflection, specimen support, and fastener preload.

INTRODUCTION

With modern machine designs using hundreds of different types of structural fasteners, the problem of fastener evaluation, especially in fatigue, is one of ever increasing complexity. While there are standards for fastener fabrication and evaluations, they are often confusing, overlapping, and fail to identify and standardize those parameters that are most critical to the actual performance of the entire installed fastener system. Consequently, each fastener manufacturer has continued to expand and propagate his own line of fasteners employing fastener evaluation procedures designed to fit the users intended application. As a result, it has been difficult to evaluate and compare realistically the performance of various fasteners in the installed condition. The problem of fastener proliferation is especially acute in the airframe industry. Cunningham [1] places the responsibility for this situation on the manufacturing industry from the user's point of view, when he asks "Why are there so many fasteners?" Chironis [2] points out that American industry buys more than one billion dollars worth of fasteners per year, a most impressive statistic. Among the 10 checkpoints for reducing cost that he itemizes, standardization plays a prominent role. Part of the proliferation problem can be attributed to the

lack of standardized fatigue test procedures. When there is a complete lack of standardization in testing to determine the fatigue properties of the installed fastener system, it is not possible to compare apparently contradictory test data. Because test results conflict, different fastener systems are selected to do the same job when one system could be used.

One of the first organizations to address this problem was the Fastener Testing and Development Group (FTDG). A research and development program was implemented in April 1971 under Navy Contract N62269-71-0450 [3] which aided the FTDG in developing a proposed Military Test Standard (part of MIL-STD-1312) to evaluate the fatigue behavior of installed mechanical fasteners. A second contract was awarded in July 1972 by the United States Air Force to the Lockheed-California Company [4] which continued the work started in the Navy program with the added requirements of: [1] determining the suitability of the proposed test standard as applied to interference fit fasteners, and [2] providing the Air Force with joint fatigue data generated by utilizing the proposed test standard in tests of fasteners which reflect current usage.

This paper will emphasize the tests performed and information gained in defining a high load transfer type elemental joint suitable for a test standard to screen mechanical fasteners as an installed system in fatigue. Equivalent effort was expended on low, median, and no load transfer joints [3] [4] [5].

SELECTION OF TEST SPECIMEN CONFIGURATION

A survey of industry and government agencies was conducted for the purposes of identifying the various fastener evaluation test methods in current use [6] During the course of the survey, over twenty-four different elemental joint geometries were identified. The most commonly used high load transfer* joint configurations are shown in Figures 1 through 8. Figure 8 is the only elemental joint especially designated for fatigue testing in any current ASTM, SAE, ASME, Federal, or Military Test Standard. However Figure 8 is applicable only to blind rivets and cannot be applied universally to any fastener diameter or fastener type due to certain rigid geometric and loading requirements [6]. Figure 7 is an elemental joint test standard used in the generation of static strength data [7] [8]. The traditional and intended use for this type is in the generation of joint yield and ultimate strength data and mode of static failure. The deficiencies of this as a dynamic test standard lie in the diagonally opposed manufactured fastener head orientation which does not represent standard usage.

No doubt, there are additional joint geometries in use today that were not identified. However, each specimen configuration identified was rated as to the degree of its desirability as a fatigue test standard using the following criteria as a basis for comparison.

*Load transfer is defined as a relative value of the amount of load transferred by the fastener from one joint member to another joint member.

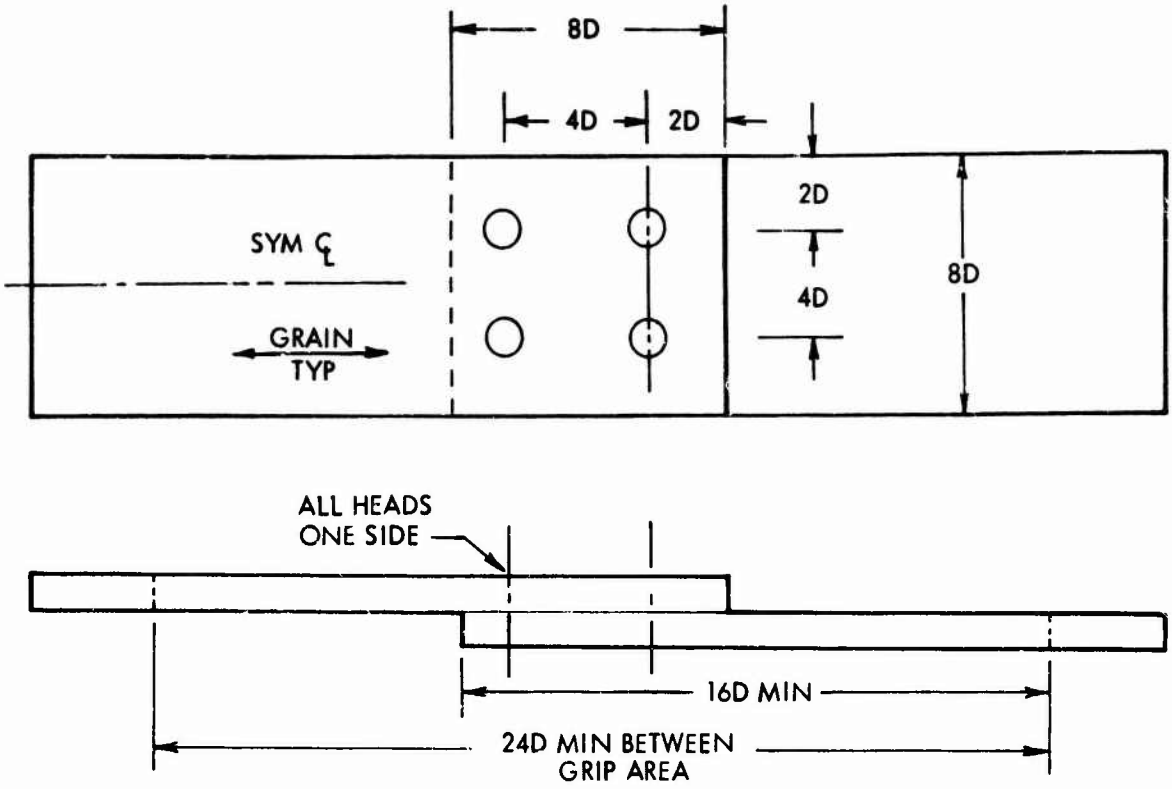

NOM DIAM	D
3/32	0.093
1/8	0.125
5/32	0.156
3/16	0.188
7/32	0.219
1/4	0.250
5/16	0.313
3/8	0.375
7/16	0.438
1/2	0.50

NOTE: 1. ALL EDGES MACHINE $\sqrt{63}$ OR BETTER

2. NO SCRATCHES, GOUGES, OR SCRIBE MARKS IN 24D AREA
3. TOLERANCE ON 2D AND 4D DIMENSIONS SHALL BE ±.005
4. CHAMFER OR RADIUS HOLES .005 MAX

Figure 1. Lap Joint Specimen - Single Shear 100% Load Transfer

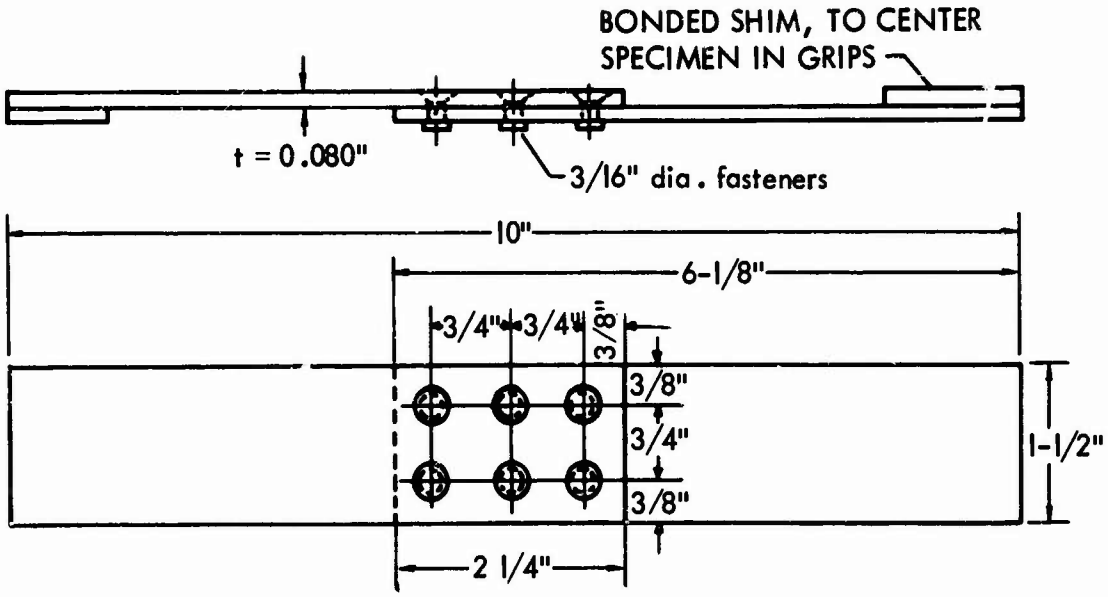

Figure 2. Six Fastener Lap Joint - 100 Percent Load Transfer

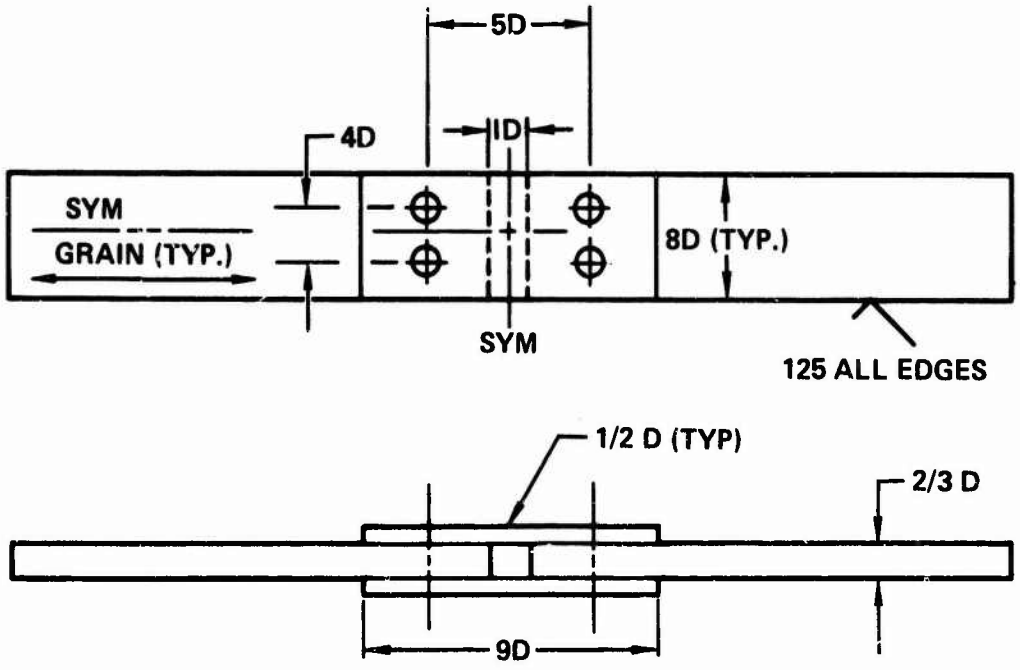

Figure 3. High Load Transfer Butt Joint - Double Shear

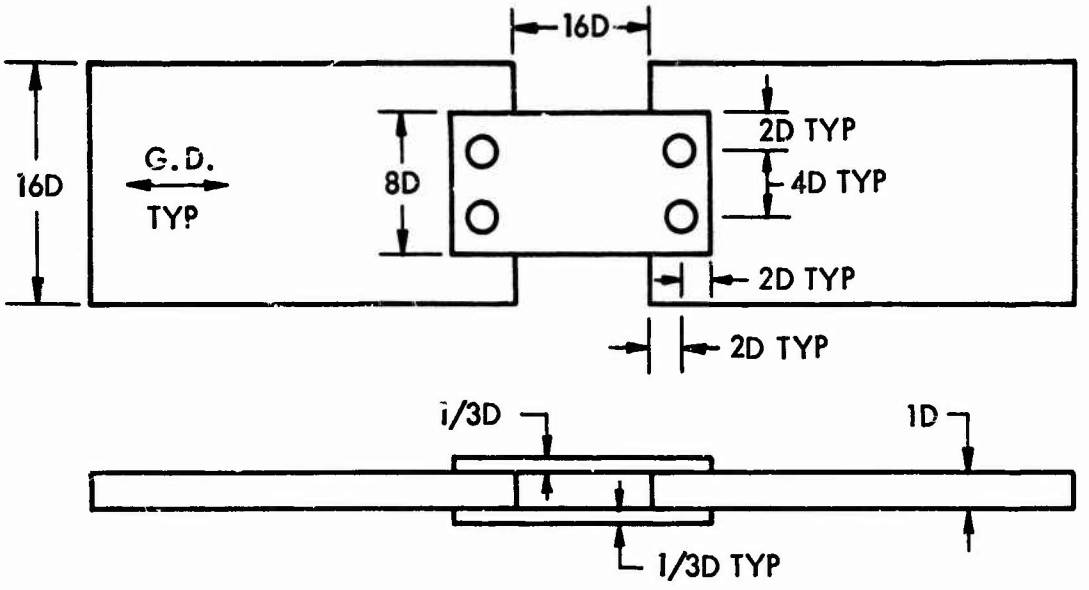

Figure 4. High Load Transfer - Double Shear

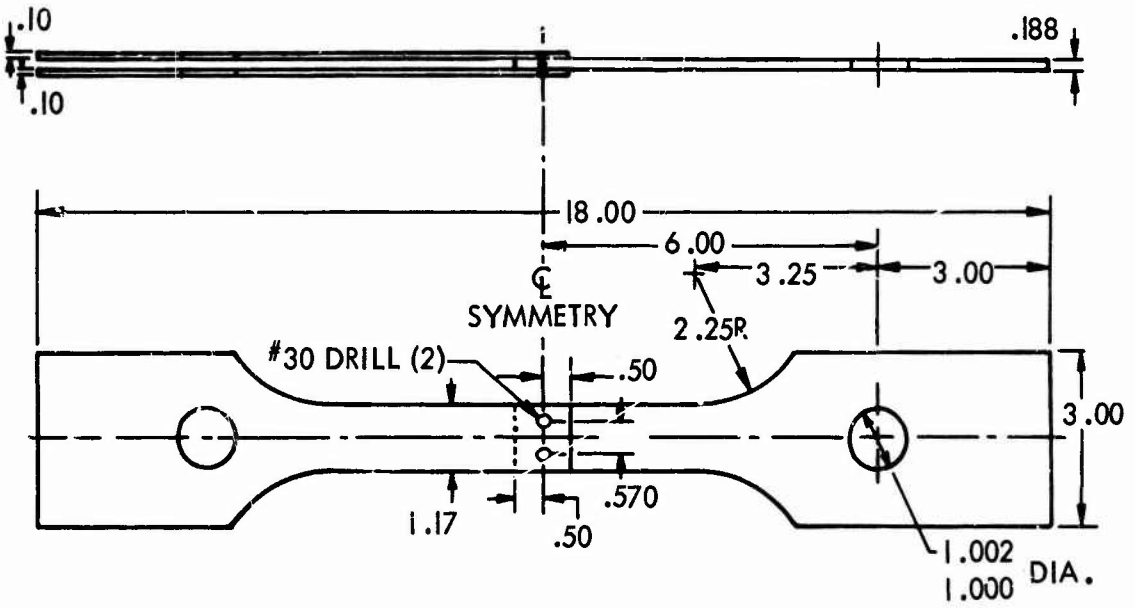

Figure 5. High Load Transfer Double Shear (2 Fasteners Side by Side)

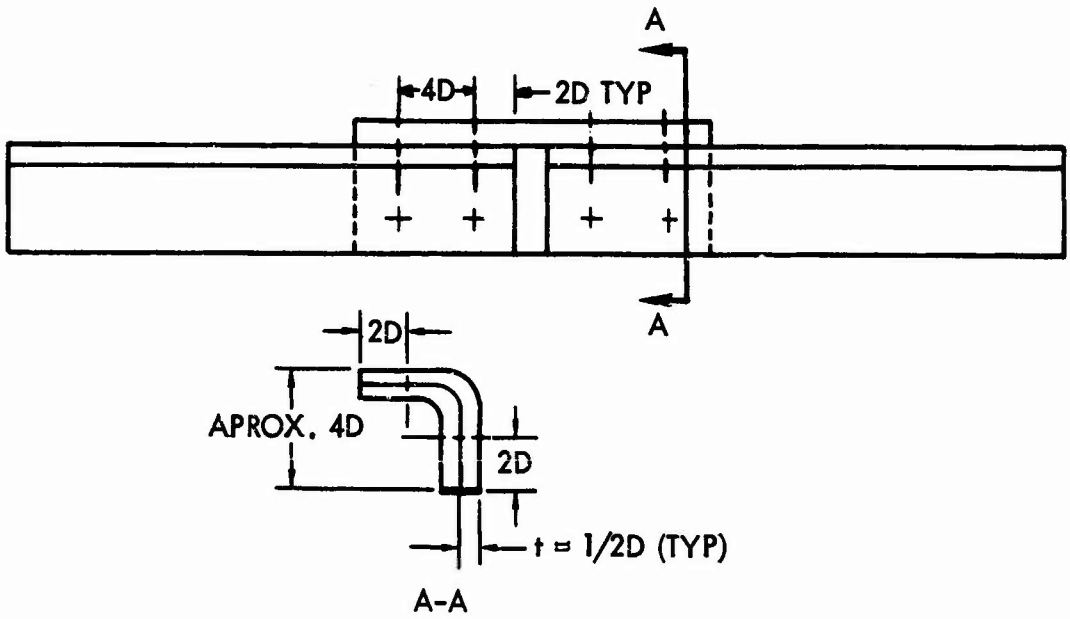

Figure 6. "Nested" Angle High Load Transfer Joint

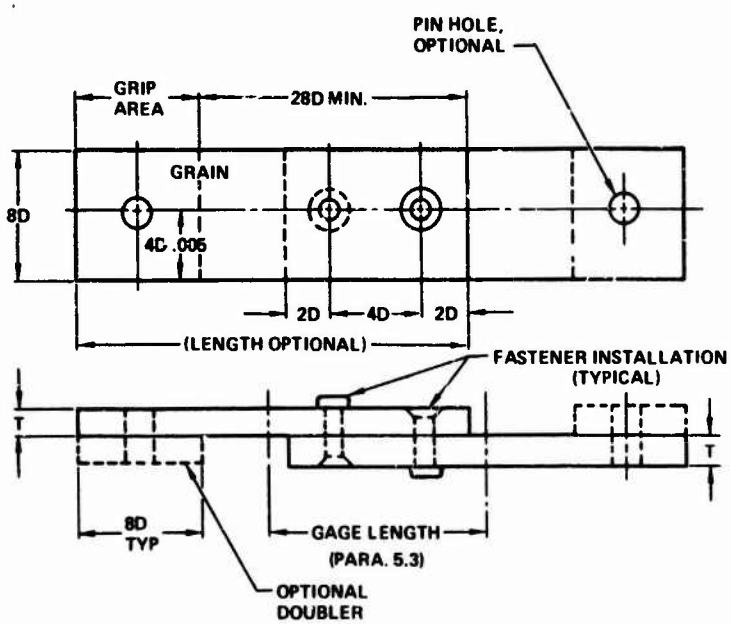

WHERE D = NOMINAL FASTENER DIAMETER
T = SHEET OR PLATE THICKNESS
FASTENER HOLES, SEE PARAGRAPH 4.2.2
TOLERANCE ON EDGE MARGIN, SPACING, AND WIDTH, 0.010 IN
STANDARD EDGE DISTANCE = 2D. FOR PERMISSIBLE DEVIATIONS, SEE PARAGRAPH 4.1.4

Figure 7. Preferred Test Lap Joint Specimen Configuration MIL-STD-1312, Test No. 4, Joint Shear Strength

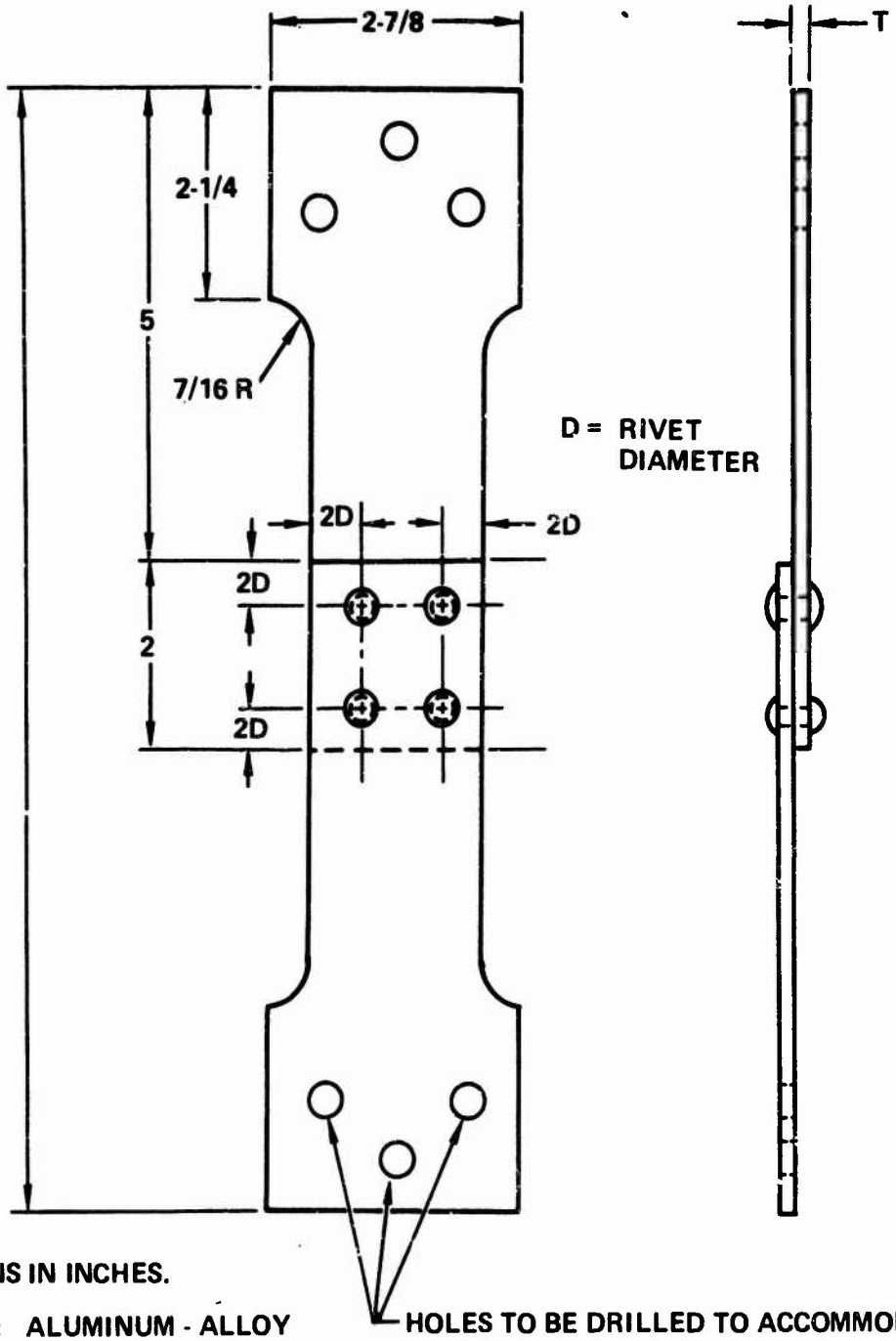

DIMENSIONS IN INCHES.

MATERIAL: ALUMINUM - ALLOY SHEET, SPECIFICATION QQ-A-355, OR CORROSION – RESISTANT STEEL SHEET, SPECIFICATION MIL-S-5059 (1/2 HARD). "T" TO BE 1/2 OF TOTAL GRIP AND BE IN ACCORDANCE WITH VALUES LISTED IN TABLE V OF MIL-R-7885B FOR APPROPRIATE SIZE RIVET UNDER TEST.

Figure 8. Specimen for Fatigue Test MIL-R-7885B, Rivets; Blind, Structural, Pull-Stem, and Chemically Expanded

- Amount of current use for that particular test specimen
- Equipment required to conduct test
- Types of failures encountered and the ease in which fracture surface characterization can be made.
- Cost of specimen fabrication
- Amount of anticipated test data scatter
- The relationships of the test specimen configuration to detail structural design.

Based on the above criteria, the seven initial candidates were reduced to two. The two selected are shown in Figures 1 and 3.

FINAL SELECTION OF HIGH LOAD TRANSFER JOINT GEOMETRY

It was desired for economic and practical reasons that only one of the two selected joint geometries be used in a fatigue test standard. Comparison fatigue tests were conducted. Statistics were used to provide a mathematical basis for the comparison. The t statistic for the mean of two samples permits a determination of whether the difference between two sets of data are real and significant [9]. The rationale for selecting the test variables was as follows: Two fastener systems of known qualities were fabricated from three different materials. One system was defined as a good system and the second was defined as a better system. For purposes of comparison, the good system selected was a MS or NAS standard rivet configuration. A rivet is a hole filling fastener in which the amount of interference fit and fastener preload is not controllable. A better system was defined as a fastener in which the interference fit and preload can be closely controlled, i.e., a close tolerance bolt with controlled hole size and torque up. Also a better fastener system could provide a greater hole cold expansion than the conventional rivet system, i.e., the slug rivet. A summary of the comparison tests, including the calculated t and percent confidence in stating a significant difference between groups tested, is given in Table I. Referring to Table I and compairing column averages it was determined that the simple lap joint, Figure 1, was consistent in generating fatigue data which indicated a significant difference between the fastener variables investigated.

PHOTOELASTIC MODELING

In an early company funded standardization program, an attempt was made to correlate elemental joint fatigue data generated by using specimen configurations developed by various investigators [5]. From the observation of the failed specimens, it was apparent that a high magnitude of bending stress is present in a axialiy loaded lap joint specimen. The testing of a simple lap joint specimen without bending restraints resulted in a majority of the fatigue

TABLE I
SUMMARY OF TEST RESULTS
FINAL SELECTION OF HIGH LOAD TRANSFER JOINT

Sheet Material: 2024-T3 Clad

Test Environment: Ambient Air

Stress Ratio: $R = 0.1 = F_{min.}/F_{max.}$

Max. Sheet Stress: 18 ksi, Minimum Gross Area

Nominal Fastener Diameter: 3/16 Inch

FASTENER SYSTEM IDENTIFICATION	SIMPLE LAP JOINT FIGURE 1	BUTT JOINT, DBLE SHEAR FIGURE 3
2117-T3 Al, Alloy		
BACR 15DH 82^{o} - 30^{o} Slug rivet	$\bar{X}$ = 143,159	85,121
MS20426AD6 Standard rivet	$\bar{Y}$ = 47,378	47,066
	t = 10.76	t = 1.78
% Confidence in Significant Diff. Btwn. $\bar{X}$ & $\bar{Y}$ ⚠	99.9%	82%
A286 Alloy		
HT3N Hi Torque Bolt	$\bar{X}$ = 115,345	874,340
NAS1199 Rivet	$\bar{Y}$ = 299,090	615,089
	t = 6.06	t = 1.28
% Confidence in Significant Diff. Btwn. $\bar{X}$ & $\bar{Y}$	99.9%	75%
Titanium Alloy		
NAS663V (Ti-6-4) Hi Torque Bolt	$\bar{X}$ = 136,599	769,037
NAS1199 (Ti B120) Rivet	$\bar{Y}$ = 68,318	384,000
	t = 4.30	t = 1.82
% Confidence in Significant Diff. Btwn. $\bar{X}$ & $\bar{Y}$	99.8%	85%
Column Average % Confidence for Constant Specimen Geometry & Variable Fastener System	Column Average 99.86%	Column Average 80.66%

⚠ Minimum of three test points per condition and the probability of being correct in rejecting the null hypothsis that $\bar{X} = \bar{Y}$ and stating that there is a significant difference between the two groups compared.

failures initiating away from the fastener hole. It was apparent that the bending of the joint was the primary cause of failure. Consequently several different methods of stiffening the lap joint (restricting joint rotation) were devised and used [5].

It became essential that the simple lap joint, recommended for use in a Military Test Standard, be restrained from bending by some standard method. To establish this method and its effect on bending stress, the use of a photoelastic model was proposed. A three dimensional photoelastic model representing a simplified version of the recommended lap joint specimen was constructed [10]. This model is detailed in Figure 9. The area of interest was the .30 inch wide by .29 inch thick strip of Homolite bonded into the center of the model surrounding the fasteners. On either side of this strip, a circularly polarized filter in an acetate cover was bonded representing the polarizer and analyzer plates of a standard transmission plane polariscope. Since the analyzer plate could not be rotated to determine partial fringes (Tardy Compensation Method), a simple tensile calibrated coupon made of the same plastic as the model was constructed. Both the calibration specimen and the photoelastic model were mounted on an optical comparator and a photometer used to measure light intensities reflected on the viewing screen. A monochromatic filter was used. The relationship between the light intensity arriving at the photocell (photometer) and the fringe value exhibited by the calibration model is sinusoidal and can be expressed as:

$$I = D + I_0 \sin^2 \alpha \tag{1}$$

$$\alpha = \frac{\pi}{f}(\epsilon_1 - \epsilon_2) \tag{2}$$

where f = fringe value of plastic

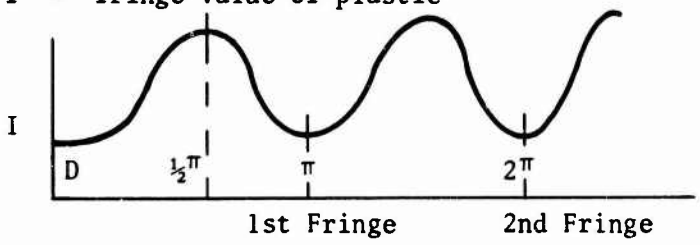

In this expression D takes into account parasitic light rays and inefficiencies of the polaroids. The minimum level occurs at every fringe, and the maximum at every half-fringe positions. The optical comparator in which the model was mounted provided a 10 to 1 magnification and the accuracy of the fringe values measured were within 1/10 fringe based on repeatability and continuity of the data.

Model relationships were developed on the basis of equal strain distributions in the model and metallic prototype.*

*Subscript m = model (photoelastic)
Subscript p - metallic prototype

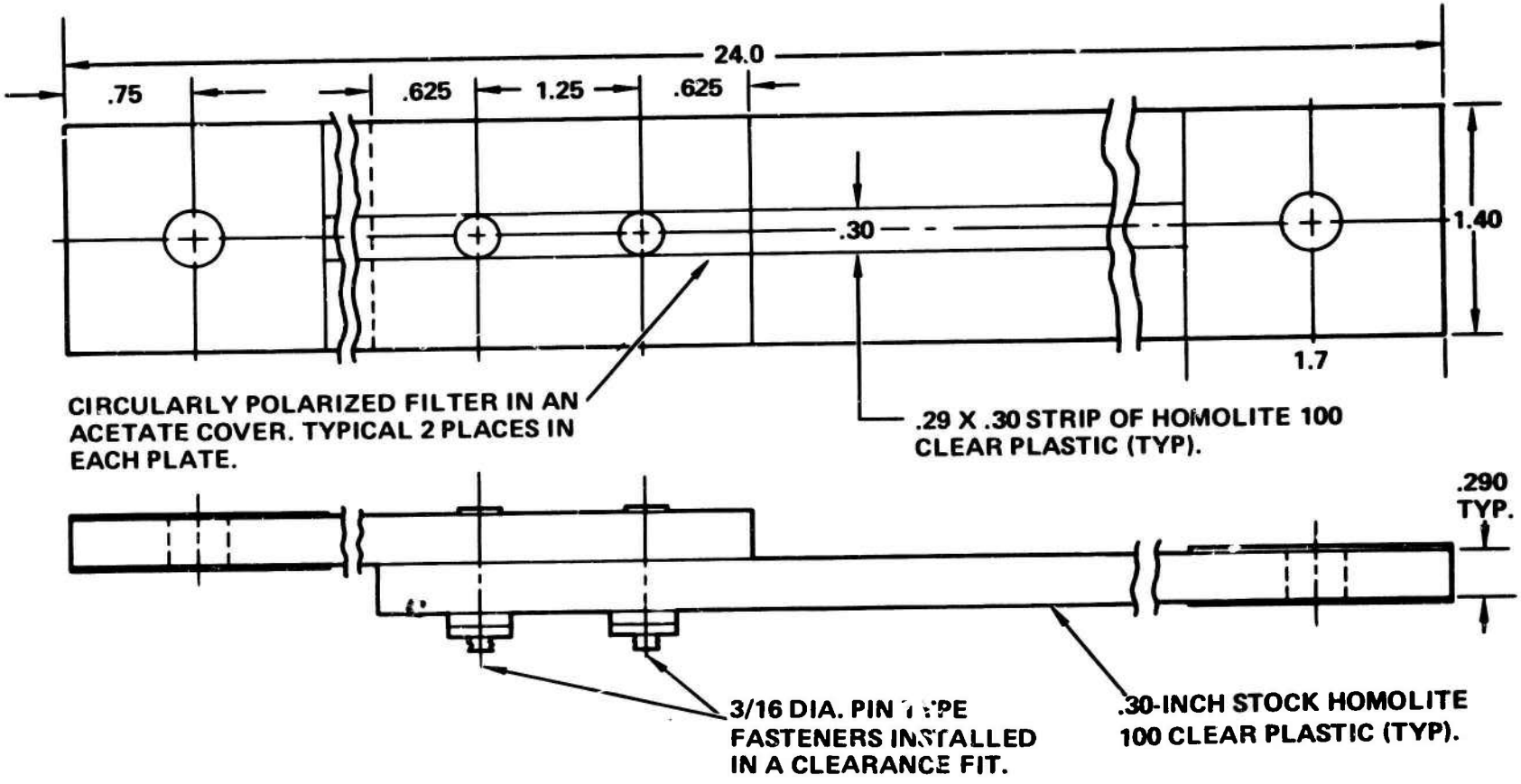

Figure 9. Photoelastic Model Configuration - Simple Lap Joint Specimen

$$\frac{(\sigma_1 - \sigma_2)_m}{(\sigma_1 - \sigma_2)_p} = \frac{E_m}{E_p} \tag{3}$$

$$(\sigma_1 - \sigma_2)_p = \frac{E_p}{E_m} (\sigma_1 - \sigma_2)_m ; \ \sigma_2 \approx o \tag{4}$$

$$(\sigma_1)_p = \frac{E_p}{E_m} (\sigma_1)_m \quad \text{but} \quad (\sigma_1)_m = \frac{Nf}{t} \tag{5}$$

N = fringe order
f = fringe constant
t = thickness of plastic

$$(\sigma_1)_p = \frac{E_p}{E_m} \times \frac{Nf}{t} \tag{6}$$

For example, to determine equivalent stress in aluminum specimen per fringe value observed in plastic model; N = 1; E_m = 350,000; E_p = 10.7×10^6; f = 155 psi/inch/fringe.

$$(\sigma_1)_{\text{aluminum}} = \frac{10.7 \times 10^6}{.35 \times 10^6} \times \frac{(1)155}{.3} = 15{,}795 \text{ psi/fringe} \tag{7}$$

Using the described apparatus and relationships presented the axial stress distribution through the thickness of the photoelastic model, one half inch away from the fastener hole, was calculated from the fringe values determined.

Joint rotations were determined from the fastener head deflections measured by using the micrometer traveling table of the polariscope. The specimen support flexures (rotation restraints), when used, were positioned and adjusted so that no bending stresses existed between the flexure supports and the specimen grips. Verification was accomplished using photometer readings.

The ability to distinguish strain/stress patterns through the width, thickness, and length of the simple lap joint specimen by means of optical measurements provided much needed quantitative data. These data included strain/stress measurements near and at the fastener due to fastener preload, joint rotation, and position of joint specimen supports. Another condition investigated was the effect of fastener preload on bearing stresses developed at the interface of two pieces of material fastened together [10].

Figure 10 shows the stress distribution through the sheet thickness as related to joint rotation (misalignment) under a constant axial load.

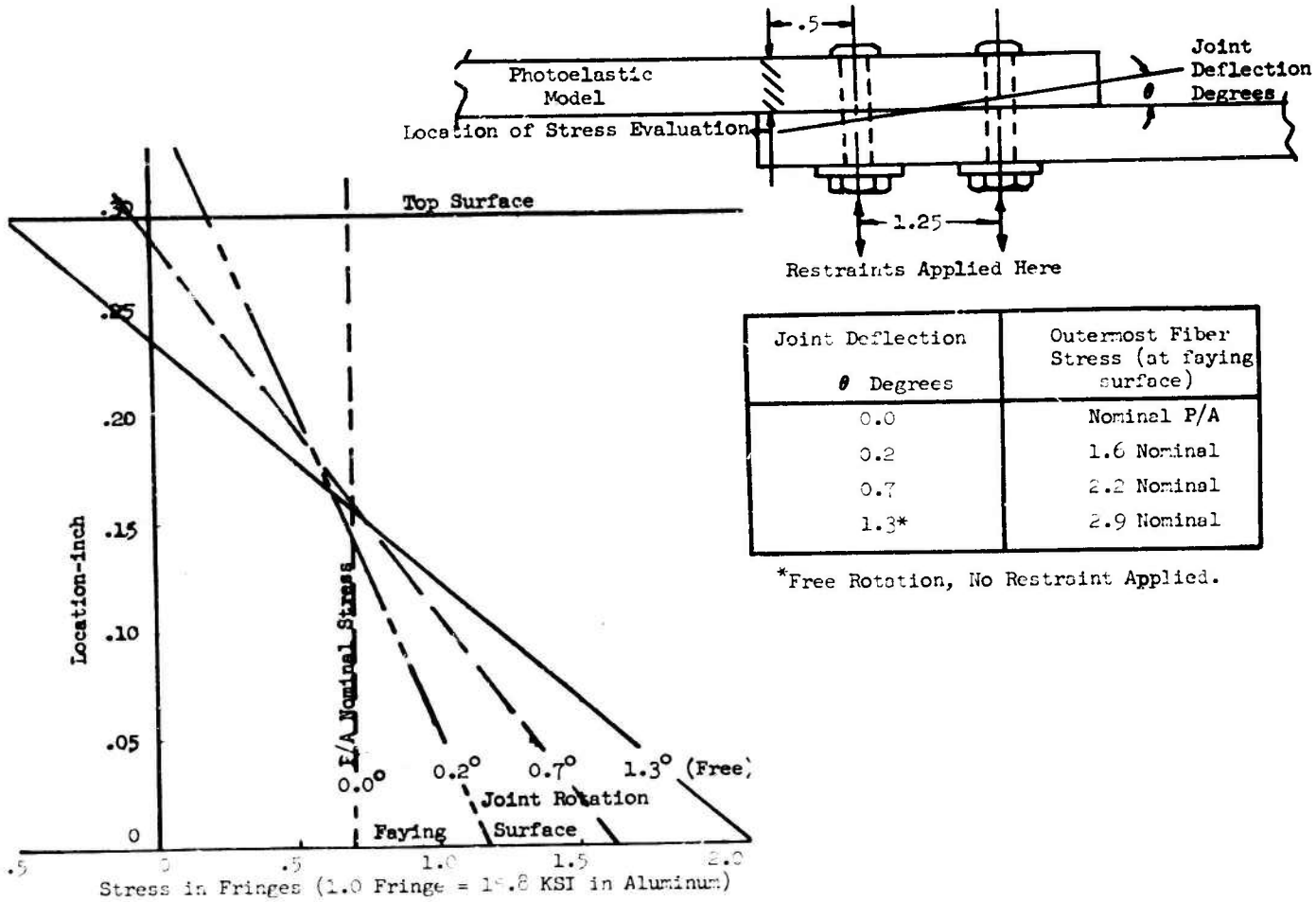

Joint Deflection θ Degrees	Outermost Fiber Stress (at faying surface)
0.0	Nominal P/A
0.2	1.6 Nominal
0.7	2.2 Nominal
1.3*	2.9 Nominal

*Free Rotation, No Restraint Applied.

Figure 10. Stress Distribution for Various Misalignments (Joint Rotation)

Originally, the joint was restrained from rotating, and as this restraint was removed the joint was allowed to deflect (bend). As shown in Figure 10, a deflection (misalignment) of only two tenths of one degree caused an increase of 60 percent in tensile stress in the outside fibers of the material in the faying surface. Without any restraints, the joint freely rotated 1.3 degrees and the tensile stresses at the faying surfaces became almost three times greater than the nominal P/A stress experienced at the ends of the specimen. These data explain why fatigue cracks almost always originate at the faying surface especially when a fretting condition exists.

Figure 11 presents data on how the position of the flexure support (location of zero bending) influences the bending stresses developed in the lapped area of the joint. When the flexures are placed directly over the two outside rows of fasteners, the specimen is restrained from bending and only the P/A nominal tensile stress exists. When the flexures are removed from the outside rows of fasteners and placed farther apart along the length of the specimen, the joint is allowed to deflect (misalign/rotate) with the bending stresses experienced dependent on the distance between flexures. As shown in Figure 11, a point is reached where further relocation of the flexures has no influence on the bending stresses experienced.

The need for using guides or joint rotation restraints on simple lap joint specimens is substantiated by the data given in Figures 10 and 11. Therefore, the joint guide arrangement, shown in Figure 12, using 90^{o} offset flexure rod supports was recommended to be included as part of the Military Test Standard. In Fall of 1972 the MIL-STD-1312 committee recommended that an additional specimen support method be developed because of difficulty in the set-up of the flexure method in certain types of fatigue machines. A sandwich type fixture was proposed by several committee members. This sandwich fixture is detailed in Figure 13. This alternate method of stiffening the lap joint was used for a small portion of tests conducted under an Air Force program [4]. In reviewing these data, it did appear that the sandwich supported specimens sustained longer fatigue lives than specimens tested using the flexure supports. However, the limited amount of data generated does not lend itself to a high confidence statistical judgment and it appears that the individual data points of specimens tested with the sandwich support fall within the scatter band exhibited by the total sample tested.

FAILURE MODES OF THE JOINTS

Several generalizations can be made about the failure modes experienced by the aluminum alloy joint specimens tested throughout the program. In the high load transfer joint, Figure 1, the failures occurred through the fastener hole when subjected to a high level of applied stress resulting in relatively short test lives. On the other hand, the same type of joint failed away from the fastener hole when testing at low stress intensity levels leading to relatively long test lives. The low load transfer specimens experienced the majority of the failures through the fastener holes regardless of the magnitude of the applied stress [4]. The reason for this occurrence is not a simple one. It is related to the amount of bending stress occurring in the

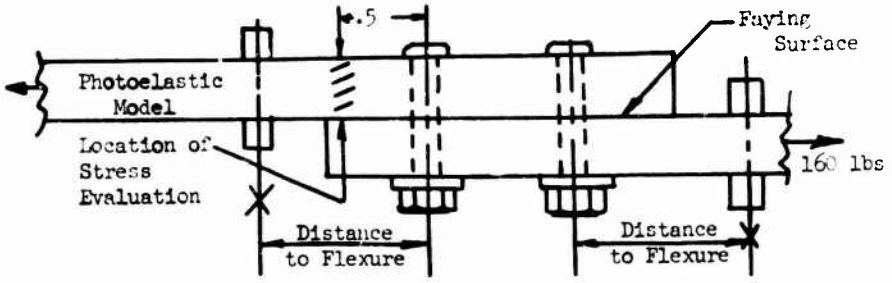

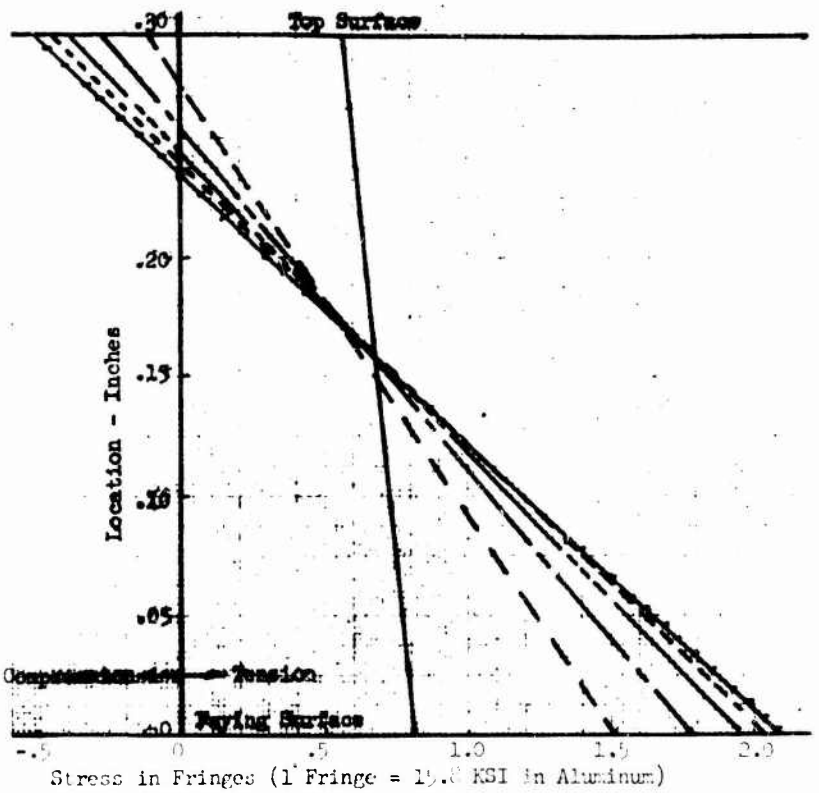

Stress in Fringes (1 Fringe = 19.8 KSI in Aluminum)

Outermost Fiber Stress (at faying-surface): Nominal = P/A

Flexure at Fasteners ———— 1.19 X Nominal
Flexure at 1.1 in. from Fasteners — — — 1.16 X Nominal
Flexure at 2.0 in. from Fasteners — - — 1.36 X Nominal
Flexure at 3.0 in. from Fasteners — - - — 1.50 X Nominal
Flexure at 5.0 in. from Fasteners - - - - 1.56 X Nominal
Flexure at {6.0 / 9.0} in. from Fasteners ←→←→ 1.64 X Nominal

Figure 11. Stress Distribution Through the Thickness for Various Flexure Locations

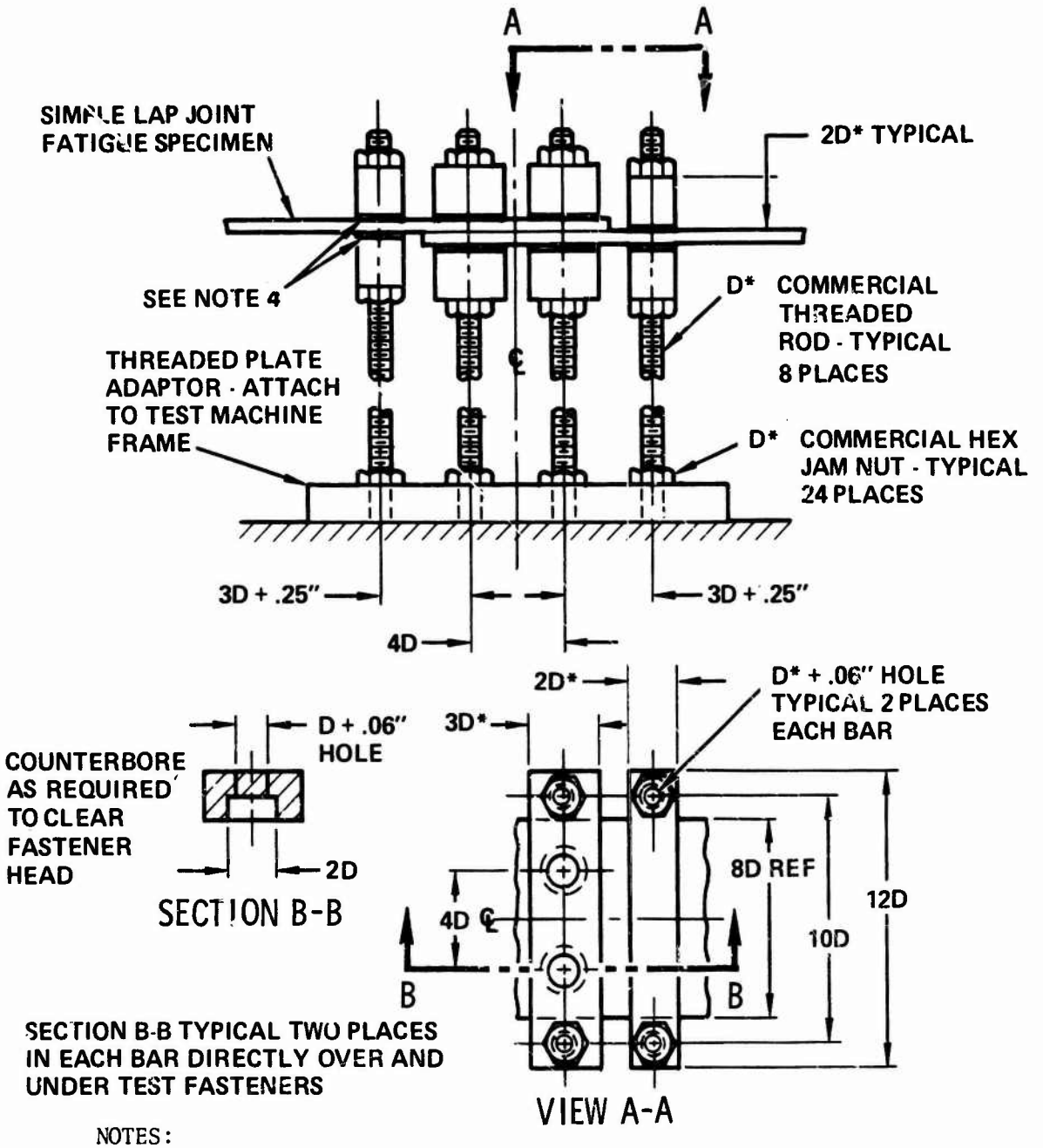

NOTES:

1. D=Nominal Fastener Diameter Under Test.
2. *D Minimum for these Dimensions=3/16".
3. Rod and Bar Material - Mild Steel.
4. Teflon, Nylon, Micarta, Etc. Must be Interfaced Between Bars and Test Specimen Surfaces

Figure 12. Details of Flexture Pivot (90° Offset) Test Specimen Restraint Fixture

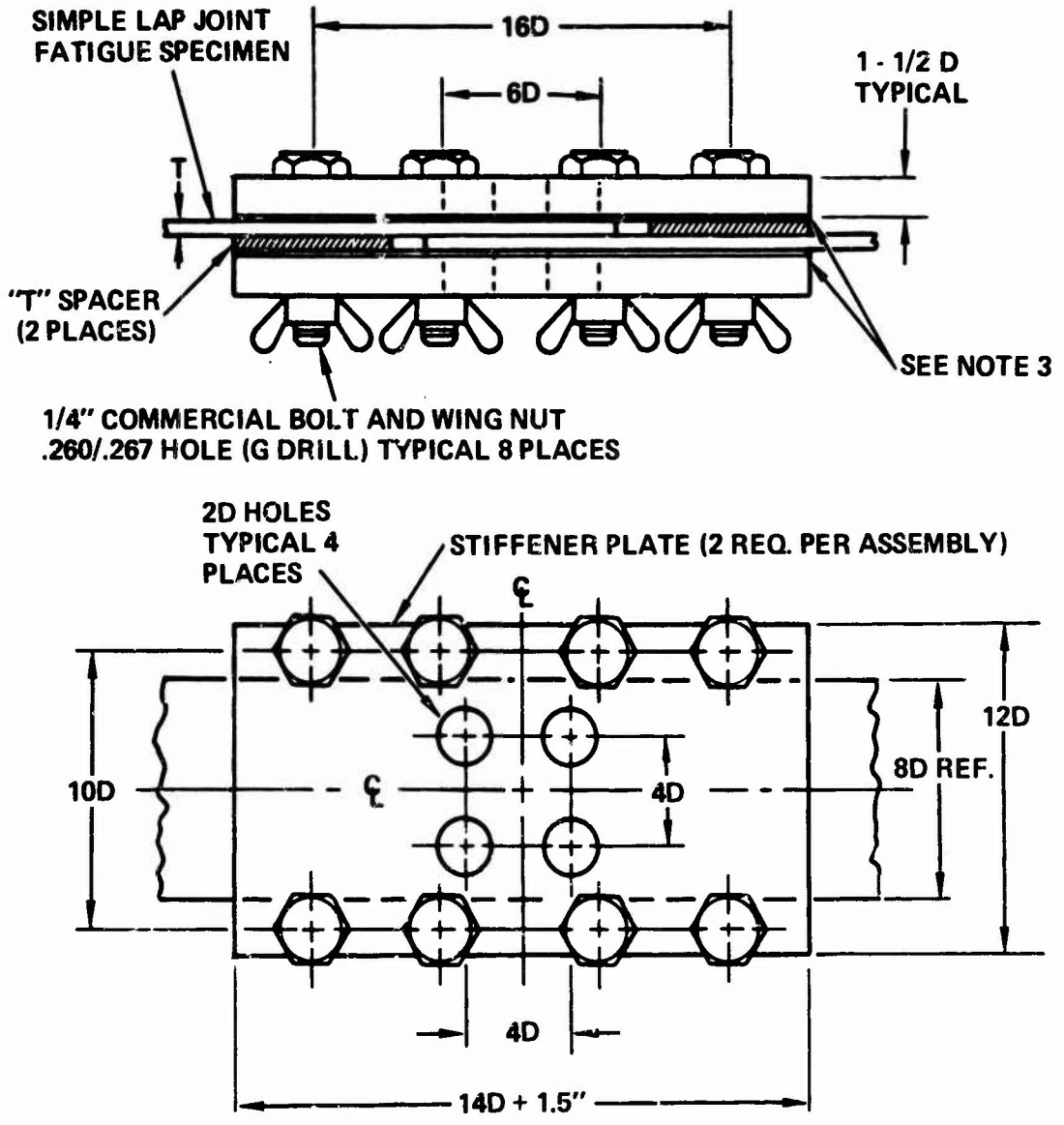

NOTES:

1. D=Nominal Fastener Diameter Under Test.
2. Stiffener Plate and Bold Material - Mild Steel.
3. Teflon, Nylon, Micarta, Etc. Material Must Be Interfaced Between Stiffener Plates and Test Specimen Surfaces.
4. Tighten Wing Nuts Only Finger Tight.

Figure 13. Details of "Sandwich" Type Specimen Restraint Fixture

joint and to the degree of fretting located at the faying surface. During long test lives, fretting pits are established and the peak stresses resulting from these pits (sharp notches) are of a greater magnitude then those occurring at the fastener hole. Exception to this behavior pattern was exhibited by all the titanium specimens which failed through the fastener holes. The reason for this apparent discrepancy is that a special faying surface treatment was used on the titanium specimens which eliminated the fretting experience by the aluminum joints. The faying surface treatment consisted of coating with Molykote 106, and was one of many treatments that was investigated in a prior Air Force sponsored program [11].

SUMMARY

Based on the test results obtained, it appears that the use of any one of the proposed joint geometries would lead to some order of discrimination between the fastener system variables being evaluated, but the choice of joint would determine the degree of reproducibility and consistency gained. In the analysis of test results, only one joint configuration indicated the high degree of consistency and confidence demanded of a universal test standard method. Based on these data, it was recommended that the simple lap joint be adopted as one of two elemental joint standard configurations. It was also recommended that the simple lap joint be fatigue tested using the flexure supports (joint rotation restraints) to reduce the bending stresses drastically. Based on the need for a second type of joint with greater sensitivity to the fastener system variables and the need to define a test relating to low-load transfer joint attachments, it was recommended that the reverse dogbone low-load transfer joint be adopted as the second type of elemental joint standard [3]. The reverse dogbone specimen possess a load transfer characteristic closely approaching many joints found in aircraft construction such as wing spanwise splices and skin stringer attachments.

ACKNOWLEDGMENT

A program of this nature would not have been possible without the encouragement and support of many individuals from all segments of government and industry. The work was conducted in the Rye Canyon Research Laboratories of the Lockheed-California Company. A continuing program was sponsored by Lockheed, by the Naval Air Development Center (Contract N62269-71-C-0450), and by the Air Force Materials Laboratory (Contract F33615-72-C-1838).

REFERENCES

1. Cunningham, H.H., "Why Are There So Many Fasteners?," Iron Age, August 19, 1971.

2. Chironis, N.P., "Fasteners Get The Spotlight As Designers Seek The Way To Save Money," Product Engineering, November 9, 1970.

3. Urzi, R.B., "Standardization of Fatigue Tests of Installed Fastener Systems," Naval Air Development Center Report, LR 25280, 17 July 1972.

4. Urzi, R.B., "Development of Fatigue Test Standards and Mechanical Property Data on Interference Fit Fastener Systems," Air Force Materials Laboratory Report, AFML-TR-73-195, August 1973.

5. Urzi, R.B., "Standardization of Fastener Tests," Lockheed-California Company Report, LR 22950, December 1969.

6. Urzi, R.B., "Interim Report On Task I, Standardization Of Fatigue Tests Of Installed Fastener Systems," Lockheed-California Company Report, LR 24773, 16 September 1971.

7. MIL-STD-1312 dtd 31 May 1967, Military Standard Fasteners, Test Methods, Test Number 4, "Joint Shear Strength."

8. MIL-HDBK-5B dtd 1 September 1971, Metallic Materials and Elements For Aerospace Structures, Chapter 8, "Structural Joints."

9. Volk, W., "Industrial Statistics," Chemical Engineering, March 1956.

10. Urzi, R.B., "Standardization Of Fastener Tests," Lockheed-California Company Report, LR 24328, December 1970.

11. Air Force Materials Laboratory, "Fretting Resistant Coatings for Titanium Alloys," Report No. AFML-TR-71-184, September 1971.

SESSION IV - FASTENERS-2

Chairman: K. Rim
Chairman, Department of Mechanics and Hydraulics
University of Iowa

STRESS INTENSITY FACTOR MEASUREMENTS FOR FLAWED FASTENER HOLES

A. F. GRANDT, JR.
Materials Engineer

T. D. HINNERICHS
Materials Engineer
Air Force Materials Laboratory
Wright-Patterson Air Force Base, Ohio

ABSTRACT

Cracks which emanate from fastener holes represent one of the most common failure sources in aircraft structural components. In order to determine the severity of such flaws, the design engineer may utilize the stress intensity factor to relate crack length, remote loading, and structural geometry. With the stress intensity factor one may calculate the critical flaw size for a given structure and loading as well as estimate the service life of components containing subcritical flaws. The purpose of this paper is to describe an experimental method which employs fatigue crack growth rates to determine stress intensity factor calibrations for complex structural joint configurations. The procedure is applied to holes which have been cold-worked with an oversize mandrel and further demonstrated with preliminary results for surface cracked holes.

INTRODUCTION

Mechanical joints significantly influence both fabrication costs and structural reliability in modern aircraft. Procuring and installing the many necessary bolts and rivets (over one million for some transport aircraft) may represent five or six percent of total airframe costs. More important, however, fasteners compose the largest single location for structural cracks encountered in service. A 1971 review of significant USAF aircraft structural failures (1)*, for example, revealed that bolt or rivet holes comprised over one third of the failure origins considered.

In view of the operational limitations imposed by early incidents of fatigue cracking in several recent aircraft, the USAF has adopted a new damage tolerance criteria (2) which places increased emphasis on an assumed initial flaw size. This criteria requires future designs to demonstrate that the service lives of fracture critical components will survive pre-existing cracks of specified length and shape. The minimum flaw size is fixed by the damage tolerance criteria and is effectively treated as a material property. Any reduction in the assumed initial crack size must be accompanied by a demonstrated capability to detect these smaller defects with production inspection methods.

---

*See List of References

The significant feature of the damage tolerance criteria for purposes of this paper lies in the fact that two of the specified initial defects are surface flaws or thru-cracks located at a fastener hole as shown in Fig. 1. The designer, is, thus, faced with determining the service lives of these precracked holes. The stress intensity factor (K_I), the linear elastic fracture mechanics parameter relating crack size, remote load, and geometry, provides the means for solving this formidable problem. With the stress intensity factor, one may determine the critical flaw size for a given component and estimate the service life of subcritical cracks which escape detection.

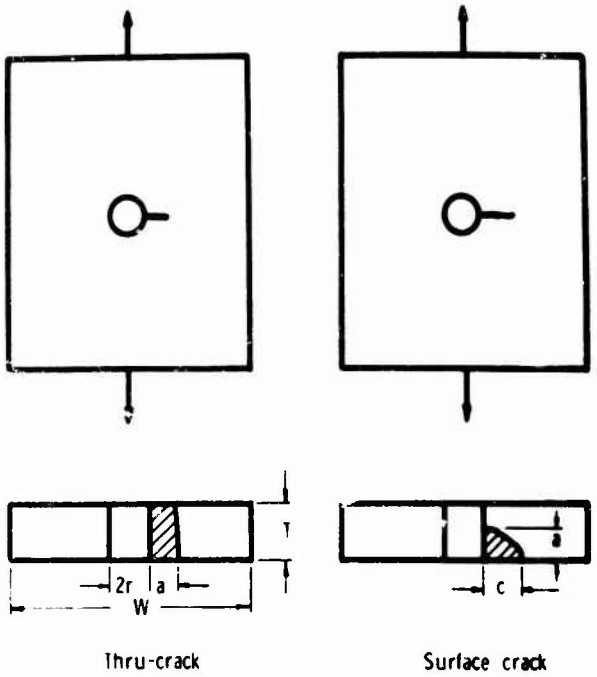

Fig. 1. Schematic of Typical Fastener Hole Flaws

Thru-cracks extending from open holes in plates loaded in remote tension were studied with complex variable methods by Bowie (3), while Crandt (4) recently developed a solution for radial hole cracks loaded with arbitrary crack face pressure. When the pressure is specified as the hoop stress surrounding an unflawed fastener hole, K_I is readily computed by the linear superposition procedure (5-9) shown schematically in Fig. 2. Stress intensity factor results obtained in this manner are given in Ref. 4 for open holes subjected to remote loads, interference fit fasteners, pin-loaded plates, and cold-worked holes. Other investigators (8-9) have used similar linear superposition techniques which employ modified analyses for thru-cracks in wide plates, but do not model the hole directly.

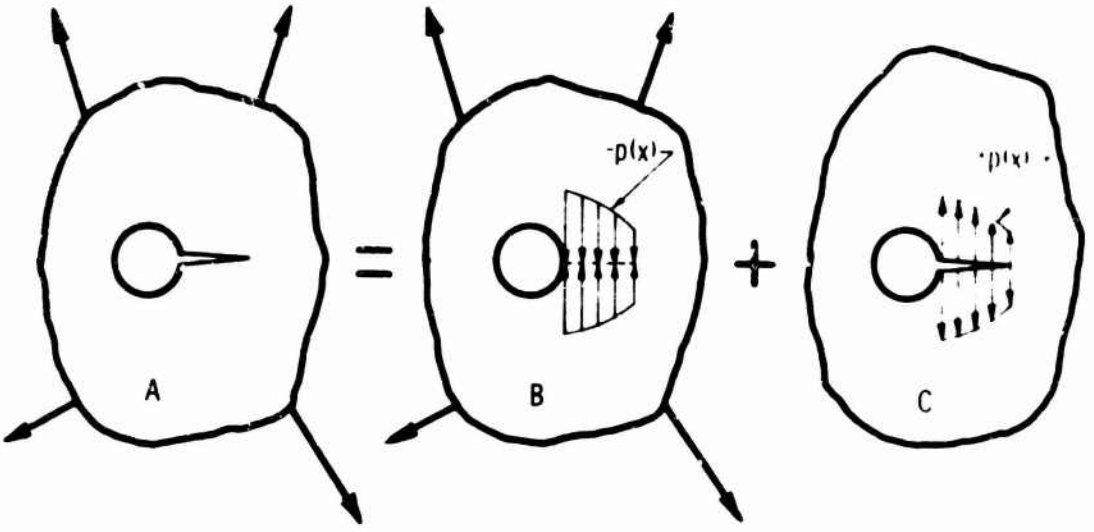

$$K_{I,A} = K_{I,B} + K_{I,C}$$

but $K_{I,B} = 0$ (no crack)

$$K_{I,A} = K_{I,C}$$

Fig. 2. Schematic of Linear Superposition Method

Since surface flaws originating at fastener holes represent an extremely difficult problem in three-dimensional elasticity, no exact solutions exist. Stress intensity factor estimates have been obtained for surface cracked holes by Liu (10), by Hsu and Liu (11), and by Hall et al (12), however, by modifying existing surface flaw solutions (13) to estimate the influence of the hole. To date, little or no work has been reported for "fatigue rated" fasteners or for load transfer through surface cracked holes.

Thus, although the new damage tolerance requirements place increased emphasis on stress intensity factor solutions for flawed fastener holes, exact analytical solutions for many practical configurations are unavailable, pointing out the need for experimental measurements. Cartwright and Ratcliffe (14) determined the strain energy release rate (which is related to K_I) for radial cracks emanating from pin-loaded holes. Although this method may, in principle, be used to study any thru-crack geometry, the experiments require extreme care in that the basic load-displacement data must be differentiated twice to obtain K_I (15). Hall and Finger (16) used fracture measurements of surface flawed holes to empirically relate flaw size and fracture strength. This method is inherently subject to scatter, however, due to statistical variations in fracture toughness. In addition, separate specimens are required for each data point, resulting in many tests for a detailed calibration curve.

It is suggested in this paper that the fatigue crack growth test be used to establish experimental K_I results for complex fastener hole configurations.

This technique is described in the next section and is then used to experimentally evaluate stress intensity factor solutions for cold-worked holes. The procedure is further demonstrated with preliminary K_I measurements in surface flawed holes.

EXPERIMENTAL PROCEDURE

Fatigue testing of mechanical fasteners is often used to evaluate the service lives of structural joints (17). These tests typically are of the endurance type (combined crack initiation and propagation) or directed to obtain crack growth data under spectrum loading. If, however, a few fatigue crack growth experiments are conducted under constant amplitude loading, it is possible to measure the stress intensity factor for flawed fastener holes.

For constant amplitude zero-to-tension cyclic loading, many materials obey the well known relation (18)

$$da/dN = C(\Delta K)^m \qquad (1)$$

Here da/dN is the cyclic crack growth rate, ΔK is the range in stress intensity factor, and C and m are empirical constants which are found from baseline experiments. By solving Eq. 1 for ΔK, measured fatigue crack growth rates may be used to calculate stress intensity factors for both thru-cracks and surface flaws. In order to minimize experimental error, the baseline data should be collected under the same test conditions as the flaw configurations under study (e.g. same specimen material, crack orientation, temperature, humidity, material thickness, R ratio = minimum load/maximum load, etc.).

James and Anderson (19), who ascribed the genesis of this scheme to P.C. Paris, ca 1962, successfully employed this procedure to find stress intensity factors for thru-cracks in thin walled aluminum cylinders, while Grandt and Sinclair (20) used the method to study surface flaws in bending. In addition, several other authors have used fatigue crack growth rates to evaluate K-calibrations determined by other means. This method was followed by Adams (21) to find curvature corrections in axially loaded cracked shells, by Kendall and Hussain (22) to evaluate finite element and compliance results for cracks in curved beams, and by Poe (23) to consider the effect of bolted and integral stringers on cracked panels.

Since the stress intensity factor is computed from da/dN, differentiating the crack growth data requires special care to prevent magnification of experimental error. All of the data analyzed here were first smoothed by a simple averaging technique. Next a least squares parabola was passed through a set of five successive data points and crack lengths calculated at four regular intervals over the range of the set. The growth rate was calculated by a standard least squares formula which approximates the derivative at the center of five evenly spaced points (24). The set was then advanced one point and the process repeated until all the data were exhausted. Slightly different formulas were used for da/dN near the ends of the range of data.

Baseline da/dN versus ΔK data obtained in this manner are shown in Fig. 3 for 7075-T6 aluminum and in Fig. 4 for polymethylmethacrylate (PMMA), a transparent polymer. The results shown in Fig. 3 represent data collected from three compact specimens and one edge-cracked strip at a cyclic frequency of 40 Hz. All specimens were machined from a single sheet of 0.25 in. thick aluminum, with specimens oriented to keep the same direction of crack growth. The PMMA data were collected at 1 Hz from one compact specimen, three three-point bend specimens, and four four-point bend members. Again care was taken to insure the same flaw orientation in the 0.75 in. thick specimens. The aluminum baseline data is used in the following section to study cold-worked holes, while the PMMA data is employed for preliminary measurements of surface cracks originating at fastener holes.

COLD-WORKED HOLES

Cold-working fastener holes with an oversized mandrel develops beneficial residual stresses which have been shown to improve the fatigue life of mechanical joints (12,17,25). Tests with precracked holes, in fact, indicated that cold-working could retard subsequent flaw extension for over 10^6 cycles in some cases (17). Grandt and Gallagher (26) explained this crack arrest in terms of the threshold level of stress intensity factor for fatigue (ΔK_{th}), suggesting that when ΔK is less than ΔK_{th}, cracks will not grow for long service lives. Since ΔK_{th} is a material property which can be measured with standard fracture mechanics specimens, the key to determining the long life crack length again rests with calculating the stress intensity factor.

Although to date no direct stress intensity factor solution exists for flawed holes which have been cold-worked, Adler and Dupree (27) have recently studied uncracked holes in 7075-T6 aluminum. Using elastic-plastic finite element techniques, they first determined the residual state of stress and strain caused by cold-working the hole, and then found the subsequent redistribution in stress and strain due to remote tensile loading. Taking their stress solutions for 0.012 in. mandrel expansion on the diameter of 0.260 in. diameter hole, and using the linear superposition technique discussed in Ref. 4 one obtains the K_I calibrations for 16 ksi and 40 ksi remote loading shown in Figs. 5 and 6. Note in both cases that the stress intensity factor is significantly reduced by the cold-working process when compared with an unworked hole (Bowie solution). The effect of cold-working is particularly significant for the 16 ksi remote load, where as seen in Fig. 5, K_I is reduced to zero for flaws as large as 0.15 in. The comparable stress intensity for 0.15 in. crack emanating from an unworked hole is calculated by the Bowie relation as 14 ksi-in$^{\frac{1}{2}}$.

In order to evaluate these linear superposition solutions, K_I was measured by the fatigue crack growth rate procedure. Specimens were machined from the same sheet of 0.25 in. thick 7075-T6 aluminum used to determine the material properties employed by Adler and Dupree (27) and to collect the baseline data shown in Fig. 3. A careful attempt was made to match the configuration modeled by the finite element solution, resulting in a nominal 0.26 in. diameter hole located on the centerline of a 2.5 in. wide plate. The 0.012 in. mandrel interference was matched by selecting a 0.257 in. diameter mandrel in

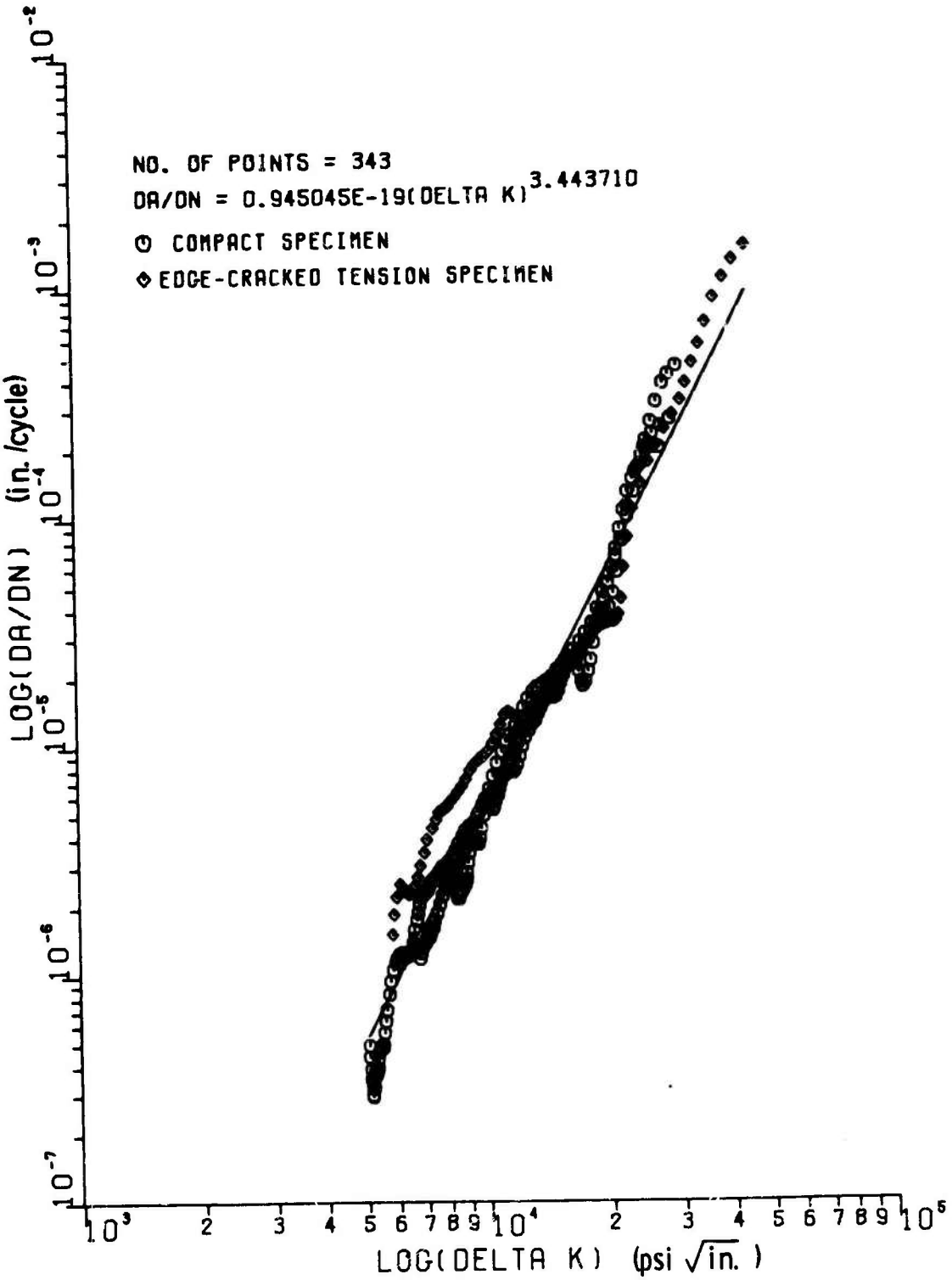

Fig. 3. 7075-T6 Aluminum Baseline Data

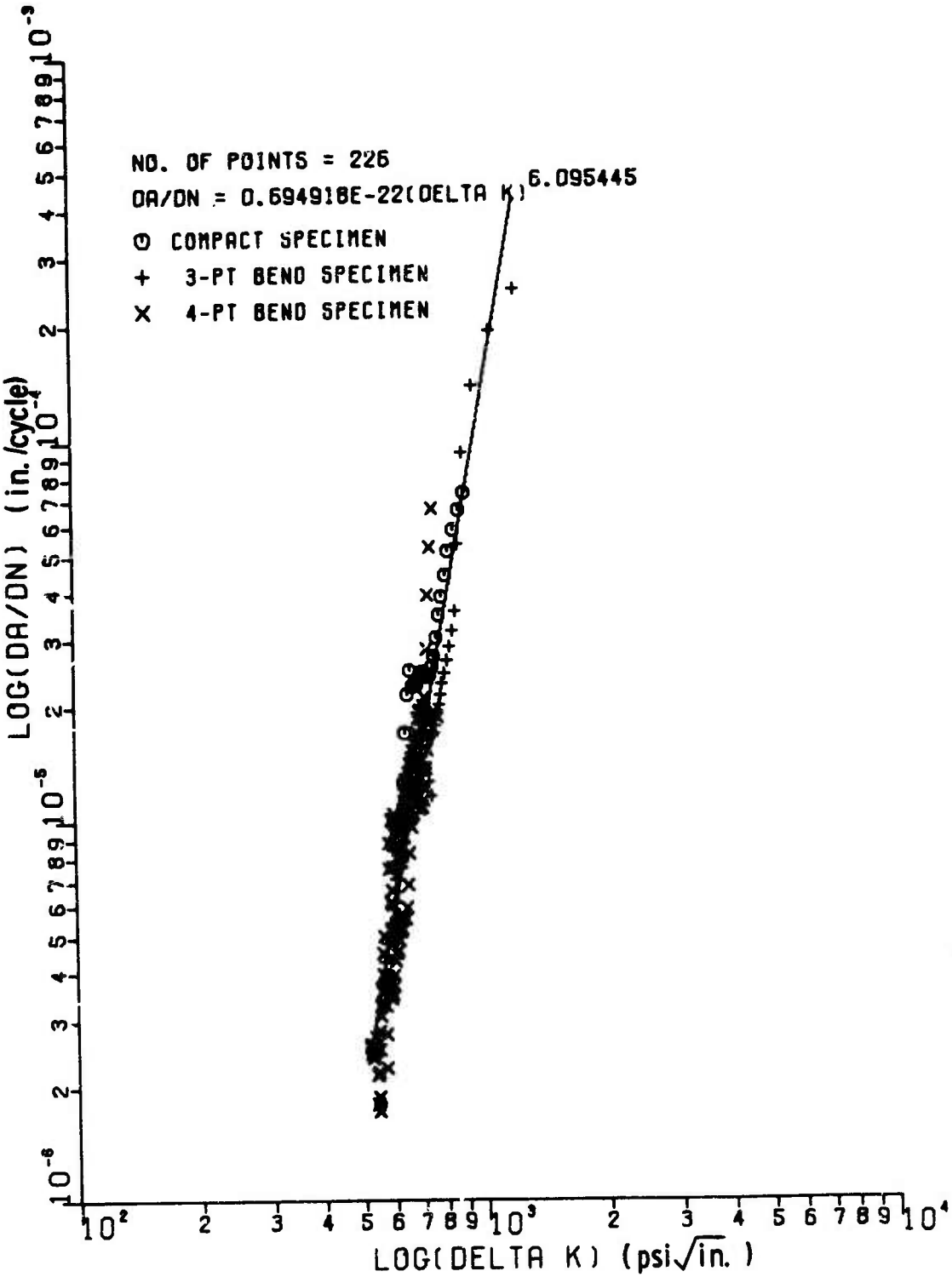

Fig. 4. PMMA Baseline Data

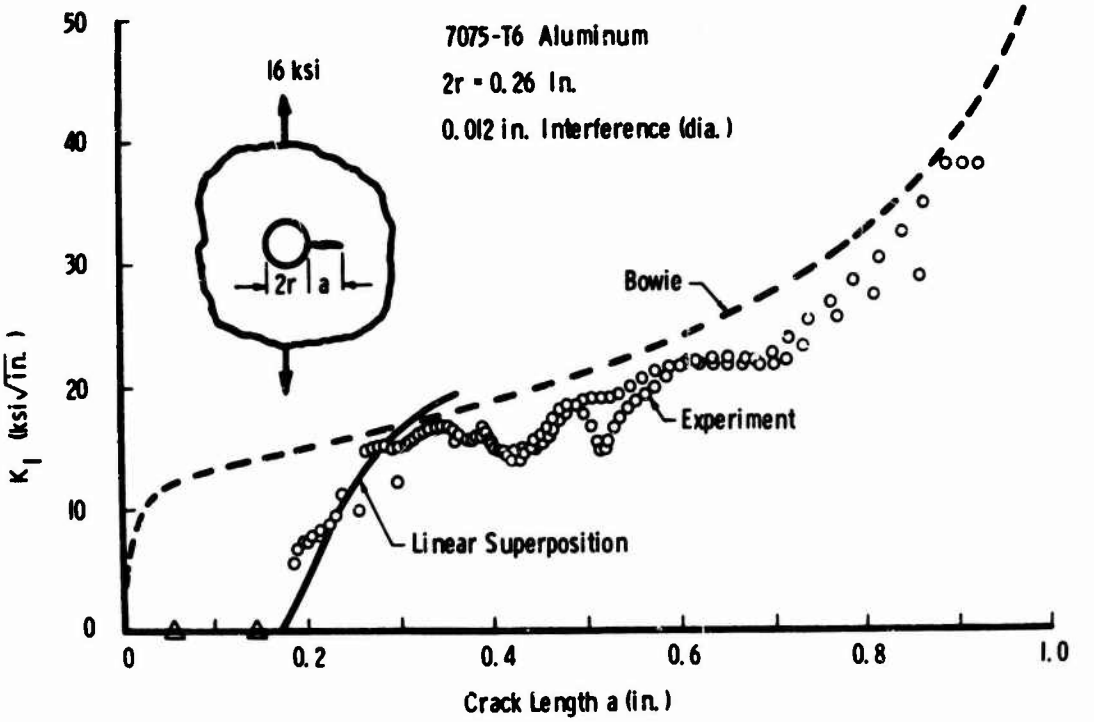

Fig. 5. Stress Intensity Factor Calibration for Cold-Worked Hole in 7075-T6 Aluminum

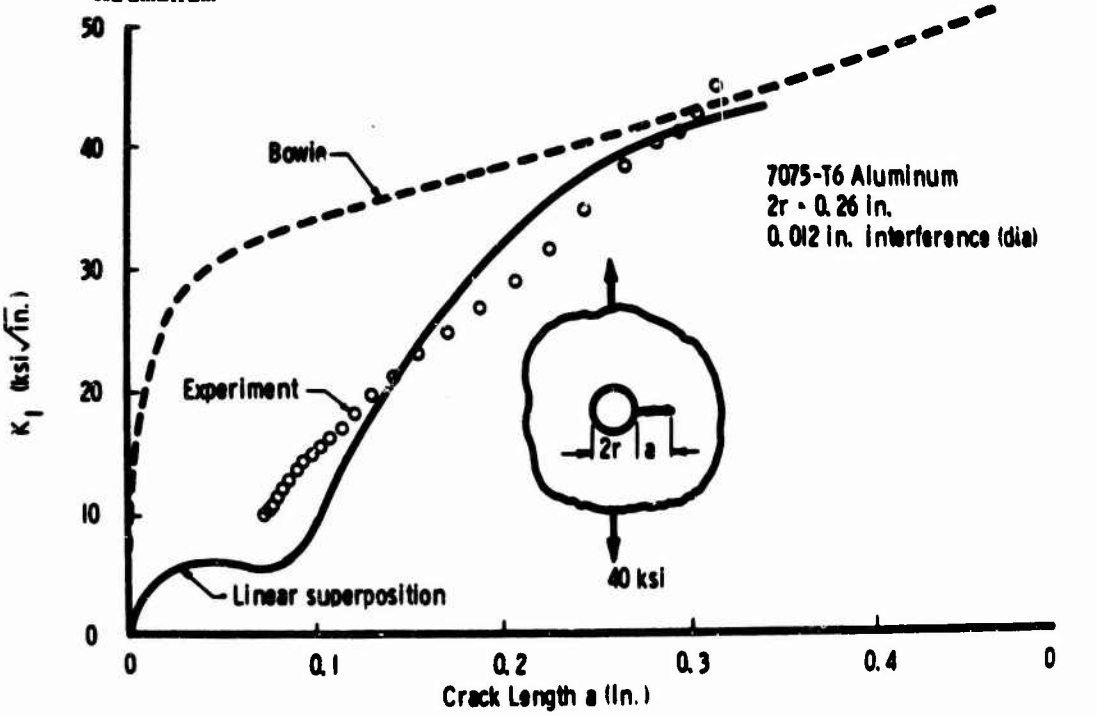

Fig. 6. Stress Intensity Factor Calibration for Cold-Worked Hole in 7075-T6 Aluminum

conjunction with a .008 in. thick seamless sleeve (28) placed in a 0.261 in. diameter hole. The holes were first precracked, reamed to final size, and then cold-worked with a fixture mounted in a standard test machine. The load required to pull the mandrel through the sleeved hole was typically 1500 lbs. under a penetration rate of 0.10 in./min.

Two cold-worked holes were cycled at 16 ksi remote stress (R approximately zero) while a third specimen was cycled at 40 ksi remote stress. The cyclic frequency for the 16 ksi remote stress was maintained at 40 Hz, while the larger loads required for 40 ksi dictated the cyclic frequency be reduced to 1.25 Hz.

A typical crack growth curve for one of the 16 ksi specimens is shown in Fig. 7. Note the increase in specimen life caused by cold-working in comparison with the predicted growth for an unworked hole. This latter curve was obtained by using the Bowie (3) solution for a cracked hole in conjunction with the da/dN versus ΔK relationship shown in Fig. 3. The cold-worked hole crack growth data were first smoothed and then differentiated to obtain da/dN as described before. The measured growth rates were then used with Eq. 1 and the baseline material properties to calculate ΔK. Since $K_{minimum}$ was close to zero, $K_I = K_{maximum} = \Delta K$. It was assumed here that the cold-working process did not alter the material properties relating da/dN and ΔK. This assumption is substantiated by data reported in Refs. 29 and 30 which indicates that changes in microstructure due to thermo-mechanical treatments had no significant effect on fatigue crack growth rates in 7075 aluminum.

The measured values of K_I are compared with the theoretical predictions in Figs. 5 and 6. Note that the experimental measurements generally agree well with the linear superposition solutions throughout their range of validity. Once the cracks grow out of the influence of the residual cold-work stresses (about one diameter from the edge of the hole), the Bowie solution provides a reasonable estimate for K_I as might be expected. A secant width correction (31) was applied to the Bowie curves shown in Figs. 5 and 6 to reflect the finite specimen width.

The two points indicated by triangles on the zero stress intensity factor axis in Fig. 5 were obtained from separate specimens precracked to the lengths shown and cold-worked as before. Both specimens were cycled at 16 ksi remote stress for over 440,000 cycles, with no observed crack growth, at which time the tests were discontinued. Although the total cycles applied to these two specimens do not satisfy the "infinite" life requirements discussed in Ref. 26, these specimens provide preliminary verification of that long life design criteria. (Here $\Delta K = 0 < \Delta K_{th}$) More rigorous testing of this selection criteria remains, however, for future work.

SURFACE FLAWED HOLES

Preliminary stress intensity factor measurements of surface flawed holes were made with the fatigue crack growth rate technique. Since it is difficult to measure subsurface cracks in metals, PMMA, a transparent polymer, was

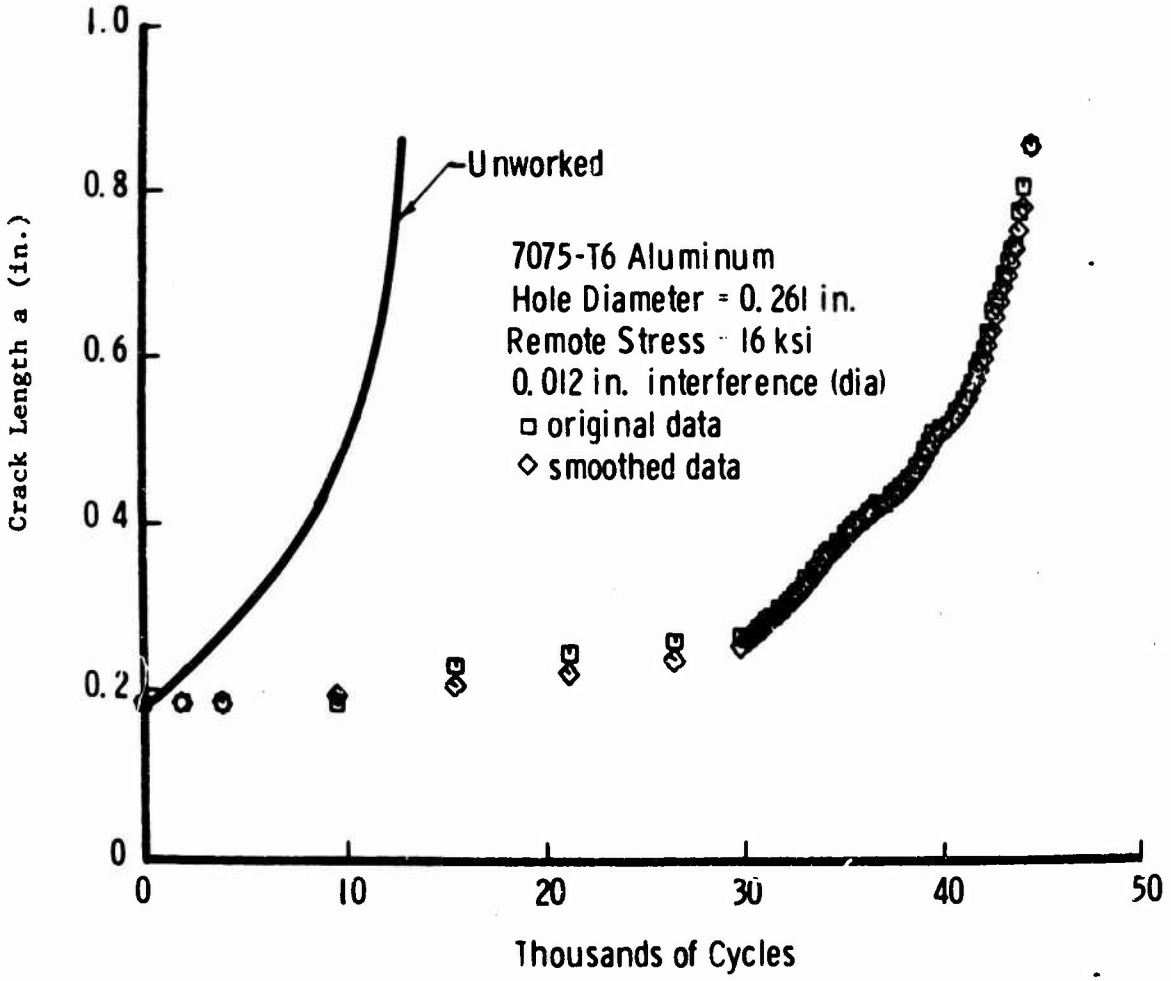

Fig. 7. Predicted Crack Growth From an Unworked Hole Compared with Experimental Data for a Cold-Worked Hole

selected as the test material. Previous work with this method in PMMA gave good results in a study of surface flaws in bending (20).

The specimens measured 8 in. wide by 14 in. long by 0.75 in. thick and contained a centrally placed 0.75 in. diameter hole. Surface cracks shown in Fig. 1 were initiated from a notch at the corner of the hole during constant amplitude cycling between zero and maximum tension. In order to view the crack front directly, the tensile load was applied through pins in metal plates bonded to the specimen with epoxy as shown in Fig. 8. A mirror placed in a cutout in the metal plates provided a direct view of the crack during the fatigue test. Crack growth was recorded on film with a 35 mm camera positioned as shown. These photographs were projected to approximately 20X in a film strip projector and measured, using the known hole diameter as a scaling distance.

A typical crack growth curve obtained in this manner is shown in Fig. 9. Note that both the crack depth a and c are plotted as a function of load

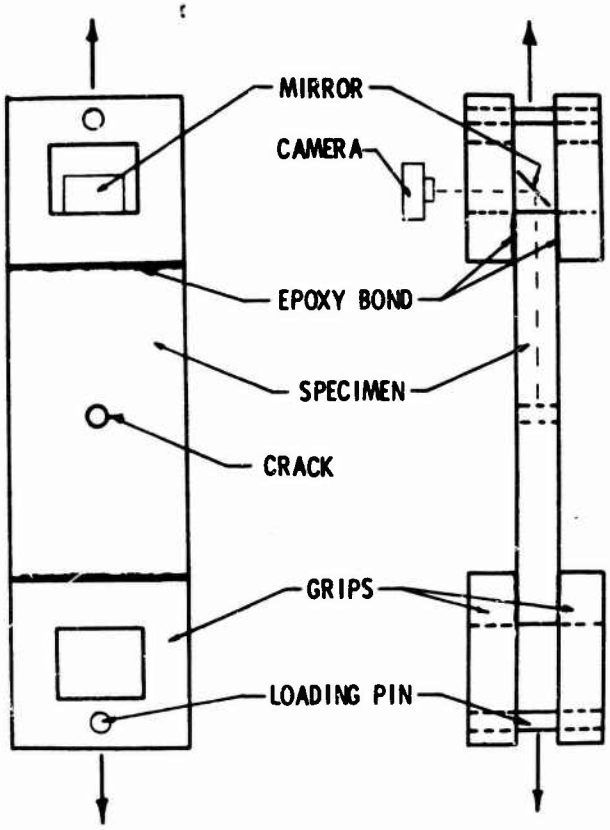

Fig. 8. Schematic of Experimental Apparatus for Surface Flawed Holes

cycles. Using the crack growth rate computed from smoothed data as before, the stress intensity factor at the point the flaw intersects the hole was calculated from da/dN and the baseline data of Fig. 4. Dimensionless K_I results for two specimens are plotted versus a/T in Fig. 10. The naturally occurring flaw shape a/c is also indicated on this figure. Notice that both tests agree fairly well with each other, but that the experimental results lie considerably below the approximate values predicted by Refs. 1 and 16.

Although this lack of agreement between experiment and theory is perhaps disturbing, the purpose for showing these preliminary measurements here is to demonstrate an application of the fatigue crack growth rate method to the complex surface flaw problem. As noted before, no exact solution has been obtained for this geometry to date. Further tests are scheduled to determine whether the differences shown in Fig. 10 are due to experimental error or have some other more fundamental basis.

CONCLUDING REMARKS

In order to prevent future operational restrictions of the type which have hampered recent aircraft, the USAF has adopted a new damage tolerance criteria which emphasizes the assumption of pre-existent flaws. The designer is required to demonstrate that initial defects will not reach critical size

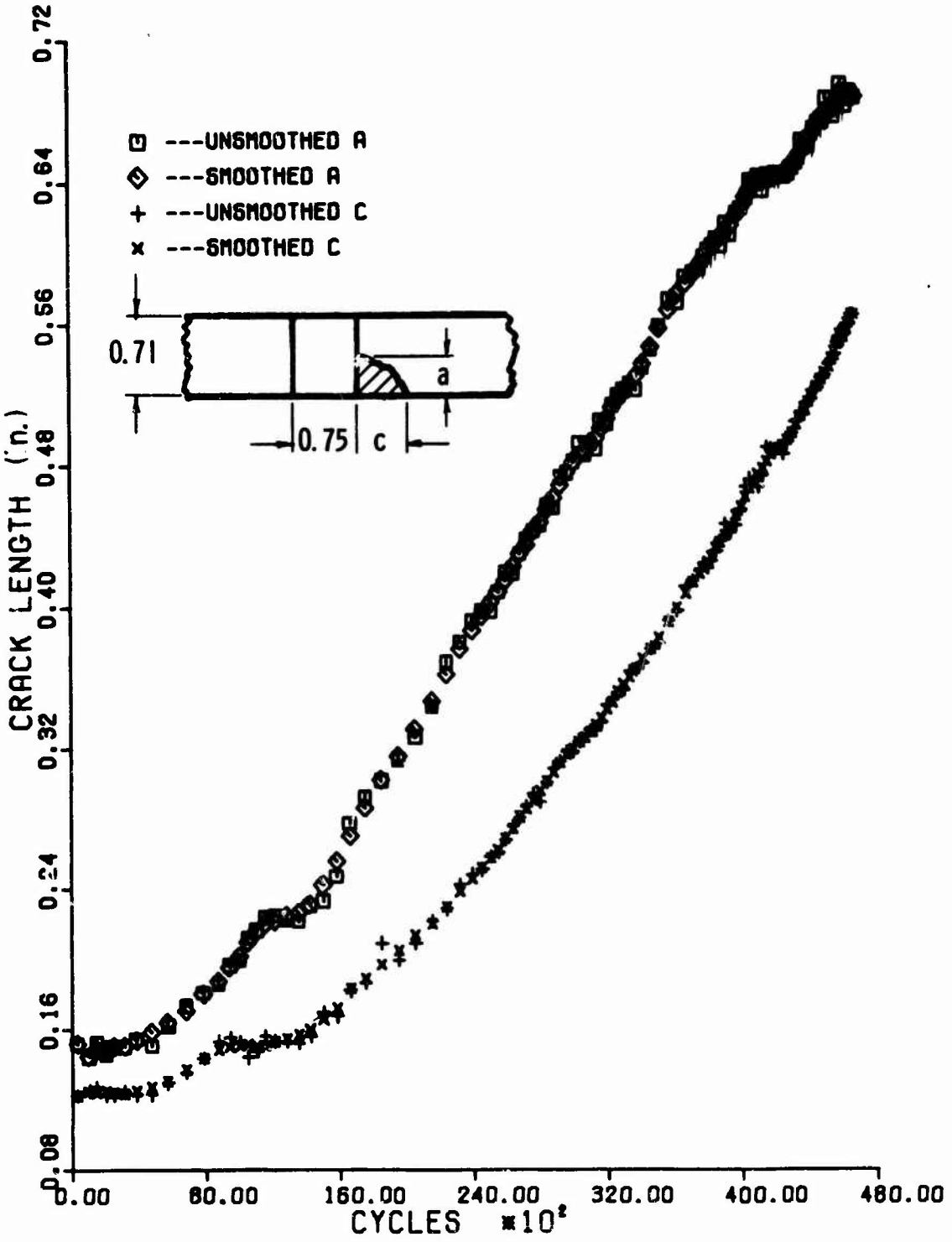

Fig. 9. Fatigue Crack Growth Data for Surface Flawed Hole

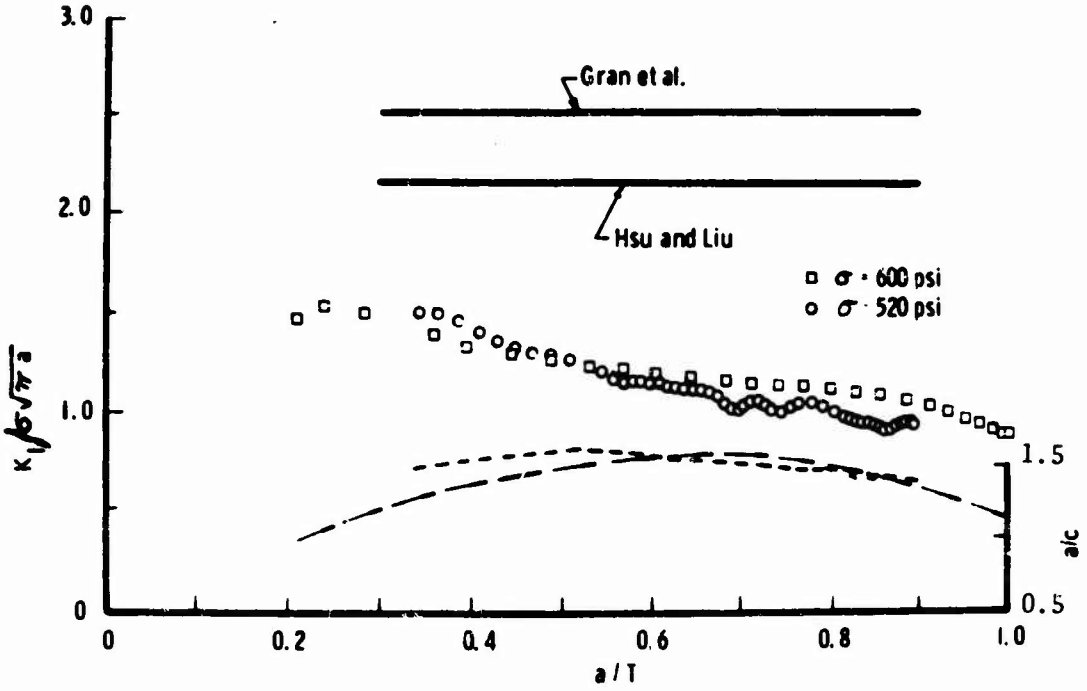

Fig. 10. Preliminary Stress Intensity Factor Results for Surface Flawed Holes at the Point the Crack Intersects the Hole

during the life of the structure. The stress intensity factor is the fracture mechanics tool which provides the key for making these crack growth analyses.

Since mechanical fasteners represent a common failure origin in aircraft structures, stress intensity factor solutions are particularly needed for fastener hole cracks. The purpose of this paper is to describe a convenient experimental procedure for obtaining these calibrations for complex structural configurations. It was shown here that fatigue crack growth rate measurements obtained under constant amplitude conditions can readily be converted to stress intensity factors through baseline data collected with standard specimens. This procedure was demonstrated with measurements in cold-worked holes and with some preliminary results with surface cracked holes.

The K_I calibrations are obtained with a minimum amount of additional cost, since the baseline data is already needed for the life predictions required by the damage tolerance criteria. Thus, the few additional fastener hole tests represent a minimal investment in terms of the K_I information obtained. Although some experimental error may be introduced by differentiating the data, many measurements are obtained from a few experiments over a wide range of crack lengths. If desired, statistical methods (32) may be used to place confidence levels on the measured values of K_I as in Ref. 20.

Stress intensity factor measurements obtained by the fatigue crack growth rate method in cold-worked holes agree well with predictions made by

the linear superposition solution given in Ref. 4. This analytical procedure provides the significant advantage that an entire thru-crack K_I calibration is obtained directly from a single unflawed stress solution. Although stress analyses for complex fastener hole problems such as cold-worked holes subjected to pin loads may require sophisticated techniques, the much more difficult task of resolving crack tip stresses is avoided.

ACKNOWLEDGEMENTS

In addition to the many colleagues who provided advice and assistance, the authors especially wish to acknowledge the assistance of M.B. Strope and H.D. Stalnaker with the fatigue tests and the aid of J.S. Wagner with the data reduction.

REFERENCES

1. Gran, R.J., Orazio, F.D., Paris, P.C., Irwin, G.R. and Hertzberg, R., "Investigation and Analysis Development of Early Life Aircraft Structural Failures," Technical Report AFFDL-TR-70-149, Wright-Patterson Air Force Base, Ohio, March 1971.

2. Proposed USAF Damage Tolerance Requirements, August 1972.

3. Bowie, O.L., "Analysis of an Infinite Plate Containing Radial Cracks Originating from the Boundary of an Internal Circular Hole," Journal of Mathematics and Physics, Vol. 35, pp 60-71, 1956.

4. Grandt, A.F., "Stress Intensity Factors for Some Thru-Cracked Fastener Holes," International Journal of Fracture (in press).

5. Paris, P.C., Gomez, M.P., and Anderson, W.E., "A Rational Analytical Theory of Fatigue," The Trend in Engineering, Vol. 13, No. 1, January 1961, University of Washington.

6. Emery, A.F., "Stress-Intensity Factors for Thermal Stresses in Thick Hollow Cylinders," Journal of Basic Engineering, Transactions of the ASME, Series D, pp 45-52, March 1966.

7. Emery, A.F., Walker, Jr., G.E. and Williams, J.A., "A Green's Function for the Stress Intensity Factors of Edge Cracks and Its Application to Thermal Stresses," Journal of Basic Engineering, Transactions of the ASME, Vol. 91, Series D, No. 4, pp 618-624, December 1969.

8. Crews, Jr., J.H., and White, N.H., "Fatigue Crack Growth from a Circular Hole With and Without High Prior Loading," Technical Report NASA TN D-6899 Langley Research Center, Hampton, Virginia, September 1972.

9. Schmidt, R.A., "An Approximate Technique for Obtaining Stress Intensity Factors for Some Difficult Planar Problems," paper presented at Fracture and Flaws Symposium, Albuquerque, New Mexico, March 2, 1973.

10. Liu, A.F., "Stress Intensity Factor for a Corner Flaw," Journal of Engineering Fracture Mechanics, Vol. 4, March 1972, pp 175-179.

11. Hsu, T.M. and Liu, A.F., "Stress Intensity Factors for Truncated Elliptical Cracks," presented at the Seventh National Symposium on Fracture Mechanics, College Park, Maryland, August 27-29, 1973.

12. Hall, L.R., Engstrom, W.L., and Shan, R.C., "Fracture and Fatigue Crack Growth Behavior of Surface Flaws and Flaws Originating at Fastener Holes," Technical Report AFFDL-TR-74-47, Air Force Flight Dynamics Laboratory, Wright-Patterson Air Force Base, Ohio, March 1974.

13. Swedlow, J.L. (editor), The Surface Crack: Physical Problems and Computational Solutions, The American Society of Mechanical Engineers, New York, 1972.

14. Cartwright, D.J. and Ratcliffe, G.A., "Strain Energy Release Rate for Radial Cracks Emanating from a Pin Loaded Hole," International Journal of Fracture Mechanics, Vol. 8, No. 2, June 1972, pp 175-181.

15. Bubsey, R.T., Fisher, D.M., Jones, M.H. and Grawley, J.E., "Compliance Measurements," Experimental Techniques in Fracture Mechanics, Society for Experimental Stress Analysis Monograph Series, Westport, Conn., 1973, pp 76-95.

16. Hall, L.R. and Finger, R.W., "Fracture and Fatigue Growth of Partially Embedded Flaws," Proceedings of the Air Force Conference on Fatigue and Fracture of Aircraft Structures and Materials, Technical Report AFFDL-TR-70-144, Wright-Patterson Air Force Base, Ohio, September, 1970, pp 235-262.

17. Tiffany, C.F., Stewart, R.P., and Moore, T.K., "Fatigue and Stress-Corrosion Test of Selected Fasteners/Hole Processes," Technical Report ASD-TR-72-111, Wright Patterson Air Force Base, Ohio, January 1973.

18. Paris, P.C. and Erdogan, F., "A Critical Analysis of Crack Propagation Laws," Journal of Basic Engineering, Transactions of the ASME, Vol. 85, Series D, No. 4, December 1963, pp 528-533.

19. James, L.A. and Anderson, W.E., "A Simple Experimental Procedure for Stress Intensity Factor Calibration," Journal of Engineering Fracture Mechanics, Vol. 1, April 1969, pp 565-568.

20. Grandt, A.F. and Sinclair, G.M., "Stress Intensity Factors for Surface Cracks in Bending," Stress Analysis and Growth of Cracks, Proceedings of the 1971 National Symposium on Fracture Mechanics, Part I, ASTM STP 513, 1972, pp 37-58.

21. Adams, N.J.I., "The Influence of Curvature on Stress Intensity at the Tip of a Circumferential Crack in a Cylindrical Shell," Damage Tolerance in Aircraft Structures, ASTM STP 486, American Society for Testing and Materials, 1971, pp. 39-49.

22. Kendall, D.P. and Hussain, M.A., "A New Fracture Toughness Test Method for Thick Walled Cylinder Materials," Paper No. 1848A, presented at 1971 SESA Spring Meeting, Salt Lake City, Utah, May 18-21, 1971.

23. Poe, Jr., C.C., "Fatigue Crack Propagation in Stiffened Panels," Damage Tolerance in Aircraft Structures, ASTM STP 486, American Society for Testing and Materials, 1971, pp. 79-97.

24. Pettofrezzo, A.J., Introductory Numerical Analysis, Heath and Company, Boston, 1967.

25. Phillips, J.L., "Sleeve Coldworking Fastener Holes," Technical Report AFML-TR-74-10, Air Force Materials Laboratory, Wright-Patterson Air Force Base, Ohio, 45433, February 1974.

26. Grandt, A.F., and Gallagher, J.P., "A Proposed Fracture Mechanics Criteria to Select Mechanical Fasteners for Long Service Lives," Fracture Toughness and Slow-Stable Cracking, ASTM STP 559, American Society for Testing and Materials, 1974, pp. 283-297.

27. Adler, W.F. and Dupree, D.M., "Stress Analysis of Coldworking Fastener Holes," Technical Report AFML-TR-74-44, Wright Patterson Air Force Base, Ohio, March 1974.

28. King-Size Cold Working Hole Sizing System, J.O. King, Incorporated, Atlanta, Georgia.

29. Posner, J.M., "Investigation of Stage II Crack Propagation in 7075 Aluminum," Thesis #GAM/MC/73-3, Air Force Institute of Technology, Wright-Patterson Air Force Base, Ohio, September, 1972.

30. Hahn, G.T. and Simon, R., "Metallurgical Control of Fatigue Crack Growth in High Strength Aluminum Alloys," Technical Report AFML-TR-72-48, Air Force Materials Laboratory, Wright-Patterson Air Force Base, Ohio, 1972.

31. Fedderson, C.E., Discussion, Plane Strain Crack Toughness Testing of High Strength Metallic Materials, ASTM STP 410, American Society for Testing and Materials, 1966, pp. 77-79.

32. Acton, F.S., Analysis of Straight Line Data, Dover Publications, New York, 1959.

SIMPLIFIED THREE-DIMENSIONAL ANALYSIS OF MECHANICALLY FASTENED JOINTS

HARRY G. HARRIS
Structural Methods Engineer, Structural Mechanics Section

IRVING U. OJALVO
Structural Mechanics Staff Engineer
Grumman Aerospace Corporation
Bethpage, New York 11714

ABSTRACT

Analytical techniques for predicting the three-dimensional stresses a deformations of mechanically fastened joints are presented. The idealization used is a set of stacked parallel plates which transfer planar loads among themselves by means of transverse fasteners. The plates are treated by finite element methods to determine their two dimensional load-deflection characteristics in the vicinity of a loaded hole. The influence coefficients so obtained are then used as equivalent elastic foundations for the fasteners. The fasteners are then treated by short beam on elastic foundation theory.

Application of the present analytical techniques was made to the problem of predicting the load-deflection behavior of single-fastener joints. Parametric studies were perfor ed to determine the effects on stress and deflection distributions of variables such as initial clearance and interference between fastener and hole, load level, geometry, and material properties of both fastener and plate. Comparison of the analysis with limited test data showed good agreement.

NOMENCLATURE

A	=	Fastener cross-sectional area ($in.^2$)
D	=	Fastener diameter or diameter of hole (in.)
ΔD	=	Difference in diameter between fastener and hole
e	=	Plate edge distances measured from the hole center (in.)
E	=	Young's modulus (psi)
G	=	Shear modulus of fastener material (psi)
I	=	Fastener cross-sectional moment of inertia ($in.^4$)
k	=	"Spring constant" or slope of the load deflection curve (lb/in.); foundation modulus (psi)
k_i	=	Foundation modulus of the i^{th} plate or i^{th} layer of the plate
M	=	Moment (in.-lb)
P_i	=	Redundant radial load; total plate tension (lb)
P_o	=	Statically determinate radial load (lb)
P^*	=	Bypass load in multifastener joint (lb)
q	=	Distributed plate interaction load per unit of fastener length (lb/in.)
Q	=	Cross sectional shear; fastener transfer load in multifastener joints (lb)

t = Plate thickness (in.)
W = Plate width (in.)
x = Fastener axial coordinate (in.)
X = Cartesian coordinate for plate
y = Fastener deflection (in.)
Y = Cartesian coordinate for plate

Greek Letters:

β = Fastener/plate bending stiffness parameter (in.$^{-1}$)
γ = Fastener/plate shearing stiffness parameter (in.$^{-1}$)
δ = Radial displacement (in.)
Δ_A = Radial displacement due to clearance or interference (in.)
Δ_B = Radial displacement due to bypass loads P* (in.)
θ = Angular measure around hole circumference (degrees)
λ = Cross-sectional shear parameter or shape factor (dimensionless)
σ_R = Ratio of peak bearing stress between a flexible and rigid fastener (see Figure 10)

Matrices:

$[A]$ = Flexibility matrix of hole due to P loads; $[A_{11}]$, $[A_{12}]$, $[A_{21}]$ and $[A_{22}]$ are partition matrices of matrix $[A]$
$[B]$ = Flexibility matrix of hole due to P* loads
$\{\delta\}$ = Vector of radial displacements around hole
$\{\Delta_A\}$ = Vector of radial displacements around hole caused by clearance or interference
$\{\Delta_B\}$ = Vector of radial displacements around hole caused by by-pass loads, P*

INTRODUCTION

The accurate structural analysis of mechanically fastened joints is an important aspect in the efficient design of many engineering structures. Because the exact analysis of such joints is highly complex, involving combined nonlinear three-dimensional stress states, more modest approaches have been developed.

Previous investigators[1,2] have employed redundant analysis procedures to determine the load associated with each fastener. Their techniques have been semi-empirical in that the load displacement relationship for a single fastener, a necessary input quantity, must be determined by test. These procedures also rely upon uniformly loaded "effective width" concepts to simulate the spring constants between fasteners, and so the stress concentrations near fastener holes are masked.

The groundwork for the application of the finite element techniques to the solution of two-dimensional contact problems dealing with the determination of stress distributions in structural joints was given by H. Loshigian. It was reported in 1967 by Mason and Balderes[3] who presented the solution of a lug problem including clearance effects and successfully compared their results to experimental data. Following a similar approach, Harris, Ojalvo

and Hooson [4] extended the cited method to interference-fit fastener problems and considered, for the first time, the non-uniform stress distribution through the plate thickness. These authors were thus able to compute the elastic load-deflection characteristics of single-fastener joints and successfully compare them to experimental results.

A planar analysis of a pin-and-eye connection where the pin elasticity was taken into account but where the contact forces were assumed to act only at nodes (similar to References 3 and 4) was presented by White and Enderby [5]. Following these works, important computational improvements for this type problem were made by Scholes and Strover [6]. Chan and Tuba [7,8] considered both two-dimensional contact and frictional interaction and their formulation can treat the problem of partial contact between nodes. Their method is more general than the above procedures and distributes the load linearly to the adjacent nodes where partial contact occurs. An excellent survey paper of these works was recently presented by Newman [9].

To reduce the dependency upon test data (as required in References 1 and 2), the present paper follows the modeling techniques of References 3, and 5 through 8, for the planar idealization. Two-dimensional finite elements are proposed as adequate models for the plates. Consistent with current state-of-the-art methods, these are capable of determining effects of geometric configuration, elastic-plastic stress states, hole clearance, and interference fit.

To determine fastener deformation effects and load variations through the plate thickness, the finite element method could be extended in conjunction with three-dimensional elements. However, this would increase the complexity of the problem by at least an order of magnitude. Rather than do this, a simplified engineering modeling approach is taken in which the fastener is treated as a short beam and the surrounding medium is idealized as an elastic foundation [4]. In this way it is possible to approximate fastener shearing and bending flexibilities, head stiffness effects, bearing stress variation, and non-uniform foundation modulus through the plate thickness, without further complicating the planar finite element analysis.

This component analogue, to simulate the actual mechanically fastened structure, is illustrated schematically in Figure 1, and detailed further, below. In addition, partial results are presented from a more thorough analytical investigation [4]

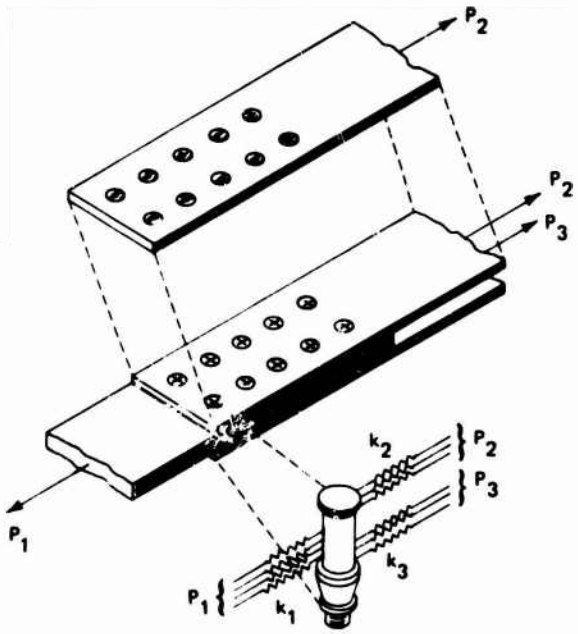

Figure 1 Modeling Scheme for Mechanically Fastened Structural Joint

which examined: the combined elastic-plastic behavior of plates with unloaded holes, the load-deflection behavior of single-fastener joints, the residual stress distributions in plates with squeeze rivets, the effect of fastener bending and shear deformation on the bearing stress distribution between fastener and plate, and the prediction of the fatigue life of typical mechanically fastened joints. In all of these cases, comparisons with test results generally gave very good correlation.

PLANAR ANALYSIS

The planar idealizations are treated by the finite element method of structural analysis. The two specific types of problems considered in the present study are: (1) the elastic nonlinear contact analysis of plates, with a single hole, loaded by rigid circular pins with arbitrary conditions of initial fit, and (2) the elastic-plastic analysis of plates with unloaded holes. Methods of analysis for problems falling into the latter category have been extensively treated in the literature and so are not detailed here. Suffice it to say that the approach used, called the "initial strain" method [References 10 to 12], is one in which plastic strains are interpreted as initial strains in a series of standard linear stiffness analyses.

The load transfer from one plate of a joint to another, through a fastener, creates a nonlinear problem. As with many contact problems, the reason for this is that as the load in the joint changes, the contact area between plate and fastener changes causing a gradual load redistribution. The degree of redistribution is a function of the load level and the initial clearance, or interference, between fastener and hole. Frictional effects may also play an important role on the contact area. However, the present analysis ignores this effect. Thus, the load direction at any point on the contact surface is always radial. Hence, the analysis procedure only permits radial interaction loads between the fastener and plate, which by the nature of contact loads, must be compressive.

The computation of radial contact forces, when limited to nodal points only, is not as great a disadvantage as was stated in [9] because a refinement of the finite element grid is always possible with more nodal points added to the anticipated contact region. We have found that this approach yields accurate plate stresses and deflections in the vicinity of the hole, which are the items of real interest.

The mathematical model chosen to study local effects of load transfer and by-pass load around a fastener is shown in Figure 2. The basis for the idealization as a single fastener is that the region of stress concentration around each fastener is fairly localized. Another assumption made is that the plate structure and load are both symmetric as indicated in Figure 2(b).

The solution of the redundant forces around the fastener are evaluated by first generating the flexibility matrix [A] for the plate in terms of the nodes 1, 2, ..., n surrounding the hole and the applied load, Q. Thus,

$$\begin{Bmatrix} \delta_P \\ \delta_Q \end{Bmatrix} = \begin{bmatrix} A_{11} & A_{12} \\ A_{21} & A_{22} \end{bmatrix} \begin{Bmatrix} P \\ Q \end{Bmatrix} \qquad (1)$$

where the matrix A_{22} is simply 1 X 1.

Additional kinematically determinate radial displacements, $\{\Delta_A\}$, will occur if the fastener has initial clearance or interference, with the plate. Eq (1) then becomes,

$$\begin{Bmatrix} \delta_P \\ \delta_Q \end{Bmatrix} = \begin{bmatrix} A_{11} & A_{12} \\ A_{21} & A_{22} \end{bmatrix} \begin{Bmatrix} P \\ Q \end{Bmatrix} + \begin{Bmatrix} \Delta_{AP} \\ \Delta_{AQ} \end{Bmatrix} \qquad (2)$$

When by-pass loads, P*, act on the plate in addition to the transfer load, Q, additional radial displacements will occur between the fastener and plate interface. Thus, the combined effects of contact forces, initial clearance or interference, and the effect of by-pass load are given by

$$\begin{Bmatrix} \delta_P \\ \delta_Q \end{Bmatrix} = \begin{bmatrix} A_{11} & A_{12} \\ A_{21} & A_{22} \end{bmatrix} \begin{Bmatrix} P \\ Q \end{Bmatrix} + \begin{Bmatrix} \Delta_{AP} \\ \Delta_{AQ} \end{Bmatrix} + \begin{Bmatrix} \Delta_{BP^*} \\ \Delta_{BQ} \end{Bmatrix} \qquad (3)$$

Where $\{\Delta_B\} = [B]\{P^*\}$.

The elements of $\{\delta_P\}$ in Eq (3) are the "gaps" which exist in the statically determinate structure, i.e., $P_i = 0$, $i = 1, 2, \ldots, n$ and $\{P\}$ are the redundant interaction forces.

Imposing the compatibility conditions $\{\delta_P\} = \{0\}$ in Eq (3), which implies that the redundants are zero if a "gap" exists, yields

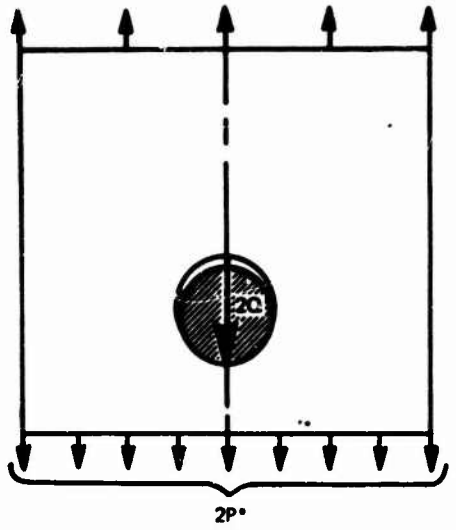

(a) REGION AROUND A TYPICAL FASTENER

Q = TRANSFER LOAD
P* = BY-PASS LOAD

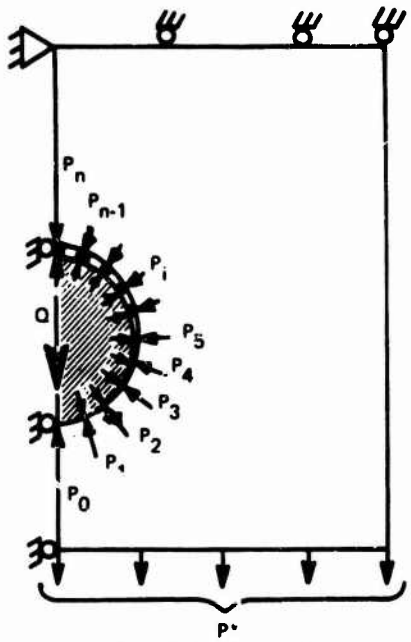

(b) IDEALIZATION USED

Figure 2 Mathematical Model of Plate Loaded Through a Fastener

$$\{0\} = [A_{11}]\{P\} + [A_{12}]\{Q\} + \{\Delta_{AP}\} + \{\Delta_{BP^*}\} \quad (4a)$$

and

$$\{\delta_Q\} = [A_{21}]\{P\} + [A_{22}]\{Q\} + \{\Delta_{AQ}\} + \{\Delta_{BQ}\} \quad (4b)$$

Solving Eq (4a) for the redundants yields

$$\{P\} = -[A_{11}]^{-1}\left|[A_{12}]\{Q\} + \{\Delta_{AP}\} + \{\Delta_{BP^*}\}\right| \quad (5)$$

The solution of Eq (5) (assuming that all the gaps between the redundants are closed) will, in general, yield some positive values for the redundants, indicating tension. Since these are physically inadmissible, the corresponding P's are set to zero and the matrix order reduced in the succeeding computation of P. By this trial and error iterative procedure, the redundants are recomputed until all are compressive and the relative radial displacements create a compatible deflected condition between plate and fastener.

Using a computer program [4] based upon this technique, several examples of aluminum and titanium joints were analyzed. A planar finite element idealization for a typical aluminum plate loaded solely by a single 0.25-inch diameter fastener is shown in Figure 3. This plate may be considered the top or bottom cover (neglecting countersink effects) of the double shear joint shown in Figure 4. The load distribution around the fastener at various load levels for one clearance and one interference fit condition is shown in Figure 5. Application of the reaction loads at each load level, Q, produced the stress concentration factors shown in Figure 6. Note that the effect of clearance tends to increase the stress concentration factor which levels off as Q increases. Such data is highly useful in the fatigue analysis of joints. The other important aspect of such information is the determination of local "spring constants", for the appropriate length of plate surrounding the hole in which local fastener effects are concentrated. These "spring constants" are then used to compute the variation of stress, through the plate thickness, by the manner discussed in the following section.

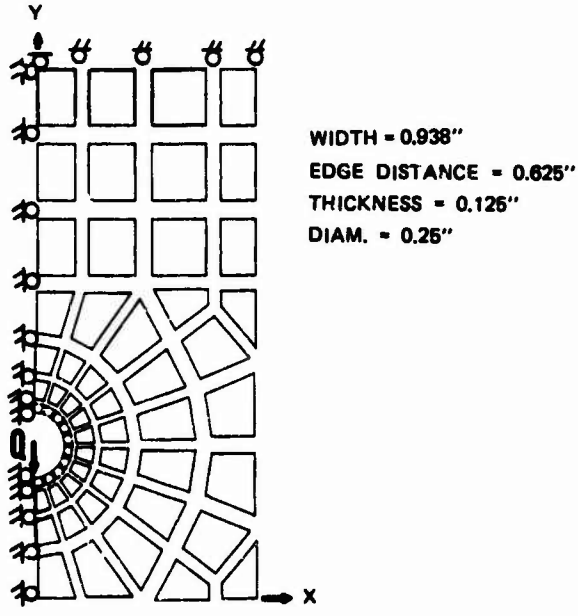

Figure 3 Finite Element Idealization of Plate (Part of an Aluminum Joint)-Plotted by Orthomat Machine to Check Data Input

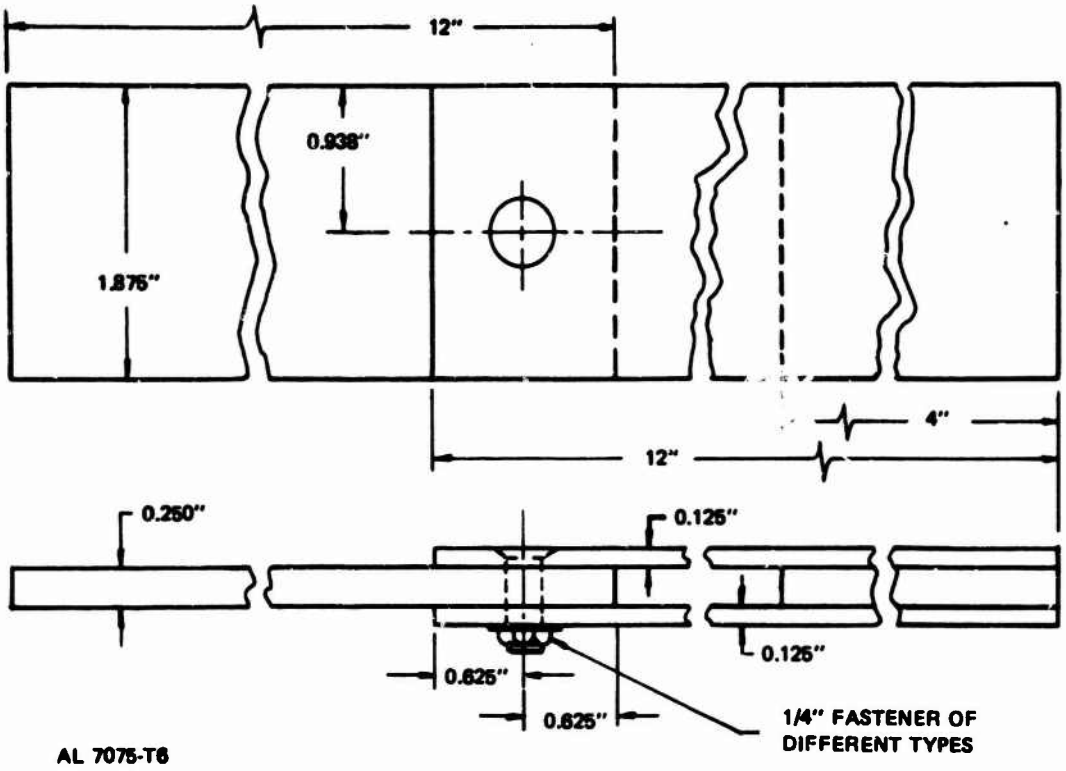

Figure 4 Test Specimen for Single Fastener in Double Shear

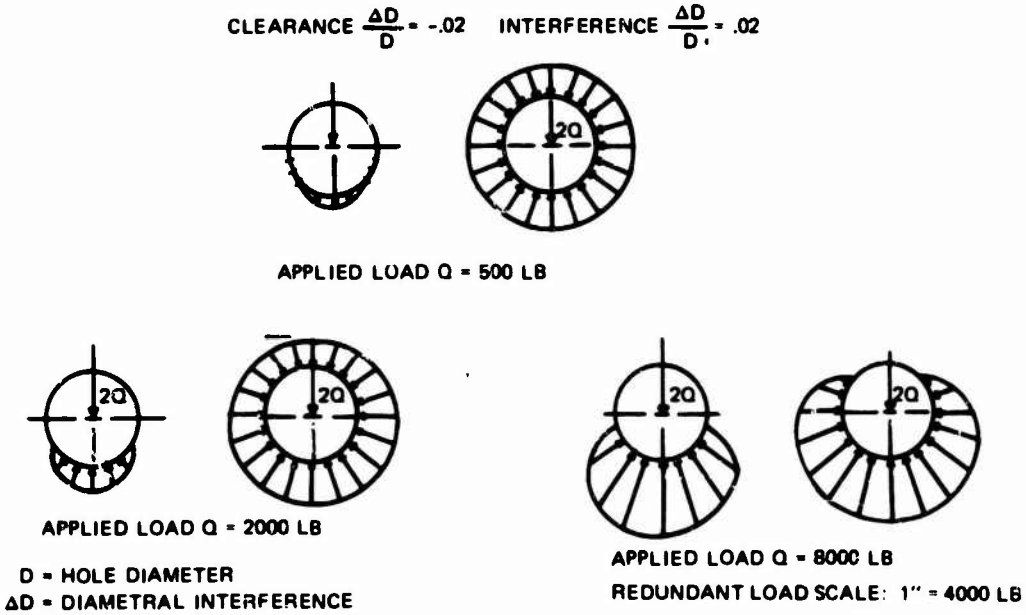

Figure 5 Load Distribution Around Fastener for the Plate of Figure 3 at Three Different Load Levels

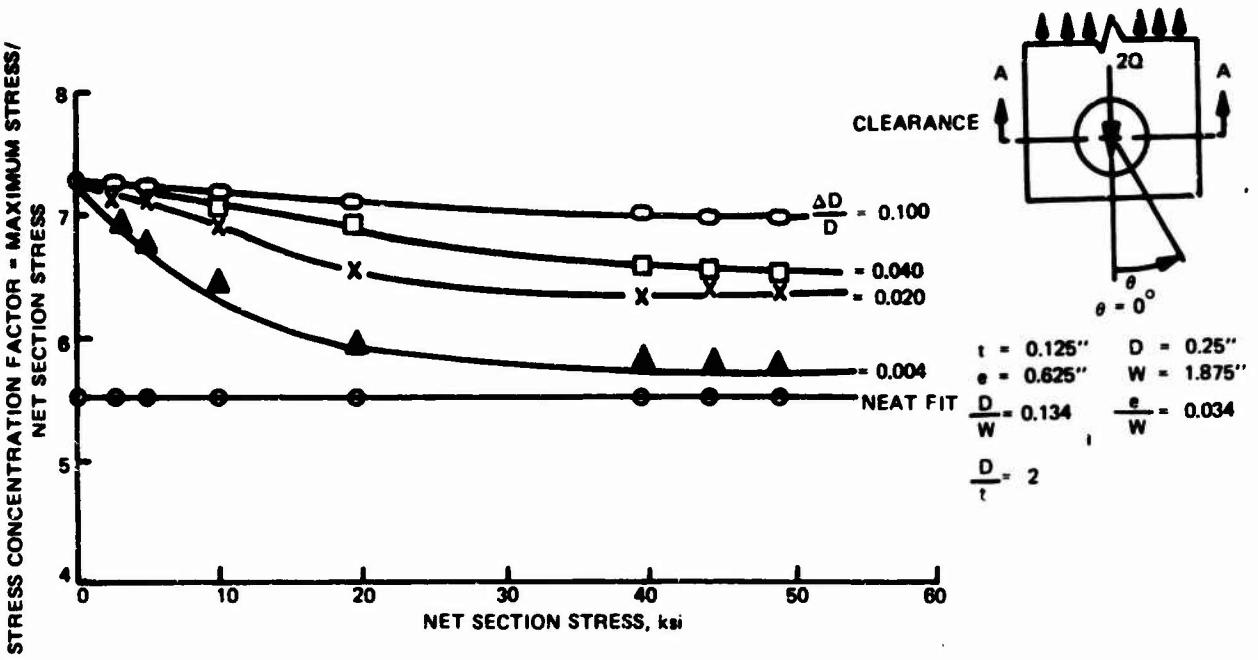

Figure 6 Variation of Stress Concentration Factor With Increasing Net Section Stress for the Plate of Figure 3

NON-RIGID FASTENER EFFECTS

In obtaining the planar finite element solutions, the effects of fastener shear, bending, and over-all pitching motion were assumed secondary and the fastener simply translated as a rigid cylinder normal to its axis. In addition, many other considerations such as fastener head shape, countersink, clampup force, and contact friction were also neglected. To account for some of these effects in a simplified way, the fastener/plate interaction is idealized as a beam resting on a continuous set of mutually uncoupled springs (Figure 7). Thus, the bearing forces per unit of axial length are directly proportional to the fastener's transverse, centerline displacements. The assumption that the springs are not coupled is equivalent to assuming that the plate's transverse shear stiffness may be neglected and that planar stress distributions, given by the methods of the previous section, vary throughout the plate thickness.

As justification of this simplification, Hetenyi [13] demonstrated its suitability for foundations with shear continuity when the ratio $E_{fastener}/k_{foundation}$ is greater than unity. Fortunately it has been found that this is the case for a wide range of mechanically fastened joints. As may be seen from Figure 8, it also appears reasonable to select k as uniform and independent of load level throughout a given plate, once all the hole slack clearance has been taken up.

The governing equations for a mechanical fastener, idealized as a beam with both shear and bending stiffnesses (λGA and EI, respectively), in contact with the i^{th} plate acting as an elastic foundation [4] are:

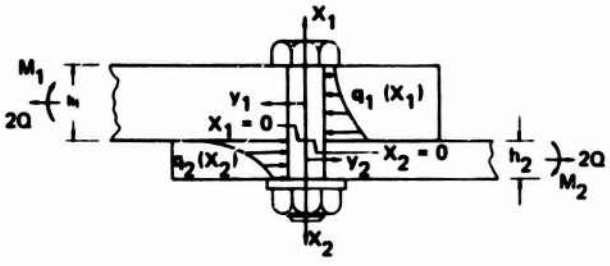

(a) Plate-Fastener Load Interaction Through Plate Thickness

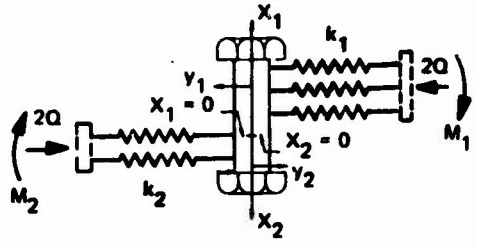

(b) Idealized Model of Plate as a Nonlinear Elastic Foundation Interacting with a Short Beam

Figure 7 Idealized Model Including Local Effects Along the Fastener Length and Through the Plate's Thickness

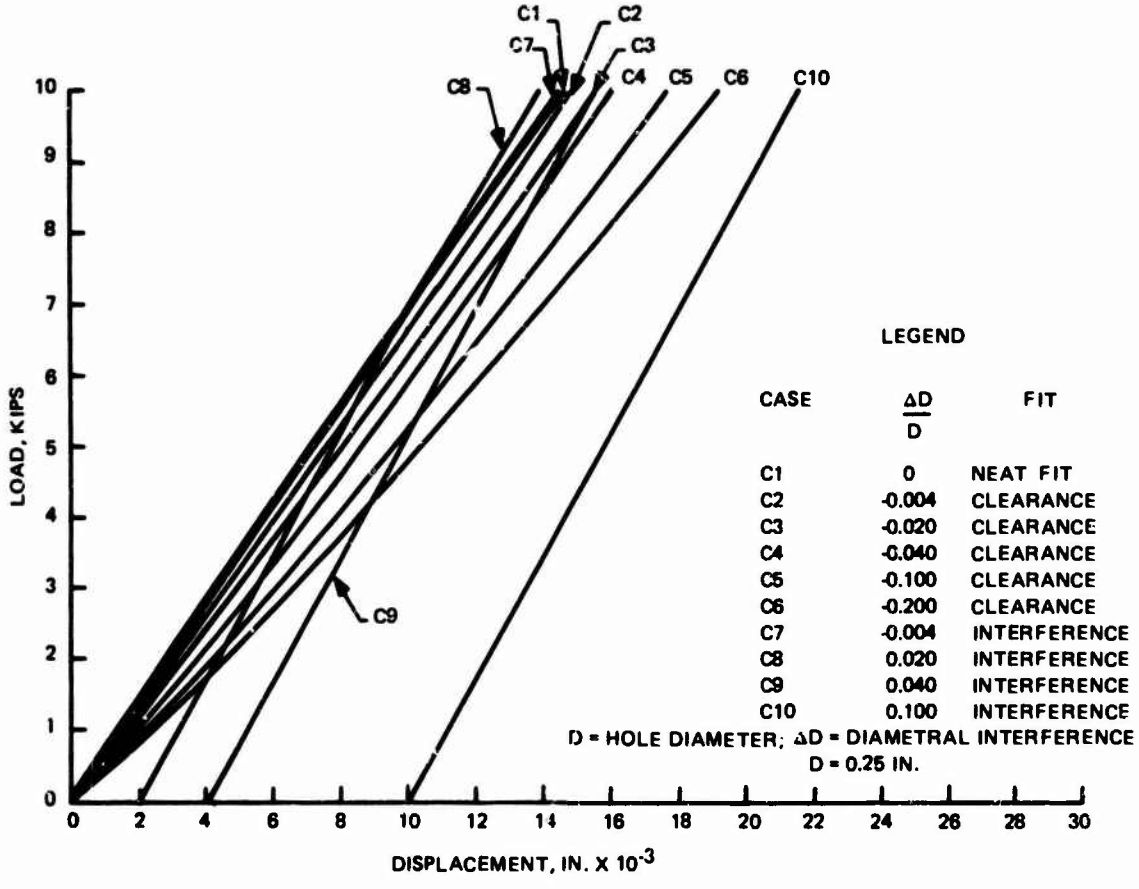

Figure 8 Computed Load-Deflection Curves for Plate of Figure 3 for a Plate Gage Length of 4D.

$$\frac{d^4 y_i}{dx^4_i} - \frac{k_i}{(\lambda GA)_i} \cdot \frac{d^2 y_i}{dx^2_i} + \frac{k_i}{(EI)_i} y_i = 0, \; i = 1, 2, \qquad (6)$$

where the variables x_i, y_i and k_i are defined in Figure 7. Note that the local bearing load, $k_i \cdot y_i$, is analogous to the value of the fastener transfer load, $2Q$, used in the planar analysis.

Two useful simplifications of this equation are possible. The first corresponds to classical beam theory in which beam shear effects are ignored ($k_i/(\lambda GA)_i = 0$), while the other simplification results from neglecting bending effects in the beam ($k_i/(EI)_i = 0$).

Application of these assumptions for a fastener of length $2t$ in anti-symmetrical single shear (with negligible head stiffness) results in

$$-\frac{ky}{2Q/t} = \frac{qt}{2Q}$$

$$= 2\beta t \left\{ \frac{\sinh \beta t \cos \beta x \cosh \beta (t-x) - \sin \beta t \cosh \beta x \cos \beta (t-x)}{\sinh^2 \beta t - \sin^2 \beta t} \right\} \qquad (7)$$

for fastener bending-only theory, and

$$-\frac{ky}{2Q/t} = \frac{qt}{2Q} = -\gamma t \left\{ \frac{\sinh \gamma x + \sinh \gamma (t-x) - \gamma t \cosh \gamma (t-x)}{\gamma t \sinh \gamma t + 2(1-\cosh \gamma t)} \right\} \qquad (8)$$

for fastener shear-only theory, where

$$\beta = \sqrt[4]{\frac{k}{EI}} \text{ and } \gamma = \sqrt{\frac{k}{\lambda GA}}$$

These solutions are compared in Table I with those for a rigid fastener, for a typical realistic set of plate-fastener parameters. As can be seen from the results, the fastener performs in an essentially rigid manner, and both shear and bending effects, acting separately, cause only a slight perturbation upon this behavior. However, of the two fastener flexibility effects considered, shear is seen to be the more important factor for the configuration and parameters treated. Therefore, in subsequent analyses, principal attention is given to solutions for the shear-only beam equations.

Note that the assumed highly-flexible-head performance of the previous configuration permits an overall cocking action of the fastener relative to the plate. However, if the fastener has stiff head attachments which tend to clamp the plate locally, then the fastener is prevented from rotating at the ends relative to the plate. Under these conditions, the resultant bearing load distribution on the plate and fastener, using shear-only theory, is:

$$-\frac{ky}{2Q/t} = \frac{qt}{2Q} = \gamma t \quad \frac{\cosh \gamma(t-x)}{\sinh \gamma t} \qquad (9)$$

and the corresponding rigid fastener solution is $qt/2Q = 1$. Results for this case are presented in Table II for the same typical parameters as were used in Table I.

Similar numerical studies [4] for a fastener in symmetrical double shear (Figure 9) are presented in Table III. Note that although the shear theory produces greater fastener flexibility effects, the difference from the bending theory results are far less pronounced than was the case for the fastener in single shear. This indicates that fastener bending is as important a factor as shear in such configurations.

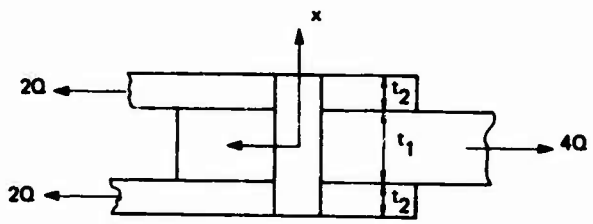

Figure 9 Fastener in Symmetrical Double Shear

Table I Load Interaction Parameter $\frac{qt}{2Q}$ For A Fastener With Negligible Head Stiffness in Single Shear

- Ref Figure 7
- $E = 30 \times 10^6$ psi, $\upsilon = 0.3$, $k = 7.68 \times 10^6$ psi, $t = 0.125$ in., $D = 0.25$ in.

x/t	Flex. Beam (Rigid in Shear) EQ 7	Shear Beam (Rigid in Bending) EQ 8	Completely Rigid Beam
0	4.003	4.032	4.000
0.1	3.401	3.410	3.400
0.2	2.800	1.796	2.800
0.3	2.199	2.190	2.200
0.4	1.599	1.588	1.600
0.5	0.998	0.990	1.000
0.6	0.399	0.395	0.400
0.7	-0.201	-0.200	-0.200
0.8	-0.800	-0.795	-0.800
0.9	-1.392	-1.392	-1.400
1.0	-1.998	-1.992	-2.000

Table II Load Interaction Parameter $\frac{qt}{2Q}$ For A Rigid-Head Fastener In Single Shear

- Ref Figure 7
- $E = 30 \times 10^6$ psi, $\upsilon = 0.3$, $k = 7.68 \times 10^6$ psi, $t = 0.125$ in. $D = 0.25$ in.

x/t	Shear Beam (Rigid in Bending)	Completely Rigid Beam
0	1.078	1.000
0.1	1.056	
0.2	1.036	
0.3	1.018	
0.4	1.029	
0.5	0.990	
0.6	0.980	
0.7	0.972	
0.8	0.966	
0.9	0.962	
1.0	0.961	1.000

PARAMETRIC STUDY

The ratio of peak bearing stress for a flexible fastener versus peak bearing stress for a rigid fastener may be employed as a stress concentration factor to account for variations in bearing load through the plate thickness. A series of bearing stress ratio curves as functions of fastener diameter to plate thickness ratio are presented in Figures 10 and 11. Results for two

Table III Load Interaction Parameter, $\frac{qt_1}{2Q}$ or $\frac{qt_2}{Q}$, for a Fastener in Double Shear

- Ref Figure 9
- $E = 30 \times 10^6$ psi, $\nu = 0.3$, $k_1 = 7.68 \times 10^6$ psi, $k_2 = 7.68 \times 10^6$ psi, $t_1 = 0.125$ in., $t_2 = 0.0625$ in., $D = 0.25$ in.

	x/t_1	Completely Rigid Beam	Free & Clamped Heads Shear Beam (Rigid in Bending)	Clamped Head Bent Beam (Rigid in Shear)	Free Head Bent Beam (Rigid in Shear)
inner plate	0	1.000	0.990	0.995	0.995
	0.1		0.991	0.996	0.996
	0.2		0.995	0.997	0.997
	0.3		1.001	1.000	1.000
	0.4		1.009	1.005	1.005
	0.5	1.000	1.020	1.010	1.010
outer plates	0.5	1.000	1.020	1.009	1.015
	0.6		1.009	1.004	1.009
	0.7		1.001	1.000	1.003
	0.8		0.995	0.997	0.997
	0.9		0.991	0.995	0.991
	1.0	1.000	0.990	0.995	0.985

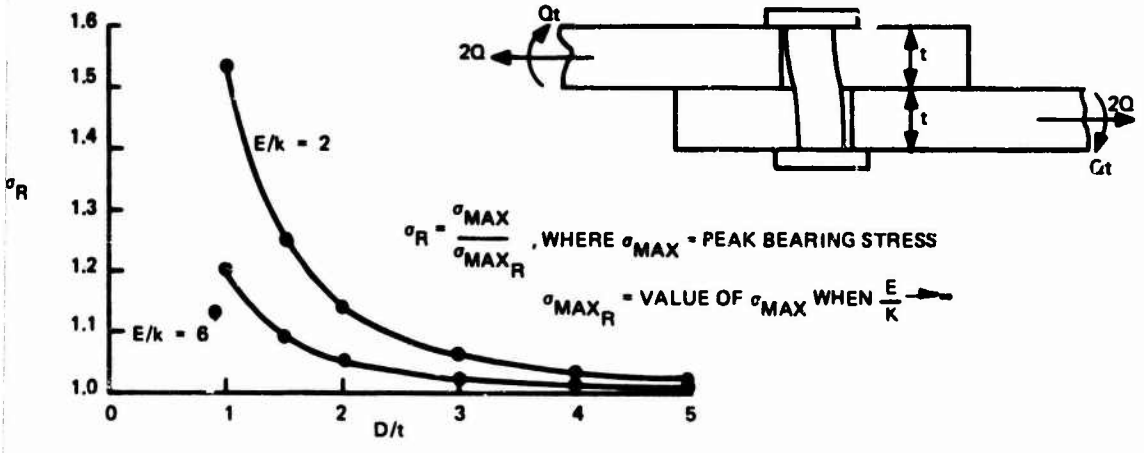

(a) SINGLE SHEAR, CLAMPED FASTENER HEAD

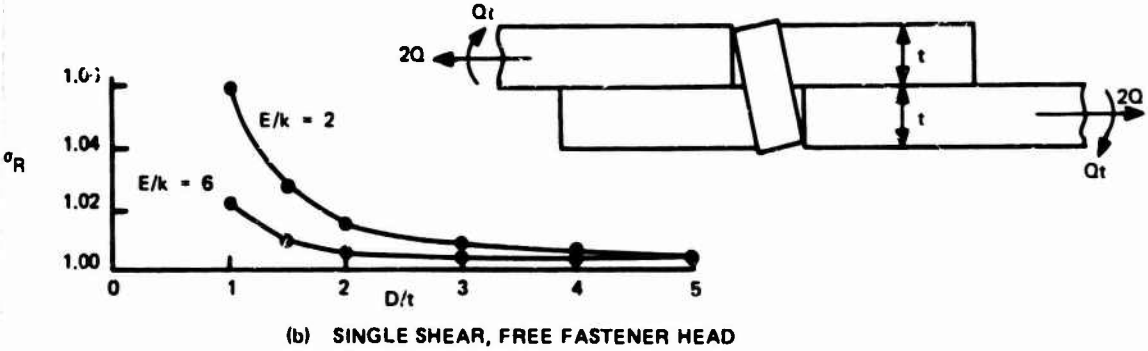

(b) SINGLE SHEAR, FREE FASTENER HEAD

Figure 10. Effect of Fastener Stiffness on Peak Bearing Stress

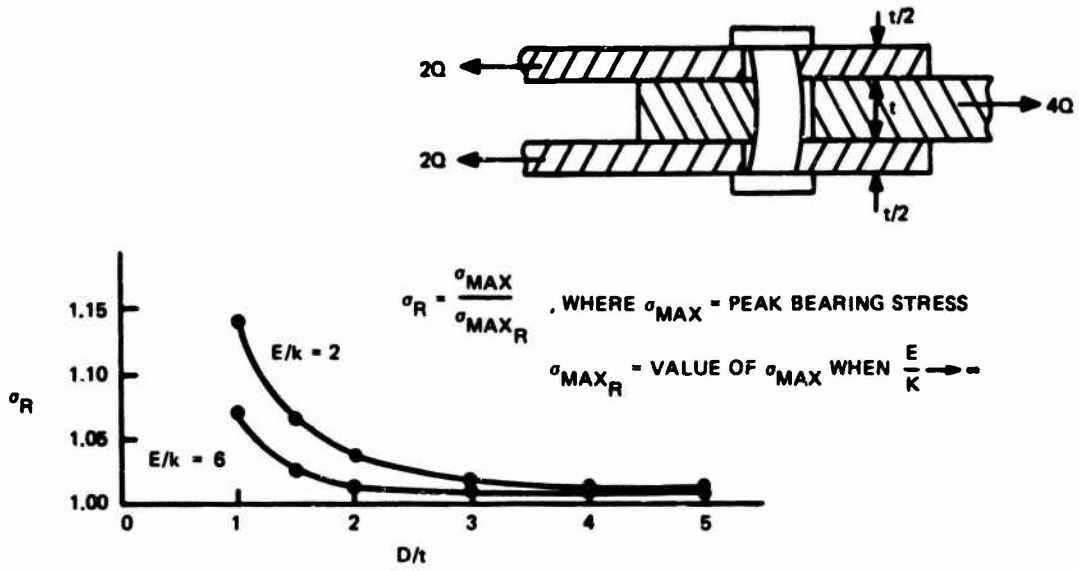

Figure 11 Effect of Fastener Stiffness on Peak Bearing Stress (Double Shear Case With Arbitrary Fastener Head End Conditions)

values of E/k, which represent approximate practical limits for this parameter, are presented. As might be expected, the stiffer fastener to plate ratios (i.e., higher E/k) and larger D/t ratios yield results which approach those for a rigid fastener.

Note that the bearing stress in each plate laminate is a measure of the two dimensional stress state level. Thus, the bearing stress ratios presented in Figures 10 and 11 may be viewed as stress concentration factors, caused by fastener flexibility, over and above the plate stress concentrations resulting from purely two-dimensional plate-fastener considerations.

COMPARISON OF TESTS WITH THEORY

Overall joint flexibilities for single fasteners in double shear, for a given gage length, were determined both experimentally and by the present methods. A series of 15 tests were performed on aluminum-plate, symmetrical, double-shear lap joints using titanium fasteners (Figure 4). Twelve of these specimens were joined by loose fitting fasteners and the remaining three by interference-fit fasteners.

A comparison of analysis and test results (Table IV) reveals the importance of fastener flexibility upon joint compliance. Excellent agreement for the loose-fitting titanium fasteners and good agreement for the interference-fit titanium fasteners was obtained. However, note that the variation of measured results test-to-test for similar conditions of fit were significant, and that Table IV gives only average values. Note also that the effects of fastener-to-hole fit, which can be observed by comparing the loose, neat, and interference fit results in Table IV, are highly important in establishing the joint's net compliance.

Table IV Analytical and Experimental Results for the Double Lap Joints Tested

Type Fit	k Plate Stiffness x 10^{-6} psi	Overall Joint Stiffness x 10^{-6} $\frac{lb}{in.}$		
		Analysis	Test	Analysis for a Rigid Fastener
Loose	4.255	0.416	0.420 (avg. of 12 tests)	0.535
Perfect (Neat)	5.330	0.610	----	0.670
Interference	6.966	0.778	0.803 (avg. of 3 tests)	0.876

CONCLUSIONS AND RECOMMENDATIONS

The proposed approach demonstrates a simple means by which two-dimensional finite element analyses may be extended to obtain first-order three-dimensional effects associated with fastener flexibility. Logical extensions to the present work include: the use of Timoshenko beam theory when both fastener shear and bending effects are important, the inclusion of friction at the fastener/hole interface, a variable foundation modulus (as would be present in a plate made of composite materials), and the presence of plate plasticity in the vicinity of the fastener. Possibly important extensions to this approach which are more difficult to accommodate are the effects of closely spaced fasteners and friction on the plate faying surfaces.

Additional experimental work to establish the level of accuracy of the proposed approach is recommended.

ACKNOWLEDGEMENT

This work was performed in the Structural Mechanics Section of the Grumman Aerospace Corporation with the support of the Air Force Flight Dynamics Laboratory of the Research and Technology Division, Air Force Systems Command, Wright-Patterson Air Force Base, Ohio, under Contract No. F33615-69-C-1263.

REFERENCES

1. McCombs, W.F., McQueen, J.C. and Perry, J.L., "Analytical Design Methods for Aircraft Structural Joints," Air Force Flight Dynamics Laboratory Technical Report AFFDL-TR-67-184, Wright-Patterson Air Force Base, Ohio, January 1968.

2. Gehring, R.W. and Maines, C.H., "A Redundant-Force Method for the Ineleastic-Analysis of Mechanically Fastened Joints," U.S. Naval Air Engineering Center Report, NAEC-ASL-1103, January 1967.

3. Mason, P. and Balderes, T., "Applications of the Finite Element Technique in Structural Aanlysis," Grumman Advanced Development Report ADR 02-11-67.5, Grumman Aerospace Corporation, Bethpage, New York, December 1967.

4. Harris, H.G., Ojalvo I.U., and Hooson, R.E., "Stress and Deflection Analysis of Mechanically Fastened Joints", Air Force Flight Dynamics Laboratory Technical Report, AFFDL-TR-70-49, Wright-Patterson Air Force Base, Ohio, May 1970.

5. White, D.J. and Enderby, L.R., "Finite Element Analysis on a Non-linear Problem - a Connecting Rod Eye Loaded by Means of a Pin," Journal of Strain Analysis, v. 5, No. 1, 1970, 41.

6. Scholes, A. and Strover, E.M., "The Piecewise-Linear Analysis of Two Connecting Structures Including the Effect of Clearance at the Connections," International Journal for Numerical Methods in Engineering, v. 3, 1971, 45-51.

7. Chan, S.K., and Tuba, I.S., "A Finite Element Method for Contact Problems of Solid Bodies - Part I. "Theory and Validation," International Journal of Mechanical Science, v. 13, 1971, 615-625.

8. Chan, S.K. and Tuba, I.S., "A Finite Element Method for Contact Problems of Solid Bodies - Part II. Application to Turbine Blade Fastenings," International Journal of Mechanical Sciences, v. 13, 1971, 627-639.

9. Newman, J.B., "Analysis of Problems Involving Non-Linear Boundary Conditions and Non-Linear Material Properties," presented at the 1973 ASME Winter Meeting - Symposium on Numerical Solution of Non-Linear Structural Problems; in Numerical Solution of Non-Linear Structural Problems, R.F. Hartung, Ed., American Society of Mechanical Engineers, AMD v. 6, New York, New York 1973.

10. Padlog, J., Huff, R.D. and Holloway, F.G., "Unelastic Behavior of Structures Subjected to Cyclic, Thermal and Mechanical Stressing Conditions," Wright Air Development Division Technical Report 60-271, December 1960.

11. Lansing, W., Jensen, W., and Falby, W., "Matrix Analysis Methods for Inelastic Structures," Proceedings of First Air Force Conference on Matrix Methods in Structural Mechanics, Air Force Flight Dynamics Laboratory Technical Report, AFFDL-TR-66-80, Wright-Patterson Air Force Base, Ohio, November 1965.

12. Armen, H., Jr., Isakson, G., and Pifko, A., "Discrete-Element Methods for the Plastic Analysis of Structures Subjected to Cyclic Loading," presented at the joint American Institute of Aeronautics and Astronautics/ American Society of Mechanical Engineers Eighth Materials, Structures, Structural Dynamics Conference, Palm Springs, California, March 1967; also a Grumman Research Department Report, RE 28LJ, February 1967.

13. Hetenyi, M., Beams on Elastic Foundation, University of Michigan Press, Ann Arbor, Michigan, 1946.

INELASTIC MECHANICAL JOINT ANALYSIS METHOD WITH TEMPERATURE AND MIXED MATERIALS

B.E. Gatewood

Professor of Aeronautical and Astronautical Engineering
The Ohio State University
Columbus, Ohio
Consultant
Rockwell International Corporation–Columbus Aircraft Division

R.W. Gehring

Member of Technical Staff
Rockwell International Corporation–Columbus Aircraft Division
Columbus, Ohio

ABSTRACT

An inelastic redundant-force method of analysis is used to determine the mode of failure and the failing load for axially loaded, multi-fastener, multi-plate splice joints under nonuniform temperature distributions. Both the plate element stress-strain relationships and the local fastener-plate load-deformation characteristics, as determined from simple two-fastener single lap test specimens, are represented by the nondimensional Ramberg-Osgood equation. The method is applied to a six-fastener, three-plate joint and to a full-scale horizontal stabilizer root end splice joint. Calculated failing loads and modes of failure agree with test results satisfactorily.

INTRODUCTION

Although a considerable amount of work has been done to obtain analysis techniques for mechanical joints with temperature present, there appears to be no practical analytical method for joints which allows for inelastic deformations, nonlinear deformations, mixed materials, mixed fastener sizes, more than two plates in the joints, and the temperature deformations and thermal load distributions. References [1], [2], and [3] discuss elastic methods with temperature present to analyze the joint. In Reference [2], some discussion of a joint flexibility factor, which must be determined experimentally, is given for inelastic and nonlinear effects.

This paper presents a method of mechanical joint analysis that considers the factors listed above by including the plate element deformation characteristics between fasteners whether elastic or inelastic, the local deformation of the fastener-plate intersection whether elastic, nonlinear, or inelastic, and strain failure criteria in the inelastic region.

METHOD OF ANALYSIS

Consider a multiple plate, multiple fastener joint with I plates and J rows of fasteners perpendicular to primary applied load direction (Figure 1). Let (i, j) be the typical plate-fastener intersection for plate i and fastener row j, and plate element (i, j) be the element of plate i between rows j and j + 1. The shear force on the fastener row j between plates i and i + 1 is S (i, j). The length of the plate elements between row j and row j + 1 is L (j, j + 1) and the axial load in plate element (i, j) is U (i, j). To calculate the loads S (i, j) and U (i, j) in the highly redundant joint, cut the fasteners between the plates for all rows except the last row j. Let X (m) be the redundant loads in the cut fasteners, where m counts over i and j up to M = (I-1) (J-1) in the order on i, j, of (1, 1), (1, 2), . . . (1, J-1), (2-1), . . . (2, J-1), . . . (I-1, J-1). Let u (m, i, j) be the axial load in plate element (i, j) in the determinate structure due to a 1-pound load at the cut fastener location m and let s (m, i, j) be the fastener shear load in the determinate structure due to the 1-pound load at location m. The elastic flexibility influence coefficients C (n, m) for the structure can be written in terms of the loads u (m, i, j) and s (m, i, j) as

$$C(n,m) = \sum_{i=1}^{I} \sum_{j=1}^{J-1} \frac{u(m,i,j)\, u(n,i,j)\, L(j,j+1)}{E(i,j)\, A(i,j)} + \sum_{i=1}^{I-1} \sum_{j=1}^{J} s(m,i,j)\, s(n,i,j) \left[\frac{1}{K(i,j)} + \frac{1}{K(i+1,j)} \right] \quad (1)$$

where A (i, j) is area, E (i, j) is modulus of elasticity at temperature, and K (i, j) is shear stiffness of fastener-plate intersection at the given temperature.

The deflections of the determinate structure due to the applied loads, $d_o(n)$, due to the temperature, $d_T(n)$, and due to inelastic effects, $d_{pr}(n)$, on the iteration r, can be expressed as

$$d_o(n) = \sum_{i=1}^{I} \sum_{j=1}^{J-1} \frac{U_o(i,j)\, u(n,i,j)\, L(j,j+1)}{E(i,j)\, A(i,j)} + \sum_{i=1}^{I-1} \sum_{j=1}^{J} S_o(i,j)\, s(n,i,j) \left[\frac{1}{K(i,j)} + \frac{1}{K(i+1,j)} \right] \quad (2)$$

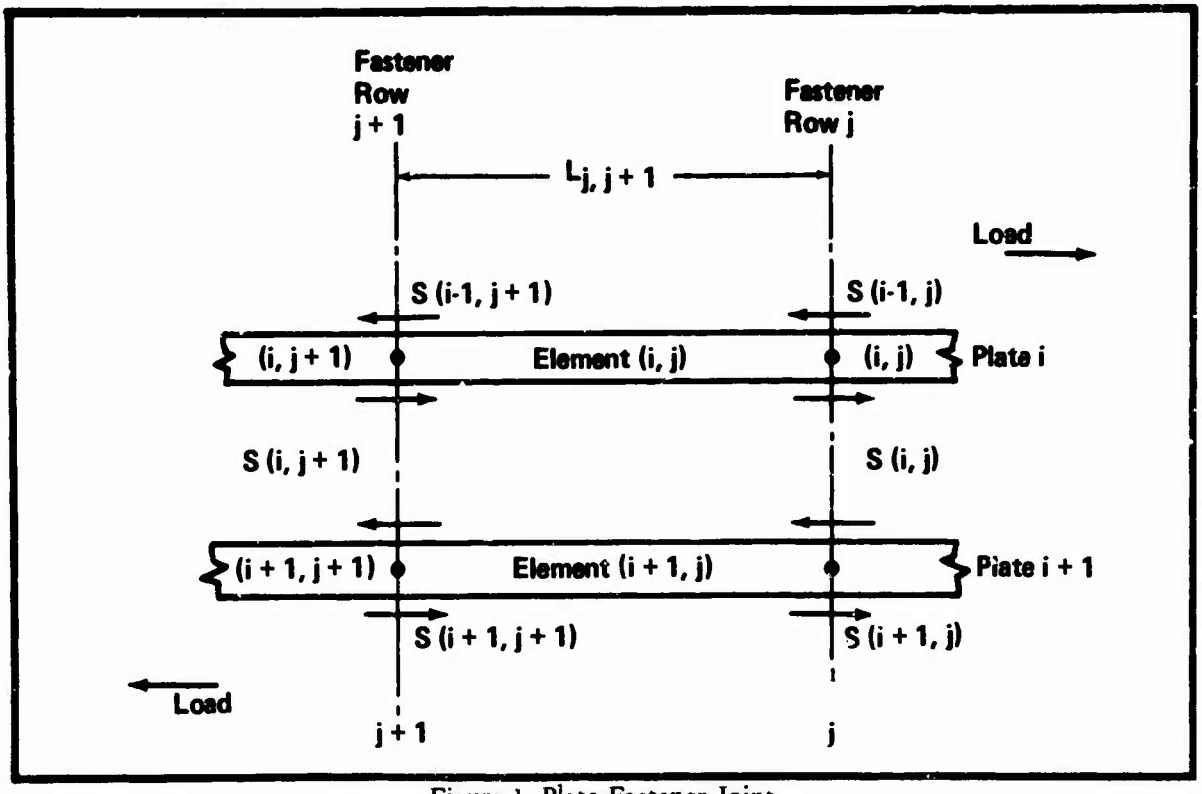

Figure 1. Plate-Fastener Joint

$$d_T(n) = \sum_{i=1}^{I} \sum_{j=1}^{J-1} \alpha(i,j)\, T(i,j)\, u(n,i,j)\, L(i,j+1) \quad , \tag{3}$$

$$\begin{aligned} d_{pr}(n) = & \sum_{i=1}^{I} \sum_{j=1}^{J-1} \left[u(n,i,j)\ L(j,j+1) \left\{ e_p(i,j) \right\}_r \right] \\ & + \sum_{i=1}^{I-1} \sum_{j=1}^{J} \left[s(n,i,j) \left\{ f_p(i,j) + f_p(i+1,j) \right\}_r \right] , \end{aligned} \tag{4}$$

where $\alpha(i, j)$ is coefficient of thermal expansion, $T(i, j)$ is temperature change from room temperature, $e_p(i, j)$ is inelastic strain, and $f_p(i, j)$ is fastener-plate nonlinear and inelastic deformation. The virtual displacement equations to determine the unknown redundant forces $X(m)$ can now be written in the form

$$\sum_{m=1}^{M} C(n, m)\, X(m) = -\, d_o(n) - d_T(n) - d_{pr}(n),\ n = 1, 2, \ldots, M \quad , \qquad (5)$$

whence the loads U (i, j) and S (i, j) are

$$U(i, j) = U_o(i, j) + \sum_{m=1}^{M} u(m, i, j)\, X(m) \quad , \qquad (6)$$

$$S(i, j) = S_o(i, j) + \sum_{m=1}^{M} s(m, i, j)\, X(m) \quad . \qquad (7)$$

The inelastic strain e_p (i, j) for plate element (i, j) at iteration r is

$$e_{pr}(i, j) = e_{p, r-1}(i, j) + \frac{U_{r-1}(i, j) - A(i, j)\, C_{r-1}(i, j)\, F_{r-1}(i, j)}{A(i, j)\, E(i, j)} \quad , \qquad (8)$$

where U_{r-1} (i, j) is the load in plate element (i, j) at iteration r-1, C_{r-1} (i, j) is the effective area factor, and F_{r-1} (i, j) is the stress in element (i, j) at iteration r-1. This stress can be obtained from a Ramberg-Osgood stress-strain curve for the plate element material at the proper temperature. Note that e_p (i, j) = 0 for the first elastic calculation and for all elements that remain elastic. The effective area factor C_r (i, j) allows for plate buckling when the plate load is compression, and can be taken as

$$C_r(i, j) = \left[\frac{e_{cr}(i, j)}{\left\{ e(i, j) \right\}_r} \right]^{1/2} \equiv H^{1/2}, H < 1, \qquad (9)$$

$$= 1, H \geq 1 \quad ,$$

where e_{cr} (i, j) is the buckling strain of plate element (i, j).

The inelastic and nonlinear fastener segment load-deformation f_p (i, j) can be obtained from experimental load-deformation data for simple lap joints representing the structural joints as to bolt size and material, and plate material. Test data indicates that the load-deformation curve with elastic slope K can be represented as a Ramberg-Osgood curve with the proper shape constants. Thus

$$f_{pr}(i,j) = f_{p,r-1}(i,j) + \frac{[S(i,j) - S(i-1,j)]_{r-1} - P_{r-1}(i,j)}{K(i,j)}, \qquad (10)$$

where P_{r-1} (i, j) is the load obtained from the curve for the total deformation f_{r-1} (i, j).

Failure criteria for the joint can be based on (a) plate strain cutoff in tension on all plate elements, (b) ultimate fastener shear allowable load at temperature for all fasteners, and (c) joint deformation cutoff based on allowable bearing deformation at temperature (some percent of fastener diameter).

MATERIAL PROPERTIES

For the axially loaded splice joint, uniaxial stress-strain curves for the plate elements and shear load-deformation curves for the fastener-plate intersection are needed to define the material properties needed in the preceding equations. It is possible to represent both curves by a Ramberg-Osgood nondimensional equation with the form

$$\frac{eE}{F_y} = \frac{F}{F_y}\left[1 + \frac{3}{7}\left(\frac{F}{F_y}\right)^{m-1}\right] \qquad (11)$$

where e is strain or deformation f, E is modulus of elasticity or shear stiffness K, F is stress or load P, F_y is yield stress or yield load P_y, and m is a shape factor for the curve. The factor m depends upon the material, temperature, and the knee of the stress-strain curve. It is about m = 10 for 2024-T3 aluminum alloy at room temperature.

Some typical load-deformation curves for simple joints are shown in Figures 2 and 3. The m factor for such joints is m = 3 to 6 and the elastic slope K is $3(10)^5$ to $6(10)^5$ for the joint stiffness. The yield load P_y is taken as the intersection of the line of slope 0.7 K with the curve. (See Figure 3.) Since it may be difficult to determine the slope K from the experimental curve for the joint, it is recommended that K, P_y, and m be calculated from Equation (11) by using three points from the experimental curve.

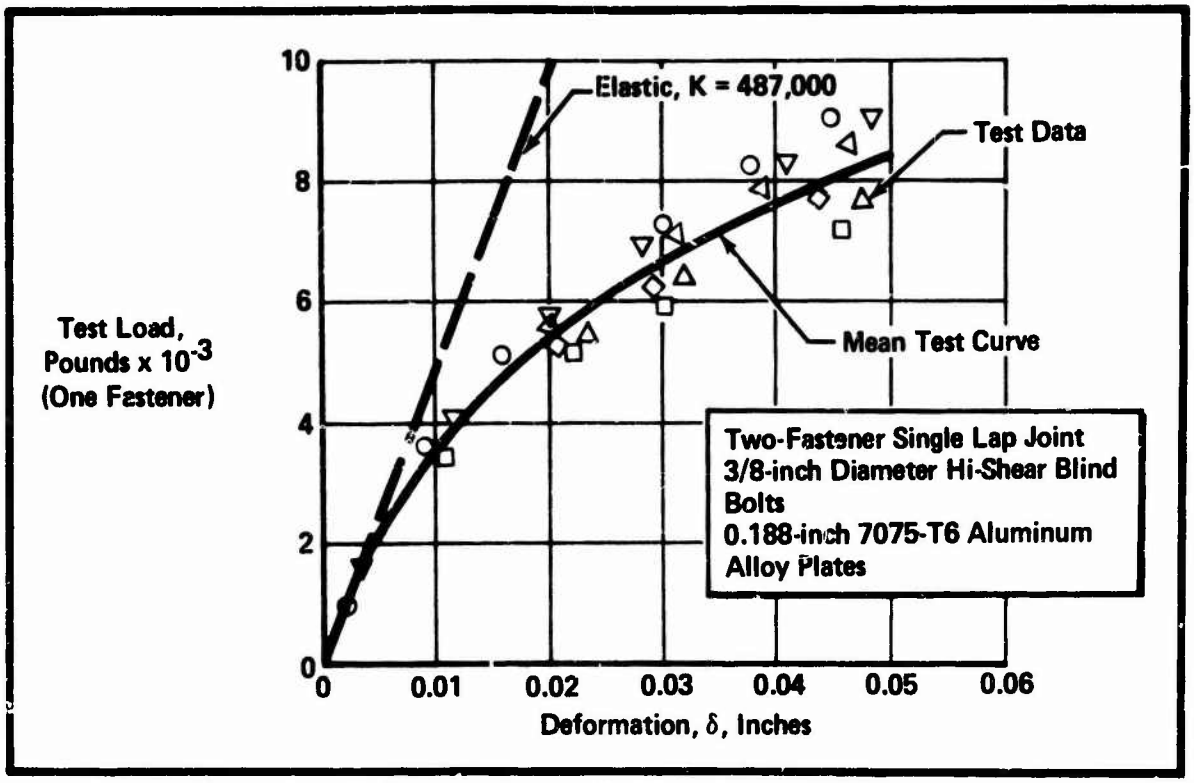

Figure 2. Typical Test Load Deformation Curves for Single Lap Joint Specimen

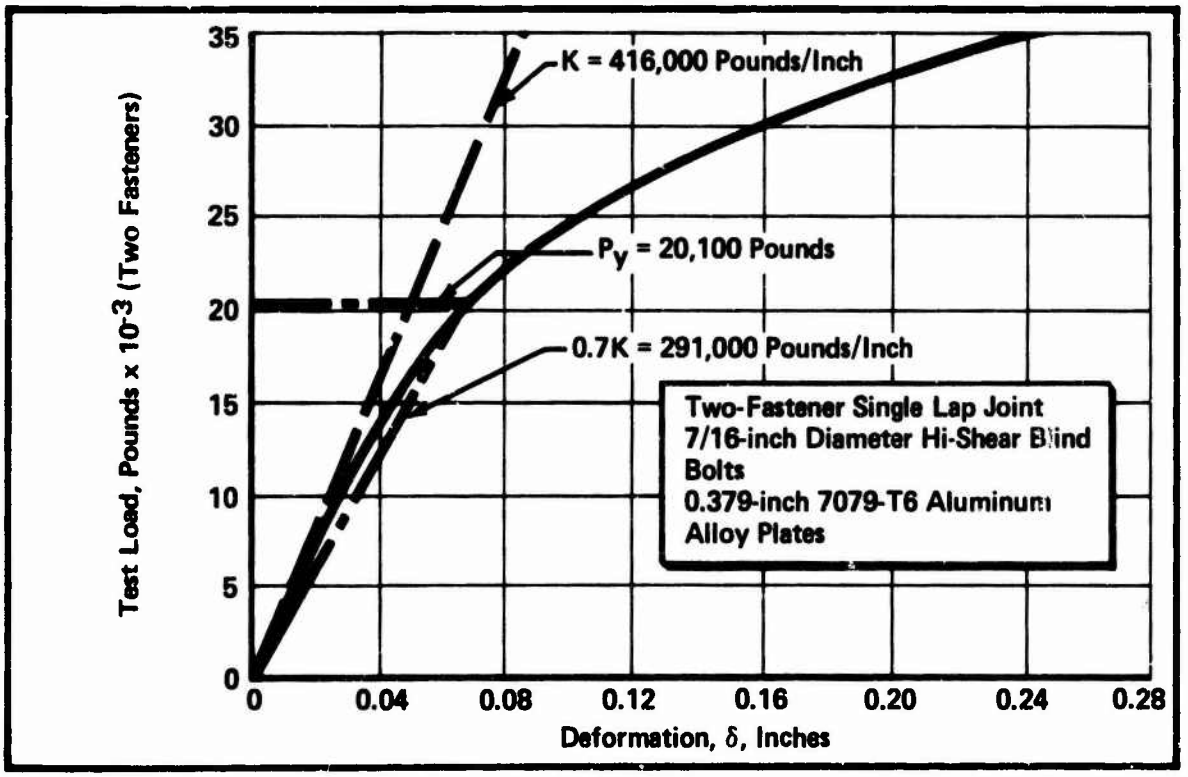

Figure 3. Typical Test Load-Deformation Curves for Single Lap Joint Specimens

EFFECT OF JOINT STIFFNESS UPON A THREE-FASTENER JOINT

The effect of the elastic stiffness factor K upon a simple joint can be evaluated in terms of one simple parameter, EA/Ks, for a three-fastener lap joint, where s is fastener spacing and A is plate area. Figure 4 shows the results, where it is evident that for $E = 10^7$ psi for aluminum alloy and $K = 4\ (10^5)$ pounds/inch (Figure 2) the value of EA/Ks will be of the order of 5 so that the load will divide nearly equally to the fasteners.

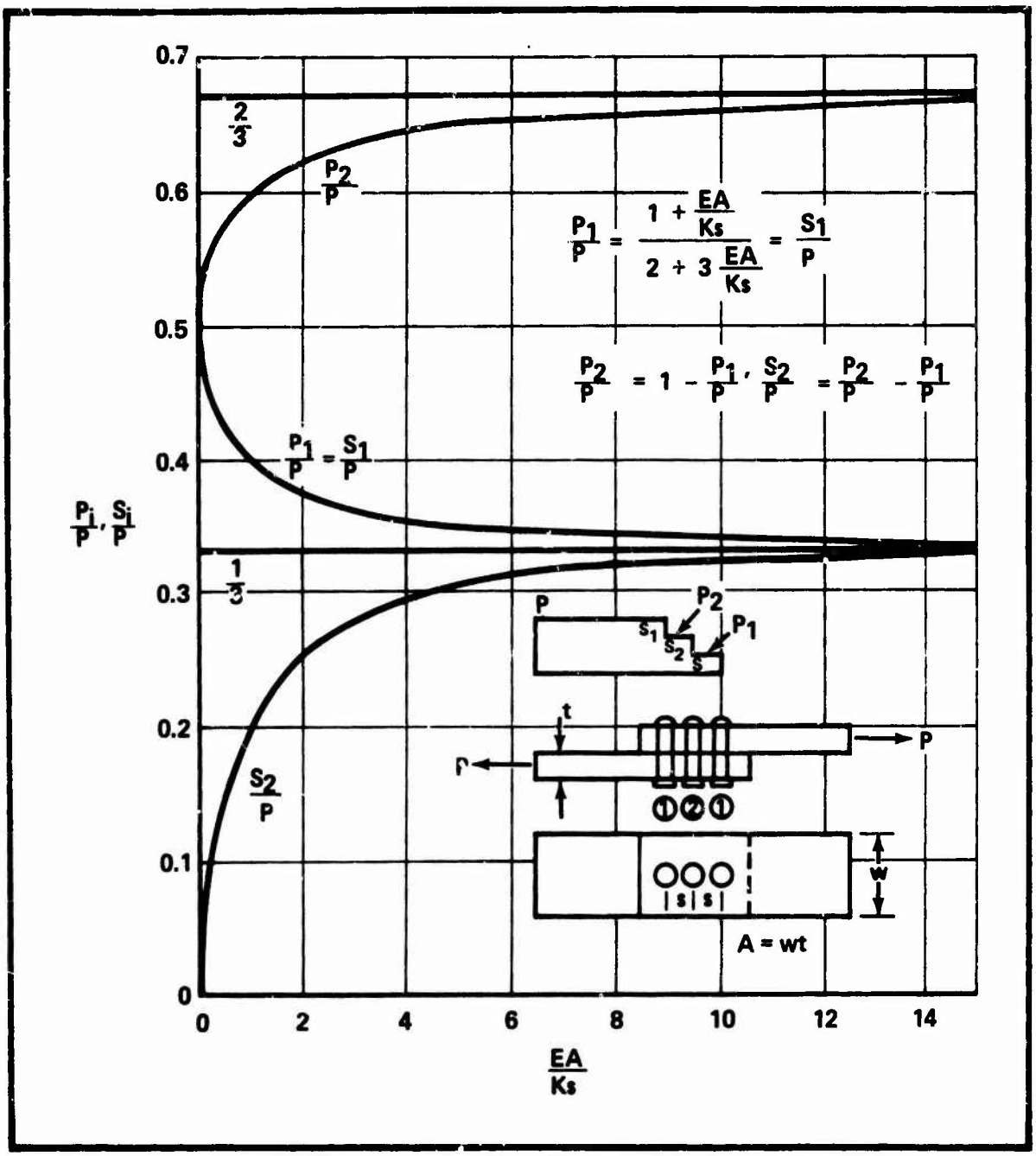

Figure 4. Elastic Three-Fastener Lap Joint

INELASTIC THREE-PLATE, SIX-FASTENER JOINT

Consider the joint in Figure 5 with two aluminum plates and a middle steel plate. The plates are separated in the figure to show the X (m) loads for the redundant solution. With the first five fasteners cut between plates one and two and between plates two and three, the unit loads u (m, i, j) and s (m, i, j) become

$$
\left.\begin{array}{l}
u(m,1,j) = 1, \quad m = 1,2,\text{----},5, \quad j = m, m+1, \text{----}, 5, \\
u(m,2,j) = -1, \quad m = 1,2,\text{----},5, \quad j = m, m+1, \text{----}, 5, \\
u(m,2,j) = 1, \quad m = 6,7,\text{----},10, \quad j = m-5, m-4, \text{----}, 5, \\
u(m,3,j) = -1, \quad m = 6,7,\text{----},10, \quad j = m-5, m-4, \text{----}, 5, \\
\text{all other } u(m,i,j) = 0 ;
\end{array}\right\} \quad (12)
$$

$$
\left.\begin{array}{l}
s(m,1,j) = 1, \quad m = j = 1,2,\text{----},5 \\
s(m,2,j) = 1, \quad m = 6,7,\text{----},10, \quad j = m-5 \\
s(m,1,6) = -1, \quad m = 1,2,\text{----},5 \\
s(m,2,6) = -1, \quad m = 6,7,\text{----},10 \\
\text{all other } s(m,i,j) = 0 .
\end{array}\right\} \quad (13)
$$

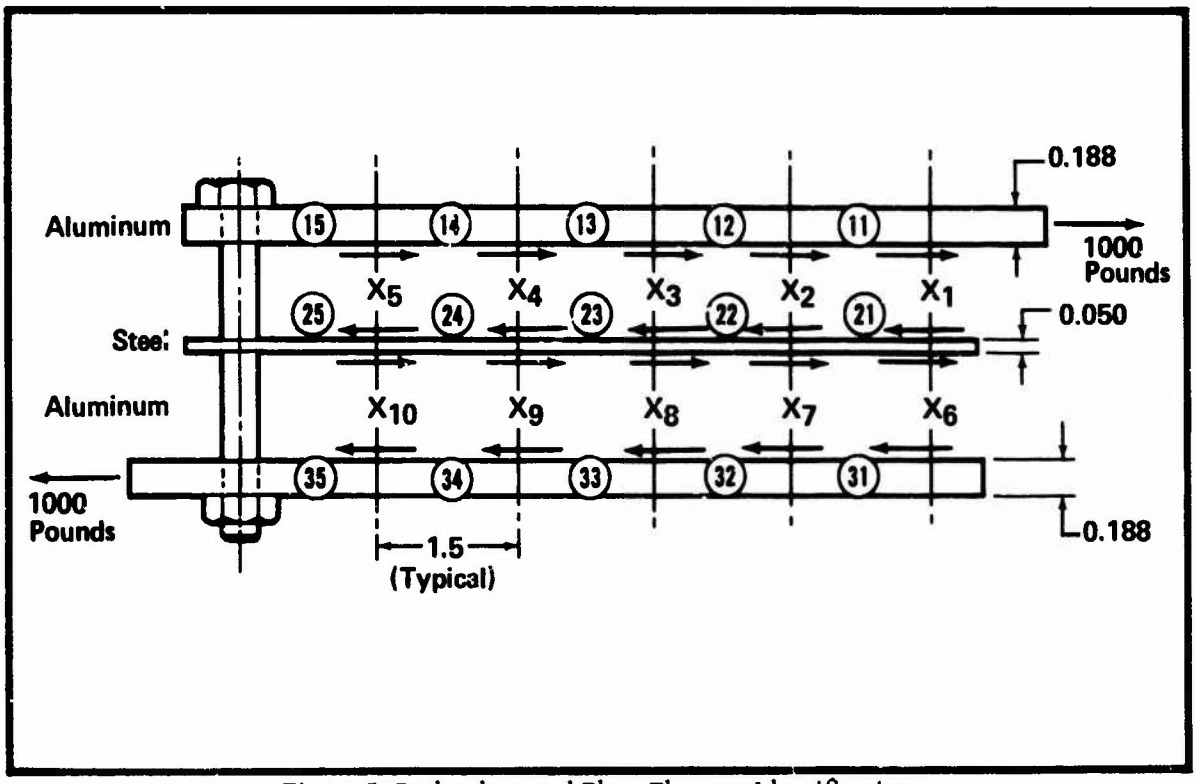

Figure 5. Redundant and Plate Element Identification

For an applied reference load of 1000 pounds in Figure 5, the U_o (i, j) and S_o (i, j) loads in Equation (2) are

$$\left.\begin{aligned} &U_o\,(1,j) = 1000 \text{ lbs}, j = 1, 2, 3, 4, 5\ , \\ &\text{all other } U_o\,(i,j) = 0 \\ &S_o\,(1,6) = S_o\,(2,6) = -1000 \text{ lbs} \\ &\text{all other } S_o\,(i,j) = 0\ . \end{aligned}\right\} \quad (14)$$

No temperature effects are considered in this example. The material properties are as follows (net areas are used):

$$\left.\begin{aligned} &\text{Aluminum plate: } A = 0.500 \text{ in.}^2,\ F_y = 71.5 \text{ ksi},\ F_{tu} = 80.3 \text{ ksi}, \\ &\qquad E = 9.92\,(10^6) \text{ psi},\ m = 10; \\ &\text{Steel plate: } A = 0.100 \text{ in.}^2,\ F_y = 110.0 \text{ ksi},\ F_{tu} = 150.0 \text{ ksi}, \\ &\qquad E = 29\,(10^6) \text{ psi},\ m = 10; \\ &\text{3/8-inch fastener-aluminum plate: } P_y = 3950 \text{ lbs},\ n = 2.75, \\ &\qquad K = 487{,}000 \text{ lbs/in.},\ P_{su} = 8300 \text{ lbs}\ ; \\ &\text{3/8-inch fastener-steel plate: } P_y = 3950 \text{ lbs},\ m = 2.75, \\ &\qquad K = 487{,}000 \text{ lbs/in.},\ P_{su} = 8300 \text{ lbs}\ . \end{aligned}\right\} \quad (15)$$

The fasteners are 3/8-inch blind bolts with fastener-aluminum plate properties shown in Figure 2. The fastener-steel plate properties are the same as for the fastener-aluminum plate.

From Equations (12) through (15), the d_o (n) values in Equation (2) can be calculated as

$$\left.\begin{aligned} d_o(n) &= (6\text{-}n)\,(303) + 4100,\ n = 1, 2, 3, 4, 5 \\ d_o(n) &= 0 + 4100,\ n = 6, 7, 8, 9, 10 \end{aligned}\right\} \quad (16)$$

Similarly, the influence coefficients in Equation (1) can be evaluated so that the redundant loads X (m) can be obtained from Equation (5) and the loads from Equations (6) and (7). With these values, e_{pr} and f_{pr} from Equations (8) and (10) can be determined to give d_{pr} (n) in Equation (4), whence the iteration can be started by resolving Equation (5) for the new X (m).

Figures 6 and 7 show results for the elastic and inelastic solutions for the bolt shear loads with a total load of 40,000 pounds. The maximum bolt load of 9204 pounds for the elastic solution decreases to 8132 pounds for the inelastic solution, indicating that an elastic design with bolt shear critical would be very conservative. On the other hand, if equal bolt loads of 6667 pounds are used for design, then the design could be unconservative for bolt shear critical. Also, the maximum tension load in the steel plate decreases from 5816 pounds (elastic) to 3839 pounds (inelastic) so that the steel plate is not very efficient. Such a splice as this with a steel plate is not recommended as a practical design.

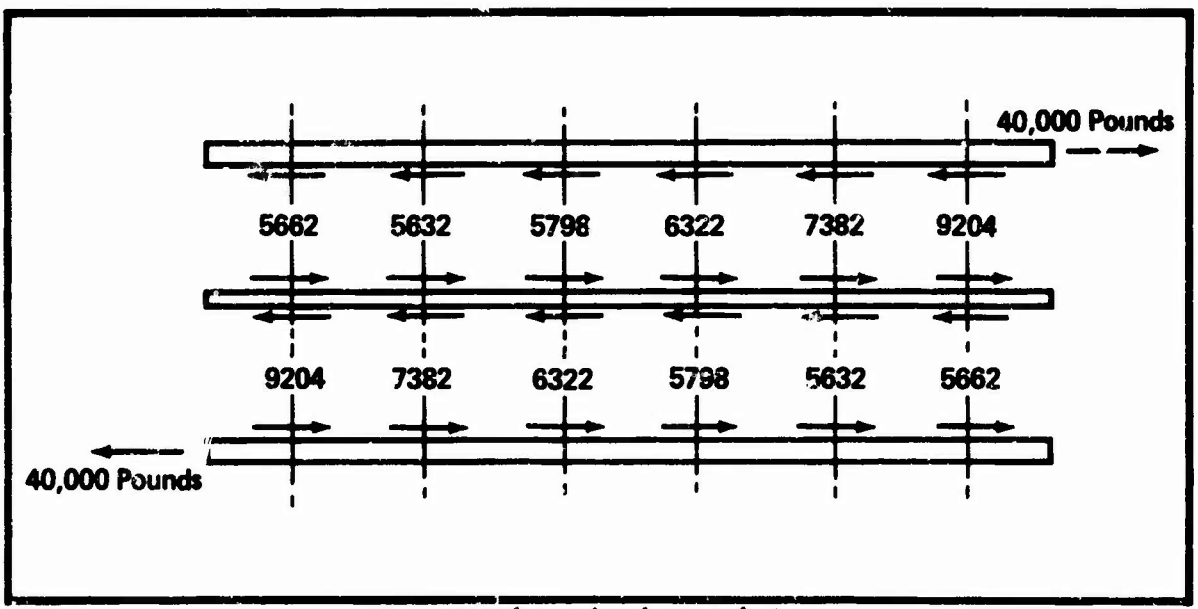

Figure 6. Bolt Loads, Elastic Solution

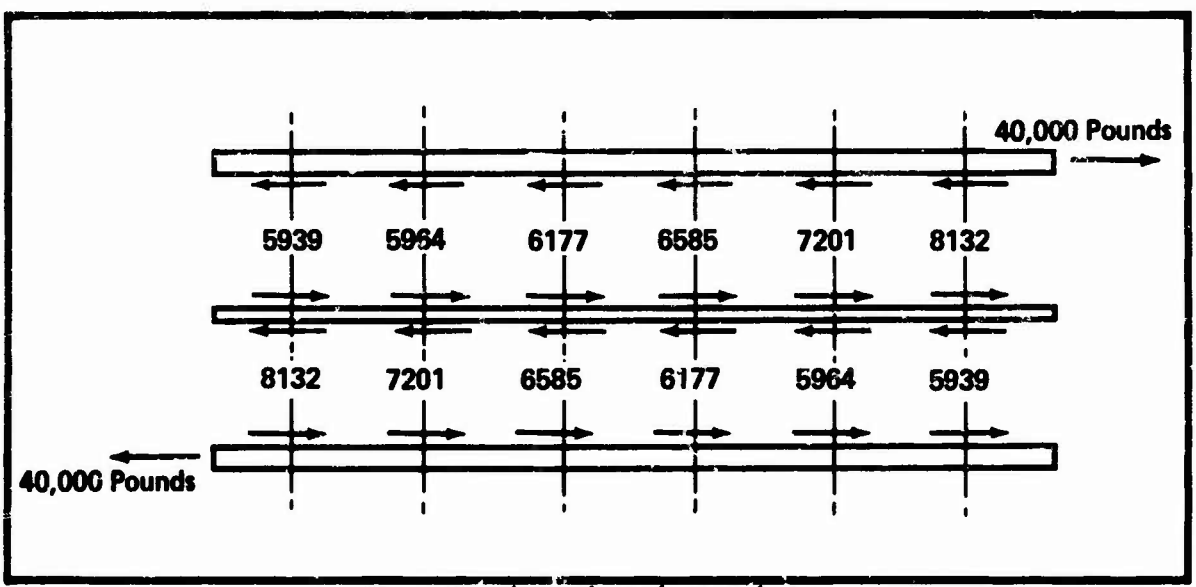

Figure 7. Bolt Loads, Inelastic Solution

TEST AND THEORY FOR FULL-SCALE HORIZONTAL STABILIZER ROOT END SPLICE JOINT

In Reference [4], tests of full-scale stabilizers at room temperature, 250°F, and 425°F are described. For the root end splice joint, equal loads were applied to two formers (Figure 8) to produce the proper moment and shear on the splice. Details of the joint splicing the 7079-T6 aluminum alloy stabilizer skin to the steel main beam fitting are shown in Figures 9 and 10. The room temperature material properties are

$$\left.\begin{array}{l}\text{Aluminum skin: } F_y = 73{,}500 \text{ psi, } F_{tu} = 79{,}600 \text{ psi, } E = 9.25\,(10^6) \text{ psi, } m = 35;\\ \text{Steel splice plate: } F_y = 163{,}000 \text{ psi, } F_{tu} = 180{,}000 \text{ psi, } E = 29\,(10^6) \text{ psi, } m = 10;\\ \text{Steel beam fitting: } F_y = 217{,}000 \text{ psi, } F_{tu} = 260{,}000 \text{ psi, } E=29\,(10^6) \text{ psi, } m = 10;\\ \text{Fasteners in Figures 2 and 3, and Equation (15), 7/16-inch, 3/8-inch, 1/4-inch Hi-Shear blind bolts.}\end{array}\right\} \quad (17)$$

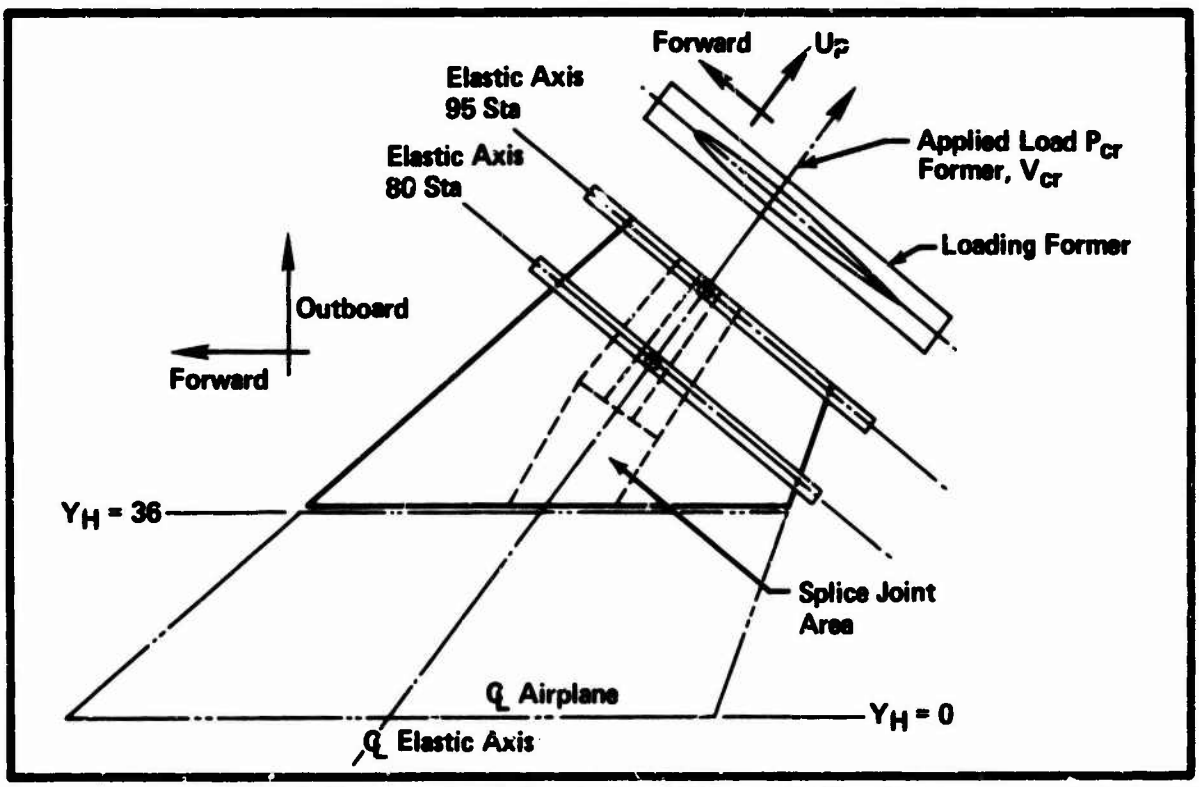

Figure 8. Horizontal Stabilizer Inboard Splice Joint Test Loading

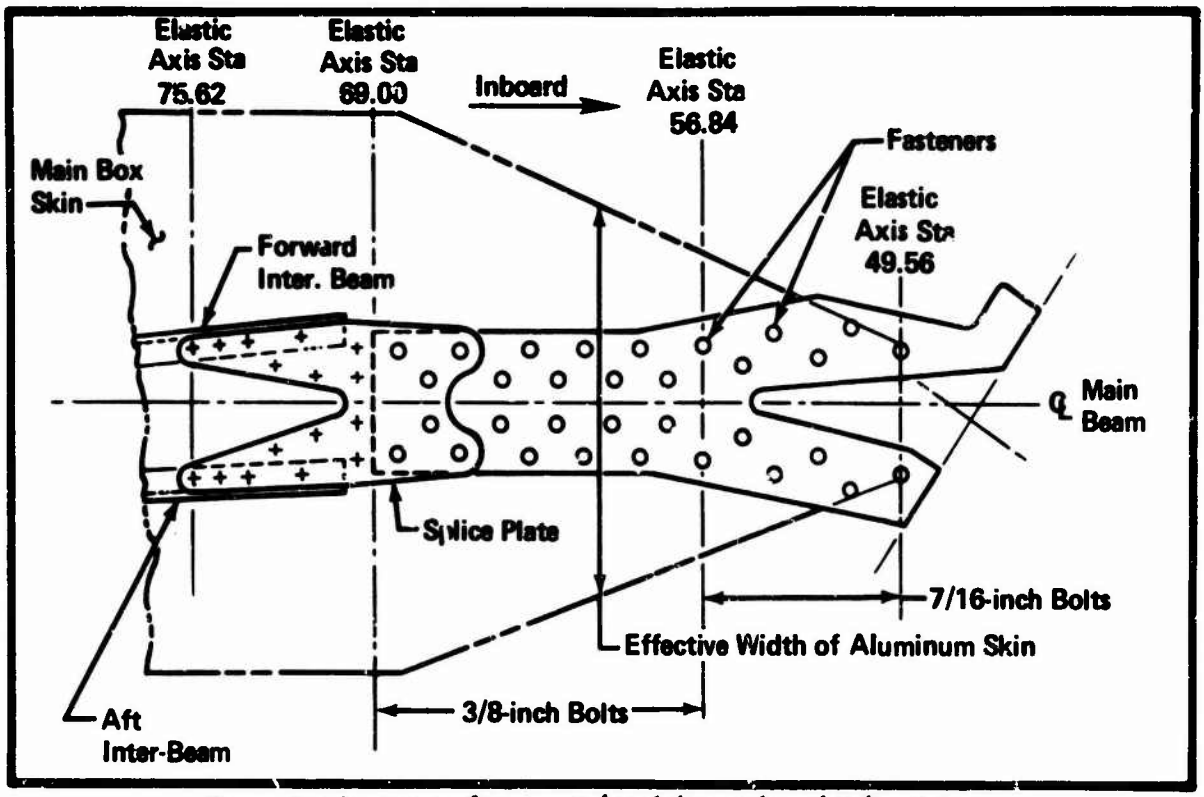

Figure 9. Plan View of Horizontal Stabilizer Inboard Splice Joint

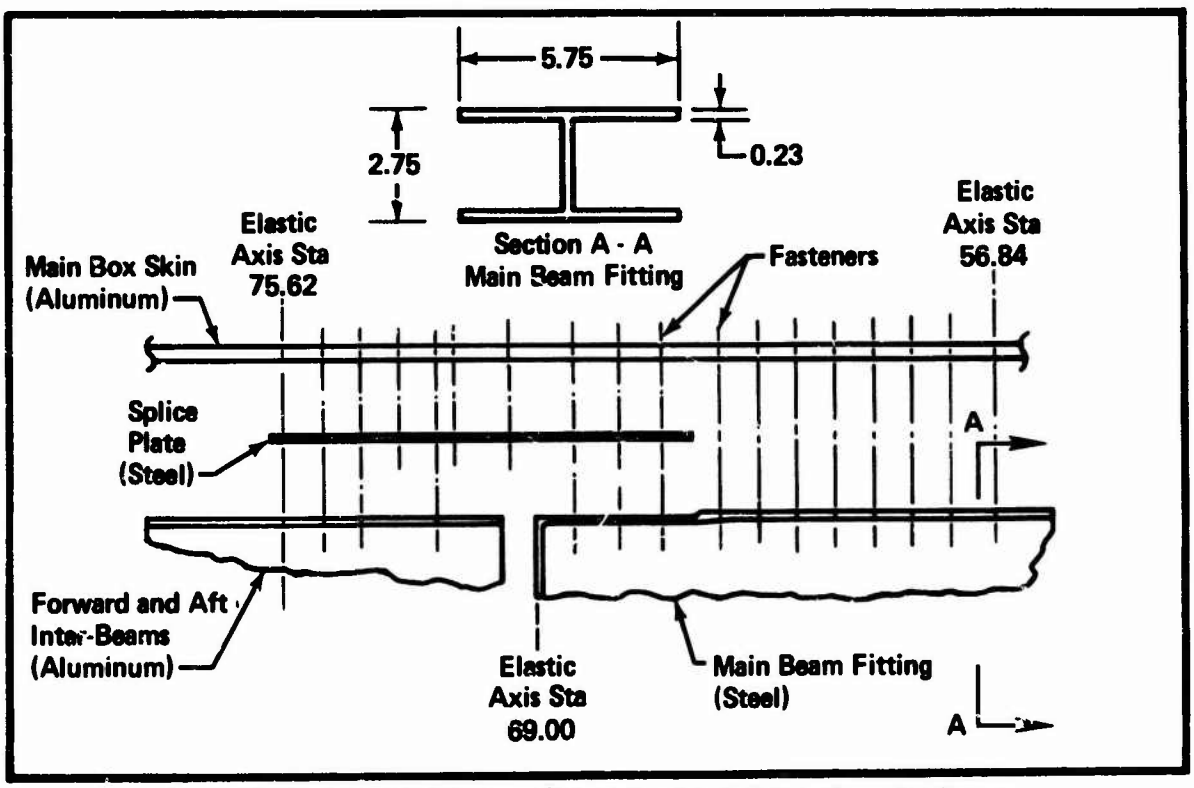

Figure 10. Exploded Side View of Horizontal Stabilizer Inboard Splice Joint

Temperature corrections for material properties for the aluminum skin were taken from MIL-HDBK-5. To obtain data on the fastener-plate intersection, simple two-bolt aluminum plate tests were made at 250°F and 450°F. The results [page 43, Volume II, Reference 4] show

$$\left.\begin{array}{lllll} \text{at } 250^{\circ}\text{F:} & P_y/(P_y)_{R.T.} = 0.98, & K/K_{R.T.} = 0.72, & m/m_{R.T.} = 1.12 \\ \text{at } 450^{\circ}\text{F:} & P_y/(P_y)_{R.T.} = 0.60, & K/K_{R.T.} = 0.68, & m/m_{R.T.} = 1.30 \end{array}\right\} \quad (18)$$

For the various bolt sizes and various plates in Figure 9, at 425°F, K varies from 268,000 to 501,000, while m varies from 3.8 to 5.6 [page 16, Volume IV, Reference 4].

Figures 11, 12, and 13 show the calculated inelastic distribution of the fastener loads and plate element loads at the calculated failure load of the stabilizer joint at room temperature, 250°F, and 425°F. The V_{cr} load on each loading former at calculated failure is 18,000, 17,250, and 12,420 pounds, showing a large reduction at 425°F. At 425°F, the aluminum skin properties for tension and bearing are about 50 percent of the room temperature values, while the steel properties are about 95 percent. The predicted modes of failure (Table I) are bolt shear and main steel beam tension at station 58 for room temperature and 250°F. At 425°F, aluminum skin bearing and main steel beam tension are critical at station 58. Since the cause of the reduction in failing load is due to reduction of properties in the 7079-T6 skin, why should main steel beam tension still be a possible mode of failure? From Figures 11, 12, and 13 it appears that the reduction in the aluminum bearing allowables causes a large change in load distribution at 425°F. The maximum loads in the 7079-T6 skin, the fasteners, and the steel fitting at station 49.56 have decreased, but the load in the main beam steel fitting around station 58 has changed very little. Thus the steel fitting may still fail at the lower applied load. Note that the fastener loads at 425°F have reduced more between station 49 and 58 than between stations 58 and 66, thus unloading the steel fitting more uniformly in Figure 13 than in Figures 11 and 12. It also should be noted that there is additional tension load in the steel fitting due to temperature, with steel having less expansion than aluminum. This thermal load peaks around station 58. In addition, the steel beam fitting carries the full shear of 2 V_{cr}, which loads the beam flanges uniformly between stations 66 and 49.

Even though the inelastic analysis tends to show more uniform loads in the fasteners than the elastic analysis (Figures 6 and 7), it is evident in Figures 11 and 12 that the end fasteners have the highest loads at the calculated failure point with all inelastic effects included. In Figure 11 at room temperature, the 7/16-inch bolts vary from 28,201 to 23,173 pounds and the 3/8-inch bolts vary from 21,702 to 13,193 pounds (load for two bolts). Note that the 3/8-inch bolt load at station 58.09 is nearly as large as the adjacent 7/16-inch bolt. This suggests that bolt sizes should not be mixed.

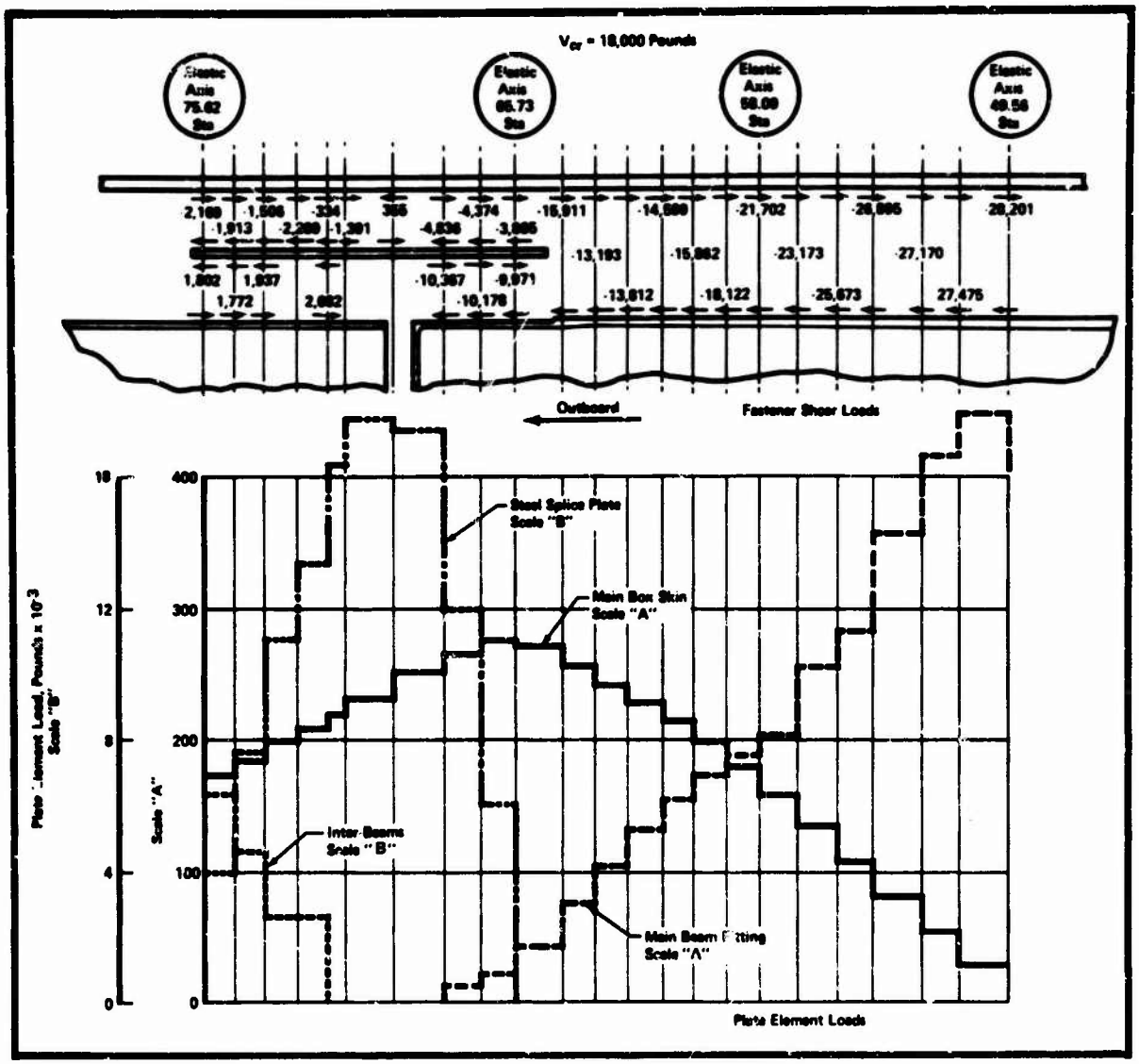

Figure 11. Fastener Shear Loads and Plate Element Loads at Failure, Horizontal Stabilizer Inboard Splice Joint, Room Temperature

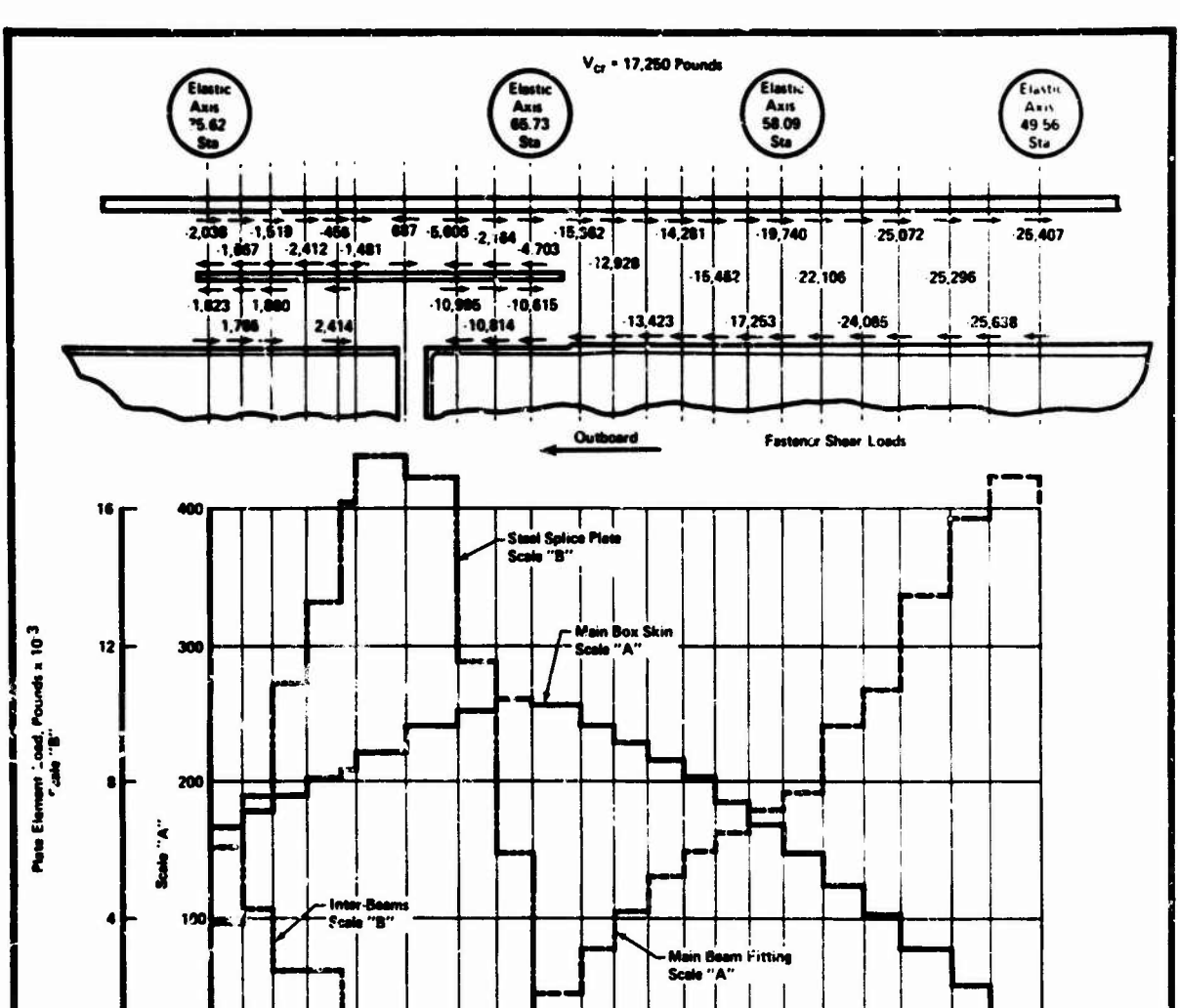

Figure 12. Fastener Shear Loads and Plate Element Loads at Failure, Inboard Splice Joint, 250°F Symmetrical

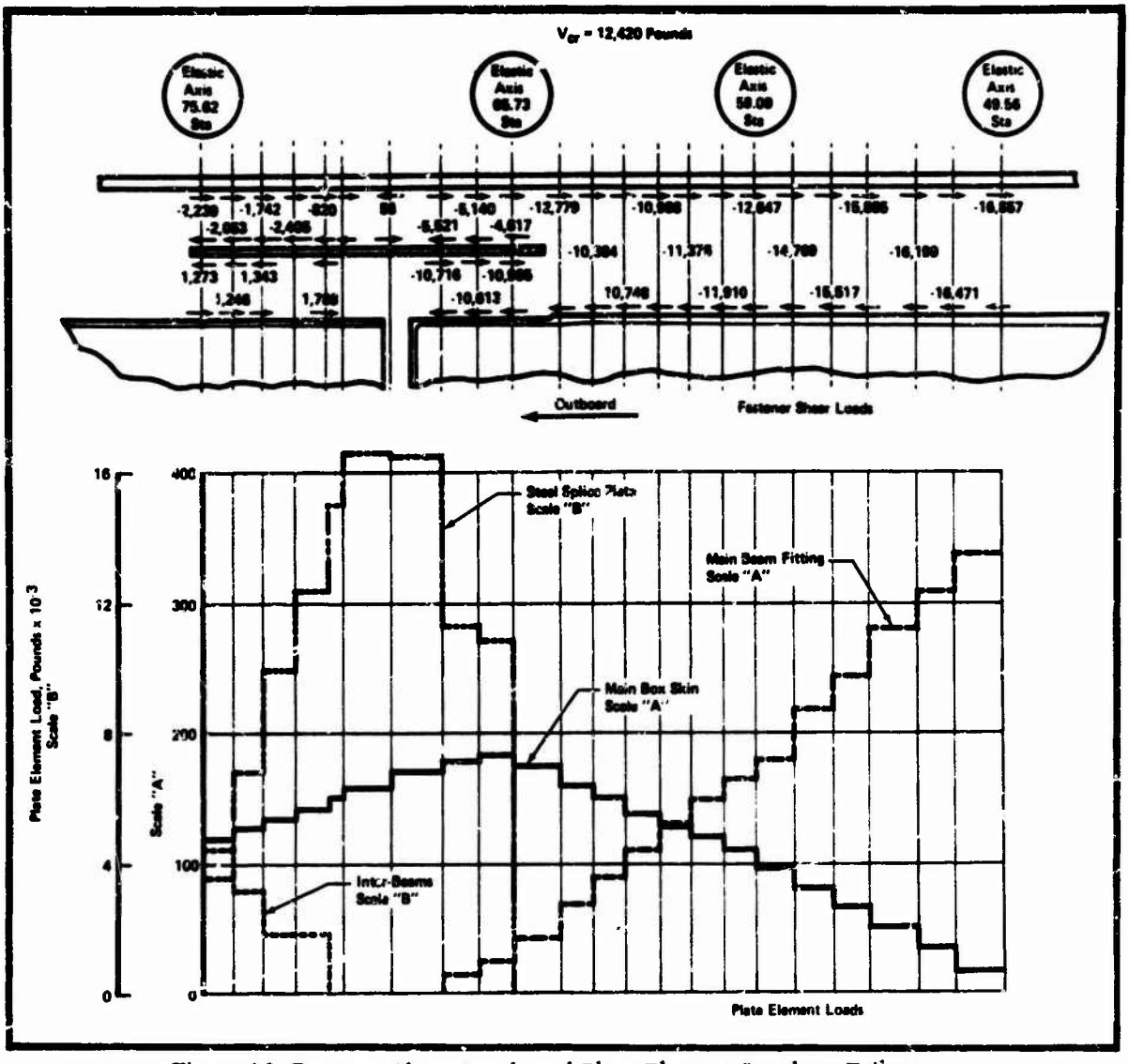

Figure 13. Fastener Shear Loads and Plate Element Loads at Failure, Inboard Splice Joint, 425°F Symmetrical

Table I shows test and calculated results for all of the tests. The calculated modes of failure agree with the predicted modes, with the 425°F test case having tension failure of the steel main beam fitting as the primary mode. The magnitude of the test loads at failure are slightly less than the calculated loads in most of the tests, but well within test tolerance.

Table I. Summary of Results, Horizontal Stabilizer Inboard Splice Joint

Temperature Environment Test Condition	Test Former Loads at Failure	Description of Test Failure	Calculated Failing Load, V_{cr}	Calculated Primary Mode of Failure and Impending Secondary Failure
Room Temperature	17,400 17,200 18,741 * 15,425	(1) Six inboard, aft fasteners sheared. (2) Same six holes in main box skin elongated inbocrd. (3) Tension failure, main beam flange, elastic axis station 58. (No failure during Test No. 7.)	18,000	(1) Fastener shear at elastic axis station 58. (2) High tension stress in main beam flange at elastic axis station 58 (Secondary).
250°F Symmetrical	15,985 (outbrd) 15,795 (inbd)	(1) Ten inboard fasteners sheared. (2) Same holes in main box skin elongated. (3) Tension failure in main beam flange at approximate elastic axis stations 54 to 55.	17,250	(1) Fastener shear at elastic axis station 58. (2) Imminent shear failure and bearing failure of inboard six fasteners (Secondary). (3) High tension stress in main beam flange at elastic axis station 58 (Secondary).
250°F Unsymmetrical	15,827 (outbrd) 15,471 (inbd)	(1) Nine inboard fasteners sheared. (2) Same holes in main box skin elongated. (3) Tension failure in main beam flange at approximate elastic axis station 54.	16,770† 17,750†	a. (See Note Below) ‡ (1) Fastener shear at elastic axis station 58. (2) High tension stress in main beam flange at elastic axis station 58 (Secondary).
425°F Symmetrical	12,440 (outbd) 12,347 (inbd)	(1) Tension failure, main beam flange, elastic axis station 57.25. (2) Holes elongated in main box skin in area of beam tension failure. (3) Inboard fasteners sheared.	12,420	(1) Box skin bearing at elastic axis station 58. (2) High tension stress in main beam flange at elastic axis station 58 (Secondary).
425°F Unsymmetrical	14,418 (outbd) 14,211 (inbd)	(1) Four inboard aft fasteners sheared. (2) Holes elongated in main box skin in area of beam tension failure. (3) Main beam tension failure at approximate elastic axis station 54 to 55.	13,030† 17,700†	b. (See Note Below) ‡ (1) Fastener shear at elastic axis station 58. (2) High tension stress in main beam flange at elastic axis station 58 (Secondary).

* Maximum total load reached prior to failure of horn and housing assembly. No fastener, main beam, or main box skin failure.

† No bending moment restraint for thermal strains.

‡ Results for full restrained-in-bending case for thermal strains.

‡ a.
(1) Fastener shear at elastic axis station 58.
(2) High tension stress in main beam flange at elastic axis station 58 (Secondary).
} 16,770 Pounds

‡ b.
(1) Main beam fitting tension failure at elastic axis station 58.
(2) Critical fastener shear and bearing; most inboard five rows of 7/16-inch diameter blind bolts (Secondary).
} 13,030 Pounds

CONCLUSIONS

The examples previously described show that the distribution of loads in a complicated splice depends on the deformation of all elements in the joint and that an inelastic, nonlinear analysis should be made to determine the mode of failure and the failing load. It appears that the method described and used in the examples is satisfactory provided load deformation data is available for a simple joint representing the desired fastener-plate combination. The method may be applied to splice joints using mixed fasteners as long as each row across the joint has the same type and size of fastener. However, the example of the stabilizer splice joint described indicates that it may be undesirable to mix fasteners in the joint. The splice plates may be of different materials, at different temperatures, and may be tapered in thickness and width. Any type of fastener can be used provided some type of load-deformation data is available for it in plates similar to the ones used in the actual joint. Although not shown in this paper, some limited application of the method has been made to bonded joints and metal structures reinforced with boron/epoxy composites where equivalent discrete fastener segments were used to represent the bond line.

ACKNOWLEDGEMENT

The authors acknowledge the support of the Naval Air Engineering Center under Contract Number N156-45330.

REFERENCES

1. Gatewood, B.E., "Thermal Loads on Joints," Thermal Stresses, McGraw-Hill Book Company, New York 1957, 5-8.

2. Switzky, H., Forray, M.J., and Newman, M., "Thermo-Structural Analysis Manual," WADD TR60-517, September 1960.

3. Lobbett, J.W., and Robb, E.A., "Thermo-Mechanical Analysis of Structural Joint Study," WADD TR61-151, January 1962.

4. Gehring, R.W., and Maines, C.H., "Application of Applied Load Ratio Static Test Simulation Techniques to Full-Scale Structures," NAEC-ASL-1094, four volumes, 1965–1966.

ANALYTICAL STUDIES OF STRUCTURAL PERFORMANCE IN MECHANICALLY FASTENED FIBER-REINFORCED PLATES

D. W. OPLINGER
Physicist-Mechanics

K. R. GANDHI
Mechanical Engineer
Army Materials and Mechanics Research Center
Watertown, Massachusetts

ABSTRACT

Analytical results are given for stresses in fiber reinforced plates loaded by circular fasteners. Single pin and periodic array configurations of fasteners are considered. The fasteners are considered as rigid circular inserts. Results are obtained with and without friction between the pin and plate taken into account. The analysis consists of a two dimensional elastic stress analysis using a complex variable formulation in conjunction with a least squares collocation scheme for satisfying boundary conditions. Iteration approaches are required: (1) for determination of the contact angle between the plate and fastener; (2) in the case where friction is considered for determining the portion of the fastener hole which is free of slip; (3) in the case of periodic fastener arrays, for determining the net lateral strain which makes the plate free of net lateral stress.

The stresses are interpreted in terms of a quadratic failure rule which is applied layer-by-layer to determine the fastener load causing failure. Results are given, which demonstrate the effects of joint geometry (edge distance and fastener spacing) as well as the composite material parameters, the most important of which appears to be the distribution of fiber orientation among various layers. Observations are made regarding principles to be used in selecting materials for local reinforcement of mechanical joints in composite plates.

NOTATION

D	- fastener hole diameter
E	- joint efficiency, $P_{f)_{min}}/P_{fo} X100$
E_L E_T	- Young's moduli of unidirectional layer along material axes
e	- axial distance from fastener center to free edge
G_{XY}	- shear modulus of laminate
G_{LT}	- shear modulus of unidirectional layer
L	- axial distance from fastener center to loaded edge of plate

P - fastener load

P_f - load producing failure at a given point in the laminate

P_{fo} - P_f at $x=-L$, $y=0$

$P_f)_{min}$ - minimum value of P_f in plate

R - fastener hole radius, $D/2$

r - radial coordinate

S_{Lt}, S_{Lc} - longitudinal tensile and compressive strengths of unidirectional layer

S_{Tt}, S_{Tc} - transverse tensile and compressive strengths of unidirectional layer

s - distance from fastener center to lateral edge of plate (single pin) or half spacing of fasteners (multi-pin)

u, v - displacement vector components in rectangular coordinates

u_R - radial displacement

v_s - vertical displacement constant at $y=s$ in multi-pin case

x, y - rectangular coordinates

δ - fastener displacement

θ - polar angle

η - contact angle

η_s - angle of non-slip

μ - coefficient of friction

σ_A - uniform axial stress at $s=-L$

$\sigma_x, \sigma_y, \tau_{xy}$ - laminate average stresses in rectangular coordinates

$\sigma_R, \sigma_\theta, \tau_{R\theta}$ - laminate average stresses in polar coordinates

$\sigma_L, \sigma_T, \tau_{LT}$ - stresses in unidirectional layer resolved along material axes

σ_u - ultimate axial stress in virgin laminate

INTRODUCTION

Structural joints have generally been recognized as a potential "Achilles' heel" for fiber reinforced structures due to the occurrence of modes of structural response which involve natural weaknesses of composites associated with low shear strength and other deficiencies. The need for special care in joint design to minimize these adverse effects is obvious. To achieve the maximum joint performance it is essential that as complete an understanding as possible of factors controlling joint performance be available.

It has been further recognized that, because of superior structural efficiency, adhesive joining would be the most desirable method of joint fabrication if problems of reliability under fatigue environments encountered with bonded concepts were well in hand. However, it appears that appreciable use of mechanical joining techniques will be unavoidable for some time to come, and optimum design of mechanical joints is a continuing need. The present study was undertaken to contribute to this end.

Although a number of analyses have been carried out on riveted or bolted isotropic plates [1-5] the amount of prior analytical work related to mechanically fastened composite structures is minimal [6-7]. Waszczak and Cruse [6] presented results of finite element analyses related to prediction of failure modes in various composite laminates for which prior experimental data was available. The first systematic analytical investigation of the effects of joint geometry and material parameters on the performance of composite mechanically fastened joints appears to have been given by the present authors in [7].

In the present paper some of the key results presented in [7] will be reviewed. Additional results on effects of pin friction and observations on concepts for introducing local strengthening around mechanical fasteners which were not previously considered will be discussed.

FORMULATION

In the present study the plate-fastener system (Fig. 1) was represented as a rectangular orthotropic plate containing rigid circular inclusions which exert load by a translation displacement in a given direction. The bulk of results have been obtained under the assumption of a perfectly fitting pin (zero clearance, non-interfering). The problem at hand reduces to obtaining a plane elastic solution under stress conditions on the outer boundary together with mixed boundary conditions at the inner boundary. The inner boundary, i.e. the circular boundary of the plate adjacent to the fastener, divides into a region of separation where zero normal and tangential stress are present, together with a contact region over which a radial displacement corresponding to simple translation of the fastener is a required condition. In addition the contact region includes a non-slip region together with a region of slip in which a linear relation between shear and contact pressure must be satisfied.

Typical fibrous composite laminates were modeled as homogeneous orthotropic

plates using simple laminate theory [8] which ignores thickness normal and transverse shear deformations. Hoffman's modified distortional energy criterion [9] was applied on a layer-by-layer basis to investigate failure considerations. This has the advantage over the standard form of distortional energy criterion considered in [6] of taking differences in tensile and compressive strength into account.

Fig. 1 shows the types of joint configuration which have been considered. Comparison of the single pin [Fig. 1(A)] and periodic array [Figure 1 (B)] configurations was of interest in assessing the effect of interactions between fasteners arranged in a parallel array. The solution for the isolated pin in an infinite plate [Figure 1(C)] gives a data base for predicting joint behavior in the case of pins widely spaced and well removed from neighboring boundaries. For the single pin and periodic array case [Figures 1(A) and 1(B)] results of interest were developed parametrically in terms of the ratios of pin spacing-to-diameter, s/D and edge distance-to-diameter, e/D.

Multilayer laminates were treated using the approach described in [8] to obtain effective compliance coefficients, a_{ij} (i;j = 1,2,6)in terms of engineering constants E_L, E_T, G_{LT} and ν_{LT} (Young's moduli, shear modulus and Poisson's ratio in material axis system of each layer). After the stresses in the laminate were obtained by the analysis discussed below, the corresponding laminate strains were used to determine stresses in individual layers, using layer stiffness coefficients determined from the engineering constants. Failure considerations were investigated by applying Hoffman's failure criterion [9] to the layer stresses.

ELASTICITY SOLUTION

COMPLEX VARIABLE APPROACH

The details of the stress analysis are given in Ref. [7] and will only be summarized here. The problem was treated in terms of a two dimensional elastic stress analysis of an orthotropic plate with boundary conditions which will be described below. The elasticity solution was obtained using the complex variable formulation of Lekhnitskii [10]. The method involves the generation of series expressions for Airy's stress functions in terms of variables related to the complex characteristics of a 4th order partial differential equation related to the two dimensional compatibility condition. The main step in the solution, determination of the coefficients of the series expressions, was accomplished by least squares boundary collocation. This involves setting up expressions for the boundary conditions in terms of the Airy stress function, stating these relations at selected points around the boundary and obtaining a system of linear equations in the unknown coefficients which minimizes the average squared error in the boundary conditions.

BOUNDARY CONDITIONS

1. Outer Boundary

The conditions on the outer boundary of the plate correspond to;

zero traction at the right hand edge (x=e); uniform axial stress at the left hand edge (x= -L); symmetry along the x-axis (y= 0); and at the lateral edge (y=s) either zero traction (single pin case) or a second condition of symmetry (multi-pin case, periodic fastener array). Formally, the conditions on the outer boundary are:

$$\underline{\text{right edge}} \quad (x=e,\ 0 \le y \le s)$$

$$\sigma_X = \tau_{XY} = 0 \tag{1.1}$$

$$\underline{\text{left edge}} \quad (x= -L,\ 0 \le y \le s)$$

$$\sigma_X = \sigma_A, \quad \tau_{XY} = 0 \tag{1.2}$$

$$\underline{\text{x - axis}} \quad (-L < x < e,\ y=0)$$

$$\tau_{XY} = v = 0 \tag{1.3}$$

$$\underline{\text{lateral edge}} \quad (-L \le x \le e,\ y=s)$$

$$\underline{\text{single pin}} \quad \tau_{XY} = 0 = \sigma_y \tag{1.4}$$

$$\underline{\text{multi-pin}} \quad \tau_{XY} = 0;\ v = \text{constant} \tag{1.5}$$

Condition (1.3) implies that the laminate properties and the stress field are symmetric about the x-axis. In the elasticity solution a half plane symmetry is therefore imposed on the terms which enter into the complex formulation. The value of vertical displacement, v, appearing in (1.5) is an unknown in the problem and must be determined by the iterative scheme discussed below.

2. Inner Boundary

The edge of the fastener hole is given by r = R, $0 \le \theta \le \Pi$. The boundary divides into: (1) a region of separation between the fastener and plate, ($\eta \le \theta \le \Pi$); (2) a contact region ($0 \le \theta \le \eta$) in which the plate boundary deforms in conformity with the rigid translation of the fastener. The parameter η is the contact angle. The contact region further divides into a non-slip region ($0 \le \theta \le \eta_s$) and a region of slip ($\eta_s \le \theta \le \eta$).

In the region of separation the hole is free of radial normal and tangential shear stress so that σ_R and $\tau_{R\theta}$ are zero. In the contact region a condition on the radial displacement, $u_R = \delta \cos\theta$ is required where δ

is the axial displacement of the fastener. Note that δ has to be defined with respect to some reference point, since δ is the difference in axial displacement between that of the pin and that of the reference point. The most convenient reference point is the intersection of the x - axis and the left-hand edge where the load is applied; x = -L, y = 0. In addition to the radial displacement condition a second boundary condition in the contact region is required. In previous work [7] the pin was considered frictionless, requiring that the tangential shear stress $\tau_{R\theta}$ be zero. In cases where friction is to be considered the most precise statement for the second boundary condition is v = 0 in the nonslip region and $\tau_{R\theta} = \mu|\sigma_R|$ where μ is the coefficient of friction, in the region of slip. Note that angle of nonslip, η_s along with the contact angle, η, are unknowns in the problem and must be determined by iteration. The details involved in the iteration procedure for η and η_s as well as the constant v in equation (1.5) are discussed below. Since the consideration of three iterative parameters could lead to considerable magnification of the computing effort, preliminary results relating to the effects of friction have been obtained with complete elimination of the region of slip by arbitrarily setting $\eta_s = \eta$ and with $\eta_s = 0$ which eliminates the nonslip region. The statement of boundary conditions on the inner boundary is formally as follows:

region of separation $(r = R, \eta \leq \theta \leq \Pi)$

$$\sigma_R = \tau_{R\theta} = 0 \qquad (2.1)$$

contact region $(r=R, 0 \leq \theta \leq \eta)$

$$u_R = \delta \cos\theta \qquad (2.2)$$

frictionless case

$$\tau_{R\theta} = 0 \qquad (2.3)$$

friction present

(nonslip region, $0 \leq \theta \leq \eta_s$) $v = 0$ (2.4)

(region of slip, $\eta_s \leq \theta \leq \eta$) $\tau_{R\theta} = \mu |\sigma_R|$ (2.5)

3. Iterative Scheme

As noted above, three unknown parameters enter into the problem. These include: the vertical displacement v_s at the lateral edge, y = S which (equation (1.5)) is required to be constant in the case of the multi-fastener configuration; the contact angle η; and the angle of slip, η_s. The uniform vertical displacement at y = s is determined by the requirement

that the net vertical force on the lateral boundary, i.e. $\int_{-L}^{e} \sigma_Y \, dx \Big)_{y=s}$ be zero (corresponding to the assumed condition that the joint is subject only to axial load). The contact angle η is established by the requirement that σ_R be strictly compressive within the contact region and go to zero in a continuous manner at the end of contact. The slip angle η_s is determined by the condition $\tau_{R\theta} \leq \mu\sigma_R$ in the nonslip region. Thus the parameters $v_s = v\ (y = s)$, η and η_s are determined by assuming initial values for them and making subsequent adjustments until the conditions

$$\int_{-L}^{e} \sigma_Y\ (y = s)\ dx = 0 \tag{3.1}$$

$$\sigma_R \Big)_{\theta = \eta} = 0 \tag{3.2}$$

$$\left[\tau_{R\theta} - \mu\sigma_R\right]_{\theta = \eta_s} = 0 \tag{3.3}$$

are met. It is noted that if equation (3.2) is satisfied, σ_R will generally be compressive for $|\theta| < \eta$ and therefore the required condition on σ_R will be fulfilled, although care must be taken to screen out cases in which the contact region may be broken up by gaps which are physically possible under some circumstances. Equation (3.3) which determines η_s is meant to be applied to the last point in the nonslip region where $v = 0$ is applied as a boundary condition. In general in the region $0 < \theta \leq \eta_s$ equation (3.3) will not be satisfied identically, but it is assumed that by varying the maximum θ where $v = 0$ is imposed and calling this η_s, a value of η_s may be found for which the condition $v = 0$ and equation (3.3) are satisfied simultaneously.

It should be noted that equation (3.1) is a linear condition, i.e. independent of the load, while conditions (3.2) and 3.3) which determine η_s and η are nonlinear since they give rise to values of η_s and η which depend on the load. In addition the left side of (3.1) is linearly related to v_s while the left hand sides of equations (3.2) and (3.3) vary in a nonlinear manner with η and η_s, respectively. As a result, two assumed values of v_s are sufficient to establish a linear trend in the left side of (3.1) which establishes the correct v_s exactly, while in the case of η and η_s, the initially assumed values must be good approximations to the correct values. For a perfectly fitting fastener (pin radius = hole radius) an initial value of η given by $\eta = 90°$ generally gives good results. An initial value of η_s equal to zero also appears to be a good guess.

FAILURE PREDICTIONS

The elasticity solution leads to a distribution of effective average stresses σ_X, σ_Y and τ_{XY} in the orthotropic plate which represents the laminate. Within the laminate the stresses vary from layer to layer because of changes in the elastic constants. The layer stresses may be related to the laminate stresses by noting that under the assumptions of simple laminate theory, in the absence of bending the strains are independent of thickness coordinate. The strains in each layer may therefore be calculated from the average laminate stresses, and lead to layer stress values by introducing the stiffness coefficients of a given layer. Once the layer stresses are determined in terms of the laminate stresses, a failure criterion may be applied to the resolved layer stresses σ_L, σ_T and τ_{LT} on a layer by layer basis to determine whether the laminate stress field corresponds to a failure in an individual layer. Since maximum fastener load is a basic requirement of joint design, it is convenient to establish what fastener load leads to a failure at a given point in the plate. This may be accomplished by noting that stresses at each point and within each layer are linearly related to fastener load P. Thus relationships of the form

$$\sigma_X (x,y) = k_X (x,y)\ P$$

$$\sigma_Y (x,y) = k_Y (x,y)\ P$$

$$\tau_{XY} (x,y) = k_{xy} (x,y)\ P$$

can be written once the elastic solution for a unit value of P is determined, the quantities k_X, k_Y and k_{XY} being equivalent to the stress distribution in the plate. Since the laminate analysis gives the resolved stresses σ_L, σ_T and τ_{LT} in each layer related to the laminate stresses σ_X, σ_Y and τ_{XY} then additional relations of the form

$$\sigma_L (x, y, j) = k_L (x, y, j)\ P \qquad (3.1)$$

$$\sigma_T (x, y, j) = k_T (x, y, j)\ P \qquad (3.2)$$

$$\tau_{LT} (x, y, j) = k_{LT} (x, y, j)\ P \qquad (3.3)$$

where j refers to layer number can be established. The latter can be used in conjunction with a failure criterion to determine the value of P producing failure at x, y and in layer j. For example the max stress criterion

$$\text{Max} \left\{ \frac{\sigma_L}{S_L} , \frac{\sigma_T}{S_T} , \frac{\tau_{LT}}{T_{LT}} \right\} \leq 1$$

reduces to

$$\text{Max} \left\{ P \frac{k_L}{S_L} , P \frac{k_T}{S_T} , P \frac{k_{LT}}{T_{LT}} \right\} \leq 1$$

or equivalently

$$P_f = \text{Min} \left\{ \frac{S_L}{k_L} , \frac{S_T}{k_T} , \frac{T_{LT}}{k_{LT}} \right\} \tag{4}$$

where S_L, S_T and T_{LT} are longitudinal, transverse and shear strengths of the layer under consideration.

The load P_f given by equation (4) is the load causing failure at x, y, layer j. By scanning over the plate and locating the point where the minimum value of P_f denoted by $P_{f|\min}$ occurs, the failure load for the joint is determined. In the present case the quadratic failure rule given by Hoffman [9]

$$\frac{\sigma_L^2 - \sigma_L \sigma_T}{S_{Lc} S_{Lt}} + \frac{\sigma_T^2}{S_{Tc} S_{Tt}} + \left(\frac{S_{Lc} - S_{Lt}}{S_{Lc} S_{Lt}} \right) \sigma_L + \left(\frac{S_{Tc} - S_{Tt}}{S_{Tc} S_{Tt}} \right) \sigma_T + \frac{\tau_{LT}^2}{T_{LT}^2} = 1 \tag{5}$$

was used. On introducing equations (3) this leads to a quadratic equation in P which must be solved at each point to determine P_f.

The structural efficiency of the joint can be defined as the ratio of axial stress σ_A which can be applied with the joint present to σ_u, the ultimate strength of the virgin laminate. If P_{fo} is the value of P_f at the reference point x = -L, y = 0, then $P_{f)_{min}}/P_{f0} \times 100$ is essentially equivalent to joint efficiency E provided the plate is long enough (i.e. L is large enough) so that the stress is essentially uniform in the vicinity of the loaded end x = -L.

RESULTS

STRESS DISTRIBUTION

Results of the study were obtained for high modulus graphite epoxy and glass epoxy. Assumed unidirectional properties of these materials are given in Table 1.

Typical radial stress distributions around the fastener are shown in Figure 2. Although all of the finite plate cases treated to date have been for the perfect fit case (pin radius = hole radius), the curve in Figure 2 labeled with triangles applies to a clearance fit (pin rad. = .99974R) for the infinite plate case and demonstrates the ability of the method to handle this situation. While the case for e=s=5 (labeled with circles) has the appearance of a "half cosine" distribution, wide departure from the cosine distribution may occur, as exemplified by the case for e=1.5R, s=2R (labeled with squares). For large plates for which the infinite plate results are accurate the distribution of σ_R has been found to be nearly linear over a large part of the contact region (θ=20° to 70°). Waszczak and Cruse [6] found that the half cosine distribution was adequate for the cases which they studied. The present results suggest that it gives good results primarily if e/D is not too small (i.e., e/D>2) and s/D is not too large.

TABLE 1. Assumed Mechanical Constants of Fiber Reinforced Materials

	Graphite Epoxy	Glass Epoxy
Elastic Constants		
E_L (10^6 psi, GN/m^2)	25.0, 172	7.00, 48.2
E_T (10^6 psi, GN/m^2)	1.0, 6.89	2.50, 17.2
G_{LT} (10^6 psi, GN/m^2)	.7, 4.82	1.20, 8.26
ν_{LT}	0.2	0.25
Strength Constants		
S_{LT} (ksi, MN/m^2)	150.0, 1032	210.0, 1445
S_{Lc} (ksi, MN/m^2)	100.0, 689	170.0, 1170
S_{Tt} (ksi, MN/m^2)	6.0, 41.3	4.0, 27.5
S_{Tc} (ksi, MN/m^2)	20.0, 138	30.0, 207
T_{LT} (ksi, MN/m^2)	10.0, 68.9	8.0, 55.0

Fig. 3 shows the distribution of axial stress, σ_X, throughout the plate for a typical case ($0_2 \pm 45$ graphite epoxy, e/D=2, s/D=0.75, L/D=4) This illustrates the expected range of disturbance of the uniform stress field by the fastener. The axial stress distribution becomes essentially uniform and equal to σ_A at about x/D= -2. On the unloading side of the fastener the stress approaches zero at about x=3 (x/D=1.5)

Effects of friction are illustrated in Figures 4 and 5. Fig. 4 shows a comparison of radial and shear stress around the fastener hole for two values of friction coefficient along with the frictionless case, for $0_2 \pm 45$ graphite epoxy, with e/D=4, s/D=1. In the cases of non-zero μ the dashed curve shows the variation of $\mu\,|\sigma_R|$ which is required to become equal to $\tau_{R\theta}$ beyond $\theta=\eta_s$, within the tolerances allowed by the least squares fit. (A vertical dashed line indicates the location of η_s). It is apparent that the presence of friction has a significant effect on σ_R in the vicinity of $\theta=0$. Fig. 5 shows a comparison of the σ_θ distribution for the frictionless case and the case of $\mu=0.25$. The behavior of σ_θ in the vicinity of $\theta=0$ is especially significant due to the fact that cleavage failures are suggested as a possible failure mode by the results obtained for the frictionless case. These are discussed below. The presence of friction tends to suppress hoop strain at $\theta=0$ and therefore sizeably reduces σ_θ at that location as indicated in Fig. 5. In view of the fact that cleavage failures are not normally observed in the $0_2 \pm 45°$ graphite epoxy configuration, the effect of friction appears to play an important role in controlling the failure mode for laminates of this type.

ELASTIC STRESS CONCENTRATIONS

The stress concentrations of interest in the joint are the ratios of the peak values of net section tension, shearout and bearing stress in the joint to the applied stress σ_A. The peak values referred to above will be taken to be defined as follows:

peak net section tension $\sigma_{NS})_{max} = \sigma_\theta$ at $\theta = 90°$, r=R

peak shearout stress $\tau_{XY})_{max}$ = maximum value of τ_{XY} at r=R

peak bearing stress $\sigma_B)_{max}$ = maximum negative value of σ_X at r=R

Cases have been observed where the peak net section tension may lie slightly away from the fastener hole but for present purposes the peak value is assumed to be identical with the hoop stress, σ_θ at r=R and $\theta=90°$. In addition it is noted that the maximum value of τ_{XY} in the joint which is presumed to cause shearout initiation is generally found to occur at r=R. The maximum bearing stress, $\sigma_B)_{max}$ is defined as the maximum compressive value of σ_X at the fastener hole and in most cases lies at $\theta=0$.
The stress concentration factors of interest are:

$$K'_{NS} = \frac{\sigma_{NS})_{max}}{\sigma_A}$$

$$K'_{so} = \frac{\tau_{XY})_{max}}{\sigma_A}$$

$$K'_{B} = \frac{\sigma_{B})_{max}}{\sigma_A}$$

The variation of these stress concentrations with joint geometry and material properties of the laminate are of interest because of their relation to the important failure modes which may occur.

Effects of joint geometry on the stress concentrations are illustrated in Figs. 6-8 for 0_2 45 graphite epoxy in a multi-pin configuration. Figure 6 shows the effect of fastener spacing, s/D for fixed edge distance e/D while Fig. 7 shows the effect of edge distance for fixed s/D. Also shown in Fig. 6 are linear trends obtained from the infinite plate solution. These are based on the view that the finite plate solution for large values of s/D and e/D approaches a situation in which all stresses become proportional to the average bearing stress, P/Dt, the proportionality factor for a given stress at a given point being given by the infinite plate results. Since the ratio of P/Dt to σ_A is proportional to s/D, the large plate trends become linear with respect to s/D as well as with P/Dt. The persistent separation between the finite and infinite plate trends in K'_{NS} (top curve in Fig. 6) reflects the lack of uniform stress terms in the infinite plate solution which must be present in the finite plate to satisfy the outer boundary condition. Although the separation persists the ratio of the stress concentrations predicted by the infinite plate and finite plate solutions approaches unity for large s/D. The trends with respect to edge distance in Fig. 7 illustrate the fact that the peak stresses become independent of e/D for e/D greater than about 2.

Of particular interest in the results shown in Fig. 6 are the minima in the curves of K'_{NS} and K'_{So} vs. s/D. Fig. 8 shows a comparison of the K'_{NS} curve with that obtained for the isotropic case [4]. The two curves appear to merge for s/D > 1.75. A minimum occurs in the isotropic case at a slightly higher value of s/D than that for the composite laminate. The presence of the minima in the K'_{NS} and K'_{so} curves indicates that the joint geometry is optimum for values of s/D equal to about 1. The interpretation of stress predictions in terms of failure levels discussed later bears this conclusion out.

Table 2 shows a comparison of the elastic stress ratios K'_{NS}, K'_{B} and K'_{so} for a fixed geometry and for various combinations of material, fiber orientation and fastener configuration. It appears from these results that the material system does not have a strong effect on the stress ratios although the effect of fiber orientation, particularly on K'_{NS} is fairly significant. A comparison of the single pin and multi-pin results for $0_2 \pm 45$ graphite epoxy shows that both K'_{B} and K'_{SO} are lower for the single pin case while K'_{NS} is somewhat higher for this case, reflecting the absence of σ_y at the lateral edge (y = s) which is generated in the periodic (multi-pin) case to provide for the uniform vertical displacement condition.

TABLE 2

ELASTIC STRESS RATIOS FOR VARIOUS CASES: e/D = 4, s/D = 1

Material	Orient'n	Fastener Configuration	K'_{NS}	K'_{B}	K'_{so}	Efficiency, %
Graphite-E	$0_2, \pm 45$	Multi-pin	4.36	2.67	1.62	11.7
Graphite-E	$0_2, \pm 45$	Single pin	4.80	2.07	1.40	12.7
Graphite-E	0/90	Multi-pin	7.76	2.01	1.06	10.7
Glass-E	$0_2, \pm 45$	Multi-pin	4.07	2.22	1.77	2.5
Glass-E	0/90	Multi-pin	4.49	1.98	1.62	4.7

It is well to keep in mind that the peak stress which has the primary effect on joint performance will depend on the strength characteristics of the laminate under consideration. Thus a large value of K'_{NS} is not necessarily the most important result to be obtained if enough 0° reinforcement is present to eliminate net tension failure. This is the case for $0_2 \pm 45$ and 0/90° laminates. In both cases there is evidence that the shear stresses exert the primary effect on failure initiation so that the variation of K'_{so} appears to be of greater interest.

Results shown in Table 3 for unidirectional and 0/90° glass epoxy illustrate this point further. In the unidirectional case cleaving failure corresponding to vertical splitting at θ=0° is the indicated failure mode for large edge distance. Thus, in addition to the three stress ratios considered previously, a knowledge of σ_y/σ_A at θ = 0°may be needed. Furthermore, while the cleaving failure is suppressed for small edge distances bending failure associated with σ_y at the right hand edge (x=e, y=0) appears to be important for unidirectional materials. When 90° material is added as in the case of the 0/90° laminate shown in the last row of Table 3, failure associated with cleaving or bending appears to have been eliminated due to tensile

strengthening of the laminate in the 90° direction. For the 0° laminate the effect of pin configuration appears to be quite significant (compare results for e/R = 1.5, s/R = 2) since it produces a relatively large change in σ_y at the failure point.

TABLE 3 TYPICAL ANALYTICAL RESULTS ON MECHANICALLY FASTENED COMPOSITE JOINTS

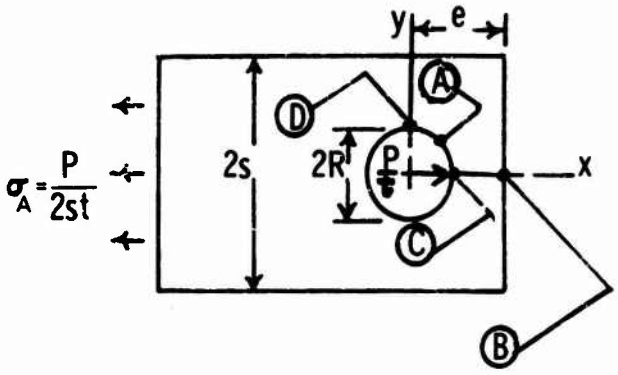

Configuration	$\frac{e}{R}$	$\frac{s}{R}$	STRESS RATIOS Ⓐ K'_{so}	Ⓑ $\frac{\sigma_y}{\sigma_A}$ (Bending)	Ⓒ $\frac{\sigma_y}{\sigma_A}$ (Cleaving)	Ⓓ K'_{NS}
0° Glass Epoxy						
Single Pin	5	5	3.22	1.51	2.78*	9.12
Single Pin	1.5	2	2.58	5.05*	3.24	9.51
Multi-Pin	1.5	2	2.85	3.41*	2.21	7.73
Multi-Pin	2.0	1.5	1.61	1.37*	0.96	6.24
0°/90° Glass Epoxy						
Single Pin	4	4	2.88*	1.90	3.31	6.82

* Denotes critically stressed point based on assumed layer failure properties in conjunction with Hoffman's failure rule.

FAILURE CONSIDERATIONS

Figs. 9 and 10 show the variation of the failure load, P_f, around the fastener hole in a $0_2 \pm 45°$ graphite epoxy laminate. Fig. 9 refers to the frictionless case while Fig. 10 corresponds to an assumed coefficient of friction of 0.25. Sizeable differences of the P_f values occur among the various layers making up the laminate. It is particularly interesting that a marked difference occurs between the + 45 and - 45° layer which is obviously a consequence of the difference between compressive and tensile strengths of the individual layers. A failure rule which ignored these differences would obscure this result. It is especially important that the difference be accounted for since failure specifically in the + 45 layer, at about 60° is indicated and at no point does a P_f value in the - 45° layer come close to the minimum value in the + 45° layer. The situation with the 0° layer is somewhat ambiguous in the frictionless case (Fig. 9) since the analytical results suggest that failure in the 0° layer may occur in the vicinity of $\theta = 0°$ at a load which is quite similar to the minimum P_f in the + 45 layer. Indeed, between the single pin and multipin cases the balance of control on failure is seen to shift from the 0° layer to the + 45 layer. The ambiguity is resolved when friction is introduced, however, since it is seen in Fig. 10 that P_f at $\theta=0°$ in the 0° layer is far removed from that in the + 45 layer, and $P_f)_{min}$ value in the latter stands out clearly as the $P_f)_{min}$ for the joint as a whole. The failure mode for the 0° layer in the frictionless case is presumed to be cleavage failure while that in the + 45 layer is assumed to be associated with shearout. No indication of net tension failure has been seen in results examined to date for $0_2 \pm 45$ graphite epoxy. It is not clear at present whether decreasing the spacing parameter s/D will tend to produce net tension failure in the analytical results. It appears from results obtained with the infinite plate case that any of the failure modes which have been discussed (i.e. net tension, bearing, shearout and cleavage) can occur even for large edge and side distances if the laminate is constructed so as to retain the directions of extreme weakness characteristic of unidirectional laminates. Thus shear and net tension failures are not necessarily restricted to small edge distances and fastener spacings.

The effect of joint geometry on structural efficiency in the $0_2 \pm 45$ graphite epoxy configuration is illustrated in Fig. 11. This is seen as a translation of the effects of s/D and e/D shown in Figs. 6 and 7 through the failure criterion. The existence of an optimum value of s/D is clearly indicated by the peak in the upper curve of Fig. 11. The numerical values of efficiency given in Fig. 11 must be assumed to be somewhat tentative due to the assumption of linearity and elastic response inherent in the analysis, in addition to the ignoring of interlaminar shear stress effects. The trends seen in Fig. 11 would be expected to manifest themselves in some fashion, however.

Results for several cases of interest corresponding to a fixed geometry (e/D=4, s/D=1) are shown in Table 2 (right hand column). In general it appears that the 0/90° and $0_2 \pm 45$ laminates give similar joint efficiencies.

The actual joint strength for the 0/90° case is about 75% of that for the $0_2 \pm 45$ corresponding to lower shear strength of the 0/90 laminate. However the strengths of the virgin laminates differ by almost the same factor, whence the nearly equal values of joint efficiency. The low values of efficiency in the fiberglass laminates reflect a higher virgin laminate strength corresponding to a higher S_{Lt} value given in Table 1 for glass epoxy and a lower laminate shear strength corresponding to a lower value of T_{LT}. The joint strength for $0_2 \pm 45$ and 0/90 laminates was found to be shear strength dependent and the unidirectional shear strength plays a relatively important part in determining laminate shear strength. The comparison of single and multipin results for $0_2 \pm 45$ graphite epoxy in Table 2 indicates a slight drop in efficiency with the multifastener configuration. This appears to be a consequence of increased peak shear stress reflected in a higher value of K'_{so} which occurs in the multipin case.

JOINT STRENGTHENING MECHANISMS

Since fiber reinforced uni-layers are excessively weak in transverse and shear loading, even relatively low stress levels for these types of loading can cause failure. As a result the high peak net section tension which is usually developed at mechanical fasteners is often not the stress of interest in determining joint failure levels. In general the joint must be strengthened to a minimal extent against cleavage failure and to a greater extent against shear failure. The addition of $\pm$ layers to 0° layers apparently accomplishes both of these steps to some extent, as illustrated by the results discussed in the previous section for $0_2 \pm 45$ graphite epoxy. The fact that failure occurs in the $\pm$ 45° layer for this type of laminate suggests that shear strengthening is not completely effective with this configuration, since if it were, it is expected that the failure mode would shift to tensile failure in the net section. A preliminary consideration of the strengthening problem suggests that stiffness of the strengthening layer plays a part along with its strength enhancement capability. For example, laminate theory predicts that $\pm$ 45° glass epoxy layers have a shear strength on the order of 100 k.s.i., as compared with a shear strength in 0° material of 8 k.s.i. However, the shear stiffness of $\pm$ 45° glass epoxy is only about twice that of 0° glass epoxy so that the strengthening layers are not loaded particularly effectively in the area of the joint where high shear stresses predominate. In the case of graphite epoxy the $\pm$ 45° layers have a shear stiffness about 7 times that of the 0° material so that more effective loading of the $\pm$ 45° layers is obtained. This appears to be an explanation of the higher joint efficiencies obtained for $0_2 \pm 45°$ graphite epoxy than for the same configuration in glass epoxy (see right hand column, Table 2).

Proceeding along this same line of thinking, it appears that addition of $\pm$ 45° boron epoxy layers to unidirectional glass or graphite would provide greater enhancement of joint efficiency than $\pm$ 45° graphite reinforcement since the shear modulus of $\pm$ 45° boron epoxy is higher than that of glass or graphite. Moreover, high modulus isotropic film interlayers have the potential for even greater shear loading effectiveness than $\pm$ 45° layers containing any of the fibrous reinforcing materials presently available since their

shear stiffnesses tend to be as high as 1/3 of their Young's moduli. Boron vapor deposited on polyimide substrate has already been studied as a joint reinforcing material [11] and shown considerable promise. Graphitic films are currently under development at AMMRC. These both appear to be capable of providing the effective shear stiffening action which is needed to obtain joint strength improvement.

The exact mechanisms by which various layers contribute to joint performance are obscured somewhat by the complicated interactions between laminate stress states and layer stress states as well as by the complexities entailed in the failure rule. The conclusion could not always be made as to whether a change in the layer strength constants or a shift in the stress state was responsible for differences in joint strength predicted for different materials. Thus the conclusion as to what specific properties are needed in joint strengthening layers can be made only on a general basis as yet. The selection of more clearcut and specific features of the strengthening layers as being important will result from further examination of the results of the analysis. The present form of the analysis appears to be capable of providing such guidance when an effective scheme for interpreting the results obtained is in hand.

CONCLUSIONS

The results of the present study clarify the effect of geometry on the structural performance of mechanical joints in fiber reinforced structures. Of particular interest is the indication of optimum fastener spacing equal to about twice the pin diameter. The need for maintaining edge distances twice the pin diameter or greater to develop full joint strength is also borne out.

Differences between the response of single pin and multipin configurations do not appear to be significant in commonly encountered laminates such as $0_2 \pm 45$ configurations. For laminates such as unidirectional configurations in which the peak level of σ_y is a consideration, fastener interactions do appear important.

The effect of friction between the fastener and the rim of the hole causes a significant reduction in cleavage stresses which accounts for the lack of observed cleavage failures in $0_2 \pm 45°$ laminates which are predicted by results obtained for the frictionless case. The results related to friction are tentative because of a current lack of knowledge of coefficients of friction which occur in actual joints. Experimental effort to determine such data is needed.

Joint strengthening approaches involving foil interlayers should make use of foil materials which provide sufficient shear stiffness to effectively load the interlayers in shear. Candidate foil materials which appear promising in this respect are boron vapor deposited on polyimide substrate and film forms of graphite.

Improvements in the analysis to allow for such effects as:

- nonlinear response
- interlaminar shear and normal stresses as well as other three dimensional effects
- restraining effects of cover plates
- layer buckling

are needed to provide for improvements in the failure predictions. In cases where bearing failures occur these appear to be strongly related to three dimensional response, i.e. splitting due to thickness deformation. In addition interlaminar failures are commonly encountered in $\pm$ 45° laminates. Thus the present analysis which restricts itself to in-plane modes of deformation needs to be supplemented by three dimensional solutions in order to have a comprehensive picture of joint behavior.

Improved concepts for modeling the progression of failure in the laminate are an important need. With the present analysis the local redistribution of load after initial failure of a given layer at a particular point cannot be accurately described. Unless load redistribution is taken into account the first failure must be assumed to represent final failure, and unreasonably low values of joint strength may be predicted. Waszczak and Cruse [6] were able to account for load redistribution using a finite element routine. From the discussion of those authors it appears that they allowed for changes in element stiffness constants corresponding to unloading of selected layers within a particular element. Although this provides a desirable step toward accounting for failure progression it must be considered tentative since it artificially ties the size of the zone of redistribution to the size of the element in which individual layer failure is identified. To obtain a correct model of failure progression, some sort of three dimensional analysis of the stress field is needed which treats the restraining effects of adjacent layers in the vicinity of a region of local fracture in an individual layer.

REFERENCES

[1] Bickley, W. G., Phil. Transactions of Royal Society of London, V. 227A, p. 383, 1928.

[2] Howland, R.C.J., "On Stresses in Flat Plates Containing Rivet Holes", Proceedings of 3rd International Congress of Applied Mechanics, Vol. II, pp 74-79, 1930

[3] Knight, R.C., Phil, Mag. Series 7, V. 19, p. 517, 1935.

[4] Theocaris, P., "The Stress Distribution in a Strip Loaded in Tension by Means of a Central Pin", ASME J. Applied Mechanics, Paper No. 55-A-34

[5] Harris, H.G., Ojalvo, I.U. and Hooson, R.E., Air Force Flight Dynamics Laboratory Report AFFDL-TR-70-49, 1970.

[6] Waszczak, J.P. and Cruse, T. A., J. Composite Materials, V. 5, p. 421, 1971.

[7] Oplinger, D.W. and Gandhi, K.R., "Stresses in Mechanically Fastened Orthotropic Laminates", Presented at 2nd Conference of Fibrous Composites in Flight Vehicle Design, May 21-24, 1974, Dayton, Ohio (To be published in the Proceedings)

[8] Halpin, J., Ashton J. and Petit, P., "Primer on Composite Materials Analysis", Technomic Publishing Co., 1969.

[9] Hoffman, O., J. Composite Materials, V. 1, p. 200, 1967.

[10] Lekhnitskii, S., "Theory of Elasticity of an Anisotropic Elastic Body", Holden-Day Inc. 1965.

[11] Padawer, G.E., "Film Reinforced Multifastened Mechanical Joints in Fibrous Composites," Journal of Aircraft, Volume 10, Number 9, September, 1973.

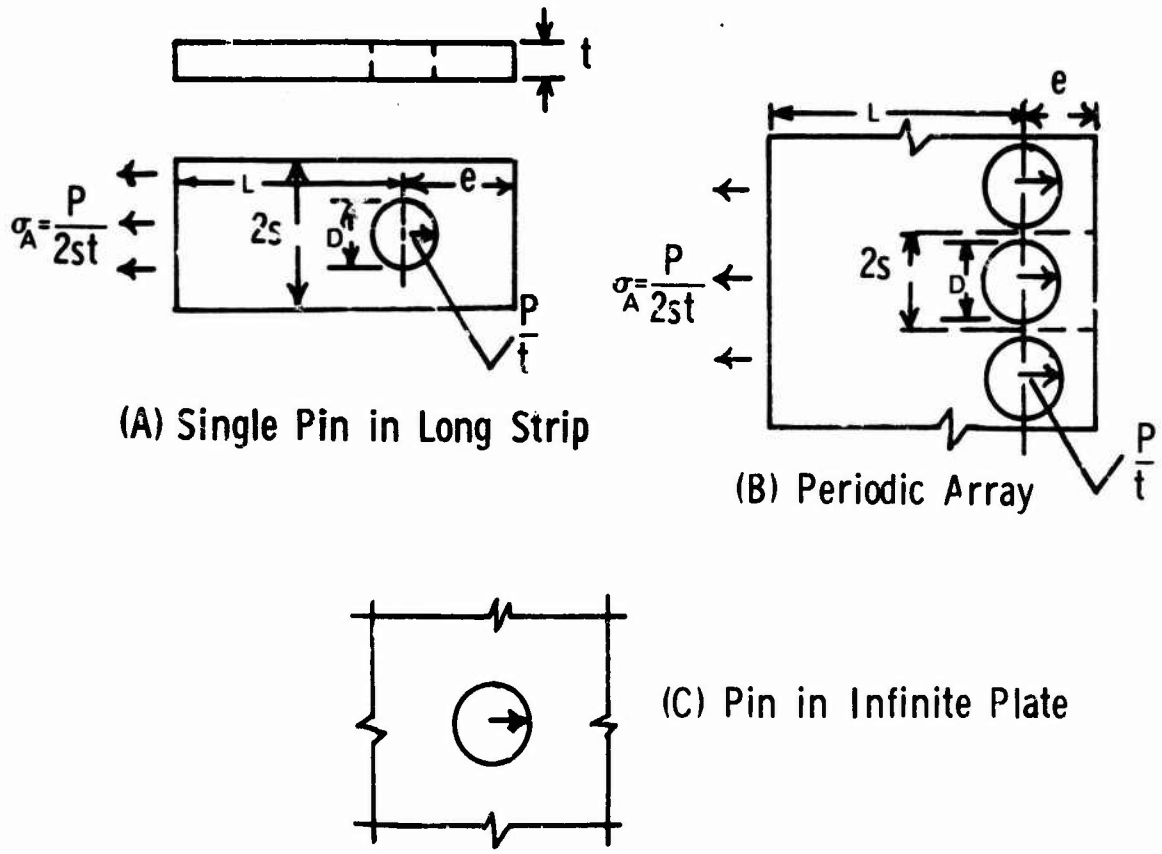

(C) Pin in Infinite Plate

Fig. 1 Mechanical Joint Configurations Under Consideration

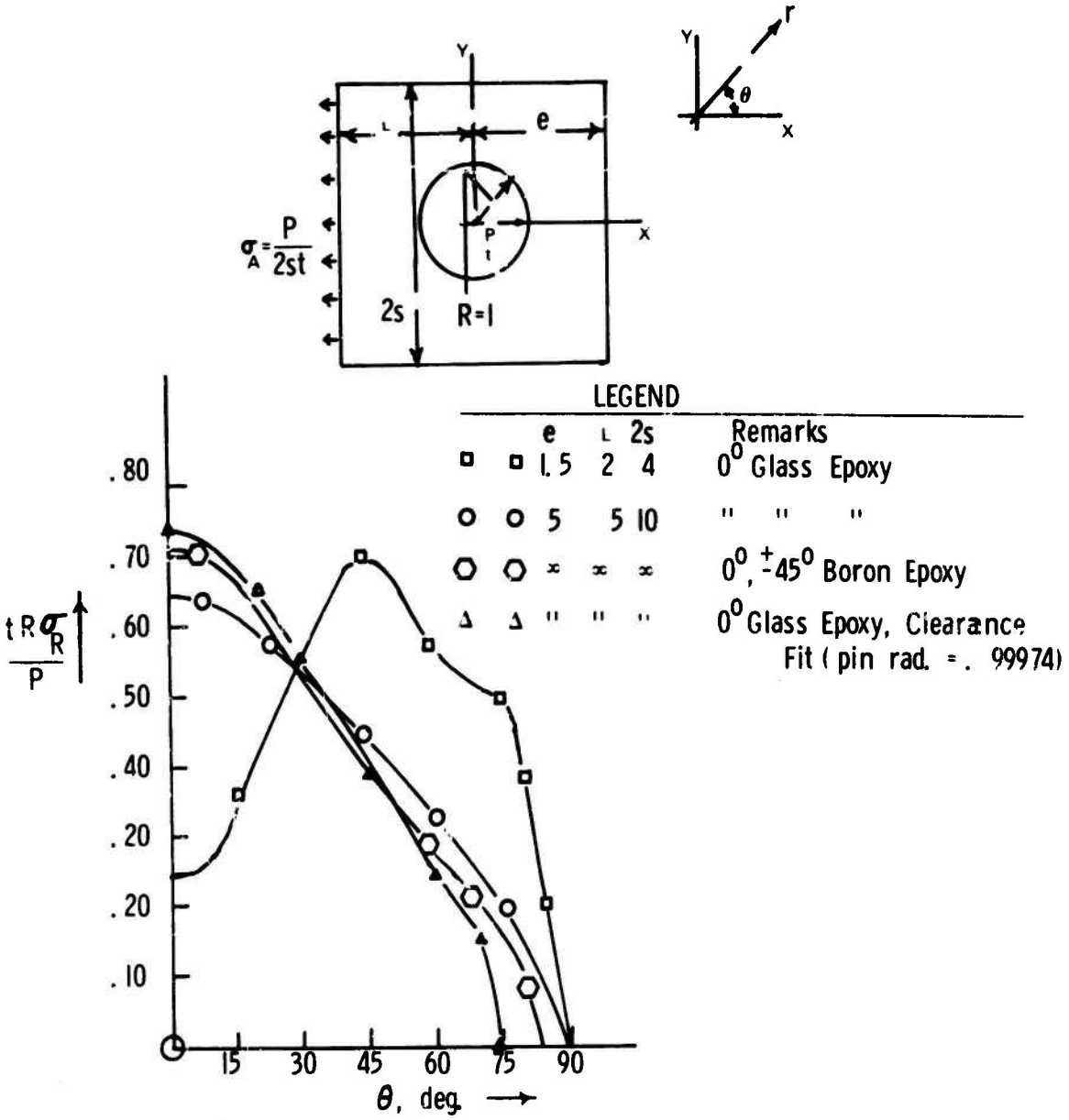

Fig. 2 Radial Stress Distribution around Fastener Hole (D = 2)

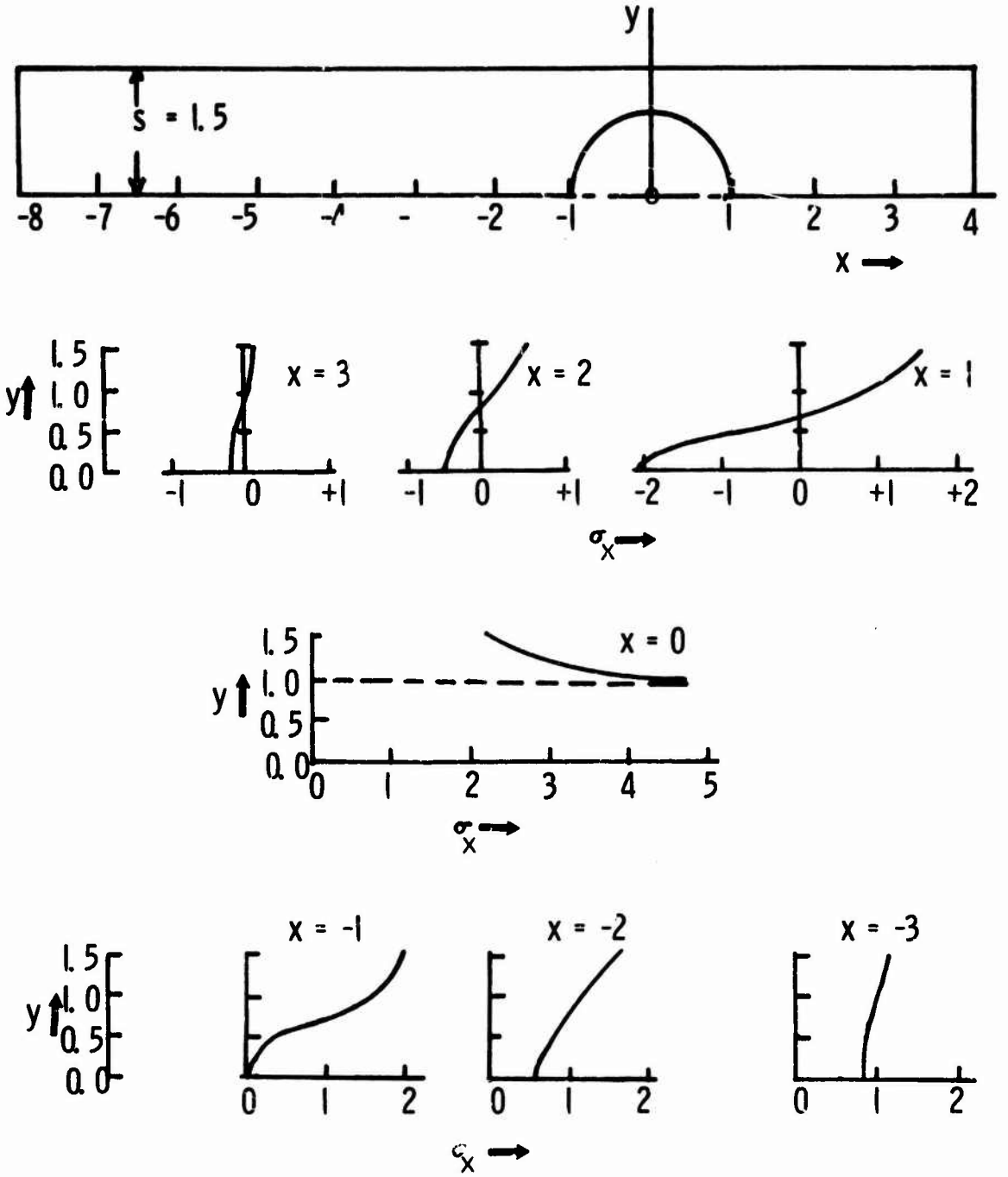

Fig. 3 Variation of Axial Stress Profile along x-Axis, $0_2 \pm 45$ Graphite Epoxy, e/D = 2, s/D = 0.75, L/D = 4 (Multi-Pin)

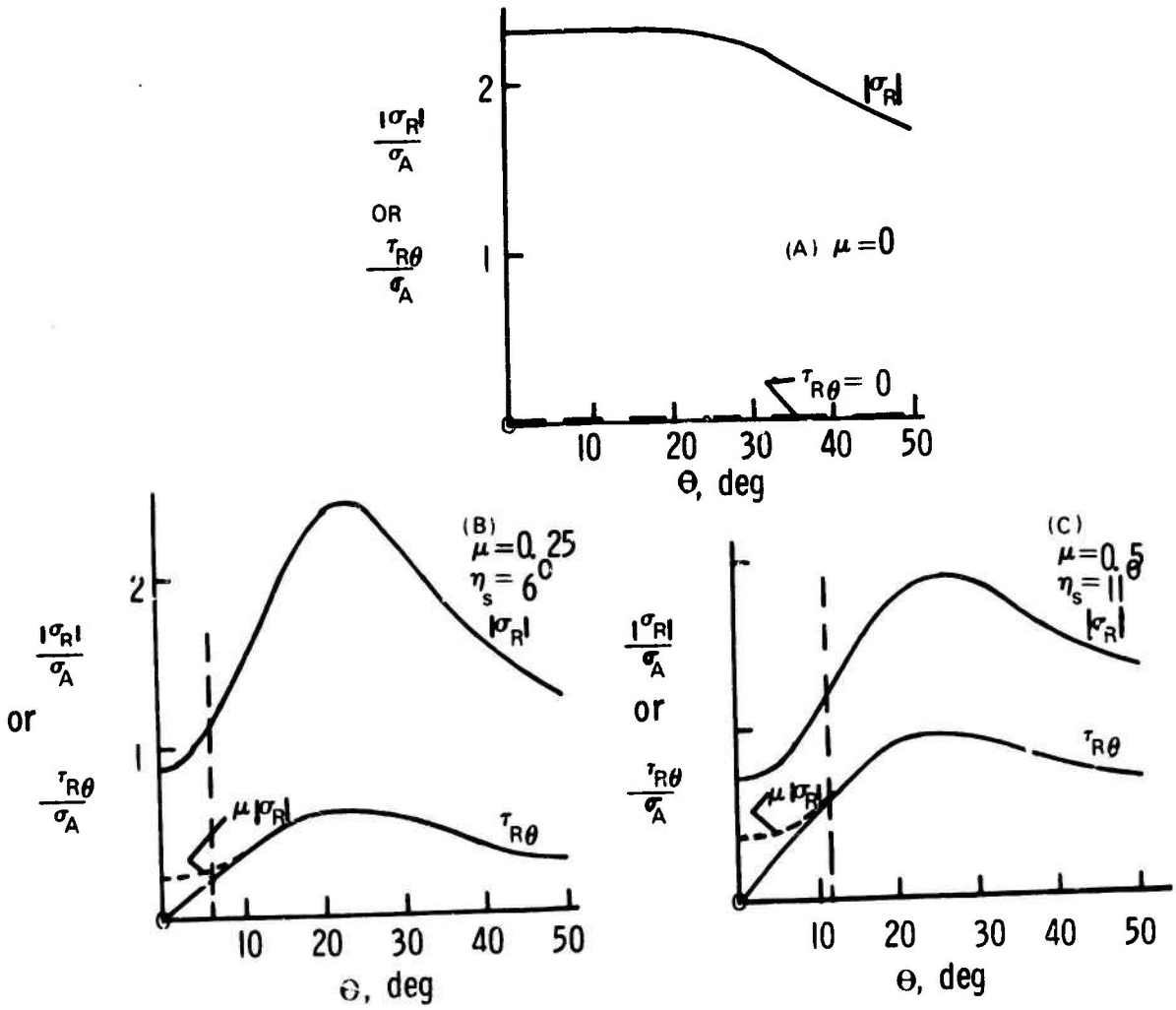

Fig. 4 Effect of Friction on Radial And Shear Stress Distribution around Fastener Hole, $0_2^{\pm}45$ Graphite Epoxy--e/D = 4, s/D = 1 (multi-pin)

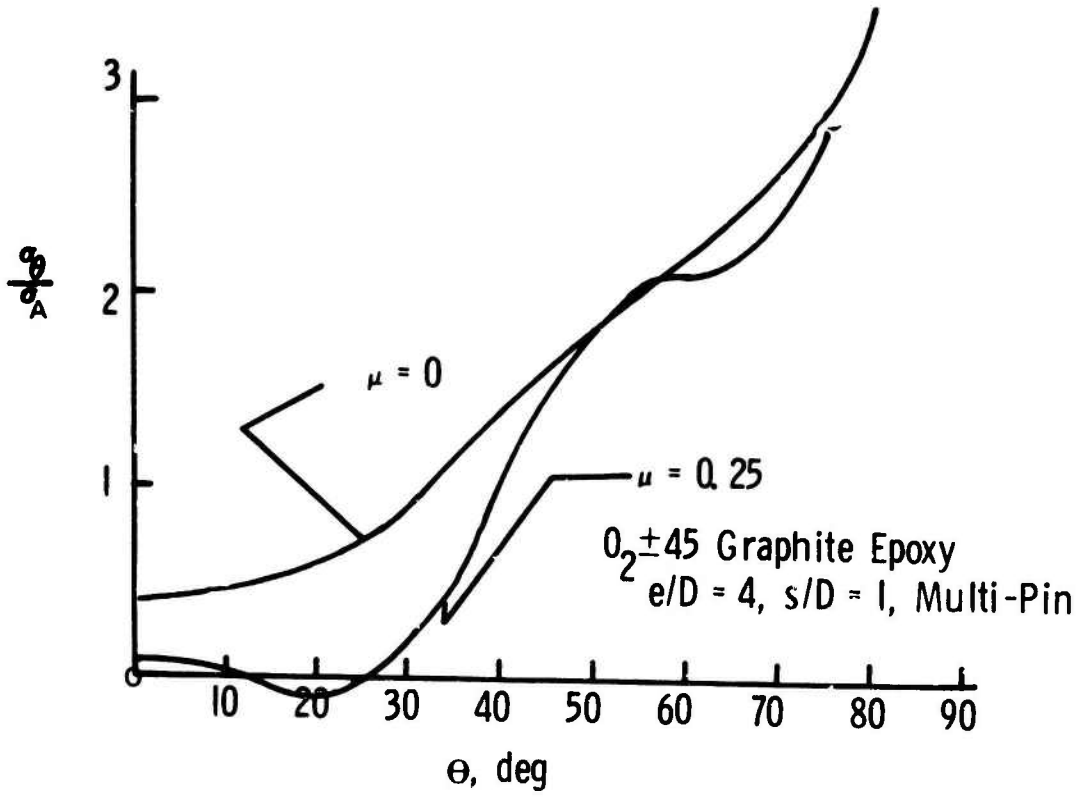

Fig. 5 Effect of Friction on Hoop Stress Distribution around Fastener Hole

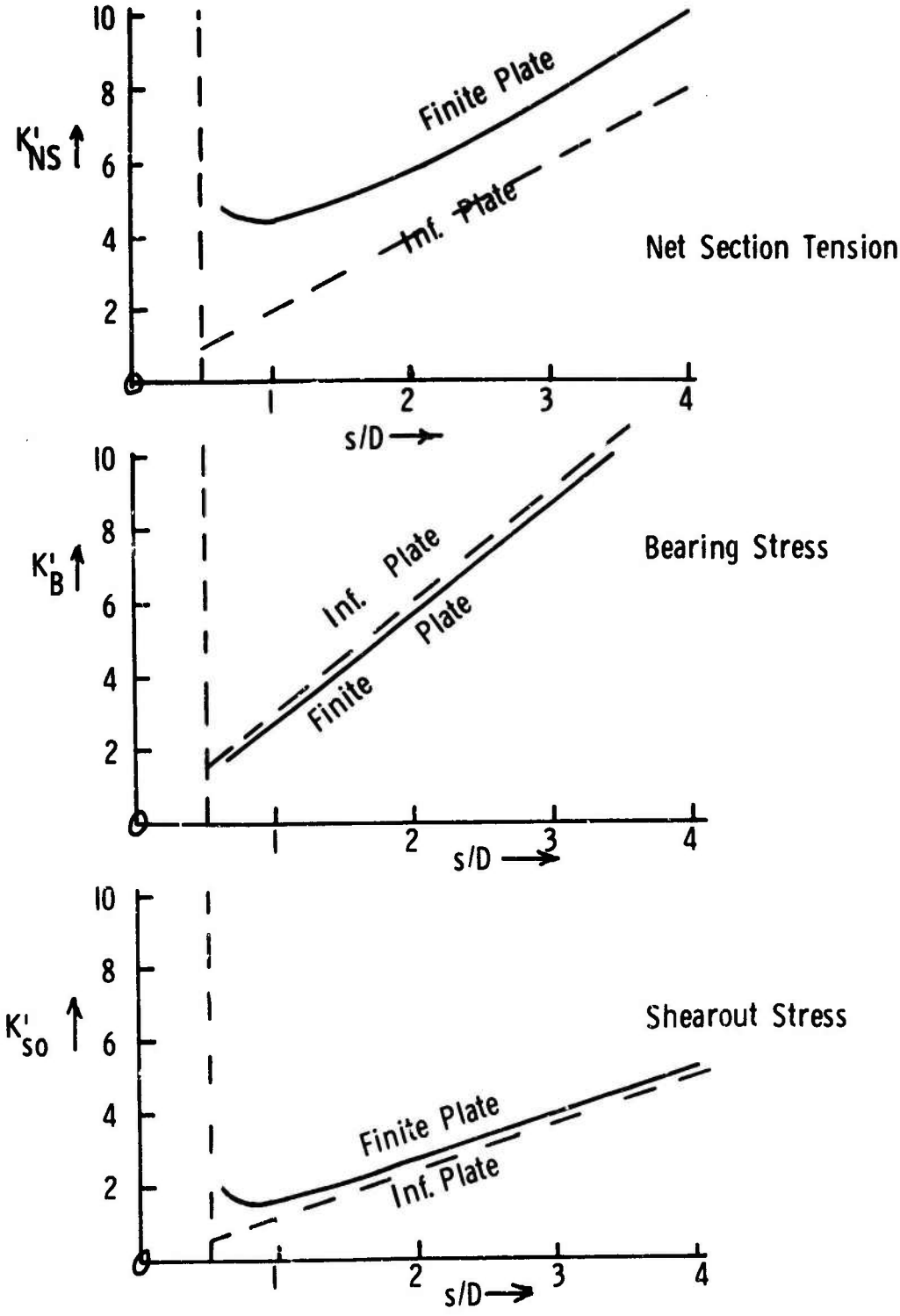

Fig. 6 Stress Ratios vs. Fastener Spacing, $0_2 \pm 45^0$ Graphite Epoxy--e/D = 4

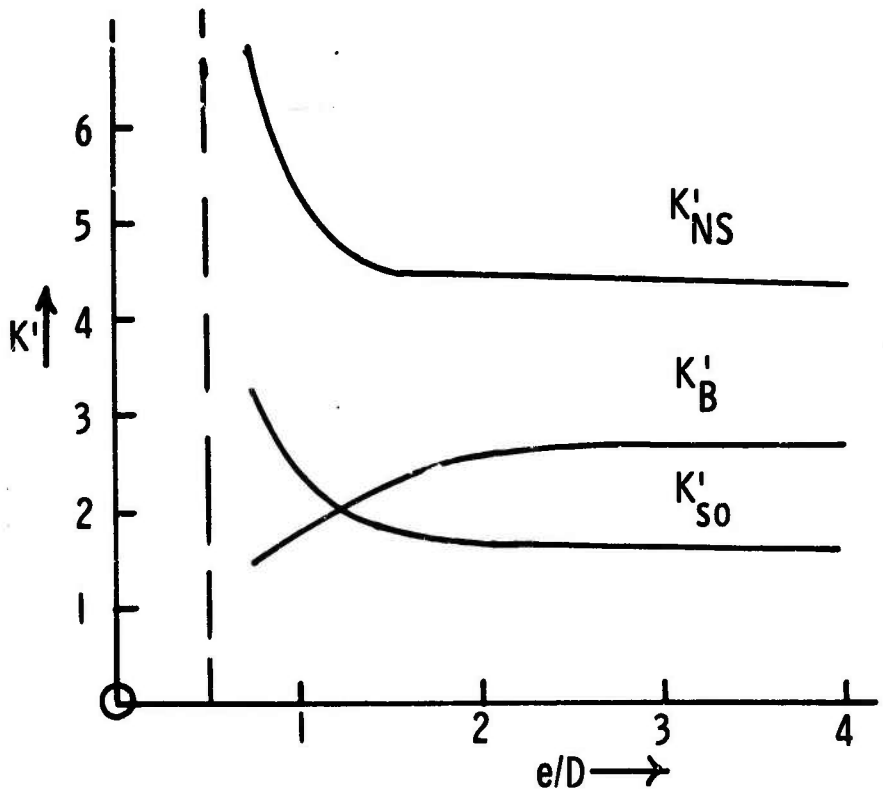

Fig. 7 Stress Ratios vs. Edge Distance, $0_2 \pm 45$ Graphite Epoxy--s/D = 1

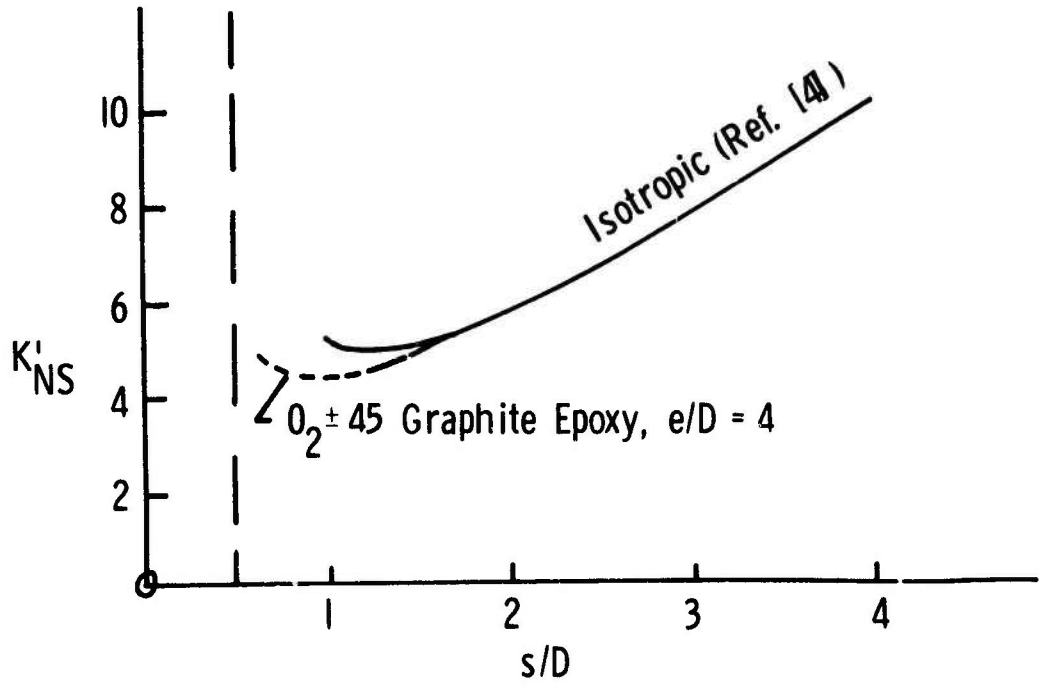

Fig. 8 Comparison of Net Section Stress Concentration Factor for Isotropic Plate and Graphite Epoxy Laminate

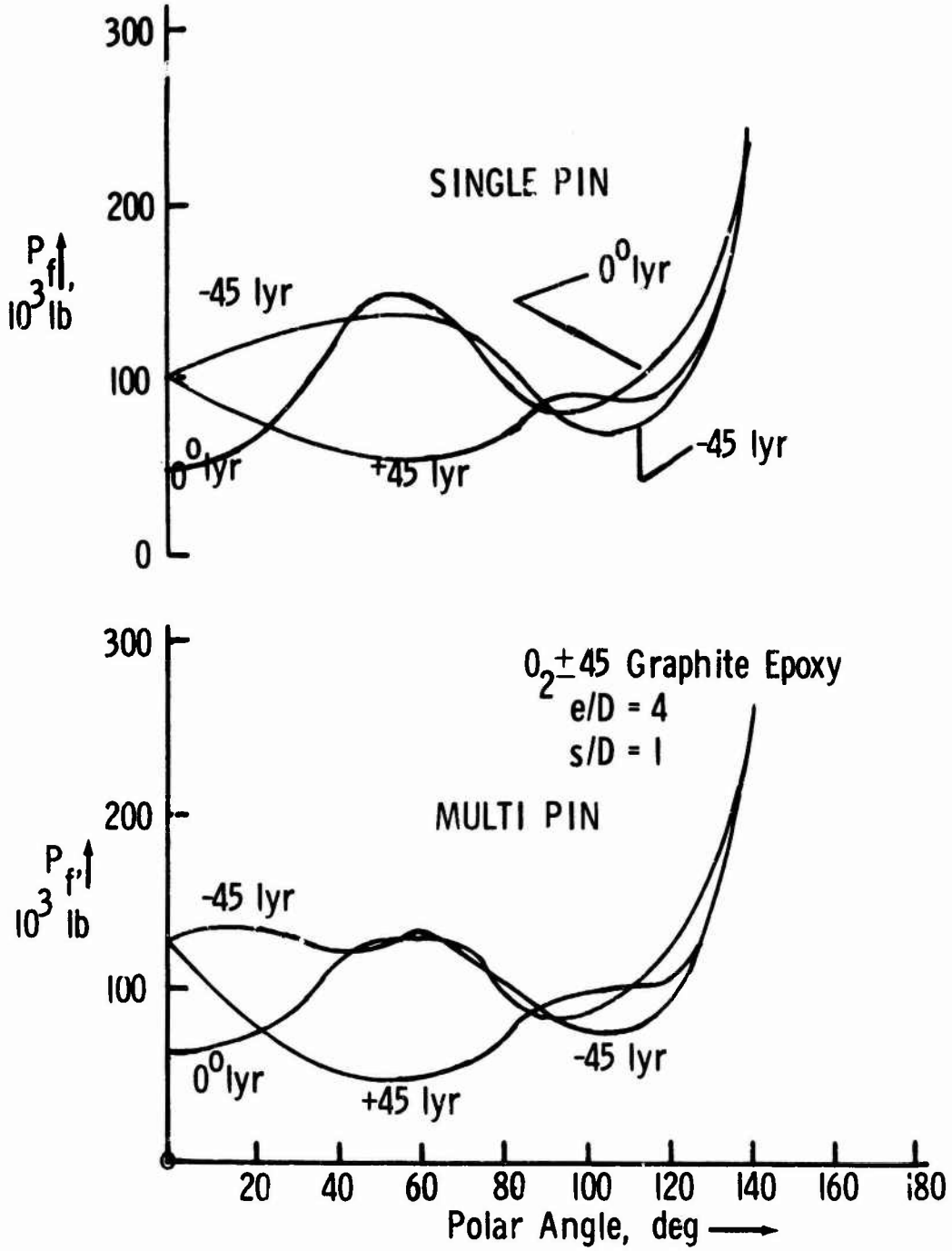

Fig. 9 Failure Load Distribution Around Fastener Hole, FRICTIONLESS

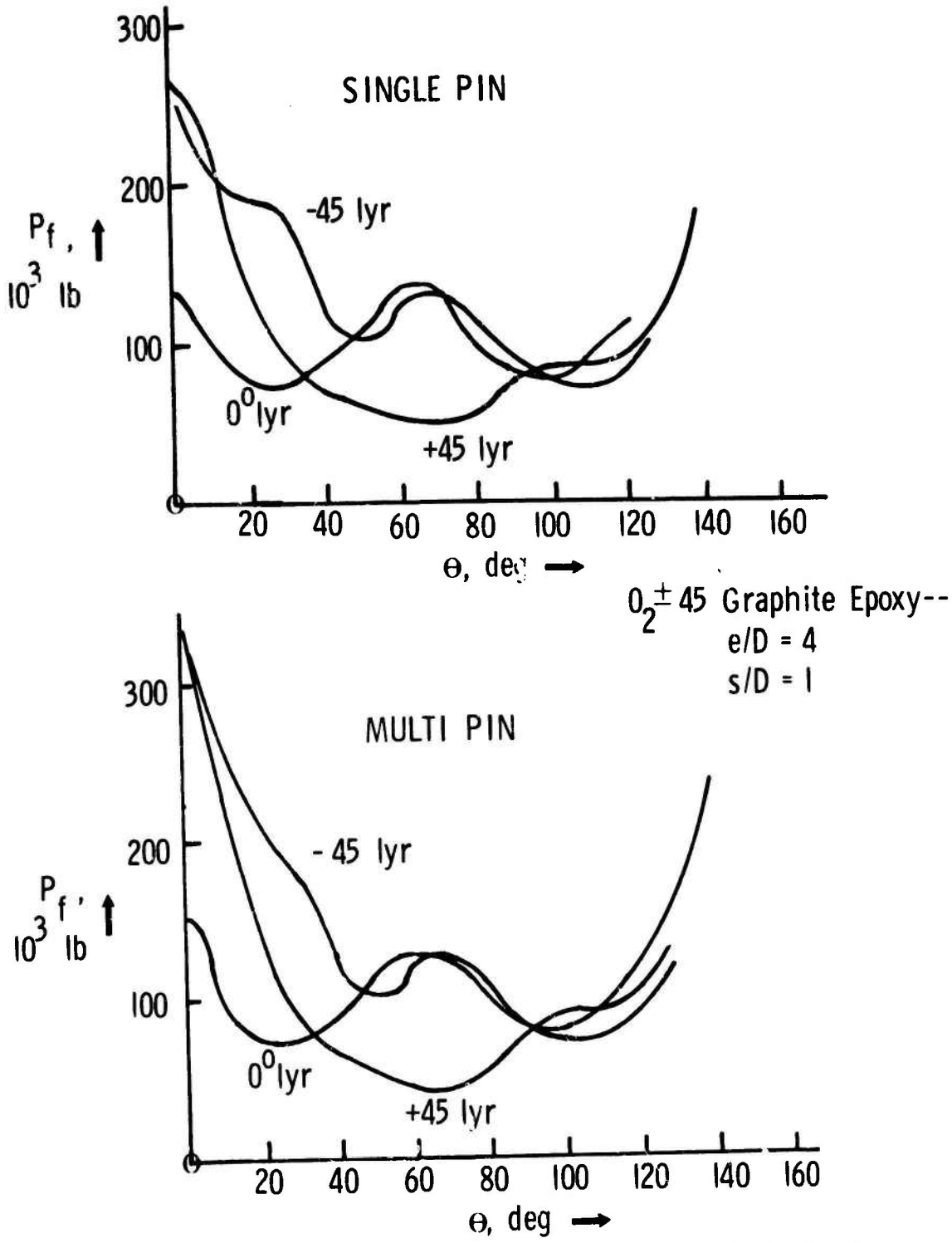

Fig. 10 Failure Load Distribution around Fastener Hole, Friction Present ($\mu = 0.25$)

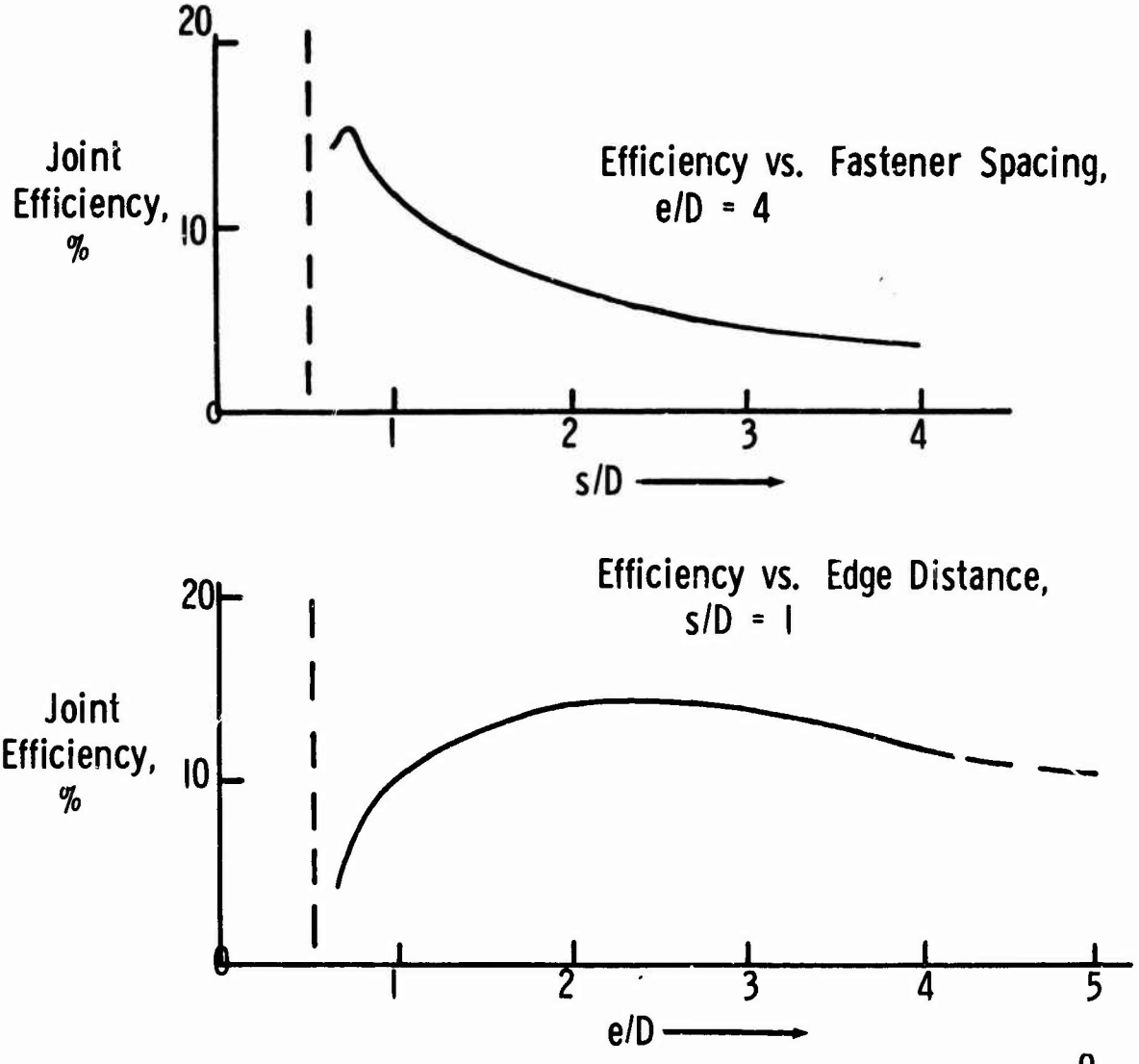

Fig. 11 Effect of Geometry on Mechanical Joint Efficiency, $0_2 \pm 45^0$ Graphite Epoxy

SESSION V - DESIGN APPLICATIONS

Chairman: I. Weitzler
Chief, Applied Technology Division, Aeromechanical Laboratory
Army Natick Laboratories

BONDED COMPOSITE-TO-METAL SCARF JOINT PERFORMANCE IN AN AIRCRAFT LANDING GEAR DRAG STRUT

W. E. HOWELL
Aero-Space Technologist
Langley Research Center
Hampton, Virginia

ABSTRACT

The structural performance of a boron-epoxy reinforced titanium drag strut, which contains a bonded scarf joint and was designed to the criteria of the Boeing 747 transport, has been evaluated. An experimental and analytical investigation was conducted. The strut was exposed to two lifetimes of spectrum loading and was statically loaded to the tensile and compressive design ultimate loads. Throughout the test program no evidence of any damage in the drag strut was detected by strain gage measurements, ultrasonic inspection, or visual observation. An analytical study of the bonded joint was made using the NASA Structural Analysis Computer Program NASTRAN. A comparison of the strains predicted by the NASTRAN computer program with the experimentally determined values shows excellent agreement. The NASTRAN computer program is a viable tool for studying, in detail, the stresses and strains induced in a bonded joint.

INTRODUCTION

Aircraft designers are continually endeavoring to develop more efficient structures. The use of high modulus fibers, such as boron and graphite, in a polymeric matrix is one such endeavor. Whether these composite materials are used for entire structural components or for selective reinforcement of metallic structures, almost all applications have structural attachments consisting of metallic fittings or concentrated load points. Developing an efficient design for the transition from composite to metal has been one of the major problem areas encountered in the use of composites. To solve this problem, a number of different bonded joint configurations such as lap shear, scarf, and step joints have been proposed (refs. 1, 2, and 3). In the design of such bonded joints, an understanding of the stresses and strains induced in the joints by applied loads is needed in order to develop the most efficient structures.

The purpose of this investigation was to conduct an experimental and analytical evaluation of a bonded scarf joint in a boron-epoxy reinforced titanium landing gear drag strut for the Boeing 747 transport. The experimental investigation consisted of both cyclic and static loading. The analytical evaluation involved the use of the NASA Structural Analysis Program NASTRAN (ref. 4) to compute the stresses and strains induced in the bonded joint. Comparisons are made between the analytical and experimental strains in the bonded joint.

The units used for the physical quantities are given in the International System of Units (SI) and in the U. S. Customary Units. Factors relating the two systems are given in reference 5.

TEST SPECIMEN

The test specimen was a boron-epoxy reinforced titanium drag strut structure designed and fabricated by the Boeing Commercial Airplane Company as a company-sponsored program. Concepts developed under NASA contract (ref. 1) were used in the design in a manner to satisfy the performance specifications of the main body landing gear of the Boeing 747 transport aircraft (fig. 1). Details of the strut are shown in figure 2. Except for the ends, where the strut is entirely laminated titanium, unidirectional boron-epoxy was used to stiffen the thin titanium cover skins and provides 80 percent of the load carrying capabilities of the strut. A titanium strap which had a uniform 0.017 rad. (1^{o}) tapered scarf and a 16-ply boron-epoxy strap in which the plies terminated at 1.02 cm (0.4 in.) steps were bonded together in a co-cured process. Eight of these straps were secondary-bonded together to form the complete load carrying portion of the flanges. (See figure 2b.)

Figure 2c is a cross-sectional view of the I-beam configured strut and shows the boron-epoxy reinforcement at the extremities of the flanges. The remainder of the strut was fabricated of titanium faced aluminum honeycomb-core sandwich. No mechanical fasteners were used; the entire strut was adhesively bonded together. The total mass of the completed strut is 34.5 kg (76 lbs), 30 percent less than the production drag strut.

TEST PROCEDURES AND RESULTS

The experimental evaluation of the drag strut was conducted at the NASA-Langley Research Center. Three different tests were performed on the drag strut: fatigue test, static tension test to the design ultimate load, and static compression test to the design ultimate load. (See fig. 3.) The behavior of the drag strut during these tests was monitored by strain gages located on the flanges in the vicinity of the bonded joints as shown in figure 2b, as well as at a number of other locations.

FATIGUE TEST

The drag strut was exposed to two lifetimes of spectrum loading in the 1.78 MN (400 kip) capacity fatigue test machine. A sample of the spectrum is shown in figure 4. This spectrum is associated with training flights, 1-hour flights, 3-hour flights, and 7-hour flights. Each of the four types of flights has distinct mean and alternating loads. The load spectrum consisted of these four different load levels randomly arranged in a block of 33 cycles. This block of loading was applied repeatedly until two lifetimes of loading (198,000 cycles) were accumulated. The cyclic load was applied at a rate of 5 Hz. No hysteresis heating was detected. The peak

load in the spectrum, 355 kN (79,800 lbs) in tension, which is only 22 percent of the design ultimate load was applied once every 100 blocks of loading for a strain survey. This data was used to monitor any changes which might occur in the strut due to the cyclic loading. A sample of this data is shown in figure 5 where strain is plotted as a function of the number of cycles of loading and shows no significant change in the strain during the test. The small, random variation is believed to have been caused by ambient temperature changes during the test.

At the conclusion of two lifetimes of spectrum loading, the strut was visually and ultrasonically inspected and no damage was detected.

TENSILE TEST

After the fatigue test was completed, the drag strut was mounted in the 5.34 MN (1,200 kips) capacity static testing machine (fig. 3) and was loaded in tension to the design ultimate load of 1.65 MN (372 kips). Figure 6 is a plot of some of the strain gage data as a function of applied load. The measured strain for the four gages positioned over the end of the first ply of boron-epoxy (gages 1, 2, 3 and 4 in fig. 2) indicates that the strut behaved in a linear manner. Maximum strain in boron-epoxy sections was approximately 0.0038 at the tensile design ultimate load. There was no indication of any damage due to the loading.

COMPRESSION TEST

Following the tensile test the strut was mounted in the compression side of the 5.34 MN (1,200 kips) capacity static testing machine (fig. 3) and loaded to the compression design ultimate load of 2.83 MN (636 kips). Figure 7 is a plot of the compression data obtained from strain gages 1, 2, 3, and 4 shown in figure 2. Maximum strain at the compression design ultimate load was approximately 0.0060 in the boron-epoxy sections. Again, the data indicates that the strut behaved in a linear manner and survived the load with no apparent damage.

Similar data was obtained from strain gages at the other end of the strut and at several locations along the length of the strut. There was no indication of any buckling condition being approached.

NASTRAN MODEL

The finite element model developed was that of a bonded step joint and represented a section of the drag strut bonded joint. The model included the face sheet, adhesive layer, titanium strap with 16 steps, one ply of boron-epoxy bonded to each step, and a second adhesive layer which is located between the first and second straps (fig. 8). Since each ply of boron-epoxy in the drag strut ended in discrete steps, a uniformly stepped joint was used to model the steps and the scarf portion of the titanium strap. Each ply of

boron-epoxy was divided into equal volumes of boron and epoxy. The boron filament volume was assumed to be distributed in a continuous, uniform layer sandwiched between equal volumes of epoxy.

The NASTRAN program used in this study computes stresses at the centroid of each element. The boundary conditions consisted of constraining the left edge of the model in figure 8 while a uniform displacement in the direction of the fibers was applied to the right edge of the model. The parameters computed in this study consisted of the shear, axial, and normal stresses; forces at the constrained grid points; and displacements of the grid points.

NASTRAN RESULTS

Shear stress data obtained for the NASTRAN model are presented in figure 9 where the normalized shear stress is plotted as a function of position along the joint model. The curve represents the shear stress pattern of the row of elements containing the epoxy matrix of the first ply of boron-epoxy. At the left edge of the model in the titanium strap the shear stress is zero. The stress remains small up to the first step, at which point the peak stress [70.0 MPa (10.20 ksi)] in the titanium occurs. The next element which is the first element of epoxy has a considerably lower stress value of 26.1 MPa (3.78 ksi); but the peak matrix shear stress 37.5 MPa (5.44 ksi) occurs in the second epoxy element. This peak matrix shear stress is approximately 50 percent of the matrix material shear strength (ref. 1). The stress drops very rapidly from this point to the second step where a second pair of shear stress peaks of considerably lower values occurs. From this point to the right edge of the joint model, the shear stress is very small, essentially zero, with pertubations from subsequent steps of negligible stress values.

In figure 10 the normalized axial stress of the first ply of boron is plotted as a function of distance along the model. The stress increases rapidly along the length of the first step. At the start of the second step there is another abrupt increase in the axial stress of the fiber to the maximum value of 1,420 MPa (206 ksi). This increase is caused by the decrease in effective area due to the epoxy bond at the end of the second fiber. From this point the stress continually decreases, with progressively decreasing pertubations at the successive steps, until the end of the titanium strap is passed. From the end of the strap to the end of the model there are no further changes in configuration and the axial stress is constant at 0.62 times the peak. This figure readily points out where the maximum stress occurs in the boron fiber and aids in understanding the axial stress profile of an individual ply in a bonded step joint.

From the results of the analytical study, the stresses induced in the critical matrix areas during the fatigue loading are small compared to the material strength. Compared to previously developed data (ref. 6), the strut has essentially an indefinite lifetime at the load levels of the fatigue spectrum. The data in reference 6 indicate that the bonded joints in the drag strut would survive at least 10 times the number of cycles they were exposed to.

In order to verify the analytical study of the joint, computed strains were compared to experimental values. This comparison is presented in figure 11 where the applied load is plotted as a function of the measured strain. The solid lines are the experimental data obtained from strain gages along the drag strut bonded joint during static loading to the tensile design ultimate load [1.65 MN (372 kips)]. The symbols represent computed values of strain at model locations that correspond to the specified strain gage locations. These computed strains correspond to the drag strut tensile design ultimate load. Agreement is excellent at the all-titanium area (gage 5), at the first ply of boron-epoxy (gage 1), and at the area beyond the joint in the all boron-epoxy area (gage 6). This figure shows that the NASTRAN finite element analysis is a viable tool for predicting realistic stresses and strains at the working stress levels in a bonded step joint.

CONCLUSIONS

An evaluation of structural performance has been conducted on a boron-epoxy reinforced titanium drag strut containing a bonded scarf joint. An experimental and analytical investigation was performed. The results of this investigation are summarized as follows:

1. Experimental strains obtained in static tensile and/or compressive loading of the drag strut can be predicted by a NASTRAN analysis.

2. The analytical study indicated that the peak shear stresses in the bonded joint were sufficiently low to preclude drag strut failure by disbonding the joint.

3. The drag strut was exposed to two lifetimes of spectrum loading and loaded in tension and compression to the respective design ultimate loads without the occurrence of any detectable damage.

REFERENCES

1. Oken, S., and June, R. R.: "Analytical and Experimental Investigation of Aircraft Metal Structures Reinforced with Filamentary Composites. Phase 1 - Concept Development and Feasibility." NASA CR-1859, 1971.

2. Corvelli, N., and Carri, R. L.: "Evaluation of a Boron-Epoxy Reinforced Titanium Tubular Truss for Applications to a Space Shuttle Booster Thrust Structure." NASA TN D-6778, 1972.

3. Hart-Smith, L. J.: "Analysis and Design of Advanced Composite Bonded Joints." NASA CR-2218, 1973.

4. McCormick, Caleb W. (Editor): "The NASTRAN User's Manual (Level 15)." NASA SP-222(01), 1972.

5. Comm. on Metric Pract.: "ASTM Metric Practice Guide." NBS Handbook 102, U. S. Dep. Com., Mar. 10, 1967.

6. Blichfeldt, B., McCarty, J. E.: "Analytical and Experimental Investigation of Aircraft Metal Structures Reinforced with Filamentary Composites." NASA CR-2039, 1972.

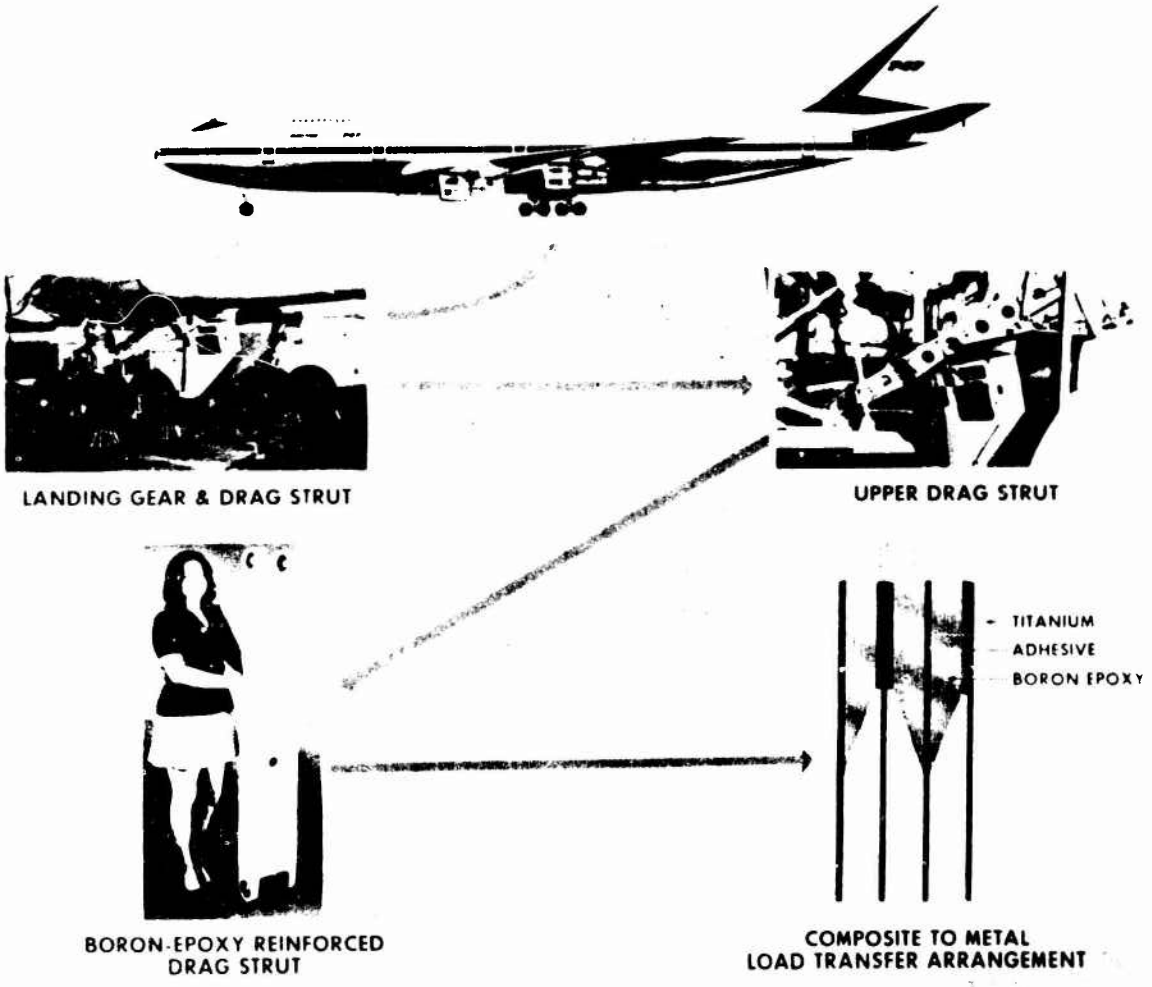

Figure [illegible] - Composite reinforced drag strut for the Boeing 747 transport.

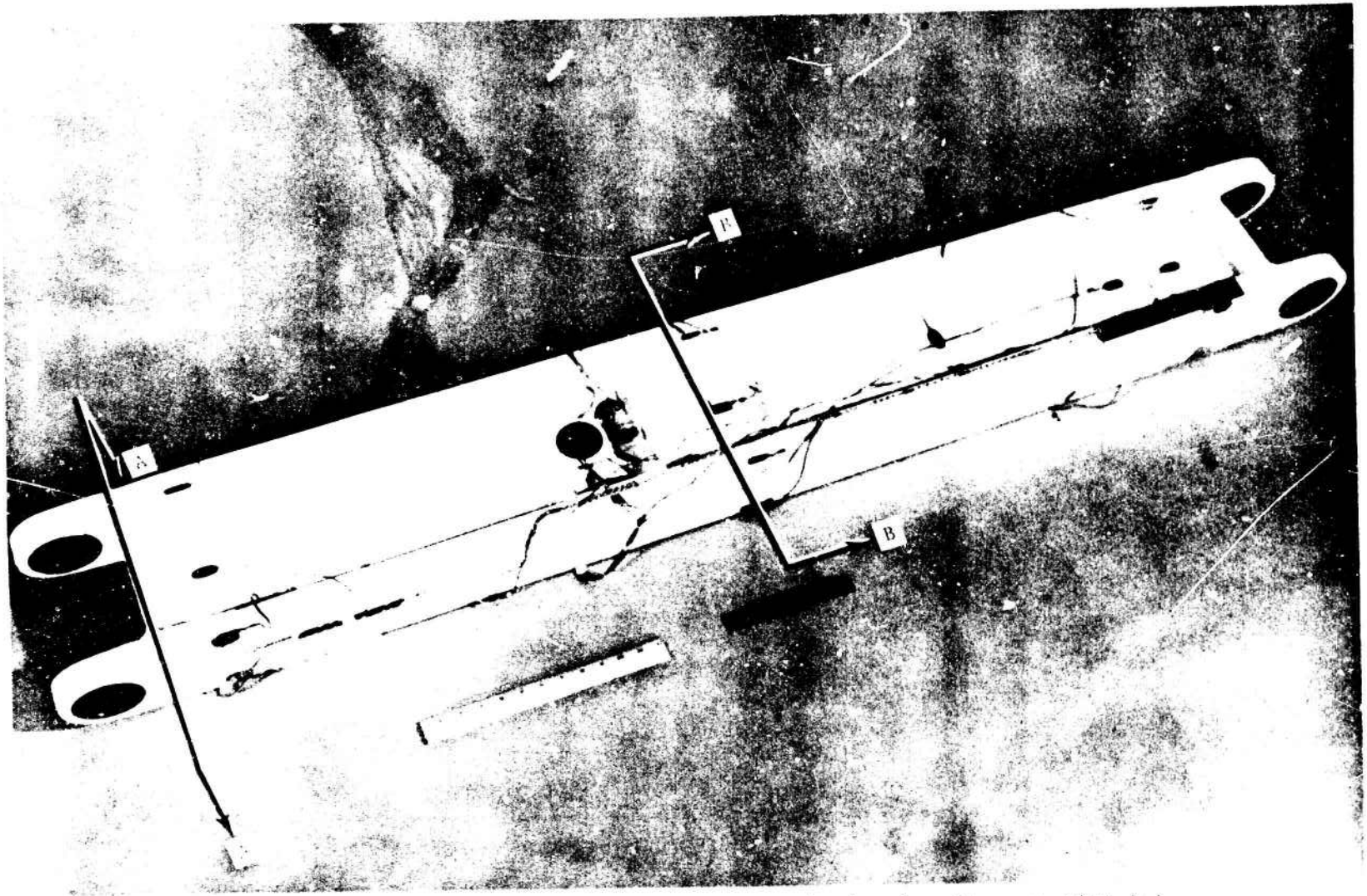

Figure 3a. - Detailed view of drag strut showing locations of view A-A (fig. 2b) and section B-B (fig. 2c).

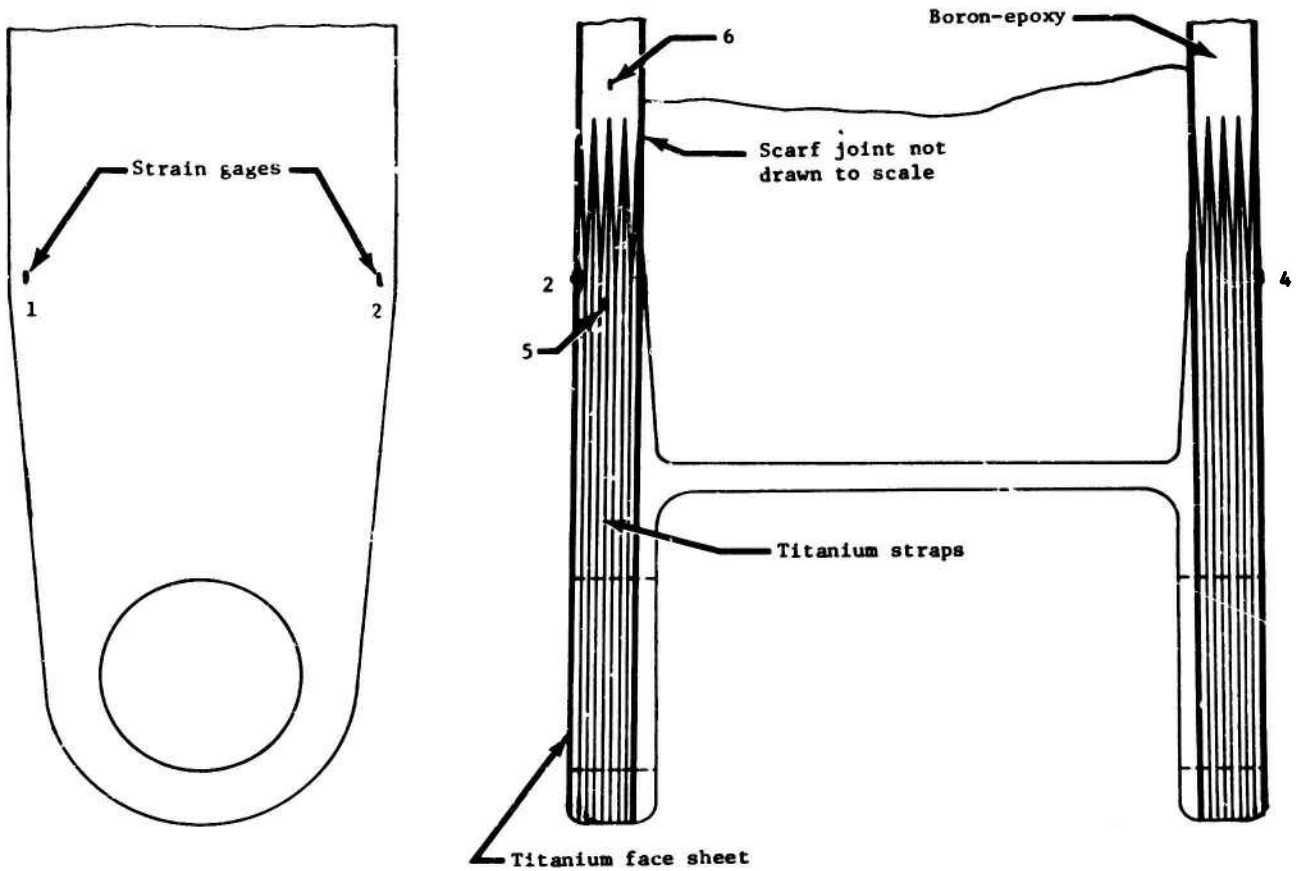

Figure 2b.- Strain gage locations at the boron-epoxy-titanium joints near the ends of the drag strut.

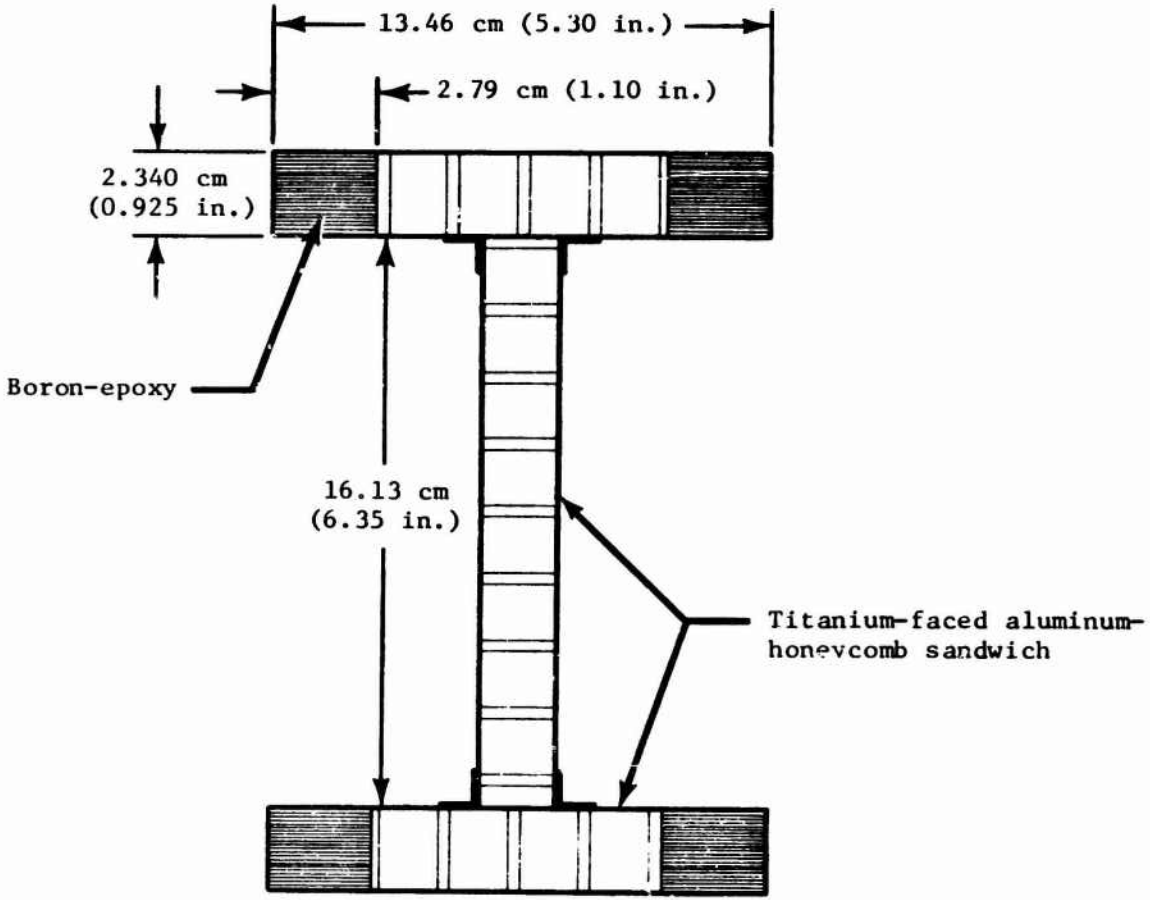

Figure 2[illegible]- Drag strut cross-section at section B-B.

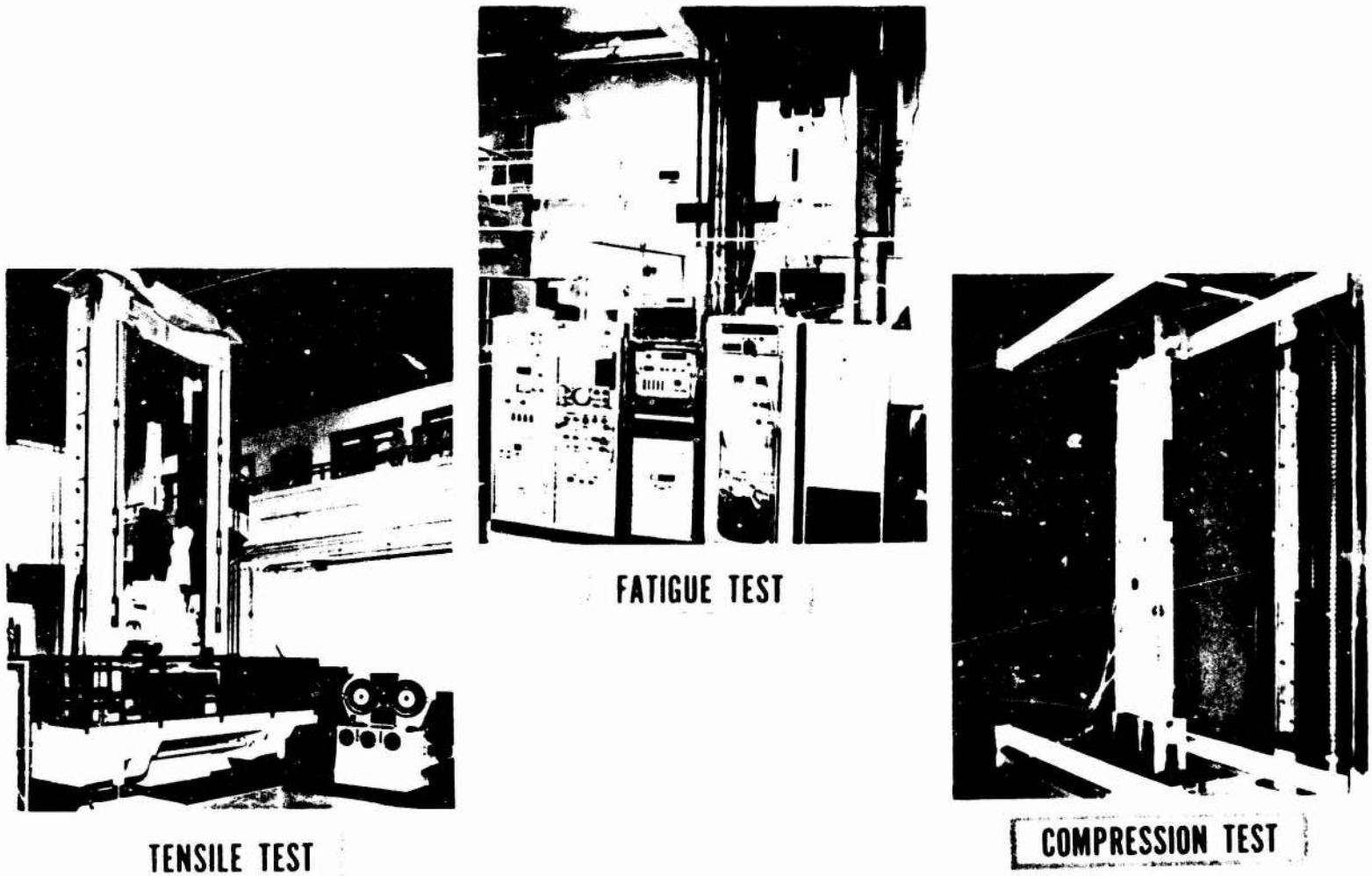

Figure 3. - Experimental test arrangements for composite reinforced drag strut.

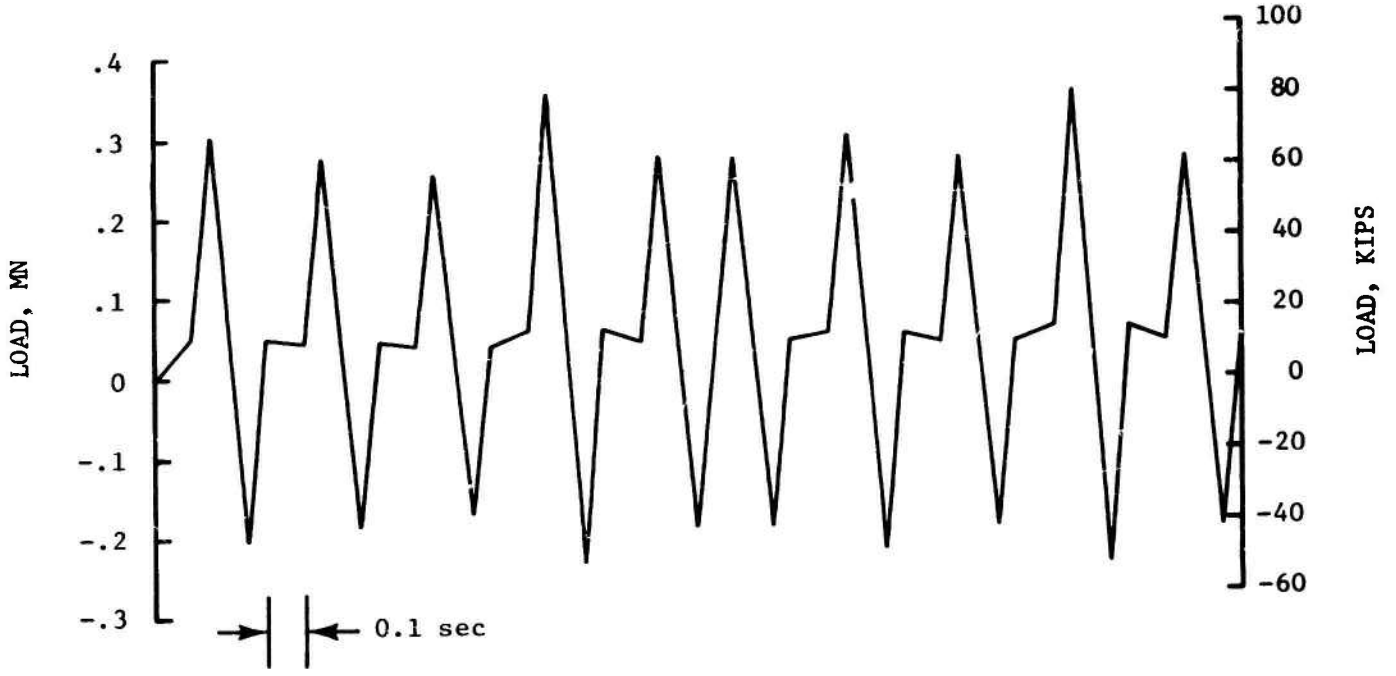

Figure 4.- Sample of the fatigue load spectrum.

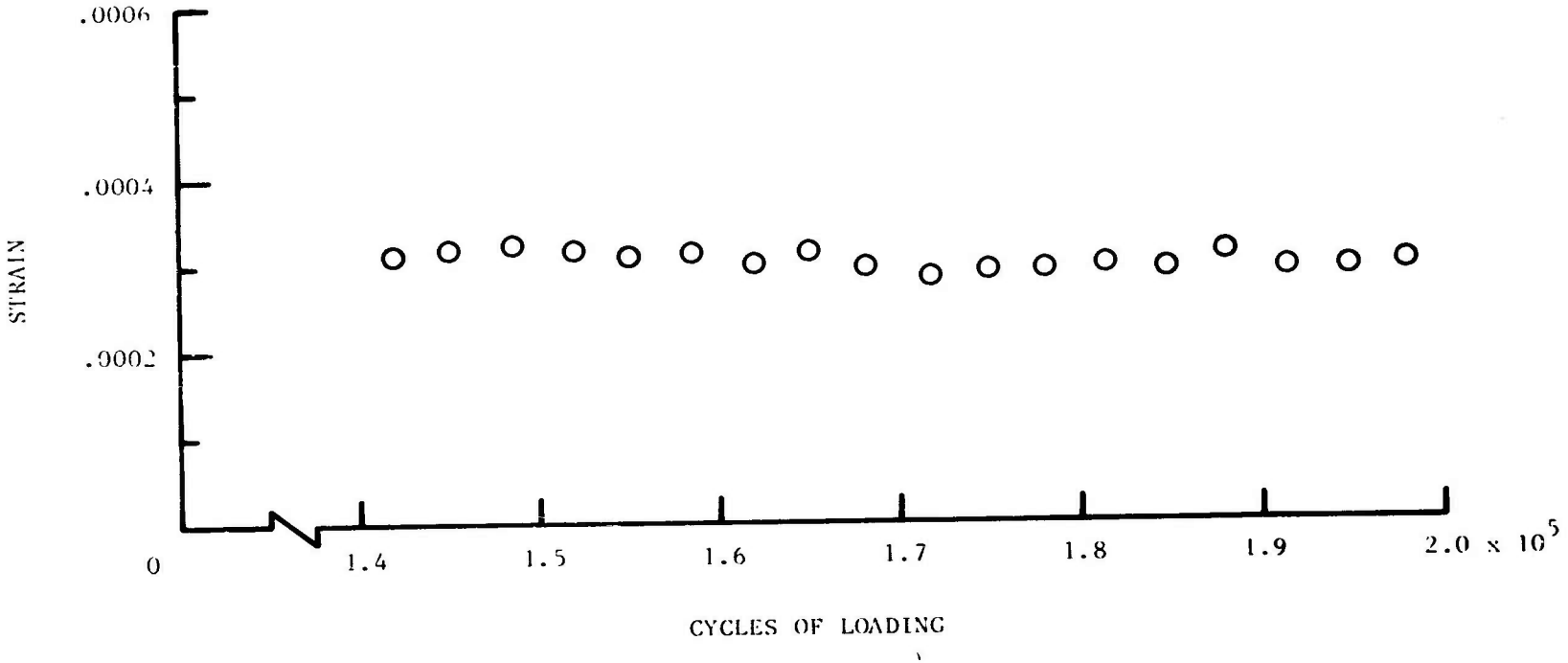

Figure 5.- Strain gage data from fatigue test (one location).

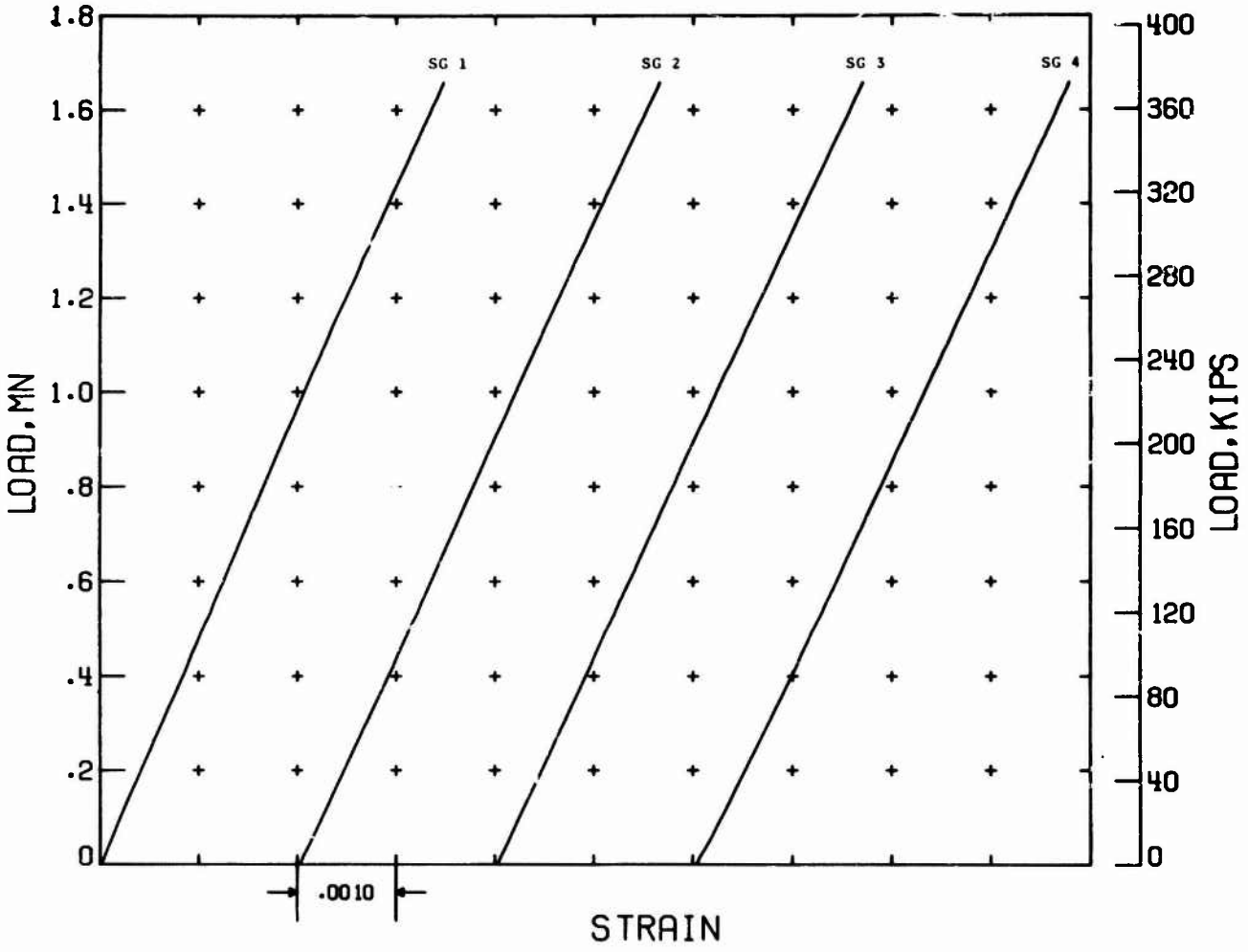

Figure 6.- Strain-gage data for the tensile design ultimate load [1.65 MN (372 kips)].

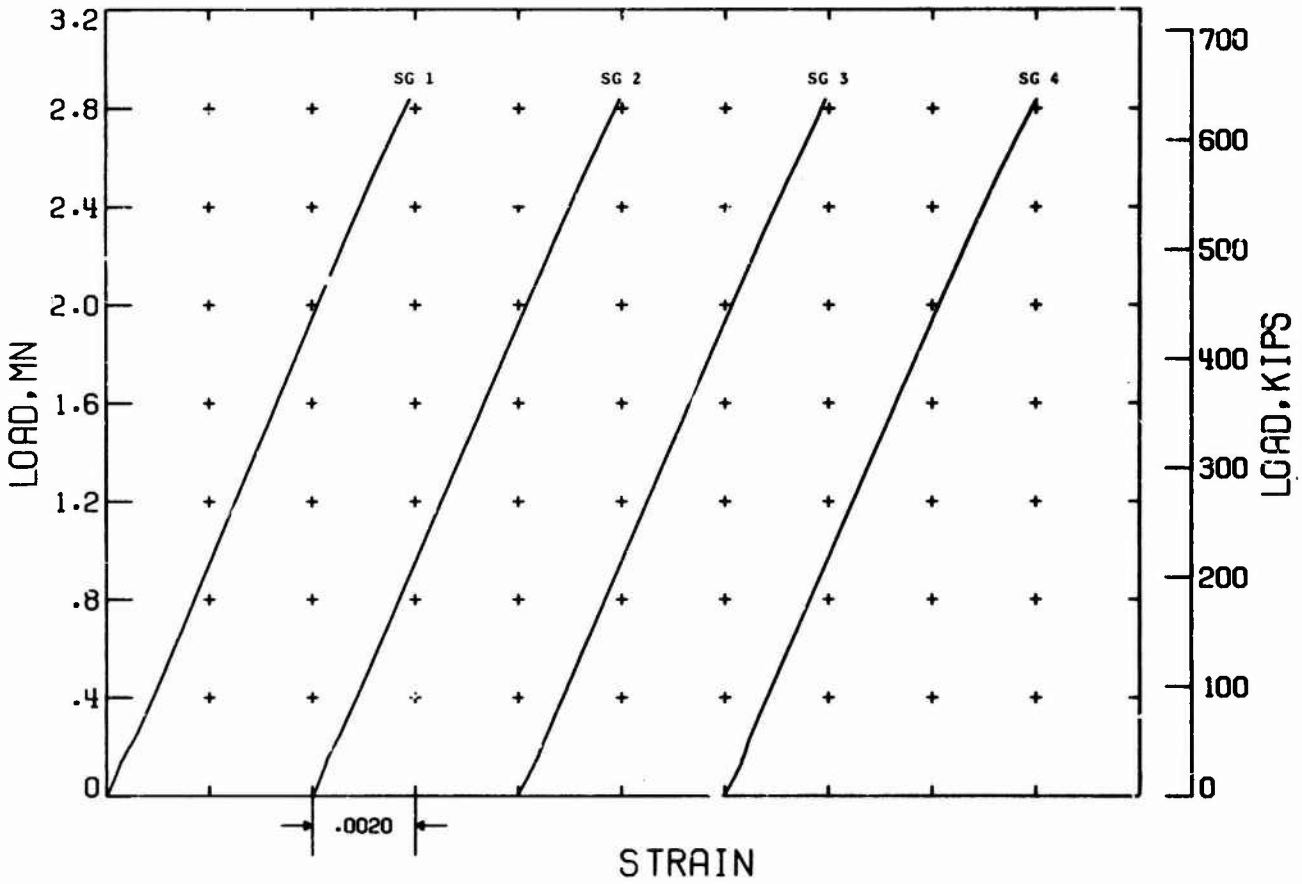

Figure 7.- Strain-gage data for the compression design ultimate load [2.83 MN (636 kips)].

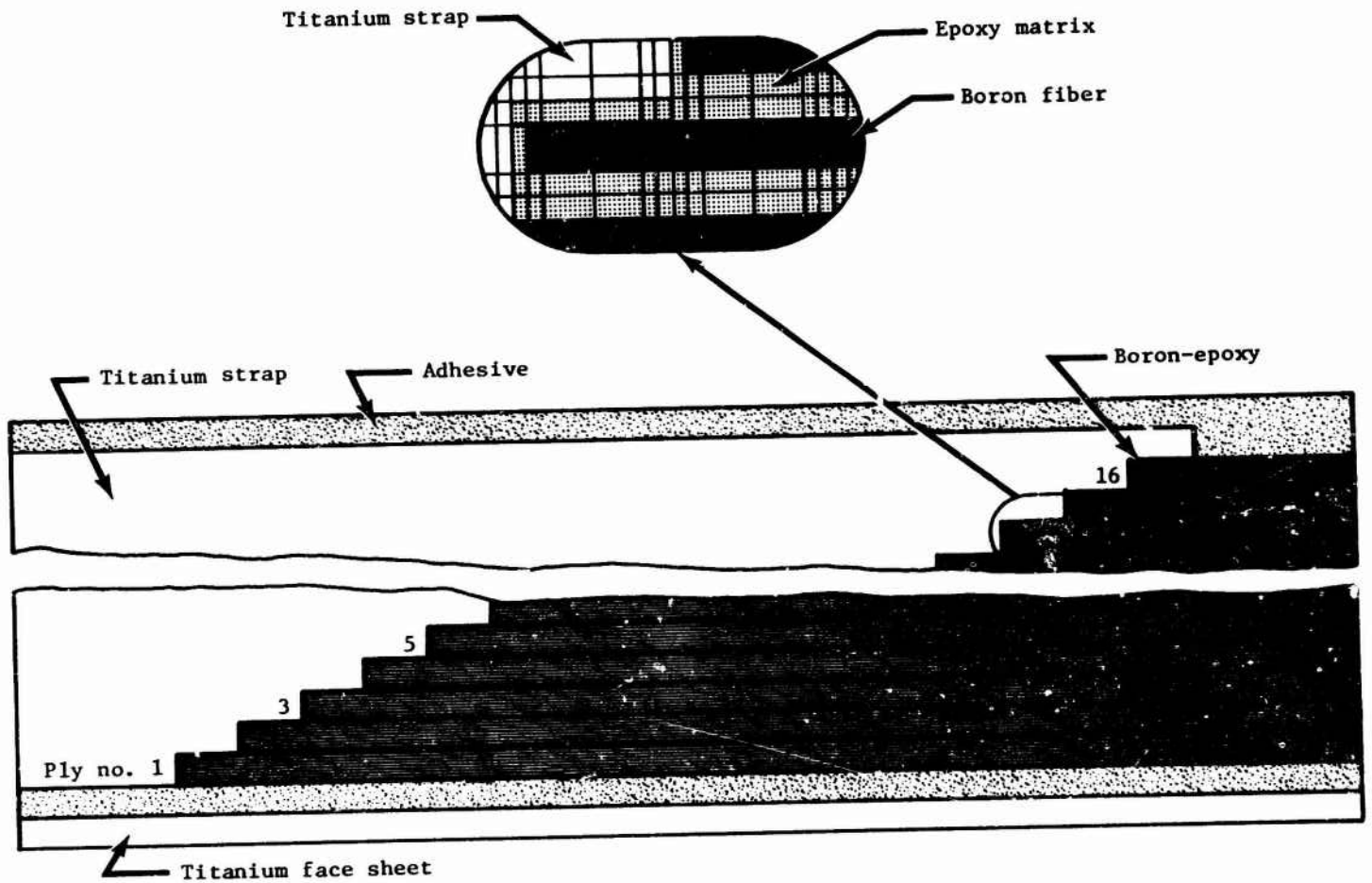

Figure 8.- Structural model used for the analytical study (NASTRAN).

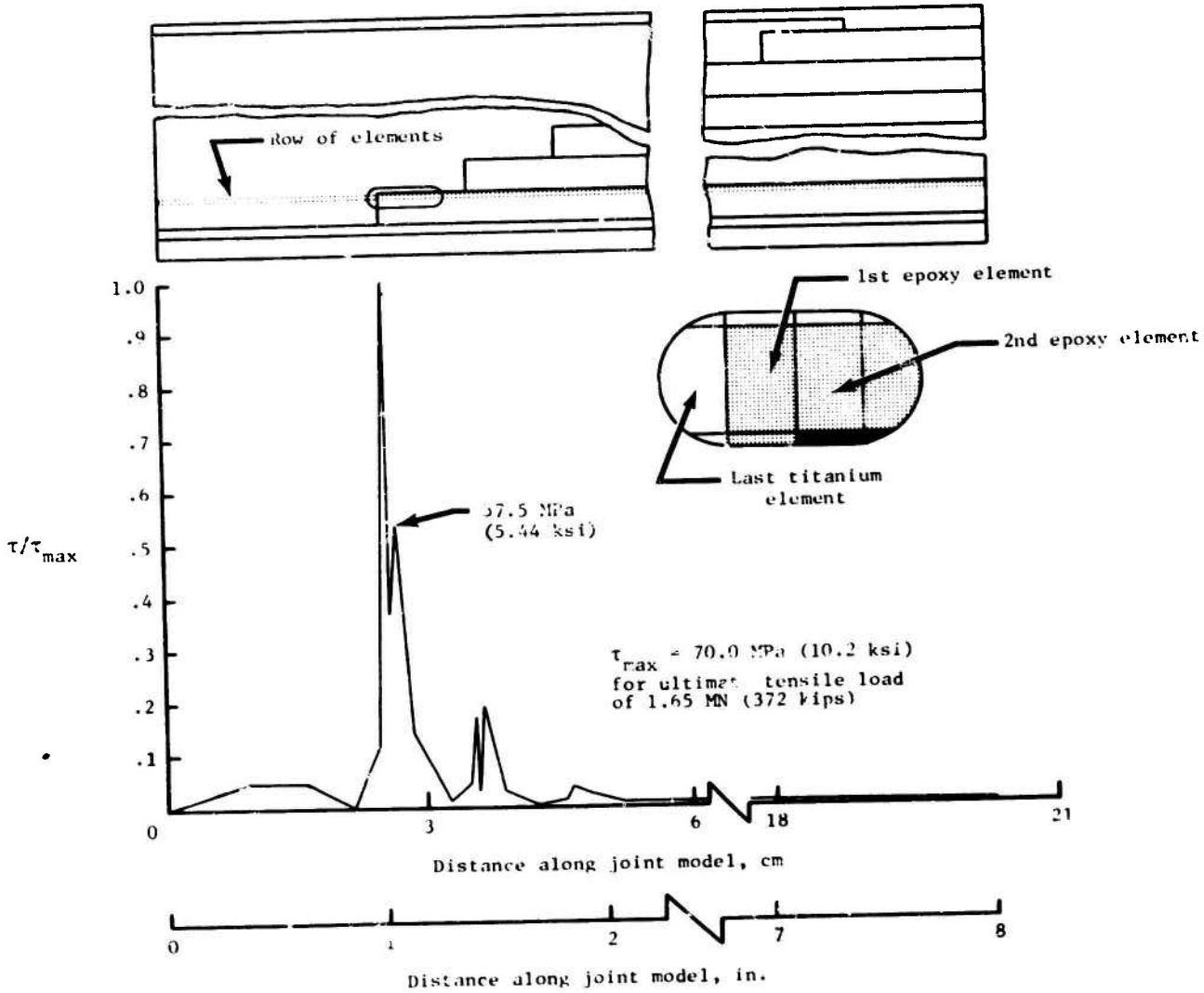

Figure 9. - Shear stress pattern of the row of elements containing epoxy matrix of the first ply of boron-epoxy.

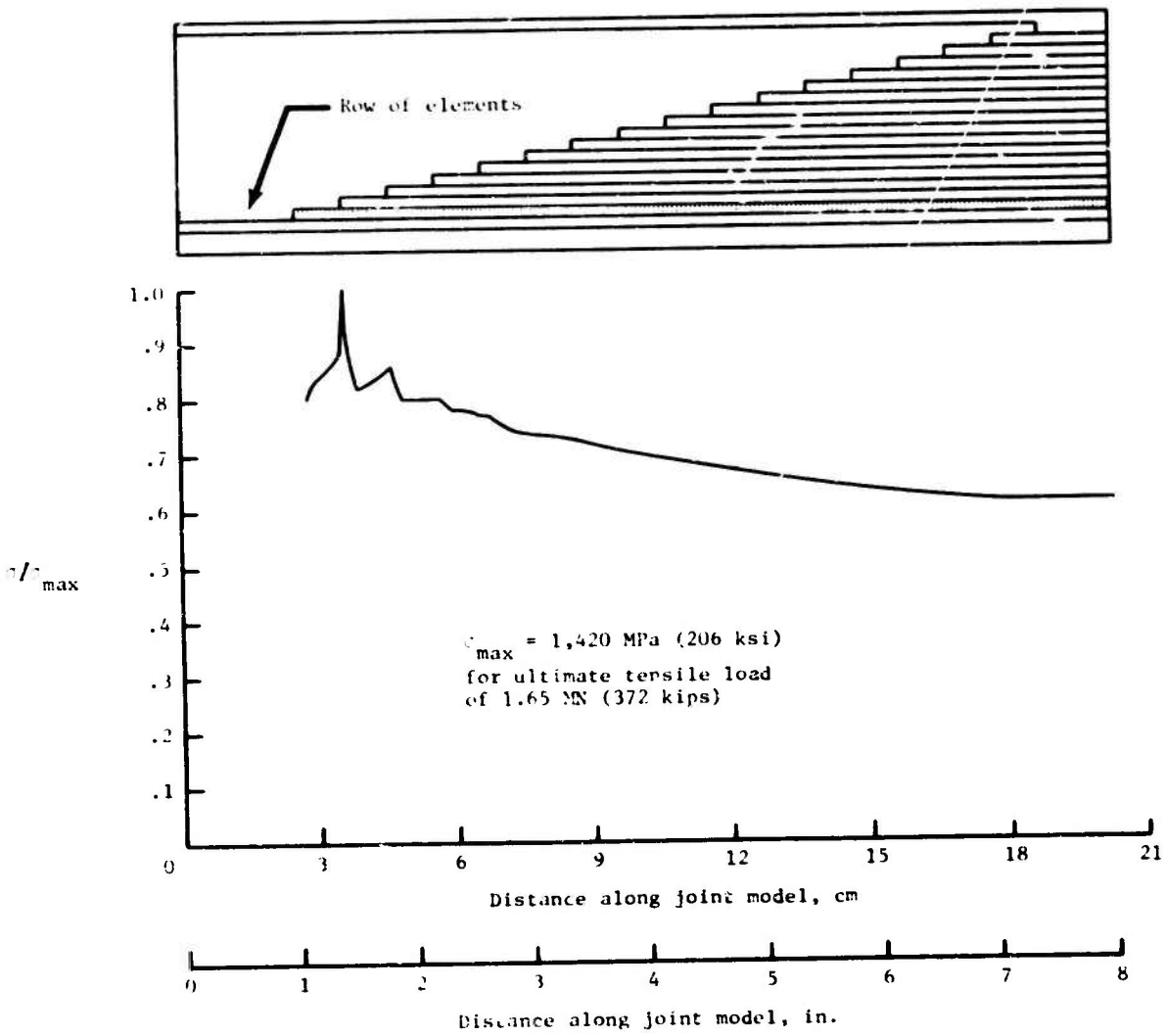

Figure 10. - Axial stress in the first ply of boron fibers.

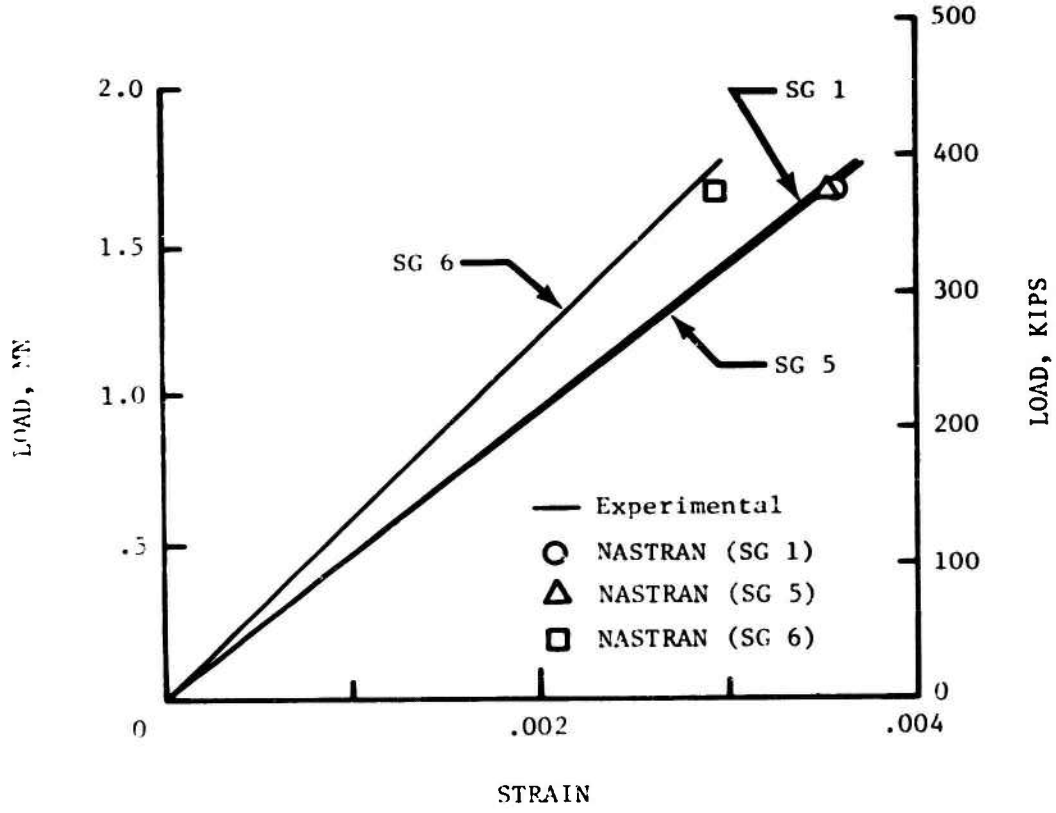

Figure 11. - Comparison of experimentally and analytically determined strains.

GAP EQUALIZATION DESIGN TECHNIQUE FOR SHELL JOINTS

FRANCIS I. BARATTA
Mechanical Engineer

WILLIAM T. MATTHEWS
Mechanical Engineer
Army Materials and Mechanics Research Center
Watertown, Massachusetts 02172

ABSTRACT

The gap equalization concept for the design of shell joints is presented. Equations are developed using a linear, quasi-static analysis. The gap equalization procedure is applied in detail to a shell joint as an illustration for designers.

NOMENCLATURE

A_1	nominal area of leg 1 (see figure 4)
A_1'	contact area of leg 1 "
A_2	nominal area of leg 2 "
A_2'	contact area of leg 2 "
A_T	total area of leg 1 and 2 "
E_1, E_2	modulus of elasticity of materials 1 and 2, respectively
ν_1, ν_2	Poisson's Ratio of materials 1 and 2, respectively
ε_Z	general strain in axial direction
ε_{Z1}	axial strain in leg 1
ε_{Z2}	axial strain in leg 2
ε_{Z2cl}	axial strain at closure in leg 2
ε_{Z2ex}	axial strain in leg 2 above closure
F	total force in joint (see figure 4)
F_{cl}	force at closure at joint
F_b	force in equivalent load system (see figure A-3b)
k_{f1}	stress concentration factor in fillet of leg 1
k_{f2}	stress concentration factor on fillet of leg 2
L	joint length
L_g	gap length

P_g	maximum gas pressure in chamber
p_i	interface pressure between cylinder 1 and 2 (see figure A-1)
p_a	pressure inside the projectile due to hydrostatic loading of explosive
σ_z, σ_θ, σ_n	general axial, circumferential and radial stress, respectively
$\sigma_{\theta 1}$	circumferential stress in cylinder 1 (see fig A-1)
$\sigma_{\theta 2}$	circumferential stress in cylinder 2 (see fig A-1)
σ_{r1}	radial stress in cylinder 1 (see fig A-1)
σ_{r2}	radial stress in cylinder 2 (see fig A-1)
σ_{Z1}	axial stress in leg 1
σ_{Z2}	axial stress in leg 2
σ_{Z1c1}	axial stress in leg i at closure
σ_{Z2c1}	axial stress in leg 2 at closure
σ_{Z1ex}	axial stress in leg 1 above closure
σ'_{Z1ex}	axial stress in contact area at leg 1 above closure
σ_{Z2ex}	axial stress in leg 2 above closure
σ'_{Z2ex}	axial stress in contact area at leg 2 above closure
t_1	thickness of leg 1
t_2	thickness of leg 2
t_{T1}	total thickness of leg 1
t_{T2}	total thickness of leg 2
r_1	fillet radius in leg 1
r_2	fillet radius in leg 2
R_b	outside radius of shell
R_i	interface radius of joint
R_a	inside radius of shell

INTRODUCTION

The increased performance requirements of gun tube-projectile systems have imposed a weight minimization consideration upon the design of shell structural components. At joints between shell components nonuniform stress distributions and locally high stresses often occur. At joints between dissimilar materials, high local stresses can occur as a result of the difference in material characteristics. Nonuniform stress distributions must be minimized to achieve an efficient, weight saving design.

The gap equalization technique is a concept which can achieve efficient design of joints between dissimilar materials. This concept was developed, in a specialized form, for application to a particular shell design *. The concept will be illustrated in idealized terms and then applied in detail to the design of a joint of the XM 517 projectile.

CONCEPT

Consider the idealized configuration shown in Fig. 1a where concentric cylinders of materials 1 and 2 are compressed between rigid heads. The displacement of each cylinder must be equal $\delta_1 = \delta_2$, or:

$$\varepsilon_1 L = \varepsilon_2 L$$

$$\frac{\sigma_1}{E_1} L = \frac{\sigma_2}{E_2} L$$

Therefore:

$$\sigma_1 = \frac{E_1}{E_2} \sigma_2$$

The stress ratio depends only on the modulii of the materials. The stiffer material will be subjected to the higher stress.

However, let it be assumed that a gap, L_g, is provided in the load path of the stiffer material (designated as material 1), Fig. 1b. As the distance between the loading heads is reduced, only the less stiff material is stressed. A schematic illustration of the stress in each material as a

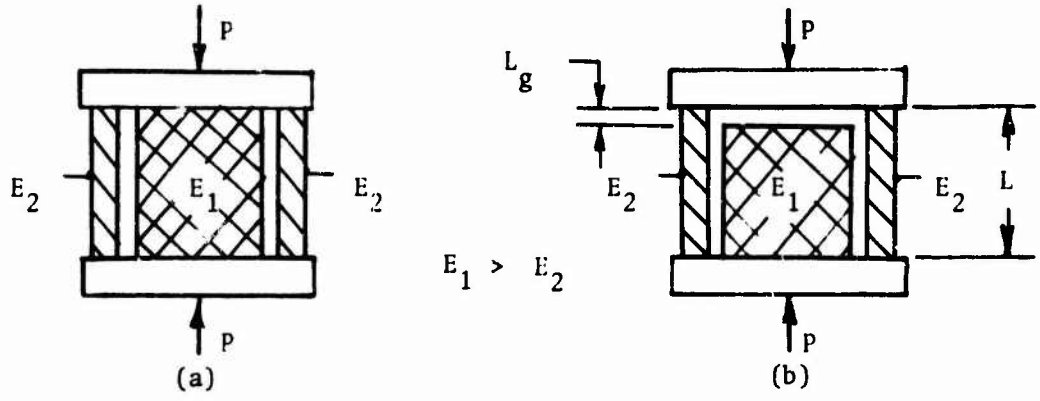

Figure 1 Stress Equalization Concept

* "XM-454 Investigation Conducted by the Staff of Watertown Arsenal", June 1962

function of head displacement or equivalent load resultant and gap length is shown in Fig. 2. Further displacement after gap closure causes stresses in both materials. The stress in the stiffer material increases more rapidly with displacement than σ_2 before gap closure. Also the rate of increase in σ_2 decreases after gap closure since material 1 provides the major resistance to the imposed displacement. The relative magnitude of σ_1 and σ_2 at a particular displacement is a function of the gap length. The gap length may be varied to provide control of these stresses. For example, equalization of stresses σ_1 and σ_2 may be achieved at a particular displacement or load level by controlling the gap length. As shown in Fig. 2, equalization of stresses occurs at load F_1 with gap length L_{g1} or at F_2 with L_{g2}. The effect of equalization of stresses on the efficiency of a practical joint design will be considered later.

It is interesting to note that stress equalization can cause a nullification of a stress concentration factor*. A stress concentration factor normally exists at the fillet between the lap and shoulder at point A in Fig. 3. If σ_1 equals σ_2, the stress is uniform everywhere in the body and the stress concentration is removed. This nullification may be beneficial in general design and in particular for certain types of shell joint configurations.

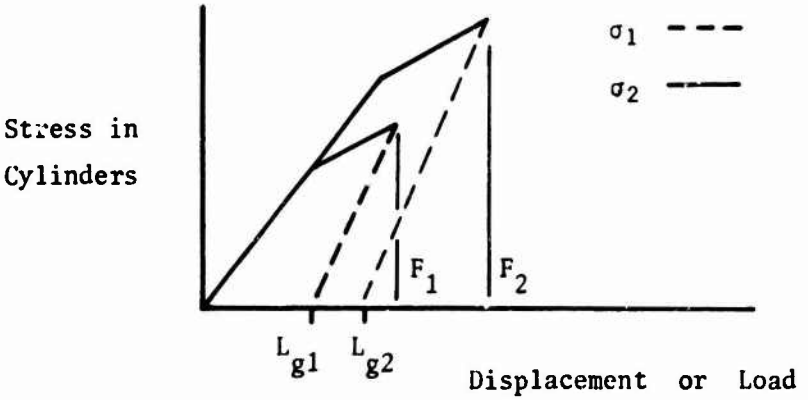

Figure 2 Schematic of Gap Eqalization Behavior

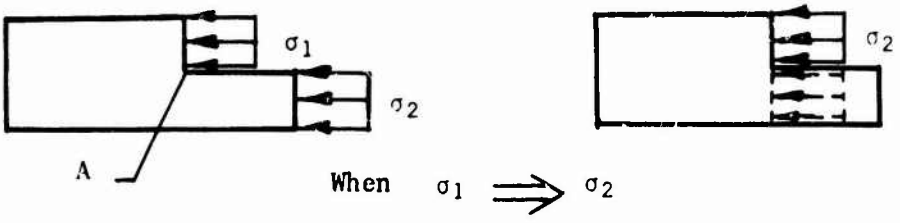

Figure 3 Nullification Of Stress Concentration

* Baratta, F.I. and Bluhm, J.I., "On the Nullification of Stress-Concentration Factors by Stress Equalization", Exp Mech. V. 7, No. 10., Oct. 1967, 35 A-41A

PRACTICAL SHELL DESIGN:

This concept may be applied to shell design by considering the loading of the lap portion of the joint to be equivalent to the compression of concentric cylinders between rigid heads. Nonsymmetric features such as pins are not considered in this simple approach. In a practical butt joint, the contact area is reduced by the presence of a chamfer. [Fig. 4]. The chamfer provides clearance for the fillet between the lap and shoulder or for a hot propellant gas seal located at the fillet. In minimum weight designs with thin shell walls, this reduction in area causes a significant increase in the normal stress level. These areas must be considered as potential maximum stress regions of the joint. In the simplified approach the maximum stress criterion is taken to be the maximum nominal stress.

In applying this design procedure a stress control criterion must be selected. The choice depends upon the shell design. If the shell wall is tapered and the cross sectional area changes within the joint, the most efficient design will result from minimizing the local normal fillet stress at the minimum cross section.

If the shell wall has a uniform thickness it can be shown that the most efficient design will result from an equalization of stresses on the minimum contact areas adjacent to the shoulder fillets. This area must resist the total axial load resultant. At each location the two dissimilar materials are in contact. The lower strength material limits the allowable stress level at each area regardless of the strength of the abutting material. The maximum normal strength in the lower strength material is minimized when the stress distribution is uniform across the entire cross section A-A. Thus the equalization of stresses on the contact areas provides the most efficient design.

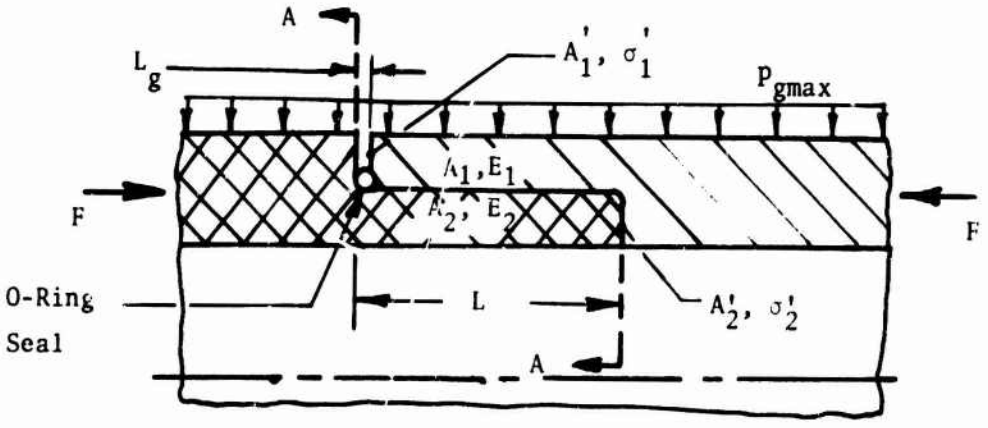

Figure 4 Model Of Shell Joint Geometry

DESIGN OF XM 517 JOINT:

The joint configuration is shown in Fig. 5. The idealization of the joint and loading is shown in Fig. 4. The forward section is 250 Maraging Steel and the rear body is Titanium. The steel has the higher modulus and is designated as material 1. The steel is located on the outside of the joint so that the gap is accessible for inspection. The joint length and the size of the cross sectional area of each lap are determined by factors which will not be considered here. The propellant gas pressure acts on the external surface of the shell and in the gap. In this design the rotating band pressure is nearly equal to the gas pressure. Therefore a uniform pressure is assumed to exist along the entire length of the shells. The compressive force on the joint is the reaction load from the acceleration of the mass of the shell forward of the joint. This load is proportional to the external gas pressure and is assumed to be given at the start of these calculations. The following quantities are given: (See Fig.5 and nomenclature.)

A_1 =	6.757 in^2	A_1'/A_1 = 0.562	E_1 = 27 X 10^6	t_1/t_2 = 1.129	
A_1' =	3.799 in^2	A_2'/A_2 = 0.872	E_2 = 16.5 X 10^6		
A_2 =	5.241 in^2	A_1/A_2 = 1.289	E_1/E_2 = 1.626		
A_2' =	4.576 in^2	R_a = 2.330 in	L = 3.68 in		
t_1 =	0.377 in	R_b = 3.041 in	ν_1 = 0.295		
t_2 =	0.334 in	R_i = 2.664 in	ν_2 = 0.33		

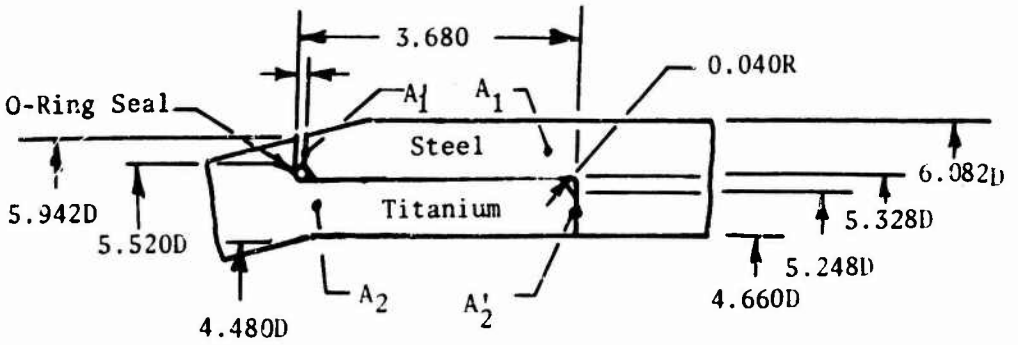

Figure 5 XM 517 Shell Joint Dimensions

This joint is essentially of the constant cross sectional area type for which equations have been obtained in the Appendix. The equalized maximum stress level at the cross sections A_1' and A_2' can be found easily from the equilibrium conditions: Equation numbers are consistent with those used in the appendix.

$$\sigma_{Z1}' = \sigma_{Z2}' = \frac{-F}{A_1' + A_2'} \qquad (1)$$

$$\sigma_{Z1} = \frac{-1.56\ 10^6}{4.576+3.799} = -186.3 \times 10^3 \text{ psi}$$

Thus the maximum stress at the contact areas under equalized stress conditions is immediately known. It is necessary to determine the gap length which causes the equalized stress condition.

$$\frac{L_g}{L} = \frac{F_{CL}}{F}\left[\frac{1}{E_2}\left(\frac{F}{A_2} - \frac{A_1}{A_2} P_{gmax} + \nu_2 \phi_2\right) - \frac{1}{E_1}\left(P_{gmax} + \nu_1 \phi_1\right)\right] \qquad (5)$$

where:

$$F_{CL} = \frac{A_2\left[\frac{F}{A_1'+A_2'}\left(\frac{A_2'}{A_2} - \frac{A_1'}{A_1}\frac{E_2}{E_1}\right) - \left(\nu_1 \phi_1 \frac{E_2}{E_1} - \nu_2 \phi_2\right)\right]}{\left[1 - \frac{P_{gmax}}{F}\left(A_2 \frac{E_2}{E_1} + A_1\right)\right]} \qquad (12)$$

$$\phi_1 = \sigma_{\theta 1} + \sigma_{r1} \qquad \phi_2 = \sigma_{\theta 2} + \sigma_{r2} \qquad (2)$$

$$\sigma_{\theta 1} = \frac{P_{amax} R_a - P_{gmax} R_b}{t_1\left(1 + \frac{E_2 t_2}{E_1 t_1}\right)} \qquad \sigma_{\theta 2} = \frac{P_{amax} R_a - P_{gmax} R_b}{t_2\left(1 + \frac{E_1 t_1}{E_2 t_1}\right)} \qquad (16)$$

$$P_{imax} = \frac{P_{amax}\left(\frac{R_a}{R_i}\right)\frac{E_1 t_1}{E_2 t_2} + P_{gmax}\frac{R_b}{R_i}}{1 + \frac{E_1 t_1}{E_2 t_2}} \qquad (15)$$

$$\sigma_{r1} = -\left(\frac{P_{gmax} + P_{imax}}{2}\right) \qquad \sigma_{r2} = -\left(\frac{P_{amax} + P_{imax}}{2}\right) \qquad (17)$$

The maximum pressure values are used in these equations since the proportionality term F_{CL}/F is used with the ϕ terms in the development of equation 5.

$$\sigma_{\theta 1} = \frac{-(53)(10^3)(3.041)}{.377\left[1 + \frac{1}{(1.636)(1.129)}\right]} = -277 \times 10^3 \text{ psi}$$

$$\sigma_{\theta 2} = \frac{-(53)(10^3)(3.041)}{.334[1 + (1.636)(1.129)]} = -169.5 \times 10^3 \text{ psi}$$

$$P_i = \frac{0 + (53)(10^3)\left(\frac{3.041}{2.664}\right)}{1 + (1.636)(1.129)} = 21.25 \times 10^3 \text{ psi}$$

$$\sigma_{r1} = -\frac{(53+21.25)10^3}{2} = -37.13 \times 10^3 \text{ psi}$$

$$\sigma_{r2} = -\frac{(21.25+0)10^3}{2} = -10.63 \times 10^3 \text{ psi}$$

These values of σ_θ and σ_r define ϕ_1 and ϕ_2.

$$\phi_1 = (-277-37.13)10^3 = -314.1 \times 10^3 \text{ psi}$$

$$\phi_2 = (-169.5 - 10.63)10^3 = -180.1 \times 10^3 \text{ psi}$$

The value of F_{CL} may now be determined.

$$F_{CL} = \frac{A_2\left[\frac{F}{A_1' + A_2'}\left(\frac{A_2'}{A_2} - \frac{A_1'}{A_1'}\frac{E_2}{E_1}\right) - (\nu_1\phi_1\frac{E_2}{E_1} - \nu_2\phi_2)\right]}{1 - \frac{P_{gmax}}{F}\left(A_2\frac{E_2}{E_1} + A_1\right)}$$

$$F_{CL} = \frac{5.241 \left\{ \frac{(1.56)(10^6)}{3.799+4.576} \left(.873 - \frac{.562}{1.636} \right) - \left[\frac{(.295)(-.3141)10^6) - (.33)(-.180)10^6}{1.636} \right] \right\}}{\left[1 - \frac{(.053)10^6}{(1.56)10^6} \left(\frac{5.241}{1.636} + 6.757 \right) \right]}$$

$$\underline{F_{CL} = 761 \times 10^3 \text{ lbs.}}$$

$$\frac{L_g}{L} = \frac{F_{CL}}{F} \left[\frac{1}{E_2} \left(\frac{F}{A_2} - \frac{A_1}{A_2} P_{gmax} + \nu_2 \phi_2 \right) - \frac{1}{E_1} (P_{gmax} + \nu_1 \phi_1) \right]$$

$$\frac{L_g}{L} = \frac{(.761)\ 10^6}{(1.56)10^6} \left\{ \frac{1}{(16.5)(10^6)} \left[\frac{(1.56)10^6}{5.241} - (1.289)(.053)(10^6) + (.33)(-.180)10^6 \right] - \frac{1}{27(10^6)} \left[(.053)(10^6) + (.295)(-.3141)10^6 \right] \right\}$$

$$\frac{L_g}{L} = \frac{.761}{1.56} (.01177) = 0.00574$$

$$L_g = (.00574)(3.68)$$

$$\underline{L_g = .0211}$$

STRESS RESULTING FROM VARIATIONS IN GAP LENGTH:

It is not possible to maintain the ideal nominal gap length during the manufacture and assembly of a shell. The deviation from the ideal gap dimension will cause unequalized stresses to occur at the contact areas A_1' and A_2'. The extent of this deviation from the equalized stress condition must be determined in order to specify the permissible tolerance in gap length dimension. Using equations from the appendix:

$$\sigma'_{Z1} = \frac{A_1}{A_1'} (\sigma_{Z1CL} + \sigma_{Z1ex}) \qquad \sigma'_{Z2} = \frac{A_2}{A_2'} (\sigma_{Z2CL} + \sigma_{Z2ex}) \qquad (20)$$

$$\sigma_{Z1CL} = - \left(\frac{F_{CL}}{F} \right) P_{gmax} \qquad (4)$$

$$\sigma_{Z1ex} = -\left[\frac{(F-F_{CL})+\left(\nu_2\,\phi_2 - \nu_1\,\phi_1\right)E_{2/E_1}\,A_2}{A_1 + E_{2/E}\,A_2}\right] \tag{18}$$

$$\sigma_{Z2CL} = -\frac{F_{CL}}{F}\left[\frac{F}{A_2} - \frac{A_1}{A_2}\,P_{gmax}\right] \tag{4a}$$

$$\sigma_{Z2ex} = \nu_2\,\phi_2 + \frac{E_2}{E_1}\left(\sigma_{Z1ex} - \nu_1\,\phi_1\right) \tag{19}$$

Rearranging equation 5, page 7, and using previous results

$$\frac{F_{CL}}{F} = \frac{L_{g/L}}{\frac{1}{E_2}\left[\frac{F}{A_2} - \frac{A_1}{A_2}\,P_{gmax} + \nu_2\,\phi_2\right] - \frac{1}{E_1}\left(P_{gmax} + \nu_1\,\phi_1\right)}$$

$$\frac{F_{CL}}{F} = \frac{1}{.01177}\,\frac{L_g}{L}$$

Let it be assumed that a tolerance of ±0.002 inches is permitted in the gap dimension:

$$L_1 = 0.021 - 0.002 = 0.019 \text{ in.}$$

$$L_2 = 0.021 + 0.002 = 0.023 \text{ in.}$$

The stresses resulting from a gap dimension of 0.019 in. are:

$$\frac{F_{CL}}{F} = \left(\frac{1}{.01177}\right)\left(\frac{.019}{3.68}\right)(1.56)(10^3)$$

$$F_{CL} = 684.3 \times 10^3 \text{ psi}$$

$$\sigma_{Z1ex} = -\left[\frac{(F-F_{CL})+(\nu_2\,\phi_2 - \nu_1\,\phi_1\,E_{2/E_1})\,A_2}{A_1 + (E_{2/E_1})\,A_2}\right]$$

$$\sigma_{Z1ex} = -\frac{(1.56-.6843)10^6 + \left[(.33)(-.1801) - \frac{(295)(-.3141)}{1.636}\right](10^6)5.241}{6.757 + \frac{5.241}{1.636}}$$

$$\sigma_{Z1ex} = -\ 86.4 \times 10^3 \text{ psi}$$

$$\sigma_{Z1CL} = -\ \frac{F_{CL}}{F}\ P_{gmax}$$

$$\sigma_{Z1CL} = -\ \frac{(.6843)\ 10^6}{1.56(10^6)}\ 53(10^3) = -\ 23 \times 10^3 \text{ psi}$$

$$\sigma'_{Z1} = \frac{A_1}{A'_1}\ (\sigma_{Z1CL}+\sigma_{Z1ex})$$

$$\sigma'_{Z1} = -\ \frac{1}{.562}\ (86.4+23.3)\ 10^3$$

$$\underline{\sigma'_{Z1} = -\ 195.1 \times 10^3 \text{ psi}}$$

$$\sigma_{Z2CL} = -\ \frac{F_{CL}}{F}\ \left[\frac{F}{A_2} - \frac{A_1}{A_2}\ P_{gmax}\right]$$

$$\sigma_{Z2CL} = -\ \frac{(.6843)10^6}{(1.56)\ 10^6}\ \left[\frac{(1.56\ 10^6)}{5.241} - (1.289)(.053)\ 10^6\right]$$

$$\underline{\sigma_{Z2CL} = -\ 100.6\ 10^3 \text{ psi}}$$

$$\sigma_{Z2ex} = (.33)(-180.1\ 10^3) + \frac{1}{1.636}\ \left[(-86.4)10^3 - (.295)(-314.1)10^3\right]$$

$$\sigma_{Z2ex} = -\ 55.6\ 10^3 \text{ psi}$$

$$\sigma'_{Z2} = \frac{A_2}{A'_2}\ (\sigma_{Z2CL}+\sigma_{Z2eX})$$

$$\sigma_{Z2} = -\ \frac{1}{.873}\ (100.6+55.6)10^3; \quad \underline{\sigma_{Z2}' = -\ 178.9 \times 10^3 \text{ psi}}$$

For the 0.019 gap dimension the maximum stress in the joint of the contact surface has been increased from the equalized stress of 186.3×10^3 psi to 195.1×10^3 psi.

The stresses which result from a gap dimension of 0.023 inches may be obtained in a similar manner:

$$\frac{F_{CL}}{F} = \frac{1}{.01177}\ \frac{L_g}{L}$$

$$F_{CL} = \frac{(1.56)(10^6)}{(.01177)}\ \left(\frac{.023}{3.68}\right) = 828.4\ 10^3 \text{ lbs.}$$

$$\sigma_{Z1ex} = -\ \frac{(F-F_{CL}) + \left(\nu_2\ \phi_2 - \nu_1\ \phi_1\ E_{2/E_1}\right) A_2}{A_1 + (E_{2/E_1})\ A_2}$$

$$\sigma_{Z1ex} = -\ \left\{\frac{(1.56-.8284)10^6 + \left[(.33)(-.1801) - \frac{(.295)(-.3141)}{1.636}\right] (10^6)\ 5.241}{6.757 + \frac{5.241}{1.636}}\right\}$$

$$\sigma_{Z1ex} = -\ 72 \times 10^3 \text{ psi}$$

$$\sigma_{Z1CL} = -\frac{F_{CL}}{F}\ P_{gmax}$$

$$\sigma_{Z1CL} = \frac{(.8284)(10^6)(\ 53)10^3}{(1.56)10^6} = -\ 28.1 \times 10^3 \text{ psi}$$

$$\sigma'_{Z1} = \frac{A_1}{A'_1}\ (\sigma_{Z1CL} + \sigma_{Z1eX})$$

$$\sigma'_{Z1} = -\ \frac{1}{.562}\ (72+28.1)\ 10^3$$

$$\sigma'_{Z1} = -\ 178.2 \times 10^3 \text{ psi}$$

$$\sigma_{Z2CL} = -\ \frac{F_{CL}}{F}\left[\frac{F}{A_2} - \frac{A_1}{A_2}\ P_{gmax}\right]$$

$$\sigma_{Z2CL} = -\ \frac{(.8284)10^6}{(1.56)10^6}\left[\frac{(1.56)10^6}{5.241} - (1.289)(.053)10^6\right]$$

$$\sigma_{Z2CL} = -\ 121.8 \times 10^3 \text{ psi}$$

$$\sigma_{Z2ex} = \nu_2 \phi_2 - \frac{E_2}{E_1} \nu_1 \phi_1 + \frac{E_2}{E_1} \sigma_{Z1ex}$$

$$\sigma_{Z2ex} = \left[(.33)(-180.1) - \frac{(.295)(-314.1)}{1.636} - \frac{(72)}{1.636} \right] 10^{+3}$$

$$\sigma_{Z2ex} = -46.8 \times 10^{2} \text{ psi}$$

$$\sigma'_{Z2} = \frac{A_2}{A'_2} (\sigma_{Z2CL} + \sigma_{Z2ex})$$

$$\sigma'_{Z2} = \frac{1}{.873} (121.1+46.8) 10^{3}$$

$$\underline{\sigma'_{Z2} = -193.1 \times 10^{3} \text{ psi}}$$

In the preceding, a gap length of 0.021 inches has been found to provide the equalized stress of -186.3 KSI on the contact areas of the joint. A tolerance of $\pm$ 0.002 inches in the gap length causes a maximum normal stress of -195.1 KSI at the contact area. The stress level at the fillet between the lap and shoulder should be determined in order to ensure that it does not exceed the normal stress on the contact area.

STRESSES AT FILLETS:

Again taking equations from the appendix:

$$\sigma_{f1} = \sigma'_{Z2} + k_{f1} (\sigma_{Z1} - \sigma'_{Z2}) \qquad (23)$$

$$k_{f1} = 1 + \left[\frac{\left(\frac{t_{T1}}{t_1} - 1 \right) \frac{t_1}{r_1}}{2.8 \frac{t_{T1}}{t_1} - 2} \right]^{0.65} \qquad (22)$$

$$k_{f2} = 1 + \left[\frac{\left(\frac{t_{T2}}{t_2} - 1 \right) \frac{t_2}{r_2}}{2.8 \frac{t_{T2}}{t_2} - 2} \right]^{0.65}$$

Given:

$t_{T1} = 0.711$ in. $\qquad t_{T2} = 0.731$ in.

$t_1 = 0.377$ in. $\qquad t_2 = 0.334$ in.

$r_1 = 0.040$ in. $\qquad r_2 = 0.040$ in.

$$k_{f1} = 1 + \left[\frac{\left(\frac{.711}{.377} - 1 \right) \frac{.377}{.04}}{2.8 \left(\frac{.711}{.377} \right) - 2} \right]^{0.65}$$

$$k_{f1} = 2.83$$

$$k_{f2} = 1 + \left[\frac{\left(\frac{.731}{.334} - 1 \right) \frac{.334}{.04}}{2.8 \left(\frac{.731}{.334} \right) - 2} \right]^{0.65}$$

$$k_{f2} = 2.7$$

With the nominal gap length 0.021 inches:

$$\sigma_{f1} = \sigma'_{Z2} + k_{f1} (\sigma_{Z1} - \sigma'_{Z2}) \qquad (23)$$

since $\sigma'_{Z1} = \sigma'_{Z2}$, from equation (24)

$$\sigma_{f1} = \sigma'_{Z2} \left[1 + k_{f1} \left(\frac{A'_1}{A_1} - 1 \right) \right]$$

$$\sigma_{f1} = -186.3 \, [1 + 2.83 \, (.562 - 1)] \, 10^3$$

$$\underline{\sigma_{f1} = +44.6 \times 10^3 \text{ psi}}$$

$$\sigma_{f2} = \sigma'_{Z1} + k_{f2} (\sigma_{Z2} - \sigma'_{Z1})$$

$$\sigma_{f2} = \sigma'_{Z1} \left[1 + k_{f2} \left(\frac{A'_2}{A_2} - 1 \right) \right]$$

$$\sigma_{f2} = -186.3 \, [1 + 2.7 \, (.873 - 1)] \, 10^3$$

$$\underline{\sigma_{f2} = -122.4 \times 10^3 \text{ psi}}$$

With the gap length of 0.019 inches:

$$\sigma_{f1} = \sigma'_{Z2} + k_{f1} \left(\frac{A'_1}{A_1} \sigma'_{Z1} - \sigma'_{Z2} \right) \qquad (23)$$

$$\sigma_{f1} = \left\{ -179 + 2.83 \, [(.562)(-195) - (-179)] \right\} 10^3$$

$$\sigma_{f1} = +17.4 \times 10^3 \text{ psi}$$

$$\sigma_{f2} = \sigma_{z1}' + k_{f2} \left(\frac{A_2'}{A_2} \sigma_{z2}' - \sigma_{z1}' \right)$$

$$\sigma_{f2} = \left\{ -195 + 2.7 \left[(.873)(-179) - 195 \right] \right\} 10^3$$

$$\sigma_{f2} = -90.4 \times 10^3 \text{ psi}$$

With gap length of 0.023 inches:

$$\sigma_{f1} = \left\{ -193 + 2.83 \left[(.562)(-178) - (-193) \right] \right\} 10^3$$

$$\sigma_{f1} = +70.1 \times 10^3 \text{ psi}$$

$$\sigma_{f2} = \left\{ -178 + 2.7 \left[(.873)(-193) - (-178) \right] \right\} 10^3$$

$$\sigma_{f2} = -152 \times 10^3 \text{ psi}$$

For these cases, which are characteristic of constant cross section shell joint designs, the stresses at the shoulder fillets have lower magnitude than at the contact areas.

NOMINAL STRESS LEVELS WITH NO GAP

The nominal stress in the XM-517 shell joint, with no gap, will be calculated for comparison with the previous results.

$$\sigma_{z1ex} = - \frac{(F - F_{CL}) + \left(\nu_2 \phi_2 - \nu_1 \phi_1 \frac{E_2}{E_1} \right) A_2}{A_1 + \frac{E_2}{E_1} A_2} \qquad (18)$$

$$\sigma_{z1ex} = - \frac{(1.56)10^6 + \left[(.33)(-.1801) - \frac{(.295)(-.314i)}{1.636} \right] 10^6 \, (5.241)}{6.757 + \frac{5.241}{1.636}}$$

$$\sigma_{z1ex} = -155.1 \times 10^3 \text{ psi}$$

$$\sigma_{z2ex} = \nu_2 \phi_2 + \frac{E_2}{E_1} (\sigma_{z1ex} - \nu_1 \phi_1) \qquad (19)$$

$$\sigma_{Z2ex} = (.33)(-180.1)10^3 + \frac{1}{1.636}\,[(-155.1)-(.295)(-314.1)]10^3$$

$$\sigma_{Z2ex} = -97.5 \times 10^3 \text{ psi}$$

$$\sigma'_{Z1} = \frac{A_1}{A'_1}\,(\sigma_{Z1CL} + \sigma_{Z1ex}) \qquad \sigma'_{Z2} = \frac{A_2}{A'_2}\,(\sigma_{Z2CL} + \sigma_{Z2ex}) \qquad (20)$$

$$\sigma'_{Z1} = \frac{1}{.562}\,(0 - 155.1)10^3 \qquad \sigma'_{Z2} = \frac{1}{.872}\,(0 - 97.5)10^3$$

$$\underline{\sigma'_{Z1} = -276 \times 10^3 \text{ psi}} \qquad \underline{\sigma'_{Z2} = -111.9 \times 10^3 \text{ psi}}$$

Fillet Stresses:

$$\sigma_{f1} = \sigma'_{Z2} + k_{f1}\left(\frac{A'_1}{A_i}\,\sigma'_{Z1} - \sigma'_{Z2}\right) \qquad (23)$$

$$\sigma_{f1} = \left\{ - 111.9+2.83\,[(.562)(-276)-(-111.9)] \right\} 10^3$$

$$\underline{\sigma_{f1} = -234 \times 10^3 \text{ psi}}$$

$$\sigma_{f2} = \sigma'_{Z1} + k_{f2}\left(\frac{A'_2}{A_2}\,\sigma'_{Z2} - \sigma'_{Z1}\right)$$

$$\sigma_{f2} = \left\{-276 + 2.7\,\,[(.873)(-111.9) - (-276)\right\} 10^3$$

$$\underline{\sigma_{f2} = + 205 \times 10^3 \text{ psi}}$$

SUMMARY

The stresses at the joint contact surfaces as a function of gap length are shown in the accompanying figure and table. The maximum normal stress is significantly reduced by the introduction of a properly sized gap. The control of the gap length within reasonable manufacturing tolerances of ±0.002 inches maintains the maximum stress level within 5% of the equalized stress level. A material being considered for use at the joint in this design should have a minimum compressive strength of 195,000 PSI.

In general, the control of stresses in joints between dissimilar materials by the introduction of a gap will be a function of the relative stiffness of the materials. A significant improvement in the efficiency of a joint between typical structural materials can be obtained by the use of the gap equalization design technique.

L_g in	σ_{Z1} (KSI)	σ_{Z2} (KSI)	σ_{f1} (KSI)	σ_{f2} (KSI
0.000	-276	-112	-234	+205
0.019	-195	-179	+17	-90
0.021	-186	-186	+45	-122
0.023	-178	-193	+70	-152

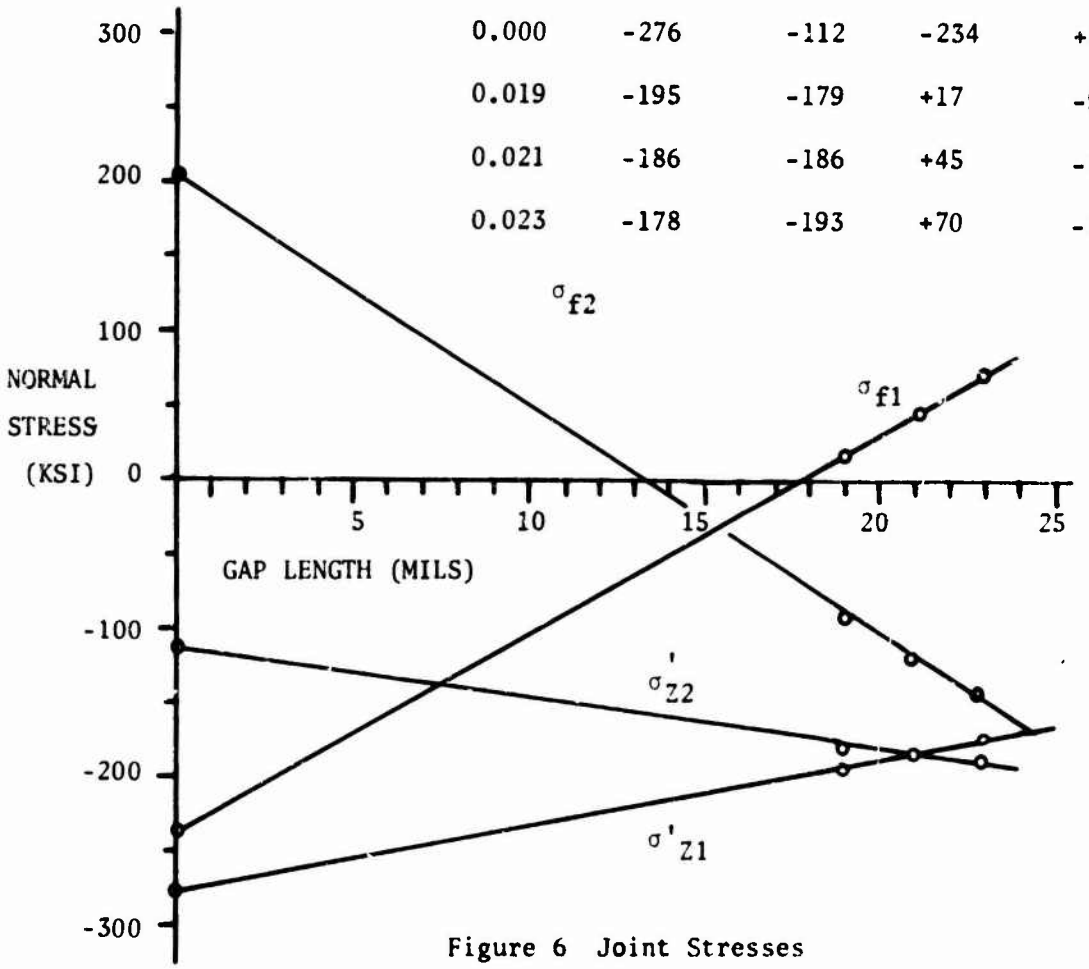

Figure 6 Joint Stresses

APPENDIX

IDEAL GAP LENGTH

The equations relating to the gap equalization design technique will be derived in general form. The joint is considered to be rotationally symmetric, Fig. A-1 Nonsymmetric local features, such as pins, are not considered. The following assumptions are made:

1. inner and outer laps are thin walled cylinders

2. the shell wall is an infinitely long cylinder with constant cross section.

3. internal and external pressure load is uniform and extends to infinity

4. bending stresses are not considered

5. stresses are elastic everywhere in the shell

6. strain occurs only in the laps, the cylinders are rigid elsewhere

7. strain is uniform in the joint, i.e., end effects in joint are neglected

8. the surface between the laps is frictionless

9. the dimensions, areas and loadings are specified or determined by other considerations

10. the failure criterion is the maximum local normal stress

The object is to derive equations which will permit the specification of a gap length (L_g) which will minimize the peak stresses in the joint which occur at peak acceleration of the shell. As noted earlier in the main text, for a shell of uniform cross section the most efficient design results from the equalization of stresses on the areas A_1' and A_2'. This equalized stress level can be easily determined from equilibrium

$$F = -(\sigma_{Z1}' A_1' + \sigma_{Z2}' A_2')$$

since $\sigma_{Z1}' = \sigma_{Z2}'$

$$\sigma_{Z1}' = \sigma_{Z2}' = -\frac{F}{A_1' + A_2'} \qquad (1)$$

Thus the maximum nominal stress at the minimum section in the joint is known immediately. The primary task is to find expressions for the gap length necessary to achieve these equalized stress conditions.

Thus, starting with the general stress-strain relationship for the axial direction:

$$\epsilon_Z = \frac{1}{E}\left[\sigma_Z - \nu(\sigma_\theta + \nu_r)\right]$$

Quantities pertaining to the stiffer material will be designated by subscript 1, and those for the less stiff material by 2.

$$\epsilon_{Z_1} = \frac{1}{E_1}\left[\sigma_{Z_1} - \nu_1\,(\sigma_{\theta_1} + \sigma_{r_1})\right]$$

$$\epsilon_{Z_1} = \frac{1}{E_2}\left[\sigma_{Z_2} - \nu_2\,(\sigma_{\theta_2} + \sigma_{r_2})\right]$$

Expressions for σ_θ , σ_{θ_2}, σ_{r_1} and σ_{r_2} will be derived subsequently, for convenience new quantities are defined:

$$\phi_1 = \sigma_{\theta 1} + \sigma_{r1} \qquad \phi_2 = \sigma_{\theta 2} + \sigma_{r2} \tag{2}$$

Using these definitions:

$$\epsilon_{Z1} = \frac{1}{E_1}\,(\sigma_{\theta 1} - \nu_1\,\theta_1), \epsilon_{Z2} = \frac{1}{E_2}\,(\sigma_{Z2} - \nu_2\,\theta_2)$$

The pressure loadings and the axial reaction load due to acceleration (F), are directly proportional, thus the strain in the single load bearing leg at closure may be expressed as:

$$\epsilon_{Z2CL} = \frac{1}{E_2}\,(\sigma_{Z2CL} - \nu_2\,\frac{F_{CL}}{F}\,\phi_2)$$

Thus the values of θ and σ are related to the full design load and pressure.

The compressive strain in leg 2 at closure is (see Fig. 4):

$$-\epsilon_{Z2C1} = L_{g/L} + (-\epsilon_{Z1C1})$$

where $(-\epsilon_{Z1C1})$ is the compressive strain in leg 1 due to gas pressure in the gap. Equating expressions for ϵ_{Z2CL}.

$$-L_{g/L} + \epsilon_{Z1CL} = \frac{1}{E_2}\,(\sigma_{Z2C1} - \nu_2\,\frac{F_{CL}}{F}\,\phi_2)$$

$$-L_{g/L} = \frac{1}{E_2}\,(\sigma_{Z2CL} - \nu_2\,\frac{F_{CL}}{F}\,\phi_2) - \frac{1}{E_1}\,(\sigma_{Z1CL} - \nu_1\,\frac{F_{CL}}{F}\,\phi_1) \tag{3}$$

The compressive stress in leg 2 at closure is obtained from equilibrium of forces:

$$-\sigma_{Z2CL} A_2 = F_{CL} + \sigma_{Z1CL} A_1$$

where $\sigma_{Z1CL} = -\frac{F_{CL}}{F} P_{gmax}$ (4)

$$\sigma_{Z2CL} = -\frac{F_{CL}}{F} \left(\frac{F}{A_2} - \frac{A_1}{A_2} P_{gmax} \right) \quad (4a)$$

Substituting stress values in equation 3:

$$\frac{L_g}{L} = \frac{F_{CL}}{F} \left[\frac{1}{E_2} \left(\frac{F}{A_2} - \frac{A_1}{A_2} P_{gmax} + \nu_2 \phi_2 \right) - \frac{1}{E_1} \left(P_{gmax} + \nu_1 \phi_1 \right) \right] \quad (5)$$

The value of F_{CL} for the desired stress equalization criterion must now be obtained.

When the axial load is greater than the closure load the joint restraint requires:

$$\varepsilon_{Z1ex} = \varepsilon_{Z2ex}$$

by definition:

$$\frac{1}{E_1} \left(\sigma_{Z1ex} - \nu_1 \phi_1 \right) = \frac{1}{E_2} \left(\sigma_{z2ex} - \nu_2 \phi_2 \right) \quad (6)$$

The equalization criterion for stresses on A_1' and A_2' is now enforced:

$$\sigma'_{Z1} = \sigma'_{Z2} \quad (7)$$

$$\sigma'_{Z1Cl} + \sigma'_{Z1ex} = \sigma'_{Z2CL} + \sigma'_{Z2ex}$$

$$\frac{-F_{CL}}{F} P_{gmax} \frac{A_1}{A_1'} + \sigma_{Z1ex} \frac{A_1}{A_1'} = -\frac{F_{CL}}{F} \left[\frac{F}{A_2} - \frac{A_1}{A_2} P_{gmax} \right] \frac{A_2}{A_2'} + \sigma_{Z2ex} \frac{A_2}{A_2'} \quad (8)$$

From equilibrium:

$$\sigma_{Z1ex} A_1 + \sigma_{Z2ex} A_2 = - (F - F_{CL}) \tag{9}$$

Solving equations 8 and 9 for σ_{Z1ex} and σ_{Z2ex}:

$$\sigma_{Z1ex} = - \frac{F A_1'}{A_1 (A_1' + A_2')} + \frac{F_{CL}}{F} P_{gmax} \tag{10}$$

$$\sigma_{Z2ex} = - \frac{F A_2'}{A_2 (A_1' + A_2')} + \frac{F_{CL}}{A_2} - \frac{F_{CL}}{F} P_{gmax} \frac{A_1}{A_2} \tag{11}$$

Substituting these stresses into the strain requirement, equation 6, and solving:

$$F_{CL} = \frac{A_2 \left[\frac{F}{A_1' + A_2'} \left(\frac{A_2'}{A_2} - \frac{A_1'}{A_1} \frac{E_2}{E_1} \right) - (\nu_1 \phi_1 \frac{E_2}{E_1} - \nu_2 \phi_2) \right]}{1 - \frac{P_{gmax}}{F} \left(\frac{A_2 E_2}{E_1} + A_1 \right)} \tag{12}$$

Substituting F_{CL} into equation 5 gives the desired expression for the gap length (L_g) necessary to obtain equal stresses on the contact areas A_1' and A_2':

$$\frac{L_g}{L} = \frac{A_2 \left[\frac{F}{A_1' + A_2'} \left(\frac{A_2'}{A_2} - \frac{A_1'}{A_1} \frac{E_2}{E_1} \right) - \left(\nu_1 \phi_1 \frac{E_2}{E_1} - \nu_2 \phi_2 \right) \right]}{1 - \frac{P_{gmax}}{F} \left(A_2 \frac{E_2}{E_1} + A_1 \right)} \times \tag{13}$$

$$\frac{1}{F} \left[\frac{1}{E_2} \left(\frac{F}{A_2} - \frac{A_1}{A_2} P_{gmax} + \nu_2 \phi_2 \right) - \frac{1}{E_1} \left(P_{gmax} + \nu_1 \phi_1 \right) \right]$$

The pressure terms ϕ_1 and ϕ_2 are required in equation 13. Recalling equation 2

$$\phi_1 = \sigma_{\theta 1} + \sigma_{r1} \qquad \phi_2 = \sigma_{\theta 2} + \sigma_{r2}$$

From figure A-1

$$\sigma_{\theta 1} = \frac{P_i R_i - P_{gmax} R_b}{t_1} \qquad \sigma_{\theta 2} = \frac{P_{amax} R_a - P_i R_i}{t_2} \tag{14}$$

$\sigma_{\theta 1}$ and $\sigma_{\theta 2}$ are the average tangential stresses in the thin cylindrical shells.

At the interface:

$$\frac{\sigma_{\theta 1}}{E_1} = \frac{\sigma_{\theta 2}}{E_2}$$

Substituting from equations (14)

$$P_i = \frac{\left(\frac{E_1 t_1}{E_2 t_2}\right) \frac{R_a}{R_i} P_{amax} + \frac{R_b}{R_i} P_{gmax}}{1 + \frac{E_1 t_1}{E_2 t_2}} \tag{15}$$

Substituting in equations (2):

$$\sigma_{\theta 1} = \frac{P_{amax} R_a - P_{gmax} R_b}{t_1 \left[1 + \frac{E_2 t_2}{E_1 t_1}\right]} \qquad \sigma_{\theta 2} = \frac{P_{amax} R_a - P_{gmax} R_b}{t_2 \left[1 + \frac{E_1 t_1}{E_2 t_2}\right]} \tag{16}$$

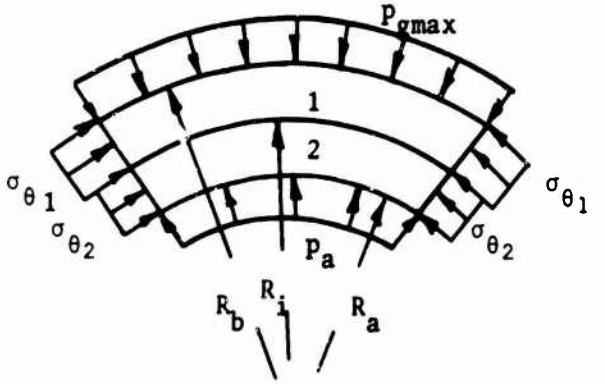

Figure A-1 Element Of Composite Cylinder

The radial stress is taken as the average stress through the thickness of the thin wall:

$$\sigma_{r1} = -\frac{P_{gmax}+P_i}{2} \qquad \sigma_{r2} = -\frac{P_{amax}+P_i}{2} \tag{17}$$

Thus, all quantities necessary for the evaluation of the ideal gap length have been determined.

STRESSES RESULTING FROM VARIATIONS IN GAP LENGTH

The relationship between contact area stress and the variation in gap length is required in order to establish tolerance limits on L_g. Previous equations incorporating the $\sigma'_{Z1} = \sigma'_{Z2}$ criterion are no longer applicable [(equations (8), (10), (11), (12), (13)]. Solving (5) for F_{CL}.

$$\frac{F_{CL}}{F} = \frac{\frac{L_g}{L}\ E_2}{\frac{F}{A_2} - \frac{A_1}{A_2} P_{gmax} + \nu_2\ \phi_2 - \frac{E_2}{E_1}\ (P_{gmax}+\nu_1\ \phi_1)}$$

Solving equation 9 for σ_{Z2ex} and substituting in 6 gives:

$$\sigma_{Z1ex} = -\left[\frac{F-F_{CL}+(\nu_2\ \phi_2 - \nu_1\ \phi_1\ \frac{E_2}{E_1})\ A_2}{A_1+\frac{E_2}{E_1}\ A_2}\right] \tag{18}$$

From (6) σ_{Z2ex} may be expressed in terms of σ_{Z1ex}

$$\sigma_{Z2ex} = \nu_2\ \phi_2 + \frac{E_2}{E_1}\ (\sigma_{Z1ex} - \nu_1\ \phi_1) \tag{19}$$

The total stresses are:

$$\sigma'_{Z1} = \frac{A_1}{A'_1}\left(\sigma_{Z1CL}+\sigma_{Z1ex}\right) \qquad \sigma'_{Z2} = \frac{A_2}{A'_2}\ (\sigma_{Z2CL}+\sigma_{Z2ex}) \tag{20}$$

Recalling equations (4) and (4a):

$$\sigma_{Z1CL} = -\frac{F_{CL}}{F} P_{gmax} \qquad \sigma_{Z2CL} = -\frac{F_{CL}}{F}\left(\frac{F}{A_2} - \frac{A_1}{A_2} P_{gmax}\right)$$

$$\sigma'_{Z1} = \frac{A_1}{A'_1}\left(-\frac{F_{CL}}{F} P_{gmax} + \sigma_{Z1ex}\right) \qquad (21)$$

$$\sigma'_{Z2} = \frac{A_2}{A'_2}\left[-\frac{F_{CL}}{F}\left(\frac{F}{A_2} - \frac{A_1}{A_2} P_{gmax}\right) + \nu_2 \phi_2 \frac{E_2}{E_1}\left(\sigma_{Z1ex} - \nu_1 \phi_1\right)\right]$$

STRESSES AT FILLETS

There is a stress concentration at the fillet between the lap and shoulder of the shell joint. The stress level at this concentration may be determined approximately from results available in the literature. The plate with shoulder geometry, figure A-2, may be considered to approximate the stress conditions in the shell joint. It is assumed that the stress state in the cross section of the cylindrical shell is approximated by the two dimensional plate of figure A-2.

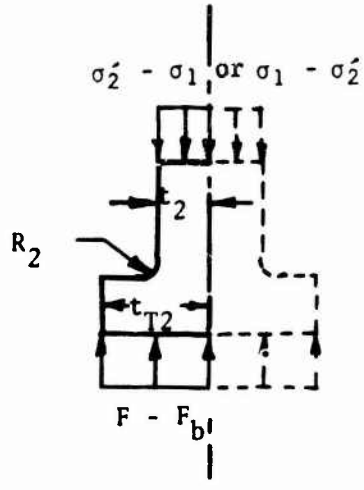

Figure A-2 Equivalent T-Head Configuration

Further, because of symmetry, the stress results for the shell cross section are equal to the results for the case of the entire plate. It can be shown, figure A-3, that the joint loading may be taken as the sum of case b and case c. The stress in case b is approximately equal to σ_{Z1}' since the body is approximately uniformly loaded. The fillet stress in case c may be determined from the results for the geometry of figure A-2 available in the literature. The stress at the fillet may be defined as:

$$\sigma_{fc2} = k_{f2} (\sigma_{Z2} - \sigma_{Z1}')$$

The stress concentration factor may be defined:

$$k_{f2} = \frac{\sigma_{fc2}}{\sigma_{Z2} - \sigma_{Z1}}$$

With the assumptions noted previously, the empirical results from Heywood* may be applied.

$$k_{fZ} \sim 1 + \left[\frac{\left(\frac{t_{T1}}{t_1} - 1 \right) \frac{t_1}{r_1}}{2.8 \frac{t_{T1}}{t_1} - 2} \right]^{0.65}$$

$$k_{fZ} \sim 1 + \left[\frac{\left(\frac{t_{T2}}{t_2} - 1 \right) \frac{t_2}{r_2}}{2.8 \frac{t_{T2}}{t_2} - 2} \right]^{0.65} \qquad (22)$$

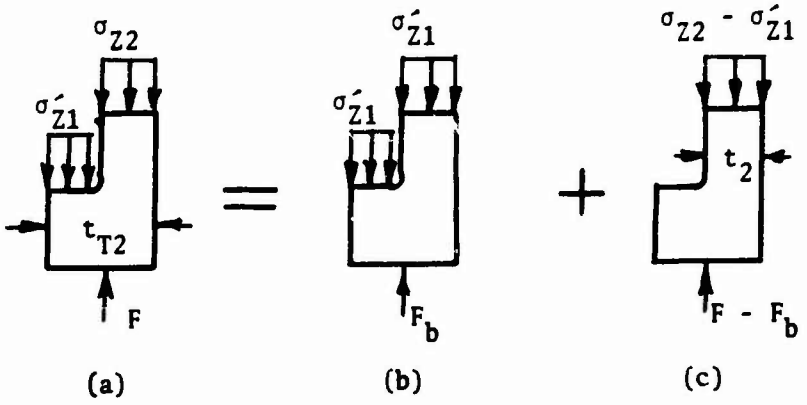

Figure A-3 Equivalent Load System

*Heywood, R.B., Designing By Photoelasticity, Chapman & Hall, London, 1952, p. 178.

The total stress at the fillet is case b plus case c:

$$\sigma_{f1} \sim \sigma'_{Z2} + k_{f1}\,(\sigma_{z1} - \sigma'_{Z2})$$
$$\sigma_{f2} \sim \sigma'_{Z1} + k_{f2}\,(\sigma_{Z2} - \sigma'_{Z1}) \qquad (23)$$

or

$$\sigma_{f1} \sim \sigma'_{Z2} + k_{f1}\left(\frac{A'_1}{A_1}\,\sigma'_{Z1} - \sigma'_{Z2}\right)$$
$$\sigma_{f2} \sim \sigma'_{Z1} + k_{f2}\left(\frac{A'_2}{A_2}\,\sigma'_{Z2} - \sigma'_{Z1}\right) \qquad (24)$$

CONNECTIONS FOR RECTANGULAR STRUCTURAL STEEL TUBING*

PEN J. FANG
Department of Civil and Environmental Engineering
University of Rhode Island

ABSTRACT

Research in recent years has served to develop a considerable amount of knowledge of the behavior of connections for tubular members and produce guidelines for design. This paper discusses the results of five types of simple connections for joining wide flange beams to a tubular column and T-type joint for two tubular members of different sizes meeting at a right angle. Tests of all connections and analytical prediction of connection elastic stiffnesses and ultimate strength of Type A and T-type connections are discussed. Some design recommendations for the connections are presented.

NOMENCLATURE

a = width of cross-section of branch member in T-type connection

b = width of tube column

d = length of connection plate in Type A connection

Fy = yield stress

L = span length of beam

t = thickness of tube wall

w = deflection of plate

q = lateral loads on plate

D = plate flexural rigidity

*This work has been supported in part by the U. S. Department of Transportation.

INTRODUCTION

Square and rectangular structural-steel tubular shapes offer structural advantages in certain types of frameworks. For example, the shape facilitates architectural details based on modular rectangular grids, and it requires only square cuts for connecting to other square tubes. Despite these and other advantages, the application of the shape has nevertheless often been hampered by a lack of detailed information on suitable connections. However, research in recent years has served to develop a considerable amount of knowledge of the behavior of connections for tubular members and produce guidelines for design. This paper discusses the results of some of the connection types which have been investigated experimentally and analytically. The connections studied are divided into two basic categories: simple framing connections for framing flanged beams into tubular members as shown in Fig. 1, and T-type "moment-resistant" connections for connecting two tubular members at a right angle, as shown in Fig. 2.

Five different types of simple connections are investigated. Type-A connection consists of a flat plate fillet-welded to the center of the tube wall. A substantial part of the investigation was directed toward the study of this connection. Type-B connection uses a length of structural tee, shop-welded along both flange edges to the tube wall. Type-C connection is an unstiffened angle seat connection consisting of the top angle and the bottom load-carrying angle proportioned such that all welding is along the corners of the tube. Type-D connection consists of a single plate fillet-welded to the tube corner at 95° to the principal axes of the tube. Type-E connection uses a single plate which is placed through a pair of slots in the tube, and fillet-welded along both sides of the plate-slot junction.

The T-type joint is formed by butt-welding a member of smaller size, all around, to a larger size member. Such a connection generally displays a semi-rigid behavior; however, the connection will be called a "moment-resistant" connection in this paper to distinguish it from simple connections.

PERFORMANCE REQUIREMENTS FOR CONNECTIONS

Requirements for adequate simple connections and moment-resistant connections will be examined briefly before considering

behavior of the several connections studied.

SIMPLE CONNECTION REQUIREMENTS

1. The connection must have adequate strength to carry safely the imposed beam reactions.

2. Because of the inherent flexibility of the flat plate wall of the tube, the connection must not induce stresses or distortions in the tubular section which are sufficient to cause an appreciable reduction in axially compressive strength.

3. A simple connection must be sufficiently flexible so that it does not transmit appreciable bending moment to the connected column.

4. The connection must have satisfactory moment-rotation characteristics, even though it is not designed to carry bending moment. Many "simple" connections, designed for beam-end reaction only, are inherently semi-rigid; but the moments actually developed in the connection have been ignored in the design. The developed moment will tend to deform the connection and unless some portion of the connection can accomodate such deformation, either elastically or nonelastically, the connecting devices (fasteners, welds) or the connection itself may become overstressed to the point of possible failure.

Therefore, any connection, no matter what its type, must be able to carry safely the end moments developed by the normal tendency of the ends of a beam to rotate when the beam is loaded. Batho's beam-line concept [1], originally presented in 1934 and well explained in modern steel design textbooks [2], provides a most convenient means for checking this particular requirement. The beam-line concept is illustrated in Fig. 3.

5. From a practical point of view, the connection should be simple to design and fabricate.

MOMENT-RESISTANT CONNECTION REQUIREMENTS

In addition to requirements 1, 4 and 5 for a simple connection discussed above, a moment-resistant connection for joining two tubes should satisfy the following requirements:

1. The joint should be able to carry a bending moment close to the full resisting moment of the connected members.

2. The joint stiffness should be equal to or greater than the stiffness of an equivalent length of the beam sections to be joined.

3. The joint should be able to sustain its elasto-plastic rotations without failure. As maximum bending moments in a rigid frame usually occur at the connection, the plastic hinges forming at or near the connections are accompanied by relatively large rotations.

DESCRIPTION OF TESTS

SIGNIFICANT CONNECTION PARAMETERS

The main parameters which influence behavior of connections of structural tubing are summarized below. Selection of test specimens is given in Tables 1 and 2.

1. Ratio of width of tube wall to tube thickness: As this ratio increases, any connection which is fastened directly to the tube wall will tend to become more flexible. Nominal width/thickness ratios for the test specimens range from 10.6 to 32.0 for simple connections and 13.3 to 24 for T-type connections.
2. Ratio of depth of connected branch member to tube column size: In the case of simple connections, this will also express the ratio of tube size to the beam web connection depth which is proportional to the depth of beam.
3. Material: Tensile yield points of the specimens in simple connections varied from 36.1 to 49.2 KSI and those of T-type connections exceeded 50 KSI.
4. Shape of tube: All tests were conducted on square tubing. It is felt that rectangular tube behavior would be very nearly the same as that for the square tube.
5. Connecting device: The total rotation of the beam end at a connection is a function of all possible sources of rotation, including distortions of the tube, deformations of the shape used in the connection, deformations of the beam end, and, in simple connections, slip of the beam web relative to the connection.

TEST PROCEDURE

The simple connection specimens consisted of a short tubular column with symmetrical cantilever beams connected to each side of the stub column. The beams were loaded at their extreme ends with hydraulic jacks until the induced rotation exceeded a predetermined amount or the connection failed. The specimens were also coated with brittle lacquer to reveal any yield patterns in

the various components. Selected specimens were also tested for direct vertical shear capacity after the moment rotation tests. A typical test setup for testing simple connections is described in Fig. 4.

It was felt that the high stresses and considerable distortions induced in the column walls by Type A connections could possibly jeopardize the ultimate compressive load capacity of the column. Therefore, column specimens with Type A connections were tested under combined axial and connection loadings. In testing an elastic column, the buckling load, P_{cr}, for the bare column was obtained by loading the column in axial compression with no connection loads applied. The P_{cr}-value was determined by means of Southwell's plotting method. After removing the column load, the connection load was subsequently applied and held constant, the column was again loaded axially until incipient buckling was reached. The column was then unloaded and the connection load was increased once more. In this cyclic loading manner, the critical column load could be determined for each increment. Such cyclic loading, however, was not appropriate in testing an inelastic column. Therefore, an inelastic column was loaded axially only once after an appropriate connection load was applied.

Nine specimens of T-type moment-resistant connections with variable b/a and b/t_c ratios were tested (Table 2). Each specimen was loaded first up to the failure load by a vertical force applied at the end of the cantilever branch tube. Then, in order to investigate the behavior of the connection under the action of both a joint moment and an axial load acting on the main tube, the specimen was unloaded and the main tube was loaded up to 60% of the nominal column yield load. The branch tube was then loaded to induce joint moment. In applying an axial load on the column, care was taken to prevent buckling in this test. Fig. 5 depicts a typical setup for testing T-type connections.

TEST RESULTS

Results of the tests will be discussed for each type of connection.

SIMPLE CONNECTIONS

Type A Connections

Results of the moment-rotation tests are given in Fig. 6. Additional details on test results are presented in Table 3. Stiffness varied considerably--tubes with a low width/thickness ratio exhibited moderate stiffness, while connections on the thinner tubes were quite flexible. The measured center of rotation (Fig. 4) was invariably at or near the intersection of the exterior face of the tube wall and the mid-depth of connection plate. Strain gage readings revealed that high stresses developed in the connected tube wall at low load levels, with critical stresses exceeding the yield level being reached in the vicinity of the ends of the connection plate. The rotation of the connection was due primarily to this deformation of the column wall, with some additional flexibility resulting from bearing deformation at the bolt holes and slipping between beam web and connection plate.

A summary of test results for the three columns under combined axial and connection loadings is given in Table 4, with the theoretical loads for a column material yield stress of 40 KSI forming a basis for comparison with test results.

Stress concentrations at both ends of the connection plate induced local warping and yielding of the tube wall, tending to reduce the effective tube cross-sectional area for resisting direct compression. Application of axial load caused additional local plastification, which in turn produced further reduction in effective column area and higher stresses in the still-elastic portion of the tube. It was hoped that the testing would reveal behavioral patterns which would enable separation of effects of critical parameters such as column slenderness ratio and tube wall b/t ratio. However, the measured reductions in column strength, as tabulated in Table 4, did not fall into any positive pattern. Nonetheless, it does appear that reduction in column capacity decreases with increasing b/t ratio of the tube wall and with increasing slenderness ratio of the column, although more extensive testing is required to substantiate this.

Type B Connections

This connection configuration permits reasonable rotation through distortion of the structural tee, and unlike the Type A connection, does not induce high stresses and distortions in the

tube wall. Maximum flexibility and minimum tube damage can be achieved by restricting all welding to the edges of the flanges. Results of four specimens tested for moment-rotation characteristics are given in Fig. 7. Extensive slipping between the tee web and beam web occurred in all connections.

Type C Connection

Design procedures for the unstiffened seat are well documented, and it was believed that no problems should arise in its use on tubular columns. The main disadvantage of this connection is its low carrying capacity, particularly if the length of the angle is not to exceed the width of the relatively narrow tubular columns. As expected, the connections proved to be extremely flexible, with the connections on the thicker tube being only slightly stiffer than those on the thin tube (Fig. 8).

Type D Connection

Easy and inexpensive to fabricate, the connection should cause relatively little tube distortion as all load is coming into the tube at a corner. Its main disadvantage involves the required 45° rotation of the tube, which would certainly complicate framing at partitions and walls. However, this factor would not be critical in many applications such as in industrial buildings or other exposed framing construction. There are no known applications of this particular connection. The test results indicated that the connections were relatively stiff (Fig. 8). Increasing the wall thickness from 3/16 to 1/2 in. increases the stiffness of the connection by nearly 50%.

Beam web yielding due to excessive bolt bearing stresses occurred in both specimens, and appreciable slip between beam web and connection plate was measured.

Type E Connection

Although similar in external appearance to Type A connection its behavior is considerably different. It is a much more rigid connection, and it should transmit only negligible local bending into the tube wall because of the continuity of the plate through the tube. Despite the expense and difficulty involved in the tube slotting operation, the connection has been used in various tabular column framing situations.

Connections on both specimens proved to be excessively stiff for use as simple connections. Stresses in tube walls remained at low levels throughout the testing. Slight residual distortion of the tube walls remained after loads were removed.

T-Type Connections

Inspection of Fig. 12 where the load-deflection curves for the nine specimens tested are plotted, shows that the connection behavior cannot be categorized as a rigid connection. Typically, the stiffness of the connection is that of a semi-rigid connection. The width of the branch tube being narrower than that of the main (or column) tube, the stiffness of the joint is essentially provided by the stiffness of the main tube wall; hence the main-tube wall width/thickness ratio, b/t_c, is the most important parameter of the connection, similar to the Type A connection discussed in the foregoing. Slight increase in the b/t_c-ratio markedly decreased the stiffness and strength of the connection. (19% increase in b/t_c value resulted in 25% decrease of stiffness; see specimens 7 and 8.) The flexibility of the column wall made it impossible for the connection to develop the yield moment of the beam section.

The test results showed that axial loads on the column up to 0.6 P_y had no effect on the moment resistance of the tubular column.

ANALYSIS OF CONNECTIONS

ELASTIC ANALYSIS

The theoretical analysis has been made to predict the elastic stiffnesses of Type A connections and T-type joints. The method of finite differences was used to Type A connection to compute the elastic response to an applied moment. Assuming the classical small deflection theory of elastic plate holds, the partial derivatives in the plate deflection equation

$$\nabla^4 w = \frac{\partial^4 w}{\partial x^4} + \frac{\partial^4 w}{\partial x^2 \partial y^2} + \frac{\partial^4 w}{\partial y^4} = \frac{q}{D} \qquad (1)$$

were replaced by their finite equivalents. The tube was considered as a closed space frame with unyielding longitudinal edges. The boundary condition at the edge was one of moment-

slope relationship which can be expressed as

$$-D \frac{\partial^2 w}{\partial x^2} = K \frac{\partial w}{\partial x} \qquad (2)$$

The constant K can be found by considering the restraint provided at the joint. It was further assumed that deflections of the tube were insignificant at a distance of about twice the length of the connection plate from the end of the plate. The tube model was therefore terminated at this distance and the wall was assumed to be resting on a simple support. A linear rotational deflection pattern was imposed onto the tube wall at the tube-connection plate interface (Fig. 9). The linear finite-difference equation set was modified to enable solving the plate-induced loading needed to produce such deflections. Results of theoretical analysis for Type A connections are shown in Fig. 5 together with the experimental data for comparison.

In the elastic analysis of T-type connections, the finite element technique through triangular discretization was used. The applied moment in the experimental setup was replaced by a system of statically equivalent forces in the mathematical models in order to shorten the computational effort (Fig. 10). The length of the column tube was four times the beam width and the length of the cantilever branch tube was twice the beam width. The end of the main tube wall was again assumed to be resting on a simple support. Accounting for symmetry and antisymmetry conditions, only one-half of the assemblage was analyzed.

The elastic finite element analysis is limited to the case of small deflections and small strains. This means that the inplane action is uncoupled from the plate bending action. Therefore, the stiffnesses were developed for two actions independently and subsequently they were combined for the plate element stiffness. The inplane stiffness is based on a 12 degrees-of-freedom membrane triangle characterized by a quadratic displacement function which leads to a linearly varying strain field in the element. For bending stiffness a 21 degrees-of-freedom triangle was used, whose deflection function is a complete fifth degree polynomial (Fig. 10a). Since the derivation of the stiffnesses is well described in literature [3], [4] and the procedure of finite element analysis through direct stiffness method is well known, the details will not be discussed here. Results of the analysis are shown in Fig. 12.

ULTIMATE STRENGTH ANALYSIS

The elastic analysis discussed in the foregoing has produced very useful results in that they have indicated where concentrations of stress are likely to occur, but they are not sufficient to provide information on the strength of the joint. The tests have indicated nonlinear behavior at fairly low to moderate loads, but they also indicate that there is a considerable amount of reserve strength. The ultimate strength of a connection could in theory be predicted by the application of the finite element technique incorporating a plasticity theory. However, the approach is inevitably expensive in that very lengthy computer time is involved. Instead, the yield line theory [5] is used in an attempt to analyze the connection strength. This method is easy to apply and, as will be seen, it yields satisfactory results.

The tube wall where the connection is welded is assumed to form a probable yield mechanism, and the ultimate load transmitted to the tube wall can be found by application of the principle of virtual work. The so-called work method gives an upper-bound solution to the true collapse load. The effect of strain hardening of steel is neglected in the theory, which, however, would somewhat offset the upper-bound solution of the method.

The collapse mechanism patterns assumed for Type A connection and T-type connection are shown in Fig. 11. By equating the virtual work done by the applied ultimate moment M_u to the energy dissipated in the plate through the rotation at the yield lines, it can be shown that

$$M_u = 2d\left(4 + \frac{2d}{b} + \frac{b}{d}\right) m_p \qquad (3)$$

for a Type A connection, and that

$$M_u = 2a\left(\frac{4\sqrt{b(b-a)}}{b-a} + \frac{2a}{b-a} + \frac{b}{a}\right) m_p \qquad (4)$$

for a T-type connection, where m_p = plastic moment per unit width of plate and can be expressed as $F_y t^2/4$ where F_y is the yield stress of steel and t the thickness of tube column wall; other notations are explained in Fig. 11. In the application of Eqs. (3) and (4), the effective dimension d should be taken greater than the nominal length of the connection plate in the

Type A connections and a greater than the nominal size of the branch tube in the T-type connections because of the weld material. Results of the ultimate strength analysis are presented in Figs. 5 & 12. The narrow yield lines assumed in the ultimate strength calculation cannot in general be identified on the test specimens; yield regions are actually much more widespread. Nevertheless, the comparison with the experimental evidence suggests that the yield line theory can be used to obtain a reasonably approximate collapse load for these types of connections in which the side walls are sufficiently strong.

CONCLUSIONS AND RECOMMENDATIONS

Judging the adequacy of connections in this report is based on the requirements for a satisfactory simple connection and a moment-resistant connection as discussed earlier. Strength in shear was more than adequate in all connections tested, and nearly all connections had sufficient strength to safely resist the moment induced by beams of ordinary L/d ratios.

SIMPLE CONNECTIONS

(a) No aboslute value can be given for maximum recommended stiffness but it is felt that connections with stiffness in excess of about 30% (as based on an L/d ratio of 25 for typical beam sizes that would ordinarily be used with the connection) should be avoided. Additional research is needed to help clarify maximum stiffness levels at which the induced column moments are at acceptable levels.

(b) To prevent excessive stiffness, connections fastened to beam webs intended to be simple connections should be not more than 2/3 the depth of the connected beam. The shorter the connection, the more flexible it will be. Also, the use of field bolting instead of field welding will permit slipping between the connection and the beam web in many situations, thus lending to increased flexibility.

(c) On the basis of the results reported herein, the Type A connection, despite its flexibility, should be used with care. The investigation revealed that the connection caused excessive distortion of the tube wall to which it is attached. These distortions in turn reduced the effectiveness of the column in carrying axial load and/or bending moment when the connection was attached at an unbraced point.

A possible use for the connection is at locations

where only a portion (say 50%) of the column strength is utilized or needed at a point immediately below the connection. It is felt, however, that if distortions should occur only at laterally braced points along the column, their effects may not be so serious. Moreover, if beams are designed with a depth to span ratio of about 1 to 25, with corresponding beam end rotations of about 0.01 radians at working load, the effects of tube distortions may not be as critical as the test conditions represented. The yield-line theory can be used to predict approximate strength of the connection.

(d) The Type B connection is suitable for general use as a simple framing connection, although it tends to be stiffer than desired for a simple connection. The following design factors should be noted:

1. The tee flange should be wide enough to permit welding along the corners of the tube wall.
2. The width-thickness of the tee flange must not be too low. As there is no rational design method for determining required flange thickness, using a width/thickness ratio of about 10 appears to be a reasonable rule of thumb.
3. Tee web thickness and welds are to be sized by conventional techniques.

(e) The Type C connection is completely satisfactory, with behavior essentially independent of the tube size. Customary design procedures for determining angle size, length, and weldments can be used.

(f) Type D is quite stiff. It also can induce distortion into the tube wall which might be of rather serious consequence, particularly in thin-walled tubes.

(g) Type E was the stiffest of the five types tested, and perhaps should be classified as a semi-rigid connection rather than a flexible connection. Recommendations for its use remain to be clarified after further study of the effects on the tubular column of the rather large moment placed on the tube by this stiff connection.

T-TYPE CONNECTION

(a) The instantaneous stiffness of a T-type moment connection depends on b/a, b/t_c, and also on the magnitude of the load transmitted.

(b) A square or rectangular tube is framed to a column of greater width, it is unlikely that the plastic moment, M_p, or

even the yield moment, My, of the beam will be developed.

(c) When loading is confined to the transmissions of the loads from the narrower beam to the wider column, which is unloaded except for the reaction forces, numerical solutions for predicting elastic stiffness proves to be satisfactory.

(d) The yield-line approximate solution for the ultimate load joint can be of practical use.

(e) The influence of a column axial load of up to 60% of the ultimate column yield load on the stiffness of the connection was relatively low. However, when the loading on the column becomes significant, the joint is likely to behave in a non-linear manner.

REFERENCES

1. Second Report, Steel Structures Research Committee, Dept. of Scientific and Industrial Research of Great Britain, H. M. Stationary Office, London, 1934.

2. Gaylord, E. H., Gaylord, C. N., "Design of Steel Structures," McGraw-Hill, N. Y., 1972.

3. Holand, I., Bell, K., "Finite Element Methods in Stress Analysis," Tapir, Trondheim, Norway, 1969.

4. Ou, J. L., "Finite Element Analysis of Elastic Stability of Thin Square Plates with a Central Cut-out Under Edge Loading," M. S. Thesis, Department of Civil and Environmental Engineering, University of Rhode Island, 1973.

5. Wood, R. H., Plastic and Elastic Design of Slabs and Plates, Thames & Hudson, London, 1961.

TABLE I SUMMARY OF SIMPLE CONNECTION SPECIMENS

Specimen	Nominal Tube Size	Nominal w/t ratio	Connection	Connection Length, in.	Welds	Beam Size	Number and Size of Bolts
A1	4x4x3/16	21.3	3/8" plate	5 1/2"	3/16"	8WF17	2 - 7/8"
A2	4x4x3/16	21.3	3/8" plate	8 1/2	3/16"	12WF31	3 - 7/8"
A3	4x4x3/8	10.6	3/8" plate	5 1/2	3/16"	8WF17	2 - 7/8"
A4	4x4x3/8	10.6	3/8" plate	8 1/2	3/16"	12WF31	3 - 7/8"
B1	4x4x3/16	21.3	ST 3.517.6	8 1/2"	5/16"	12WF27	3 - 7/8"
B2	4x4x3/8	10.6	ST 3.517.6	8 1/2"	5/16"	12WF27	3 - 7/8"
B3	8x8x1/4	32.0	Piece of	11 1/2"	7/16"	18WF55	4 - 1"
B4	8x8x1/2	16.0	18 I 54.7	11 1/2"	7/16"	18WF55	4 - 1"
C1	6x6x3/16	32.0	Angle	-	7/16"	12WF27	-
C2	6x6x1/2	12.0	5x3 1/2 x 3/4	-	7/16"	12WF27	-
D1	6x6x3/16	32.0	3/8" Plate	8 1/2"	3/16"	12WF27	3 - 7/8"
D2	6x6x1/2	12.0		8 1/2"	3/16"	12WF27	3 - 7/8"
E1	6x6x3/16	32.0	3/8" Plate	8 1/2"	3/16"	12WF27	3 - 7/8"
E2	6x6x1/2	12.0		8 1/2"	3/16"	12WF27	3 - 7/8"

TABLE II SUMMARY OF T-TYPE SPECIMENS

Specimen	Column Size	Branch Member Size	b/a	b/t_c	Nominal Branch Failure Load P2	Nominal Column Failure Load P1
1	6x6x.250	5x5x.250	1.20	24.0	8.30	276
2	Do	4x4x.188	1.50	Do	4.00	Do
3	Do	3.5x3.5x.188	1.71	Do	3.05	Do
4	5x5x.250	4x4x.210	1.25	20.0	4.40	227
5	Do	3.5x3.5x.188	1.43	Do	3.05	Do
6	Do	3x3x.150	1.60	Do	1.79	Do
7	4x4x.250	3x3x.188	1.33	16.0	2.08	174
8	4x4x.210	Do	Do	19.0	Do	149
9	4x4x.188	Do	Do	21.3	Do	137

TABLE III TEST RESULTS OF SIMPLE CONNECTIONS

		Moment-Rotation Test				Shear Test		
Specimen	Tube Size	(1) M_F in-k	(2) M_{25} in-k	(3) % Stiff	(4) $M_{.01r}$ in-k	Design Load kips	Test Load kips	F.S.
A1	4x3/16	507	17	8.2	16	19.6	60	3.06
A2	4x3/16	578	40	6.9	37	34	58	1.71
A3	4x3/8	207	68	32.8	74	19.6	62	3.16
A4	4x3/8	578	127	22.0	132	34	54	1.59
B1	4x3/16	500	120	24.0	123		-	
B2	4x3/8	500	150	30.0	161	30.6	83.5	2.73
B3	8x1/4	1440	230	16.0	240		-	
B4	8x1/2	1440	360	25.0	375	69	156	2.64
C1	6x3/16	500	33	6.6	30	20	83	4.15
C2	6x1/2	500	40	8.0	37	20	70	3.5
D1	6x3/16	500	130	26.0	140		-	
D2	6x1/2	500	185	37.0	183		-	
E1	6x3/16	500	178	35.6	185		-	
E2	6x1/2	500	190	38.0	191	30.6	111.5	3.64
CT2	3x3/16	207	25.5	12.3	27.5		-	
CT4,5	6x3/16	500	20	4.0	18		-	

(1) Fixed end moment for connected beam.
(2) Connection moment for beam with L/d = 25.
(3) Ratio of (1)/(2).
(4) Connection moment for rotation of 0.01 radians.

TABLE IV TEST RESULTS OF TYPE A CONNECTION EFFECTS ON COLUMN CAPACITY

Specimen	Column	Conn. Plate Length (in)	L/r	CRC COLUMN LOADS F_y=36 KSI P_{cr} (kips)	CRC COLUMN LOADS F_y=40 KSI P_{cr} (kips)	P_{cr} from Southwell Plot (kips)	Beam Moment (in-kips)	Max. Col. Load (kips)
CT-1	3x3x3/16	5 1/2	52.9	66.3	73.0	-	0	-
							45	66.0
CT-2	3x3x3/16	5 1/2	105.9	47.0	49.2	44.2	0	42.0
							12	39.2
							24	33.0
							36	29.6
CT-3	3x3x3/16	5 1/2	166.0	21.0	21.0	22.5	0	21.5
							6	21.5
							18	21.2
							30	20.0
							39	18.5
CT-4	6x6x3/16	8 1/2	39.1	158.5	175.2	-	0	-
							36	133.5
CT-5	6x6x3/16	8 1/2	79.9	133.0	143.8	-	0	-
							36	122.0

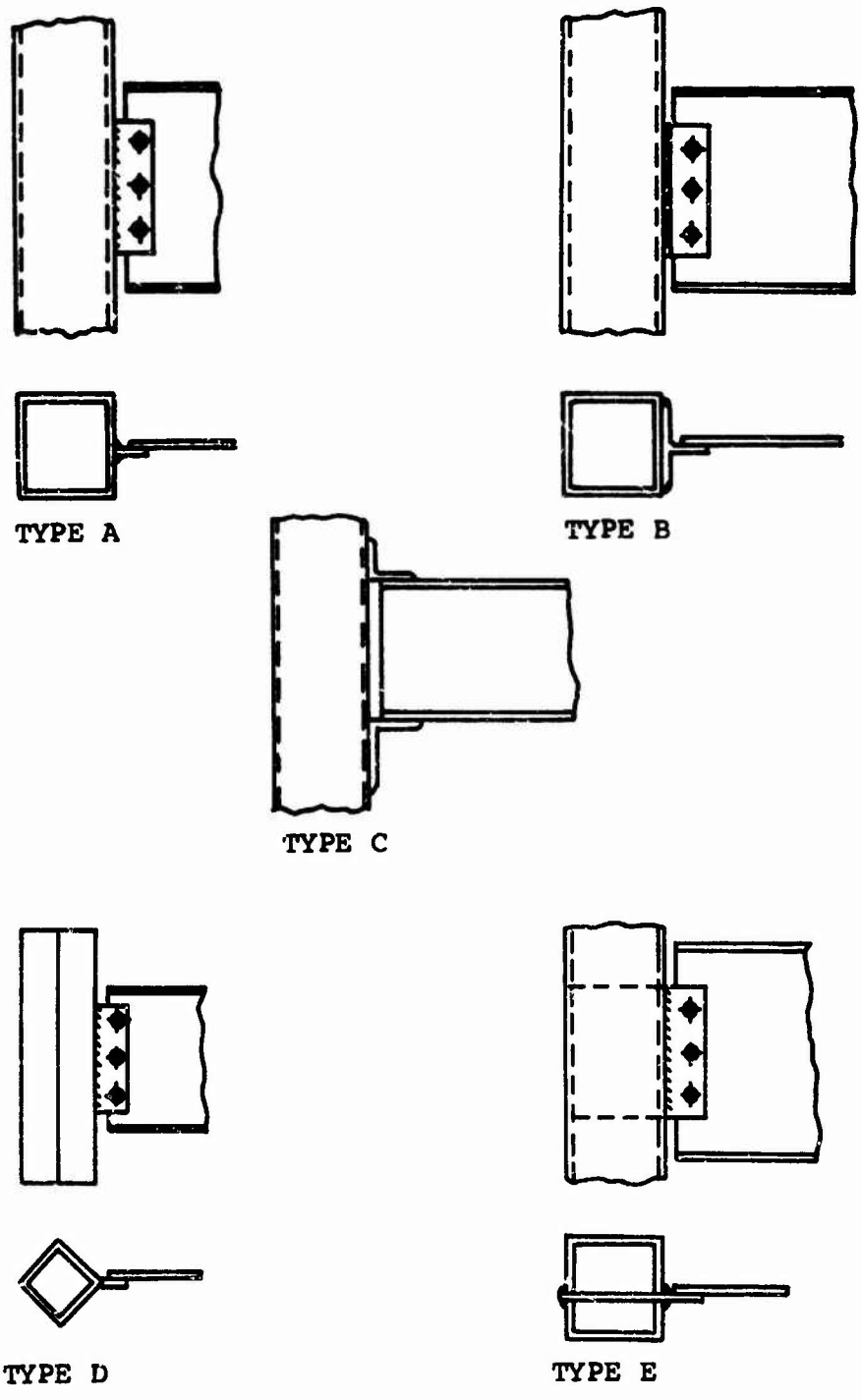

FIG. 1 WF TO TUBE SIMPLE CONNECTIONS

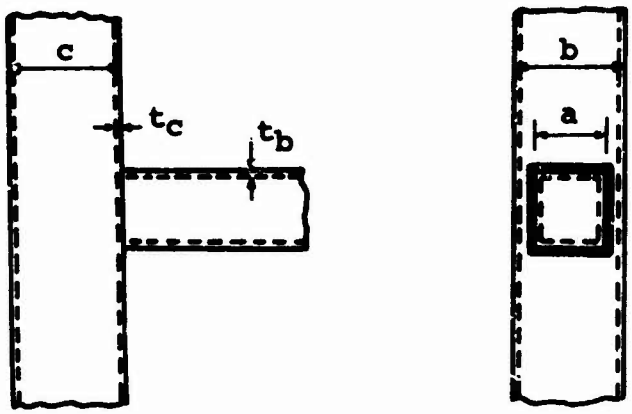

FIG. 2 MOMENT RESISTANT CONNECTION

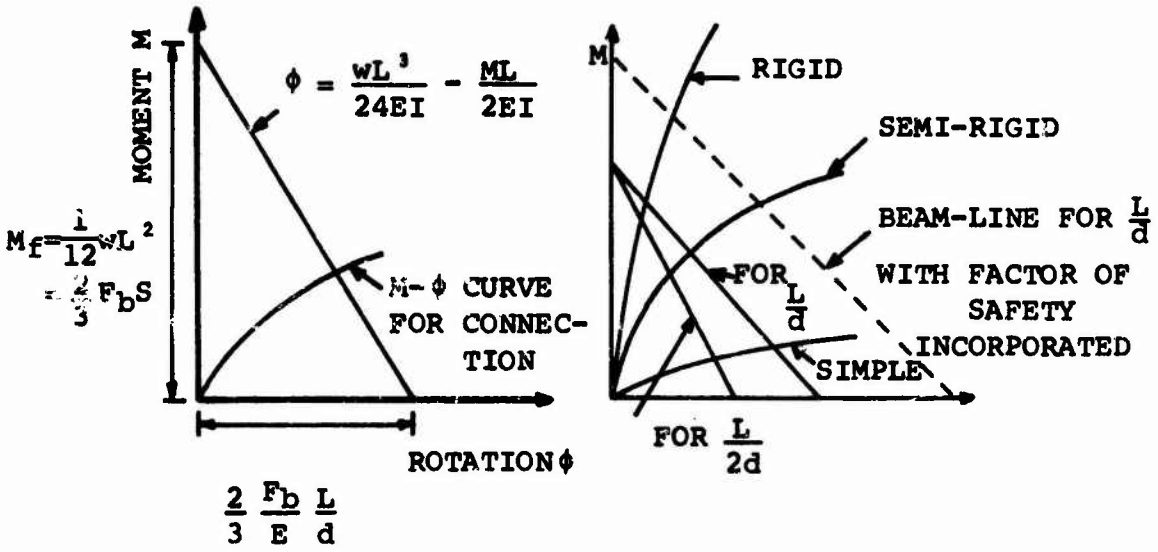

(a) BEAM-LINE FOR UNIFORMLY LOADED BEAM

(b) M-φ RELATIONS FOR DIFFERENT CLASSES OF CONNECTIONS

FIG. 3 BEAM-LINE CONCEPT

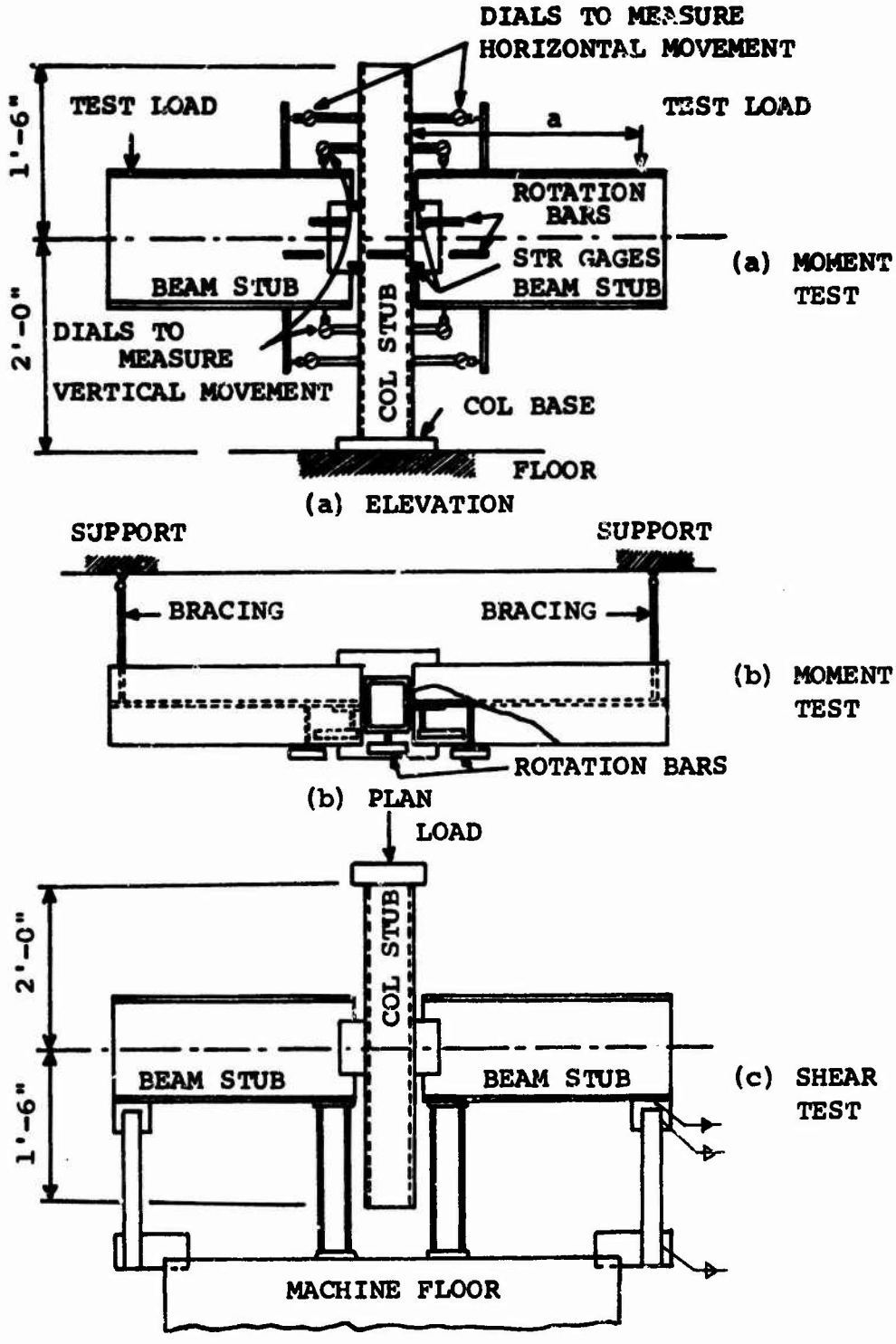

FIG. 4 TEST SET-UPS

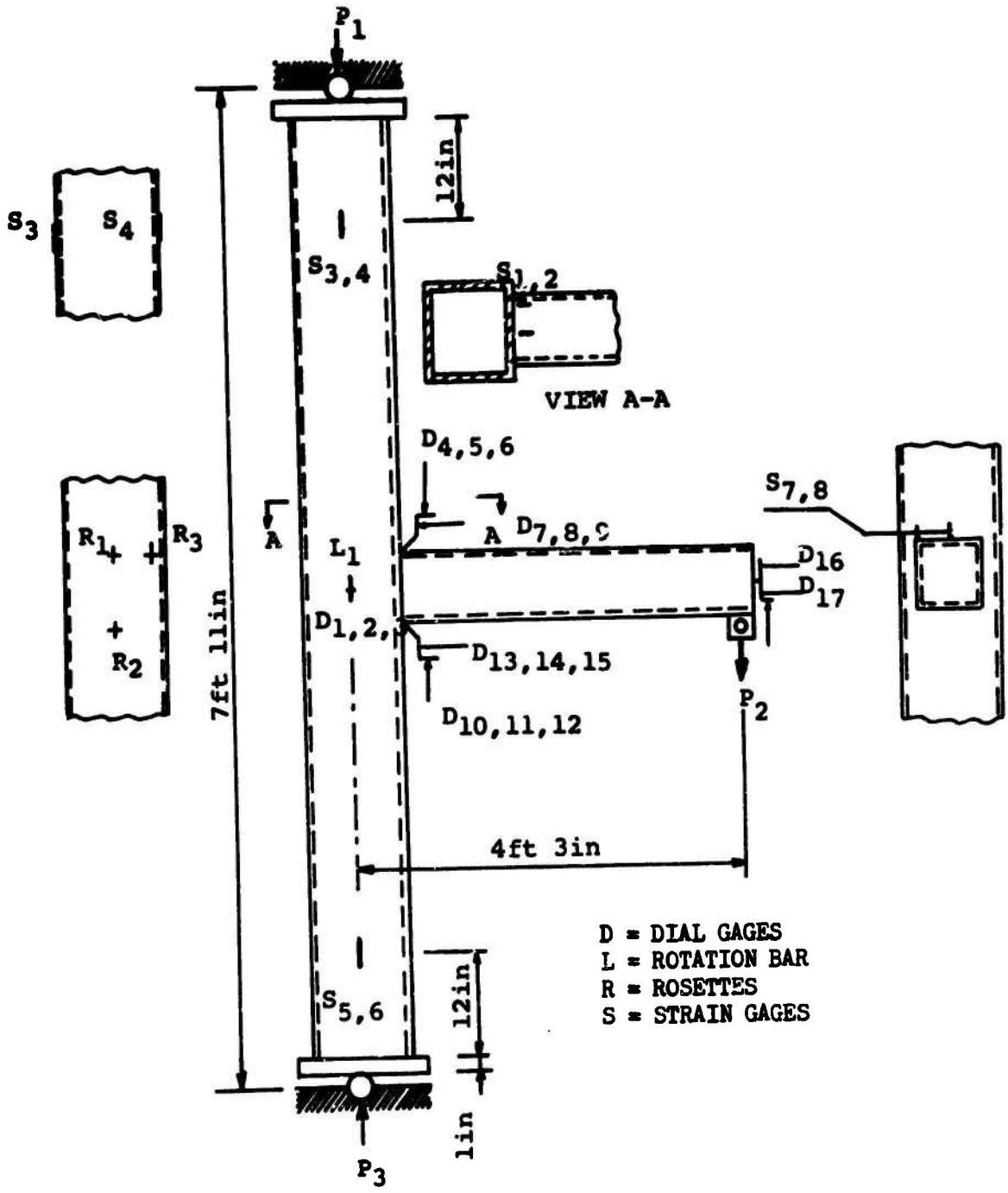

FIG. 5 TEST SETUP AND INSTRUMENTATION FOR T-TYPE JOINTS

MOMENT M IN INCH-KIPS
ROTATION ϕ IN RADIANS

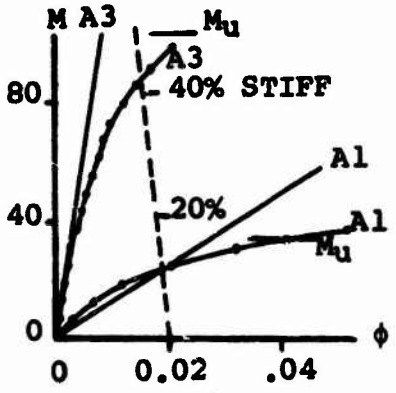

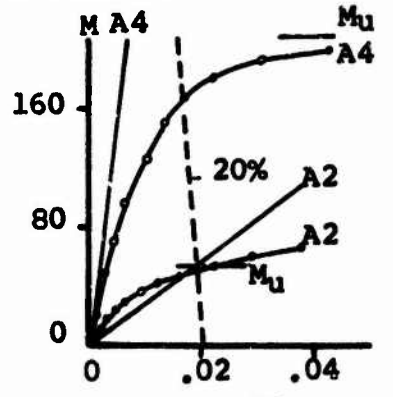

A1: 4"x$\frac{3}{16}$" TUBE; 5$\frac{1}{2}$" PLATE

A2: 4"x$\frac{3}{16}$" TUBE; 8$\frac{1}{2}$" PLATE

A3: 4"x$\frac{3}{8}$" TUBE; 5$\frac{1}{2}$" PLATE

A4: 4"x$\frac{3}{16}$" TUBE; 8$\frac{1}{2}$" PLATE

(NOTE: PLOTTED BEAM-LINES ARE FOR UNIFORMLY LOADED BEAMS WITH L/d=25 FACTOR OF SAFETY = 1.65)

FIG. 6 TYPE A CONNECTIONS

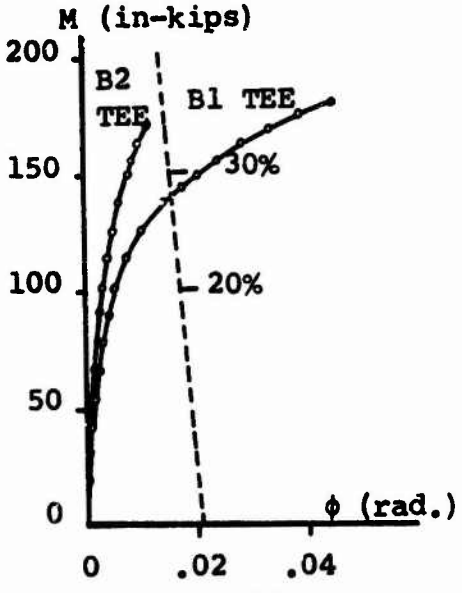

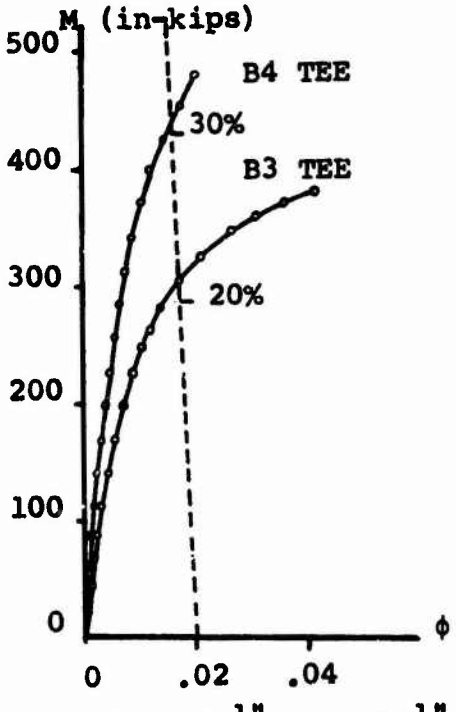

B1: 4"x$\frac{3}{16}$" TUBE; 8$\frac{1}{2}$" TEE

B3: 8"x$\frac{1}{4}$" TUBE; 11$\frac{1}{2}$" TEE

B2: 4"x$\frac{3}{8}$" TUBE; 8$\frac{1}{2}$" TEE

B4: 8"x$\frac{1}{2}$" TUBE; 11$\frac{1}{2}$" TEE

FIG. 7 TYPE B CONNECTIONS

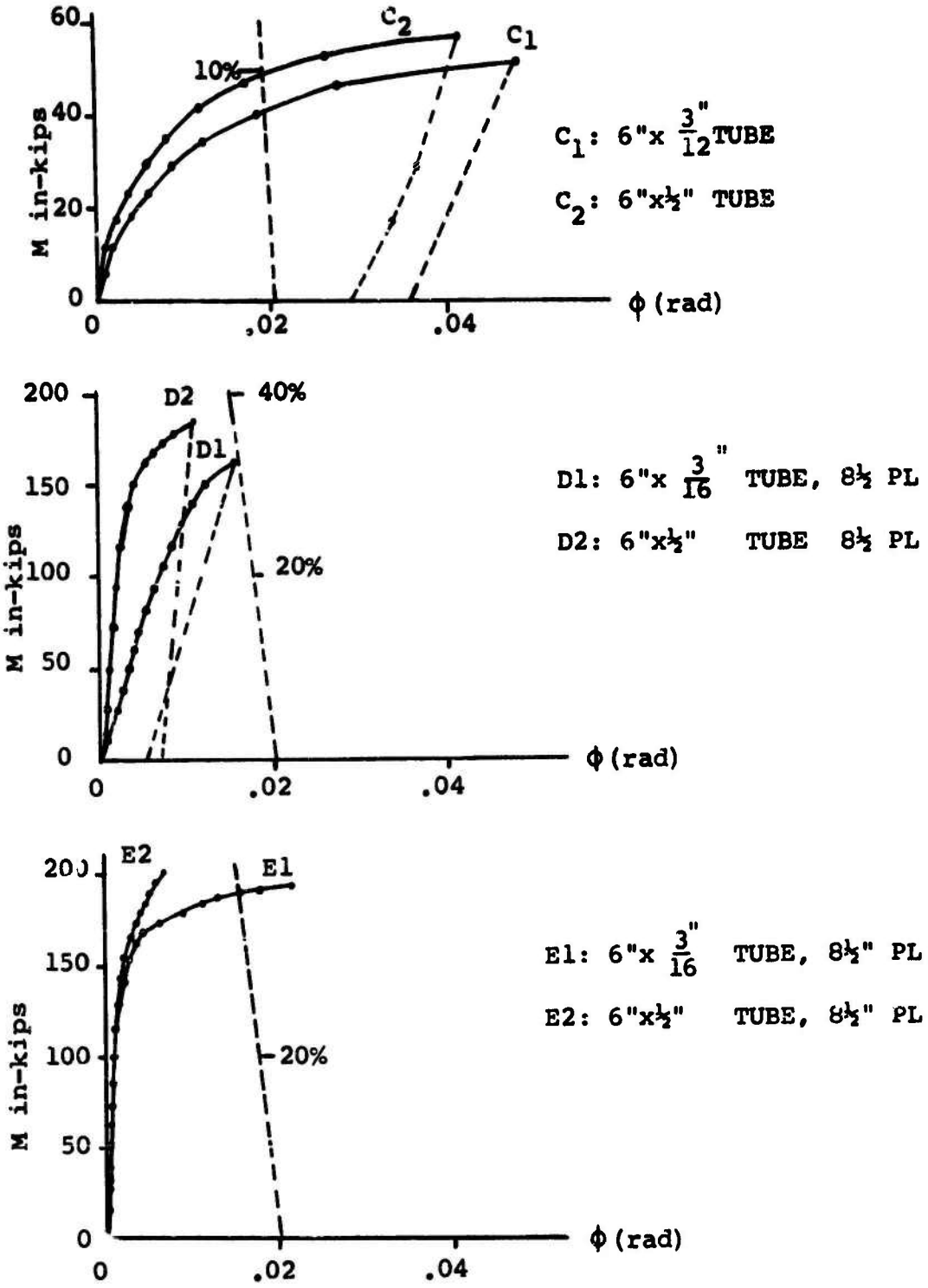

FIG. 8 TYPE-C, D, AND E CONNECTIONS

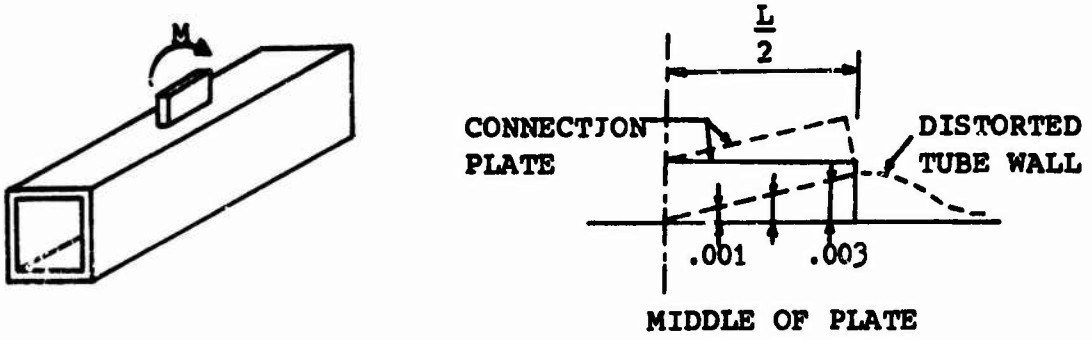

FIG. 9 TUBE MODEL FOR A-TYPE ANALYSIS

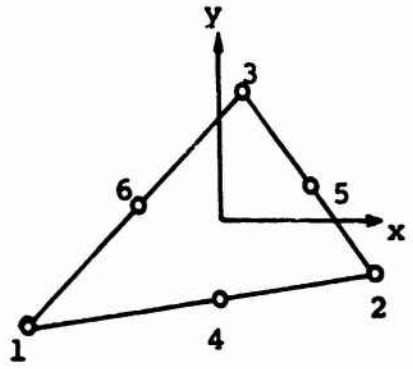

NODAL VECTOR:

$$\{r_p\}_i = \begin{Bmatrix} u \\ v \end{Bmatrix}_i \quad (i=1,2....6)$$

(a) PLANE STRESS ELEMENT

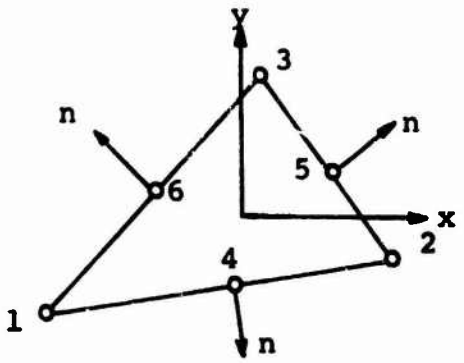

NODAL VECTOR:

$$\{r_b\}_i = \begin{Bmatrix} w \\ w,_x \\ w,_y \\ w,_{xx} \\ w,_{xy} \\ w,_{yy} \end{Bmatrix}_i \quad (i=1,2,3)$$

$$\{r_b\}_j = \{w,_n\}_j \quad (j=4,5,6)$$

(b) BENDING ELEMENT

FIG. 10(a) PLANE STRESS AND PLATE BENDING FINITE ELEMENTS

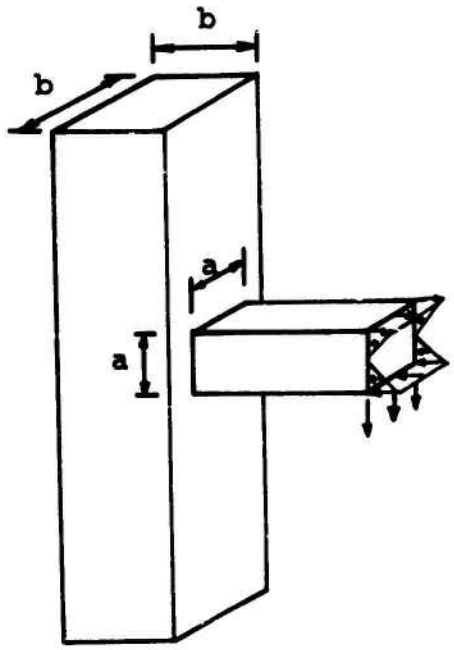

FIG. 10(b) TUBE MODEL FOR T-TYPE ANALYSIS

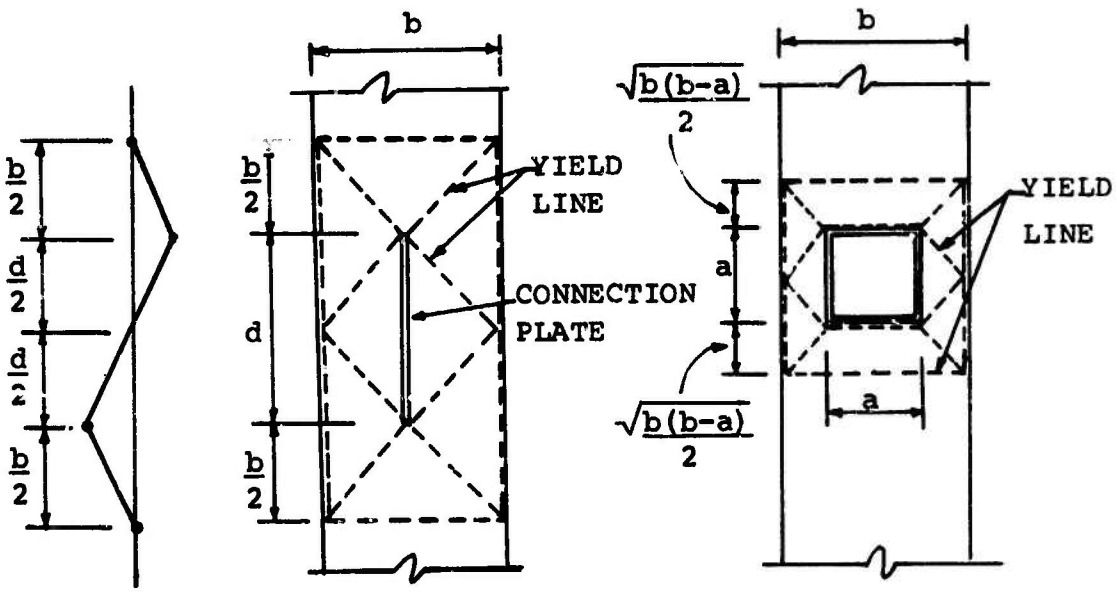

(a) TYPE-A SIMPLE CONNECTION (b) T-TYPE CONNECTION

FIG. 11 YIELD LINES

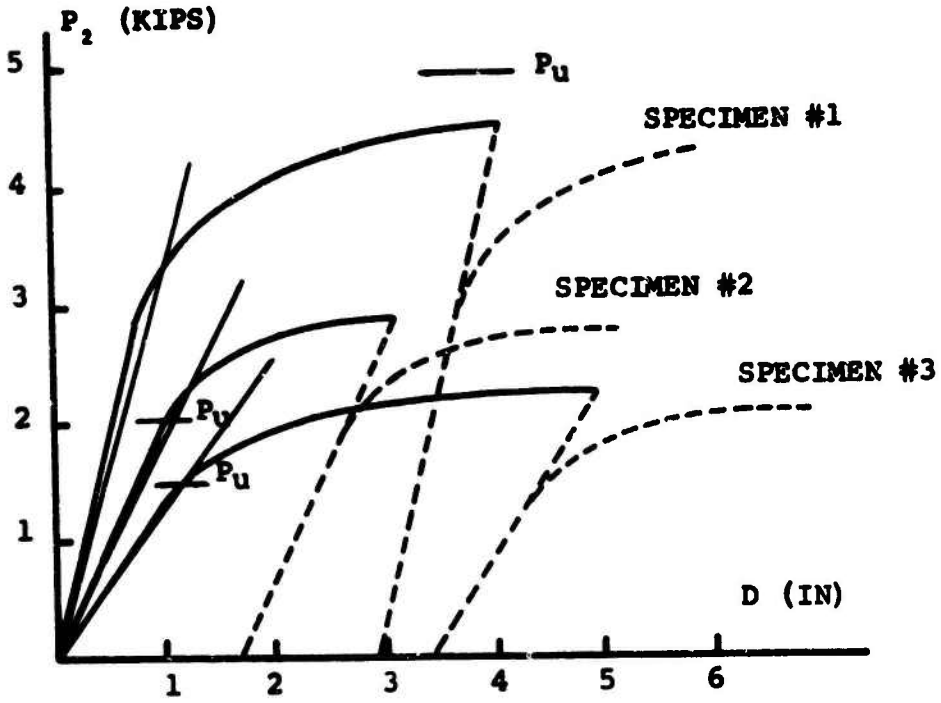

FIG. 12(a) LOAD-DEFLECTION CURVE FOR b/t_c = 24 AND b/a VARIABLE

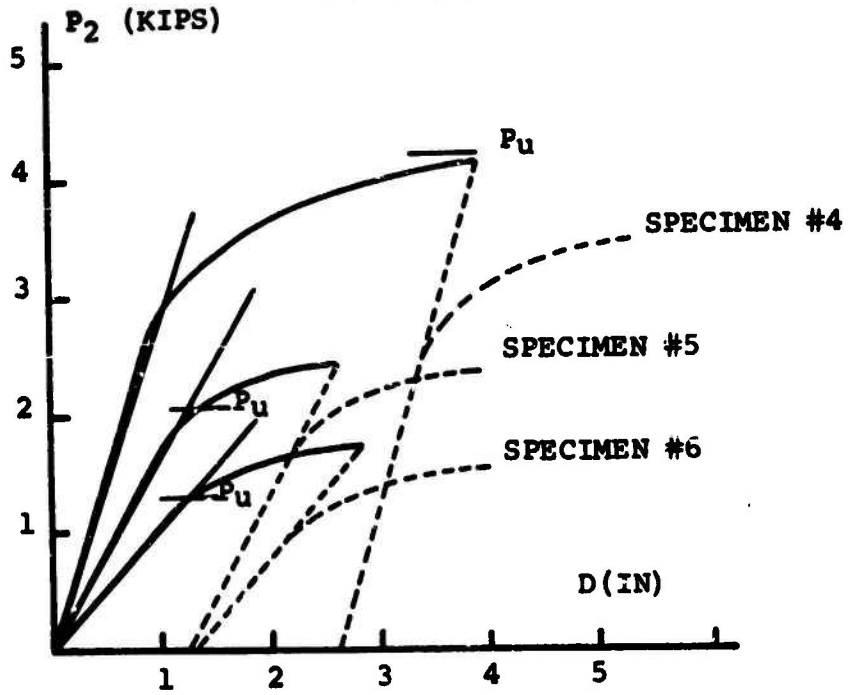

FIG. 12(b) LOAD-DEFLECTION CURVE FOR b/t_c = 20 AND b/a VARIABLE

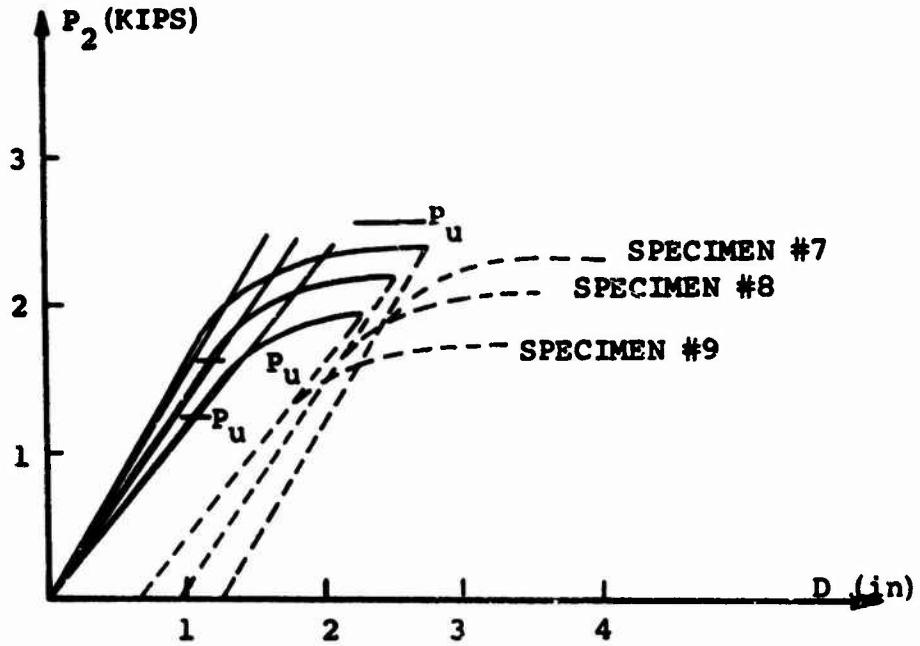

FIG. 12(c) LOAD-DEFLECTION CURVE FOR b/a=1.33 AND b/t_c VARIABLE

A FILAMENT-WOUND, STRUCTURALLY EFFICIENT COMPOSITE JOINING TECHNIQUE

MICHAEL HANSON
Eustis Directorate,
USAAMRDL,
Fort Eustis, Virginia

DALE P. ABILDSKOV
and
LARRY J. ASHTON
Fiber Science, Inc.
Gardena, California

ABSTRACT

Composite materials are finding increasing usefulness in structural members; however, the advantages offered by composite materials, particularly low weight, are often lost because large, heavy, inefficient end fittings are used at the structural joints.

A novel composite joint has been developed consisting of a flared filament-wound fitting which mechanically entraps a small lightweight metallic plug. The winding process places the fibers in essentially a tensile field, thus providing optimum structural efficiency. The fabrication is totally automated, resulting in a highly repeatable and cost-effective process.

The end fitting is being evaluated in conjunction with a program to test composite fuselage sections for helicopters. The test sections have sandwich type construction with filament-wound skins and PVC foam. The simulated fuselage sections are 18-inch-diameter and 40-inch-long hollow cylindrical elements. There are four end fittings on either end of the section to simulate the four bolt fittings on the tail boom of the helicopter. The composite fittings are designed to have sufficient strength to fail the four 3/8-inch attachment bolts.

NOMENCLATURE

(Reference Figure 3)

FS	Factor of safety.
P	Load, lb.
p	Pressure acting against fitting windings in the plug dome.
R_e	Radius at mid band where winding angle is 90 degrees, in.
R_i	Radius to inside of windings at fitting tangent line, in.
R_n	Radius to mid wall of underformed fitting at point "n", in.
R_o	Radius to outside of windings at fitting tangent line, in.
t_n	Thickness of windings at point "n", in.
t_o	Thickness of windings at fitting tangent line, in.
X	Dimension measured from fitting tangent line, in.
α	Angle between filaments and a meridian line, deg.

α_n Winding angle (angle between filaments and a meridian line) at point "n", deg.
α_o Winding angle at fitting tangent line, deg.
σ_α Composite (fibers and resin) stress in direction of fibers, psi.
σ_x Composite (fibers and resin) stress in axial direction, psi.
τ_b Average bond stress between fitting windings and structure to which fitting is bonded, psi.

INTRODUCTION

Composite materials, especially graphite/epoxy advanced composites, are finding more and more applications in light-weight aircraft structures. Advantages can be accrued due to the lower weight and improved fatigue characteristics of structural components and also, in many instances, a significant improvement in production costs.

In the case of hi-modulus composite components, a primary aircraft structural item may be tailor-made to be lighter, stiffer and with significantly improved fatigue life as compared to the corresponding traditional metal hardware. With a predicted decline in the price range of graphite fiber to the $5.00 to $10.00 per pound level many applications will be generated for stronger, lighter, more fatigue resistant and more cost-effective primary structure.

A significant problem area or roadblock to the widespread adaptation of composite materials is the relative difficulty in design and the abnormally high weight penalty paid for making structural connections between composite structure and mating or adjoining metal sections. Typical of these problems has been the difficulty in making a light-weight, highly efficient structural joint between the new all-composite graphite/epoxy flaps, ailerons, divebrakes, and other structural control surfaces used in the newest fighter and bomber aircraft. Also, typical of the problems of connection of light-weight composite primary structures to existing all-metallic structure is the interest in attaching a composite helicopter aft fuselage or tail boom to a helicopter main fuselage. A number of programs have been accomplished -- both paper studies and actual hardware -- to show that significant weight and cost savings are possible in replacing entire aft fuselage sections of such helicopter aircraft as the Bell UH-1 and AH-1 series (see Figure 1). In these studies the difficulty in developing a light-weight attachment from the composite structure through the four bolt arrangement to the main fuselage has seriously degraded the weight advantages gained from using graphite/epoxy.

A significant improvement in structural joints can be realized if concentrated loads at the joint connection points can be directly transmitted into fiber material such that the fibers are operating in their most efficient mode; namely - tension and compression. Where attachment is handled in tension and compression rather than interlaminar or bonding shear, the fatigue life is found to be greatly improved. A number of schemes have been developed for manufacturing helicopter rotor blades of composites where continuous fibers wrap around the root-end connection. The physical arrangement and design of blades allows for this superior attachment

scheme. Testing on composite blades for loads and fatigue is so promising it is expected that all helicopter rotor blades will eventually be designed and built of composites.

It is impractical to terminate all fibers in an aircraft flap or aft fuselage application around a single point in a continuous fiber manner achieving the excellence of design and efficiency mentioned for the rotor blade. However, a technique is discussed herein where continuous fibers can be used efficiently in a light-weight arrangement to fasten composite construction to localized point loading. The technique involves filament winding continuous fiber around a metal attach fitting in a manner to allow a geodesic and natural tensile loaded path of the fiber to the fitting. The filament-wound structure is wound as back-to-back conical sections making two attach fittings in a single operation. The windings are deformed before cure into a flat section - providing a long and increasingly large bonding area for tying the continuous filament wound fibers to the basic composite structure.

This paper addresses a program performed at Fiber Science, Inc. in Gardena, California, under the direction of the Department of the Army, USAAMRDL, Eustis Directorate, Structures Area, Fort Eustis, Virginia, Contract No. DAAJ02-74-C-0011.

In this program, the technique of filament winding back-to-back conical attach fittings has been demonstrated and practically applied to a short 18-inch-diameter, 40-inch-long simulated fuselage section. The simulated fuselage section with four attach fittings at either end, located on the circumferential periphery, is loaded in tension, compression and torsion and subjected to ultimate and fatigue testing to determine the structural characteristics of the new attach fitting scheme.

COMPOSITE FITTINGS DESIGN AND ANALYSIS

In the simulated fuselage program with Fort Eustis (the subject herein) the local replacement of the 1/2" PVC sandwich core material with the deformed conical filament wound attach fitting was shown. The fittings have also been designed and applied to a full scale AH-1G aft fuselage where the fitting locally replaces 5/8" Nomex Honeycomb. Figure 2 shows a cross-section of the assembly.

The attach fittings (see Figure 3) were designed to redistribute (spread out) localized axial tension or compression loads before transferring them through a bonded shear joint into the skins of a sandwich wall monocoque structure. A metallic plug is used in much the same way as a polar ring in a filament-wound pressure vessel to feed load into the windings. The windings are placed on a geodesic path which wraps them around the fitting and then fans outward to create a large bonding surface to the monocoque shell. By wrapping around the metallic plug, the problem of low interlaminar shear strength, prevalent in all composite structures, is eliminated and the strength problems become primarily the strength of the windings and the bonding strength between the flared composite fitting and the shell faces.

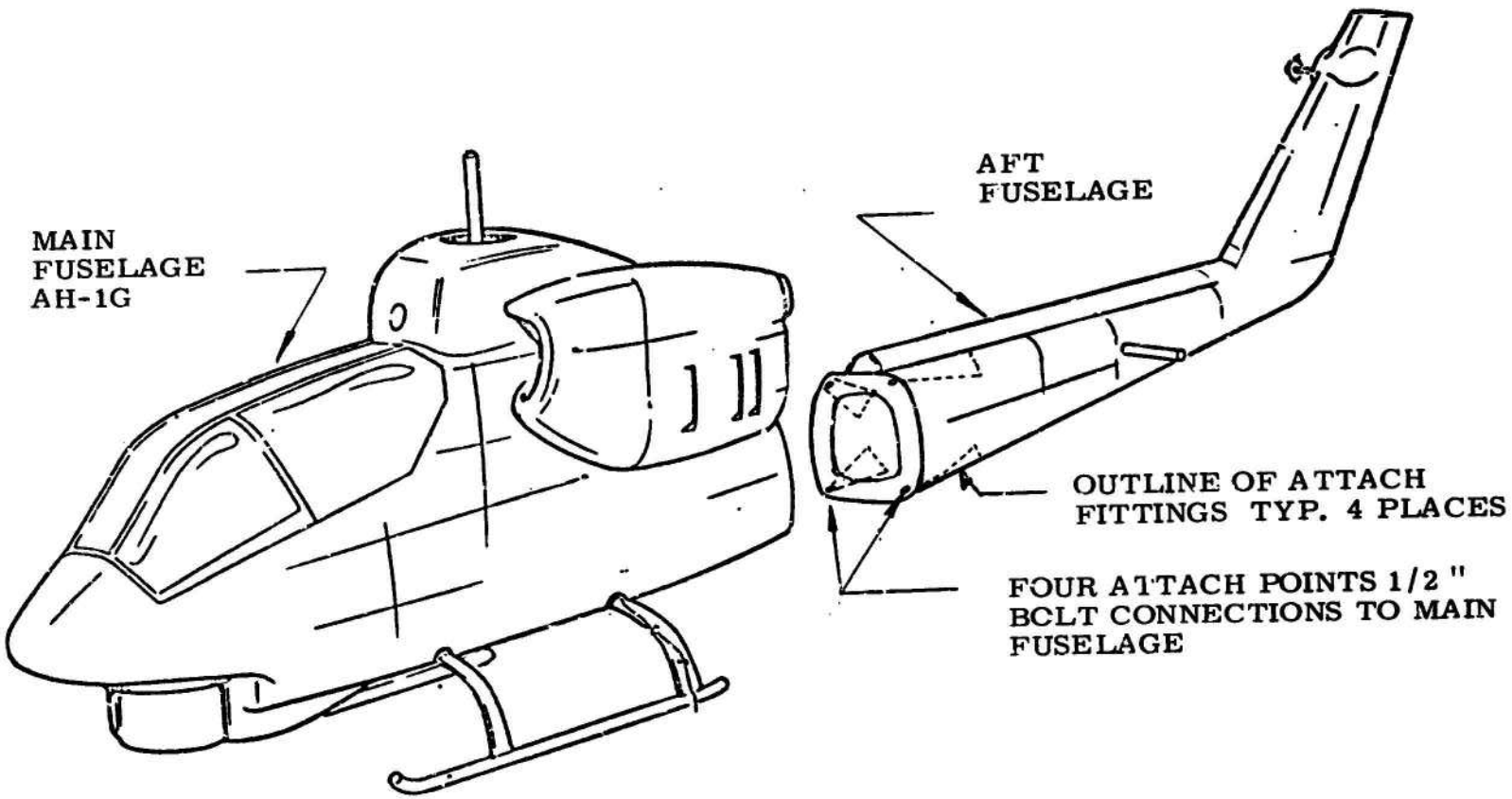

FIGURE 1. TYPICAL MAIN FUSELAGE CONNECTION ON BELL HELICOPTER.

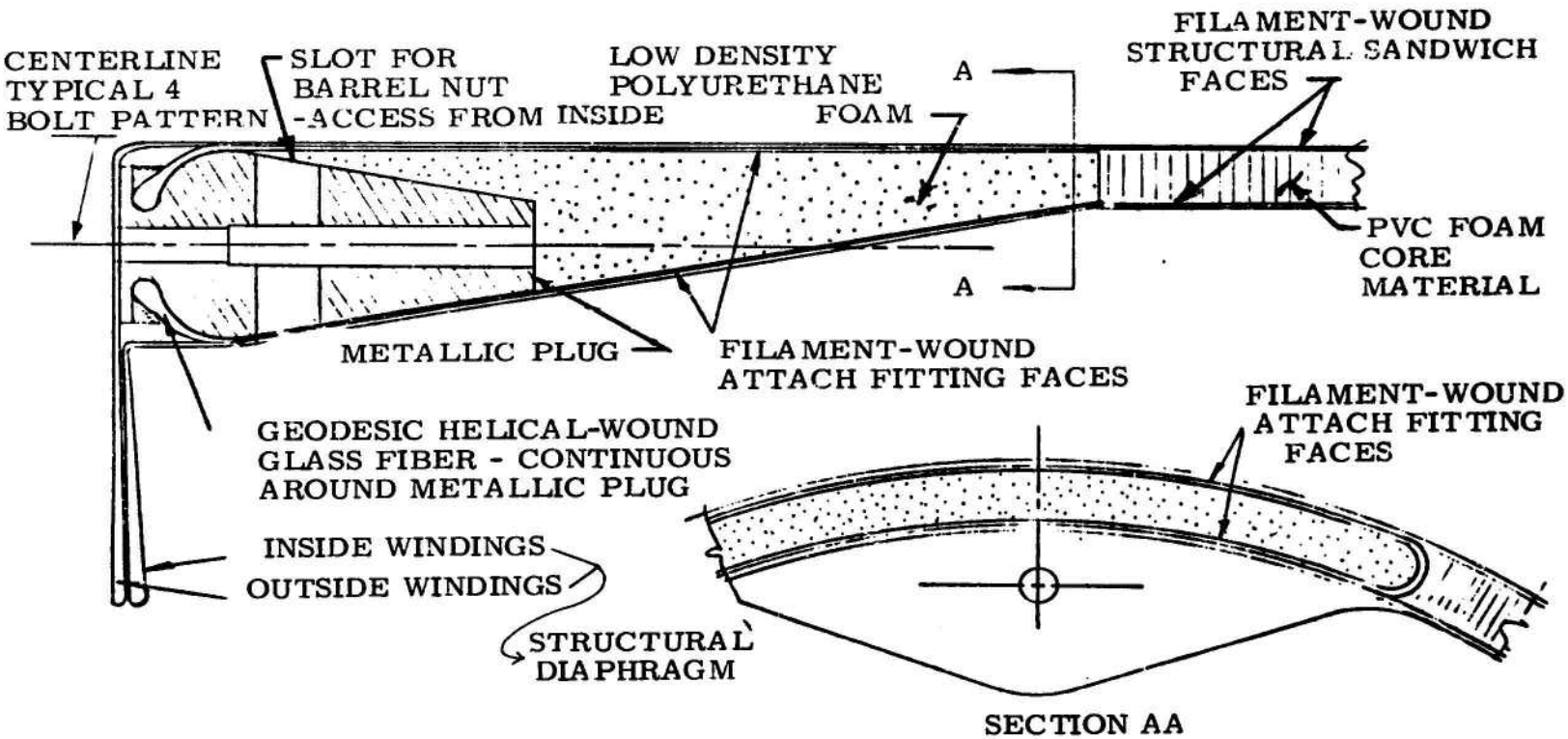

FIGURE 2. ATTACH FITTING - LOCALLY DISPLACING SANDWICH WALL

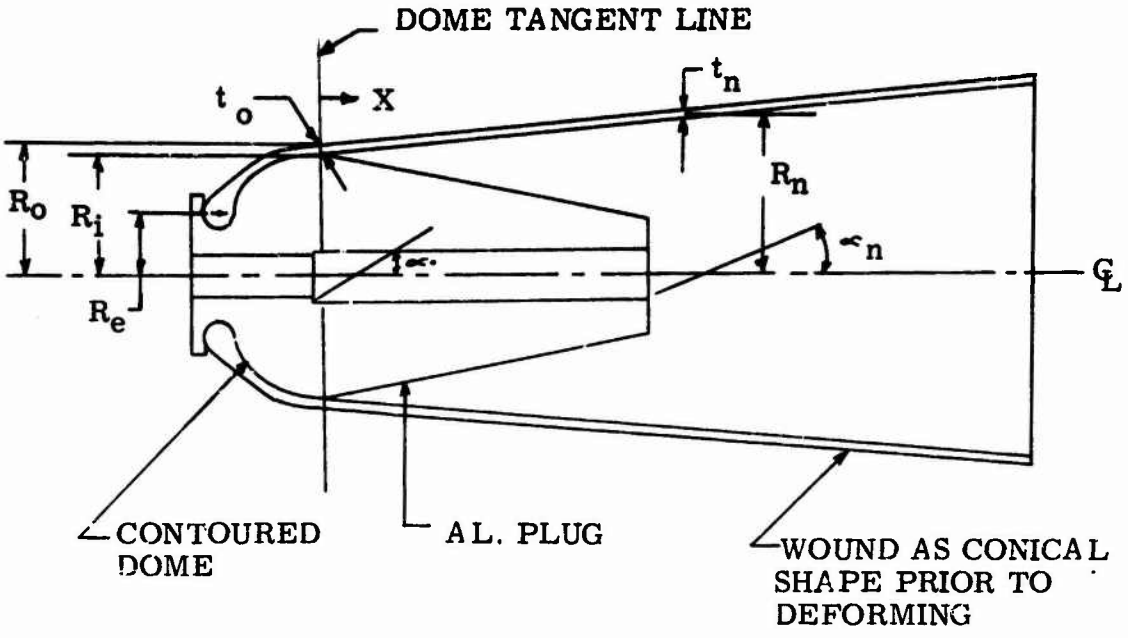

FIGURE 3. ATTACHMENT FITTING PRIOR TO BEING CONFIGURIZED AND CURED

The flared filament-wound portion of the fitting is foam filled and formed either in place or in female tooling prior to curing to fit virtually any contour. The large planform area of the flared portion provides a very effective bond area and efficient load transfer. The foam filled sandwich allows the windings to react efficiently to tension or compression loads.

The portion of the plug (metallic attach fitting) which contacted the windings was configured similar to the ideal (constant stress) shape for a filament-wound pressure vessel. Thus the pressure acting against the windings is nearly uniform and the stress level in the windings over the dome are constant. The most critical stress area is just aft of the dome tangent line where the loads are no longer parallel to the fibers.

The stresses in the windings over the dome portion of the fitting plug are;

P = 21,000 lbs. (design fitting tension load)

t_o = .0718 in.
R_i = 1.0540 in.
R_o = 1.1258 in.
α_o = 30 deg.

} See Figure 3

$$p = \frac{P}{\pi R_i R_o} = 5633 \text{ psi} \quad (1)$$

$$\sigma_{\alpha} = \frac{p(R_o + R_i)}{4 t_o \cos^2 \alpha_o} = 57,004 \text{ psi.} \quad (2)$$

The allowable composite strength of S-glass epoxy is assumed at 175,000 psi. (See Figure 3).

$$FS = \frac{175,000}{57,004} - 3.07 \quad (3)$$

The stress in the winding just aft of the plug tangent line are;

$$\sigma_X = \frac{P}{\pi (R_o^2 - R_i^2)} = 42,700 \text{ psi} \quad (4)$$

The allowable single cycle composite tensile strength at = $\pm$ 30 deg of S-glass/epoxy is 86,000 psi. (See Figure 4).

$$FS = \frac{86,000}{42,700} = 2.01 \quad (5)$$

The bonding area between the fitting windings and the fuselage skins is 126 in.^{2} giving an average bond stress of;

$$\tau_b = \frac{21,000}{126} = 167 \text{ psi} \quad (6)$$

Figure 5 shows a plot of winding angle and thickness versus the distance from the plug dome tangent line. The thickness and winding angle variations are desirable for accomplishing uniform load transfer from the fitting to the basic structure.

FABRICATION INCLUDING TOOLING APPROACH

Simulated fuselage sections were manufactured using the filament winding approach. Both S-Glass/epoxy and Kevlar 49/epoxy materials were incorporated for comparison. The fuselage sections were filament wound over an inflated preformed mandrel shown in Figure No. 6 using conventional filament winding equipment and standard sandwich wall construction. The filament wound faces, both internal and external, were wound to a thickness of .050 inches and PVC foam of 4 #/ft.^{3} density was used as the core material.

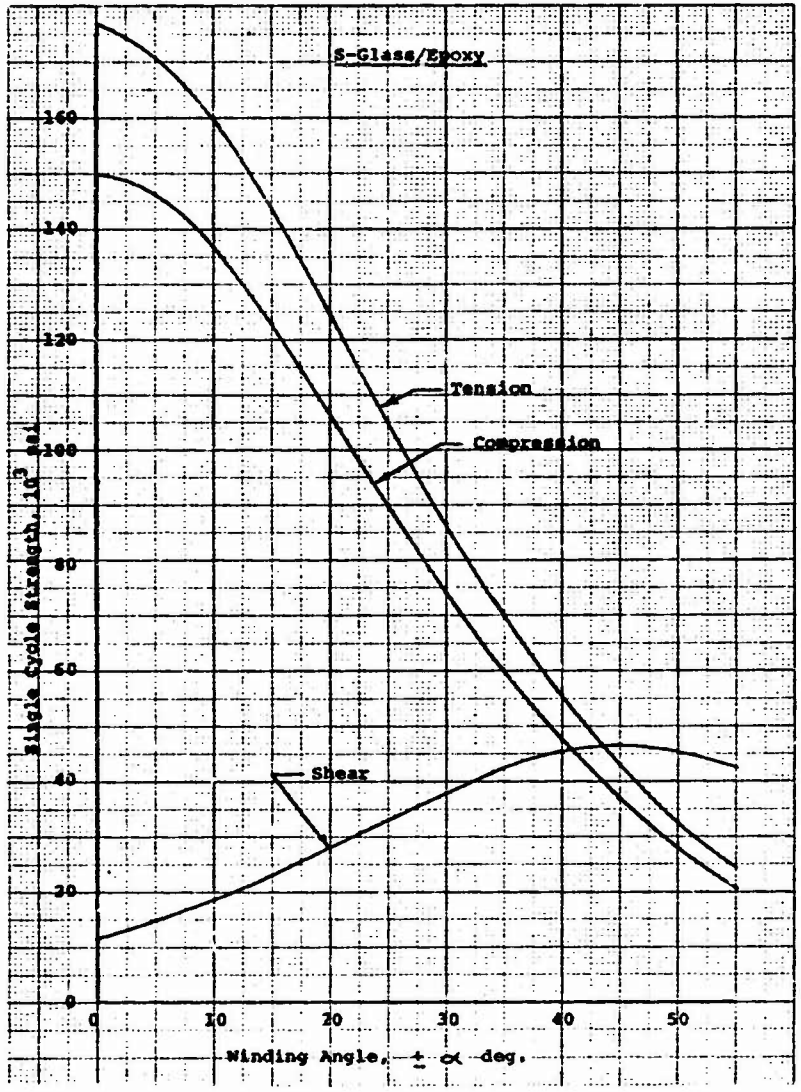

FIGURE 4. STRENGTH -VS- WINDING ANGLE, S-GLASS/EPOXY.

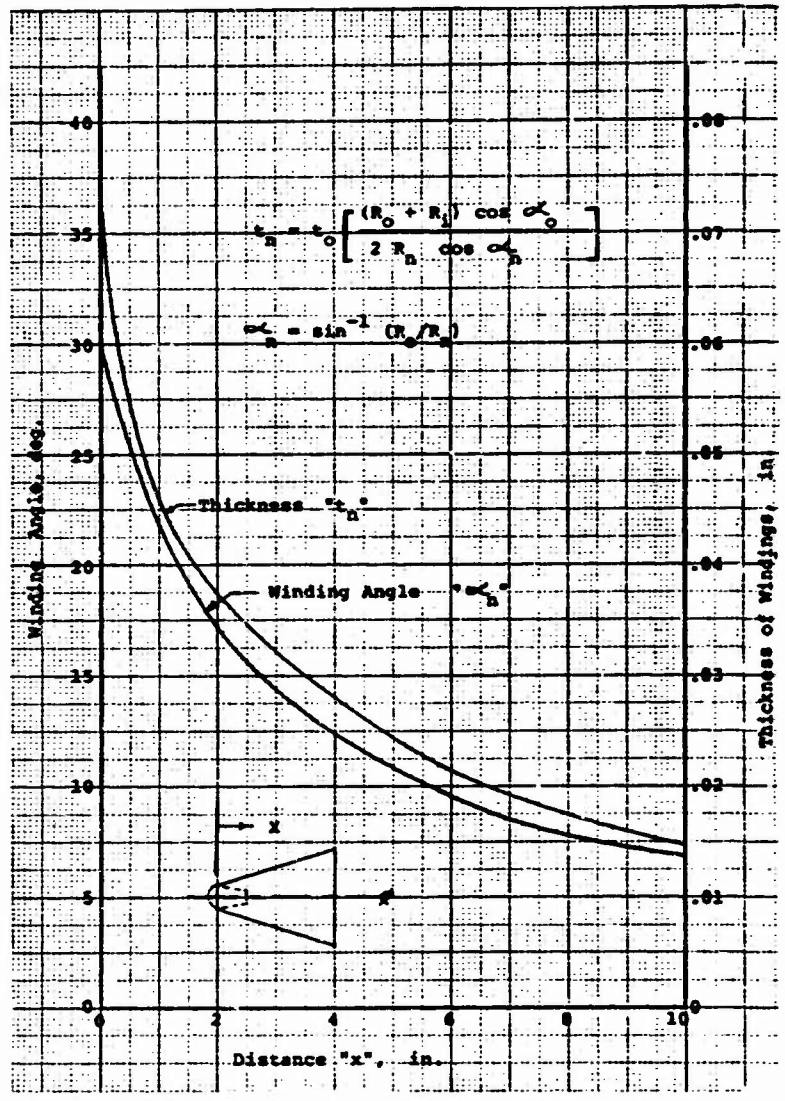

FIGURE 5. THICKNESS OF WINDINGS, & WINDING ANGLE -VS DISTANCE

The flared attach fittings were filament wound over a back-to-back conical mandrel whose apex terminates in the metallic polar plug. A winding shaft passes through the plug and back-to-back conical mandrel for support in the winding machine. Figure 7 indicates the winding of the attach fitting over the back-to-back mandrel and metallic plug.

Reinforced plastic tooling was manufactured in the shape of a split mold to define the flared-out contour of the composite attach fitting (See Figure 8). The flared-out portion was formed to terminate to half-inch core thickness used in the basic simulated fuselage structure. Upon completion of the attach fitting winding, the wet-impregnated assembly was deformed into the split tooling and the internal space filled with a light-weight polyurathane expanding foam to provide the expansion pressure to place the deformed winding into final configuration in the mold. Upon cure of both the foam and the laminate, the fittings are removed and are prepared for bonding.

Figures 9 and 10 indicate the assembly operation of the fuselage, including the placement of the attach fittings , and final winding configuration. Note that the winding operation results in a natural partial diaphragm or ring frame at the end of the cylinder; thereby, automatically providing an integral and necessary part of the structure. Figures 11 and 12 show both the internal and external surfaces of the finally wound simulated fuselage. Note the location and placement of the attach fittings.

CONCLUSION

The fabrication of a structurally efficient integrally filament-wound attach fitting was one hundred percent successful with regards to proving the advantages of a machine wound, highly redundant and cost-effective joining technique. The winding of both the attach fittings and the cylindrical structure was performed using the wet filament winding technique and accomplished in a very short period of time. For example, attach fittings by the pair were wound in approximately 15 minutes. The winding of each phase of the cylindrical sandwich wall construction required approximately 30 minutes.

With the speed, accuracy, reproducibility and basic low-cost of the wet filament wound materials, the entire scheme of a light-weight structurally efficient attach fitting was conclusively proven.

At the time of printing the test sections (two each Glass/epoxy and two each Kevlar 49/epoxy) are awaiting structural testing at the Army Test Facility at Fort Eustis.

The simulated fuselage program has a direct bearing to the attachment of a fuselage typical in the Helicopter UH-1 or AH-1 series as well as others in that four attach bolts are used for securing the aft fuselage to the main fuselage. A program is presently under way through the Eustis Directorate with the Hughes Aircraft Company, as a prime contractor and Fiber Science, Inc., as the composite subcontractor to demonstrate and flight test a Bell Cobra AH-1G with a composite (graphite/epoxy) aft fuselage attached to the standard metal main fuselage in a manner similar to

that presented in this paper.

Two of the Cobra aft fuselages have been fabricated from filament-wound graphite epoxy and have been tested for fitting integrity at Hughes Aircraft. The maximum capability of the fitting is unknown since failure has occurred in the basic fuselage section at 150% of limit loads.

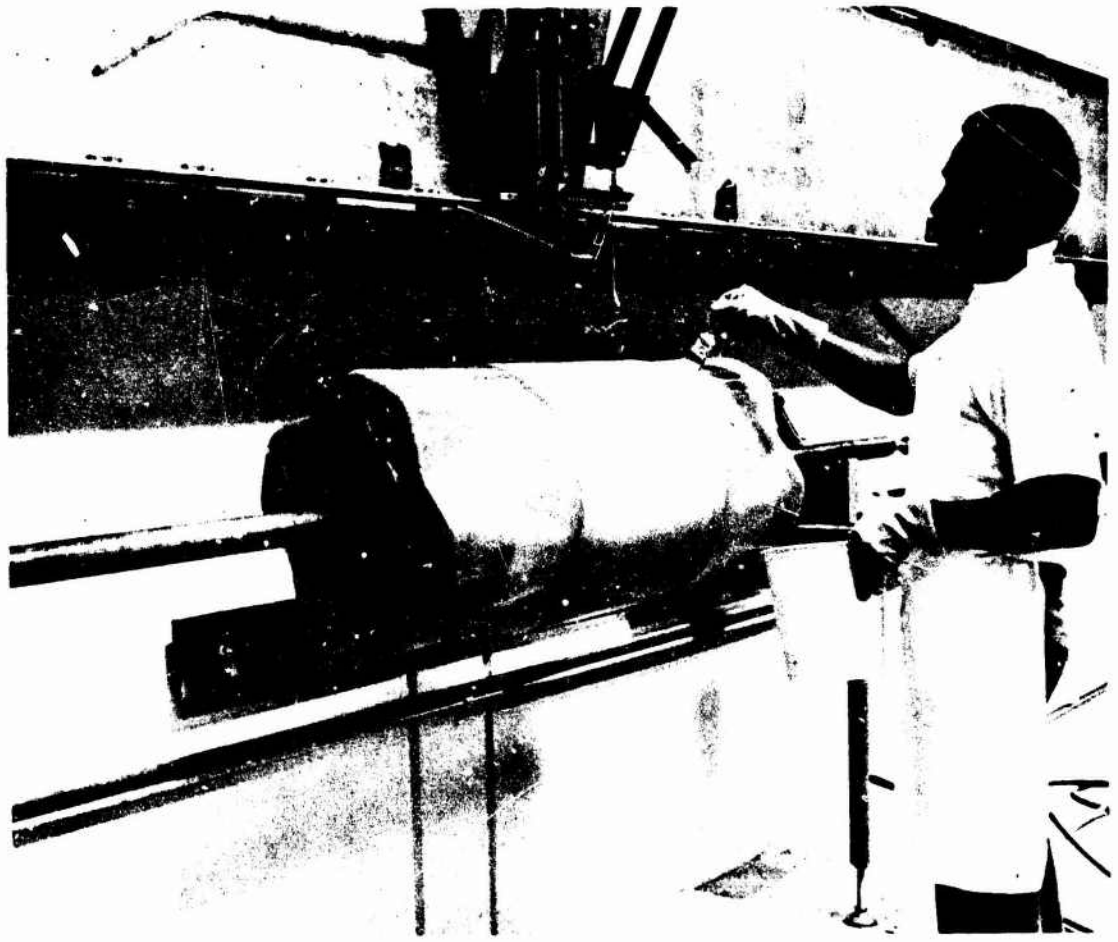

FIGURE 6. BASIC INFLATABLE TOOLING

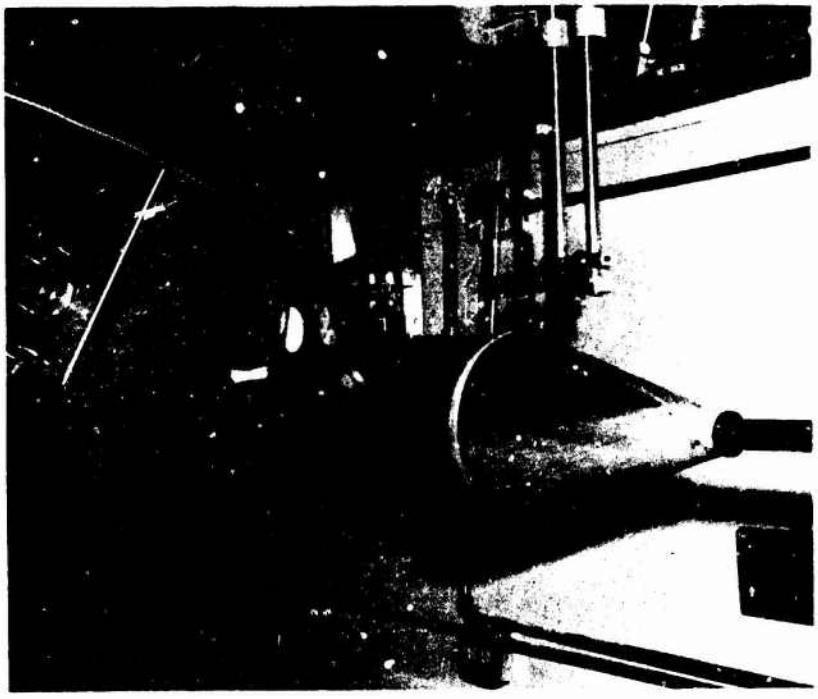

FIGURE 7. WINDING ATTACH FITTINGS

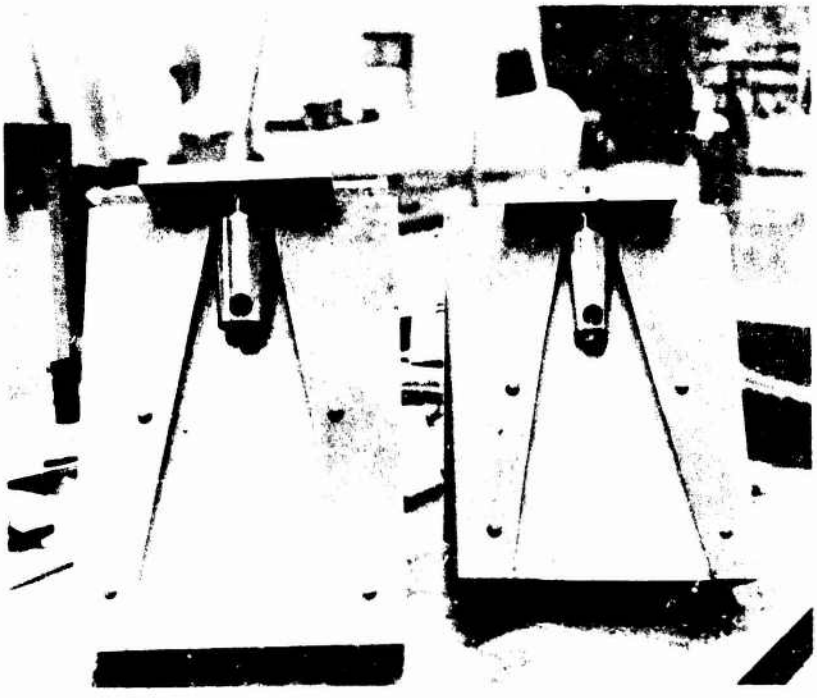

FIGURE 8. SPLIT MOLDS FOR FORMING ATTACH FITTINGS

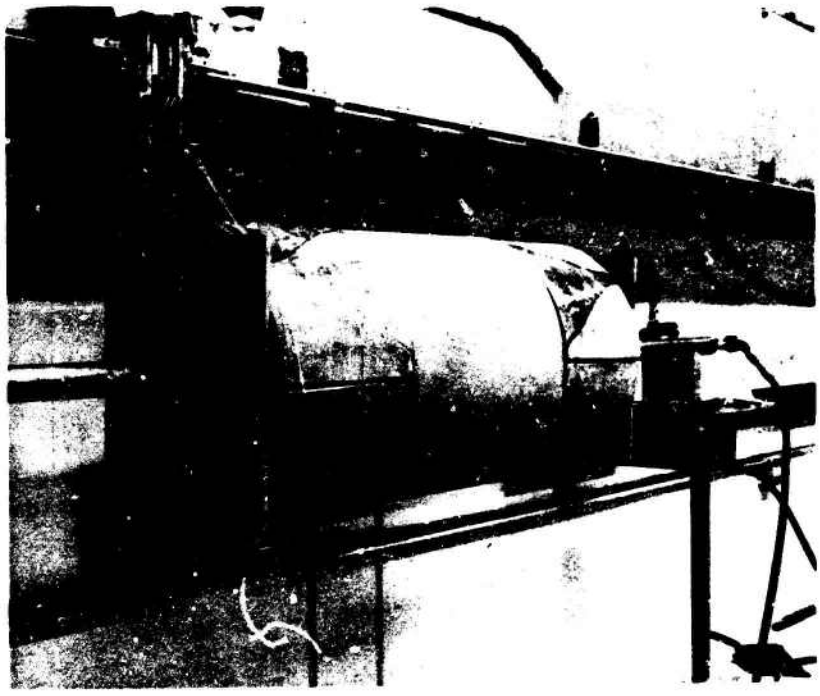

FIGURE 9. ASSEMBLY OF ATTACH FITTINGS AND PVC FOAM OVER INNER WINDINGS PRIOR TO WINDING EXTERNAL SANDWICH FACE.

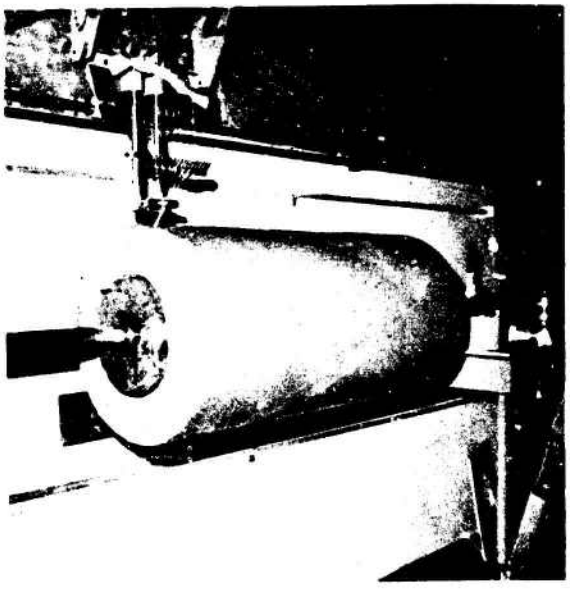

FIGURE 10. WINDING OF SIMULATED FUSELAGE

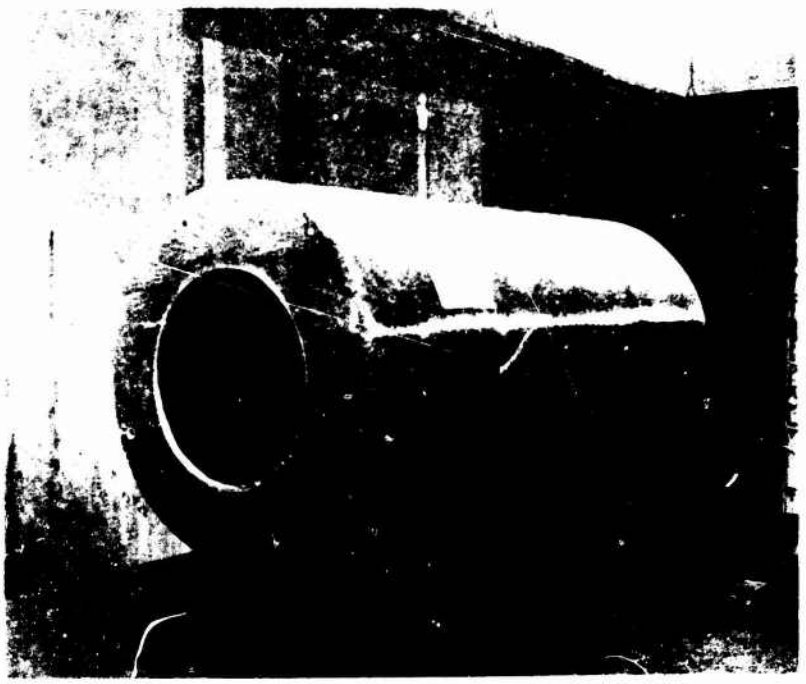

FIGURE 11. FINISHED SIMULATED FUSELAGE SECTION

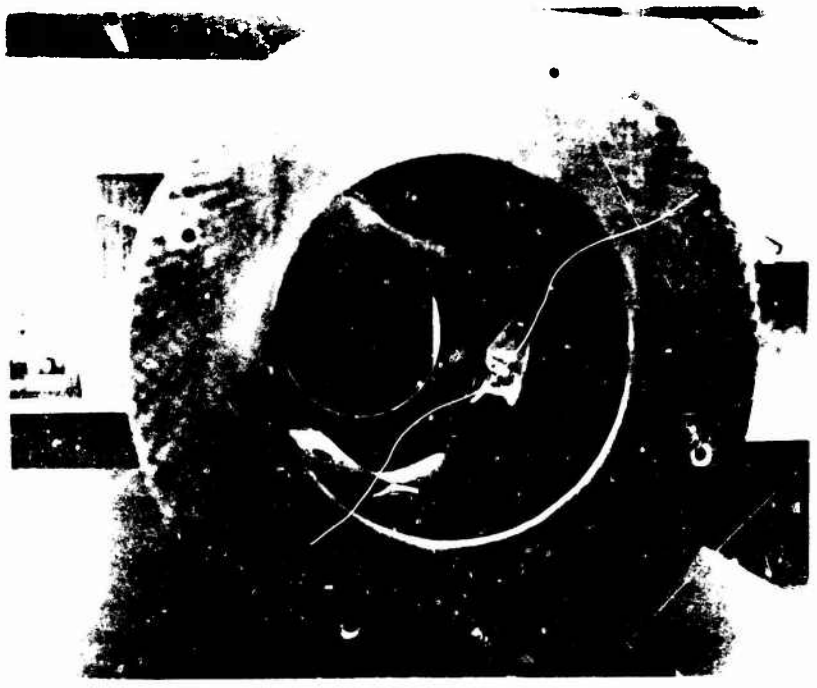

FIGURE 12. INTERNAL VIEW FINISHED SIMULATED FUSELAGE SECTION

FINITE ELEMENT ANALYSIS OF A MULTI-COMPONENT KINETIC ENERGY PROJECTILE

LEONARD M. GOLD
Mechanical Engineer
Stone & Webster Engineering Corporation*
Cherry Hill, New Jersey

NANCY A. STOWELL
Physicist
Pitman-Dunn Laboratories
Frankford Arsenal
Philadelphia, Pennsylvania

ABSTRACT

Finite element techniques are used to perform a launch stress analysis on a multi-component 27.5 mm kinetic energy projectile. The five parts of the projectile are each analyzed separately utilizing a layer of false boundary elements to determine the interaction between each component and those in contact with it. The stress history in the boundary elements is utilized as boundary conditions for the adjacent components. The analysis proceeds from the forward components toward the rear providing the additive inertia load to each. The resulting launch stress fields are shown for each component and the advantages and disadvantages of this approach are discussed. The analysis of this round generally indicated no serious problems and will act as an aid in the verification of actual projectile performance.

INTRODUCTION

A launch stress analysis is performed using finite element techniques on a 27.5 mm multi-component kinetic energy projectile for a new weapons system (see figure 1.) The Kinetic Energy round consists of five parts which are: 1) nose cone, 2) nose plug, 3) sabot, 4) projectile and 5) base. Each part is analyzed separately under launch conditions. To simulate the interaction between parts, a false layer of boundary elements is placed on each part where it comes in contact with an adjacent part. The layer of false boundary elements were constrained to remain elastic throughout the analysis. A Young's modulus of 10×10^6 psi was assigned to these elements. The false layer nodes were constrained in the axial or radial or both directions to prevent rigid body motion of these elements. The stress history calculated in the false layer is used to generate the boundary conditions for the next component.

*Formerly with Pitman-Dunn Laboratories, Frankford Arsenal, Phila., Pa.

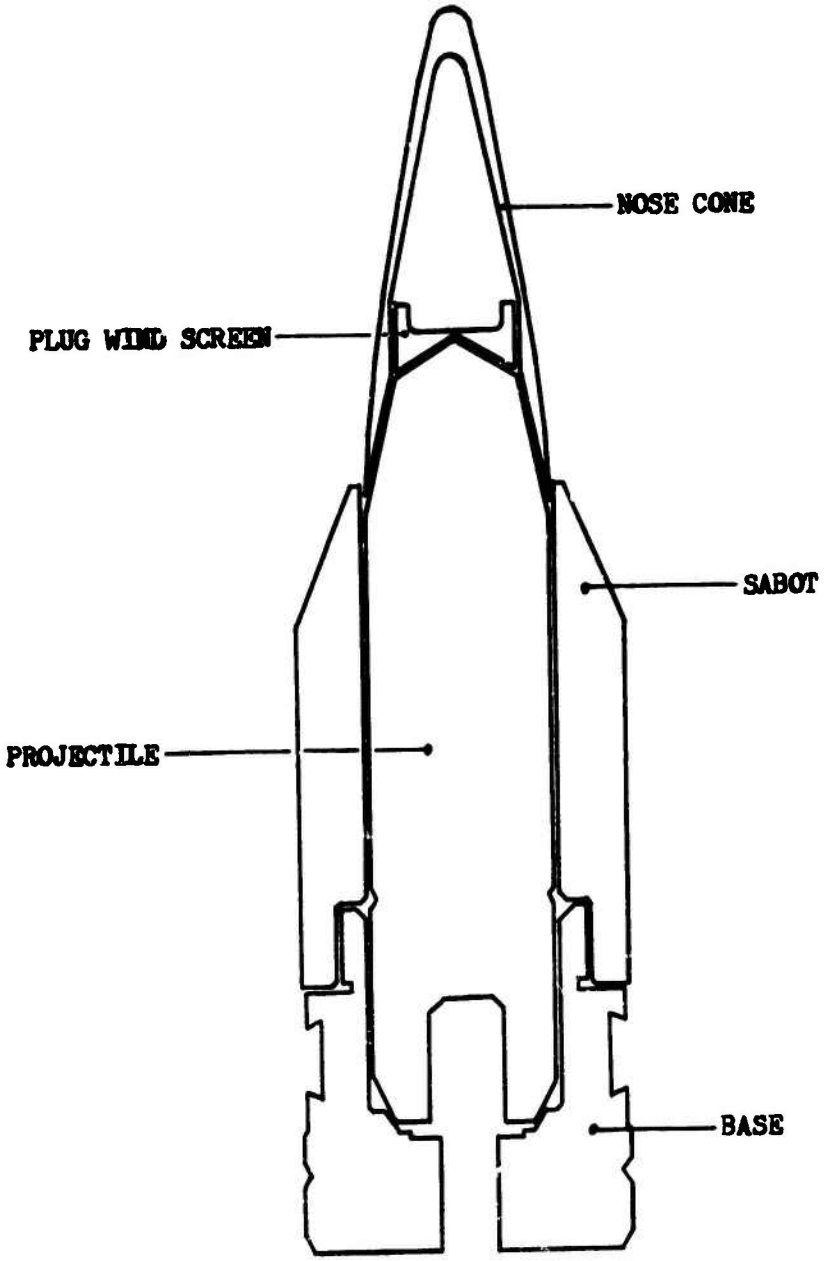

Figure 1. Multi-Component Kinetic Energy Projectile

The analysis proceeds from the nose cone toward the rear of the round. As each part is analyzed, the data provides the boundary conditions or transmission of loadings to the next part. The transmitted loads are programmed as normal stresses and simulated shear stresses. When a component is in contact with more than one part, then a combination of boundary conditions and false layers are utilized as the previous analyses dictate.

The loads generally applied throughout the projectile are shown in figures 2a, 2b and 2c. Figure 2a shows the propellant pressure and longitudinal acceleration which have the same history. The values are normalized to the peak. Figure 2b shows the ratio of angular velocity squared to peak angular velocity squared. This value multiplied by the center point radius for each element gives the local centrifugal force. Figure 2c shows the assumed band pressure loading applied to the aluminum base. The value of band pressure was unknown and assumed equal to the peak propellant pressure. From previous experience it is known that band pressure peaks sometime during engraving then drops to approximately two-thirds of the peak value for the remainder of the launch period. The peak band pressure was chosen approximately halfway through the engraving of the band.

A discussion of the generation of boundary conditions and the launch stress fields for the components is provided with iso-stress plots showing the effective stresses at peak launch pressure (56,547 psi).

The general technique utilized in this analysis is then discussed as to both advantages and shortcomings. Since this technique is the first approach to this problem suggestions are made which will enhance the capability of determining interfacing conditions and consequently improving launch stress analysis of multi-component projectiles.

The program used in this analysis is the Franklin Institute Two Dimensional Structural Analysis program called CRTPLS (1),(2). The program is capable of handling 400 nodes and 300 elements in its present form. Elastic-Plastic analysis is accomplished using a multilinear representation of the stress-strain curve. The von-Mises yield criteria is used along with isotropic strain-hardening. The tangent modulus of the stress-strain curve at the beginning of each loading is used for each load step. If the load progresses into the next linear portion of the stress-strain curve, the stresses are ratioed to bring them down to the stress-strain curve. Two simultaneous boundary pressure histories may be applied with varying local peak intensities. Longitudinal acceleration and centrifugal force histories can be applied. Nodal point loads in the radial and axial directions can also be applied. The program is also capable of accepting boundary displacements.

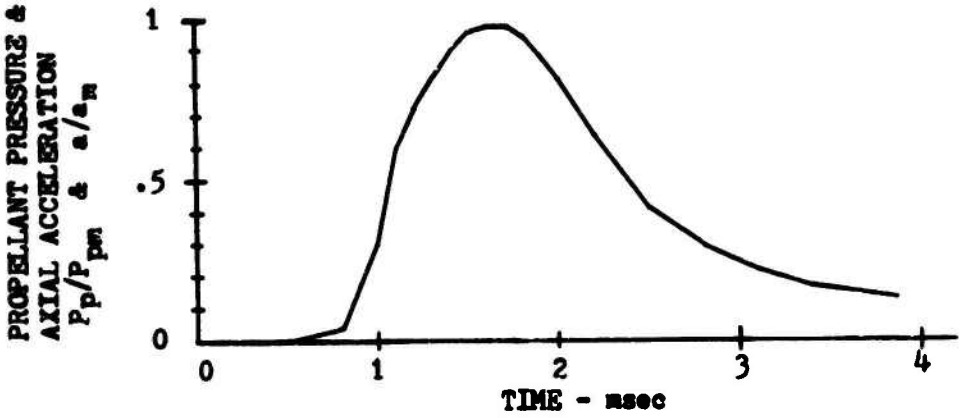

Figure 2a. Propellant Pressure and Axial Acceleration History

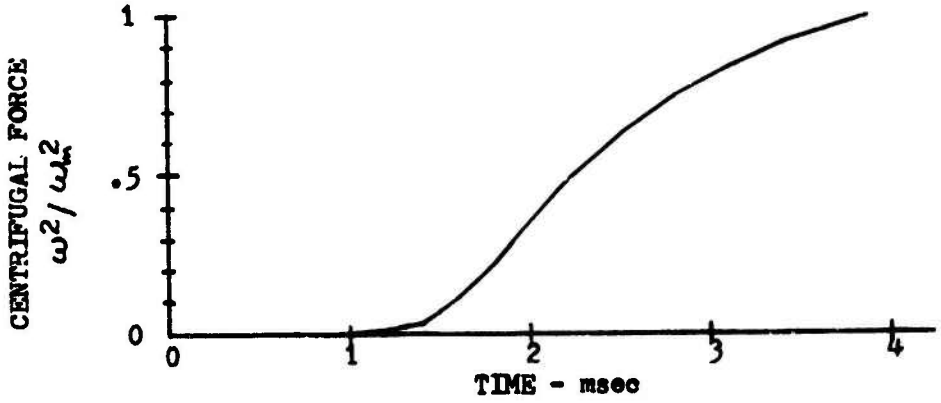

Figure 2b. Angular Acceleration History

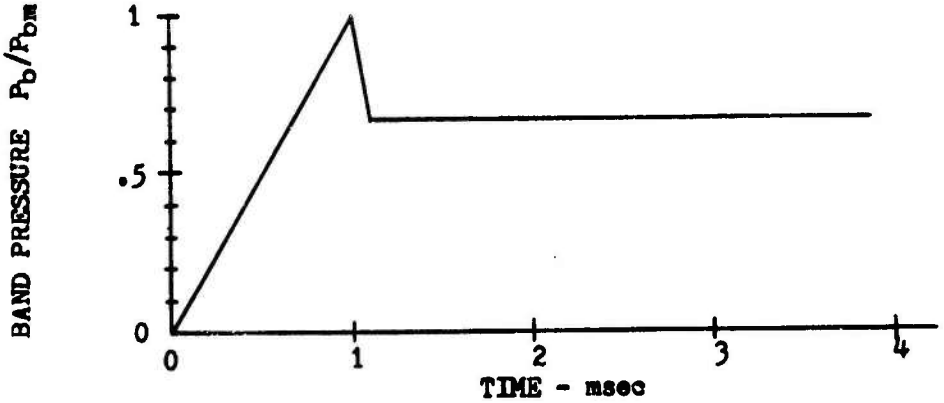

Figure 2c. Band Pressure History

NOSE CONE

The first component to be analyzed is the round nose cone simply because the only loads acting on this part are: 1) longitudinal inertia (setback), 2) centrifugal force and 3) interaction with adjacent components. With projectile acceleration and rotation as known histories the only concern for the analysis of this part is the interaction with the nose plug, projectile and sabot. The nose cone is aluminum with a yield strength of 33,850 psi and an ultimate strength of 46,300 psi at seven (7) percent elongation. The finite element grid used with the false boundary elements is shown in figure 3. The boundary conditions applied to the external nodes of the false elements restricted axial motion only on those elements representing contact with the nose plug and the projectile. The nodes of the elements representing contact with the sabot were restricted in both the axial and radial direction. This technique allows a determination of compressive stresses on the sabot due to the centrifugal loading. Shear stresses are determined as a result of the restriction on axial motion. Constraint of both axial and radial motion on upper and lower boundary elements is overly restrictive on radial expansion of the nose cone due to rotation.

Figure 4 is an iso-stress plot of effective stresses in the nose cone at peak propellant pressure which corresponds with peak longitudinal acceleration. Note that a maximum effective stress of 5000 psi occurs approximately at the contact point between the nose cone and the sabot. This stress level is insignificant and should create no difficulties in the functioning of this part.

PLUG WIND SCREEN

The second part to be analyzed was the plug wind screen which fits over the nose of the projectile. The plug wind screen is fabricated from a copper alloy with a yield strength of 45,000 psi and an ultimate strength of 78,000 psi at thirty-five (35) percent elongation. The finite element grid with false boundary elements and boundary conditions is shown in figure 5. The boundary elements at the trailing edge represent contact with the tungsten alloy projectile. The normal and shear stresses on the upper boundary were determined by the results of the analysis of the false boundary elements on part 1 in that region. Note that only compressive normal boundary stresses are utilized. Tensile stresses would indicate separation between the plug wind screen and the nose cone. The shear stresses are used to compute nodal point forces in the axial direction. The boundary stresses direction shown in figure 4 represent the direction of peak values determined in the analysis of part 1. The appropriate fractions of this value are applied as a loading history corresponding to the longitudinal acceleration and centrifugal force histories.

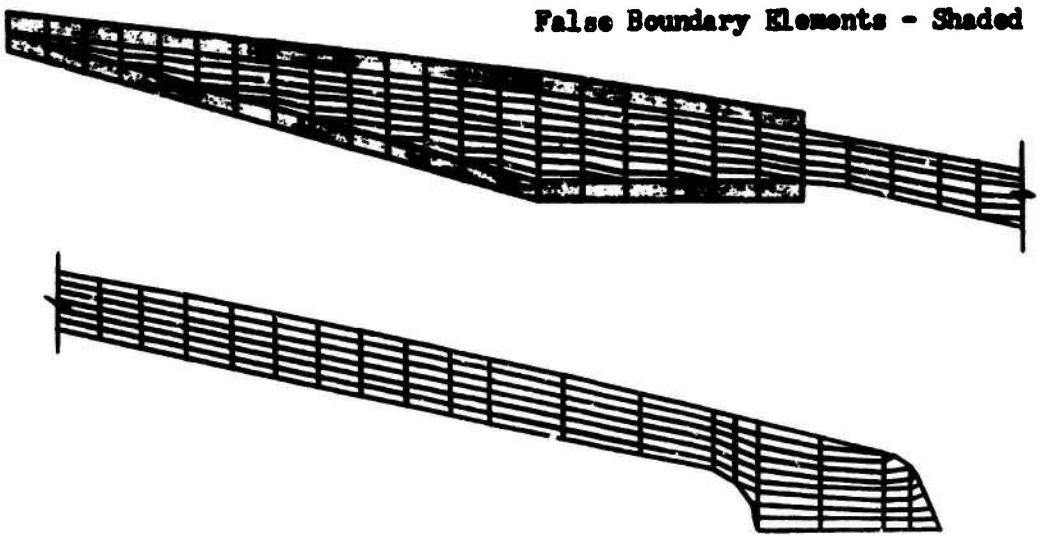

Figure 3. Finite Element Grid for Nose Cone

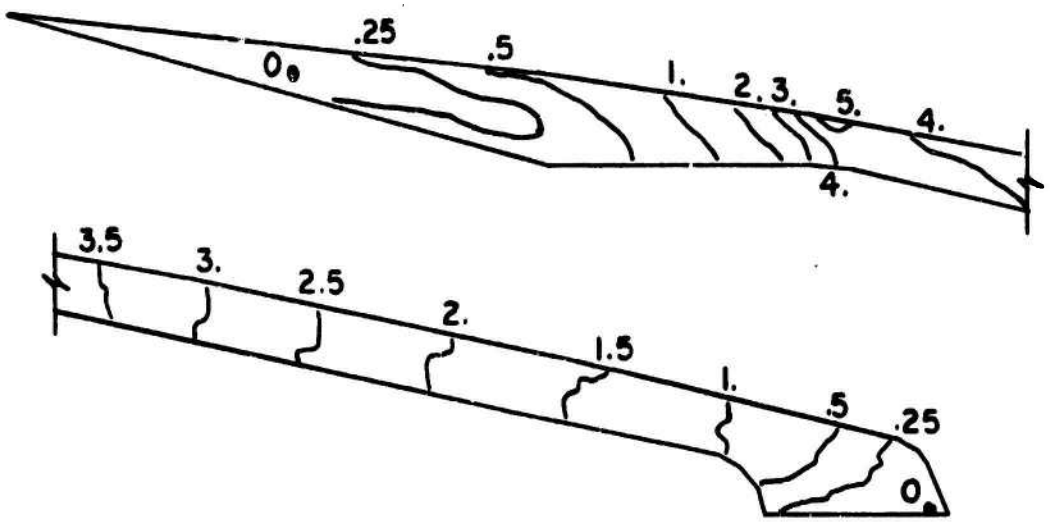

Figure 4. Iso-Stress Plot of Effective Stress at Peak Propellant Pressure for Nose Cone (ksi)

False Boundary Elements - Shaded

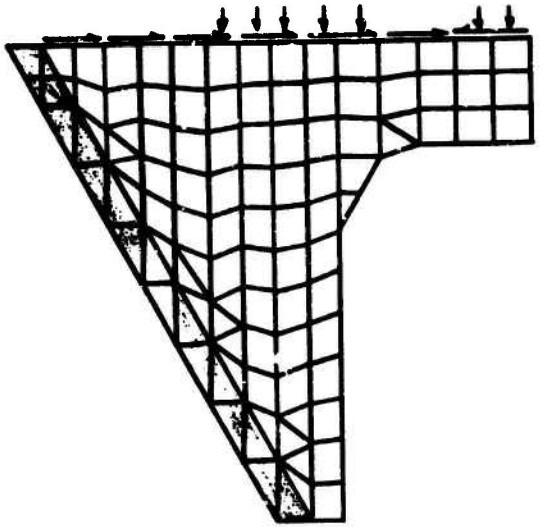

Figure 5. Finite Element Grid for Plug Wind Screen

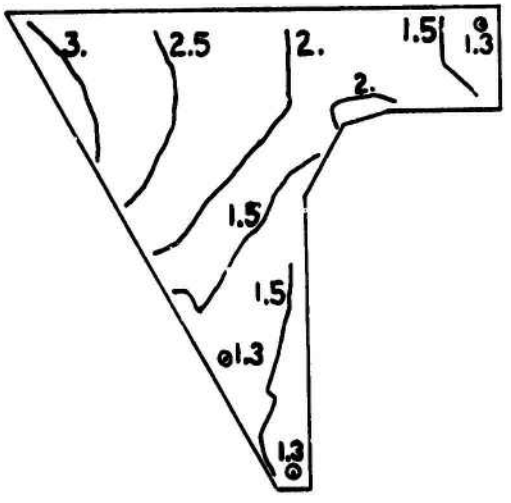

Figure 6. Iso-Stress Plot of Effective Stress at Peak Propellant Pressure for Plug Wind Screen (ksi)

Figure 6 is an isostress plot of peak effective stresses for part 2. As in the case of the nose cone, stresses are very low and should not interfere with the functioning of the part. The effect of longitudinal acceleration and centrifugal force show up as increasing values of effective stresses moving toward the rear and top of the plug wind screen; however, the effective stress never reaches 3500 psi.

SABOT

The finite element grid for the sabot and false boundary layer elements is shown in figure 7. The boundary elements at the rear of the projectile represent interfacing with the aluminum base. At the inner radius near the rear of the projectile the boundary elements also represents the interfacing with the base. The remainder of the boundary elements represent contact with the tungsten projectile. The compressive radial stresses and axial shear stresses applied to the sabot at the forward portion of the inner radius are determined from the false boundary elements on the nose cone (part 1). The remainder of the applied loadings include the longitudinal inertia and the centrifugal force. Interaction between the sabot and the barrel is an unknown which could not be accounted for because of time and funding allotted for this project. The sabot is formed from a plastic with a yield strength of 5,500 psi and an ultimate strength of 10,000 psi at fifteen (15) percent elongation.

The isostress plot of effective stresses is shown in figure 8 for peak pressure. The largest stresses occur in the forward region of the sabot. However, even in this region the stresses are sufficiently small to be considered as neglible. The effective stresses were reviewed for this part at peak centrifugal forces and found to be still less than 2000 psi which should cause no concern as to the functioning of the part.

PROJECTILE

The primary component of the round, the tungsten alloy projectile, is the fourth part to be analyzed. It has a yield strength of 80,000 and an ultimate strength of 100,000 psi at an elongation of three and one-half ($3\frac{1}{2}$) percent. The grid used for the analysis is shown in figure 9. The false boundary elements at the rear of the projectile and at the rear of the outer radius represent the interaction between the projectile and the aluminum base. The radial and shear loadings shown on the center and forward part of the outer radius are the interaction loads calculated from the false boundary layer stresses determined in the analysis of parts 1, 2 and 3.

False Boundary Elements - Shaded

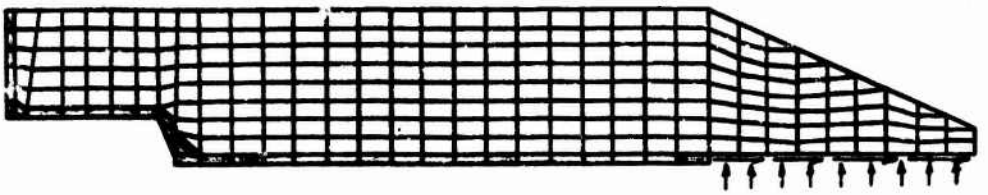

Figure 7. Finite Element Grid for Sabot

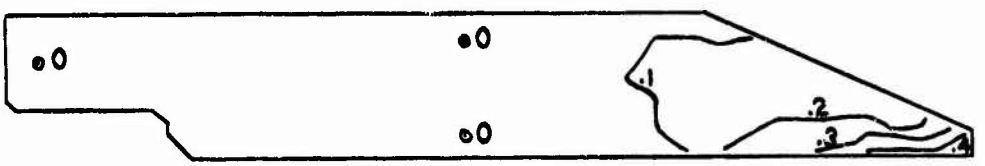

Figure 8. Iso-Stress Plot of Effective Stress at Peak Propellant Pressure for Sabot (ksi)

False Boundary Elements - Shaded

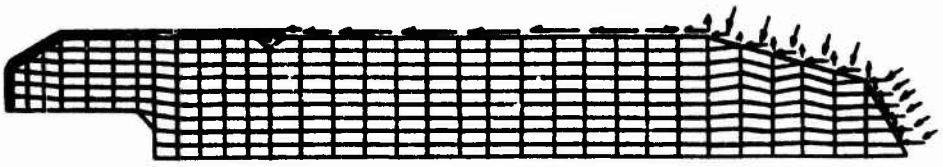

Figure 9. Finite Element Grid for Projectile

Yield Stress = 80,000 psi

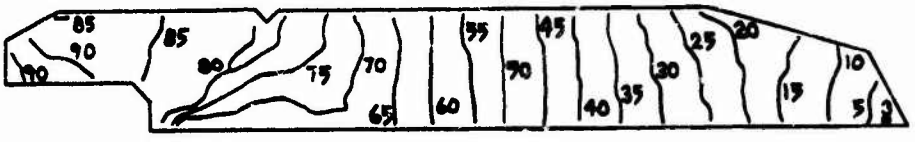

Figure 10. Iso-Stress Plot of Effective Stress at Peak Propellant Pressure for Projectile (ksi)

The plot of the effective stresses at peak pressure is shown in figure 10. The forward half of the projectile shows a stress gradient which is almost constant from the nose to more than halfway back. The effective stresses are about 3000 psi at the nose and increase to over 65,000 psi through the gradient. From that point to the rear along the outer radius the stress increases gradually to 92000 psi. A steep stress gradient is shown near the forward portion of the tracer cup. The elastic-plastic boundary runs from the tracer cup to the groove on the outer boundary. All of the material to the rear of this boundary has yielded but not failed. The projectile will survive launch and perform as expected.

BASE

The last part to be analyzed was the aluminum base. The finite element grid used for this part is shown in figure 11. The arrows indicate directions of applied loading. Along the rear of the base and along the outer radius just forward to the band seat, propellant pressure was applied. Band pressures were used inside the band seat. On the forward portion of the outer radius the loads are a result of interaction with the sabot. The arrow parallel to the boundary indicates an applied shear stress. Along the inner radius in the forward portion of the base, the loading represent contact with the projectile. In addition to these loadings, longitudinal inertia and centrifugal force were applied. The base is manufactured from aluminum with a yield strength of 75,000 psi and an ultimate strength of 84,800 psi @ eight (8) percent elongation.

The isostress plot of effective stresses is shown in figure 12. The stresses at the forward tip are extremely low; however, the stress gradient is very large and the results indicate material failure in the vicinity of the groove in the forward portion of the base. The stresses drop slightly but increase again to failure level under the band seat. The material remains at failure level halfway through the thick portion of the base and along the inner radius or tracer cavity. The stresses drop off somewhat toward the outer radius at the rear of the base.

It is interesting to note that almost the entire component has yielded (75,000 psi). In the main region of failure (84,000 psi) the cause appears to be large tensile hoop stresses; however, under the band seat large compressive radial and axial stresses appear to be the principle causes of failure. It is not clear from the analysis whether the material will actually crack or just deform excessively within the confinement of the rotating band and the lands and grooves of the gun tube. It is possible that excessive material flow could cause the base to adhere to the projectile and not be pulled off by aerodynamic drag.

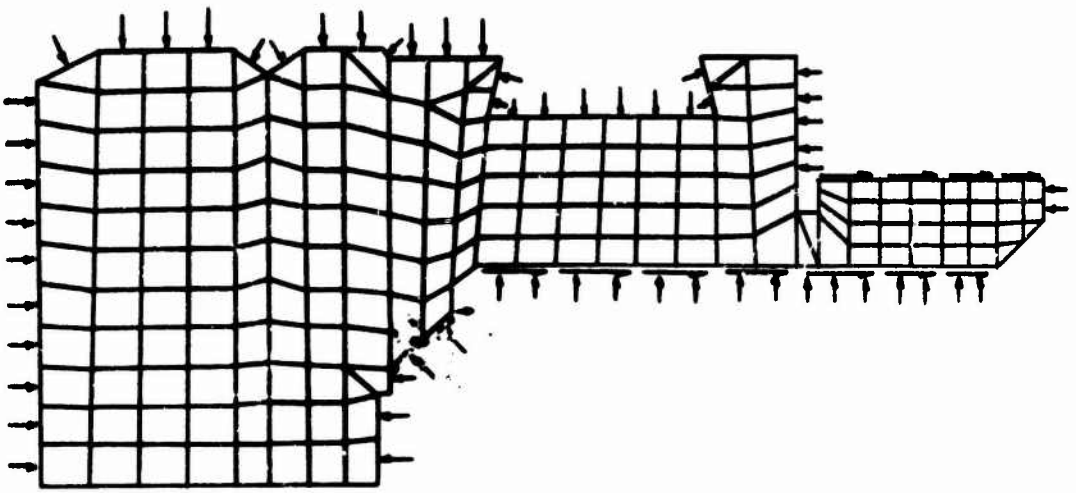

Figure 11. Finite Element Grid for Base

Yield Stress = 75,000 psi

Ultimate Stress = 84,000 psi

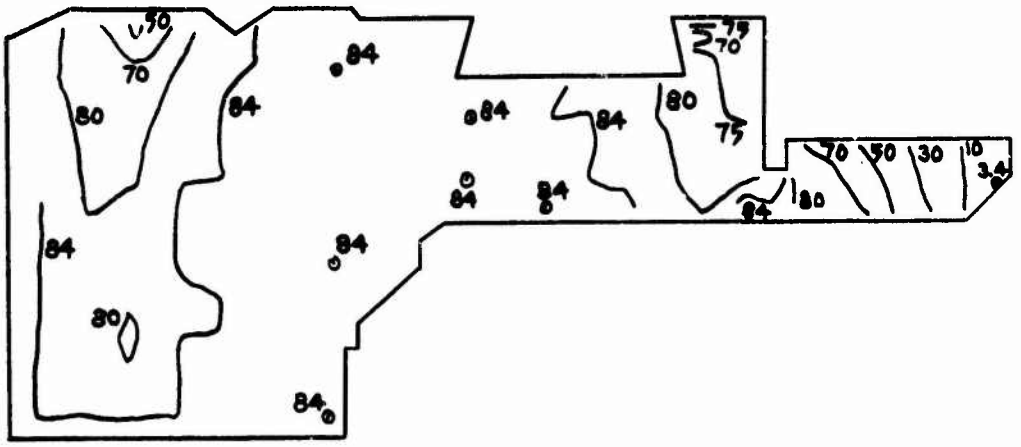

Figure 12. Iso-Stress Plot of Effective Stress at Peak Propellant Pressure for Base (ksi)

DISCUSSION & CONCLUSIONS

The general technique for simulating the boundary conditions at the interface between adjacent components is to applied loadings as determined from the analyses of adjacent parts and to provide a layer of false boundary elements where a part is in contact with other components which have not been analyzed. As each component is studied the stresses determined in the false boundary elements is used to compute boundary loads for the next part.

The nose cone, which was the first part analyzed, interfaces with the sabot, nose plug and projectile. The false boundary elements utilized at these and all other junctures were given a Young's modulus of 10×10^6 psi and a Poisson's ratio of 0.3. The concern is not with the behavior of these boundary elements but rather in the loads transmitted through them. Since the nose cone does not receive external loadings, for the purposes of this analysis, other than contact with adjacent parts, longitudinal acceleration and centrifugal forces, it is the logical place to begin the analysis. In addition to this, by starting at the front of the round and working toward the rear the additive inertia loading is transmitted from one part to the next through the boundary elements.

The nose plug is the logical choice to be second since its loadings consist of interaction with the nose cone and projectile and accelerations. The shear loads applied to this part by the nose cone false boundary elements are calculated by using the shear stresses in the nose cone boundary to determine the ring loads which can be applied at the boundary nodes of the plug. The false boundary elements at the rear of the plug are used to provide loads to the first conical section of the projectile.

The choice of the third part to be analyzed was arbitrary and could have been either the sabot or the projectile. With the results available from the analysis of the nose cone and plug, either part could have sufficient boundary conditions along with boundary elements to perform an analysis. The sabot was chosen as third and the study proceeded in exactly the same manner as for the nose plug and nose cone. The projectile was fourth to be analyzed using the same procedure as used for the sabot.

The aluminum base was the last part to be analyzed and was the only part to indicate a potential problem area. The base was loaded with the inertia of all the forward components as well as its own longitudinal inertia and centrifugal force. In addition, the base experienced all the propellant and band pressure. No false boundary elements were necessary for the base analysis since all adjacent components had already been studied.

The use of the false boundary elements should provide a reasonable approximation to the loads being transmitted to adjacent parts simply because of equilibrium requirements. This, however, assumes that all shear stresses are totally transferred to the component in contact with the part being analyzed. This can only be true if there is no slippage between parts. Any slippage between components would have to be compensated for by an increase in longitudinal components of normal stress due to equilibrium requirements. Therefore one must conclude that the shear stresses found in the false boundary elements are high and should be adjusted before application as a boundary condition on an adjacent component. A first approach to accomplish this would be to scale down the transmitted shear stresses by multiplication with a coefficient of friction between the components. The resulting decrease in axial force would then have to be added to the longitudinal normal stresses.

Another approach to this problem involves the use of friction elements. While this is a capability of the CRTPLS program, it has never been tested. This allows a coefficient of friction to be applied to certain boundary elements for the determination of friction forces. This would also require a test program to determine the coefficients of friction between the various materials used to manufacture this projectile.

RECOMMENDATIONS

The problem which has been discussed was initiated because of a need for analysis of the specific multi-component round. The interfacing study was an inherent requirement to accomplish the task. Since there are many multi-component rounds in use and in design, a procedure should be refined to handle the interfacing. A research study should be initiated which has as its prime purpose the developing of techniques to provide boundary conditions for multi-component rounds.

REFERENCES

1. Zudans, Fishman and Reddi, USERS MANUAL FOR THE CRTPLS COMPUTER PROGRAM, Vol. I "Analyst's Guide", 1970

2. Zudans, Fishman and Reddi, USERS MANUAL FOR THE CRTPLS COMPUTER PROGRAM, Vol. II "Theory and Programmer's Guide", 1970

AUTHOR INDEX

Vaishnav, R.N.	The Catholic University of America	Washington, DC	45
Van Siclen, R.C.	Aircraft Division, Northrup Corporation	Hawthorne, CA	120
Vinson, J.R.	University of Delaware	Newark, DE	7